



HAL
open science

Galaxy Evolution in dense environments observed by the IFS MUSE, a kinematic approach

Valentina Abril-Melgarejo

► **To cite this version:**

Valentina Abril-Melgarejo. Galaxy Evolution in dense environments observed by the IFS MUSE, a kinematic approach. Astrophysics [astro-ph]. Aix Marseille Université (AMU); Laboratoire d'Astrophysique de Marseille, CNRS, CNES, 2020. English. NNT : . tel-03193238

HAL Id: tel-03193238

<https://theses.hal.science/tel-03193238>

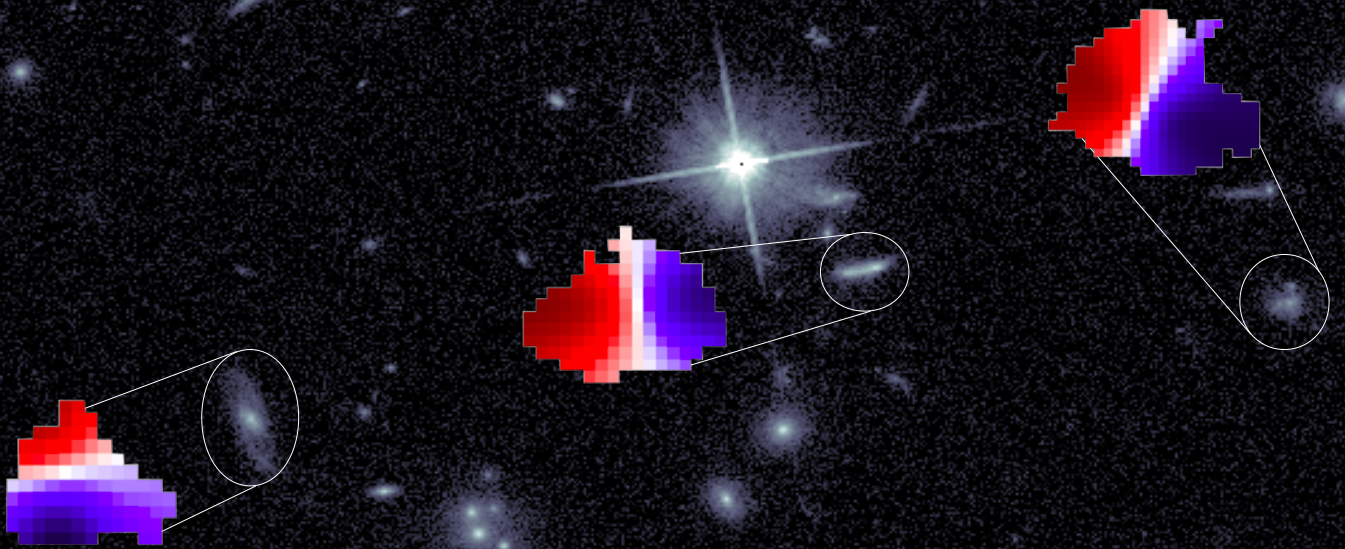
Submitted on 8 Apr 2021

HAL is a multi-disciplinary open access archive for the deposit and dissemination of scientific research documents, whether they are published or not. The documents may come from teaching and research institutions in France or abroad, or from public or private research centers.

L'archive ouverte pluridisciplinaire **HAL**, est destinée au dépôt et à la diffusion de documents scientifiques de niveau recherche, publiés ou non, émanant des établissements d'enseignement et de recherche français ou étrangers, des laboratoires publics ou privés.

Galaxy Evolution in dense environments observed by the IFS MUSE

A Kinematic approach



PhD Thesis, Aix Marseille-Université / LAM

Valentina Abril Melgarejo

2020



AIX-MARSEILLE UNIVERSITÉ
ÉCOLE DOCTORALE DE PHYSIQUE ET SCIENCES DE LA MATIÈRE ED 352
Laboratoire d'Astrophysique de Marseille

**Thèse présentée pour obtenir le grade universitaire de
Docteur en Sciences**

Discipline: Physique et Sciences de la Matière
Specialité: Astrophysique et Cosmologie

Valentina Abril Melgarejo

**Evolution des galaxies dans des environnements denses
observées par l'instrument MUSE, une approche
cinématique**

*Galaxy Evolution in dense environments observed by the IFS MUSE, a
kinematic approach*

Soutenue publiquement le 19/10/2020 au Laboratoire d'Astrophysique de Marseille
Devant le Jury composé de

Prof. Laurence TRESSE	CRAL, Université de Lyon	Rapportrice
Dr. Mathieu PUECH	GEPI, Observatoire de Paris	Rapporteur
Prof. Cláudia MENDES DE OLIVEIRA	IAG, Univ. São Paulo	Examinatrice
Prof. Bernd VOLLMER	OAS, Université de Strasbourg	Examinateur
Prof. Véronique BUAT	LAM, Aix-Marseille Univ.	Examinatrice
Prof. Philippe AMRAM	LAM, Aix-Marseille Univ.	Directeur
Dr. Benoît EPINAT	LAM, Aix-Marseille Univ.	Co-Directeur



Esta Tesis no hubiera sido posible sin el apoyo fundamental del Ministerio de Ciencia Tecnología e Innovación de la República de Colombia

Cette Thèse n'aurait pas été possible sans le soutien fondamental du Ministère de la Science la Technologie et l'Innovation de Colombie

This Thesis would not have been possible without the fundamental support from the Ministry of Science Technology and Innovation of Colombia

© *Valentina Abril-Melgarejo*

Contents

Contents	ii
Acknowledgments/ Remerciements / Agradecimientos	ii
Résumé	vi
Abstract	xvi
Resumen	xviii
List of Tables	xx
List of Figures	xxi
1 Introduction	1
1.1 Morphological Classification of Galaxies	1
1.2 Galaxies throughout Cosmic Time	6
1.3 Galaxy kinematics	10
1.4 The Tully-Fisher Relation	15
1.5 Environment, from cosmic voids to clusters of galaxies	20
1.6 Outline	26
2 Spectroscopic Instrumentation in Astrophysics	28
2.1 Introduction to Spectroscopy	28
2.2 Spectrographs	29
2.2.1 Multi-Object Instruments	30
2.2.2 Introduction to Integral Field Spectroscopy	31
2.2.3 IFS Techniques	34
2.3 Spectrometers	38
2.3.1 Fabry-Perot	39
2.3.2 IFTS - Michelson	41
2.4 MUSE: The Multi Unit Spectroscopic Explorer	44
2.5 Comparison of data from Spectrographs used in this study	49
2.5.1 Redshift, wavelengths range and emission lines used as kinematics tracers	49
2.5.2 VIMOS (VLT) and DEIMOS (Keck) MOS Spectrographs	55
2.5.3 IFS SINFONI and KMOS (VLT)	57
2.5.4 Technical Comparison	60
2.6 Future IFS Instruments	63

3	Definition of the sample	67
3.1	The Cosmic Evolution Survey (COSMOS)	67
3.2	Existing IFS surveys to study galaxy evolution	71
3.3	The MUSE gAlaxy Groups In COSMOS, the MAGIC Survey	74
3.4	Group sub-samples in the MAGIC Survey	77
4	Morphological and kinematic Modeling	82
4.1	HST-COSMOS PSF modeling	83
4.2	Two-component surface brightness Morphological modeling	87
4.2.1	GALFIT Modeling of galaxies and some Results	91
4.2.2	Determination of Global Properties: R_e and B/D, B/T ratios	98
4.3	Inclination distribution of a randomly selected sample	100
4.4	MUSE LSF and PSF determination	103
4.5	Kinematics Extraction	108
4.6	Kinematics modeling	113
4.6.1	Recovering velocity and σ maps from Light distribution	116
4.7	Summary of the Morpho-Kinematics Analysis	118
5	The TFR and the determination of Dark Matter content	120
5.1	Metodology	120
5.2	Selection Criteria to define the Kinematic sample	122
5.3	Definitive Selection Criteria using the [OII] Flux from MUSE narrow band images	126
5.4	Ionization mechanisms: AGN identification	128
5.5	Paper I: TFR in dense environments in the MAGIC survey	131
6	Summary and Conclusions	183
7	Perspectives	188
A	Appendix A	190
A.1	Paper II: Ram pressure stripping in CGr32. Boselli et al. 2019	191
B	Appendix B	202
	Bibliography	203

Acknowledgments / Remerciements / Agradecimientos

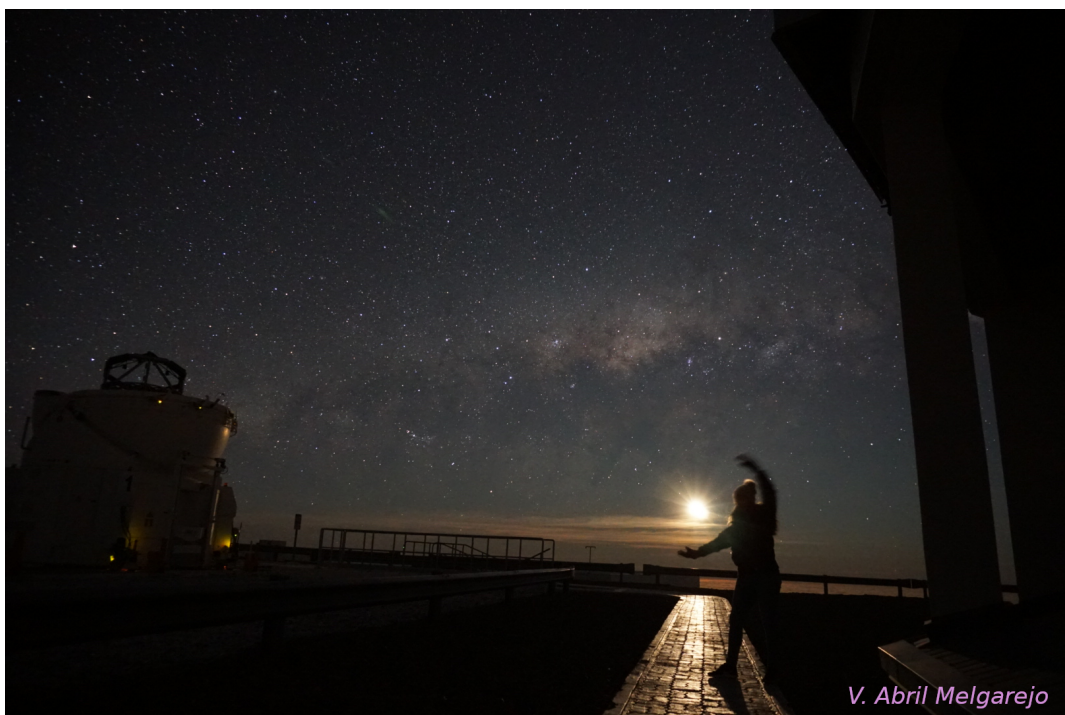


Figure 1: The Milky Way and the Moon at Paranal VLT. October 2018.

Our place in Universe is a question that has puzzled humankind for ages. Thanks to the enormous curiosity and hard work of valuable women and men in our history, we have observed deeper in the immensity of the Universe trying to solve the huge amount of questions that implies to understand Nature. I feel very honored and fortunate of all that heritage of knowledge and to be able to appreciate the beauty of a dark sky wondering for all the mechanisms happening there. It was at the age of 4 when I observed a total lunar eclipse for the first time and since then I have been connected to the sky. Later in the farmlands of my beautiful country, Colombia, when I was 13 I witnessed the entrance of a meteorite and its disintegration in a breathtaking spectacle I will never forget. That was a clear signal for me that I wanted to address my professional life to the study of the Universe. The path has been difficult and full of challenges, failures and obstacles but also of great achievements and satisfactions. I remark the fact that still there are few female astrophysicist, specially from developing countries, so this is an additional reason for me to keep working for gender equality in this field.

No he recorrido este camino complejo sola, he tenido a mi lado a mi familia. Mi padres y mi hermana quienes son mi motor, de quien soy reflejo y a quienes debo todo lo que soy. Su apoyo incondicional ha sido fundamental en la construcción de un sueño que parecía muy lejano y atípico, convertirme en Astrofísica. A mi madre reconozco su gran dedicación a nuestra familia, es una mujer admirable, fuerte, tierna y muy inteligente. A mi padre agradezco todos sus cuidados, su gran sentido del humor y todas sus enseñanzas en el campo de la arquitectura que me maravillan siempre. Mi hermana ha sido mi compañera de vida, a ella toda mi admiración como Médico especialista y más en estos momentos de pandemia en los que ella está luchando por salvar la vida de sus pacientes y es una guerrera valiosa en esta complicada situación que enfrenta la humanidad. Este logro es de ustedes, su apoyo me ha permitido continuar en la lucha y no desfallecer en los momentos más difíciles. Deseo también rendir un homenaje muy especial a mi abuelito, la persona más sabia que he tenido la fortuna de conocer, un hombre honesto, honrado y humilde que sacó adelante a una numerosa familia con grandes dificultades. Desde hace más de un año su vida se apagó, pero ahora ha vuelto a ser parte de la Naturaleza en forma de polvo de estrellas. Sé que él está muy orgulloso de mí y a él debo mi curiosidad científica y el pensamiento crítico que me inculcó desde pequeña. Allá en la eternidad e inmensidad del Universo nos volveremos a encontrar un día.



Figure 2: Magellanic clouds at Paranal VLT. October 2018.

Lorsque j'ai décidé de quitter mon pays pour entamer une nouvelle aventure académique et personnelle en Europe, je n'imaginai pas les beaux endroits que je visiterais et les gens formidables que je rencontrerais. La vie peut réserver de belles surprises en liant les histoires des personnes. Je me sens très chanceuse d'avoir croisé Romain, malgré la longue distance entre les Andes colombiennes et les Pyrénées. C'est une personne merveilleuse et très intelligente, qui a donné de la joie et de la couleur à mes journées. Nous nous soutenons et admirons mutuellement et je suis très fière que nous ayons tous les deux conclu nos Doctorats ensemble, après

beaucoup d'efforts, ¡lo logramos chico!. J'ai beaucoup appris à ses côtés, nous avons toujours des discussions très agréables et intéressantes sur la vie, le monde, l'humanité et la science. Je suis également très reconnaissante envers sa famille, que je considère maintenant comme faisant partie de la mienne. Jeannine, Jessica et Jean-Paul je vous remercie beaucoup pour votre soutien, votre hospitalité et les bons moments que nous partageons ensemble, vous avez été une partie très importante de tout ce processus en m'encourageant à donner le meilleur de moi-même.

I'm enormously grateful with my supervisors for the great opportunity they gave me to pursue this amazing and interesting PhD research project, to investigate the complex cosmic laboratories in which I've always been interested, the galaxies. Thanks to Professors Benoît Epinat and Philippe Amram for believing in me, for taking this challenge to work in team to devote their time and efforts to guide me towards the goal. I deeply admire them, I learned a lot from them and besides being great scientist they are also great human beings. They provided me with the best advice to start my life in France, that implied to face tones of administrative procedures that I successfully overtook thanks to them. They always were very kind so I felt welcome and supported since the first day. They offered me a very encouraging and nice environment to make high quality research, implying international collaborations and nice observational missions. Thanks a lot for allowing me to work at the Very Large Telescope, that was a dream came true, one of the best experiences of my professional life, as proof of this, the pictures [1](#) and [2](#) show part of the amazing sky at Paranal including the Milky way and the Magellanic Clouds. Benoît, I thank you for your guidance and advice, your amazing ideas and for working hard at my side day after day. Philippe, thank you for sharing your expertise and for your advice, the meetings and the support in every aspect, academic or administrative. Benoît and Philippe, you are the captains of this boat that successfully fulfilled its trip arriving safe and sound to firm land, even with the pandemic that imposed an additional challenge to our project. All my deepest admiration and respect for you both for ever.

Je tiens également à rendre un hommage particulier à Françoise Maxant, un être humain extraordinaire, toujours disposée à assurer le bien-être de tous les doctorants du Laboratoire. Quel que soit le problème ou le conflit, Françoise fait le maximum pour le résoudre. Son amitié est précieuse pour moi, elle est comme un rayon de lumière dans l'obscurité, une étoile très brillante. Finally, I thank to the institution that hosted me during three years, my academic home, the Laboratoire d'Astrophysique de Marseille with its unique and kind environment. I had the opportunity to meet there amazing people, thanks to Jesus, Alfonso, Simona, Davide, Jorge, Frédérique, Elena, the PhD students, postdocs, researchers and administrative personnel who made my time at LAM so nice.

Thanks to all of you!
¡A todos ustedes gracias!
Merci à vous tous !

Valentina

Résumé

L'étude de l'Univers est fondamentale pour comprendre sa formation et son évolution, depuis une distribution homogène primitive observée dans le Fond Diffus Cosmologique (FDC, $z \sim 1100$) jusqu'à la configuration du réseau cosmique que nous observons aujourd'hui. Les galaxies sont les éléments constitutifs des structures à grande échelle de l'Univers, réparties le long de filaments, de parois, de groupes, d'amas et de vides; tous façonnés par la répartition des halos de matière noire qui constituent la majeure partie du budget de la masse de l'Univers.

Les galaxies ont subi d'importantes transformations morphologiques et cinématiques depuis le maximum de la densité du Taux de formation des étoiles (TFE) cosmique ($z \sim 2$) jusqu'à aujourd'hui: depuis les disques granuleux et les galaxies perturbées avec une cinématique complexe (différents composants) jusqu'aux spirales régulières bien définies et aux galaxies elliptiques passives. Il a été observé qu'il existe une forte corrélation entre l'environnement dans lequel une galaxie se forme et évolue et ses différentes propriétés physiques, comme sa capacité à former de nouvelles étoiles, sa taille, sa cinématique et son contenu baryonique. Par conséquent, l'époque comprise entre $z \sim 1,5$ et $z \sim 0,3$ est une période de transition fondamentale au cours de laquelle les galaxies ont activement évolué.

L'évolution des galaxies est fortement influencée par l'environnement et aussi par la contenu en masse stellaire. Il y a deux principaux processus d'extinction de la formation stellaire (quenching) en jeu, l'un dépendant de la densité de l'environnement et l'autre de la teneur en masse. Les galaxies massives ont la plus grande fraction de galaxies inactives de tous les environnements, ce qui indique que pour ces galaxies, le blocage de la formation stellaire est principalement due à des processus internes.

Des groupes de galaxies se sont formés, ont rassemblé leur masse et se sont virialisés, après que le maximum de densité de TFE cosmique, en affectant fortement l'activité de formation d'étoiles et la morphologie des galaxies qui y résident. Ceci est dû au fait que dans les environnements denses, il y a une probabilité plus grande qu'une galaxie interagisse avec d'autres galaxies et avec son environnement par le biais de différents mécanismes, ce qui implique que les galaxies situées dans des environnements denses éteignent leur activité de formation d'étoiles avant les galaxies de champ pour les régimes de galaxies de masse faible à intermédiaire ($10^9 M_\odot < M_\star < 10^{11} M_\odot$, [Peng et al. 2010b](#)).

La cinématique des galaxies est un outil fondamental pour la compréhension des processus et des mécanismes qui régissent la formation et l'évolution des galaxies, car pour les systèmes dominés par la rotation, elle permet de tracer la distribution du contenu de la masse totale, y compris les composantes baryonique et de matière noire. Ensuite, la comparaison des car-

actéristiques cinématiques et physiques pour des échantillons de galaxies à différents décalages spectraux vers le rouge représente une stratégie robuste pour suivre l'évolution des galaxies. À partir de la cinématique, il est également possible de séparer les composantes dynamiques (baryonique et noire), en modélisant la courbe de rotation, si l'on a accès au contenu baryonique total (y compris la fraction gazeuse). Les cartes de vitesse donnent des informations sur les interactions dans l'histoire de l'évolution des galaxies par l'identification de cinématiques complexes provenant de perturbations internes ou d'interactions externes. La cinématique est également liée à d'autres propriétés physiques comme la morphologie, les systèmes dont le support gravitationnel est dominé par la rotation étant principalement des galaxies à disque, et ceux dominés par la dispersion correspondant principalement à des galaxies précoces (e.g. galaxies elliptiques). Ce n'est pas le cas à grand redshift ($z > 1$), car les galaxies particulières et irrégulières représentent une fraction élevée des galaxies dominées par la rotation aux premières époques (Delgado-Serrano et al., 2010).

L'observation des galaxies lointaines représente un défi en termes de pouvoir de résolution, en particulier pour les galaxies de faible masse. Pour étudier la cinématique interne et la distribution de masse, il est crucial d'avoir accès à des données spatialement résolues. Jusqu'à présent, la spectroscopie à longue fente (long-slit) était la technique la plus utilisée pour extraire la cinématique, mais elle présente plusieurs inconvénients, car la fente doit être placée le long du grand axe du disque afin de suivre la rotation de la galaxie, et l'angle de position photométrique (PA, Position Angle en Anglais) n'est pas toujours le même que le PA cinématique, ce qui peut fortement affecter les estimations cinématiques.

Dans ce contexte, la dernière génération d'instruments de spectroscopie à champ intégral (IFS) comme MUSE et KMOS, offre une solution intégrale fournissant simultanément des images dans le plan du ciel (α, δ) et des informations spectrales dans la dimension de la longueur d'onde (λ). Dans le cas de MUSE (instrument monté sur un télescope de 8 m de l'Observatoire Very Large Telescope VLT), l'échantillonnage spatial correspond à $0,2''/\text{pix}$ dans son mode grand champ (WFM), tandis que la couverture spectrale s'étend dans l'intervalle optique et le infrarouge (IR) proche [4800 Å – 9300 Å], avec une résolution spectrale allant de 1700 dans le bleu à 3600 dans le IR proche. L'extension du champ de vue de MUSE de 1 armin^2 sur le plan du ciel, correspond à 500 kpc dans le repère associé aux galaxies au redshift moyen des structures étudiées ($z \sim 0,7$), ce qui est adapté à la taille des groupes et des amas ciblés. Ces caractéristiques font que les instruments utilisant spectrographie à champ intégral montés sur des télescopes de classe 10m sont adaptés pour effectuer des études de propriétés physiques spatialement résolues dans les galaxies à redshift intermédiaire. Les observations IFS sont complétées par des images à haute résolution du Télescope Spatial Hubble (HST) dans une bande IR pour étudier la distribution de la lumière du continuum stellaire, obtenant ainsi la morphologie globale des galaxies dans l'échantillon.

Des observations du Télescope Spatial Hubble et des données spectroscopiques à champ intégral pour un total de ~ 330 galaxies dans des structures denses ont été obtenues dans l'intervalle de redshift $0.3 < z < 0.8$, à partir du sondage MAGIC MUSE-GTO, dont les observations sont effectuées à l'intérieur du champ HST COSMOS (Scoville et al., 2007a). Le gaz ionisé est utilisé pour extraire la dynamique des galaxies dans l'échantillon, et compte tenu des limites de détection des raies nébulaires pour MUSE, le doublet [OII] $\lambda\lambda 3727, 3729$ Å est utilisé comme

traceur cinématique puisqu'il s'agit de la raie d'émission la plus brillante disponible dans tout l'intervalle de redshift.

La relation Tully-Fisher (RTF) est une relation d'échelle très connue et utilisée pour étudier les propriétés dynamiques des galaxies en forme de disque qui lie la luminosité ou la masse stellaire/baryonique à la vitesse de rotation maximale d'un système, ce qui est un indicateur de la distribution de la matière noire. Cette relation fournit des informations clés sur le support dynamique, la distribution de la masse et sur la formation et l'évolution des galaxies.

Comme le but de mon projet de thèse est de déterminer l'influence de l'environnement et les mécanismes qui permettent d'éteindre plus tôt l'activité de formation des étoiles dans les environnements denses, j'ai effectué une étude morpho-cinématique approfondie et une analyse plus poussée de la RTF de la masse stellaire (smRTF) et de la RTF baryonique (bmRTF) des galaxies dans les groupes denses à $z \sim 0,7$. Les résultats ont ensuite été comparés à la smRTF dérivée à partir d'autres échantillons de la littérature dans différents environnements: deux dans des environnements de faible densité (KMOS^{3D}, Übler et al. 2017 ; et KROSS, Tiley et al. 2019) et l'autre provenant de galaxies en amas (ORELSE, Pelliccia et al. 2019).

Objectifs scientifiques

- ▷ Quels sont les moteurs de l'évolution des galaxies et de leur transformation morphologique au cours du temps cosmique?
- ▷ L'environnement a-t-il un rôle fondamental dans le taux de formation stellaire (SFR) cosmique?
- ▷ Quand les mécanismes d'extinction de formation stellaire deviennent-ils efficaces ?, comment agissent-ils sur la distribution de la masse baryonique et sa fraction dans les halos de matière noire ?

Ce sont des questions qui font encore l'objet de débats en astrophysique et ce projet vise à donner des indications solides pour les comprendre, ceci en menant une étude morpho-cinématique et en analysant l'évolution de la RTF dans différents environnements, ce qui est décrit en détail ci-dessous. Il s'agit de la première étude utilisant conjointement des observations IFS et de l'imagerie à haute résolution, permettant d'augmenter les statistiques sur la caractérisation des galaxies dans les structures denses à redshift intermédiaire.

Méthodologie et Résultats

J'ai principalement appliqué l'analyse sur le sous-échantillon à z intermédiaire composé de 250 galaxies à $0,5 < z < 0,8$ provenant de 8 groupes denses (Section 3.4), puisque cet échantillon trace la période de l'évolution cosmique après le maximum cosmique de formation stellaire (FS), avec les observations MUSE les plus profondes contenant les structures les plus grandes/denses. Les résultats sont principalement issus de l'analyse morpho-cinématique effectuée sur ces 250 galaxies et de la détermination des caractéristiques dynamiques et structurelles de 77 galaxies

avec formation stellaire dominées par la rotation. Ci-dessous, je résume les méthodes et les principaux résultats de ce projet de recherche dont l'analyse est détaillée dans l'article [Abril-Melgarejo et al. 2021](#) (Section 5.5).

- J'ai calculé les valeurs PSF (Point Spread Function) pour les données photométriques de HST-ACS F814W et des images MUSE à bande étroite [OII] en WFM (Wide field mode), en utilisant l'algorithme d'analyse GALFIT. Pour les images HST, j'ai utilisé 27 étoiles sélectionnées dans l'ensemble des champs pour déterminer les paramètres de la PSF. Celle-ci est modélisée avec un profil de Moffat avec $\text{FWHM}=2,84$ pixels (85 mas) et $\beta = 1,91$, ce qui est équivalent à une échelle physique de $\sim 410\text{--}620$ pc (dans le repère de la galaxie), dans la gamme de redshift $z=[0,34\text{--}0,75]$. Dans le cas de MUSE, la PSF a été calculée pour chaque champ et chaque groupe en extrayant des images à bande étroite des étoiles du champ à la longueur d'onde [OII] décalée vers le rouge à la moyenne z du groupe. Dans ce cas, j'ai utilisé des profils gaussiens pour prendre en compte les effets de la turbulence atmosphérique sur la résolution des observations (seeing), avec une moyenne $\text{FWHM}=0,652''$ correspondant à une distance physique équivalente de 4,7 kpc à $z\sim 0,7$. La FWHM varie dans l'échantillon de $\sim 0,578''$ à $0,741''$.
- L'étude a été réalisée sur des groupes denses et massifs avec une densité projetée au moins 25 fois plus grande que les densités moyennes des galaxies à l'intervalle de décalage spectral vers le rouge de l'échantillon, calculées en utilisant la méthode établie par [Beers et al. \(1990\)](#) et [Cucciati et al. \(2010\)](#). Les masses du Viriel se situent entre 3.1 et $81.4 \times 10^{13} M_{\odot}$ avec une masse médiane de $8.5 \times 10^{13} M_{\odot}$.
- Avec les résultats de l'ajustement de la distribution spectrale d'énergie (DSE) appliqué aux données de photométrie disponibles dans COSMOS pour les champs du sondage MAGIC, j'ai utilisé la relation entre masse stellaire et TFE pour séparer de manière cohérente la population des galaxies passives et de celles avec formation stellaire, situées respectivement dans la séquence rouge et la séquence principale (SP) du diagramme. L'échantillon de galaxies avec FS active est composé de 178 galaxies qui couvrent une large gamme de masses entre $10^{7,5} M_{\odot}$ à $10^{11,5} M_{\odot}$ et de TFE de $10^{-2} M_{\odot} \text{ an}^{-1}$ à $10^2 M_{\odot} \text{ an}^{-1}$. Toutes les galaxies de l'échantillon cinématique (galaxies dominées par la rotation) font partie de la séquence principale (représentant 43% des galaxies avec FS), dont la masse médiane est de $7,2 \times 10^9 M_{\odot}$ et le TFE médian vaut $1,74 M_{\odot} \text{ yr}^{-1}$.
- En utilisant les images haute résolution HST-ACS F814W disponibles pour les champs MAGIC, j'ai effectué une décomposition morphologique des galaxies avec un bulbe et un disque pour modéliser la brillance de surface (BS) de 330 galaxies, incluant l'échantillon à faible décalage spectral vers le rouge. L'objectif de la modélisation morphologique est d'obtenir, grâce à cette décomposition morphologique, des estimations précises des tailles des galaxies, des rapports de lumière des deux composantes bulbe et disque, et des paramètres de projection (PA, i). J'ai utilisé des profils de Sérsic pour la composante bulbe sphéroïdale et des profils exponentiels pour décrire la distribution de la lumière du disque. J'ai calculé la taille globale (rayon effectif global R_{eff}), la luminosité globale et les rapports de luminosité à partir de la décomposition bulbe-disque. Il existe une grande diversité de morphologies dans l'échantillon présenté au chapitre 4 montrant des disques granuleux, des disques perturbés, des anneaux, des bras ouverts et des barres. Dans les

cas de morphologie complexe, j'ai inclus la modélisation de certaines structures internes et pour les champs avec des galaxies voisines proches; j'ai modélisé simultanément ces galaxies afin de minimiser leur influence sur les résultats.

- J'ai estimé les rapports bulbe-disque afin d'établir la contribution de chaque composante au profil de lumière. Les rapports lumineux bulbe sur disque (B/D), bulbe sur total (B/T) et disque sur total (D/T) sont importants pour déterminer la composante dominante et pour vérifier les relations avec le TFE et le support dynamique. Il y a 34 galaxies dominées par le bulbe (B/D>1) dans la séquence rouge représentant 53% de cette population. Pour les galaxies de la séquence principale, 44 galaxies ont B/D>1, ce qui représente 25% des galaxies avec formation des étoiles. En comparant ces résultats morphologiques pour les galaxies dans des groupes et pour des galaxies dans des environnements moins denses (de l'échantillon MAGIC) avec les catalogues morphologiques COSMOS (réalisés par W. Mercier), un accord a été trouvé entre la décomposition morphologique avec le type morphologique: les galaxies spirales et irrégulières étant principalement composées de galaxies dominées par des disques et les galaxies elliptiques ayant principalement des profils dominés par des bulbes. J'ai ensuite utilisé ce résultat pour écarter les galaxies dominées par des bulbes de l'échantillon cinématique final.
- J'ai obtenu la distribution des inclinaisons des échantillons parent et cinématique à partir de la modélisation morphologique, montrant qu'ils suivent approximativement (à l'intérieur des erreurs) la fonction de probabilité théorique des orientations aléatoires des disques. L'inclinaison médiane de l'échantillon parent est $i_{MEDIAN} = 65.2^\circ$ et pour l'échantillon cinématique $i_{MEDIAN} = 63.9^\circ$, valeurs qui sont proches de l'inclinaison médiane $i_{MEDIAN} = 60^\circ$ de la distribution théorique. J'ai ensuite démontré la nature aléatoire de l'échantillon sans biais dû à la présélection.
- J'ai étudié la différence entre les estimations morphologiques et cinématiques du PA et j'ai trouvé pour 174 galaxies que la différence absolue $|\text{PA}_m - \text{PA}_k| > 40^\circ$ pour 30% de l'échantillon SF. Ce résultat montre les avantages des données IFS permettant d'extraire des cinématiques spatialement résolues par rapport aux observations spectroscopiques à longue fente, en raison de la difficulté pour estimer avec précision le PA cinématique de l'échantillon 1D.

J'ai effectivement extrait et modélisé la cinématique de 178 galaxies SF dans l'échantillon en utilisant le formalisme des moments dynamiques (Epinat et al., 2012) appliqué sur la carte de flux [OII] pour obtenir les cartes de vitesse et de dispersion de vitesse respectivement. J'ai ensuite extrait la vitesse de rotation à 2.2 fois la longueur de l'échelle du disque ($R_{2.2}$) en utilisant un modèle de rampe pour ajuster la courbe de rotation, en tenant compte de l'effet de la résolution spatiale (PSF et Line Spread Function-LSF). La vitesse de rotation et la dispersion de vitesse intrinsèque ont été obtenues pour l'échantillon cinématique à $z \sim 0.7$, soit 92% de systèmes dominés par la rotation ($V/\sigma > 1$) et 8% de systèmes dominés par la dispersion (6 galaxies). Je liste ci-dessous les résultats concernant l'analyse cinématique.

- J'ai mis en place une nouvelle stratégie de sélection pour la construction de l'échantillon cinématique, basée sur la taille globale (R_{eff} de la morphologie) par rapport à la résolution spatiale de MUSE (FWHM_{MUSE}), ainsi que sur le rapport signal sur bruit (S/B) du flux du doublet [OII] utilisé pour produire des cartes cinématiques fiables. La sélection est

ensuite basée sur les limites $S/B \geq 40$ et $R_{eff}/FWHM_{MUSE} \geq 0,5$, limites qui garantissent de contraindre l'échantillon à des galaxies suffisamment résolues et avec une émission suffisante du gaz ionisé, afin de récupérer des mesures cinématiques robustes. Cette sélection est en bon accord avec une inspection visuelle des cartes de vitesse pour évaluer l'étendue du gaz ionisé et la cohérence du gradient de vitesse. Après application de cette méthode, 77 galaxies se trouvent au-dessus des limites de sélection, ce qui correspond à 43% de l'échantillon de galaxies avec formation stellaire active. Le fait que seules 6 galaxies de l'échantillon cinématique soient dominées par la dispersion montre l'efficacité de la méthode de sélection, qui sélectionne directement les systèmes dominés par la rotation sans aucune hypothèse a posteriori comme c'est généralement le cas lorsque le rapport vitesse sur dispersion (V/σ) est utilisé.

- Afin d'avoir des estimations appropriées de la masse stellaire, la masse de l'ajustement SED a été corrigée puisqu'une ouverture photométrique fixe de 3" a été utilisée pour calculer la masse, ce qui pourrait ne pas être approprié pour tracer le contenu stellaire à partir du profil lumineux pour les galaxies petites ou trop étendues, donnant des valeurs avec des incertitudes variables. Nous avons plutôt mesuré la masse à l'intérieur du $R_{2,2}$ correspondant à chaque galaxie, qui est en moyenne 1,4 fois plus faible qu'à l'intérieur de l'ouverture de 3" de diamètre.
- J'ai appliqué deux diagnostics (Lamareille 2010, Juneau et al. 2011), efficaces à un redshift intermédiaire pour déterminer les mécanismes d'ionisation dans le but d'identifier les galaxies à noyaux actifs (AGN) dans l'échantillon cinématique. Le diagnostic a été complété par une inspection visuelle des spectres pour rechercher des raies élargies ou la présence de niveaux d'ionisation élevés comme la raie [NeIII]. Sept galaxies dans tout l'échantillon ont été confirmées comme possédant des AGN et deux cas ambigus étaient probablement dus à une faible activité des AGN. Deux AGNs ont été écartés de l'échantillon cinématique car ils sont dominés par la composante centrale, dans ces cas l'activité AGN (ionisation par chocs) domine l'émission du gaz ionisé par rapport à l'activité de formation d'étoiles dans le disque. Un autre AGN a été conservé dans l'échantillon cinématique car il présente un disque étendu pour lequel on peut différencier l'émission ionisante provenant des régions HII, d'où la possibilité de déterminer la vitesse de rotation.
- J'ai utilisé la limite $B/D > 1$ pour identifier les éventuelles galaxies de type précoce (ETG) dans l'échantillon, comme cela a été discuté précédemment. J'ai ensuite retiré 8 ETG de l'échantillon cinématique final. D'autre part, en tenant compte de la limitation de la résolution spatiale qui affecte principalement les petites galaxies, une limite supplémentaire a été fixée sur la masse stellaire pour les galaxies avec $M_* \geq 10^9 M_\odot$, laissant l'analyse fortement contrainte à 54 galaxies avec formation stellaire dominées par la rotation. Cette limite permet également d'effectuer une comparaison plus appropriée avec d'autres études dans la littérature qui sont limitées aux galaxies massives.
- La fraction de masse de gaz pour l'échantillon cinématique a été calculée en utilisant la forme inverse de la loi de Kennicutt-Schmidt (KS) (Kennicutt, 1998), en utilisant le TFE de l'ajustement des SED corrigé par l'extinction des poussières. La masse de gaz médiane de l'échantillon correspond à $\log(\overline{M}_g) \sim 9.45 M_\odot$, tandis que la valeur médiane de la masse stellaire est $\log(\overline{M}_*) \sim 9.71 M_\odot$. Les résultats confirment que les fractions de gaz dans les

galaxies à redshift intermédiaire sont en moyenne plus importantes que celles à faible redshift. De même, certaines galaxies de la séquence principale (dont le TFE a été calculé à partir de l’ajustement SED par photométrie multibande) ne présentent pas ou ont très peu d’émission de gaz ionisé, ce qui suggère que ces galaxies pourraient passer par un processus d’extinction (quenching) de leur formation stellaire. D’autres galaxies sont trop petites pour que leur flux d’émission [OII] puisse être déterminé de manière fiable. En revanche, parmi les ETG massifs, j’ai trouvé quatre cas de formation d’étoiles actives en leur centre, ce qui montre qu’elles ont une activité de SF localisée. L’émission d’AGN a été écartée pour ces galaxies.

- Les deux, les RTF stellaire et baryonique ont été dérivées en étudiant l’impact de la méthodologie de sélection. Pour obtenir la RTF dans chaque cas, un ajustement linéaire a été effectué et les paramètres de pente et de point zéro obtenus ont été comparés à d’autres études sur la RTF à des décalages spectraux vers le rouge similaires des grandes relevés IFS comme KROSS (Tiley et al., 2019) et KMOS^{3D} (Übler et al., 2017), et avec une longue fente en utilisant ORELSE (Pelliccia et al., 2019). Deux estimateurs dynamiques différents ont été utilisés, $V_{2.2}$ la vitesse de rotation à $R_{2.2}$ et V_{circ} la vitesse circulaire de relevés Übler et al. 2017 incluant un terme pour tenir compte de la dispersion des vitesses.
- Lorsque V_{circ} est utilisé, la dispersion intrinsèque de la RTF diminue considérablement, en particulier pour les petites galaxies, ceci dû au fait que V_{circ} inclut la vitesse de dispersion dans le budget dynamique et que les petites galaxies sont principalement dominées par la dispersion de vitesses et présentent de faibles vitesses de rotation. Quand V_{circ} est employée, l’effet est toujours le même pour tous les échantillons utilisés: la pente est plus élevée et le point zéro de la RTF est plus petit comparé au cas où seule la vitesse de rotation est considérée.
- L’ajustement de la pente de la smRTF avec les données MAGIC est tout à fait cohérent avec les trois études de comparaison, utilisant soit $V_{2.2}$ soit V_{circ} . Cependant, lorsque la pente est fixée à celle trouvée avec les échantillons de référence, le point zéro est systématiquement décalé vers des valeurs de masse plus petites et des vitesses plus grandes pour l’échantillon MAGIC par rapport aux échantillons de comparaison.
- En comparant les masses stellaire et baryonique avec la masse dynamique (calculée en utilisant à la fois $V_{2.2}$ et V_{circ}) les fractions correspondantes ont été calculées pour l’échantillon MAGIC. Il a été clairement constaté que les fractions de masse stellaire augmentent en fonction de la masse stellaire de 10% pour les galaxies de faible masse jusqu’à 50% pour les galaxies massives. Pour la fraction baryonique, une tendance globale comparable a été constatée, qui reste inférieure à 50% même pour les galaxies massives, ce qui pourrait être dû aux incertitudes dans l’estimation de la masse de gaz pour les petites galaxies où une forte dispersion est présente dans la fraction baryonique.

Le résultat le plus pertinent de cette étude est le déplacement du point zéro de la RTF de l’échantillon MAGIC par rapport aux autres échantillons dans le même domaine de redshift, pour lequel deux hypothèses ont été proposées. Dans la première hypothèse, qui suppose que la cinématique trace la masse du halo de matière noire – c’est-à-dire que pour une vitesse donnée, la masse du halo de matière noire est constante – alors le déplacement vers des masses inférieures dans les groupes denses est le résultat de mécanismes d’extinction de la formation

estellaire actifs à l'intérieur d'environnements denses (décrits dans la section 1.5). En supposant une diminution du TFE de 0,3 dex due à l'environnement (Tomczak et al., 2019), le temps d'interaction dans lequel les galaxies sont entrées dans les structures est estimé entre 1 et 3 Gyrs. Dans un second scénario, l'effet de la contraction de la distribution de masse dans $R_{2,2}$ (pour un M_* donné) implique une augmentation de la vitesse de rotation. Un facteur de contraction compris entre 0,07 et 0,13 a été trouvé et semble expliquer au moins la moitié des décalages observés. Comme la fraction de matière noire est importante, cela indiquerait donc que la matière noire est également contractée ou que les halos de matière noire sont plus massifs. La contraction environnementale des baryons a été documentée dans la littérature par plusieurs études (Weinmann et al. 2009, Maltby et al. 2010 et Fernández Lorenzo et al. 2013 et Matharu et al. 2019) qui sont en accord avec cette hypothèse.

En conséquence les différences de smRTF et de bmRTF entre les échantillons dans des environnements de différentes densités sont probablement liées à la fois à l'extinction de la formation stellaire et à la contraction de la distribution de masse dans les environnements denses. De même, l'influence de chaque mécanisme dépend du régime de masse (différentes fractions de masse). Néanmoins, afin d'obtenir une comparaison plus robuste, limitant les effets de sélection et d'erreurs systématiques liés à l'utilisation de différents instruments, nous soulignons la nécessité d'un échantillon de comparaison approprié, ce qui implique d'utiliser la même qualité de données, une extraction et une modélisation cinématiques similaires, ainsi qu'une stratégie de sélection et une analyse semblables. C'est la prochaine étape à mettre en œuvre, afin de caractériser de manière robuste le rôle de l'environnement dans l'évolution des galaxies, pour ce faire, nous comparerons les résultats de cette Thèse avec une étude utilisant une stratégie et une analyse similaires sur les galaxies dans des environnements peu denses de l'échantillon MAGIC.

Perspectives du projet

Les résultats présentés dans cette Thèse correspondent à la première étude utilisant l'échantillon MAGIC pour déterminer le rôle de l'environnement dans les propriétés dynamiques des galaxies. Ce projet a montré le grand potentiel et les avantages des études de spectroscopie 3D (IFS) sur l'étude des propriétés spatialement résolues de grands échantillons qui permettent d'effectuer des analyses statistiquement significatives. Dans le cas de MUSE, sa capacité exceptionnelle à recueillir des observations IFS profondes à l'intérieur de son champ de vue (FoV) étendu permet d'étudier les propriétés et l'évolution de structures grandes et denses comme les groupes et les amas à des décalages spectraux vers le rouge intermédiaires. Je m'intéresse à la caractérisation de telles structures en étudiant leur distribution de masse, leur densité (nombre de galaxies par Mpc^2), la détermination de la position du barycentre, la densité radiale projetée, la dynamique et les interactions à grande échelle (accrétion de gaz et galaxies entrant dans les structures). Ceci est actuellement en cours avec la description du sondage MAGIC et la caractérisation de cet échantillon de groupes de galaxies dans l'article [Epinat et al. en prep.](#), auquel je participe activement. Les observations complémentaires dans le domaine des hautes énergies (rayons X avec les observations de Chandra et XMM) sont particulièrement utiles pour réaliser ce type d'études.

Parallèlement à l'obtention de la smRTF en utilisant le doublet [OII] comme traceur dy-

namique, j'ai travaillé sur le calcul de la vitesse de rotation dans d'autres bandes étroites ($H\alpha$ -[NII] pour l'échantillon à faible décalage spectral vers le rouge et [OIII]- $H\beta$ pour l'échantillon entier). Il s'agit d'un projet en cours qui vise à déterminer la cohérence entre les estimations des paramètres cinématiques en utilisant différentes phases du gaz ionisé en évaluant le niveau de concordance entre les différents RTFs à ces bandes.

Par ailleurs, la décomposition morphologique que j'ai effectuée pour cette étude offre la possibilité de réaliser plusieurs études complémentaires comme la caractérisation des résidus morphologiques pour quantifier les asymétries (lopsidedness), la concentration des profils de lumière, pour identifier les structures internes comme les anneaux, les bras et les barres, et le calcul de statistiques sur la fraction de galaxies ayant une morphologie perturbée en fonction du redshift. Il serait également intéressant de caractériser les disques granuleux en effectuant des histogrammes sur la distribution radiale des profils de luminosité de surface. Ensuite, sur la base de notre décomposition bulbe-disque et de l'analyse structurale sur les asymétries, disques granuleux et les composantes internes (barres, anneaux, bras, etc), il sera possible d'obtenir notre propre classification morphologique sur l'échantillon MAGIC et d'effectuer la comparaison avec d'autres catalogues morphologiques.

Les résultats de ce travail montrent la grande efficacité de notre méthodologie pour sélectionner de manière cohérente les galaxies dominées par la rotation au sein d'un échantillon, en se basant sur la capacité à extraire des informations fiables en utilisant des critères de résolution et de limites S/B. Comme cela est introduit dans la section 3.3, l'échantillon MAGIC inclut d'autres groupes de galaxies (CGr35, CGr87, CGr172) et de nouvelles observations sur les groupes existants, dont les données ont été récemment réduites. Enfin, dans le cadre des programmes MUSE-GTO consortium, des observations IFS de structures denses sont effectuées dans d'autres champs de vue observés par le Télescope Spatial Hubble comme l'UDFS (Ultra Deep Field South) et l'HUDF (Hubble Ultra Deep Field). Ces échantillons de données supplémentaires enrichissent la diversité des environnements sur lesquels l'analyse proposée dans cette thèse peut être appliquée.

L'étude des effets environnementaux dans l'évolution des galaxies, en utilisant une approche dynamique a été l'objectif principal de ce travail, Je participe désormais à l'analyse et à l'identification des différences substantielles entre la RTF des galaxies en structures denses et celui des galaxies en champ dans l'échantillon MAGIC, ceci en appliquant la même méthodologie que celle proposée dans cette étude pionnière. Cela permettra de prouver la cohérence des résultats de notre comparaison avec d'autres échantillons IFS obtenus avec des instruments différentes et utilisant des méthodes différentes pour extraire la cinématique. Grâce à cette comparaison de groupes et de champs impliquant des galaxies dans l'échantillon MAGIC, nous pourrions obtenir des indicateurs robustes sur le rôle de l'environnement et les différences dans la distribution de la masse stellaire, de la masse baryonique et des halos de matière noire, à l'intérieur des intervalles de redshift et de masse bien déterminés. Pour cette étude des galaxies en champ, j'ai extrait les cartes de vitesse et de dispersion de la vitesse pour tous les objets dans les champs MAGIC (à l'exception des trois champs nouvellement publiés mentionnés ci-dessus), y compris les galaxies isolées, et j'ai modélisé la cinématique complète des galaxies dans les structures les plus denses sélectionnées.

Comme le débat sur l'évolution de la RTF de masse stellaire est encore ouvert, je suis intéressé par une étude plus approfondie des différences entre la smRTF dans l'Univers local et les galaxies à redshift intermédiaire en utilisant les données IFS (e.g. WEAVE, SAMI et MaNGA dans l'Univers local contre KMOS et MUSE à redshift plus élevé). Il y a d'ailleurs un manque de caractérisation de l'environnement dans les échantillons de l'Univers local, ce qui offre un grand potentiel de recherche.

À partir de la modélisation cinématique, une autre possibilité est de construire la distribution radiale de la composante de la matière noire, en se basant sur les distributions de masse baryonique et dynamique obtenues dans cette étude. Cela complétera l'étude structurelle sur l'échantillon de galaxies dans structures denses. Je souhaite également poursuivre ce projet de recherche en étudiant la distribution du moment angulaire pour l'échantillon MAGIC. Cela permettra de caractériser les processus d'évolution de ces galaxies et de mieux comprendre la manière dont l'environnement impacte cette évolution.

Abstract

Galaxies form and evolve in different environments, arranged at large scales, in structures shaped by the distribution of dark matter halos, like filaments, walls, clusters and cosmic voids. The evolution of galaxies in low-density environments significantly differs from those embedded in large crowded structures like groups or clusters of galaxies, where environmental drivers are more prominent reducing the gas content and consequently quenching their star-forming capacity earlier than their isolated counterparts.

The goal of this work is to study the Tully-Fisher relation (TFR) for galaxies at intermediate redshift ($z \sim 0.7$) in groups of galaxies. The TFR links the maximum rotation velocity of galaxies – a proxy of dark matter halo mass distribution – to their stellar and/or baryonic mass content. This relation provides key information on the dynamical support, and on formation and evolutionary state of galaxies. The advent of powerful Integral Field Spectroscopy instruments like MUSE, allows to reach a resolution high enough to perform spatially resolved studies at intermediate redshifts and recover essential physical parameters.

This research is based on the exploitation of an unique sample of 12 dense galaxy groups selected in the COSMOS field, from the Guaranteed Time Observations MUSE gALaxy Groups In Cosmos (MAGIC) Survey, spanning the redshift range $0.3 < z < 0.8$. I performed a morphokinematics analysis on a total of ~ 350 galaxies in those groups, from which ~ 70 are distributed in 4 structures at lower redshift ($z < 0.4$).

My analysis was centered on the sub-sample of 8 groups at $0.5 < z < 0.8$, containing ~ 280 galaxies, for which the kinematics was extracted using the $[\text{OII}]\lambda\lambda 3727, 3729 \text{ \AA}$ doublet. A bulge-disk decomposition was applied on high resolution ACS-HST F814W images, in order to retrieve the projection parameters, an accurate global size and the light contribution of the bulge and disk components. Subsequently, a 2D kinematic modeling was applied to recover the maximum rotation velocity at $2.2 R_d$ (disk scale-length radius), the intrinsic velocity dispersion and the dynamical mass. In order to get robust kinematic measurements, I performed a rigorous sample selection in setting suitable limits on the spatial resolution and on the signal-to-noise ratio. This selection is not based on a posteriori assumption, like it is typically done when the velocity-to-dispersion ratio is used. The effects of selection criteria were carefully evaluated on the TFR: I found the selected galaxies are mostly rotation dominated disk systems and are besides enough resolved in order to retrieve reliable dynamical parameters. I compared my results with previous studies in similar dense environments (e.g. ORELSE) and in lower density environments (e.g. KMOS^{3D}, KROSS) for which the selection criteria were less restrictive, pointing out the advantages of our method which considerably reduces the number of dispersion-dominated outliers in the TFR. Likewise, I analyzed the stellar and baryon

mass fractions within stellar disks and found they both increase with stellar mass. A technical comparison of the results from this research with the previously mentioned studies is provided considering they are based on different types of environments with the purpose to determine possible shifts in mass and rotation velocity.

The most relevant result is the finding of a clear offset of the TFR zero-point between galaxies in low and high density environments implying that at fixed stellar or baryonic mass, galaxies in dense environments rotate faster than in low-density environments. Thus, the evolution of the TFR in dense environments could be due to a combination of quenching of star-formation and of contraction of the baryonic content, depending on the mass regime. These hypotheses are supported by evidences presented by previous environmental studies in literature.

Resumen

Las galaxias se forman y evolucionan en diferentes ambientes, dispuestas a gran escala, en estructuras formadas por la distribución de halos de materia oscura, como filamentos, paredes, cúmulos y vacíos cósmicos. La evolución de las galaxias en ambientes de baja densidad difiere significativamente de aquellas que están incrustadas en extensas y densas estructuras como grupos o cúmulos de galaxias, donde los factores ambientales son más prominentes reduciendo el contenido de gas y, por consiguiente, apagando su capacidad de formación estelar antes que sus homólogas aisladas.

El objetivo de este trabajo es estudiar la relación Tully-Fisher (RTF) de galaxias en grupos a corrimiento al rojo intermedio ($z \sim 0.7$). La RTF vincula la máxima velocidad de rotación de las galaxias – directamente relacionada con la distribución de masa del halo de la materia oscura – con su contenido de masa estelar y/o bariónica. Esta relación proporciona información clave sobre el soporte dinámico, la formación y el estado evolutivo de las galaxias. El advenimiento de poderosos instrumentos que utilizan Espectroscopia de Campo Integral (IFS) como MUSE, permite alcanzar una resolución lo suficientemente alta como para realizar estudios espacialmente resueltos a corrimientos al rojo intermedios y recuperar parámetros físicos esenciales.

Esta investigación se basa en la explotación de una muestra única de 12 grupos densos de galaxias seleccionados dentro del campo HST-COSMOS, con Observaciones de Tiempo Garantizado del survey MAGIC (MUSE gALaxy Groups In Cosmos), que abarca el rango de desplazamiento al rojo $0.3 < z < 0.8$. Sobre esta muestra, realicé un detallado análisis morfo-cinemático de un total de ~ 350 galaxias en estos grupos, de las cuales ~ 70 se encuentran distribuidas dentro de 4 estructuras a menor corrimiento al rojo ($z < 0.4$).

Mi análisis se centró en una submuestra de 8 grupos a $0.5 < z < 0.8$, que contiene ~ 280 galaxias, para las cuales la cinemática fue extraída usando el doblete de $[\text{OII}]\lambda\lambda 3727, 3729 \text{ \AA}$. Se aplicó una descomposición bulbo-disco a la distribución de brillo superficial de las galaxias usando imágenes de alta resolución ACS-HST F814W, con el fin de recuperar los parámetros de proyección, tamaño global preciso y la contribución en brillo de las componentes bulbo y disco. Posteriormente, se aplicó un modelado cinemático 2D para determinar la máxima velocidad de rotación a $2.2 R_d$ (radio de escala del disco), la velocidad de dispersión intrínseca y la masa dinámica. Con el fin de obtener mediciones cinemáticas robustas, implementé una rigurosa estrategia de selección de galaxias dominadas por rotación, estableciendo límites adecuados en resolución espacial y en proporción señal a ruido (SNR). Esta selección no se basa en un supuesto posterior, como suele hacerse cuando se utiliza el cociente velocidad a dispersión (V/σ). Los efectos de estos criterios de selección se evaluaron cuidadosamente en la RTF, encontrando que las galaxias seleccionadas son en su mayoría sistemas de discos dominados por rotación y

además están lo suficientemente resueltas como para recuperar parámetros dinámicos fiables. Comparé mis resultados con estudios anteriores en ambientes densos similares (e.g. ORELSE) y en ambientes de menor densidad (e.g. KMOS 3D , KROSS), para los cuales los criterios de selección eran menos restrictivos, señalando las ventajas de nuestro método que reduce con siderablemente el número de valores atípicos de sistemas dominados por dispersión en la RTF. Asimismo, analicé las fracciones de masa estelar y bariónica dentro de los discos estelares y encontré que ambas aumentan con la masa estelar. Se proporciona una comparación técnica de los resultados de esta investigación con los estudios mencionados anteriormente, considerando que se basan en diferentes tipos de ambientes con el propósito de determinar posibles cambios en la masa y la velocidad de rotación.

El resultado más relevante consiste en el hallazgo de un claro desplazamiento del punto cero de la RTF entre las galaxias en ambientes de baja y alta densidad, lo que implica que a una masa estelar o bariónica fija, las galaxias en entornos densos rotan más rápidamente que en entornos de baja densidad. Por lo tanto, la evolución de la RTF en ambientes densos podría deberse a una combinación de apagado de la formación estelar y/o de la contracción del contenido bariónico, dependiendo del régimen de masa. Estas hipótesis están respaldadas por evidencias presentadas en anteriores estudios ambientales en la literatura.

List of Tables

2.1	General characteristics of the MUSE WFM and NFM	48
2.2	Redshift ranges for nebular lines observable by MUSE	50
2.3	Technical Comparison of Spectrographs in this study	60
3.1	Technical comparison of the current major IFS Surveys	72
3.2	List of groups in the MAGIC Survey their main observational characteristics . .	74
3.3	General properties of the galaxy groups and clusters in the parent sample of galaxies in groups from the MAGIC survey	79
4.1	Parameters of HST PSF modeling for 27 stars	86
4.2	Threshold velocity dispersion and FWHM_λ (LSF) for the most important nebular lines	105
4.3	MUSE PSF results for [OII] and $\text{H}\beta$ -[OII] narrow band images	106
4.4	MUSE PSF results for $\text{H}\alpha$ -[NII] and [SII] narrow band images	106

List of Figures

1	The Milky Way and the Moon at Paranal VLT.	iii
2	Magellanic clouds at Paranal VLT	iv
1.1	Hubble tuning fork morphological diagram	2
1.2	Schematic SFR vs. M_{\odot} diagram, showing different population of galaxies	4
1.3	Cosmo models and observations	6
1.4	Morphological Evolution of the Hubble Diagram across cosmic time	8
1.5	Rotation curve with its dynamical components and examples of rotation curves from different different type of Spirals	11
1.6	Kinematics of the neutral gas (HI line) of NGC 6946 from the THINGS Survey compared to optical detection by the DSS	12
1.7	Baryonic mass models and rotation velocity components by McGaugh et al. (2016)	14
1.8	smTFR evolution studies from Übler et al. (2017) and Tiley et al. (2019)	18
1.9	Evolution of morphological type fractions in function of projected density by Dressler (1980)	20
1.10	Fraction of passive galaxies in function of environment density and stellar mass from Peng et al. (2010b)	22
1.11	Global size in function of environment from Matharu et al. (2019)	24
2.1	Spectrographs using diffraction gratings	29
2.2	MUSE datacube representation from ESO	31
2.3	Three types of Integral Field Units (IFUs)	33
2.4	Fiber bundle MaNGA IFU	35
2.5	Microlens array of OASIS and Micropupile configuration	36
2.6	Configuration of image slicer IFU	38
2.7	Schematic of a Fabry-Perot Spectrometer	39
2.8	Fabry-Perot interference pattern and transmission function	41
2.9	Schematic view of an IFTS-Michelson Spectrometer	42
2.10	The MUSE instrument and Yepun Telescope	44
2.11	Slicer image strategy from MUSE	45
2.12	MUSE Observation control panels	46
2.13	Image of Neptune using MUSE NFM	47
2.14	MUSE integrated spectra of three galaxies at different redshifts	52
2.15	MUSE sky spectrum with AO in NFM	53
2.16	Sky emission emission spectrum at JHK near-IR bands	54
2.17	KMOS instrument and KARMA visualization software	58
2.18	Main Science cases of HARMONI	63

3.1	The Cosmic Evolution Survey (COSMOS) field compared with other HST-ACS surveys	68
3.2	Left: COSMOS Probability to detect overdense structures according the survey area. Right: ACS-HST image from the COSMOS survey of the CGr30 field of the MAGIC sample.	69
3.3	Cosmic SFR density as a function of look-back time and redshift and the relative coverage of different IFS surveys of distant galaxies	71
3.4	Distribution of MAGIC groups in function of the virial velocity dispersion and the light surface brightness at the physical scale at a redshift range $0.35 < z < 1.5$	75
3.5	HST-ACS F814W high resolution image and stacked white MUSE image of the Field CGr84.	77
3.6	Distributions of z , SFR and stellar mass for the total sample of galaxies in groups from MAGIC	78
3.7	Color-Color and Color-Mass diagrams of the galaxy groups sample	80
4.1	Comparison of Moffat vs. Gaussian PSF profiles	85
4.2	PSF modeling example on HST F814W images	85
4.3	Graphic scheme of the applied bulge-disk morphological decomposition	87
4.4	Projection Parameters of a disk galaxy (inclination and PA)	89
4.5	Morphological models of Early type galaxies	92
4.6	Morphological models of Late type galaxies	93
4.7	Morphological models of Clumpy disks	94
4.8	Morphological models of Crowded fields	95
4.9	Morphological models of disks with strong bar, arms or rings	96
4.10	Distribution of inclination of the parent sample of intermediate z galaxies	101
4.11	Diagram explaining the 2D kinematic extraction based on an spaxel by spaxel emission-line modeling and the corresponding cleaning process.	109
4.12	Kinematics extraction product maps: Flux, S/N, v_{rot} , σ_v	111
4.13	Example of an ETG with extended [OII] coherent emission	112
4.14	Difference between PA_m and PA_{kin}	115
4.15	Summary Diagram of the followed Morpho-Kinematics analysis	118
5.1	SFR versus $Mass_*$ diagram for the parent sample in color scatter function of the R_{eff}/PSF ratio	123
5.2	Selection effects diagram using the flux estimations from the integrated spectrum for SNR.	125
5.3	Flux comparison between SED fitting and narrow band images	126
5.4	Kinematics extraction for the QSO CGr84-50	128
5.5	Diagnostic diagrams of ionizing mechanisms and AGN identification	130

Chapter 1

Introduction

1.1 Morphological Classification of Galaxies

Galaxies are complex physical systems composed of stars, gas and dust, all gravitationally bound and associated to a dark matter halo. The distribution of these components, specifically the stellar luminosity shows a wide variety of morphologies, mainly observed in optical bands. Morphological classification is based first on the global dominant features like spheroids and disks. In more detail, the presence of structures like arms and bars or other less common structures like rings on disks results in a more specific and diverse morphology.

Morphological features were first classified by Edwin Hubble with his pioneering work on “Extra-Galactic Nebulae” (Hubble, 1926), and latter described in “The Realm of the Nebulae” (Hubble, 1936), where he proposed a classification system relying on the observed structures of galaxies latter denominated as the Hubble sequence as it is presented in Figure 1.1. The morphological sequence goes from galaxies completely dominated by a spheroidal component –elliptical galaxies–, passing through galaxies with a faint disk with no internal structures and a prominent bulge –lenticulars–, continuing with disk dominated galaxies with spiral arms and in some cases also presenting bars –spirals–. Finally, there is a category of galaxies outside the Hubble sequence which are disk-like galaxies with no regular or defined shapes –irregulars–. Lenticular galaxies are in the center of the Hubble diagram since they are considered as a transition (intermediate) type between ellipticals and spirals. There is also a small fraction of galaxies with mixed and perturbed morphologies known as peculiars.

From the above description of changes in the bulge and disks components across the different morphological types, we can see that the primary parameter to distinguish morphology is the bulge-to-disk light ratio (B/D). The B/D parameter is defined as the rate between the luminosity contribution of the bulge with respect to the luminosity contribution of the disk and in turn each component can be weighted with respect to the total brightness profile giving origin to bulge-to-total B/T and disk-to-total D/T ratios (see Section 4.2.2). A study on B/D related to morphological types and kinematic scaling relations are presented in Chapters 4 and 5.

Hubble implemented a notation for morphological types to be split into early-type galaxies, including ellipticals and lenticulars, located on the left-hand side of the Hubble sequence and late-type spirals located on the right-hand branches of the empirical diagram. For a long time

this configuration has been misinterpreted as a temporal sequence suggesting a direction in morphological evolution from spheroidal to spiral disk-like galaxies. However, this concept is inaccurate since the terminology early and late-type solely obeys to the location of galaxies in the observed configuration in the tuning fork diagram from left to right, as Hubble pointed out. Even today we use these terms for practical purposes when distinguishing in a general way between passive and disk-like galaxies, although it is known that the idea about evolution is wrong. Below I give a more specific description summarizing the most important characteristics of each morphological class going from early to late types (See Figure 1.1).

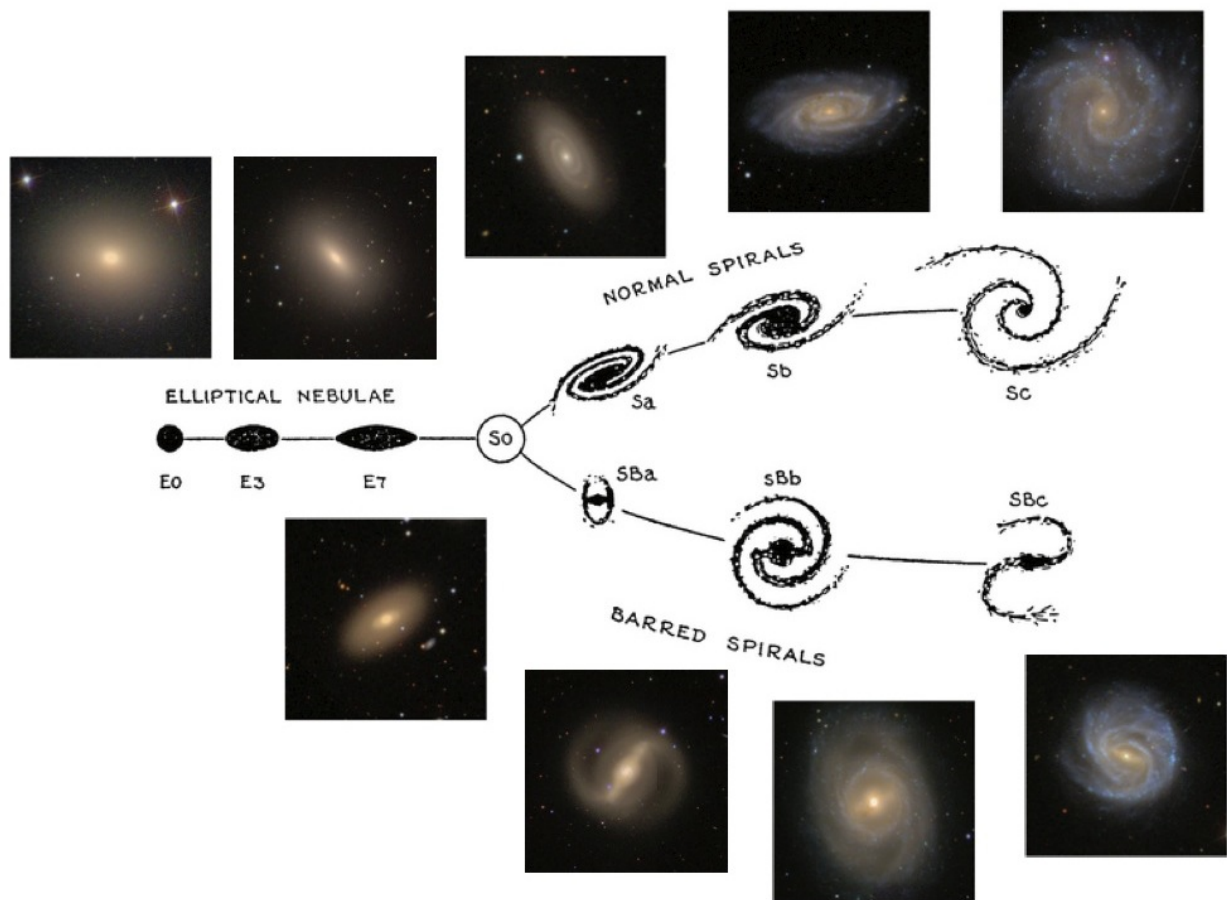


Figure 1.1: Hubble Sequence / Hubble tuning fork as was presented in “The Sequence of Nebular Types” published by Hubble in 1936. The original diagram is complemented with *gri* images from the Sloan Digital Sky Survey (SDSS) as part of the Galaxy Zoo project. Credits: This Image was taken from the document “A Zoo of Galaxies” (Masters, 2013).

Elliptical galaxies (type E_n) present a spherical or elliptical light distribution with no or little change in color from the center to the outskirts denoting a lack of young stellar populations. Their shape is further classified according to the ellipticity of their luminosity profile with index $n = 10 \times \epsilon$ (Liller, 1966), where ϵ is the eccentricity defined as $\epsilon = 1 - b/a$ being b/a the axial ratio of the light profile. The ellipticity index n ranges from 0 denoting a spherical light distribution to 7 corresponding to the most elongated galaxies. As was mentioned above

elliptical galaxies are completely dominated by a spheroidal component, there is no evidence of the presence of a disk so the bulge-to-disk ratio is $B/D \geq 1$. The luminosity profile of these galaxies is better described by a de Vacouleurs' profile ($r^{1/4}$) for a spherical distribution or a Sérsic profile ($r^{1/n}$) that depends on the concentration parameter n , with large values of n that correspond to concentrated inner profiles (See a detailed description on morphological modeling in Section 4.2).

Lenticular galaxies (type S0) show a bright central bulge (with $0.5 \leq B/D < 1$) and a diffuse flat disk-like structure surrounding the central component. These galaxies are dominated by old stellar populations and are characterized by the absence of spiral arms and a low gas and dust contents, however some present extended dust lanes and/or bars. Lenticulars owe their name to the lens shape that is observed when their disk is in edge-on orientation along the line-of-sight. Lenticulars can be further classified as a function of their dust content/attenuation as it is established by Ciesla et al. (2012).

Spiral galaxies (type S and SB) are dominated by a flattened disk presenting spiral arms, and a central bulge. Although B/D is generally ≤ 0.5 , spirals can contain prominent bulges. They are split in two main categories one denoting the presence of a bar (SB, barred spirals) and the other denoting the classical spiral galaxies with no bar (S). In most spiral galaxies star-forming activity is concentrated in the arms, so there a color gradient from the center with red-yellowish to bluish bands in the arms is observed denoting younger stellar populations and star-forming regions in the outskirts of the disk. Spiral sub-classes go from Sa(or SBa) to Sm (or SBm) primarily denoting the decrease of B/D values being the Sa type galaxies those with the most prominent bulges and less luminous disks. Global luminosity then has the same tendency as the B/D ratio, since while Sa galaxies are dominated by old stellar populations Sd and Sm are dominated by star-forming regions (some presenting star-bursts) and are besides rich in gas and dust, then they are dominated by luminous young stellar populations. The sub-sequence from a to m also denotes how closed are the spiral arms, being Sa spirals those with the most closed arms around the center and Sc, Sd and Sm those presenting open extended arms.

Irregular galaxies (Irr) do not present a defined shape and are characterized by asymmetrical light profiles. They are not composed of a regular disk nor of a spheroidal bulge, so irregular galaxies are not included into the Hubble sequence, they are represented outside the morphological diagram. They neither exhibit spiral arms although they sometimes present bars or stellar dense filaments. Irregulars present large fractions of gas and dust (Schmidt & Boller, 1993) and their structure is dominated by clumps of star-formation (Hunter 1997, Walter et al. 2007), then they are mostly composed of young stellar populations and some present strong star bursts.

According to observations in the local Universe and at low redshift ($z < 0.4$), using the criteria implemented by Delgado-Serrano et al. (2010) to account for the fractions of different morphological types, the dominant morphological types correspond to disk-like galaxies accounting for $\approx 80\%$ (including spirals and irregulars) and letting the remaining $\approx 20\%$ represented by early type galaxies (composed of lenticulars S0 and ellipticals E), from which only 3% are ellipticals (see for example, Dressler 1980, Blanton et al. 2003 and Delgado-Serrano et al. 2010). From late-type galaxies 15% are irregulars and the remaining are classical and barred spirals, from

which galaxies presenting bars represent from 60% to 70% and just $\sim 30\%$ are unbarred spirals (Sheth et al., 2008). All the above presented morphological fractions apply only in the Local Universe.

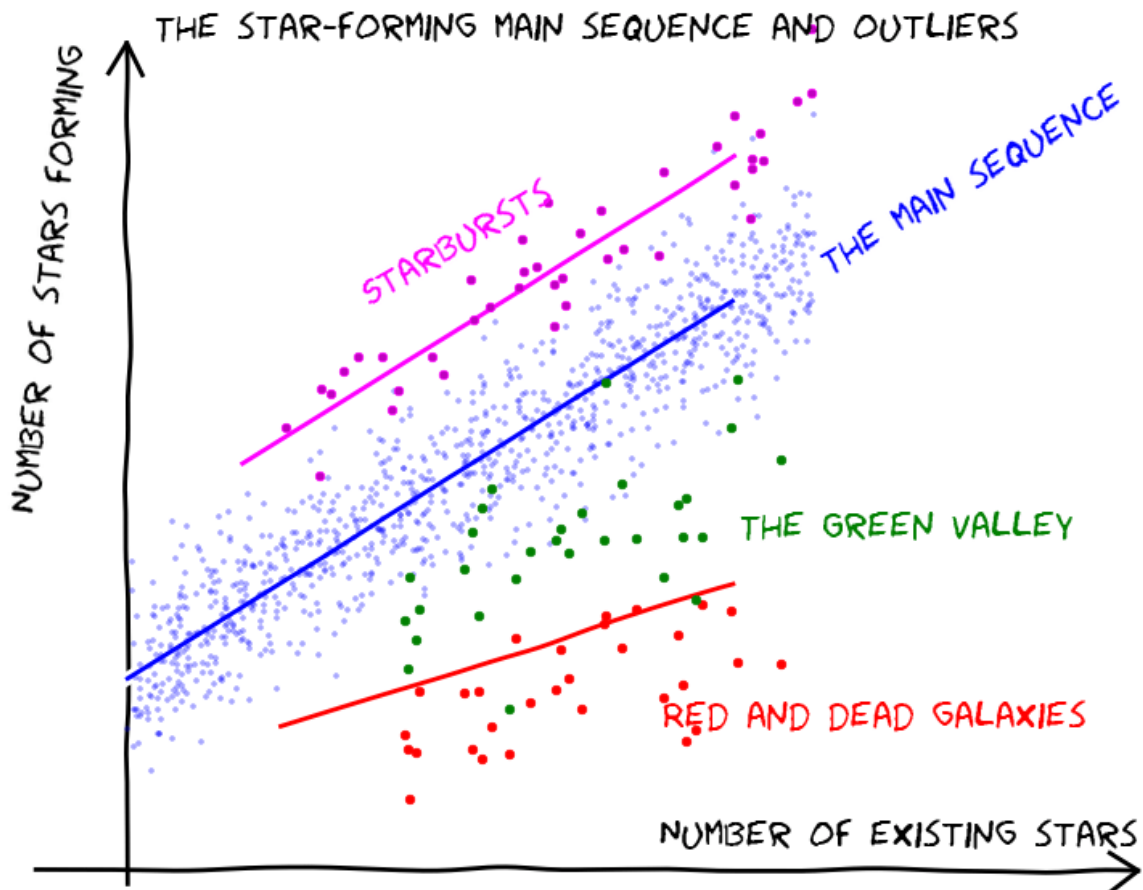


Figure 1.2: Schematic SFR vs. M_{\odot} diagram, showing different population of galaxies in function of their star-forming capacity: starburst, main sequence, green valley and Red sequence. Credits: Brian Koberlein

Another way to classify galaxies is by comparing their capacity to form stars known as Star Formation Rate (SFR) in function of their content of stellar mass. Figure 1.2 shows a schematic representation of the different populations of galaxies that can be found in this diagram and which are also related with morphology. Most of the galaxies lie on what is known as the **main sequence**, in which galaxies are actively forming stars according to their stellar masses. Galaxies having higher SFRs than the average of the main sequence for a given mass are those experiencing a **starburst** episode that is an intense period of star formation. Typically galaxies lying on the main sequence and above are spiral galaxies with a high fraction of gas in different phases allowing the formation of new stars. Galaxies with low star-formation constitute the **Red sequence** of passive galaxies, this population is mainly composed of ellipticals and lenticulars dominated by old stellar populations. Galaxies in the transition zone between star-forming and quenched galaxies are part of what is known as the **green valley**. In all the cases, for each type

of galaxies we can see a direct correlation between SFR and the stellar mass content of galaxies.

Hubble classification is based on galaxies of the local Universe. From recent deep photometric surveys it has been observed that an important fraction of distant galaxies lack of regular structures, and instead they have a more clumpy and fragmented composition due to large SF regions as it is discussed in Section 1.2. This morphological evolution seems to be related to several physical factors among others SF activity, size, gas budget and environment. This is a topic still under study both using observational techniques and theoretical simulations. This study is more focused on evaluating the change in global size and in star-formation capacity of galaxies in environments with different densities.

1.2 Galaxies throughout Cosmic Time

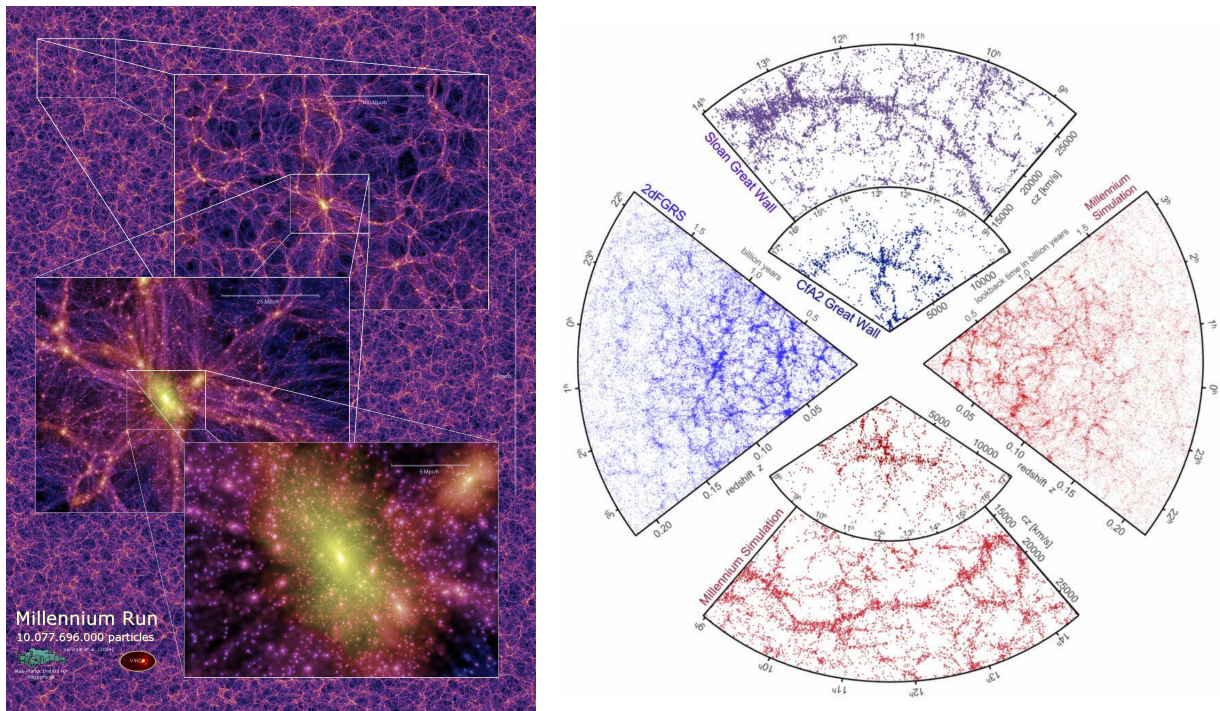


Figure 1.3: Left: This image shows a projected DMH density field with a 1 Gpc/h scale as output of the Millennium simulation (Springel et al., 2005) at $z=0$. Three overlaid consecutive panels zoom in on a galaxy cluster by a factor of 4 for each time, enlarging the regions inside the white frames with reference scales of 100 Mpc, 25 Mpc and 5 Mpc. Anisotropies are evident at scales <100 Mpc while for larger scales the distribution denotes homogeneity. Credit: Figure taken from the Millennium simulation Project website of the Max-Planck Institute for Astrophysics. Right: Galaxy distribution from the SDSS and 2dFGRS spectroscopic redshift surveys (in blue) and from mock galaxy catalogs produced using the cosmological Millennium simulation (in red). Credit: Springel et al. (2006)

The study of the distribution of matter and the structure of Universe at different epochs is fundamental to understand how it was formed and how it has evolved. Likewise, a robust and realistic model is necessary to theoretically describe the different evolution stages by comparing the theoretical predictions with observations and statistical properties of multiple empirical surveys of galaxies, as in Figure 1.3 right, where the observations in blue from SDSS and 2dFGRS match with the predictions from the cosmological Millennium simulation (Springel et al., 2006). Currently, the most accepted standard cosmological model is the Λ Cold Dark Matter (Λ CDM), since it gives the best description of the observed evolution of the Universe. The Λ CDM model establishes that the Universe was originated with a Big Bang 13.7 billion years ago (Peebles 1993, Planck Collaboration et al. 2016), has a flat configuration (no curvature), is homogeneous and isotropic at large scales (>100 Mpc) and is expanding continuously since its origin. In contrast with the large-scale homogeneity, at lower scales (<100 Mpc) clear dense structures like filaments, walls, groups, clusters and superclusters of galaxies are observed which represent anisotropies that compose a configuration known as the cosmic web, which is observed in Figure 1.3 left, that presents the distribution of Dark matter halos from the Millennium simulation (Springel et al., 2005) at $z=0$ at four different scales: 1 Gpc, 100

Mpc, 25 Mpc and 5Mpc, going from an homogeneous distribution zooming into a galaxy cluster.

The Universe is basically composed of baryonic or visible matter (stars, gas in different phases, dust and metals), dark matter and dark energy; this last responsible for the accelerated expansion observed in the Universe (Riess et al. 1998, Perlmutter et al. 1999). The Cosmic Microwave background (CMB) corresponds to the relic radiation from the Big Bang at the epoch of recombination when Universe transform from being opaque to transparent. According to an unprecedented study on the temperature variations on the CMB (of the order of microkelvins, tiny fluctuations that are thought to be the progenitors of the first galaxies), performed by the Planck mission, the fractions of the composition of the Universe correspond to 68% of Dark Energy, 27% of Dark Matter and only 4.9 % of baryonic matter (Planck Collaboration et al., 2016). As summary, the aim of cosmological models is then to propose scenarios that match observations from the Cosmic Microwave Background (CMB at $z \sim 1100$), reproducing the primordial cosmology to the matter distribution in the local Universe as the Λ CDM has proven to achieve. Based on this, throughout this work I assume a Λ CDM in order to perform the necessary computations to derive the physical properties of galaxies at intermediate redshift.

Galaxies have undergone significant morphological transformations from the maximum of the Cosmic SFR (Madau & Dickinson, 2014) at $z \sim 2$ to today ($z=0$), from clumpy disks composed of huge star-forming regions and perturbed galaxies by interactions (with wraps, bars, tidal tails, double nucleus, external rings, etc), to well defined regular spirals and passive elliptical galaxies. In Figure 1.4 it is observed that the Hubble sequence changes considerably at high redshifts containing galaxies with less defined morphologies. In fact it has been proven by van den Bergh (2002) that the Hubble sequence built with images of galaxies in the local Universe is valid as a good approximation of morphological arrangement up to $z \leq 0.5$. They argue that at $z \geq 0.5$ the fraction of galaxies with bars is very low since young disks are still to unstable (hot disks) to host regular structures like bars. At higher redshift the merger fraction is higher so this gives origin to very chaotic morphologies. In van den Bergh (2002) they also observe that the fraction of peculiar galaxies is higher for late-type galaxies (Sbc-Sc) with 69% than for early types (E-Sa-Sab), which implies that early-type galaxies get their final morphologies faster than the late-type galaxies.

Several observational campaigns have been designed in order to get deep images at high resolution and study the evolution of morphology and physical characteristics of galaxies with redshift. Some examples come from the following surveys: COSMOS (Cosmic Evolution: Scoville et al. 2007a) with a redshift coverage of $0.5 < z < 6$; GEMS (Galaxy Evolution from Morphologies and SED; Rix et al. 2004) with a coverage from $z=0$ to $z=1.1$ or GOODS (Great Observatories Origins Deep Survey; Giavalisco et al. 2004) achieving observations up to $z \sim 6.3$. Then using deep data from this kind of surveys, it is observed at intermediate and high redshifts ($z > 0.5$) that the fraction of irregular/peculiar galaxies increases considerably with respect to the local Universe. According to Delgado-Serrano et al. (2010) the fraction of irregular/peculiar galaxies in the local Universe is about $10 \pm 3\%$ while the fraction considerable increases at $z \sim 0.65$ is up to the half of the total sample ($52 \pm 9\%$), while the fraction of early type galaxies remained unchanged representing $\sim 4\%$. So from this study the main morphological transformation from 6 Gyrs ago seems to have been from peculiar galaxies to spirals with regular structures and less SF activity at $z=0$.

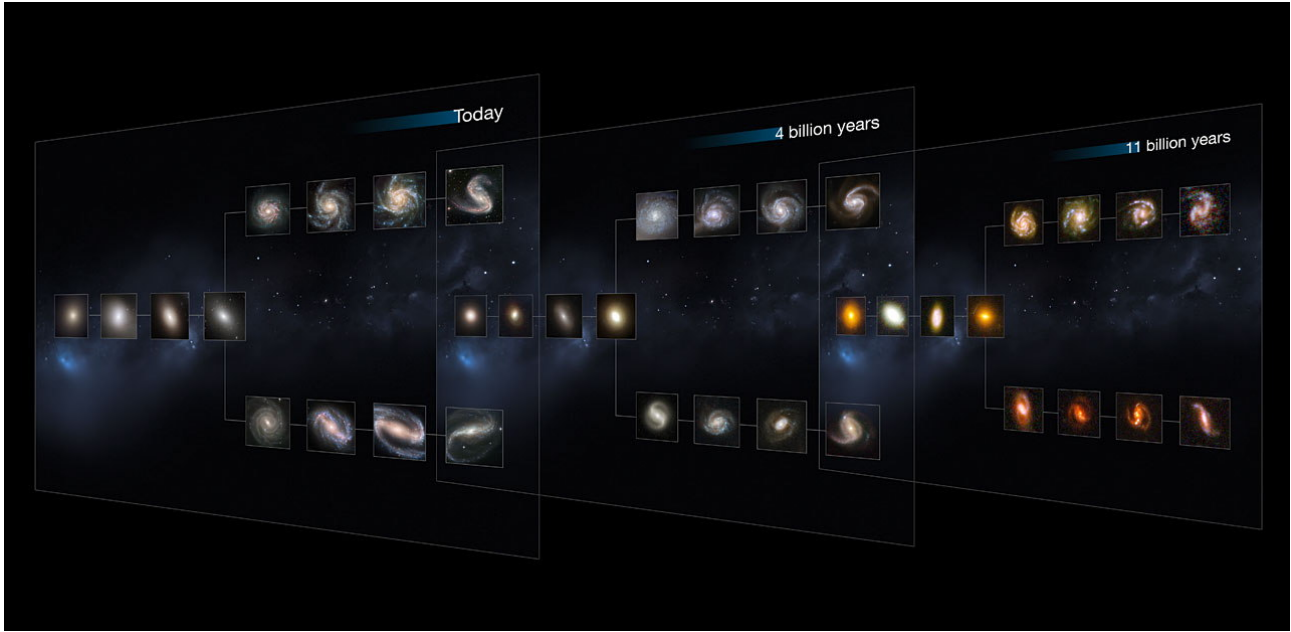


Figure 1.4: Morphological Evolution of the Hubble Diagram across cosmic time. Credits: NASA, ESA, M. Kornmesser.

In the absence of regular recognizable structures in peculiar galaxies, it is not very clear to correlate morphology with other physical properties of galaxies like their kinematics, mass content and SF activity, so the Hubble turning fork seems to partially approximate to the morphological distribution between $1 < z < 2$. Beyond $z=2$, it is not so reliable to apply this classification due to the difficulty in estimating the abundances of galaxies by morphological type since samples of distant galaxies are strongly affected by incompleteness issues which increase with redshift. Besides, most of the distant galaxies that can be resolved show morphologies that are outside the Hubble diagram.

In the local Universe there is a tight relation between kinematic properties and morphological type, being disks dominated by rotation and spheroidal components dominated by dispersion, so spiral galaxies are rotating systems and elliptical galaxies are systems supported by dispersion. At high redshift where the peculiar galaxies are abundant it seems this morpho-kinematics correlation is not yet settled at that epoch. There are interesting results in literature at different redshifts studying the morpho-kinematics correlation that have contrasting results. At intermediate redshift ($0.4 \leq z < 0.7$), (Neichel et al., 2008) using a sample of 52 galaxies from the Intermediate-mass Galaxy Evolution Sequence (IMAGES), found that there is a match between their dynamical support and their morphology since 80% of rotation dominated systems (15 galaxies) correspond to late-type galaxies and 92% of galaxies with peculiar/irregular morphologies (37 galaxies) have multiple kinematics components with complex dynamical systems. Nevertheless, other studies have shown that the scenario for galaxies at high redshift ($z > 1$) does not always follow this morpho-kinematics relation prescription, since not negligible fractions of clumpy and perturbed galaxies are supported by rotation (Förster Schreiber et al. 2009, Puech 2010, Jones et al. 2010, Tacconi et al. 2013, Wisnioski et al. 2015).

Inside galaxies there are other processes that trigger star formation and initiate the cycle of matter which suffers multiple transformations. Along galaxies with active star-formation, gas is accumulated in Giant Molecular Clouds (GMC) which collapse in the densest and coldest regions to give origin to new stars of different masses and luminosities. Stars that are formed from a single GMC give origin to a group of stars with the same age and initial metallicity which is known as a stellar population. Depending on their mass, stars from a same stellar population have different periods of life producing different elements along their lives releasing them into the inter-stellar medium (ISM), enriching the gas from which new generations of star are later formed. Energetic events like Super-nova explosions give origin to elements heavier than iron. Some complex molecules form aggregates that later give origin to dust grains, which absorb the radiated energy by stars playing an important role in the cooling of the gas which enables the formation of new stars. Star formation is regulated by massive stars which radiate high energetic photons that ionize the gas and destroy the molecular phase of gas. This baryonic matter cycle is affected by the environment in which galaxies develop since the gas supply into galaxies can be strongly affected by different interactions with other galaxies and with the environment, as I detail in Section 1.5.

Galaxies as complex systems have all the information from their different components stored and integrated inside their spectra. Each component and physical process contribute to the energy distribution from X-rays to Radio spectral regimes. The Spectral Energy Distribution (SED) then contains information about physical features, current and past mechanisms at play inside the galaxy and the state of each of its components. Stellar populations are responsible for the continuum emission from ultra-violet (UV) to the far-infrared (FIR) and also for some absorption lines originated in their atmospheres with different configurations depending on the spectral type of the stars (given by their mass and temperature). Emissions lines come mainly from the ionized gas by different mechanisms (massive stars UV radiation, AGN, shocks, etc). Emission and absorption lines allow to study chemical abundances and their ratios to retrieve the distribution of metallicity along their extension. SED also provides information about kinematics of stars and gas, the stellar mass content, star formation rate and dust attenuation. SED analysis then allows to quantify key physical parameters and scaling relations among them. Along this Thesis project I make use of different strategies in order to analyze the spectro-photometric data available from MUSE and HST to extract diverse type of information from galaxies in dense structures; specifically their baryonic mass content, SFR and kinematics.

1.3 Galaxy kinematics

Spiral galaxies are flattened rotating systems, their baryonic components (stars and gas) move in nearly circular orbits with velocities depending on their distance from the center of the gravitational potential, which provides the inward acceleration to produce the circular motion. The variation of the circular velocity as a function of the position in the disk along the major axis is known as rotation curve. Using the force balance, the rotational velocity V_{rot} of an object at a stable radius r measured from the center of a gravitational potential Φ_g is given by:

$$\frac{d\Phi_g}{dr} = F_g \rightarrow \frac{GM(r)}{r^2} = \frac{V^2(r)}{r} \quad (1.1)$$

$$V^2(r) = r \frac{d\Phi_g}{dr} = \frac{GM(r)}{r} \quad (1.2)$$

where $M(r)$ is the mass within a radius r , all this assuming a spherical distribution of mass and G is the gravitational constant. In order to have reliable values of the intrinsic rotation velocity it is necessary to account for the projection effects caused by the inclination of galaxy disks. The rotation velocity can be expressed in terms of the velocity along the line of sight—that is basically the observed velocity—, accounting for projection parameters as follows:

$$V_{rot} = \frac{V_{obs}}{\sin(i) \times \cos(\theta)} \quad (1.3)$$

where i is the inclination of the disk that is the angle between the plane of the disk and the sky plane, and θ is the azimuth on the plane of the disk, with the major axis as the reference ($\theta=0$). The inclination angle is derived from the precise determination of the apparent size of the disk (by measuring the major and minor axis), from a morphological analysis using high resolution photometry as I describe in Chapter 4. If a flat disk is assumed the inclination is derived as $\cos(i) = b/a$ where a and b are the semi-major and the semi-minor axis respectively. The complete expression to determine the inclination taking on account thickness of the disk is given in equation 4.7 in Section 4.2.

The measurements of rotation velocity accounting for the inclination of the disk are achieved computing the Doppler effect in emission lines from the ionized gas, the 21cm line produced by the neutral gas, CO lines associated to the molecular gas, or absorption lines from stars which are the main rotation tracers. The first attempts to measure the rotation curves were performed on nearby galaxies more notably on Andromeda galaxy (M31) by Pease (1918), obtaining a rotation curve of the central parts of the galaxy (up to 3 arcmin from the center) and Babcock (1939) with a more extended range of velocity measurements up to 100 arcmin corresponding for that study to ~ 6 kpc.

Later by 1970 radio astronomy became a powerful tool to investigate the properties and dynamics of the neutral gas with the HI emission line at 21 cm, whose distribution in the disk extends more than twice compared to that of the stars and ionized gas in optical bands, as it is shown for galaxy NGC 6946 in Figure 1.6, which compares the integrated emission of the neutral gas from The HI Nearby Galaxy Survey (THINGS, Walter et al. 2008) and the optical image of the same area from the Digitized Sky Survey (DSS). THINGS is composed of radio data obtained with the Very Large Array (VLA) to study the distribution and kinematics of

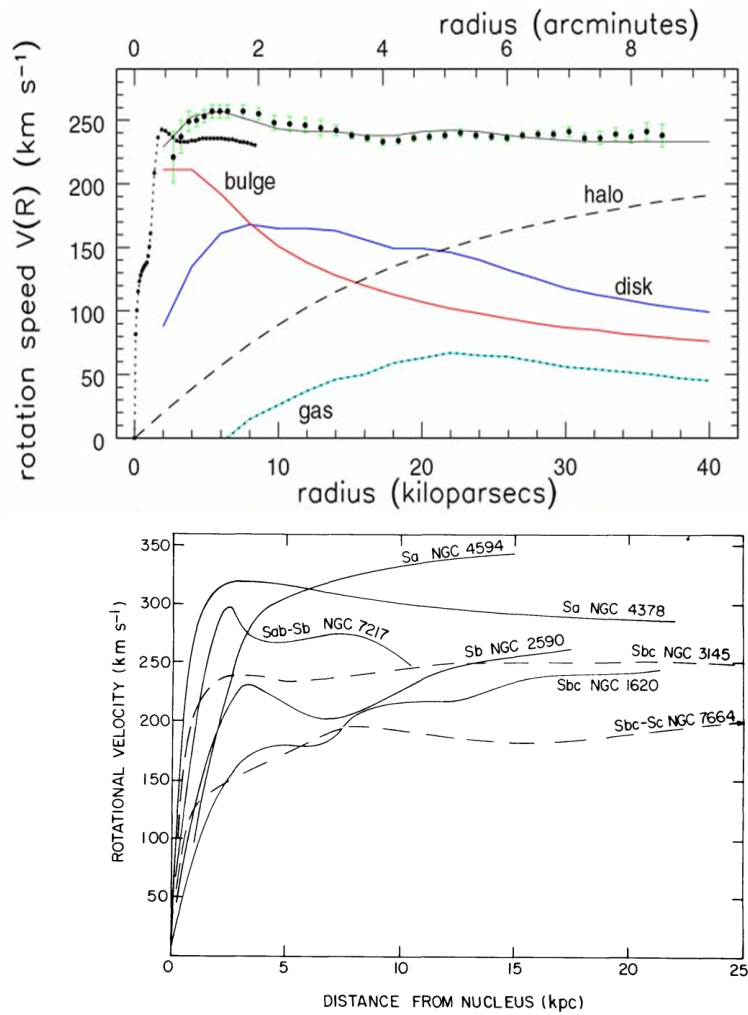


Figure 1.5: Upper panel: Rotation curve of NGC7331 and the model of its different dynamical components from the study performed by Begeman et al. (1991). The black dots correspond to observational values of HI (21cm) velocity, the solid black line is the total rotation curve model, the bulge rotation curve is presented in red, the stellar disk in blue, the gas in cyan and the dark matter halo is represented by the dashed line. The dotted line in the central part of the galaxy corresponds to velocity values from CO data. Credit: Taken from the book “Galaxies in the Universe” (Sparke & Gallagher, 2007). Lower panel: Examples of rotation curves for seven galaxies spanning in morphological type from Sa to Sc from Rubin et al. (1978b). All rotation curves are flat in the external parts of the disks which does not match with the shape of a velocity curve of a system only composed of visible matter. The most important and visible result from this study is that the amplitude of the velocity curves is larger for early types (Sa) than for late types (Sc). Credit: Figure taken from Rubin et al. (1978b).

the neutral gas of 34 nearby galaxies, in Figure 1.6 the rotation velocity and velocity dispersion maps of NGC 6946 are also presented showing a larger extension of the disk than that of the optical DSS image.

Rotation curves of spiral galaxies have shown they do not decrease with radius but instead, after reaching a maximum value of rotation velocity they are basically flat in the outer regions of the disk (as is showed in Figure 1.5). This implies rotation velocities in those regions are

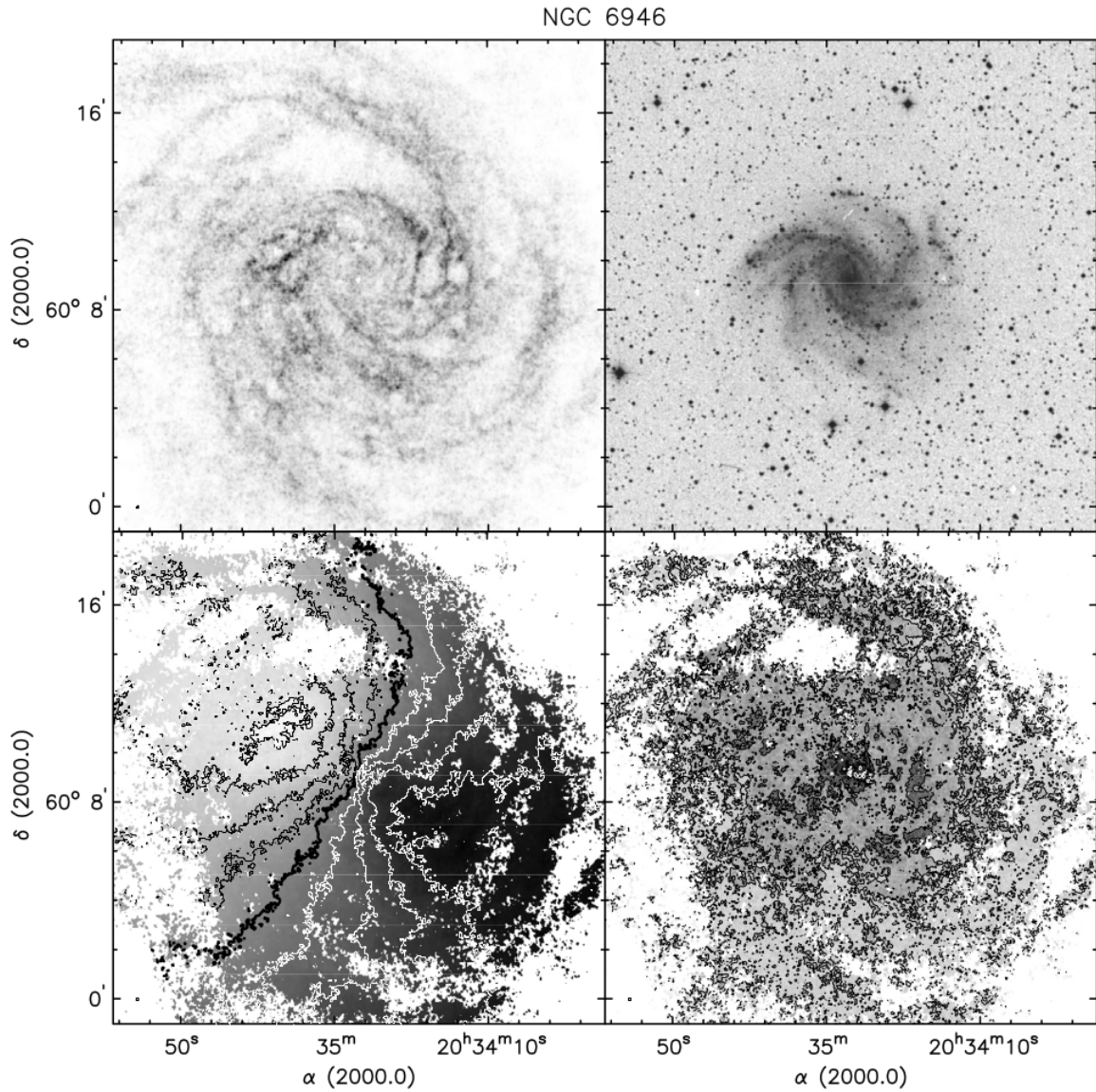


Figure 1.6: Kinematics of the neutral gas (HI line) of NGC 6946 from the THINGS Survey compared to optical detection from the Digitized Sky Survey DSS. Top left: integrated emission map. Top right: Optical image from DSS. Bottom left: HI velocity map with contours indicating a $\Delta V = 25 \text{ km s}^{-1}$ and a systemic velocity (black line) of $V_{sys} = 200 \text{ km s}^{-1}$. Bottom right: HI velocity dispersion map with contours at 20, 10 and 20 km s^{-1} . For definition of kinematic maps and terms see Chapter 4. Credits: Taken from [Walter et al. \(2008\)](#).

faster than what is expected from the Kepler law and the luminosity profiles that fall to vanish at large radii (see Figure 1.5 upper panel and [Rubin et al. 1978b](#), [Rubin et al. 1978a](#), [Rubin 1983](#)).

One of the most powerful applications of rotation curves is that they allow to determine the total mass content and its distribution inside galaxies as it is established in Equation 1.2. Another way to compute the mass is through the luminosity profile using the mass-to-light ratio, however these values do not match with the dynamical mass since the M/L ratio method

only accounts for the visible matter. An additional discrepancy comes from the assumption of a constant M/L ratio across the disk that a Keplerian description involves, since the observed flat rotation curves in fact imply a radial increase of the M/L ratio as was empirically demonstrated by [Bosma \(1978\)](#) by studying the variation of the M/L ratio as function of the distance to the center. From all these evidences, it was therefore concluded that spirals are embedded in a halo of an invisible matter, denoted as dark matter ([Rubin, 1983](#)).

The dark matter approach to explain the rotation curves of spiral galaxies was hardly debated and taken with reserve inside the astronomical community after being announced by V.C. Rubin in [1980](#) and in [1983](#), where she robustly argued flat rotation curves implied a linear grow of galaxy mass from the center which suggests that either Newtonian gravity does not have an universal character at galactic scales or that more than the half of the total mass of galaxies is composed of an unknown type of matter non-interacting with light, which is distributed in what latter was cataloged as dark mater halo. Today, the existence of dark matter is the most favored hypothesis and kinematics of spiral galaxies constitutes one of the most important evidences.

An important parameter to take into account to derive reliable mass computations is the radius r at which rotation velocity is measured. To ensure the total mass is enclosed, rotation velocity should be measured after the turn-over radius at which the velocity plateau (V_t) is reached. So farther from the center it is more likely to reach the flat part of the curve, the problem is that the luminous profile of stars and gas vanish in some cases before reaching the plateau, like in the case of low mass galaxies or for distant galaxies with noisy rotation curves. This is why rotation curve models ([Courteau 1997](#), [Epinat et al. 2012](#) and references therein) are used to infer the maximum rotation value. In the case of this study for galaxies sufficiently resolved by the spectroscopic data dynamical masses were computed at $2.2R_d$ (2.2 scale-length radius), which was in turn calculated using the high resolution morphological modeling of the stellar continuum light profiles. At that radius which is extended enough we expect to trace most of the mass and reaching the maximum rotation velocity in most of the cases, as it is explained in detail in [Section 4.6](#).

From rotation curves it is also possible to determine the contribution of each baryonic and dark components to the global mass distribution. In [Figure 1.5](#) upper panel, there is a decomposition of the dynamical components from the study made by [Begeman et al. \(1991\)](#), taking into account that the baryonic mass follows a keplerian configuration (specially the bulge and stellar disk profiles) with a constant M/L. The halo is then computed to compensate the lack of mass to achieve the observed rotation curve when all the components are added. In the lower panel of [Figure 1.5](#) there is a sample of seven rotation curves of different type of spirals from Sa to Sc morphological class from [Rubin et al. \(1978b\)](#), showing early type Sa galaxies rotate faster in average than late types Sc galaxies, so there is a correlation between morphology and dynamics. In a more recent study by [McGaugh et al. \(2016\)](#), they present an analysis of the dynamical decomposition and the change in fractions of baryonic components in function of morphology, using infrared data for the stellar continuum and HI data to characterize the gas from the Spitzer Photometry and Accurate Rotation Curves (SPARC) survey. In [Figure 1.7](#) there are three examples of mass models from [McGaugh et al. \(2016\)](#) presenting different fractions of baryonic components for three rotationally dominated systems with different mor-

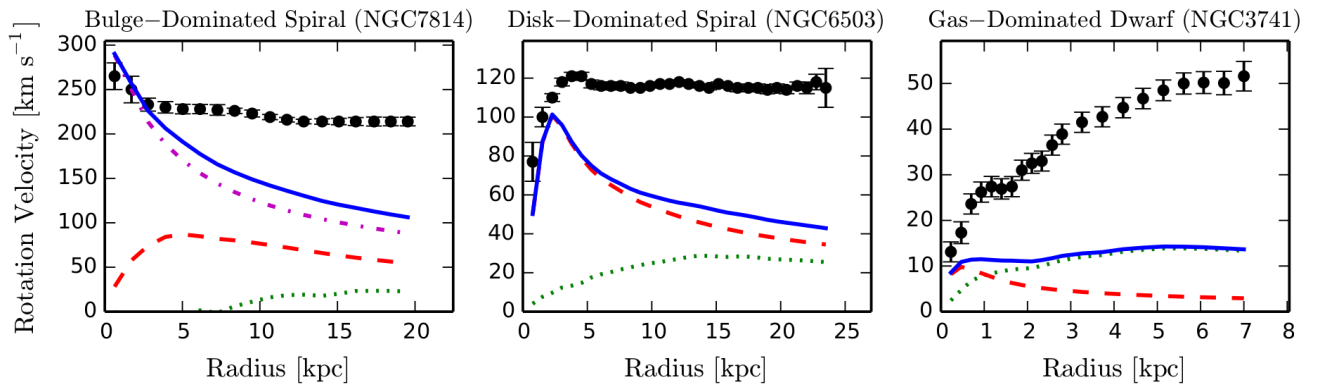


Figure 1.7: Baryonic mass models and rotation velocity components (McGaugh et al., 2016) for three galaxies with different morphologies: to the left NGC7814 a bulge dominated galaxy, in the center NGC6503 a disk dominated spiral galaxy and to the right a Dwarf gas dominated galaxy. Each baryonic component corresponds to: dotted green lines for the gas, dashed red lines for the stellar disk, and dash-dotted magenta lines for the bulge, when present. The sum of these components corresponds to the baryonic mass model represented by the blue solid line. Credits: Taken from McGaugh et al. (2016).

phologies. The bulge-dominated galaxy NGC7814 seems to have a larger fraction of baryons being the bulge the most prominent component, although its fraction of gas is small and restricted to the outer parts of the disk. For the disk-dominated galaxy NGC6503 the most important mass contribution comes from the stellar disk and the gas is found from the center to the outskirts being an important component while the bulge is negligible. For the dwarf galaxy NGC3741 dominated by gas the global baryonic contribution to the rotation velocity is the lowest, which means this system is dominated by dark matter.

Galaxy kinematics is a fundamental tool in the understanding of the processes and mechanisms that govern formation and evolution of galaxies, this due to the different correlations between dynamical features with other physical characteristics. From kinematics it is possible to determine the total mass content and to separate the dynamical components (baryonic and dark), contributing to the total radial mass distribution. The study of velocity maps permits to identify complex kinematics due to disturbances in the systems originated during interactions in the evolution history of galaxies. Using rotation curves models allows to infer the amount of dark matter and its distribution inside the dark halo. Finally, comparing kinematic and physical characteristics at different redshifts enables one to trace the evolution of different properties of galaxies.

1.4 Relation between the dynamical and baryonic components: The Tully-Fisher Relation

Galaxies gather their mass and evolve inside dark matter halos (DMH) through two main mechanisms: first by accreting cold gas from the intergalactic medium at large-scales (e.g. [Dekel et al. 2009](#)) and second by hierarchical growing (mergers of galaxies). Nevertheless, it is not completely understood how baryons are accreted inside dark matter (DM) structures and if there is a correlated evolution of the DM and baryonic components. The Tully-Fisher relation (TFR, [Tully & Fisher 1977](#)) is the tight linear dependence between stellar mass content and the maximum rotation velocity of star-forming (SF) galaxies. The TFR can be used to answer the previously mentioned questions, since it links the total mass content (from which DM fractions and its evolution can be traced) of a population of galaxies to their luminosity/stellar mass content.

Using optical photometry and observations in radio at 21cm of nearby spiral galaxies in the Virgo Cluster and the M81 group [Tully & Fisher \(1977\)](#) found for the first time a tight relation between the maximum rotation velocity (computed from the HI line-width) and their luminosity in optical bands, known as the Tully-Fisher relation (TFR), which applies on rotation dominated systems. Since the TFR allows to determine the intrinsic luminosity by means of kinematics, it has been largely used as cosmological distance indicator (e.g. [Freedman 1990](#), [Sakai et al. 2000](#), [Tully & Pierce 2000](#), [Sorce et al. 2013](#)). Nevertheless, as was also indicated by [Tully & Fisher \(1977\)](#) this correlation is also fundamental in the study of structure and properties of disk-like galaxies, and also to investigate formation and evolution scenarios. Besides, there is a small dispersion presented by the TFR specially when luminosity is measured in infrared, sub-milimeter and radio bands ([Verheijen, 1997](#)), as longer wavelengths are less affected by dust extinction and also by the effect of the ongoing star-formation. This low scatter allows to study the relation between the dynamical mass (including dark matter) and the luminous matter, which allows intrinsically to probe the connection between the baryonic or stellar mass and the dark matter distribution ([Verheijen, 1997](#)).

There are two ways to obtain the maximum rotation velocity V_{max} , either from the spatially resolved rotation curve (as described in the above Section 1.3) or in the case of HI data by extracting the Doppler width from an integrated spectrum of the 21-cm line which corresponds to $\sim 2V_{max}$ [Schneider \(2007\)](#). [Verheijen \(2001\)](#), found that the TFR has a lower dispersion when the maximum rotation velocity is computed from the plateau of the HI rotation curve in comparison with the HI line width method. [Tully & Fisher \(1977\)](#) proposed a correlation between the HI line profile width ΔV_{HI} corrected by projection effects (i) and the luminosity (computed from M_B), given by a power law of the form:

$$L_B \propto \Delta V_{HI}^\alpha \quad (1.4)$$

where $\alpha = 2.5$ from this initial study, however from further studies it has been determined this slope is more constrained around the interval $\alpha = [3-4]$ and can vary depending on the band in which the luminosity is obtained, being larger for infrared to microwave bands ([Sakai et al. 2000](#), [Verheijen 2001](#)). Observations in radio providing a visualization of the distribution of neutral gas are those reaching the largest radius of detection (see Figure 1.6). Unfortunately, HI radio data are not always accessible in the local Universe and becomes undetectable at higher

redshifts due to the limitations of the current radio facilities. Instead various emission lines from the ionized gas with rest-frame wavelengths in the optical are used to trace kinematics. The most commonly used emission lines to recover dynamical features are: [OII] $\lambda\lambda 3727, 3729$, [OIII] and the Balmer lines H $\beta\lambda 4861$ and H $\alpha\lambda 6563$.

The computation of velocity is typically set at certain radii that trace most of the luminous profile, as a compromise between the dark matter halo extension and that of the kinematics tracer. The ideal configuration is to have detection at least until the turn over radius r_t at which V_{max} is reached. Another typical radial value used in literature to estimate the maximum velocity is r_{80} which contains 80% of the total luminosity, whose velocity is labeled as V_{80} . In addition, the velocity at $R_{2.2} = 2.2R_d$, denoted as $V_{2.2}$ is extensively used since $V_{2.2}$ traces the luminosity profile until the disk luminosity has decreased by an amount of $e^{2.2}$, in other words is where the peak of the rotational curve is expected to be reached for a pure exponential disk. As I previously mentioned in this study I used the $V_{2.2}$ value to build the TFR for our sample in order to encompass most of the luminous mass for disk-dominated galaxies. Sometimes velocity is also measured at $3.2R_d$ –a more extended radius for exponential disks– which corresponds to $V_{3.2}$, however for faint or small galaxies at intermediate redshift it is difficult to have detection at that extended radius. In a study from Courteau (1997) the scatter of the TFR was investigated using two different dynamic estimators: $V_{2.2}$ from H α observations and the integrated HI linewidths for local galaxies. Courteau (1997) found that the dispersion of the TFR is lower using $V_{2.2}$ compared to other TFR optical calibrations (using $V_{3.2}$, the turn-over velocity V_t), making these measurements the ones that best coincide with integrated ΔV results in radio wavelengths for galaxies in the local Universe.

Another version of the TFR that has proved to be consistently tight is the stellar mass Tully-Fisher relation (smTFR, see Figure 1.8), given by replacing the luminosity by the stellar mass computed from the M/L ratio applied to the light profile or from SED fitting. This is due to the direct relation between luminosity and the stellar mass content since for most of the rotation dominated galaxies the luminosity profile is dominated by the stellar continuum. Now if the fraction of gas can be computed the baryonic mass fraction can be used to prove the correlation with kinematics through the baryonic Tully-Fisher relation (bmTFR). The fraction of dust is assumed to be negligible so basically the baryonic mass corresponds to $M_b = M_\star + M_{gas}$. McGaugh et al. (2000; 2005) found that the smTFR has a large dispersion for small gas dominated faint galaxies, since their baryonic content is dominated by the gas and the luminous velocity might be underestimated. From the results it is observed the bmTFR is tighter than the smTFR, having low dispersion even for small galaxies. This is true in the cases in which data from the neutral gas is available since it constitutes most of the gas content in a galaxy. Nevertheless, accurate gas masses are not yet available at intermediate redshift, therefore some alternative indirect methods to determine the gas fraction from the emission line flux of ionized gas have been adapted in literature. One of the most used methods consists in inverting the Kennicutt-Schmidt (KS) law, which is the relation between the SFR and gas surface densities (Kennicutt, 1998), this assuming the gas density to be constant inside r at which V_{rot} is computed (Erb 2008, Mannucci et al. 2009, Puech 2010, Miller et al. 2013). It is also necessary to correct this estimation by dust extinction in order to have more reliable values of the gas fraction. In a study of the comparison between two different methods to estimate the gas mass performed by Miller et al. (2013), one using the inverted KS law and the second using an an-

alytical empirical formulation derived from CO observations presented by [Miller et al. \(2011\)](#). From the comparison it is concluded that the KS method leads to an underestimation of the gas mass with a ratio of $M_{\text{g}_{\text{CO}}}/M_{\text{g}_{\text{KS}}}$ equivalent to 1.1 for disk-dominated galaxies and 1.43 for the rest of the sample. The KS method was adapted to the [OII] doublet and applied to our sample. The estimations of gas mass fraction and the bmTFR are presented in [Abril-Melgarejo et al. \(2021\)](#) in section 5.5.

Multiple studies on the smTFR have been performed in the local universe ([Bell & de Jong 2001](#), [Masters et al. 2006](#), [Pizagno et al. 2007](#), [Torres-Flores et al. 2011](#), [Reyes et al. 2011](#), [Gómez-López et al. 2019](#)) showing a very good correlation between stellar mass and maximum rotation velocity. To trace evolution of the smTFR in terms of its zero point and its slope, it is necessary to have access to large datasets with a suitable sample selection strategy and sufficiently resolved data at intermediate and high redshifts. The pioneering study on the smTFR at intermediate redshift was performed by [Conselice et al. \(2005\)](#) at $z=1.2$ using long-slit data and near infrared photometry from 101 SF galaxies, finding no evolution with respect to the smTFR in the local Universe.

Afterwards, with the advantages of Integral Field Spectroscopy (IFS) which is an observational technique that allows to recover the spatial and spectral information of an object in a single exposure, obtaining a data-cube (see Section 2.2.2), it is possible to obtain spatially resolved kinematics. There is an increasing interest in the study of the TFR during and after the peak of the cosmic star-formation ($0.5 < z < 3$, [Madau & Dickinson 2014](#)) so some studies using IFS have been performed with this aim. [Puech et al. \(2008\)](#) was the first study using IFS data from the IMAGES sample at $z \sim 0.6$ finding evolution of the zero point towards lower masses in the IR luminosity and stellar mass TFRs, later [Puech \(2010\)](#) found no evolution for the baryonic TFR using the same sample. They also found high dispersion on the TFR attributing this to the fact that distant galaxies are more likely to have peculiar or perturbed kinematics.

At higher redshifts [Cresci et al. \(2009\)](#) using the SINS sample at $z \sim 2$, and [Gnerucci et al. \(2011\)](#) from the LSD/AMAZE sample at $z \sim 3$ found some evolution of the TFR. However [Vergani et al. \(2012\)](#) with results from the MASSIV survey at $z \sim 1.2$ did not find evidence of evolution. Other samples using long slit observations at $z \sim 1$ did not find any evolution (eg. [Miller et al. 2012](#), [Pelliccia et al. 2017](#)) although [Miller et al. \(2012\)](#) found an important offset in the B-band TFR ($\Delta M_B = 0.85 \pm 0.3$) towards lower luminosities between $1 \leq z \leq 0.3$. It is important to remark that for all these studies their parent samples had less than ~ 100 galaxies mainly composed of disk SF galaxies, which represents between 10% – 20 % of current IFS samples used for the same purpose.

Recently new samples have been enlarged up to ~ 1000 galaxies, including in some cases data from IFS instruments. That is the case of the multi-object IFS KMOS surveys KMOS^{3D} ([Wisnioski et al. 2015, 2019](#)) and the KMOS Redshift One Spectroscopic Survey (KROSS, [Stott et al. 2016](#)) which have been used to derived physical properties of distant galaxies. Even with the new IFS large surveys available the debate about the evolution of the TFR is still open.

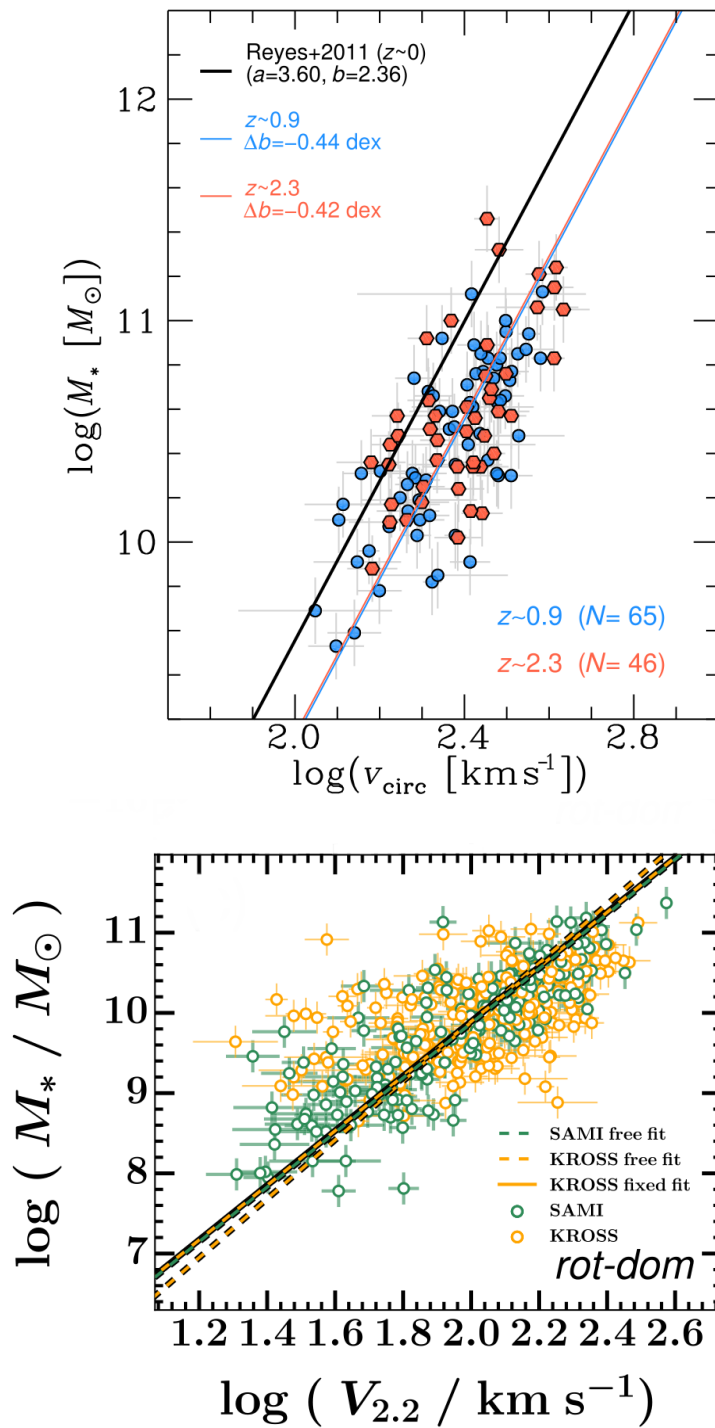


Figure 1.8: Upper panel: smTFR from \ddot{U} bler et al. (2017) comparing the fitting of two sub-samples from KMOS^{3D} at $z \sim 0.9$ (in blue) $z \sim 2.3$ in blue. They used the circular velocity (V_{circ} , this estimator uses a term to account for the velocity dispersion) from H α . The slope is fixed to that found by Reyes et al. (2011) in the local Universe. For the two subsamples at intermediate and high redshift there is a clear offset in the TFR zero point of $\Delta b = -0.44$ and -0.27 dex at $z \sim 0.9$ (in blue) $z \sim 2.3$ respectively. Lower panel: smTFR study from Tiley et al. (2019) using two samples of rotation dominated galaxies, one in the local universe observed by SAMI (Sydney-Australian-Astronomical-Observatory Multi-object IFS) and the other at $z \sim 1$ from KROSS. The slope is fixed for the local sample. There is no evidence of evolution from the comparison of the samples using $V_{2.2}$.

This is seen from recent results from a kinematic study using the KROSS sample (Tiley et al., 2019) from which there was no evidence of evolution of the smTFR with respect to results in the local Universe (see Figure 1.8 lower panel), whereas Übler et al. (2017) using the KMOS^{3D} sample found a clear offset in the zero point with respect to the results from (Reyes et al., 2011) for local galaxies (see Figure 1.8 upper panel). As can be seen, significant efforts have been made to study how the TFR evolves with cosmic time using various samples but the evolution of this relation with redshift is still a matter of debate due to the contrasting results among different studies. Besides, comparisons are not straightforward due to the differences in instrumental set-ups, the selection sample strategies and the methodology to extract kinematics.

1.5 Environment, from cosmic voids to clusters of galaxies

Galaxies form and evolve in different environments. They are arranged at large scales in structures shaped by the distribution of dark matter halos, like filaments, walls, clusters, and voids; in what is commonly known as the cosmic web. The evolution of a galaxy in a cosmic void – a low density environment – , may significantly differ from those embedded in big crowded structures like groups or clusters. After the maximum of cosmic SFR density (at $z \sim 2$) galaxy groups formed, assembled their mass and got virialized strongly affecting the star formation activity and morphology of galaxies inside them. So the intermediate redshift period between $z \sim 1.5$ to $z \sim 0.3$ is a fundamental transformation period during which galaxies actively evolved.

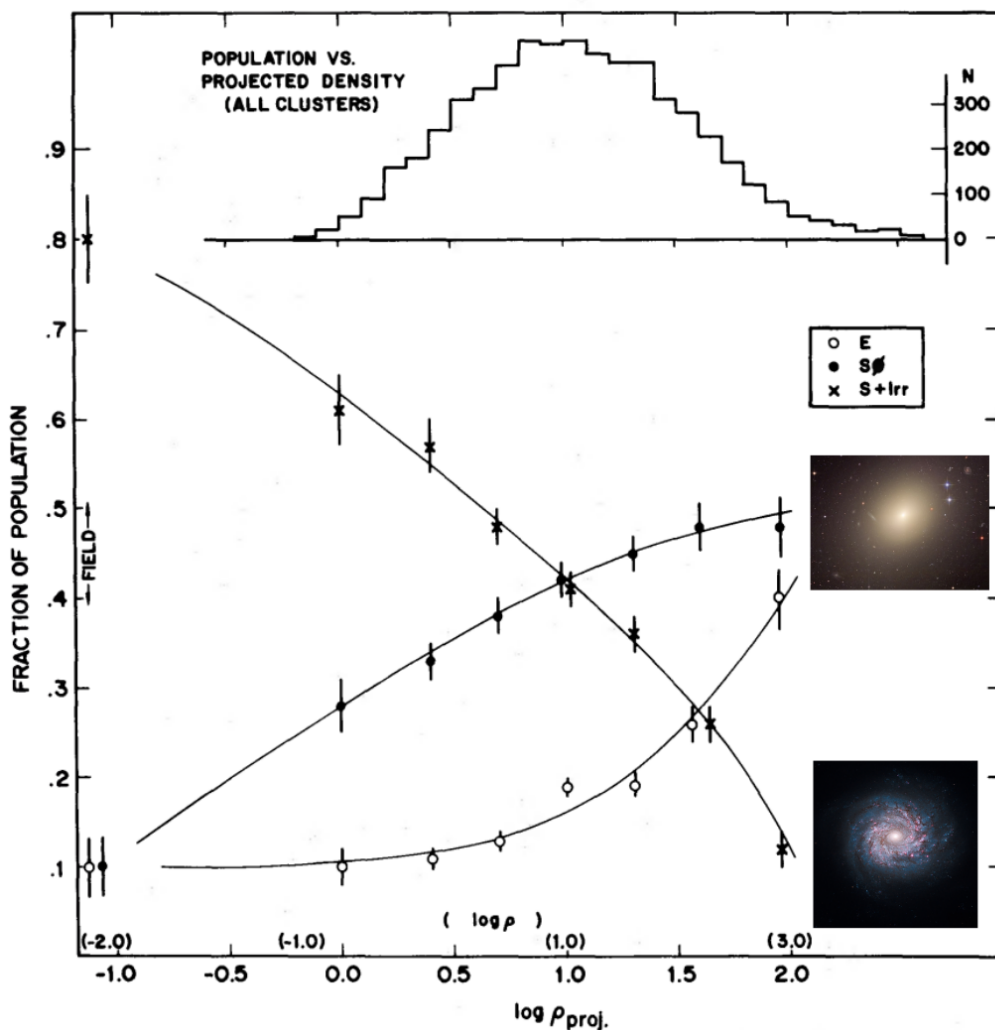


Figure 1.9: Evolution of morphological type fractions in function of projected density of the environment by Dressler (1980). Elliptical galaxies are represented by open circles, lenticulars by black dots, and disk-like galaxies (S and Irr) by crosses. Both the fraction of ellipticals and lenticulars increase with environment being the growing curve more pronounced for ellipticals. Regarding disk-like galaxies the tendency is the opposite, they are more present in low density environments. In clusters the presence of spirals and irregular is relatively low.

Some evidences of significant changes in some physical properties of galaxies in function of environment density have been observed in the local Universe and at intermediate redshift. Since the study performed by Dressler (1980) to investigate the fraction of different morphological types (E, S0 and S) in function of the projected density of 55 clusters (up to $z \sim 0.06$), it was established that dense environments are dominated by early-type passive galaxies contrasting with the observations in field where the largest fraction of about 65% is composed of spirals whose fraction decreases to about 35% in regions of high galaxy density (Schneider, 2007). In Figure 1.9 it is observed that when the density of environment increases, the fraction of late-type galaxies (blue curve) decreases considerably down to $\sim 10\%$ while the fractions of ellipticals (red curve) and S0s (black curve) increase up to almost 40 to 50% for each subcategory of passive galaxies.

Now I introduce the term *quenching* which makes a general reference to the decrease or cessation of star-formation by a set of different processes. From a very general point of view, quenching manifests as the change in color as a result of the migration of galaxies from the main sequence (known also as blue cloud) to the red sequence where the star-formation activity is low or negligible. Quenching is thought to be a determinant factor in the evolution of galaxies through cosmic time. Peng et al. (2010b) present a robust study on the mass and environment as drivers of galaxy evolution using data from the SDSS ($z < 0.1$) and zCOSMOS ($0.3 < z < 0.6$), finding on the one hand a correlation between the density of environment and the fraction of passive galaxies for low mass galaxies and on the other hand, a direct dependency of the increase of red galaxies fraction with the stellar mass for massive galaxies. In Figure 1.10 it is observed that if the average density of environment is larger, the fraction of passive galaxies increases, specifically for low and intermediate mass regime ($10^9 M_\odot < M_\star < 10^{11} M_\odot$), this effect is the so called ‘environmental quenching’. In Figure 1.10, for massive galaxies ($M_\star > 10^{11} M_\odot$) the fraction of quenched galaxies is high in all the environments being the stellar mass content a more determinant factor for quenching than environment, this is known as ‘mass quenching’.

All this empirical evidence suggests that galaxies in dense environments are quenched before their field counterparts. One of the aims of this project is to determine what are the mechanisms involved in the decrease of star-formation activity by determining which are the mechanisms at play to reduce the gas budget of galaxies, specifically in dense environments and also when those processes get efficient. In literature there are some mechanisms that have been identified as responsible of the gas loss in galaxies in dense environments. These mechanisms are the products of interactions of different nature: among galaxies, galaxies with the potential of the group or cluster or hydro-dynamical interactions with the intra-group/cluster medium, accretion of gas at large-scales or internal processes inside the galaxies.

Quenching mechanisms that efficiently remove gas from galaxies can be summarized as follows:

- ▷ **Starvation:** It is the halting of gas accretion from the large-scale intergalactic medium, known also as cosmological inflow (see Schawinski et al. 2014 and Trussler et al. 2020). Another mechanism that contributes to the supply of gas is the cooling of the hot gas present in the galactic halo which can become inefficient due to the heating of the infalling gas from the inter-galactic medium (IGM) by shocks when the mass of the halo is $M_{halo} \geq 10^{12} M_\odot$, this effect is known as ‘halo quenching’ (Schawinski et al. 2014 and

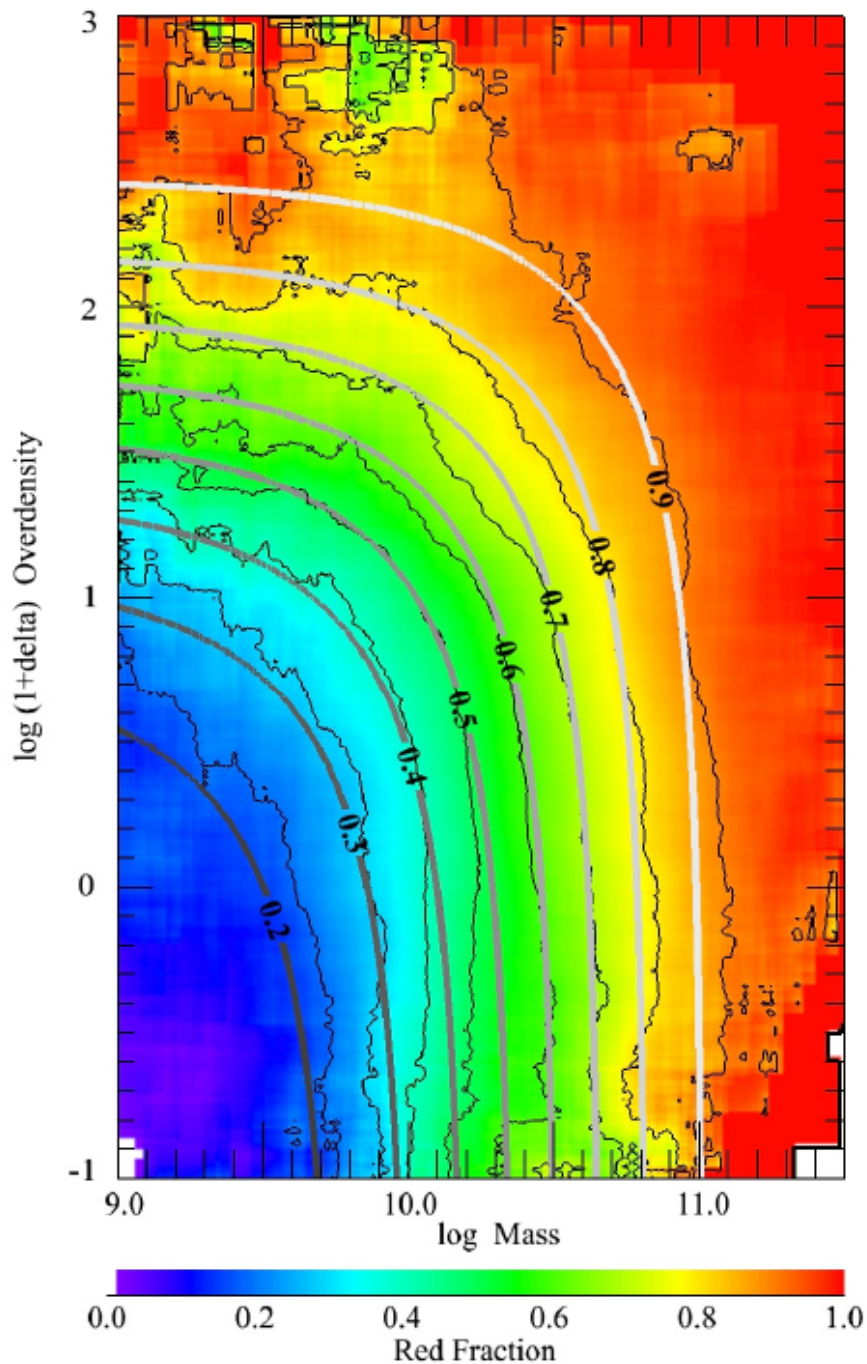


Figure 1.10: Fraction of passive galaxies in function of environment density and stellar mass from Peng et al. (2010b).

references therein). These two processes stop the supply of cold gas into the galaxies producing an unbalance between inflows and outflows conducting the galaxy to its quenching of activity.

- ▷ **Gravitational Interactions:** Interactions among galaxies are relatively common in dense environments. There are basically two types of these interactions:

- **Harassment:** It is due to multiple fly-by interactions with other galaxies and with the cluster gravitational potential. These processes can strongly disturb the morphology of the involved galaxies, producing in some cases visible changes like warps, asymmetrical distributions of stars, tidal tails, bars and localized episodes of starburst. Some studies have been performed on the rate of occurrence of this kind of interaction in a cluster (being higher in the central densest parts), and the effects on the morphology transformation induced by harassment (see for example, [Bialas et al. 2015](#)).
- **Tidal Interactions:** This kind of interactions consist on the merge of galaxies or strong interaction with the potential of the cluster or group. Both can radically change the pre-existing morphology of the involved galaxies.
 - galaxy-galaxy interactions: it can be minor or major mergers depending on the ratio of mass. Minor mergers are fed by small satellites or small transiting galaxies that are absorbed by the most massive one. Major mergers give origin to a completely new galaxy from the original galaxies in interaction and happens if the ratio in mass is at least $M_1/M_2 \leq 0.25$, i.e. if the smallest galaxy has at least a quarter of the mass of the largest galaxy ([Hopkins et al., 2010](#)). The most common result of a major merger is an elliptical passive galaxy.
 - galaxy-cluster interaction: in that case, the interaction between the galaxy with the cluster gravitational potential strongly affects the structure of the galaxy.
- ▷ **Ram pressure stripping:** A loss of gas is produced by hydro-dynamical interaction between a galaxy transiting through a dense structure and the intra-cluster medium (ICM), which can have high temperatures and densities. In the local Universe, galaxies with bright filaments of gas going out from their main structures have been observed. These filaments are oriented in the opposite direction to the galaxy trajectory, sometimes presenting star-formation along them which gives origin to long bright tails behind galaxies. These galaxies are known as jellyfish galaxies for their particular morphology that reminds those sea animals. In other scenarios, the stripped gas forms a diffuse gas structure around the affected galaxy, although sometimes it can be extended to several galaxies.
- ▷ **Internal triggered outflows:** These outflows of gas can be caused by Supernovae explosions, or driven by AGN or other objects like post-AGB stars or planetary nebula.

Another evidence of the influence of environment comes from the dependency of the mass-size relation on environment density at different redshifts. In the local Universe disk-like galaxies in clusters are more often found to be smaller than in less dense environments ([Weinmann et al. 2009](#), [Maltby et al. 2010](#) and [Fernández Lorenzo et al. 2013](#)); while this tendency is not completely clear for quiescent galaxies (see the review presented in [Matharu et al. 2019](#) and references therein). At intermediate redshift ($z \sim 1$) the studies from [Raichoor et al. \(2012\)](#) on early-type galaxies (ETGs) and [Matharu et al. \(2019\)](#) early and late types, support the decrease of the size of galaxies in function of environmental density. In the specific case of the most recent study ([Matharu et al., 2019](#)), it was performed using data from the Gemini cluster Astrophysics Spectroscopic Survey (GCLASS) and the Spitzer Adaptation of the Red Sequence (SpARCS), where they identified 10 massive galaxy clusters separating ~ 500 cluster member and 600 field galaxies. They found that on average, star-forming and passive galaxies in cluster have smaller sizes than the comparison sample in field by 0.07 dex for SF galaxies and 0.08 dex

of size offset for quiescent galaxies (see Figure 1.11).

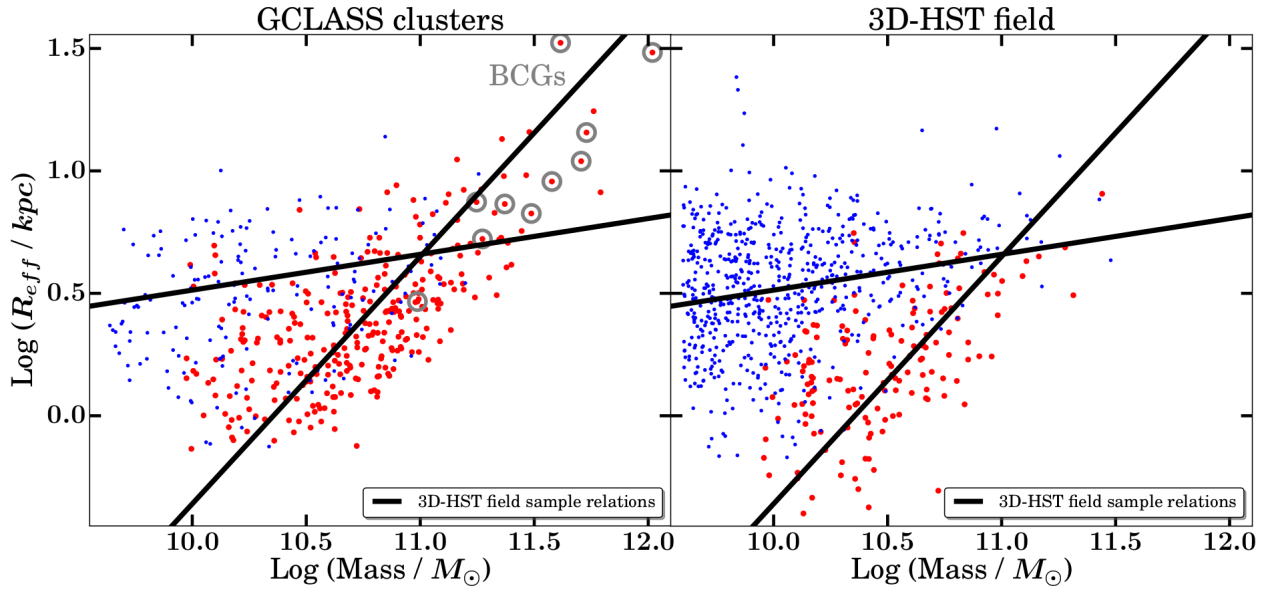


Figure 1.11: Global size of galaxies in function of environment from Matharu et al. (2019)

In this study of the variation of the global size of galaxies in clusters they also found that sizes of galaxies in clusters are equivalent to the sizes of SF and passive galaxies in fields in a previous epoch at $1.2 \leq z \leq 1.5$, which means environment has prevented the growth of galaxies between that period and $z \sim 1$. In Figure 1.11 a comparison between the mass-size relation for galaxies in clusters and in field is presented. Star-forming galaxies are represented as blue dots and passive galaxies as red dots in both relations. The lines of reference correspond to the mass-size relation in field for ETGs and disk-like galaxies. There are two main aspects that are visible in this comparison, the first is that there is a bigger fraction of passive galaxies in clusters and a larger fraction of star-forming galaxies in fields which is in agreement with results of prior studies in the local Universe and at intermediate redshift. The second result establishes that passive galaxies are in average more compact than star-forming galaxies at a given mass for both environments, so this configuration makes galaxies in clusters, which are mostly composed of passive galaxies, smaller than galaxies in field. Therefore, there is an effect of contraction directly proportional to the density of the environment. This result is important for our study as antecedent of the role of environment on galaxy size.

As summary, the main effects of environment on the physical properties of galaxies that are studied in this project are the quenching of star-formation and the impact on the size on a sample of galaxies in dense groups at intermediate redshift by their relation with changes in their kinematics parameters. This is done by means of a dynamical approach in which I extract the morphological and kinematics information to evaluate the changes in the stellar mass TFR with respect to other kinematics studies performed in denser environments (clusters) and in field. I then relate the kinematic evolution with the physical changes suffered by galaxies in terms of star formation rate (SFR) and the mass-size evolution. Additionally I also derive the stellar mass and baryonic mass fractions with respect to the total mass content given by the

dynamical mass estimation. All these gives enough information to propose hypothesis on the changes observed for each parameter in function of environment and taking into account all the evidences and antecedents I have introduced along this Chapter.

1.6 Outline

Below I briefly describe the structure of this Manuscript going through different instrumental techniques, the datasample, the methodology of analysis, the results of the research and the associated conclusions and future perspectives:

- ▷ In Chapter 2, I present a complete review on spectroscopy, spectrographs (Multi-Object and Integral Field Units) and spectrometers (Fabry-Perot, IFTS Michelson), used to derive physical properties of galaxies. I give an introduction to Integral Field Spectroscopy (IFS) and a detailed description of the IFS instrument MUSE-VLT, from which I use the data to study the kinematic properties of galaxies in dense environments. I also present a review on the main features of other IFU instruments like SINFONI and KMOS. I summarize some physical principles on the ionized gas nebular emission spectrum and I present the detection limits of the different instruments according to the redshift range of galaxies in the datasample. I give a technical comparison between 3D spectrographs (IFS) and instruments using two-dimensional spectroscopy with long-slit technique like VIMOS and DEIMOS. Finally, I present a summary of future IFS instruments to be used by the next generation of 30 meter ground-based telescopes and the James Webb Space Telescope (JWST).
- ▷ In Chapter 3, I introduce the high resolution photometrical data from ACS-HST and MUSE fields from the MAGIC (Muse gALaxy Groups In Cosmos) survey available for this study. I summarize the main properties of the studied galaxy groups splitting the sample into low ($z < 0.5$) and intermediate redshift ($0.5 < z < 0.8$). I make a comparison with other datasets available in literature for the study of morphology and kinematics of galaxies at intermediate redshift and I discuss why the MAGIC sample is the most suitable sample to study the impact of the environment on galaxy evolution. I present a summary on the selection strategy of the members of the galaxy groups applied to all the MUSE fields based on accurate spectroscopic redshifts. Through the inclination distribution, I argue the fact that the sample was randomly selected, this by comparing the observed distribution with the theoretical random distribution of inclinations.
- ▷ In Chapter 4, I describe in detail the morphological modeling on HST images and the kinematics extraction from the MUSE datacubes. I also describe the PSF computation process for HST images and for narrow band images from MUSE using Moffat and Gaussian profiles respectively. I give a mathematical description of the Sérsic and disk exponential profiles used for the bulge-disk morphological decomposition. I also provide a description of the computation of the global size (global effective radius R_{eff}), global luminosity and the luminosity ratios from the bulge-disk decomposition. I present examples on the diversity of morphologies found in the sample and how I include the modeling of some internal structures and other galaxies nearby the central galaxy in the field. I describe in detail the kinematics extraction of observed velocity and velocity dispersion maps. Finally, using a ramp velocity model I recover the maximum rotation velocity at a certain radius and the modeled velocity and velocity dispersion maps, among other kinematic parameters.
- ▷ In Chapter 5, I present the results of the Morpho-kinematic analysis described in Chapter 4, applied on the intermediate redshift sample and using the [OII]doublet flux. I

present the effects of the new selection criteria proposed to select the kinematic sample based on studying the impact of the size of the stellar distribution compared to the size of the MUSE PSF, and of the S/N of the [OII]doublet used to derive meaningful kinematics maps. The core of this Thesis project corresponds to the research article titled: "Galaxy Kinematics and the Tully-Fisher relation in dense environments from MUSE at $z\sim 0.7$ " ([Abril-Melgarejo et al. 2021](#)), which gives rise to a robust analysis on the scientific questions introduced in this Chapter 1. The article is presented in Section 5.5.

- ▷ In Chapter 6, I summarized the main results from the applied Morpho-kin analysis and I present the derived conclusions on the different hypothesis proposed to explain the results on the TFR. I also start a discussion on the implications/contributions of the proposed innovative kinematic selection strategy and the obtained results on ongoing and future research studies as a continuation of this project.

Chapter 2

Spectroscopic Instrumentation in Astrophysics

2.1 Introduction to Spectroscopy

Extracting most of the information contained in the light arriving from different astronomical sources is made through two main different techniques: photometry and spectroscopy. Photometry is the study of the flux or intensity of light from sources observed by deep images achieved by instruments with extended Field of Views (FoV), at high resolution, devoted to make big surveys covering big zones of the sky. These instruments are denoted as Imagers whose data in multiple bands are used to study color, morphology, computation of mass, dust attenuation, etc. On the other hand, spectroscopy is devoted to the study of the dispersed light in different wavelengths to extract physical characteristics as the chemical composition, dynamics, and in the case of galaxies it is useful to distinguish their different components as stellar populations, dust, gas and dark matter (more details are given in Chapter 1). In general, the instruments used to obtain the decomposition of light along the wavelength axis (spectrum) are Spectroscopes. Depending on the way how the generated spectrum is registered by the instrument, we can have Spectrographs or Spectrometers.

The main technical difference resides in the fact that a spectrograph obtains a unique image of the exposure during a unique reading of the image sensor, meanwhile the spectrometer obtains a scanning sequence from several readings of the image sensor. In other words, the spectrometer measures the intensity of the incoming light in short increments of wavelength in a determined range while the spectrographs generate the spectrum in a unique reading on a multichannel (multi-wavelength) detector.

Nowadays Imagers, Spectrographs and Spectrometers are the most common instruments used in Astrophysics Research. Typically, many astronomical observations start with the usage of imaging surveys with the aim to determine the targets of interest according to the study. This is complemented by spectroscopic observations to extract the physical characteristics that are only possible to obtain using spectroscopy as the ones mentioned above. There are two inconveniences with this methodology, one due to the time consuming observations in two fronts, with two different instruments and the second is the pre-selection of targets that limits the covered fields and introduces biases on the spectroscopic observations. To solve this, Integral Field

Spectroscopy ¹ (IFS) technique was developed combining in one instrument the capabilities of imagers and spectrographs/spectrometers.

2.2 Spectrographs

In general, a spectrograph is composed of an entrance aperture (slit mask placed in the focal plane of the telescope), a dispersive optical system, collimator and ancillary optics and a detector. This configuration allows the spectrograph to gather the light from the aperture, disperse it and register its spectrum that carries information about the medium in which the light was emitted and also the media with which light has interacted along its journey to the observer.

The aperture is typically a point or a long slit, the idea is to limit the entrance of light to get the spectrum of a very specific zone of the observed object. The slit also provides a stable spectral resolution. If no slit is used, then the dispersion will produce spectra all over the FoV causing the overlapping of the spectra from different sources including the sky background, which contaminates the target exposure. However, slitless spectroscopy is sometimes used by instruments on space telescopes given the low background in space and the high spatial resolution; in fact HST, EUCLID and JWST are all equipped with this mode.

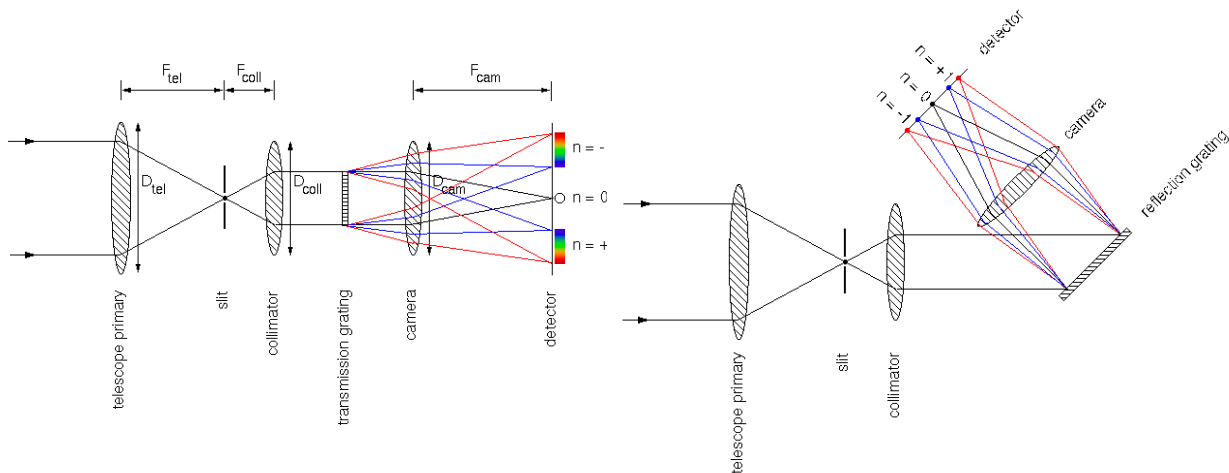


Figure 2.1: Left: Simplified Scheme of a Spectrograph using a transmission diffraction grating, showing the first order diffraction level spectra. Right: Similar scheme for a Spectrograph using a reflection grating. Credit: Both images were taken from the academic online article titled: [Basic Spectrograph design](#)

The dispersion of light is done by using a prism, a diffraction grating, or a combination of both devices. The prism works with the principle of refraction of light due to the difference of two propagation media (the air and the optical material from which the prism is made). Light changes its trajectory depending on the difference of refraction indexes between two different media. The deviation is also given by the variation of the refraction index of the glass (prism

¹Also known as 3D spectroscopy

material) which depends on wavelength of the incoming light. Then a light beam will be deviated after entering into the prism, in different angles corresponding to the different component wavelengths. The produced spectrum does not have a high resolution, since the dispersion power is too limited.

The diffraction grating is an arrangement of a large number of closely spaced consecutive grooves. These gratings can operate by transmission or reflection of the diffracted light beams (see Figure 2.1), causing different deviations at different wavelengths by an interferometry effect. The spectra produced by these gratings have a high resolution but the energy is distributed at different spectral orders (interference orders). To control this, sometimes the hybrid devices between gratings and prisms known as Grisms are used. The prism is used to control the dispersion order and the grating is used to obtain a high resolution spectrum. Usually, the spectrum is produced along the perpendicular direction with respect to the aperture.

As I previously mentioned, the apertures used are one-dimensional (a point or a line), sampling a very limited region of an object or FoV, so the solution strategy is to apply multiple slits on a FoV or to move/rotate a single long-slit along the observed object in different exposures depending on the science goals.

2.2.1 Multi-Object Instruments

Multi-object spectroscopy (MOS) is an efficient approach to simultaneously obtain the spectra of various objects in an extended FoV. These instruments are equipped with a multi-slit, multi-fibers or multi-hole mask system, produced with high precision laser-milled masks. For the MOS system tens to hundreds of small slits/holes are placed on a reception plate according to the target zones or objects under study. The plate contains several small slits/holes within the spectrograph's entrance aperture. The FoVs generated by these instruments are wide, ranging from 2 – 6 arcmin², so they also have a wide field imager mode, offering deep and extended survey observations. Many MOS instruments count also with longslit modes to study just one or few extended objects, that is the case of GMOS (Gemini North-South Multi-Object Spectrograph).

The imager mode is used to take exposures with broad filters and to pre-select the targets for a subsequent spectroscopic study. Several advantages are offered by MOS instruments: they have a high throughput sampling several objects in one exposure, the size of the slits can be adjusted as needed, there is a very good subtraction of the sky since most of the FoV is masked and the slits can be placed close together in the telescope focal plane. The drawbacks come from the considerable variations on the wavelength coverage due to the slit size and its position. The λ coverage could be very limited if a lot of slits are placed on the FoV. Under this configuration the area of the detector is not always used efficiently. Another inconvenience is the impossibility to sample all the two-dimensional FoV for an extended object in one exposure.

Despite the limitations, these instruments are currently widely used in the biggest observatories worldwide mainly due to the efficient sampling of many objects per exposure. Some examples using minislits masks are: VIMOS (VIisible Multi-Object Spectrograph), FORS2 (FOcal Reducer/low dispersion Spectrograph 2) and FLAMES (Fibre Large Array Multi El-

ement Spectrograph) at VLT; DEIMOS (DEep Imaging Multi-Object Spectrograph) at the Keck II telescope in Hawaii ; GMOS at the Gemini Observatory at Mauna Kea, Hawaii, among others. The MOS using multi-hole masks have been used to produce huge galaxy surveys like SDSS (Sloan Digital Sky Survey) and BOSS(Baryon Oscillation Spectroscopic Survey) both using the BOSS spectrograph MOS with a multi-hole mask, mounted on the 2.5m Telescope at APO (Apache point Observatory) in United States.

2.2.2 Introduction to Integral Field Spectroscopy

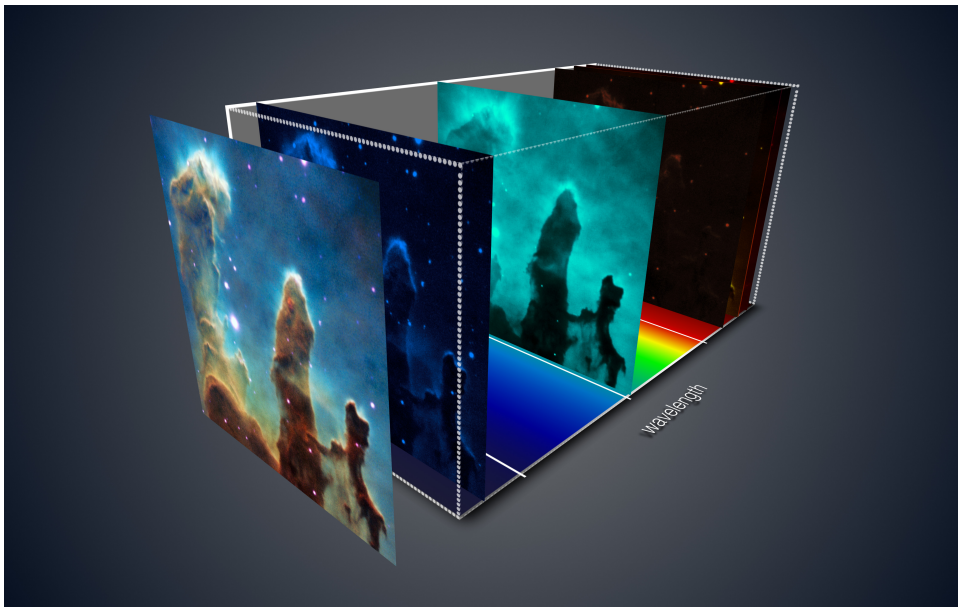


Figure 2.2: Graphic representation of a data cube using images from the MUSE data of the iconic pillars of creation nebula (in the star-forming region Messier 16) at different wavelengths. The front image is the stacked image obtained by collapsing all the datacube in λ direction. Each pixel in the spatial configuration contains information about the physical properties and the dynamics of the gas at that point. Credit: ESO

Integral Field Spectroscopy (IFS) is a relatively recent instrumental technique used in astronomical surveys, that allows to obtain by means of complex optical designs spatial and spectral information simultaneously, which offers different ways to perform research in Astrophysics. The beginnings of this technique go back to the 80s and 90s when different groups worked in instrumental designs using different optical elements. The technique was known by diverse names like spectral imaging, bidimensional spectroscopy, 3D spectroscopy, surface spectroscopy, IFS, among others. From that moment IFS has evolved a lot not only instrumentally but also in the reconstruction of the images, data reduction pipelines and data analysis. This technique has shown to be very powerful providing spatially resolved data, fundamental in the study of a variety of astrophysical phenomena which strongly increases the scientific interest on IFS. Nowadays, there are IFS instruments in several big telescopes (from primary mirror diameter of 3m on), around the world (See Table 1.1 of the book [Mediavilla et al. 2011](#)). The next generation of Space Telescopes will also have this kind of instruments, as an example the NIRSpec, an integral field Unit in the near infrared will be mounted on the James Webb Space Telescope

(JWST), see Section 2.6 for more details.

Commonly in Astrophysics photometric and spectroscopic studies are performed separately using different instruments and techniques. In traditional spectroscopy point like and long slit apertures are generally used in the focal plane of a telescope in order to collect a small quantity of light from the observed object (from a limited area of an extended object) which is in turn directed towards a dispersive element (prism, diffraction grating, or grism). Finally the decomposed light is directed towards a detector. The main drawback of this technique is that a very limited quantity of the total incident light from an extended object, is gathered, only a point or a line can be sampled each time. The last do not represent a problem for distant objects which angular size is smaller than the fiber or slit size used to sample it. Due to differential atmospheric refraction observations are greatly affected by the seeing conditions and when long slit are used there is a loss of light in the borders that has a strong dependence on wavelength (λ). Normally, to study an extended object various consecutive exposures are made by changing the position of the long slit aperture along the object, which could be time consuming. Besides, from one exposure to the other there could be a lot of changes like in the positioning of the slit, the seeing, etc. Since one of the objectives of this research is to retrieve the spatially resolved physical properties of the ionized, we need IFS observations that allow us to sample the distribution and the kinematics of the different components of a galaxy.

The IFS technique allows to collect light from an extended Field of view (FoV) by means of small aperture elements achieving a quasi-continuous sampling, this using specialized optical configurations. The light from each aperture is concentrated and addressed towards a spectrograph and finally to a detector. There are two main components in an Integral Field Spectrograph: an integral field Unit (IFU) and a spectrograph. The IFU splits the two-dimensional spatial plane into a continuous array depending on the optical structure. Each IFU has several spatial units to sample the small apertures of the FoV and are known as spaxels (spatial pixel). There are three different optical elements to build an IFU: lenslets (micro-converging lenses), optic fiber bundles and slicer mirrors (Figure 2.3). Each of these IFS techniques are explained with more detail in section 2.2.3.

In summary, we can define the Integral Field Spectroscopy as an observational method composed of an Integral field Unit, a spectrograph and a detector that obtains spectral information for each of the spatial elements of the IFU on a FoV, therefore an individual spectrum is associated to each spaxel. In practical terms IFS implies the decoupling of the image plane in the detector from the focal plane of the telescope, so the reconstruction of the original spatial distribution at each wavelength requires the usage of robust pipelines. The final product of the IFS observations is a datacube that is basically a composition of stacked images of the same FoV at different wavelengths. The datacube has three dimensions, two spatial x and y axis, usually corresponding to Right Ascension (RA) and Declination (DEC) and the wavelength along the z axis (See Figure 2.2).

The IFS has opened a new view on the study of extended sources, especially from galaxies since now it is possible to obtain bidimensional distribution maps of an object as illustrated in Figure 2.2 that represents a MUSE datacube of the star-forming nebula known as pillars of creation in the region of Messier 16. The advancement in Astronomical instrumentation has

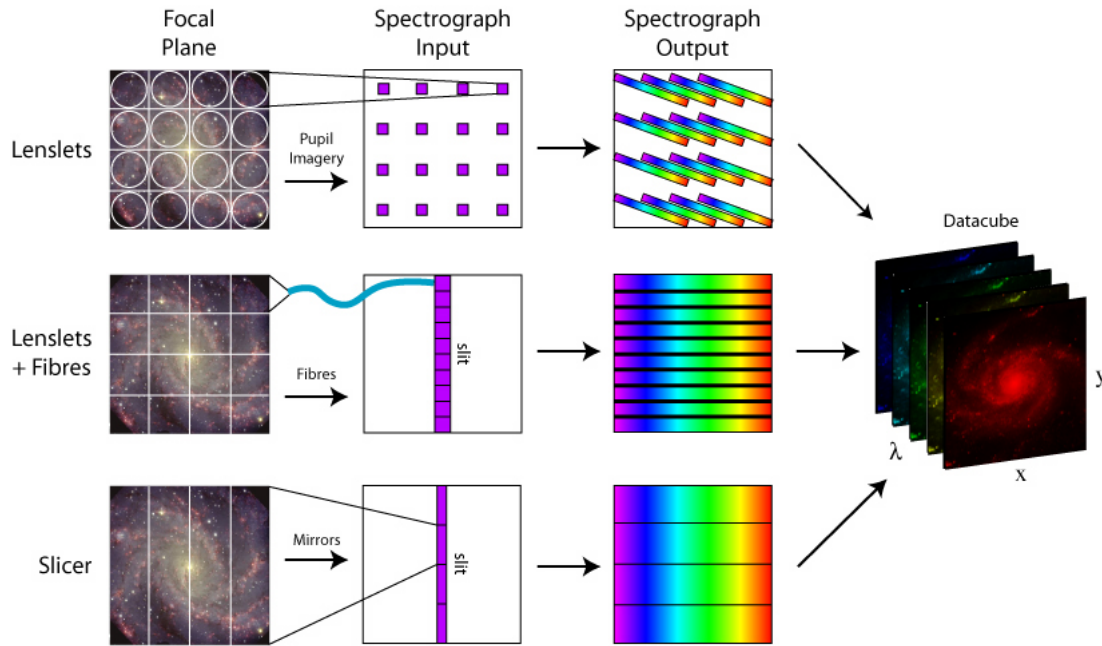


Figure 2.3: Three types of IFUs using different optical elements and arrays. Credits: M. Westmoquette, image adapted from Allington-Smith et al 1998. The image was taken from [IFS academic Wiki](#)

allowed the advent of big photometric and spectroscopic surveys, which have provided information on the integrated properties of galaxies. Nevertheless, these surveys have limitations in resolution and in 1D spectroscopy there are important aperture effects. The necessity to create new technologies to integrate the photometric and spectral information to disentangle the spatial distribution of the different components of a galaxy, is therefore obvious. A datacube gives information of multiple phenomena along the object what contrasts with the information given separately by photometric or 1D spectroscopic data.

Some challenges arise from the complexity of IFS datacubes like the spatial reconstruction from the image to the detector plane. Very efficient methods to solve this have been developed as I describe in this Chapter 2. From some of the instrumental devices used to sample and split the FoV it is evident that the spatial resolution is somehow more limited with respect to data from imagers, nevertheless with the advent of new optical technology and the Adaptive Optics techniques, extremely high resolutions can be achieved with IFS instruments (see Section 2.4).

In this work I use data from the Multi Unit Spectroscopic Explorer (MUSE; [Bacon et al., 2015](#)), instrument mounted in one of the 8m class Telescopes of the ESO Very Large Telescope Observatory at Paranal (Chile). MUSE is composed of 24 IFUs operating with slicer mirrors, in a wavelength range of 4650 – 9300Å. In the image plane MUSE samples a FoV of 1 arcmin² with a spatial resolution is 0.2"/pixel and a spectral sampling is of 1Å/pixel. More technical and scientific details are given in Section 2.4. All these instrumental specifications allow to sample galaxies at intermediate redshift ($0.3 < z < 0.8$) with enough resolution to extract maps of distribution of their physical characteristics. One of the objectives of this project is to extract and study the two-dimensional kinematics of the ionized gas of star-forming galaxies in dense

environments at intermediate redshifts, so the size of the FoV, the spatial resolution and the spectral coverage of MUSE make it suitable to perform such study, as will be showed along this document.

2.2.3 IFS Techniques

As was mentioned above, the goal of an IFU is to dissect a FoV on the sky into tiny areas, resulting in the spaxels of the produced datacube. The Euro3D ² consortium introduced the term spaxel to differentiate spatial elements in the in the focal (image) plane of the telescope from pixels that are the spatial elements in the plane of the detector (Mediavilla et al., 2011). After the reconstruction of the image plane, the spaxel can have different shapes depending on the optical pupils used in the IFU configuration. Then spaxels can be classified according to their geometry. The most common are the orthogonal spaxels (squares and rectangles) as product of a superposition of orthogonal exposures with slicers. When optical fibers or lenslets are used the spaxels can be circular or hexagonal (see Figure 2.5a). Likewise the size of the spaxel also depends on the IFU pupil size. To split the FoV there are basically four different methods using different optical elements: fiber bundles, lens arrays, combinations of lens and fibers and slicer mirrors.

Fiber Bundles

The optical Fiber technology was the first to be applied in the production of IFUs, and although the first prototypes were not optimized in efficiency, stability and other aspects, the first designs showed to be useful in the splitting of a FoV. Optical fibers are composed of three elements: a nucleus made of high refractive glass, a thin layer made of a less refractive material and a thick plastic protective layer. Fibers act like waveguides, when light enters at a certain angle (lower than the critical angle), it is reflected in the transition of the highly refractive nucleus and the less refractive external layer. The incident light beam performs several consecutive internal reflections, directing the light towards the other extreme of the fiber. When the incident angle is higher than the critical value, the beam doesn't complete the internal reflection being absorbed by the external plastic layer, then there is a certain light loss.

In terms of instrumental configuration fibers offer a practical advantage thanks to their flexibility, this maximizes the stability and gives more options of design of the instrument. In the IFUs, fibers are organized in bundles configured into several shapes, the most used arrays are square, hexagonal or circular. Each fiber will obtain a small contribution of light from the extended object which is transmitted to the spectrograph. As can be seen in Figure 2.4 the filling factor of the fiber bundles is incomplete for two reasons: the collecting area of a fiber is limited to the nucleus (the external layers do not contribute) and due to the circular shape of the fibers the consecutive packing of fibers let some void areas. To solve this issue some consecutive exposures are taken slightly changing the position of the fibers, this technique is know as dithering and assures the complete sampling. IFUs using fibers have a relatively low

²The Euro3D consortium gathers IFS Science produced by several instruments like PMAS, SAURON, VIMOS-IFU, GIRAFFE, OASIS among others, from 2003 to 2006. <https://www.aip.de/archive/www/Euro3D/publications.html>

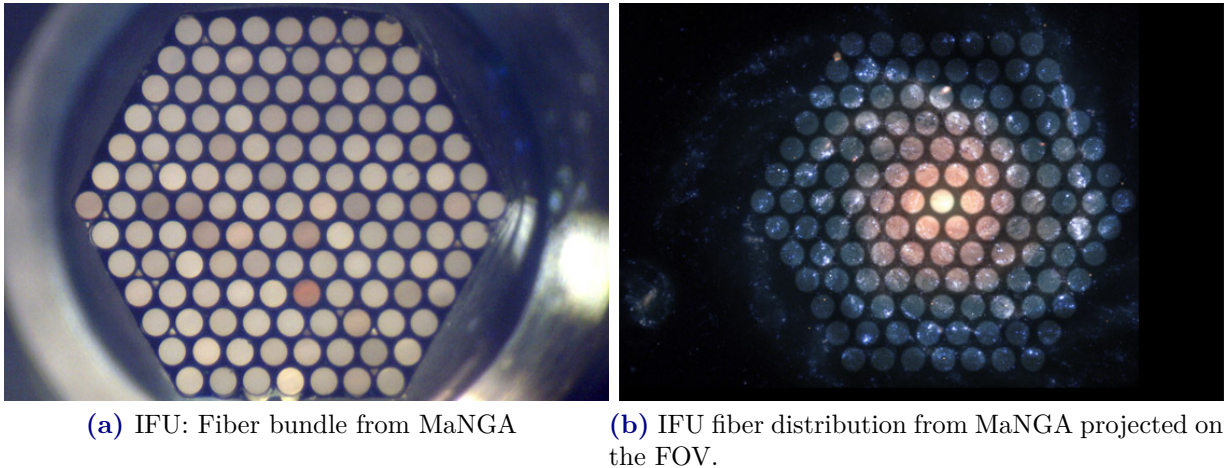


Figure 2.4: Left: Fiber bundle in an hexagonal array of the MaNGA IFU. Right: Scheme of the spatial configuration of the fiber bundle on the image plane from the MaNGA instrument. This illustrates how the IFU samples the galaxy in the example. Credits: Left: [MANGA SDSS](#). Right: [SDSS website](#)

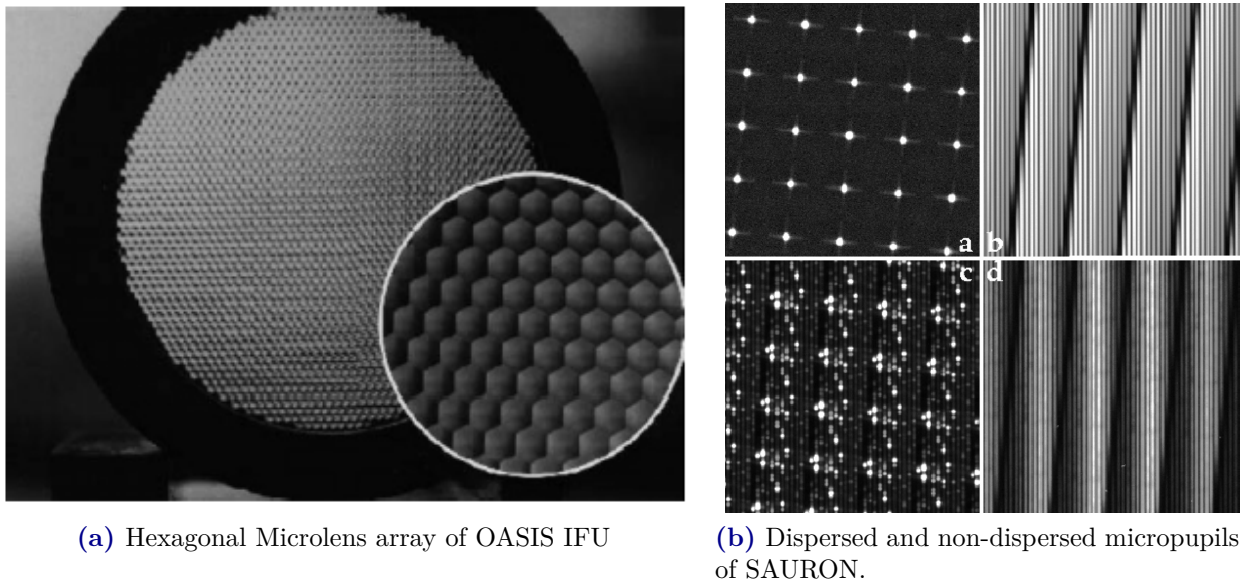
number of spaxels directly affecting the spatial resolution of the final datacube, on the other hand, a wide wavelength coverage can be achieved depending on the used spectrograph .

Currently highly efficient fiber IFUs are designed using several dithered exposures per datacube. Some instruments operating with this IFS technique are the Sydney-AAO Multi-object Integral field spectrograph (SAMI) mounted on the 3.9 Anglo-Australian Telescope (ATT), the Sloan Mapping Nearby Galaxies at APO (MaNGA) mounted on the 2.5m wide-angle optical Telescope at Apache Point Observatory and the Calar Alto Legacy Integral Field Area (CALIFA) with its IFU PPAK mounted in the 3.5 m telescope of the Centro Astronómico Hispano Alemán (CAHA). The three instruments operate in the optical range and are devoted to the study of galaxies in the Local Universe.

Lenslets: Microlens Arrays

Microlens Arrays (MLA) known in IFS as lenslets, are used to split the input image into small regions by concentrating the incident light from each lens into a point. Then the light is addressed towards a spectrograph to be dispersed. Lenslets operate by a principle of micropupil image that corresponds to the image of the aperture concentrated by the lens, that in this case is microscopic (see Figure 2.5b). Micropupils are equally spaced from the adjacent dot images so there is no spatial superposition, what allows to obtain a continuous sample of the image.

The drawback of this technique resides in the distribution of the spectra limiting the wavelength coverage, since the light is dispersed in the same position of the concentrated light from adjacent lenses, thus there is a limited space for the spectra as it is illustrated in the superior panel of Figure 2.3 that shows the spectrograph output for this technique. This directly reduces the efficiency of the CCD detector when the spectra are packed in this way. In order to maximize the usage of the detector's area and to avoid overlapping of the spectra, the dispersive element is slightly rotated producing an array of diagonal spectra in the focal plane of the



(a) Hexagonal Microlens array of OASIS IFU

(b) Dispersed and non-dispersed micropupils of SAURON.

Figure 2.5: Left: IFU of the OASIS instrument composed of hexagonal microlenses. Right: Example of the images produced in the detector of the instrument SAURON: a) non dispersed micropupils, this is the image of the incident light after been split by the MLA. b) flat field exposition. c) exposition of a calibration lamp d) Exposition of an astronomical object. Images taken from [Mediavilla et al. \(2011\)](#).

spectrograph, increasing a bit the wavelength coverage. Some truncated spectra can be also present in the borders of the detector.

The idea to use MLA to conduct astronomical observations comes from [Courtès \(1960\)](#). The first instrumental application of MLAs to perform 3D spectroscopy was the implementation of the prototype instrument TIGER1 in collaboration between the Observatory of Lyon (nowadays the Centre de Recherche Astrophysique de Lyon) and the Observatory of Marseille (current Laboratoire d’Astrophysique de Marseille), mounted on the Canada-France-Hawaii Telescope (CFHT) in 1987. This instrument was devoted to study galaxy nuclei but its potential to study other objects was evident, however it needed to be improved since it had a low spatial resolution of $1.2''$ per pixel and 80 spaxels. The instrument evolved improving its resolution to $0.7''$ /pixel and having 350 spectra per field in comparison with the 80 spectra in its beginnings. With the implementation of Adaptive Optics at the CFHT, and based on the design of TIGER1, the OASIS (Optically Adaptive System for Imaging Spectroscopy; [Bacon et al., 1995](#)) instrument was assembled in Lyon and latter tested at the Observatoire de Haute Provence in 1997. OASIS was first mounted at the CFHT but in 2003 was moved to the William Herschel Telescope (WHT), achieving high resolution datacubes ($0.09 - 0.42''$ / pixel) from small FoVs (from $2.7''$ to $12''$) and limited wavelength coverage ($\sim 800 \text{ \AA}$ per exposure). With the usage of different filters and grisms OASIS increased its wavelength coverage but this implied to take different exposures of the same object.

Compared with the fiber bundles, lenslets have a considerable advantage regarding the spatial sampling since the space between adjacent lens is small, avoiding big regions of no detection

between the spaxels. Nevertheless between neighbor microlenses there is an interface zone with no detection that represents a small percentage of the area covered by the MLA. Examples of instruments using MLAs are: TIGER1 at the CFHT, OSIRIS at the Keck Observatory and SAURON and OASIS, both mounted at the William Herschel Telescope (WHT).

Hybrid arrays: Lenslets & fiber bundles

As solution to the problem of overlapped and truncated spectra for the instruments using only MLAs, fiber bundles are incorporated in the composed IFUs. Like this there is a double advantage since the coverage of the FoV is more continuous and the spectral range is not longer limited to the detector's area when the fibers are used to transfer the light to the spectrograph. Each fiber receives the micropupil light in the output plane of the MLA. In such a way, the geometry of the MLA can be modified into a pseudo slit, thus all the extension of the detector can be used in the direction of the dispersion.

Unlike the instruments only using fibers or lenslets, these hybrid arrays suffer additional losses of light because the incident beams have to pass by this combination of optical elements. Such losses depend on the image quality of the MLAs, the precision of the alignment between the fiber and the micropupil, and the losses due to the fibers. Some examples of instruments using this hybrid arrays are: SPIRAL (rectangular array of lenslets and fibers)+AAOmega(spectrograph) in the Australian Astronomical Observatory (AAO), GMOS-IF at the Gemini Observatory, FLAMES(GIRAFFE)-IFU at the VLT and the VIMOS (IFU mode) at the VLT.

Image Slicers

IFUs using slicer mirrors are the most efficient in sampling an extended FoV and do not have limitations in the spectral coverage, thus is the preferred technology for IFS instruments to operate on the biggest telescopes in the world. That is the case of current instruments like SINFONI, MUSE, KMOS at VLT; and the next generation of instruments like Blue MUSE projected for VLT and HARMONI which will be mounted on the Extremely Large Telescope (ELT, ESO Armazones).

The input image is formed on a segmented mirror, composed of several horizontal slices (see Figure 2.6). Each slice is slightly rotated with respect to the previous one, so each slice conducts the incident beam into different directions. A second segmented mirror (the pupil mirror) are configured to reorganized the space configuration of the slides, so that instead to be one over the other they are side by side with the aim to reproduce the spatial distribution of the slit at the entrance of the spectrograph. Finally, the last group of mirrors (slit mirrors) direct the slices of the original FoV towards the long slit of the spectrograph. This technique gives a continuous spatial sampling with a high resolution in the image plane. This kind of IFU technique is the most suitable to achieve an ideal integral field spectroscopy since up to now splitting the FoV in slices is the most efficient way to get a continuous sampling, light losses between slicer mirrors are the lowest compared to the other methods. The main disadvantage are the high production costs of the optical components, mainly due to the required microscopic precision in the production of the slicer, pupil and slit mirrors, and the complexity of the design

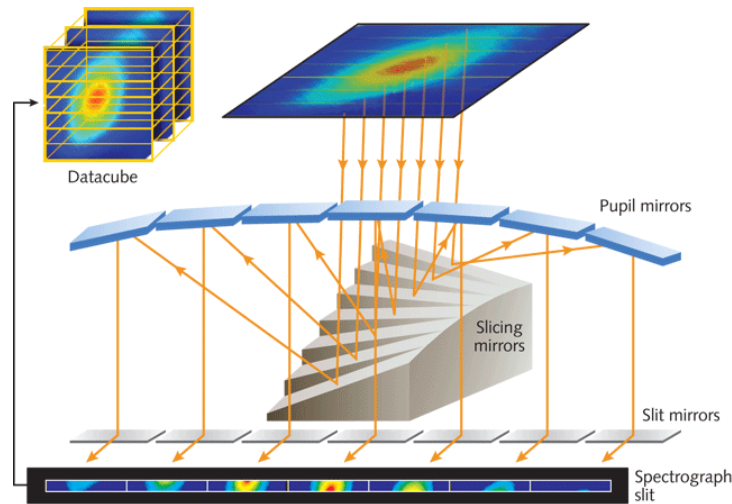


Figure 2.6: Configuration of an IFU using a slicer mirror that dissects the input image in N horizontal slices. The light from all the slices is reorganized and directed towards the spectrograph slit. Credits: STScI/NASA

of slicer mirror IFU instruments.

If the goal is to achieve the maximum number of spaxels with the least possible loss of light, then the slicer technique is the most efficient compared with fibers and lenslets. Slicer IFUs are besides designed to minimize slit losses of the conventional spectroscopy. Furthermore slicer IFUs offer the most efficient and densest packing of information in the detector. The first image slicers were used by instruments operating in the near infrared, like SINFONI. In the 2010s with new technology in the micro polishing the diamond-turning technique was created in order to produce spherical or aspherical lenses and mirrors with an extremely smoothed surface. Only then was possible to get low scatter high-quality optical elements required to perform the slicer technique in the optical domain (Bacon & Monnet, 2017). It was like this that the creation of the instrument MUSE was possible.

Some other instruments using image slicers are: WiFeS mounted on the 2.3m telescope of the Australian National University Observatory; NIFS in the Gemini Observatory and FRIDA on the Gran Canarias Telescope (GTC).

2.3 Spectrometers

Spectrometry makes reference to the measure of the spectrum, in other words it is a technique to measure different properties stored in the observed distribution of energy. A Spectrometer is then an instrument used to probe a property of light as a function of wavelength, frequency or energy. Usually the measured property is related to the flux or intensity of light, and in some cases the polarization can also be used. Spectrometers can technically cover a wide range of the electromagnetic spectrum but most of them operate in specific ranges, depending on the used instrumental technique.

We are interested in two specific instruments which use interferometric scanning systems

(known also as scanning filters [Bacon & Monnet 2017](#)): the Imaging Fourier Transform Spectrometer (IFTS) and the Fabry-Perot interferometer. These instruments are based on the optic interference phenomenon, modulating the incoming flux allowing the imager part of the instrument to work independently, at a high performance. The decomposition of light in these devices is obtained from the obtained interferograms. The splitting of the incoming light in two or several paths, makes the light beams to interfere at the output configuration. The output signal corresponds only to the interference pattern of transmitted wavelengths (determined by the lengths of the light paths interfering), then making a scanning on different wavelengths the intensities of each one can be retrieved with high precision. As a result, it is possible to recover the spectral information from the output interferograms, thus these spectrometers are also considered as Integral Field Units, allowing to obtain a datacube of an observed FoV. All this is done by means of different optical arrangements I further describe in the upcoming subsections.

2.3.1 Fabry-Perot

A Fabry-Perot Spectrometer is composed of two parallel semi-reflective plates, between them light is reflected several times (see [Figure 2.7](#)). After each reflection part of the light is transmitted and reaches the outer surface. Then, at the output of the device all the resulting beams from each reflection pass through an optic converging system and they finally interfere at the detector plane. Due to the numerous rays interfering a high resolution interference pattern is produced, this is comparable to the case of spectrographs using gratings since the number of grooves in a diffraction grating increases its resolution. The wavelength is regulated directly by the spacing between the plates, since only the wavelengths as entire multiple of the spacing will interfere constructively ($m\lambda \sim d$), consequently only those wavelengths will be effectively transmitted. The spectra is therefore obtained by making a sequential scanning by varying the spacing by small steps.

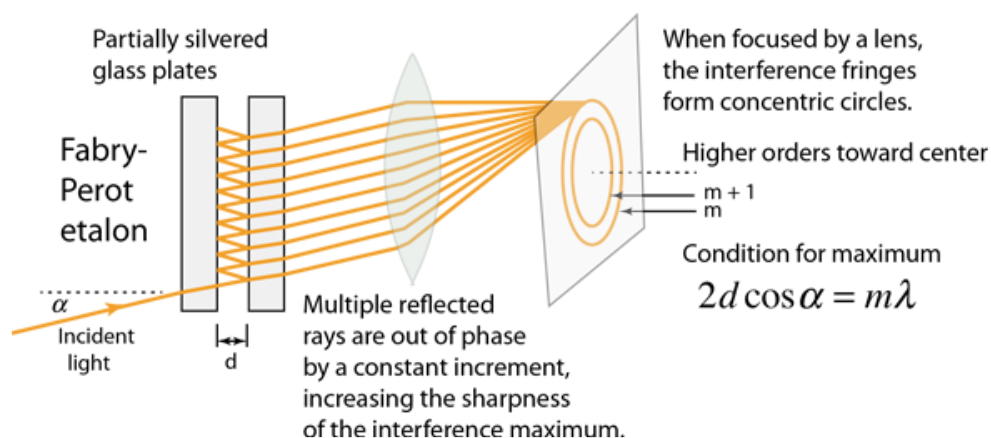


Figure 2.7: Diagram of the basic components and functioning of a Fabry-Perot interferometer. Light beams enter into an interference box composed of two parallel plates which are highly reflective in their internal surfaces. The parallel rays transmitted by the etalon are after focused on the detector plane where a concentric ring interference pattern is obtained. Credit: [HyperPhysics](#)

The parallel glass plates have highly reflective ($R \geq 90\%$) coating in their internal surfaces while an anti-reflective coating in the outer surfaces to avoid artifacts and external interference. The spacing between the plates varies from microns to few millimeters for astrophysical purposes. The separation of the plates must be checked at $\sim 1\%$ of λ precision, which implies an important challenge in the visible and infrared ranges (Bacon & Monnet, 2017).

A beam with an incident angle α with respect to the normal of the first plate (incident surface), suffers several reflections inside the Fabry-Perot cavity (etalon) with an optical length of $2nd \cos\alpha$, between consecutive reflections. In this expression n corresponds to the refractive index inside the etalon, then we assume $n=1$ (the refractive index of air). Since the wavelength of transmitted rays is proportional to the separation of the plates and assuming an ideal case where interference is perfectly constructive the difference between consecutive output beams is proportional to wavelength, this led us with an interferogram of concentric very thin circles represented by the canonical Fabry-Perot phasing equation:

$$2d \cos\alpha = m\lambda \quad (2.1)$$

where m is the etalon order, usually a positive integer in the range 200 – 2000. All the light rays fulfilling this condition will be fully transmitted while the others will be reflected back in the source direction. The transmission percentage in function of wavelength (the transmission function), for the ideal case of 100% transmitted light at any fixed incident angle α , is a Dirac peak function (zero width) at the wavelength of the source light (see left Figure 2.8). If just one wavelength is subject to study the other peaks are filtered out by the usage of special interference filters, this is the most common method to define the desired wavelength range. According to the phasing equation 2.1, the wavelength varies on the field with a circular symmetry, this agrees with the concentric rings interferogram that is obtained from the observation of monochromatic light (see left Figure 2.8). Each ring corresponds to an interference order and has a radii of α_m given by the phasing equation 2.1. Then different wavelengths correspond to a set of rings with different sizes.

There is a parameter to measure the quality of the transmission that is known as finesse. It is defined as the ratio between the free spectral interval (separation between peaks) and their full width at half maximum (FWHM), as $F_\lambda = \Delta\lambda/\delta\lambda$. This parameter is translated into the number of independent spectral bins that are distinguished (in the data), which corresponds to the number of transmitted parallel rays from a single source ray (in the etalon). The finesse parameter is also defined in terms of the reflectance factor R as $F_R = \pi\sqrt{R}/(1-R)$. Then the normalized intensity of the transmitted light as a function of λ is an Airy Function (Bacon & Monnet, 2017),

$$I_T(\lambda, \alpha) = \frac{1}{1 + F^2 \sin^2 \pi \frac{(\lambda - \lambda_0)}{\Delta\lambda}} \quad (2.2)$$

where $\Delta\lambda$ is the free spectral interval and λ_0 is wavelength of the maximum transmission. $\Delta\lambda$ also depends on the order of interference $\Delta\lambda = \lambda_m/(m - 1/m)$ which is simplified to $\Delta\lambda = \lambda/m$ for big orders. Taking the definition of finesse as $F_\lambda = \Delta\lambda/\delta\lambda$ and the definition of the free spectral interval $\Delta\lambda$, we can determine the spectral resolution that by definition is $R_\lambda = \lambda/\delta\lambda$, as equivalent to $R_m = mF_\lambda$, in terms of the finesse and the interference order. From these definitions we can observe that the resolution is related with the FWHM of the

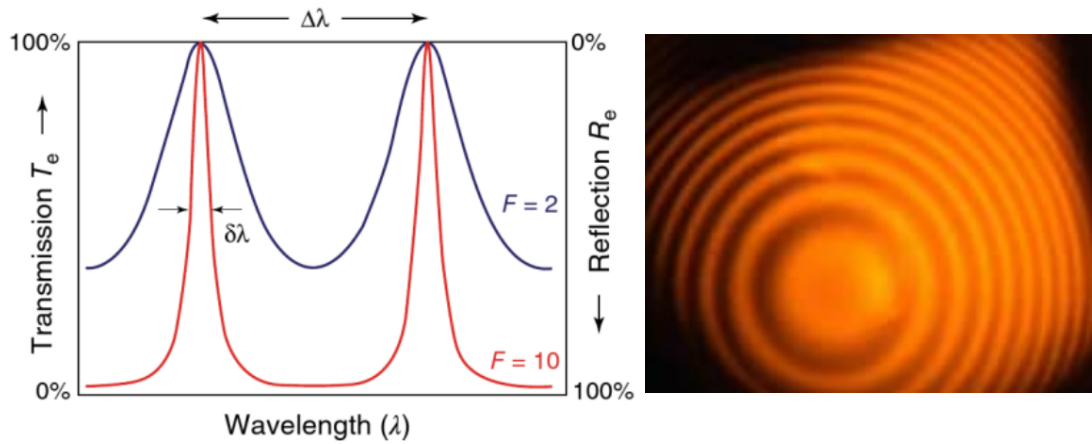


Figure 2.8: Left: Transmission function showing the pick of transmission and their different FWHM ($\delta\lambda$ in the image) depending on the finesse of the interferogram. $\Delta\lambda$ corresponds to the free spectral interval. Sharper maximums denote higher reflectance of the interior etalon surfaces. Credit: [Bacon & Monnet \(2017\)](#). Right: The concentric ring interference pattern obtained using a sodium lamp from a commercial Fabry-Perot interferometer. Credit: [HyperPhysics](#)

rings in the interferogram, being high F values corresponding to very thin rings (red peaks in Figure 2.8) and thicker rings corresponding to a lower finesse (blue peaks in Figure 2.8).

The versatility of these instruments resides on the possibility of adjusting the wavelength range to that of the expected spectral patterns of the observed object. This applies very well to the kinematics of extended objects like nebulae and galaxies. At LAM our research group widely uses this kind of instruments producing research on the kinematics of galaxies in the local Universe. The group uses the PUMA instrument (the UNAM scanning Fabry-Perot interferometer, [Rosado et al. 1995](#)), installed in the Observatorio San Pedro Mártir in Mexico and the GHASP instrument (PI: P. Amram) operating at the Observatoire de Haute Provence (OHP) in France, both mounted on 2m class telescopes. Some successful surveys and studies have been developed with these instruments (e.g. [Epinat et al. 2008](#) and [Gómez-López et al. 2019](#)), due to the high spectral and spatial resolution to retrieve kinematics maps of the main nebular lines in the optical.

2.3.2 IFTS - Michelson

An IFTS is equipped by a Michelson interferometer and a two-dimensional imaging detector. The interferometer works with a beamsplitter plate that directs half of the light towards two different mirrors, one fixed and one movable, located perpendicularly to each other, forming two paths with different length. The beams have a second reflection on the mirrors and are reflected back to the beam splitter where part of the light is transferred towards the detector where the interference pattern is recorded. The movable mirror can be moved in the direction of the incoming light, then the interferometer scans the optical path difference (OPD) of the two wavefronts by a step by step variation method. The detector records the interference map of all the pixels of the FoV simultaneously, making an efficient usage of the detector area. The datacube containing the spectral information is recovered after applying the Fourier transform

of the 3D interferogram.

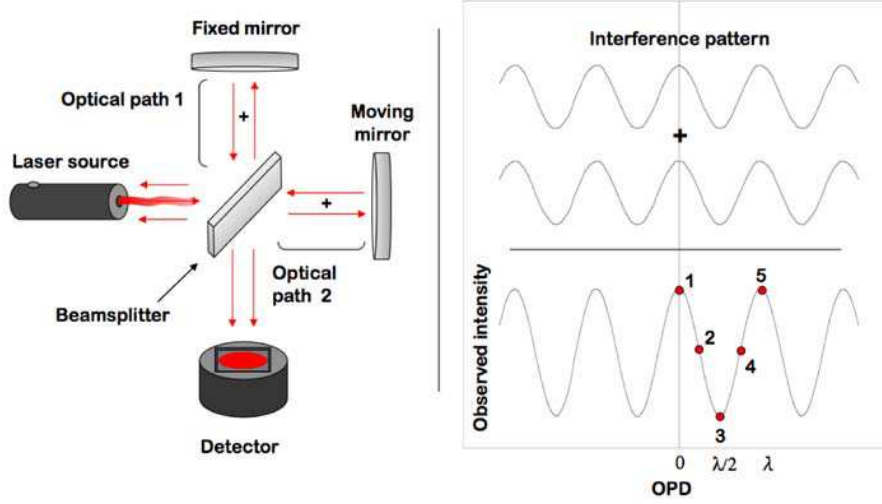


Figure 2.9: Configuration of a classical Michelson interferometer and the recording of the interferogram at the detector, due to the Optical path difference of the two beams interfering. The intensity in the detector varies according to the length of the displacements of the movable mirror. Taken from [SITELLE instrument website](#).

The fringes from the interference pattern vary their position when the OPD is scanned by moving the mirror away from the zero path difference (ZPD). Indeed the OPD is not constant in all the FoV since light enters at different angles from pixel to pixel. The output interference pattern depends on the configuration of the mirrors, i.e. for classical Michelson interferometer circular fringes are detected but some interferometers have an off-axis configuration, registering just the edges of the interference pattern. What is obtained in the end are interferogram cubes composed of the image of the sky with the interference fringes on it, so for each spatial pixel there is a corresponding interferogram. The Fourier transform of the interferogram cube is then the spectral cube.

The Rayleigh criterion establishes the minimum separation of two emission lines to be resolved as separated objects, so the distance between the two peaks of the lines should be larger than the length between their peaks and their first minimum ($\lambda/2$). Minimizing the Fourier transform of a monochromatic signal with a spectrum of the form $\text{sinc}(x) = \sin x/x$ – where $x = 2\pi L(\varphi_1 - \varphi_2)$, φ is the wavenumber and L is the maximum OPD scanned by the IFTS –, the spectral resolution can be obtained as follows:

$$2\pi L(\varphi_1 - \varphi_2) = \pi \quad (2.3)$$

then

$$(\varphi_1 - \varphi_2) = \frac{1}{2L} \quad (2.4)$$

Thus the minimum separation between two lines that can be resolved, in terms of wavenumber is $1/2L$.

There are three main advantages of these IFTS over other IFS instruments. The spectral resolution can be adjusted/modulated with the variation of the OPD ($\delta\varphi = 1/2L$). The signal-to-noise ratio (S/N) is considerably higher compared to a spectrograph (even with multiple IFUs), due to the fact that an entire bandpass is observed/registered at each step of the scanning (The multiplex or Fellgett advantage). An IFTS can gather more power obtaining higher intensities than a spectrograph, given a comparable collecting area and spectral resolution (the throughput advantage). As we see, IFTS offers the most flexible selection of spectral resolution and size of the FoV, achieving high values for both parameters (Maillard et al., 2013).

IFTS instruments currently operating in the visible up to sub-milimetric domains are few. Two examples are SITELLE (Fourier Transform Imager Spectrometer for the study of the long and wide of emission lines, from its acronym in French), Mounted in the Cassegrain focus of the 3.6 m CFH Telescope and SPIRE (Spectral en Photometric Imaging Receiver) operating on the Herschel space telescope in mid-infrared. Due to all the advantages we mentioned there are several projects to build this kind of instruments in the near future like OFIUCO (Optical Fourier-transform Imaging Unit for Cananea Observatory) to be mounted on the 2m telescope at the INAOE Cananea Observatory in Mexico. Another example is the Molecular Hydrogen Explorer (H2EX), a medium class mission proposed for ESA 2015 - 2025 Cosmic Vision Call. Although it has not been yet selected by ESA, the idea is that H2EX will be equipped with an IFTS whose aim is to detect and to map the distribution of molecular Hydrogen in objects from young star clusters to distant galaxies (Boulanger et al., 2009).

2.4 MUSE: The Multi Unit Spectroscopic Explorer



Figure 2.10: Left: Image of the MUSE instrument mounted on the Nasmyth B platform. The complex structure of the instrument is evident in this image showing the 24 cylindrical compartments corresponding to the different image splitter and IFU modules. Behind, the structure of the UT4 Yepun Telescope and its secondary deformable mirror as part of the Adaptive Optics Facility (AOF). Right: An external view of the building hosting the Yepun Telescope and the Four sodium Lasers operating as part of the AOF. In the background the UT1, UT2 and one ancillary VLT telescopes. On the sky the center of the Milky way can be observed. Credits: V. Abril-Melgarejo/ MUSE GTO P102-28 Observing run on Oct 2018

The Multi Unit Spectroscopic Explorer (MUSE) is a second generation panoramic integral-field spectrograph designed for Yepun, one of the Unit Telescopes (UT4) with a primary mirror of 8.2m at VLT. MUSE was conceived in 2001 with the main goal to explore the very distant Universe by combining simultaneously the survey capability given by an extended FoV and the spectroscopic facility given by the IFUs. The conceptualization, design, construction, calibration and implementation took around 13 years with the participation of seven European research institutes which constitute the MUSE consortium³ CRAL (Centre de Recherche Astrophysique de Lyon - France), IRAP (Institut de Recherche en Astrophysique et Planetologie), AIP (Astrophysics Institute Potsdam - Germany), ETH (Institute of Astronomy Zurich - Switzerland), IAG (Astrophysics Institute of Gottingen - Germany), Leiden Observatory (Netherlands) and ESO (European Southern Observatory). The data analyzed in this research project comes from the Guaranteed Time Observations (GTO) from the MUSE consortium, under the program to investigate the role of environment in galaxy evolution in the past 8 Gyrs (PI: T. Contini).

³The Laboratoire d'Astrophysique de Marseille (LAM), participates as support Laboratory, two researchers and one PhD student are to the date part of the MUSE consortium. The GRD group at LAM is also involved in the AOF development for MUSE and on maximization image processing.

The first light of the instrument was obtained on 31st January 2014 after a careful assembling and calibration process of three years at CRAL and the shipping and mounting process on the Telescope for two months. Since then, MUSE has proved to be a very powerful instrument, producing huge quantities of information (400 Gbytes/ min) for multiple scientific purposes. Although MUSE was in principle optimized to study formation and evolution of galaxies, it can be used for a wide range of research topics like the study of globular clusters, HII regions and AGNs in nearby galaxies, stars and resolved stellar populations, production of massive spectroscopic surveys of stars, the study of atmospheres of outer planets (solar system in general), serendipity, etc (Bacon et al., 2006).

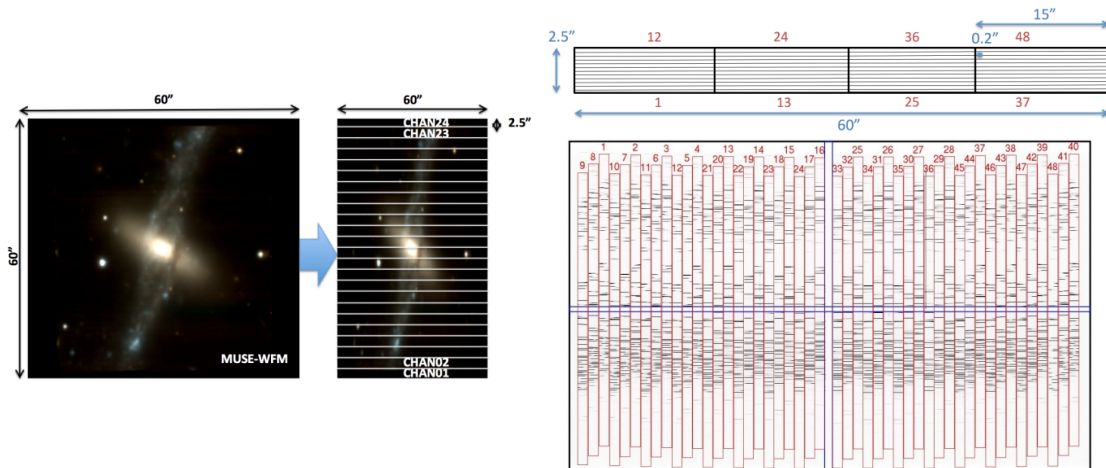


Figure 2.11: Left: MUSE image of the galaxy NGC 4650A in WFM observed by MUSE is first split into 24 slices, each corresponding to a channel and to an IFU. Right superior panel: The spatial configuration of the sliced image from one channel after being split by the slicer mirrors, the main optical component of the MUSE. Right inferior panel: The arrangement of the 48 spectra obtained by the Spectrograph in the detector plane. Credit: ESO.

MUSE is mounted in the Nasmyth B focus platform of the UT4 (the one corresponding to the optical range, See Figure 2.10 - Left), accompanied in the same telescope by HAWK-I in the Nasmyth A focus. MUSE is a complex instrument composed of 24 modules each one equipped with two series of 48 slicer mirrors (IFUs), 48 spherical focusing mirrors, a spectrograph and a $4k^2$ CCD detector.

Hereafter, I briefly describe the splitting process of the image of the observed object and the reconstruction of the image in the plane of the detector. The light from a galaxy for example, is collected in the telescope and directed to the Nasmyth focus where it arrives to the entrance aperture of the instrument, which in turn translates into a FoV of 1×1 arcmin² for the Wide Field Mode (WFM) and 7.5×7.5 arcsec² for the Narrow Field Mode (NFM). There, light is received by a fore-optics complex starting by a derotator that compensates for the field rotation at the Nasmyth focus, later the image is stabilized and magnified to be sent to a field splitter mirror that divides the original FoV into 24 sub-fields (see the left panel of Figure 2.11). Each sub-field is addressed to 24 different modules containing the IFUs, where each of the original 24 slices are further split into 48 minislits of $15'' \times 0.2''$ (see the right superior panel of Figure 2.11), giving a total of 1152 mini slits for all the modules. The light reflected by each of the small

mirrors enters into the spectrograph where light is dispersed and finally arrives to the detector, obtaining the image of the spectra of the mini slits (see the right inferior panel of Figure 2.11). Each spectrograph is composed of a collimator, a volume phase holographic grating (VPHG, transmission grating Renault et al. 2010) and a CCD camera. The dispersion of the mini slits is achieved perpendicularly to the grating components. All this process happens simultaneously in each of the 24 IFUs giving as result a ~ 400 Mpixel datacube, with 90000 spaxels and 4000 spectral pixels.

Since the image has been split and sliced multiple times (see Figure 2.11) the reconstruction of the image plane is very complex and it is made through visualization and reduction algorithms designed specifically for these tasks. The visualization is achieved using equivalence maps between the image and the detector planes. The reduction algorithm also calibrates with high precision the sky coordinates of the image (geometrical calibration) and the wavelength using the calibration lamps spectra (arc lamps). It performs also a cleaning of the sky emission lines (telluric correction), bad pixels, cosmic rays and spurious emissions due to the electronics of the detector as it is traditionally made to obtain Science exposures. During observations there are displays to control the splitting image process, the spectral calibration and the star guiding objects outside the MUSE FoV, in order to assured the right astrometry and the stability of the observation along all the exposure time. In Figure 2.12, the control panels are displayed: on the left we find the imaging and spectra monitoring interface and to the right the stellar guiding process is carefully followed. I give more details on the data acquisition process in Chapter 3, related to the description of the instrument to have a complete framework of the observational strategy.

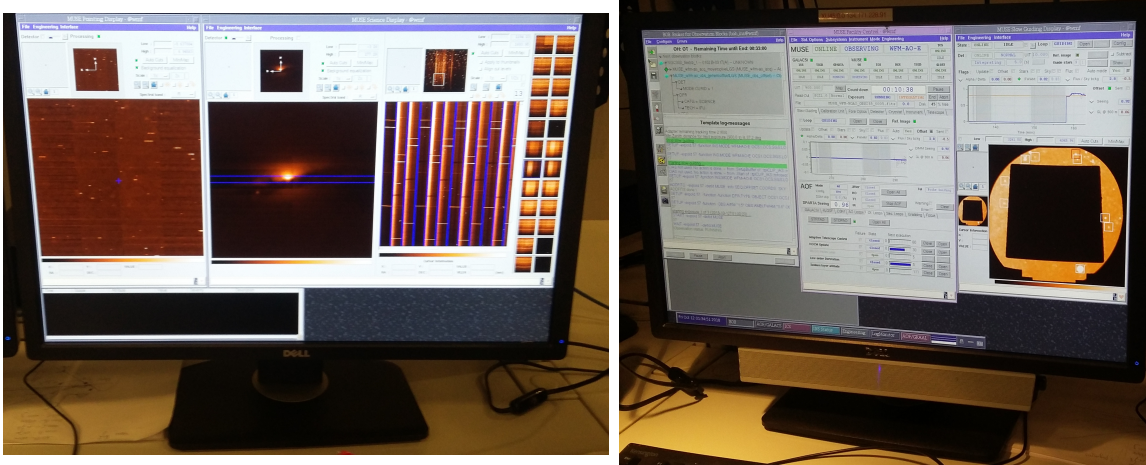


Figure 2.12: Left: Image slicer and spectral calibration interface. Right: Star Guiding monitoring system to assure right astrometry and stability of the exposures. Credits: V. Abril-Melgarejo/ MUSE GTO P102-28 Observing run on Oct 2018

The Yepun Telescope counts from 2018 with a complete Adaptive Optics Facility (AOF, commissioned in 2017), devoted to correct a considerable part of the atmospheric turbulence. This is done by observing the variations in the shape and brightness of four artificial stars created with the 4 Laser Guide Star Facility (4LGSF), which generates four 20W beams of sodium (Na) light ($\sim 5890\text{\AA}$, see Figure 2.10 - Right). Atmospheric turbulence varies with altitude but

the most important disturbances occur in the first km above the soil what is known as Ground Layer (the most turbulent layers of the atmosphere), on which AO corrections are applicable. The laser beams reach about 80 – 100 kms, where they excite the sodium atoms in the upper atmosphere. These atoms then re-emit the light becoming artificial stars, which are referred as Laser Guide Stars (LGSs), necessary to monitor the variations in the atmosphere just above the Telescope in the direction of the observed object. The wavefront sensors in the adaptive optics module GALACSI (Ground Atmospheric Layer Adaptive Corrector for Spectroscopic Imaging), use the LGSs to determine the atmospheric variations 1000 times per second calculating the necessary deformation of the 1.1m secondary mirror (deformable active mirror) of the telescope to compensate for the turbulence and to efficiently flatten the wavefronts. One natural star in IR bands nearby the FoV is also used to correct the remaining atmospheric tip-tilt distortions. The GALACSI module was exclusively designed to provide the AO corrections for MUSE enhancing the resolution of its imager capacity. Besides, MUSE was the first second generation instrument at VLT to operate with the AOF facility.

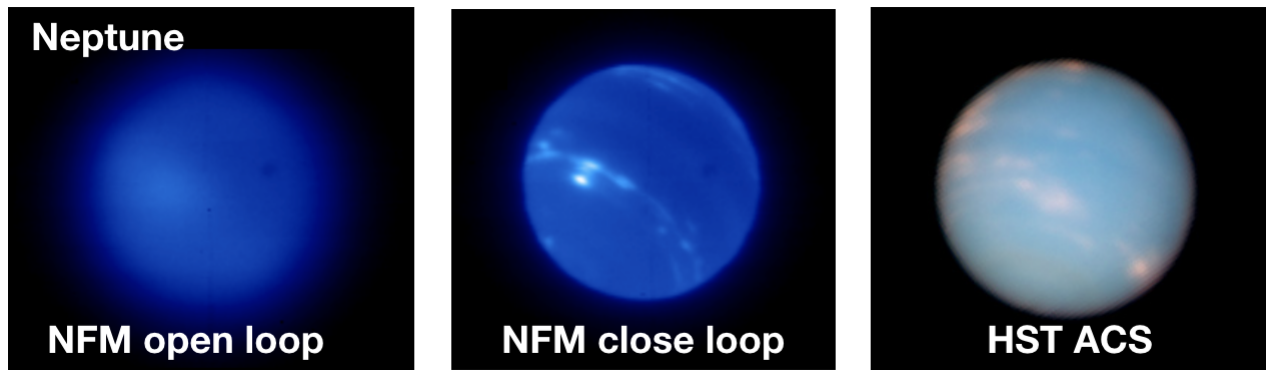


Figure 2.13: Observations of Neptune using the NFM of MUSE. Left: No-AO blurry image of the planet. Middle: The sharp image using AO tomographic mode, including details of the methane clouds in the Neptune’s atmosphere. Right: Image from the Hubble Space Telescope with ACS showing less detail. Credit: AIP/P. Weilbacher.

MUSE has three operational modes: The Wide Field Mode (WFM) using the AOF, the non-AO WFM and the Narrow Field Mode (NFM) which operates always in conjunction with the AOF. The WFM covers an extended FoV of 1 arcmin^2 with a spatial sampling of $0.2''$. The spectral resolution ranges from 1770 at 4650 \AA and 3590 at 9300 \AA . The NFM uses an additional optical system installed in the fore-optics module (before the field splitting process), in order to change the spatial sampling from $0.2''$ to $0.025''$ per spaxel. This resolution is comparable to that achieved by the Advanced Camera for Surveys (ACS) in the Hubble Space Telescope with a spatial sampling of $0.03''$ (see Figure 2.13). The FoV is proportionally reduced to $7.5'' \times 7.5''$. To operate the AOF with this NFM the guiding stars are projected closer to the scientific FoV but are maintained outside, in contrast the tip-tilt star should be inside the FoV (see Table 2.1). With the AOF corrections it is possible to obtain a near diffraction limited image (image free of the turbulence effect of the atmosphere) at a Strehl ratio $\geq 23\%$ at 7500 \AA (Bacon & Monnet, 2017). For comparison of the most important technical aspects of each observing mode I present Table 2.1.

Parameter	Wide Field Mode	Narrow Field Mode
Field of View	59.9' \times 60.0'	7.42" \times 7.43"
Spatial Sampling	0.2"/pixel	0.025"/pixel
Spatial Resolution(FWHM)	0.4"–0.7"	55 – 80 mas
Resolving power	1770 (4800 Å) – 3590 (9300 Å)	1740 (4800 Å) – 3450 (9300 Å)
Limiting Magnitude ^a	R _{AB} =22.70 mag (6500 Å)	R _{AB} =22.30 mag
AO performance	Double the ensquared energy in one spaxel at 7500 Å	5% Strehl at 6500 Å
Type of AO correction	Ground Layer AO	Laser Tomographic AO
Tip tilt star brightness	<17.5 R-mag	<15 J-Hmag
Tip tilt star location	52" to 105" off axis >70% sky coverage	On axis, within 7.5" diameter
Laser Guide Star separation	4 LGS 64" off axis	4 LGS 10" off axis

Table 2.1: Comparison of technical specifications between the WFM and NFM of MUSE, including the AO effects. ^a The registered limiting magnitude in R band corresponds to a 1hr exposure observation of a point source at airmass=1.0, with 0.8" seeing at V band. Credits: ESO

The next quotation from Roland Bacon the Principal Investigator (PI) of MUSE can summarize the importance of this instrument in the Astrophysical research: *"It seems strange that this seven-tonne collection of optics, mechanics and electronics is now a fantastic time machine for probing the early Universe. We are very proud of the achievement — MUSE will remain a unique instrument for years to come"*.

2.5 Comparison of data from Spectrographs used in this study

So far, I have highlighted the most important features of different type of instruments and techniques in order to retrieve the physical information of observed sources. In this section I am focusing on specific spectrographs that have been used in this work as comparison references, whose data is related to the study of galaxy kinematics. I will briefly check the most relevant parameters from VIMOS, DEIMOS, KMOS and SINFONI, to have a general framework of their technical characteristics and scientific goals.

Data from these instruments have allowed to develop several studies on different properties of galaxies at similar redshift ranges as this study, so our aim is to objectively compare the output results from these studies using different spectrographs, with our MUSE observations. The HR-COSMOS is a sample of 82 star-forming galaxies in low density environments, observed by VIMOS presented in [Pelliccia et al. \(2017\)](#). In a subsequent study using together long-slit data from DEIMOS and multiple photometric data, the Observations of Redshift Evolution in Large-Scale Environments (ORELSE) survey of galaxies in dense clusters was the source of the study of kinematic properties of galaxies in clusters at $z \sim 9$ by [Pelliccia et al. \(2019\)](#), this to probe the environmental effects on the kinematic properties. SINFONI data was used in the MASSIV survey to study dynamical properties of ~ 80 star-forming galaxies at $0.9 < z < 1.6$ in different environments ([Contini et al. 2012](#), [Epinat et al. 2012](#), [Vergani et al. 2012](#)). On the other hand, the IFS data from KMOS has been used to construct two important galaxy surveys: KMOS^{3D} ([Wisnioski et al. 2015, 2019](#)) and KROSS ([Stott et al., 2016](#)). These KMOS surveys have been used to produce the kinematic characterization of the star forming galaxies, published in several studies ([Übler et al. 2017](#), [Tiley et al. 2016](#) and [Tiley et al. 2019](#)). I further describe each of these studies in Chapter 5.

2.5.1 Redshift, wavelengths range and emission lines used as kinematics tracers

As I introduced in Chapter 1 the research project on kinematics of galaxies at intermediate redshift is based on the study of nebular emission lines from the ionized gas in the interstellar medium (ISM) of the studied galaxies. The main source of ionization are the young massive stars (with OB spectral type) born inside dense nebulae. These OB stars dominate in luminosity inside a stellar population, since their black-body peak emission is in the highly energetic blue and ultraviolet bands. These stars are generally embedded into clouds of neutral and molecular gas which are photoionized by the high energy photons released in their photospheres. The bright diffuse nebula in the regions of star formation are known as HII regions. The H α hydrogen Balmer line at 6562.8Å is the most prominent emission line (see Figure 2.14) and it is commonly used to trace star formation and kinematics ([Übler et al. 2017](#), [Tiley et al. 2016](#), [Gómez-López et al. 2019](#), [Tiley et al. 2019](#), [Bloom et al. 2017](#), [Bassett et al. 2017](#), among others). Balmer lines are used to determine SFR since inside ionization-bounded HII regions (the ionization has a limit given by the equilibrium with the recombination rate), Balmer fluxes scale proportionally to the ionizing photons from the star, so SFR can be determined from the emission fluxes. The ionizing photons from OB stars are sufficiently energetic to ionize heavier

elements than H, like O, S, N, among others. This is how in HII regions we can find several emission lines in the optical besides Balmer lines like [NII], [OII], [OIII], [SII], also linked to star-formation activity.

Emission lines have their origin in transitions of quantum states from neutral atoms that are ionized by interactions with energetic photons (photoionization), free electrons or free ions (collisional excitation), emitting photons as product of the recombination of electrons returning into an equilibrium state. Emission lines can be produced as single lines known as singles or as double lines due to a change of spin from one state to the other having very similar energetic transitions. The last case is known as doublet and is due to a system with two possible states, where not all electrons are paired in spin. In systems in which all electrons are paired (zero net angular momentum), the decay to lower energy levels of the excited atoms is produced via radiative transitions, which is the origin of the H Balmer and Paschen series of lines, all of them in singlet states.

In the case of [OII] the emission is produced by collisional excitation producing two possible transitions according to the initial spin state. The [OII] λ 3727 and [OII] λ 3729 lines are produced by the radiative transitions between the atomic levels $2D^{3/2} \rightarrow 4S^{3/2}$ and $2D^{5/2} \rightarrow 4S^{3/2}$ respectively (Osterbrock, 1989). These transitions produce the [OII] doublet which is one of the most important emission features of the nebular spectrum in the visual range (see Figure 2.14). Taking into account the typical temperatures and densities in HII regions of $T \sim 10^4$ K and $N_e \sim 10^3 - 10^4 \text{ cm}^{-3}$, the excitation energy between the $2D$ upper levels and the lower level $4S^{3/2}$ is of the order of the thermal electron energy kT . Therefore, the [OII] doublet is related to collisional excitation/ de-excitation which is in turn linked to the electronic density N_e (Osterbrock, 1989).

Emission Line	H α	H β	H γ	H δ	[OII]	[OIII]	[NII]
λ_{emit} vacuum (\AA)	6564.6	4862.7	4341.7	4102.9	3727.1 3729.9	5008.2	6549.9 6585.3
λ_{obs} $z \sim 0.7$ (\AA)	11159.8	8266	7380	6974.9	6336 6340.8	8514	11134.8 11194.9
z range MUSE	[0–0.42]	[0–0.91]	[0.1–1.13]	[0.15–1.26]	[0.27–1.49]	[0–0.85]	[0–0.41]

Table 2.2: List of the primary emission lines available in the visible and infrared wavelengths from sources at intermediate redshifts. The first row corresponds to the emitted wavelength in the source frame, the second row shows the observed wavelength if the object is at a redshift of $z \sim 0.7$ and the third row lists the redshift ranges of detection according to the nominal wavelength coverage of MUSE.

Detection of emission lines depends on the redshift of the observed objects and is limited by the spectral coverage of the detectors. The redshift of a light source can be defined from the relative difference between the emitted and observed wavelengths $z = (\lambda_{obs} - \lambda_{emit}) / \lambda_{emit}$, so $1+z = \lambda_{obs} / \lambda_{emit}$. I present in Table 2.2 the most important emission features generated in the ISM, their emitted wavelength in the source frame, their redshifted wavelengths according

to the average redshifts of the galaxy groups studied in this Thesis ($z \sim 0.7$) and the range of detection by the MUSE spectral coverage (see also Figure 2.14).

As we can observe from Table 2.2 and taking into account the nominal spectral coverage of MUSE ($4750\text{\AA} - 9300\text{\AA}$), the $H\alpha$ line and the [NII] doublet are no longer observable after $z \sim 0.4$, while [OII] is observable up to $z \sim 1.5$, [OIII] up to $z \sim 0.86$ and $H\beta$ up to $z \sim 0.9$. To visualize the effect of redshift on the emission lines I present Figure 2.14, that shows three MUSE integrated spectra from three different galaxies at different redshifts in our sample: CGr23-119 at $z = 0.354$, CGr79-104 at $z = 0.530$ and CGr84-276 at $z = 0.697$. These are star-forming galaxies and are part of the kinematics sample (see Chapter 5). The spectra were extracted in rectangular areas of the MUSE datacube to cover all the extension of the galaxies (the selected area corresponds to the size of the clean flux maps with pixels with enough S/N, see Section 4.5), so a subdatacube was created for each galaxy. Then all the flux in all the pixels inside the selected area were collapsed into the wavelength dimension.

In Figure 2.14, all the spectra show strong emission line pattern due to star formation in the disks of the selected galaxies, but due to the different redshifts the part of the spectrum covered by MUSE is different in each case. For galaxy CGr23-119 $H\alpha$ [NII] and [SII] are still observable, while for CGr79-104 and CGr84-276 the most prominent emission line corresponds to [OII]. In all the three spectra the absorption features of the H Balmer series (due to stellar atmosphere of stars of low mass inside the stellar populations), are observable to the right of the [OII] line. The continuum level in each galaxy corresponds to the different stellar populations integrated in the area of each galaxy. In all the cases the observable wavelength axis on the bottom is related to the rest frame wavelength on the top axis, according to the redshift of each galaxy. The different emission lines are indicated with discontinuous lines and the names of the ion responsible for each emission, in some cases the λ is also indicated. I used colors to indicate the emission in the rest frame, since all of them are in the source inside the optical range.

Our sample of galaxies in groups ranges from $z \sim 0.3$ to 0.8, so all the red emission lines are redshifted towards infrared bands where many prominent sky emission lines are present. As an example, Figure 2.15 from Vogt et al. (2017), shows a high-resolution and flux calibrated sky emission spectrum from MUSE using AO in WFM during the commissioning of the 4LGSF facility. The AO facility uses 20 W sodium (Na) lasers to produce the LGSs, whose light is scattered by the atoms in the atmosphere (through Rayleigh and Mie scattering), producing a residual line. It is then necessary to filter the spectrum around $\lambda_{4LGSF} = 5889.959\text{\AA}$ otherwise the detector would be saturated by the dispersed light from the laser. In order to filter most of the dispersed light from the lasers a filter with $\sim 225\text{\AA}$ wide and $99.7 \pm 0.2\%$ efficiency is used (Vogt et al., 2017), this means that using AO leads the filtered interval of the spectrum around λ_{4LGSF} unusable. Regarding the high continuum values of the spectrum in the blue this is due to the Full Moon conditions in which the sky spectrum was taken. The O_2 and N_2 lines at 6484.39\AA and 6827.17\AA respectively, observed in Figure 2.15, are additional spectral features product of the Raman effect due to inelastic collisions of photons from the AO lasers with the molecules in the atmosphere.

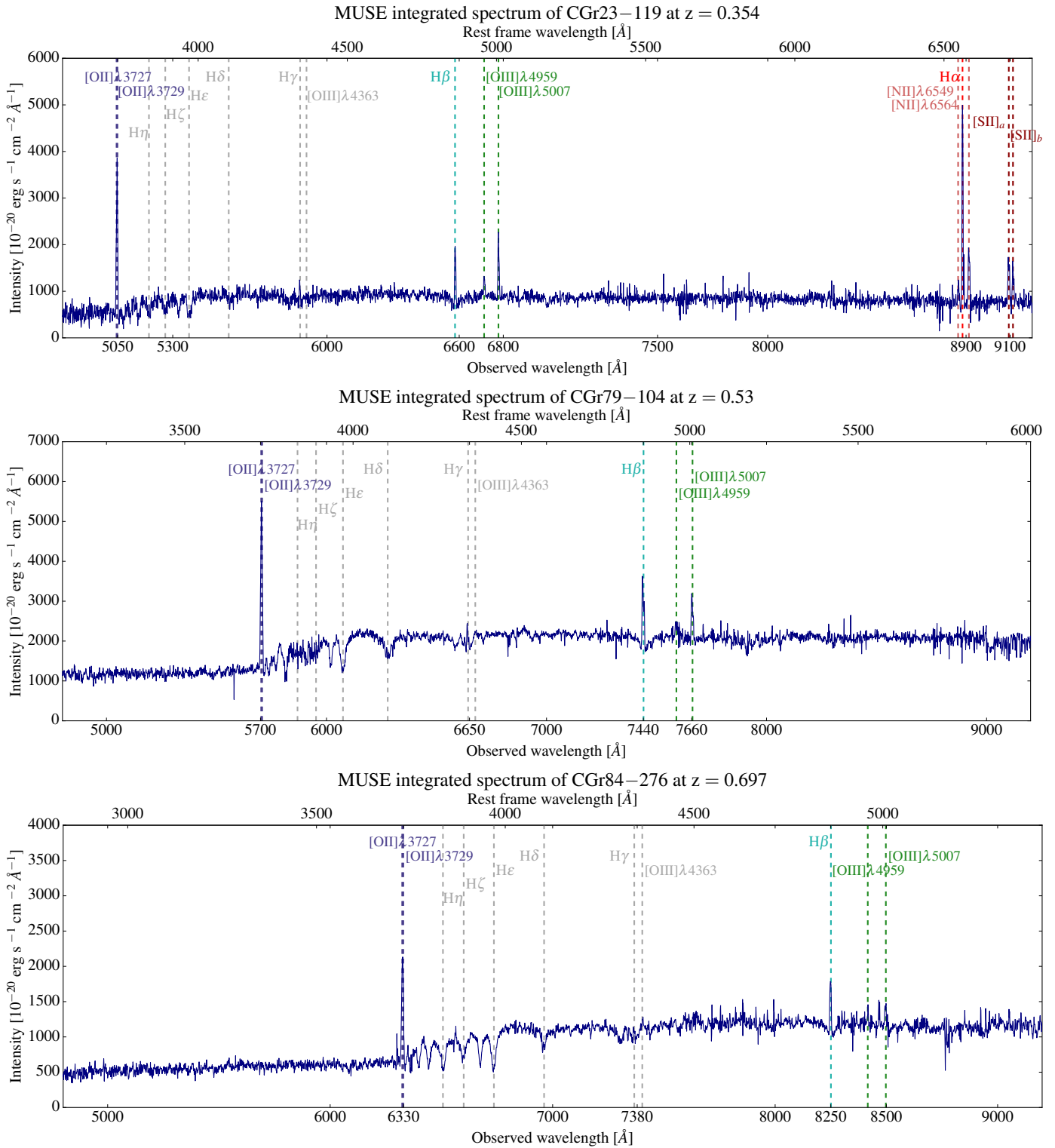


Figure 2.14: MUSE integrated spectra from three different galaxies at different redshifts: CGr23-119 at $z = 0.354$ (superior panel), CGr79-104 at $z = 0.530$ (middle panel) and CGr84-276 at $z = 0.697$ (inferior panel). This Figure shows the effect of redshift on the spectral coverage with MUSE, since H α [NII] and [SII] are observable for CGr23-119 at low redshift but are not detectable at intermediate redshifts. The most prominent emission lines are indicated with discontinuous lines and their corresponding names. Credits: V. Abril-Melgarejo.

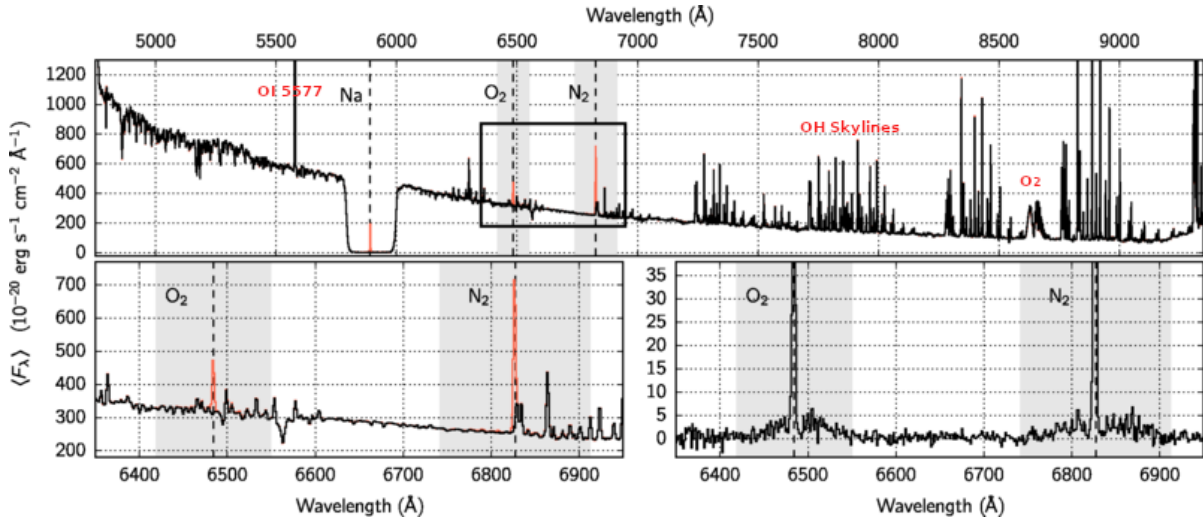


Figure 2.15: MUSE sky spectrum taken during the commissioning of the 4LGSF Adaptive Optics facility operating in WFM. This spectrum is product of observations of 60s exposure of empty sky fields are airmass ~ 1.8 , with and without AO and during full Moon conditions. The skylines start to be important after 7000\AA and they considerably increase in intensity towards the IR bands. The bottom panels make a zoom in the region where O₂ and N₂ Raman scatter lines from lasers are produced without and with AO, left and right respectively. Credit: Taken from Vogt et al. (2017) and the ESO-MUSE User Manual.

In Figure 2.15 it is evident that sky emission lines start to appear in the red part of the spectrum and then increase their intensity towards larger wavelengths. These emission lines are due mainly to the emission from vibrationally excited OH (created by the reaction of H and ozone) and O₂ molecules in the atmosphere. At infrared bands (JHK) sky features have a larger intensity being the H band the most affected, therefore the calibration and correction of the sky lines is more challenging and impacts more severely these observations compared to the optical bands as it is showed in Figure 2.16.

Another important challenge of near-IR observations is the management of the thermal noise since all the background, the telescope and the instrument itself radiate at those bands. The strategy to deal with the thermal noise in which the detector is embedded, is to cool down all the instrument to temperatures close to the absolute zero using cryogenic techniques as it is explained in the case of the KMOS instrument in subsection 2.5.3. This allows to have access to the faint IR studied sources. Regarding sensitivity, it is measured by the quantum efficiency of the detector that basically is the counting of how many photons arriving to the detector surface are converted into a current of electrons by the photoelectric effect. Considering that infrared photons are less energetic than optical photons the quantum efficiency depends on this factor. Different type of CCD detectors have been developed especially to deal with the lower energy photons in the IR achieving good performance, nevertheless detectors remain more sensible in the visible range. Despite the different operational characteristics and performances in the IR and the optical, the spectral resolution in both domains of the instruments used in this study is quite similar with an average of $R=3000$ (See Table 2.3).

In summary, the collisionally excited [OII] $\lambda\lambda 3727, 3729$ doublet is the most prominent emis-

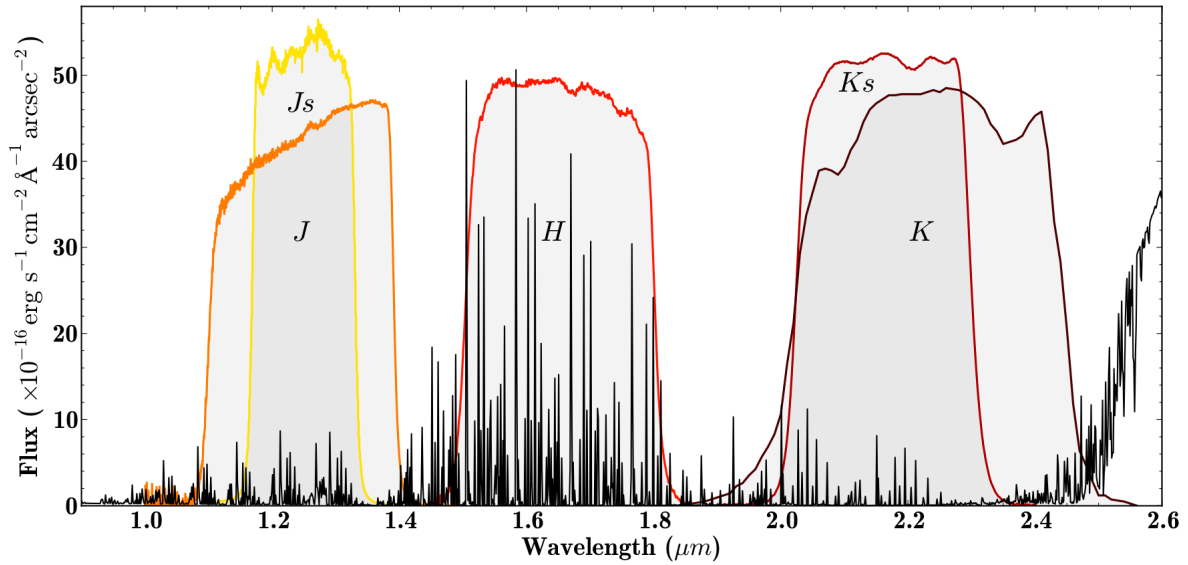


Figure 2.16: Sky emission spectrum in black at JHK near-IR bands in the interval $[1\text{--}2.6]\mu\text{m}$. The profiles of the JKS and Js and Ks band-pass filters are overplotted to distinguish each band. The most prominent sky emission lines are produced in the K band. Credit: [Paulan Thony Wilson](#)

sion feature after $\text{H}\alpha$ having an average integrated flux (adding the flux of the two lines) that is at least equivalent to the half of the $\text{H}\alpha$ flux and can even be equivalent to $\text{H}\alpha$ for corrected extinction fluxes, showing a strong dependence of the $[\text{OII}]/\text{H}\alpha$ ratio on the dust content and metallicity in nearby galaxies as it is shown by the studies from [Mouhcine et al. \(2005\)](#) and [Feng et al. \(2010\)](#). Now, based on the spectral coverage of MUSE, the redshift range of our sample of galaxies and the advantages of observing in the optical regime, I make use the $[\text{OII}]$ doublet integrated flux and a combination of the $\text{H}\beta$ and $[\text{OIII}]\lambda 5007$ fluxes in order to have enough S/N to trace the kinematics of the ionized gas as it is presented in Chapters 4 and 5.

2.5.2 VIMOS (VLT) and DEIMOS (Keck) MOS Spectrographs

The **VI**isible **MU**lti-**O**bject **S**pectrograph (VIMOS, [Le Fèvre et al. 2003](#)), is a MOS instrument equipped with wide field imager, Multi-Object spectrograph and IFU modes. It was mounted at the Nasmyth B focus of the 8.2 m third Unit Telescope (Melipal) at VLT. This instrument was built and developed by the VIRMOS consortium in association with ESO. The VIRMOS Consortium was conformed by six Institutions from France and Italy led by LAM and its PI: Olivier Le Fèvre. The instrument had its first light on February 2002 until March 2018 when was decommissioned. The VIMOS FoV is split in four quadrants corresponding to the different four $2048 \text{ pix} \times 4096 \text{ pix}$ EEV CCD detectors, mounted in four different arms. The detectors are separated by a gap of $\sim 2'$ in between, nevertheless they are not independent, they can operate simultaneously in just one mode per exposure. Hereafter I briefly describe the different modes of the instrument.

- **IMG:** The Imager mode is used with a series of broad band filters (UBVRiz) that produce high resolution images necessary for photometry and for preselection of targets for subsequent spectroscopic studies. The FoV is quite extended taking on account that each of the 4 sensors has a FoV of $7' \times 8'$, with a spatial sampling that corresponds to $0.205''/\text{pix}$.
- **MOS:** Multi-Object spectroscopy implements a multi slit mask per sensor that can host a maximum of 150 – 200 slits, so 40 maximum per quadrant. The spectrograph uses 6 different grisms (LR blue, LR red, MR, HR blue, HR orange and HR red) jointly with 4 filters (OS-blue, OS-red, GG475, GG435) in 7 different configurations (see the configurations at [VIMOS-ESO website](#)). These configurations allow a total wavelength coverage from 360 to 1000 nm, with a spectral resolution varying from $R \sim 200$ (with 40 slits/mask/quadrant) to $R \sim 2500$ (for 200 slits/mask/quadrant). When the grisms operating at near IR bands are in use the MOS mode is denoted as NIMOS (Near Infrared Multi-Object Spectrograph).
- **IFU:** The VIMOS IFU mode is composed of an array of 6400 fibers placed along pseudo slits creating what is known as IFU masks. It uses the same set of grisms than for the MOS mode, so the spectral and spatial resolution are similar for both modes. The image resolution provided by the IFU mode varies from $0.67''$ to $0.33''$ per spaxel, producing FoVs of $54'' \times 54''$ and $13'' \times 13''$ respectively.

VIMOS was designed specifically for the study of galaxy mass assembling and evolution, specially for high redshift galaxies ($z \geq 0.8$) aiming to get large and representative samples at $0 < z < 5$, thus it also has been used to study intermediate z and nearby galaxies. Its configuration is devoted to generate deep surveys of galaxies using its extended FoV and its massive capacity to collect spectra of hundreds of objects per exposure.

One of the examples of surveys made using VIMOS is the HR-COSMOS Survey (PI: L. Tresse) used in the kinematics study performed by [Pelliccia et al. \(2017\)](#). In this study they used spectroscopic data of $\sim 10\text{k}$ sources observed with the medium ($R=580$) and high resolution configurations ($R=2500$) of the MOS mode, with a magnitude limit of $I_{AB} < 22.5$ and maximum redshift of $z \sim 1.2$. For the medium resolution configuration (with the MR grism) is

used with the OS-red filter with a spectral coverage for a slit of 1" width positioned in the center of field of 5500–8700 Å with a spectral sampling of 2.5Å/pix. In the case of the high resolution mode the HR-red grism is used in conjunction with the GG475 filter with a spectral coverage in the center of field of 6300–8700 Å and a spectral sampling of 0.6Å/pix. The main spectral features studied by VIMOS for galaxies up to $z \sim 0.8$, are the set of $H\alpha$, [NII] and [OIII] λ 5007.

The DEep Imaging Multi-Object Spectrograph (DEIMOS, Faber et al. 2003), has three available observing modes: a high resolution imager a Multi-Object spectrograph and longslit spectroscopy. It is mounted in the Nasmyth focus of the 10 m Keck II telescope since June 2002. The instrument was developed by the University of Central Oklahoma and the Lick Observatory under the leadership of Sandra M. Faber, DEIMOS Principal Investigator (PI). DEIMOS is equipped with eight CCD detectors arranged in a mosaic of $8k \times 8k$ pix². I list below the main features of the different observing modes.

- Imager mode, covers a wide range of bands using the BVRIZ standard filters, so the imaging wavelength range spans from 4000Å to 10000Å. The FoV produced is quite extended with a size of $16.7' \times 5.0'$. The spatial resolution corresponds to 0.1185"/pixel.
- MOS mode, uses slit masks with maximum of ~ 100 targets (up to 130 slitlets with 1.5" gaps among them) per mask or ~ 1000 point-source targets using narrow-band filters. The usable total slit length (subtended by detector pixels) is 16.3 arcmin. The maximum achieved spectral resolution is $R \approx 6000$ in a spectral range from 4100Å to 11000Å. The spectrograph operates with 4 different blaze reflecting gratings (see Table 2.3) with different coatings but there are only 2 available grating slots per exposure. The gratings operate in different configurations with 3 different filters (GG400+5000, GG455+7000 and OG550+8000) in order to give different wavelength coverage (see the configurations at [DEIMOS keck website](#)).
- Long slit mode, is designed to study large sources and provides a variety of fixed widths, from 1" (nominal) to 0.5" (good seeing). The same spectral range than from the MOS mode is applicable depending on the gratings used.

DEIMOS was optimized to obtain the multi-image and spectroscopic data of faint-objects widely distributed on the sky. With this aim several imaging and spectral surveys of distant galaxies have been generated to study their physical properties. That is the case of ORELSE (Observations of Redshift Evolution in Large-Scale Environments Survey, Lubin et al. 2009), which contains multi-wavelength photometric and spectroscopic observations covering in a total FoV of 5 deg², targeting 15 fields containing large-scale structures like groups, clusters and field galaxies in a redshift range of $0.6 < z < 1.3$. Specifically in the case of the study of environmental evolution of kinematic features of galaxies in ORELSE, performed by Pelliccia et al. (2019), the spectroscopic observations were obtained using DEIMOS with the 1200-grooves mm⁻¹ grating blazed at 7500Å and slits with 1" width, located in different slit masks. With this instrumental configuration a spectral sampling of 1.7Å/pix and a spectral coverage of [6385–9015]Å were achieved (Pelliccia et al., 2019). With this instrument the core of the observations are performed at the [OII] $\lambda\lambda$ 3727,3729 doublet, and additionally the [OIII] and $H\beta$ lines are also used to determine kinematic properties of the ionized gas.

2.5.3 IFS SINFONI and KMOS (VLT)

The Spectrograph for INtegral Field Observations in the Near Infrared (SINFONI, Eisenhauer et al. 2003), is a near-infrared IFS complemented by an adaptive optics module. It was built by German and Dutch institutions and later mounted on the Yepun Telescope (UT4) at VLT where it operated from August 2004 to June 2019 when it was decommissioned. The spectrograph has 4 gratings covering the J,H,K and H+K bands equivalent to a spectral range of $1.1\mu\text{m} - 2.45\mu\text{m}$. The spectral resolution for the J,H,K and H+K is 2000, 3000, 4000 and 1500 respectively. Each band is fully sampled on the 2048 pixels of the Hawaii 2RG (2k \times 2k) detector in the wavelength direction. SINFONI is equipped by a slicer IFU that splits the sky FoV into 32 slitlets. The slices are after rearranged one next to the other obtaining a long slit output.

There are three different observing modes depending on the width of desired slices, the choices are 250mas, 100mas and 25mas, producing a FoV of 8'' \times 8'', 3'' \times 3'' and 0.8'' \times 0.8'' respectively. Each of the 32 slices is imaged using 64 pixels in the detector plane, thus in total 64 \times 32 spectra are generated. The widest FoV (8'' \times 8'') is generally obtained without AO, although it can also be assisted by AO. For all the modes the AO facility is used with a natural guiding star (NGS) and/or a Laser guiding star (LGS). SINFONI operates at temperatures between -150°C and -273°C in order to reduce thermal noise.

Data from SINFONI were used to build the Mass Assembly Survey with SINFONI in VVDS (MASSIV), which was devoted to structural and kinematic studies of galaxies at high redshift ($1 < z < 1.6$) in the VIMOS VLT Deep Survey (VVDS) field. Galaxies in MASSIV were observed using the J and H gratings in two close spectral intervals: $1.08\text{--}1.41\mu\text{m}$ and $1.43\text{--}1.86\mu\text{m}$ with resolution $R \sim 2000$ and ~ 3000 respectively. Most of the observations were performed without AO with a FoV of 8'' \times 8'' and a space element of size of 0.125'' \times 0.25''. Few observations (11 galaxies) were AO assisted with a 3'' \times 3'' FoV and a spaxel scale of 0.1'' \times 0.05''. MASSIV was designed to study the H α and [OII] λ 3727 lines from HII regions of distant galaxies. In order to avoid the effects sky lines, in Vergani et al. (2012) they apply an important constraint consisting in including in the survey only those galaxies for which H α and [OIII] lines fall in a region relatively free of OH sky-lines. The final MASSIV sample is composed of a total of 84 galaxies.

Among the Science goals of SINFONI are the study of compact objects like star-forming regions, active galactic nuclei (AGN), distant galaxies (formation and evolution), the galactic centre, etc.

The Kband Multi Object Spectrograph (KMOS, Sharples et al. 2006; Davies et al. 2013), is a second generation IFS instrument designed for the VLT, where it had its first light on November 2012. KMOS was developed by a consortium of 4 British and three German institutions. It is mounted on the Antu telescope (UT1), operating in the Nasmyth B focus. The most important feature of KMOS is its capacity to get IFS data in the near-infrared, performing parallel observations for 24 targets. KMOS is a multiplexed instrument, composed of 24 deployable arms that locate pick-off mirrors at different positions in the focal plane previously determined by the user (see figure 2.17). The light is sent to 24 slicer IFUs that split each subfield into 14 slices, with 14 pixels along each slice. KMOS has three cryogenic reflecting grating spectrographs which generate 14 \times 14 spectra (~ 1000 Nyquist-sampled spectral resolution elements) for each of the subfields. Each spectrograph has five diffraction gratings covering five

wavelength bands, providing the possibility to sample different wavelength ranges according to different astrophysical studies. Only one grating is used per spectrograph, per exposure, in order to generate the spectra of the 24 subfields.

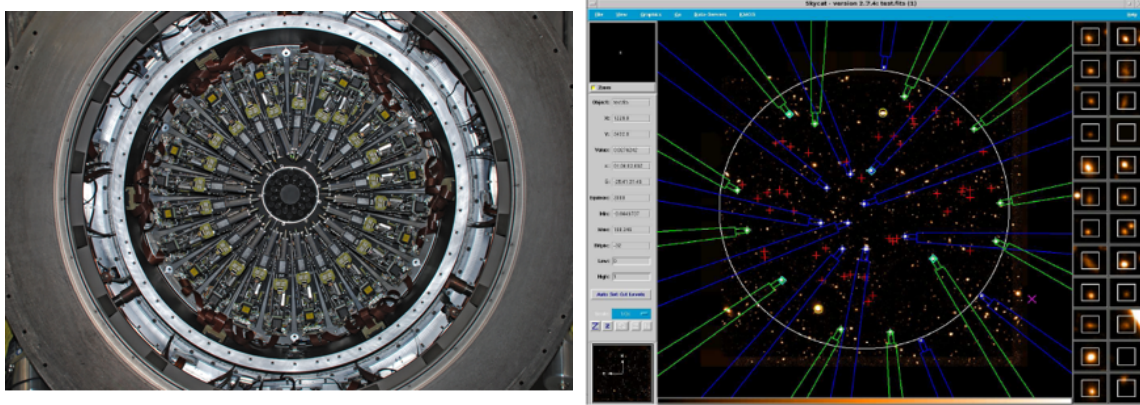


Figure 2.17: Left: Front section of KMOS containing the 24 deployable arms. Right: Display of the KARMA software, where the positions of targets and individual IFUs (pick-off mirrors) can be visualized. Images taken from the Oxford University website dedicated to [KMOS](#).

Operating in the NIR bands implies that all the working parts of the instrument need to be cooled down to below -130°C , while for the detector the operative temperature is even lower, below -200°C . To achieve those low temperatures the instrument is inside a vacuum cavity inside a cryostat, all this in order to prevent icing or extra head load and thus to minimize the thermal noise. Inside the cryostat there is a central section equipped with filter wheels to limit the spectral coverage and also the 24 IFUs which take the light from the arms and reorganize the image of the sky into a long slit. This is done by combining the light from 8 individual arms per spectrograph into its corresponding slit, so the total output is composed of three long slit format.

The patrol FoV where the pick-off mirrors can be located has a diameter of $7.2''$ (size of the unvignetted field in the focal plane). The square FoVs generated by each mirror have a size of $2.8'' \times 2.8''$, with a spatial sampling of $0.2'' \times 0.2''$ (with the Nyquist sampling of ~ 2 spectral pixels at the detector plane). The spectral resolution ranges from 3000 – 4000. The covered spectral bands are **I**Z ($0.779\mu\text{m} - 1.079\mu\text{m}$), **Y**J ($1.025\mu\text{m} - 1.344\mu\text{m}$), **H** ($1.456\mu\text{m} - 1.846\mu\text{m}$), **K** ($1.934\mu\text{m} - 2.460\mu\text{m}$) and **H+K** ($1.484\mu\text{m} - 2.442\mu\text{m}$), which corresponds to a total wavelength coverage of $0.8\mu\text{m}$ to $2.5\mu\text{m}$. The advantage of the free-moving mirrors is evident for crowded fields, to study separated elements in an extended field which is similar to the MOS configuration but with the advantage of achieving the detection of spatially resolved spectral information. The mirrors can be also operated to collect light from contiguous areas using an 8-point or 16-point dithering pattern.

The study of distant galaxies (at intermediate and high redshift) is the main objective of KMOS since for these galaxies, light is redshifted showing some of their most prominent spectral features in the infrared bands. These galaxies also have smaller apparent sizes that can still be resolved by the instrument, providing valuable information on the spatially resolved

physical properties.

In the specific cases of KROSS and KMOS^{3D} surveys, both were designed to detect and obtain H α + [NII] and [SII] observations from distant galaxies, although the lines [OIII] and H β can also be detected for lower redshift some objects. I highlight the instrumental configurations to obtain the data used by the kinematic studies by [Tiley et al. \(2019\)](#) and [Übler et al. \(2017\)](#), using KROSS and KMOS^{3D} respectively. In the one hand, KROSS observations of a total of 795 galaxies at $0.6 < z < 1$, were performed using the YJ filter with a spectral coverage of 1.02–1.36 μm and a resolution ranging from $R \sim 3000$ to $R \sim 4000$ from shorter to longer wavelengths. On the other hand, KMOS^{3D} data for 739 galaxies at $0.7 < z < 2.7$ were obtained using the YJ, H and K near-IR pass-band filters, obtaining a spectral range between 1.02 μm and 2.46 μm , with spectral resolutions R of ~ 3600 , 4000 and 4200 respectively ([Wisnioski et al., 2015](#)).

Similarly to MUSE, KMOS has different usages for different science goals, including the study of stellar populations in nearby galaxies, the formation and evolution of massive stars, a survey of molecular clouds in the Milky way, among others.

2.5.4 Technical Comparison

In Table 2.3 below, I present a summary of the most important features of the most relevant instruments for this research project: MUSE, KMOS, DEIMOS, SINFONI and VIMOS. As it was previously mentioned, the studies subject to comparison use data from these instruments so it is important to have a general framework of their capabilities compared to the performance of MUSE. From all the information gathered for each instrument, the most relevant characteristics presented are: the type of instrument according to the technique to acquire images and spectra, the dispersion system used to produce the spectra, wavelength range, spectral resolution, size of the generated FoV with their corresponding spatial sampling and average resolution (FWHM), the operation observatory, the type of telescope where the instrument is mounted with the initial year of operation and some comments on particularities about their structure and data acquisition.

Instrument	Type	Dispersive system	λ coverage	Spectral Resolution	Spatial Sampling	Observatory Telescope Type	Comments
MUSE	IFS	Volume phase holographic grating (VPHG) Bragg grating - 639 l/mm	4800Å– 9300Å	1770 – 3590 WFM 1740 – 3450 NFM	WFM FoV 1 arcmin ² - 0.2"/px FWHM AO 0.46"(0.75 μ m) FWHM No AO 0.65"(0.75 μ m) NFM FoV 7.42"×7.43" - 0.025"/px FWHM NFM 55–80 mas	VLT UT4 (8.2m) Nasmyth B focus First light: 2014	24 slicer IFUs 1 spectrograph per IFU
KMOS	IFS with MOS sampling	5 cryogenic reflecting gratings (IZ, YJ, H, K and H+K)	0.8–2.5 μ m	3400(IZ), 3600 (YJ), 4000 (H), 4200 (K) 2000(HK)	Patrol FoV: 7.2' in diameter FoV pick-off mirrors: 2.8"×2.8" 0.2"/px	VLT UT1 (8.2m) Nasmyth B focus First light: 2012	24 deployable arms, 24 pick-off mirrors, 24 slicer IFUs, 3 spectrographs
DEIMOS	Spectro-imager MOS	4 blaze reflecting gratings 600 l/mm (7500Å blaze, Al) 830 l/mm (8640Å blaze, Au) 900 l/mm (5500Å blaze, Al) 1200 l/mm (7500Å blaze, Au) +3 Filters	4100–11000Å	FWHM - spec. R 3.5Å - R ₁ ~ 2200 2.5Å - R ₂ ~ 3500 2.1Å - R ₃ ~ 2600 1.1–1.6Å - R ₄ ~ 4700–6800	FoV 16.7'×5.0' 0.12"/px	Keck II (10m) Nasmyth focus First light: 2002	130 slitlets or ~1000 holes per mask.
SINFONI	IFS	4 reflecting gratings (J,H,K and H+K)	1.1–2.45 μ m	1500(H+K), 2000 (J), 3000 (H), 4000 (K)	No AO FoV 8"×8" - 250 mas/px AO FoV 3"×3" - 100 mas/px AO FoV 0.8"× 0.8" - 25 mas/px	VLT UT4 (8.2m) Cassegrain focus First light: 2004	1st IFS AO assisted Decommissioned since 2019
VIMOS	Imager/MOS/ long-slit	6 Grisms + 4 filters	0.36 – 1.0 μ m	200 – 2500	IMG: FoV 7'×8' - 0.205 "/px IFU: 54"× 54" – 13"× 13" 0.67"/pix – 0.33/pix	VLT UT3 (8.2m) Nasmyth B focus First light: 2002	Decommissioned Since 2018

Table 2.3: Comparison of the main technical features from MUSE, KMOS, DEIMOS, SINFONI and VIMOS.

In order to achieve a wide sample of galaxies in dense environments and to retrieve their spatially resolved properties we need to fulfill two essential requirements, one is a high multiplex spatial coverage and the second to have access to imaging and spectral high resolution capabilities. The first requirement refers to the number of objects sampled in a FoV per exposure, so to be able to cover all the extension of galaxy groups a wide FoV is necessary. The second requirement points out to the usage of IFS. From the three IFS instruments in Table 2.3 we see that the largest FoV corresponds to MUSE with a spatial sampling similar to those of KMOS (0.2"/px) and the one of the configurations of SINFONI (0.8"×0.8" with 0.25"/px). KMOS and SINFONI have a spectral coverage in the near infrared suitable to trace H α and [NII] lines at intermediate redshift, which are the most luminous spectral features in the emission spectrum of the ionized gas in the ISM and ICM. Nevertheless, KMOS is limited to 24 small FoV for which a data cube is obtained despite its very extended patrol circular field of 7.2' of diameter. In the case of SINFONI, its spatial resolutions are similar to those of MUSE WFM and NFM modes but its FoV configurations are too small (limited) compared to MUSE. The spectral coverage for SINFONI and KMOS is achieved by the usage of a limited number of different configurations of reflecting gratings per exposure so the spectral range in Table 2.3 is nominal, the actual ranges vary according to the observational configuration as was mentioned above on the sections corresponding to each instrument.

Only SINFONI and MUSE are AO-assisted instruments in this list. Furthermore, SINFONI was the first IFS instrument in the world to be assisted by an addaptive optics facility (Bacon & Monnet, 2017). We can observe the improvement for both intruments in the spatial sampling but at expenses of considerably reducing the FoV. Fortunately, as I explained in Section 2.4, the NFM can also use the AO facility without affecting the size of the FoV and slightly improving the FWHM of observations from 0.65" to 0.46 in average as it is registered in Table 2.3.

The spectral capacity of MUSE is given by its identical VPHG transmission gratings (one per IFU / per spectrograph), achieving a wide spectral range from the optical to the near infrared. For the galaxies studied in this project we trace the [OII], [OIII] and H β lines, being the [OII] $\lambda\lambda$ 3727,3729 doublet the most prominent emission feature after H α .

Concerning the MOS/imagers DEIMOS and VIMOS, they have very extended FoVs with the aim to perform extended photometric surveys and to host masks with multiple holes, slits or long slits configurations. The spatial sampling of DEIMOS is slightly better than MUSE, while the imager mode of VIMOS has a very similar spatial sampling to MUSE but it decreases considerably for the VIMOS IFU configuration. Regarding the spectral coverage VIMOS and DEIMOS use different configurations of their dispersion systems with different filters to produce spectra in different bands (see subsection 2.5.2). Their spectral sampling is limited to one dimensional elements (holes or lines) of the observed object or to data cubes with low spatial and spectral resolutions in the case of VIMOS. To trace the kinematics of galaxies with slits or long slits the ideal configuration is to place the slit in the direction of the major axis of their velocity field, but it is not possible to know apriori the kinematic position angle (subtended angle from the north direction to the mayor axis of the velocity field measured counter-clockwise) of a galaxy. In Pelliccia et al. (2019) they explain the limitation they have determining the orientation of the slit having to discard an important quantity of spectra of galaxies whose PA differ for more than 45° from the position of the slit. I discuss more about the effects of the

origin of spectral data in the kinematic analysis in Chapter 5. Another disadvantage in using long slit or MOS configurations is how challenging could be to study crowded fields due to the risk of overlapping of the generated spectra. Along this chapter I presented and discussed all the advantages of IFS instruments over long slit or MOS techniques.

All the above mentioned reasons conducted us to perform the morpho-kinematic analysis on galaxies in dense structures at intermediate redshift with MUSE, which is currently the most suitable instrument to perform this study. It is important to mention that we are also interested in follow-up studies using KMOS based on our results to trace on the same objects, the dynamics given by the emission lines in the red part of the spectrum and to make a direct comparison/complementing our results with the [OII] doublet. A KMOS observational proposal was prepared by B. Epinat in 2017 to perform follow up observations in the multiple diffuse ionized gas structures that have been found in the dataset of groups in the MAGIC survey (See description on this survey in Chapter 3), this is the dataset on which my research is performed. Service mode time was granted to the proposal but the observations were not performed at the expected depth. Two papers have been published on this respect using MUSE data, one is the study of [Epinat et al. \(2018\)](#) and the other study corresponds to [Boselli et al. \(2019\)](#) in which I actively participated. These studies characterize two extended diffuse emission structures among galaxies in two galaxy groups from the MAGIC survey that were serendipitously founded by extracting narrow band images from the MUSE datacubes. This shows the huge potential of MUSE to retrieve a large quantity of information from objects at different redshifts in its extended FoV obtaining with high resolution image and spectra for each exposure. This opens the opportunity to perform many studies with diverse research approaches, for example in the same datacube where we extract kinematic information of galaxies at intermediate redshifts, there is also information from more distant galaxies that can be studied by their Lyman alpha emission ($\text{Ly}\alpha$ emitters, LAEs). Moreover, we have identified several group structures at different redshifts in all the MAGIC FoVs.

2.6 Future IFS Instruments

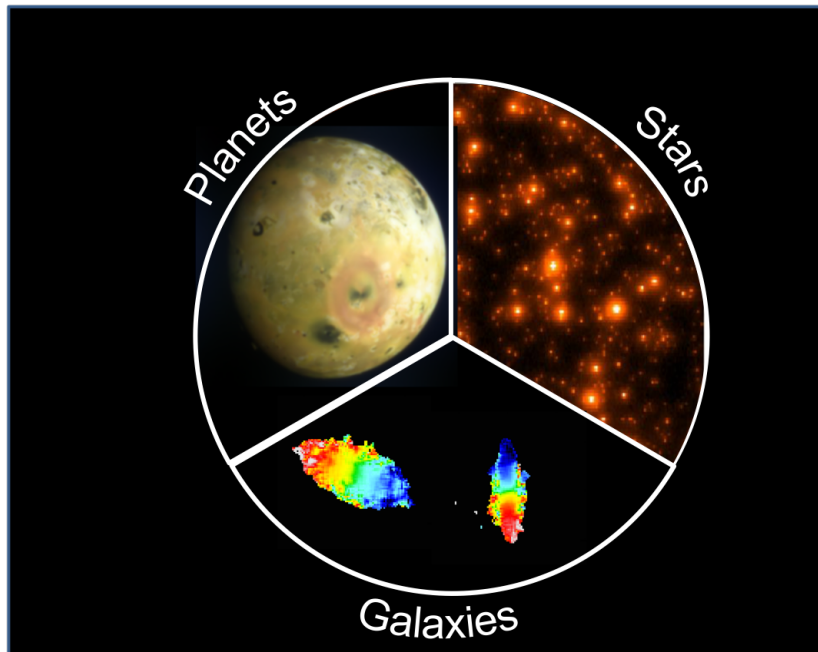


Figure 2.18: These are the results simulated observations with HARMONI, corresponding to the image obtained for Jupiter’s moon Io, a crowded field of stars and the velocity fields of two distant galaxies at a very high resolution. These observations will allow to determine with high precision masses of the different components of the galaxies and the determination of their evolutionary state. Credits: Oxford University website dedicated to [HARMONI](#).

With the advent of the new 30m class telescopes in the next decade and the future launching of outstanding observational missions like the James Space Webb Telescope (JWST), new instruments have been developed or are in planning stage to enrich our knowledge of the Universe. I mention here some of these instruments based on the IFS technique, which has proven to be the most efficient and versatile tool in the study of extended sources. The previous based on the high scientific production from IFS instruments. With new technology and larger collecting areas, new instruments will provide a lot of data with unprecedented resolution that will allow studies of the evolution of galaxies at different redshifts and cosmic scales. I start with BlueMUSE which will be part of the new generation of instruments for the VLT in the next decade, using a very similar instrumental structure as MUSE but centered in the blue part of the electromagnetic spectrum (near UV and the visible). I continue with a general description of the IFS HARMONI and the MOS-IFS MOSAIC instruments operating in the visual and near infrared ranges, which will be mounted on the Extremely Large Telescope (ELT) as part of the first light, first generation instruments respectively, for this giant European facility, at cerro Armazones in Chile. I finish with NIRSpec one of the main instruments embarked on the James Weeb Space Telescope, which uses an IFU mode and operates in the near infrared domain.

- **BlueMUSE** is a panoramic IFS with an extended field of view of 1.41 arcmin^2 , seeing-limited, blue-optimized with a wavelength coverage in the range $350\text{nm} - 600\text{nm}$ and an

average spectral resolution of $R=4000$ (Richard et al., 2019). The spatial sampling is expected to be as good as the resolution for MUSE ($0.2''$), they estimate a sampling of $0.3'' \times 0.3''$ per spaxel. The BlueMUSE consortium is considering to use a curved sensor (for which one of the prototypes has been developed at LAM), but more performance studies need to be done, in order to define a final spatial resolution and a real gain with respect to the typical flat sensors. The spectral coverage goes from the atmospheric cut-off of transmission to the middle of the R band with a sampling of 0.58\AA per spectral bin, allowing to study different science cases from the solar system (specifically the chemical composition of comets) to the study of high redshift galaxies. It is inspired on MUSE, using the same instrumental architecture and also several similar systems (it will also contain 24 IFUs), but with output data characteristics very different from MUSE like a larger FoV and higher spectral resolution. BlueMUSE opens possibilities to new studies beyond the capacities of MUSE, like for example, a survey of massive stars in our galaxy and neighbor galaxies, to study stellar evolution. Robust estimations of the properties of rest-frame UV nebular lines (HeII, [CIII], [CIV]), at intermediate redshift will allow to detect faint emission structures product of the exchange of material among galaxies (gas outflows around and between galaxies) and many other emission phenomena. By 2030 most of the new large facilities will be focused on infra-red observations, while BlueMUSE will be the only instrument performing complementary observations in the UV/blue spectral range, which are crucial for high energy studies. The BlueMUSE consortium (of which LAM is currently part) estimates a period of 7 years of building and commissioning. The project will enter in Phase A of evaluation at ESO by late 2021.

- **HARMONI:** The High Angular Resolution Monolithic Optical and Near-infrared Integral field spectrograph, is an adaptive optics assisted IFS designed for the ELT. Its redshift range spans from $0.47\mu\text{m}$ to $2.45\mu\text{m}$, with a spectral resolution varying from $R \sim 3500$ to $R \sim 18000$. The instrument produces ~ 31000 spaxels arranged in a FoV of $152 \text{ pix} \times 204 \text{ pix}$. HARMONI represents the central spectroscopic capability of the ELT, with the option to select the spaxel scale according to the science cases. The coarsest spatial scale corresponds to spaxels of $0.03'' \times 0.06''$ (already one order of magnitude sharper than WFM MUSE spaxels), resulting in a FoV of $6.1'' \times 9.1''$, suitable for AO and seeing limited observations. The sharpest scale is 15 times finer with 4×4 milli-arcseconds/spaxel, Nyquist sampling the diffraction limit of ELT in the NIR domain, producing a FoV of $0.62'' \times 0.82''$. With each pixel scale there is a possibility to select the type of AO facility to use (LTAO, SCAO) or to perform not AO observations. The main Science cases of HARMONI (see Figure 2.18), cover also the ELT science pillars like solar system observations, characterization of earth size exoplanets, resolved stellar populations, galaxies at high redshift, and Ultra Luminous Infrared Galaxies (ULIRGs). HARMONI will work in synergy with ALMA being the angular resolution similar in both cases, and with JWST having a similar sensitivity. Along with Oxford University and other 9 institutions LAM is also part of the HARMONI consortium participating actively in the instrumentation development and science cases among them the kinematics of high redshift galaxies.
- **MOSAIC:** is a multi-object and multi-integral field spectrograph that will operate at the ELT. It will produce the largest possible FoV for the ELT with a circular technical FoV of 5 arcmin diameter and a science field of 3.19 arcmin diameter ($\sim 32 \text{ arcmin}^2$). MOSAIC will have three operating modes: two multi-IFU integral field modes, the first

to study the Inter-Galactic Medium (IGM mode) and the second the high definition mode (HDM) that will provide spatially resolved observations in near-infrared; and the last, the high multiplex mode (HMM) that is basically the MOS mode. The HMM mode allows to sample simultaneously 200 objects in the optical range ($0.45\mu\text{m} - 0.8\mu\text{m}$) and 100 in the near-infrared ($0.8\mu\text{m} - 1.8\mu\text{m}$). The apertures change depending the spectral range, $0.8''$ diameter for the optical band and $0.6''$ for the near-infrared, both achieving spectral resolutions from 5000 to 15000. The HDM mode uses 10 pick-off mirrors in the focal plane that direct the light towards 10 hexagonal fiber-bundle IFUs, combined with the multi-object adaptive optics system (MOAO). This mode provides data cubes for 10 objects in 10 hexagonal $2'' \times 2''$ FoVs distributed inside the science field ($3.2'$ in diameter). The spectral coverage is only in the infrared ($0.8\mu\text{m} - 1.8\mu\text{m}$) with a resolution of $R=5000$. The spatial sampling corresponds to 75mas/spaxel . Finally, the IGM mode operates in seeing limited conditions (No AO) with pick-off mirrors that direct the light of 6 subfields to a bundle of fibers resulting in a FoV of $3'' \times 3''$. Spectral range and resolution are the same for both HMM and IGM IFS modes. The main science drivers for MOSAIC include the study of resolved stellar populations in the local group of galaxies to perform astro-archeology, to map the inter-galactic medium, the co-evolution of super-massive black holes and galaxies, the study of dwarf galaxies, exoplanetary science and the study of the first galaxies. The MOSAIC consortium is composed of 12 partner institutions mainly based in France, from which LAM is part providing scientific and instrumental contributions to the project. More details about the instrument can be consulted at the [MOSAIC website](#).

- **NIRSpec:** The Near Infrared Spectrograph will operate on board of the JWST, covering a spectral range of $0.6\mu\text{m} - 5\mu\text{m}$ with spectral resolutions of 100, 1000 and 2700, operating in long-slit, MOS and IFU modes. One of the main purposes of NIRSpec relies on the study of the farthest observable galaxies, so in order to achieve this it will perform long exposure surveys. The multi-object capacity has a maximum of 100 sources observed simultaneously, also extracting their spectra. The MOS mode works with a micro-shutter assembly (MSA) array with about a quarter million of tiny cells that can be opened and closed with the usage of varying magnetic fields. This configuration allows to vary the masks as needed. NIRSpec IFU uses a slicer mirror to split the field of view into 30 slices. Each slice has dimensions: $0.1''$ wide and $3''$ long on the sky. The FoV is further dissected at obtaining perpendicular slicing images, giving a mapping of 900 spaxels, each one with a dimension of 0.1 arcsec^2 . For the dispersion of the spatial elements, combinations of the different dispersion gratings and filters available for the other modes are usable giving to the IFU mode the same total spectral coverage $[0.6-5.3]\mu\text{m}$. Depending on the configuration of gratings and filters available for NIRSpec ⁴, there are basically 4 wavelength ranges for the IFU mode: $[0.90-1.27]\mu\text{m}$, $[0.97-1.89]\mu\text{m}$, $[1.66-3.17]\mu\text{m}$ and $[2.87-5.27]\mu\text{m}$, with two possible values of resolution, $R_1 \sim 1000$ and $R_2 \sim 1000$. The NIRSpec IFU mode was designed mainly to the study of astronomical targets with an extension of few arcsecs or for sampling sub regions inside the extended sources. This involves mainly the study of kinematics of distant galaxies up to the study of atmospheres of objects in the solar system. The produced FoV has a size of 9 arcmin^2 in MOS

⁴Gratings: G140M, G235M, G395M, G140H, G235H and G395H. Filters: F070LP, F100P, F170LP and F290LP. All the configurations and wavelength ranges for NIRSpec can be found at the [STScI webpage](#)

mode and of $3 \times 3 \text{ arcsec}^2$ using the IFU and 5 fixed slits to perform high-contrast long-slit spectroscopy. NIRSpec will be the first spectrograph in space combining all these techniques. NIRSpec was built by the European Space Agency (ESA), Airbus and Space Germany.

Chapter 3

Definition of the sample

3.1 The Cosmic Evolution Survey (COSMOS)

The Cosmic Evolution Survey (COSMOS, [Scoville et al. 2007a](#)) is a wide-field, deep and multiwavelength survey, covering an area of $\sim 2 \text{ deg}^2$ in the equatorial region of the constellation of Sextans, centered at RA = 150° 00' 28.6" and DEC= +2° 12' 21.0" (J2000.0) as part of the Hubble Space Telescope (HST) treasury program. The equatorial location of the field ensures visibility for current and future ground based facilities, which is also the reason for this field to be one of the most observed regions in the sky and a likely target for the next generation of instruments operating on the upcoming 30m-class optical/IR telescopes. COSMOS was conceived to study the evolution of galaxies, star formation, active galactic nuclei (AGNs) and dark matter (DM) and the correlation with the evolution of large-scale structures (LSS) within a wide redshift range $0.5 < z < 6$. The survey contains data from X-ray, UV, optical, near and mid-IR, submm and millimeter wavelengths, from observations of space telescopes (XMM, Chandra, GALEX, Hubble, Spitzer, Herschel) –including mainly HST imaging from the Advanced Camera for Surveys ACS instrument– and ground based telescopes (VLA, ESO-VLT, Subaru, Keck, CFHT, among others).

The total projected area of 1.8 deg^2 on the sky surveyed by the HST-ACS instrument corresponding to the COSMOS field is shown in Figure 3.1 upper panel, together with a visual comparison of the angular sizes of the moon and other HST-ACS surveys like GOODS ([Giavalisco et al., 2004](#)), GEMS ([Rix et al., 2004](#)) and the Hubble Ultra Deep Field (HUDF, [Beckwith et al. 2006](#)). In the lower panel of Figure 3.1 a technical comparison of the depth and the extension of the previously mentioned surveys ([Scoville et al., 2007b](#)) is presented, showing the COSMOS field corresponds to the largest area with a depth that is comparable to that of GOODS (320 armin^2) and GEMS (900 armin^2). The mosaic image of the COSMOS-HST field is the largest survey area ever observed by HST and was achieved using the ACS instrument to produce parallel single-orbit *I*-band F814W exposures during 581 orbits within HST cycles 12 and 13 (performed from 2003 to 2005, [Scoville et al. 2007b](#)). For each orbit four exposures of 507 s (2028 s in total) were performed in a four-position dithering configuration, with the purpose to cover the gap of 90 pixel wide between the arrays of the HST-ACS CCD detector ([Scoville et al. 2007b](#), [Koekemoer et al. 2007](#)).

The ACS-F814W exposures with individual FoV of $203'' \times 203''$, represent the primary HST

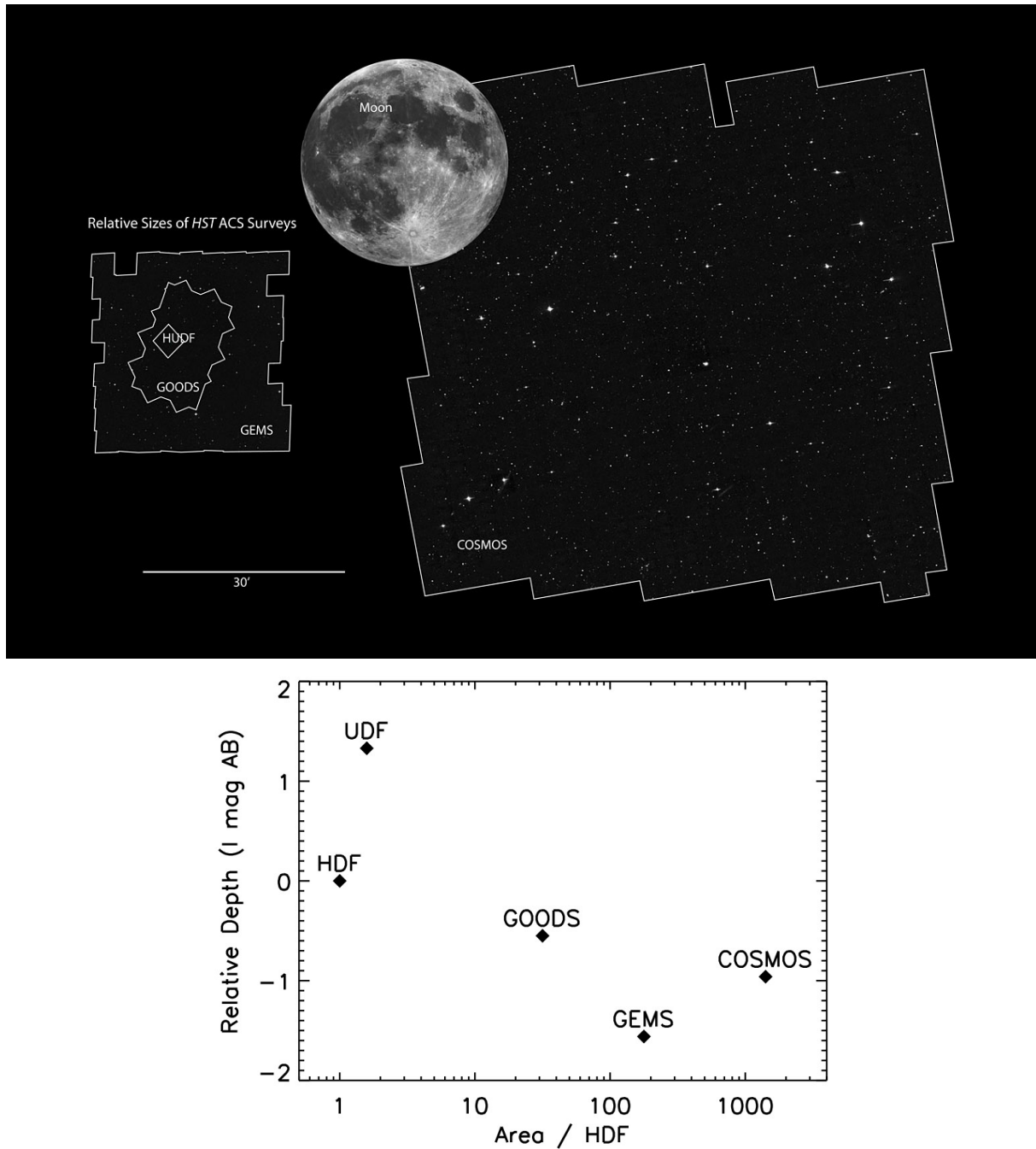


Figure 3.1: Upper panel: The Cosmic Evolution Survey (COSMOS) field compared in size with other HST-ACS surveys (UDF, GOODS and GEMS) and the angular size of the moon. Credit: Z. Levay (STScI) and NASA - ESA. Lower panel: Comparison of sizes and sensitivities of the major HST surveys at 8000 \AA , relative to the extension and sensitivity of the HDF survey. COSMOS field is 9 times larger than the GEMS, and has a sensitivity 1.4 times lower than GOODS data. Credit: [Scoville et al. \(2007b\)](#).

observations of the COSMOS field, additionally 9 orbits were carried out with the ACS-F475W g band filter. Parallel observations were also performed with NICMOS (F160W/H-band filter) and WFPC2 (F300W/U-band, F450W/B-band filters) HST instruments sampling in the first

case 6% (330 arcmin²) and in the second 55% (1.07 deg²) of the ACS area. COSMOS survey observations spanning in all the electromagnetic spectrum represent one of the most uniform, deepest and largest astronomical publicly available dataset ¹.

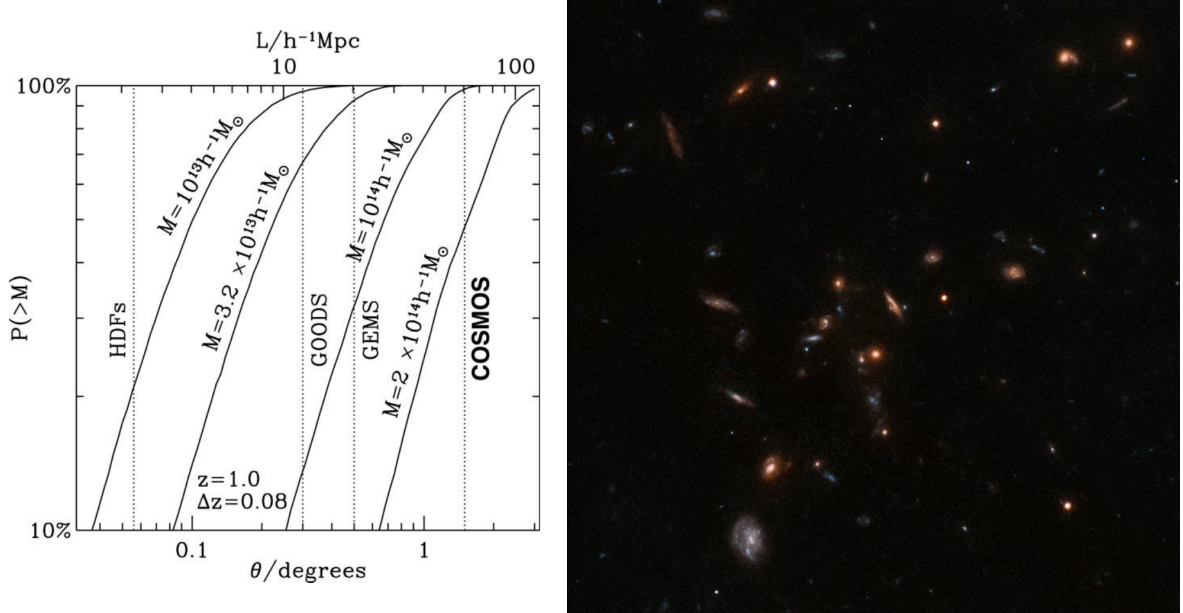


Figure 3.2: Left: Probability to detect at least one overdense structure in function of the survey area at $z=1$ for HDF, GOODS, GEMS and COSMOS (Scoville et al., 2007a) from the Virgo consortium Λ CDM simulation (Frenk et al., 2000). The indicated masses correspond approximately to those of the local group, a "poor" cluster, the Virgo cluster and 30% of the Coma super-cluster. Credit: (Scoville et al., 2007a). Right: ACS-HST image from the COSMOS survey of the CGr30 field of the MAGIC sample. This is one of the most massive galaxy groups in our sample with $M_{vir} \sim 6.5 \times 10^{13} M_{\odot}$. Credits: Thierry Contini (IRAP) and Benoît Epinat (LAM).

Thanks to the high sensitivity and resolution ($0.03''/\text{pix}$) of COSMOS observations it is possible to perform deep studies on the evolution and physical properties of numerous distant galaxies, through morphological determination from the stellar continuum distribution, multi-band photometric stellar mass and SFR computations, luminosity functions, environmental studies, AGN and gravitational lensing identification, and so on. One of the scientific motivations of the survey relies on the poor understanding of the evolution and interaction of LSSs and the mass assembling of galaxies and dark matter halos within them, by multiple mechanisms like merging, star-formation, AGN feedback, IGM gas accretion, etc. With this purpose the wide area of COSMOS was designed to sample the complete dynamic range of LSSs from voids and filaments to compact groups and massive clusters, which matches with our purpose of determining the role of environment in the evolution of galaxies in groups.

According to the Virgo consortium Λ CDM simulation (Frenk et al., 2000) overdense structures have masses up to the order of $10^{14} M_{\odot}$ and the probability of detecting such structures directly depends on the surveyed area as is shown on the left panel of Fig. 3.2. This Figure 3.2 presents the detection probabilities of structures at $z = 1$ for the HST surveys HDF, GOODS,

¹All the COSMOS survey multiwavelength observations are available at <http://cosmos.astro.caltech.edu/>

GEMS and COSMOS for masses of $10^{13} M_{\odot}$, $3.2 \times 10^{13} M_{\odot}$, $10^{14} M_{\odot}$ and $2 \times 10^{14} M_{\odot}$ corresponding approximately to the masses of the local group, a "poor" cluster, the Virgo cluster and 30% of the Coma super-cluster respectively (Scoville et al., 2007a). The COSMOS survey is then one of the biggest surveys which encompass a sufficiently large area to study the linked evolution of LSS and galaxies. According to Scoville et al. (2007a) the largest structures that are expected to be enclosed at intermediate redshift have a maximum mass (baryonic+dark) value of $2 \times 10^{14} M_{\odot}$. One example of such structure in our sample inside the COSMOS field is the group CGr30 presented in Figure 3.2 composed of 44 galaxies, with a virial mass of $\sim 6.5 \times 10^{13} M_{\odot}$ (Abril-Melgarejo et al. 2021, see Table 1 Section 5.5). More details about the selection of fields and galaxy groups are given in Section 3.3.

Among the HST observations in the COSMOS fields only the ACS-F814W exposures are available for all the sample of galaxies in groups analyzed in this study (see section 3.4) to perform a detailed morphological modeling (see Section 4.2).

3.2 Existing IFS surveys to study galaxy evolution

In several studies on the evolution of the cosmic SFR, it has been observed that there was a maximum of SF between $z \sim 1$ and $z \sim 2$ (see Figure 3.3), corresponding to the period in which dense structures were formed and got virialized. It is also an epoch of important morphological transformation of galaxies (see Section 1.2).

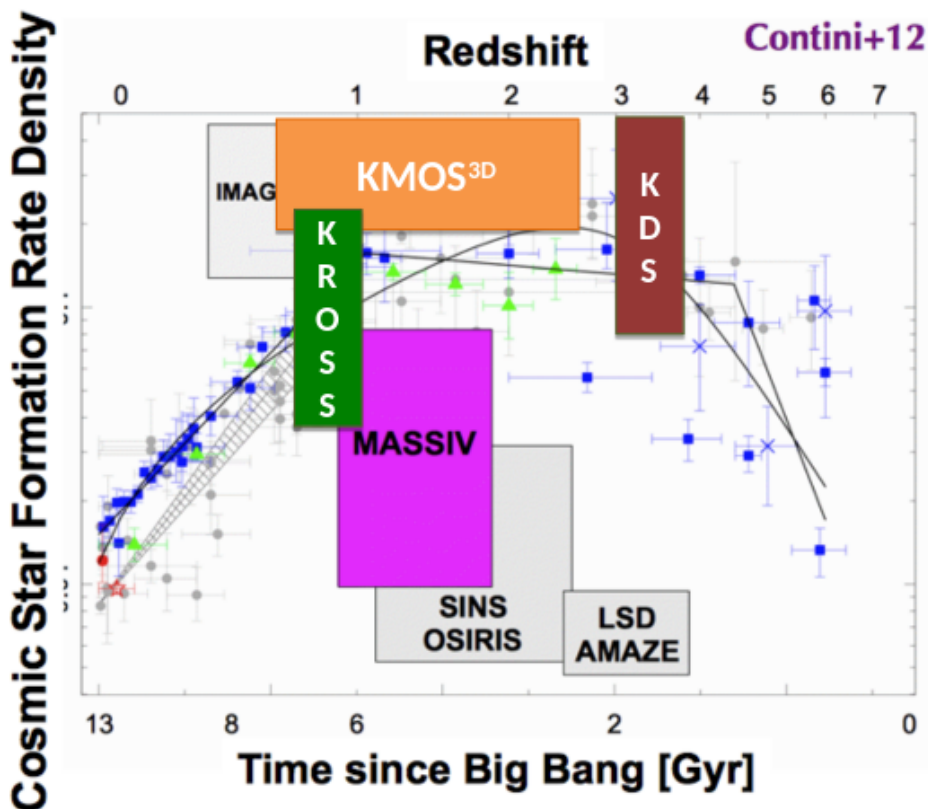


Figure 3.3: Cosmic SFR density as a function of look-back time and redshift and the relative coverage of different IFS surveys for distant galaxies from Contini et al. (2012). The evolution of the SFR density curve peaks at $z \sim 1 - 2$ followed by an important decrease. The coverage in redshift is presented for different IFS surveys: MASSIV ($z \sim 0.9 - 1.8$), SINS/OSIRIS ($z \sim 1.4 - 2.6$), LSD/AMAZE ($z \sim 2.6 - 3.8$), IMAGES ($z \sim 0.4 - 0.75$), KROSS ($0.6 - 1$) and KMOS^{3D} ($0.6 - 2.7$) and the KMOS deep Survey KDS ($3 - 3.8$, Turner et al. 2017). The vertical projection of each box represents the number of galaxies in each survey. Credit: Contini et al. (2012) and B. Epinat (LAM).

The Cosmic SFR density as a function of look-back time and redshift (presented in Contini et al. 2012 adapted from Hopkins & Beacom 2006) is presented in Figure 3.3, showing the evolution of the SF activity in cosmic time. After the maximum of SF there is an important general decrease of the SF activity in the Universe. The quenching of star formation is one of the most debated topics in astrophysics so several observing campaigns are devoted to study the different processes involved in the decrease of the SF capacity of galaxies. Some of the most important existing IFS galaxy surveys: LSD/AMAZE (Maiolino et al. 2008, Mannucci et al. 2009), IMAGES (Ravikumar et al. 2007, Puech et al. 2008, 2010), SINS/OSIRIS (Förster

Schreiber et al. 2006, Law et al. 2007), KROSS, KMOS^{3D} and the KMOS deep Survey (KDS, Turner et al. 2017), were built to study galaxy evolution at intermediate redshift around the peak of cosmic SFR ($z \sim 0.4 - 3.8$). The surveys are presented in Figure 3.3, showing their redshift coverage and a vertical projection representing the sample size.

Up to now several IFS datasets at intermediate redshift have been built with observations of hundreds of galaxies like KROSS or KMOS^{3D}, each with 795 and 739 galaxies respectively. However, most of the existing IFU data samples are focused on massive objects ($> 10^9 M_\odot$) of the galaxy population and they do not take into account the possible role of both the local and global environments in their evolution, this due to observational techniques and sample pre-selection strategies, see Table 3.1 in which the technical features of IMAGES, SINS, MASSIV, KMOS^{3D}, KROSS and KDS surveys are compared to those of the MAGIC survey. The main differences with MAGIC are the larger number of galaxies (mainly composed of SF galaxies but including all objects with secured spectroscopic redshift, see Section 3.3) in different environments (groups, clusters and field) and the lower mass limit having the possibility to extract morpho-kinematic properties of galaxies with low masses down to $10^{7.5} M_\odot$.

Table 3.1: Technical comparison of the current major IFS Surveys to study galaxy evolution at intermediate redshift. I introduce some characteristics of the MAGIC Survey (described in Section 3.3) in the last row. The columns from left to right correspond to: the name of the survey, the number of galaxies (mainly composed of SF galaxies), the median stellar mass or the range of masses, the median SFR or range of SFR, the operating band and instrument with which the observations are performed.

Survey	N gal.	z	$\log(M_*)$ M_\odot	$\log(\text{SFR})$ $M_\odot \text{ yr}^{-1}$	Operating band
IMAGES	68	0.4 – 0.75	10.2 – 11.1	2	Optical–NIR FLAMES GIRAFFE
SINS	80	1.3 – 2.6	10 – 11.1	1.14 – 2.9	J,H,K SINFONI
MASSIV	84	0.9 – 1.8	10.15 ± 0.3 9 – 10	1.5 ± 0.31 0.7 – 2.6	J, H SINFONI
KMOS 3D	739	0.6 – 2.7	9 – 11.4	1.56 -0.7 – 2.5	YJ, H, K KMOS
KROSS	795	0.6 – 1	10.0 ± 0.1	5 ± 1	J KMOS
KDS	77	3 – 3.8	9.8 9 – 10.5	– 0.2 – 2.4	K, HK KMOS
MAGIC	1080	0.2 – 1.5	– 7.5 – 11	– -2 – 2.6	Optical MUSE

As an example, in the particular case of KMOS data (from which KMOS^{3D}, KDS and KROSS surveys are composed), due to the observational strategy using 24 individual small pick-off mirrors and deployable arms (as it was described in Section 2.5.3), only individual

galaxies are targeted per IFU (inside a small FoV of $2.8'' \times 2.8''$, see Figure 2.17), which corresponds to 24 galaxies per exposure. This strategy does not allow the study of field galaxies or projected neighbor galaxies in structures at different redshifts inside the FoV. The multi-object configuration also implies to perform a pre-selection process biasing the sample towards massive SF galaxies ($>10^9 M_\odot$) which are the objects with larger S/N (stronger emission lines).

In the case of MUSE the WFM $1' \times 1'$ FoV is extended enough ($1'$ corresponds to ~ 500 kpc at $z \sim 0.7$), suited to detect large structures like compact groups at intermediate redshifts per exposure and lower mass galaxies than in other surveys. This was demonstrated by the study of kinematic properties of galaxies in the MUSE Hubble Ultra Deep South (HUDS) field performed by Contini et al. (2016), in which the TFR for 28 SF main sequence galaxies was obtained in a wide range of masses with an average of $10^9 M_\odot$ and down to $10^8 M_\odot$. Another study by (Boogaard et al., 2018) using MUSE deep data obtained the SFR vs. stellar mass relation constraining the low mass end ($10^7 \leq M_\odot \leq 10^{10.5}$), from a sample of 179 SF galaxies at $0.11 < z < 1$ in the HUDF.

3.3 The MUSE gAlaxy Groups In COSMOS, the MAGIC Survey

As was introduced above the COSMOS field is one of the most studied regions in the sky which gives the advantage of having a wide range of complementary datasets to perform multipurpose science on galaxy evolution. This section is focused on how MUSE-IFS data is suitable to the study and understanding of galaxy evolution at intermediate redshift with a morpho-kinematic approach. Thanks to the size of the MUSE FoV in wide field mode (WFM, 1 arcmin²), any exposure larger than 4 hours on blank fields produces observations enough resolved for kinematic extraction for several tens of galaxies at intermediate redshift, covering a large range of masses with minimum values of $10^8 M_{\odot}$.

With this purpose the MAGIC Survey (MUSE gAlaxy Groups In Cosmos; [Epinat et al. in prep](#)) was created, as part of the MUSE-GTO observing program specifically designed to investigate the role of the environment on galaxy evolution over the past 8 Gyrs (PI: T.Contini). The MAGIC survey is a 70h observing campaign, containing 18 blindly selected fields (no pre-selection bias), targeting 16 massive groups at $0.25 < z < 0.85$ (see Table 3.2), which are known overdense structures registered in catalogs of galaxy groups in COSMOS ([Knobel et al. 2009, 2012](#)) and in the VIMOS VLT Deep Survey (VVDS, [Cucciati et al. 2010](#)) field.

Table 3.2: List of groups in the MAGIC Survey their main observational characteristics

Group	z	Magic Fields	Exp. time (h) seeing (AO)
CGr32	0.732	CGr32 M1/M2/M3	3×4.35 (3.35)
CGr34	0.732	CGr34	5.25
CGr30	0.725	CGr30	9.75
CGr35	0.731	CGr35	4.69 (4.69)
CGr87	0.726	CGr87	2.68 (2.68)
VGr189	0.706	VGr189	2.25
CGr172	0.697	CGr172	4.69 (4.69)
CGr84	0.680	CGr84 / CGr84-North	5.25 / 4.35 (3.35)
CGr84b	0.696	CGr84 / CGr84-North	5.25 / 4.35 (3.35)
CGr114	0.659	CGr114	4.38 (2.18)
CGr79	0.531	CGr79	4.35 (3.35)
CGr28	0.530	CGr28	4.35 (3.35)
CGr26	0.439	CGr26	1
CGr61	0.362	CGr61	1
CGr23	0.354	CGr23	1
CGr51	0.341	CGr51	1

Among the observations 50% have been performed assisted with Adaptive Optics (AO, see Section 2.4) and the remaining half correspond to seeing limited observations with an average FWHM for all the sample of $\sim 0.7''$ at the [OII] narrow band (see Section 4.4 for details on the

determination of the MUSE-PSF). Regarding the exposure time per field the MAGIC sample is composed of 6 fields with snapshot exposures ($<3h$) and 12 fields with deep observations ($>4h$ up to $9h$). MAGIC groups are identified by the notation CGr (COSMOS group) or VGr (VVDS group), accompanied by their Group ID number according to [Knobel et al. \(2012\)](#) and [Cucciati et al. \(2010\)](#) for COSMOS and VVDS fields respectively (see Table 3.2).

The MUSE extended FoV has the advantage to cover structures an multiple objects at different redshifts, allowing to detect the spectroscopic redshift of ~ 200 galaxies in average (up to $I_{AB}=29.5$) per field. The determination of spectroscopic redshifts was made using the strategy described in [Inami et al. \(2017\)](#). The MARZ redshift finding algorithm ([Hinton et al. 2016](#), [Inami et al. 2017](#)) was used to identify the most prominent emission and absorption spectral features and to compute from them the average redshift values for each galaxy (for more details on the spectroscopic redshift determination for our sample see Section 5.5 and [Epinat et al. in prep.](#)).

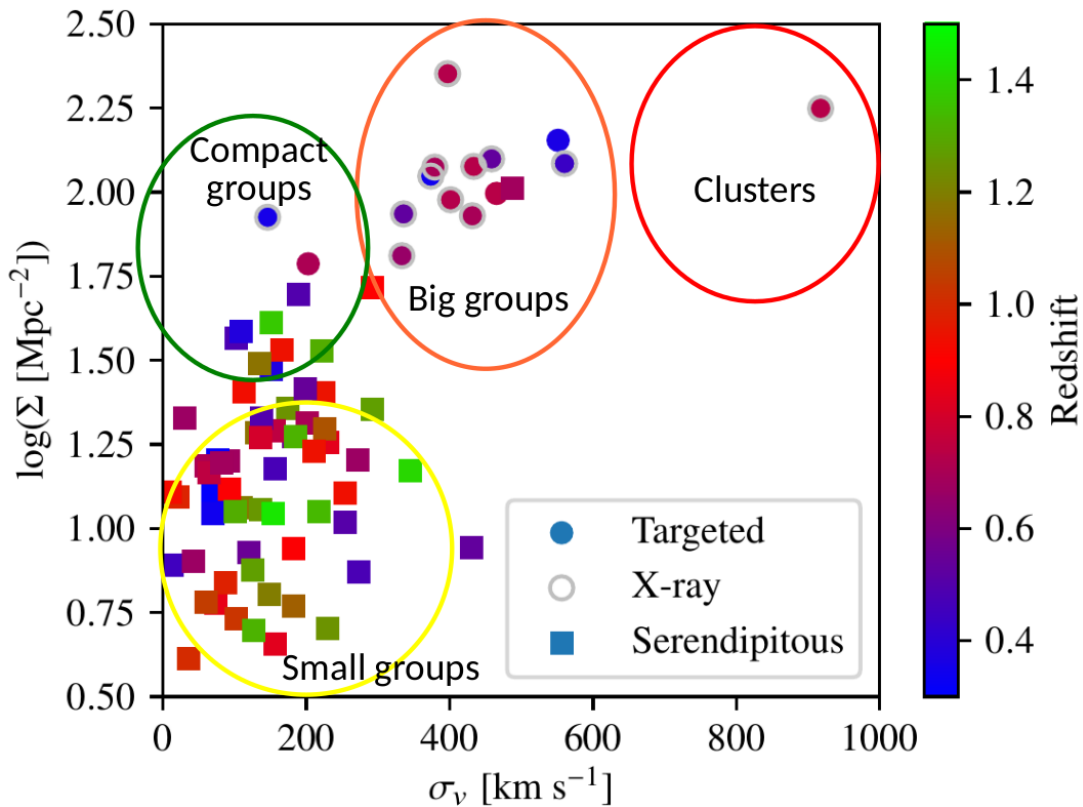


Figure 3.4: Distribution of MAGIC groups expressed as the galaxy density (number of galaxy members per Mpc^2) in function of the velocity dispersion of galaxy groups. The 16 most massive structures are targeted (filled circles) as dense environments (>10 galaxy members) from compact groups to clusters, at a redshift range $0.35 < z < 1.5$ (color code). Those groups with X-rays ancillary data are highlighted by gray circle contours. Galaxy groups newly discovered inside the MAGIC fields are represented by squares, most of them being small groups. Credit: [Epinat et al. in prep.](#)

The identification of the membership of galaxies to structures was made by applying a Friends of Friends (FoF) algorithm, imposing for each galaxy a maximum linking length (angular separation in the sky) of $\Delta L = 450$ kpc and a maximum velocity separation of $\Delta V = 500$ km s⁻¹ with respect to the nearest neighbor galaxies. Therefore, galaxies under these thresholds are considered as part of an structure (for more details on the FoFs methodology see Section 5.5 and [Epinat et al. in prep](#)). Following this criteria we identified several type of groups starting with small groups of 3–5 galaxy members, as it is shown by the diagram in Figure 3.4, which corresponds to the galaxy density (number of galaxies per Mpc²) in function of the velocity dispersion of galaxy groups. The average redshift for each group is color coded ranging from $z=0.3$ to $z=1.5$. All the groups represented by squares were not previously listed in the COSMOS and VVDS group catalogs and were discovered/identified by the precise spectroscopic redshift determination of MUSE observations. The targeted groups (filled circles) are the most massive structures (with at least 10 galaxy members), spanned in a wide range of velocity dispersion values which are related to the variety of masses of these structures. The variety of environments in the MAGIC sample is also evident in Figure 3.4, showing different kind of dense structures from compact groups to cluster environments.

The number of secure spectroscopic group members is increased by a factor of 2 – 4 with respect to the existing photometric catalogs (e.g. [Laigle et al. 2016](#)), like it was also shown in the study performed by [Bacon et al. \(2015\)](#) with MUSE deep observations (27 h) on the HUDF. This shows the power of MUSE data to increase the statistics for both galaxies in field and in dense environments by gaining detection from low mass galaxies. In MAGIC the total number of detected objects is as high as 2377, from which 1080 galaxies (including galaxies in fields) have reliable spectroscopic redshift values and enough S/N in [OII] to extract their kinematics.

Regarding MUSE observations, for groups CGr30 and CGr34 two different kind of datacubes were created. The first type of datacubes were generated by stacking all the observations (generating the possible longest exposure) to gain in depth, denoted as deep (D for CGr30) and mid-deep (MD for CGr34) datacubes. The second type datacubes were generated only considering observations with seeing $<0.7''$, denoted best-seeing (BS for both groups) datacubes (see Table 4.3 in Chapter 4). For all galaxies in groups in these fields the kinematics extraction and modeling was performed using both type datacubes, nevertheless the analysis was performed only on the deep exposures. Structure CGr32 is the most extended and massive in the MAGIC survey, it is in fact considered as a cluster ([Boselli et al., 2019](#)) with a total of 106 galaxies. Since it is more extended than the size of the MUSE FoV, a multi-field strategy was adopted collecting data from three sub-fields M1, M2 and M3. In the case of field CGr84 two extended groups relatively close in redshift (CGr84 at $z \sim 0.697$ and CGr84b at $z \sim 0.681$) were identified, as for CGr32 two sub-fields were necessary to sample these structures, both are extended inside two MUSE sub-fields: CGr84 (Figure 3.5) and CGr84-North.

This Thesis is based on the analysis of two subsamples of galaxy groups from the MAGIC survey, gathering a total of 329 galaxies at low and intermediate redshift dense structures as it is described in detail in the following Section 3.4.

3.4 Group sub-samples in the MAGIC Survey

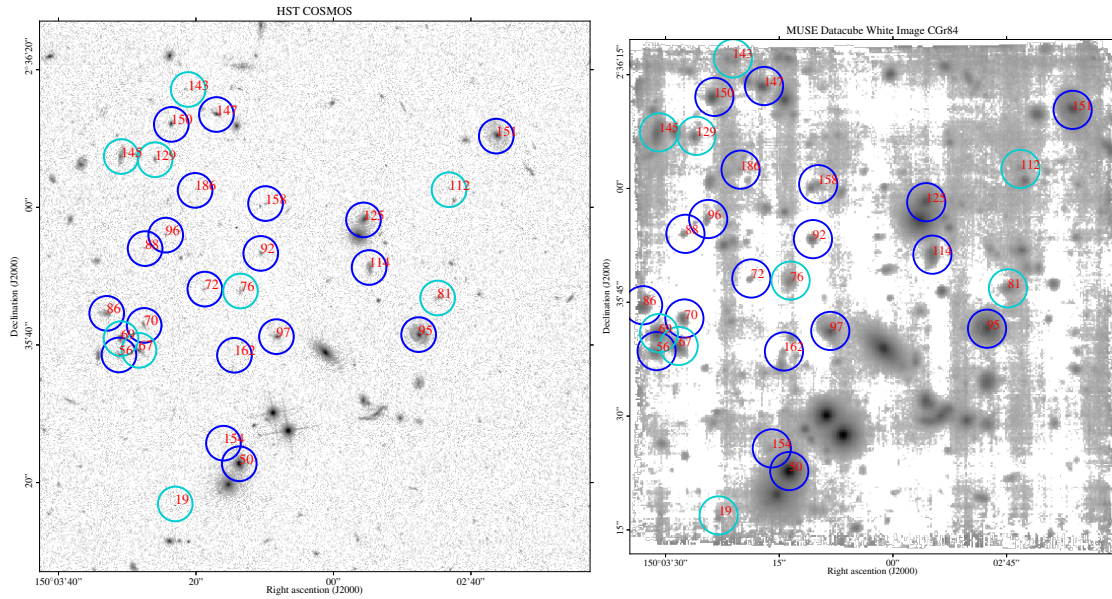


Figure 3.5: HST-ACS F814W high resolution image (left) and stacked white MUSE image of the Field CGr84. The MUSE white image was produced by collapsing the data cube along the λ axis. All galaxy members of groups CGr84 (blue contours) and CGr84b (turquoise contours) are circled indicating their location inside the field. These are extended structures observed with a multi-field strategy. Groups CGr84 and CGr84b were observed are sampled inside two MUSE subfields. Only south field in this configuration is shown to illustrate the differences between the HST-ACS images and the MUSE IFS output observations.

The goal of this study is to understand the mass assembly processes and the evolution of galaxies inside overdense structures through a morpho-kinematics analysis. This, by first modeling the surface brightness profile of galaxies in groups and then by extracting and modeling their kinematic properties (See Chapter 4). Later, with the aim to determine the link between DM and baryons, the stellar mass TFR is obtained and analyzed (see Chapter 5). Finally, by comparing the results derived from this study with others performed on galaxies at lower density environments, I look for evidences of the role played by the local and global environment on galaxy evolution.

In order to accomplish the study described above, I make use of high resolution HST-ACS F814W images and a sub-sample from the MAGIC survey containing the IFS observations from MUSE of 14 galaxy groups (e.g. Figure 3.5), from which 9 groups are part of the intermediate redshift sample ($0.5 \leq z < 0.75$) and 5 groups compose the low redshift sample ($0.3 \leq z \leq 0.5$). Both samples and their main features are indicated in Table 3.3. For group VGr189, the [OII] flux, rotation velocity and velocity dispersion observed maps were extracted, however the photometry available for this field from GEMS and CFHT was not enough resolved to perform a reliable morphological analysis. Therefore, VGr189 was not included in the analysis, although it is presented in Table 3.3 to report the MUSE observations as part of this project. Hereafter the reported parameters involving statistics of several groups do not have into account the values from VGr189. All the observations were performed using both seeing limited and

AO assisted with depths from 1 to 10 hours per datacube, spreading over 10 MAGIC FoVs for the intermediate redshift sample and 4 FoVs for the low redshift sample, where we identified 8 and 4 galaxy groups respectively. The total sample of galaxies in groups is composed of 330 galaxies, from which 278 reside at intermediate redshift structures and 52 at $z < 0.5$ groups.

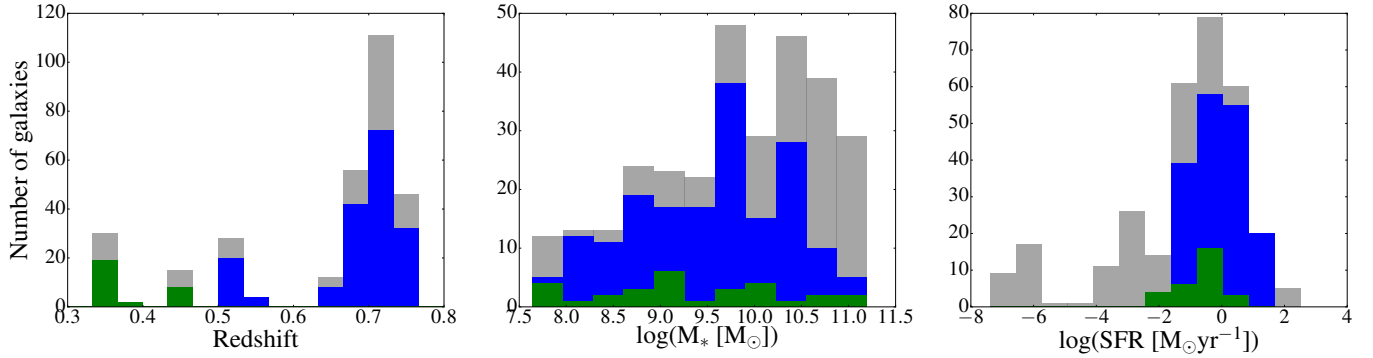


Figure 3.6: Distributions of z , SFR and stellar mass for the total sample of galaxies in groups analyzed in this thesis from the MAGIC survey. The parent sample corresponds to grey histograms, SF galaxies at intermediate redshift compose blue histograms and the SF low redshift sample corresponds to green histograms.

As was described above (Section 3.3), the existing IFS surveys have different preselection strategies, with observations performed independently from the environmental effects and in the high mass regime. So for the first time we have access to a suitable and unique sample composed of deep IFS observations in the optical range and high resolution photometry, covering different environments and gaining detection from low mass galaxies which represent an important part of the galaxy population.

In contrast with the features of the current intermediate redshift IFS major surveys presented in Table 3.1, the parent sample in groups covers a wide range of stellar masses: $10^{7.5} M_{\odot} \lesssim M_{*} \lesssim 10^{11.5} M_{\odot}$, and SFR: $-7.17 \lesssim \log(\text{SFR}) \lesssim 2.52 M_{\odot} \text{ yr}^{-1}$. Stellar masses and SFR values were computed using the extensive photometry available for the MAGIC fields (32 bands from the COSMOS2015 catalog; Laigle et al. 2016) by performing SED fitting using the code FAST (Kriek et al., 2009), all the details on the parameters used for the SED modeling are given in Section 5.5. Figure 3.6 shows the distributions in redshift, stellar Mass and SFR for the parent sample of galaxies in groups (grey histogram), the SF galaxies with spatially resolved kinematics in [OII] at intermediate redshift (blue histogram) and at low redshift (green histogram). From the redshift distribution most of the galaxies are at $0.65 < z < 0.75$ with the peak of the distribution around ~ 0.7 and a gap is observed at $0.55 < z < 0.65$. The median redshifts for the subsamples correspond to $z_{int} \sim 0.689$ and $z_{low} \sim 0.364$. The parent sample and the SF sample at intermediate redshift cover all the range of mass mentioned above, whereas the low redshift SF galaxies ranges between $8 < \log(M_{*}) < 11$. Both the intermediate and low redshift samples are mainly composed by SF galaxies with ranges $-3 < \log(\text{SFR}) < 2$ and $-2 < \log(\text{SFR}) < 1$ respectively.

General observational properties of all the studied galaxy structures are listed in Table 3.3, separating the intermediate and low redshift samples. Since the intermediate redshift sample traces the period of cosmic evolution after the cosmic maximum of SF, and has the deepest

ID COSMOS Group	R.A. (J2000)	Dec. (J2000)	Exp. Time (h)	z	Seeing (")	N galaxies (all/SED/MS/KS _{ini})
CGr 28	150°13'32.3"	1°48'42.5"	1	0.530	0.65	10/10/9/3
CGr 30	150°08'30.0"	2°04'01.2"	9.75	0.725	0.64	44/39/33/19
CGr 32-M123	149°55'19.0"	2°31'15.5"	3 × (1 + 3.35)	0.730	0.6-0.62-0.72	106/92/50/16
CGr 34	149°51'31.6"	2°29'28.1"	5.25	0.732	0.65	20/20/17/10
CGr 79	149°49'15.0"	1°49'18.1"	4.35	0.531	0.66	19/19/15/10
CGr 84	150°03'23.7"	2°36'09.0"	5.25 + 1	0.697	0.62-0.58 & 0.65	31/26/21/8
CGr 84b	150°34'41.5"	2°15'32.6"	5.25 + 1	0.681	0.62-0.58	35/32/25/9
CGr 114	149°59'50.3"	2°15'32.6"	2.2	0.659	0.74	12/12/8/2
VGr 189	149°55'19"	2°31'15.5"	2.25	0.706	0.72	12/-/-/3
Median				0.689	0.645	
Total			41.9			277/250/178/77
CGr 23	149°47'22.5"	2° 10'14.5"	1	0.355	0.83	8/8/7/5
CGr 26	150°29'32.8"	2° 04'10.3"	1	0.440	0.74	15/15/8/4
CGr 51	149°59'01.1"	1° 47'56.7"	1	0.340	0.78	10/10/6/6
CGr 51b	149°58'52.7"	1° 48'10.2"	1	0.480	0.72	5/5/4/4
CGr 61	149°43'37.1"	1° 55'08.2"	1	0.364	0.78	14/14/8/6
Median low z				0.364	0.78	
Total low z			4			52/52/33/25
Median ALL				0.531	0.66	
Total ALL			46.9			329/302/211/102

Table 3.3: General properties of the galaxy groups and clusters in the parent sample of galaxies in groups from the MAGIC survey. (1) COSMOS Group ID. (2)and (3) J2000 coordinates of the centres of the galaxy groups.(4) Total Exposure time per field. (5) Median redshift of the group. (6) MUSE seeing of the narrow band image around the projected λ of the [OII]doublet at the group's redshift (from PSF determination as described in Section 4.4) (7) Total number of member galaxies per group according to the applied Friend of Friends analysis as described in Section 3.3. (8) Number of galaxies per field with well defined velocity fields suitable for kinematic analysis (initial kinematic sample, See Chapter 5 for more details on the final sample selection).

MUSE observations and the largest structures, it is the sample used to perform the study in [Abril-Melgarejo et al. 2021](#) (see Section 5.5). The information in Table 3.3 is presented as follows: The group ID in MAGIC, the coordinates of the group centre (J2000), total exposure time of the analyzed datacubes, median redshift of the group, MUSE seeing in [OII] narrow band (determined as it is described in Section 4.4) and total number of galaxies. The counting of galaxies with SED modeling (those with multiband photometry), galaxies in the main sequence of SF and galaxies in the kinematic sample (those with spatially resolved kinematics of the ionized gas, see Chapter 5), are also presented. A total of 47 h of observations are accumulated by the parent sample, from which 42 h correspond to observations in the fields of the intermediate z groups and only 4 h are devoted to the low redshift (all in snapshot mode with 1h exposure time). The average FWHM in [OII] for the intermediate and low z samples are 0.66" and 0.78" respectively, this difference is mainly due to the variation on the seeing conditions during observations as it is discussed in Section 4.4.

In order to verify the consistency between photometric rest frame color- color ($M_{NUV}-M_R$ versus M_R-M_J) and the color ($M_{NUV}-M_R$) versus stellar mass diagrams with SFR values, I obtained these diagrams for the intermediate redshift sample in groups using the COSMOS

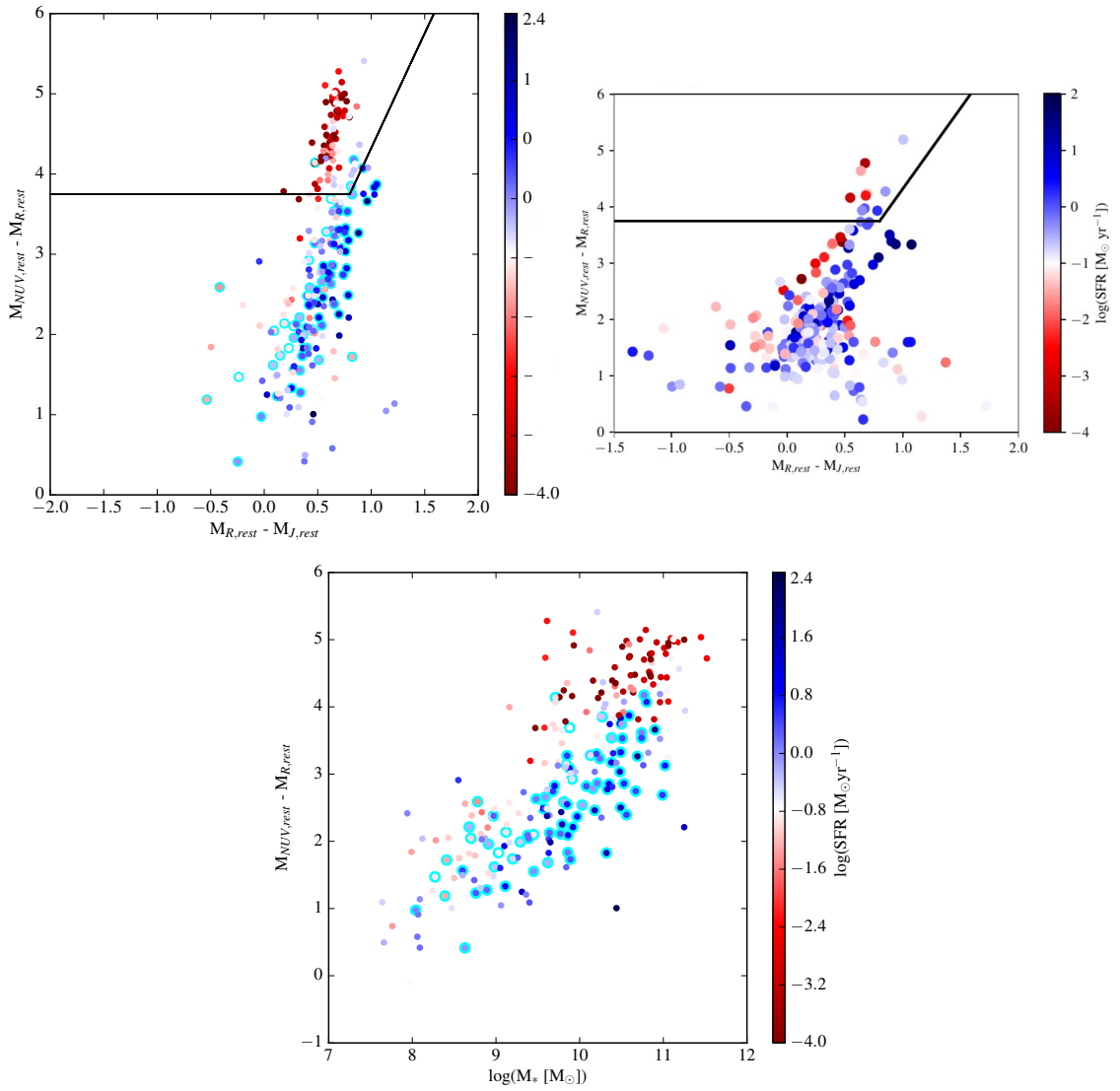


Figure 3.7: Upper panel: Rest frame $M_{NUV} - M_R$ versus $M_R - M_J$ color-color diagram for the intermediate z sample (left) and for the sample of galaxies in field (right), color coded in function of the SFR being SF galaxies those in blue and passive in red. The black line marks the limit between SF galaxies (below the line) and passive galaxies (above the line) adopted from [Lemaux et al. \(2014\)](#). Credit for the upper right diagram: B. Epinat(LAM) and W. Mercier(IRAP). Lower panel: Color (rest frame $M_{NUV} - M_R$) versus stellar mass diagram in function of SFR for the intermediate z sample. For the diagrams corresponding to galaxies in groups (upper left and lower panels), the points enclosed by turquoise contours correspond to the kinematic sample at intermediate redshift, which is entirely composed of galaxies residing in the main sequence of SF. The separation between main and red sequence galaxy populations is noticeable in these diagrams.

photometry and the stellar mass (computed from SED fitting), color coded in function of SFR (SED) as in shown in Figure 3.7. In these diagrams there is a clear separation between SF galaxies (blue dots) and quiescent galaxies (red dots), matching in most of the cases with the expected locations for SF and passive galaxies in the photometric diagrams. In the Color-Mass diagram we can observe the fraction of quiescent galaxies increases with stellar mass, being

important for $M_* > 10^{10} M_\odot$, in agreement with the Mass quenching hypothesis discussed in Section 1.5. The fraction of passive galaxies in groups corresponds to 30.1% for the total parent sample, 36.6% for the intermediate z sample and 28.8% for the low redshift sample. From a preliminary study performed on galaxies in field within the MAGIC sample by W. Mercier, it has been observed this sample in lower density environments has a small fraction of quiescent galaxies, being mainly composed of galaxies in the main sequence at the redshift range $0.5 < z < 0.8$ (the same of our group sample at intermediate z) as it is showed in the upper-right panel of Figure 3.7. Moreover, the fraction of passive galaxies in structures is not negligible and might indicate there are active quenching processes inside them which are more efficient than in field.

In Summary, thanks to the extensive ancillary datasets available for COSMOS fields including high resolution HST images (as it was described in Section 3.1) and to the deep MUSE-IFS observations, both kinematics and morphology can be reliability modeled and analyzed for hundreds of galaxies in groups and in field, offering an unprecedented IFS dataset for the study of the role of environment including the low mass galaxy population. The evolution of galaxies in groups was extensively studied in this project using the intermediate redshift sample as it is presented in Chapters 4 and 5.

Chapter 4

Morphological and kinematic Modeling

Morphology is a key global characteristic of galaxies, giving information about their structure (geometrical distribution of its visible components), their interactions with other galaxies and/or with the environment and their evolutionary status. In order to trace the evolution of Morphology it is necessary to gather high resolution observations at different redshifts to follow the changes in structure in cosmic time. The main limitation with distant galaxies is that their apparent sizes become considerably small, specially for low mass galaxies which in some cases can not be resolved. For this reason, I make use of high resolution images from the HST-COSMOS Survey (see Section 3.1) to model the morphology of the entire sample of galaxies in groups.

The luminosity distribution of galaxies in two dimensions is known as surface brightness, in other words it is the total flux per unit of solid angle on the sky of an extended object. Accounting for the gradient of luminosity from the center to the outskirts is fundamental to determine the physical properties of galaxies, specifically the distributions of their components and their size. According to the different morphologies from the Hubble sequence introduced in Chapter 1, in the local Universe we have three main morphological categories: elliptical galaxies dominated by a spherical bulge and an extended stellar halo, spiral galaxies with a central bulge and a disk containing in some cases structures like bars and/or arms and irregular galaxies with undefined morphologies sometimes presenting clumps of star-formation HII regions. At intermediate redshift however, the diversity of morphologies is more complex since irregular, peculiar galaxies with clumpy disks are more common than in the local Universe, representing up to $\sim 50\%$ of the galaxy population at $z \sim 0.7$ (Delgado-Serrano et al., 2010), which implies Hubble sequence based on regular features only holds at low redshift, as was introduced in detail in Section 1.2.

Images from the HST-COSMOS survey at the near infrared band F814W have a spatial sampling of 30 mas/pix (Scoville et al., 2007a), which corresponds to ~ 200 pc per pixel at a redshift of $z \sim 0.7$ (see Section 4.1). At this band the stellar continuum from the old stellar population dominates the integrated light so I can recover with high resolution the morphological features. Considering the Hubble sequence, I use the two most prominent morphological components, a spherical bulge and an exponential disk to obtain a composite model as it is detailed in Section 4.2. The model was performed on both the low and intermediate redshift samples for a total of 328 galaxies.

To perform the model of light profiles for stars and galaxies I used the algorithm GALFIT¹ (Peng et al. 2002 and Peng et al. 2010a), designed to fit light profiles of galaxies and PSF determination, using two dimensional analytic functions (more details in section 4.2).

The data analysis algorithm GALFIT uses some of the most typical two-dimensional analytic functions in literature to create surface brightness models for galaxies and stars, among them: Nukker, Moffat, Gaussian, Sérsic/ de Vaucouleurs, exponential (Peng et al., 2010a) and a user defined PSF (created as described in Section 4.1). There are other functions available like sky to account for the sky background emission in a FoV, a Ferrer profile which is adapted to model bars, and an edge-on disk to account for possible vertical structures. There are also options to describe more complicated shapes based on ellipsoids this by using Fourier models, bending, truncation, etc. GALFIT generates different models in consecutive iterations from the initial parameters set in an input file. Then GALFIT searches for the best model varying the parameters set as free using a minimization engine based on the Levenberg-Marquardt algorithm (downhill gradient), stopping iterations until the convergence is reached.

4.1 HST-COSMOS PSF modeling

The Point Spread Function PSF is the response of an optical system to a point-source due to the diffraction limit (finite aperture), the spatial resolution of the detector and optical aberrations proper of the system. In other words, the PSF denotes the ability of the instrument to resolve a point-source. In the ideal image with no aberration from the optical system and within an infinite aperture the PSF should be represented by a delta function (δ , an infinitely thin profile), or in the case of a circular aperture an Airy function (interference pattern produced by diffracted light when it passes through a circular aperture) is obtained. However, in reality the observed effect of the instrumental response is the blurring or spreading of a point-source in the focal plane that is characteristic of each instrument. In the case of ground based telescopes the PSF also contains information about the variations due to the diffraction produced by the turbulence of different layers of the atmosphere, which is characterized by a factor known as astronomical seeing (See Section 4.4 on the determination of the PSF for MUSE observations). For space telescopes the PSF is only related to the variations introduced by the optical composite system telescope+instrument.

In any case it is necessary to model the PSF which is based on theoretical profiles to account for the mentioned blurring effects, this with the aim to correct the images before proceeding with the scientific analysis. One way to determine the PSF is to model the luminosity profiles of non-saturated stars in a FoV of the observed objects since stars are natural point sources. Nevertheless if the FoV is too extended (to the order of arcmins), the PSF can vary along the FoV. The ideal is to have various stars per field at different locations in the FoV. Since images from the ACS-HST camera are very stable and have a high spatial sampling, this effect does not considerably affect the exposures. Besides, the final ACS-HST images have been processed and contain several individual exposures so the effects due to the position in the camera field are accounted by averaging all the exposures. In Section 4.4 we have taken this into account

¹This is an open source algorithm available at [GALFIT website](#)

basically using a similar strategy since datacubes are the product of different exposures which are averaged in the reduction process, besides I used narrow images of stars at different locations of the MUSE FoVs. In our datasample for a 1 arcmin² FoV we have from 2 to 4 stars per HST field with a total of 27 stars which are enough to have a good statistics on the PSF parameters and their possible variations. The most common profiles used to characterize a PSF are the Gaussian and the Moffat profiles. A Gaussian normalized profile is described as follows:

$$G(r, \sigma) = \frac{1}{2\pi\sigma^2} e^{-\frac{r^2}{2\sigma^2}} \quad (4.1)$$

while a Moffat normalized PSF profile is defined as:

$$M(r, \alpha, \beta) = \frac{\beta - 1}{\pi\alpha^2} \left[1 + \left(\frac{r^2}{\alpha^2} \right) \right]^{-\beta} \quad (4.2)$$

where $\alpha \neq 0$ and $\beta > 1$.

From these mathematical formulations we can observe that both profiles have a circular symmetric variation. The Gaussian profile is the most basic approximation of a PSF having a single free parameter σ related with the profile dispersion whose Full Width Half Maximum (FWHM) is given by $\text{FWHM} = 2\sigma \sqrt{2 \ln 2}$. The problem with Gaussian profiles is that the flux in the wings of the observed PSF could be underestimated (Trujillo et al., 2001). In contrast a Moffat profile has two free parameters α and β , being α the characteristic profile width correlated to $\text{FWHM} = 2\alpha \sqrt{2^{1/\beta} - 1}$ and β is the parameter that controls the extension of the wings (quantity of light in the wings) with respect to the central part of the profile. The effect of the variation of β is showed in Fig 4.1 for profiles with the same FWHM, for $\beta = 10, 3$ and 1.5 . When $\beta < 10$ the Moffat profile has a sharper and smaller peak with more extended wings in comparison with a Gaussian PSF (red curve), while when $\beta \sim \infty$ it becomes a Gaussian curve (Trujillo et al., 2001).

Previous to the galaxy surface brightness profile modeling, I performed a careful calculation of the PSF for HST images at F814W band. I first identified the stars taking all the objects with $z \sim 0$ and a confidence parameter $\text{CONF} > 1$ (CONF varies between 0 and 3, where 3 is the maximum confidence for redshift measurements) from the MUSE redshift measurements performed using the method established by Inami et al. (2017) (for more details see Section 3 of paper Abril-Melgarejo et al. 2021 at 5.5). I then cross-checked with photometric and spectroscopic catalogs within the SIMBAD² database to confirm these objects as stars. The PSF was computed by modeling the profile of all the stars in the fields using Moffat functions due to the fact that this profile samples better the PSF sharpness and the extension of the faint end (light wings). It is important to highlight that for all the modeling performed with GALFIT (stars and galaxy light profiles), I used a background profile (sky function in GALFIT) to account for the sky background emission in the center of the fitting region, this in order to recover more reliable PSF and photometrical parameters. To illustrate the PSF determination process for ACS-HST images, Fig 4.2 shows an example of the PSF fitting, presenting from left to right: the observed HST image of the star, the Moffat model and the residual in consecutive panels.

The modeling was applied on 27 stars in 11 MUSE Fields using two different strategies. In order to check for asymmetric bias I let the position angle (PA) and the parameter b/a (ellip-

² Administrated by the Centre de Donnés Astronomiques de Strasbourg (CDS) [SIMBAD](#)

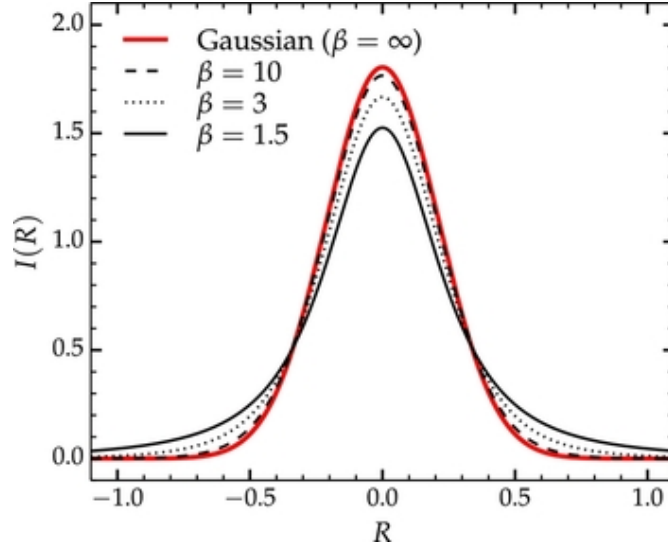


Figure 4.1: Comparison of Moffat and Gaussian PSF profiles, showing for small β values a sharper Moffat profile with a lower peak and more extended wings compared to a Gaussian curve (red curve). When $\beta \sim \infty$ both profiles become indistinguishable. Taken from the [Cambridge Core PROFILER website](#) based on the PSF study from [Trujillo et al. \(2001\)](#)

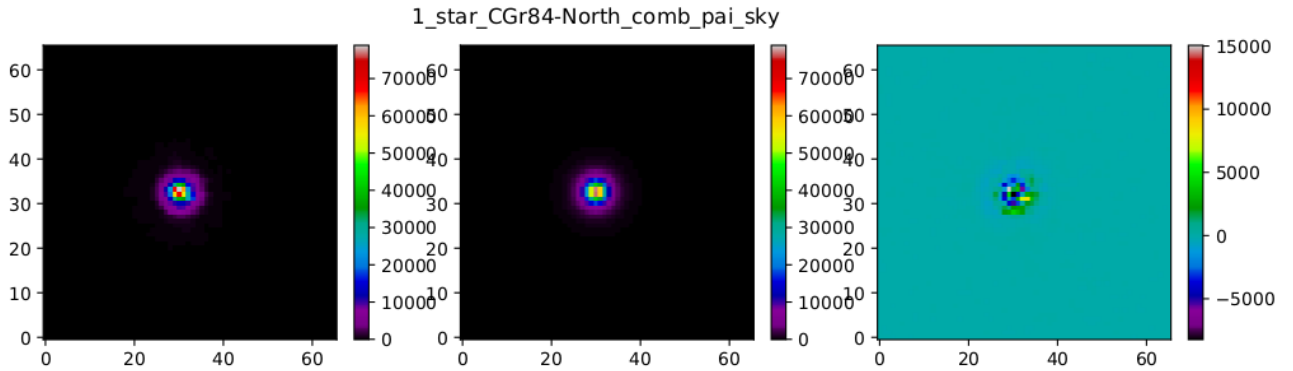


Figure 4.2: PSF fitting process showed in images at arbitrary flux units. Left: Original HST image of a star in Field CGr84 in F814W band. Center: Model obtained with GALFIT. Right: Residual image.

ticity of the PSF) free. I obtained a PSF with median parameters: $b/a = 0.96$, $\text{FWHM} = 2.94$ and $\beta = 1.93$. Now using a circular Moffat profile (with fixed $b/a = 1$), I obtained a PSF with median $\text{FWHM} = 2.8371$ pixels which is equivalent to 85 mas and a median control parameter of $\beta = 1.9102$. Since the b/a obtained using a free symmetry parameter is close to 1 there is no a systematic asymmetry in the sample of stars. Therefore to construct the PSF I used to correct the instrumental distortions on the images of galaxies necessary to perform the morphological modeling, I took into account the parameters derived from the symmetric Moffat profiles. The resulting parameters with their errors from the best fittings corresponding to each star, and the average values in bold with which the PSF function is created using GALFIT are presented in Table 4.1.

Assuming a Λ CDM Cosmology with $H_0 = 70 \text{ km s}^{-1} \text{ Mpc}^{-1}$, $\Omega_M = 0.3$, and $\Omega_\Lambda = 0.7$, the

Table 4.1: PSF parameters determined with Moffat models for 27 stars in COSMOS fields using GALFIT. Since GALFIT provides an arbitrary integrated magnitude, I adopted the GALFIT magnitude of the brightest star $m_{\text{GALFIT}} = 12.6$ as reference value, this in order to compare the relative brightness among the modeled stars. From left to right the columns correspond to: , the FWHM and its corresponding error dFWHM and the β control parameter with its corresponding error $d\beta$. The values in bold on the last row of the Table are the median values used to create the HST-COSMOS PSF.

Mag	FWHM	dFWHM	β	$d\beta$
3	2.79	0.02	1.88	0.01
2	2.86	0.02	1.93	0.01
2	2.78	0.02	1.87	0.01
3	3.31	0.03	2.1	0.02
2	2.77	0.02	1.84	0.01
4	2.76	0.02	1.86	0.01
3	2.81	0.02	1.91	0.01
2	2.97	0.02	1.99	0.01
2	3.08	0.02	2.05	0.01
3	2.90	0.03	1.98	0.02
1	2.99	0.02	2.02	0.01
0	3.56	0.08	2.33	0.06
3	2.75	0.02	1.71	0.01
4	2.79	0.03	1.70	0.02
0	3.72	0.05	2.28	0.03
1	2.88	0.02	1.99	0.01
1	2.83	0.02	1.87	0.01
0	4.17	0.05	2.82	0.04
2	3.18	0.03	1.92	0.01
2	3.50	0.03	2.27	0.02
1	2.79	0.02	1.91	0.01
3	2.76	0.02	1.73	0.01
5	3.77	0.06	2.29	0.04
4	2.84	0.04	1.72	0.02
0	2.70	0.02	1.90	0.01
2	2.84	0.02	1.87	0.01
4	2.51	0.03	1.65	0.01
2	2.84	0.02	1.91	0.01

median FWHM in Table 4.1 corresponds to an aperture of 85 mas which is in turn equivalent to a physical scale of $\sim 410\text{--}620$ pc (in the galaxies' frame), in that redshift range of $z=[0.341\text{--}0.75]$ including the sample of galaxies in groups.

4.2 Two-component surface brightness Morphological modeling

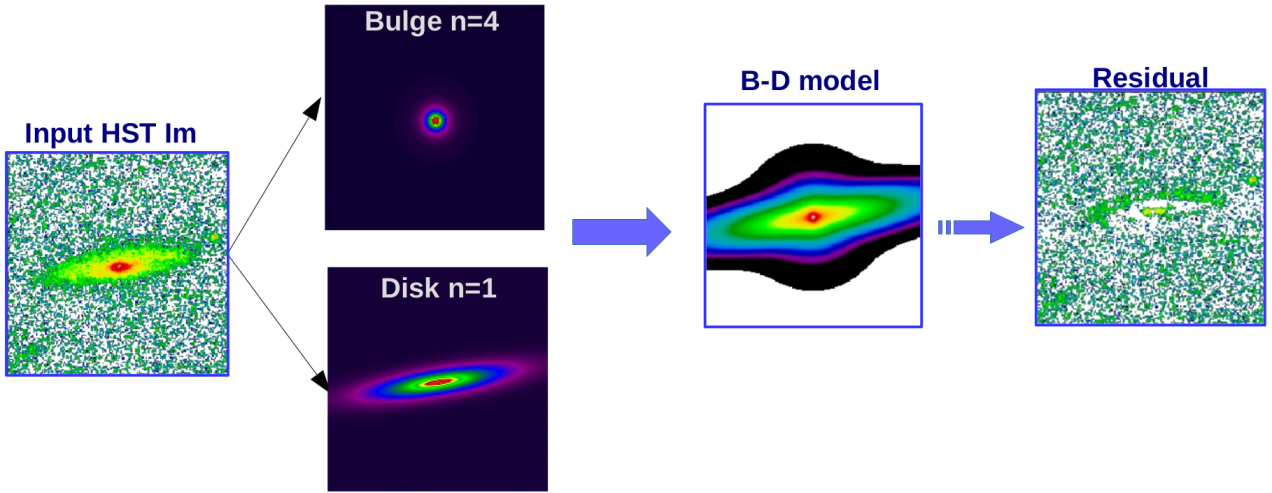


Figure 4.3: Graphic scheme of the bulge-disk morphological decomposition applied to all the sample. To illustrate the decomposition method I use the F814W HST image of galaxy CGr34-59 on the left, followed by the separated model profiles corresponding to a de Vaucouleurs bulge ($n=4$, left part of Eq.4.6) and to an exponential disk ($n=1$, right part of part of Eq.4.6). To the right the diagram shows the composite morphological model and the residuals, where internal structures like a bar and the arms are revealed.

With the aim of obtaining the geometrical information, the morphological type, size and particularities relative to each galaxy of the sample, I performed a detailed morphological modeling of the surface brightness distribution. I made use of high resolution images from the HST Advanced Camera for surveys (ACS), obtained with the F814W filter which at $z \sim 0.7$ corresponds to a central rest-frame wavelength of $\sim 5000 \text{ \AA}$. At red rest-frame bands it is possible to trace the continuum emission from the old low-mass stellar populations, which dominates the mass budget of the stellar component. Besides, the high resolution equivalent to $0.03''/\text{pix}$ using the same F814W band from the whole COSMOS photometric survey (Section 3.1), ensures a homogeneous sampling of the surface brightness for all the sample. This is the highest resolution publicly available photometry for our sample, which allows recovering the structural features of studied galaxies at sub-kiloparsec scales as was discussed in section 4.1.

The geometrical parameters to be obtained as first guesses for posterior kinematic modeling (see Section 4.6) are the major axis position angle (PA) and the inclination (i) of the disk component (for late type galaxies). Later the effective radius is used for analysis and to determine rotation velocities, classification, size, etc. The size of a galaxy can be normally determined by two characteristic values, either the effective radius or in the case of disk-like galaxies the disk scale length. The effective radius or half-light radius R_e is the radius at which 50% of the total luminosity is enclosed, while the disk scale length R_d is the radius at which the brightness of the disk component has declined by a factor of e from the galactic center, assuming an exponential

decreasing surface brightness profile.

Since the pioneering studies of de Vaucouleurs (1948 and 1953, de Vaucouleurs' 'law') and King (1962 and 1966, proposing the King profile), there have been several analytical descriptions for the light profiles of galaxies. Currently, the most commonly used model is that proposed by Sérsic (1963) with a $R^{1/n}$ model (see Eq. 4.3), which implies that the higher the index n , the more concentrated/sharper the profile in the center. This Sérsic function has proven to accurately model a broad variety of spheroidal components from bulges in the centers of late type galaxies to highly concentrated and luminous spheroid centers of early type galaxies surrounded by an extended faint halo, this by varying the concentration index n (known also as Sérsic index). The Sérsic function is defined as it is presented in (Peng et al., 2010a) and in turn as it was established by Graham (2005³ and 2013⁴):

$$\Sigma(r) = \Sigma_e e^{-b_n \left[\left(\frac{r}{R_e} \right)^{1/n} - 1 \right]} \quad (4.3)$$

where the fundamental parameters are the radial distance to the profile center r , the effective radius R_e , the surface brightness at that radius Σ_e and the concentration index n . The parameter b_n is obtained by integrating the surface brightness $\Sigma(r)$ (Eq. 4.3) over a circular projected area $A = \pi r^2$ with $r \rightarrow \infty$, to obtain the total luminosity (L_T). A second integration is made to recover the half light radius R_e where $L_e = L_T/2$. The parameter b_n is defined in terms of the Sérsic index such that:

$$\Gamma(2n) = 2\gamma(2n, b_n) \quad (4.4)$$

where Γ and γ are the complete and incomplete gamma functions respectively. The incomplete gamma function is given by:

$$2\gamma(2n, x) = \int_0^x e^{-t} t^{2n-1} dt \quad (4.5)$$

From all these definitions and assuming a spherical symmetry to model spheroidal components from different morphological types, I set $n=4$ obtaining a de Vaucouleurs profile $R^{1/4}$ (see Figure 4.3). Regarding the disk component, from studies like de Vaucouleurs (1957) and Freeman (1970), among others, it is determined that light profiles of flat disks are approximately exponential, setting the Sérsic index at $n=1$ obtaining a profile of the form $I(r) = I_0 e^{-r/R_d}$, where I_0 is the central surface brightness and R_d is the disk scale length. This function is known as exponential disk profile (see Figure 4.3). Finally having all these elements settled, the two-components morphological model I applied to obtain the surface brightness profile consists of a spheroidal de Vaucouleurs bulge and an infinitely thin exponential disk such that:

$$\Sigma(r) = \Sigma_b(R_e) e^{-b_4 \left[\left(\frac{r}{R_e} \right)^{1/4} - 1 \right]} + \Sigma_d(0) e^{-r/R_d} \quad (4.6)$$

³The original formulation from Sérsic (1963) is given in function of the brightness of isophotes with SB m such that $B(s) = 10^{-0.4m''} e^{-n \left(\frac{s}{s_0} \right)}$, which is equivalent to the modern form of surface brightness in function of radius in Eq. 4.3

⁴This is a summary review of all the light profiles derived in literature from the Vaucouleurs law, passing by Sérsic and other formulations

where $\Sigma_b(R_e)$ is the bulge surface brightness up to the effective radius and $\Sigma_d(0)$ is the central brightness of the disk. To illustrate this decomposition method, Figure 4.3 shows a diagram with the original HST image of the disk galaxy CGr34-59, followed by a sequence of SB profiles of the individual de Vaucouleurs bulge and exponential disk, the composite model and the resulting residual. Assuming a circular original shape of the disk component implies that a face-on disk galaxy ($i=0^\circ$) should have a surface brightness (SB) characterized by circular concentric isophotes (contours enclosing areas with the same light quantity), therefore its stellar light distribution is observed to have a circular symmetry. Under this general assumption of symmetric light profiles, the disk of galaxies with $i > 0^\circ$ have an apparent elliptical SB distribution due entirely to geometrical projection. I then use the observed elliptical light distributions of galaxies to determine the morphological center, the ellipticity (ε), the inclination and the orientation of the disk with respect to its semi-major axis (PA).

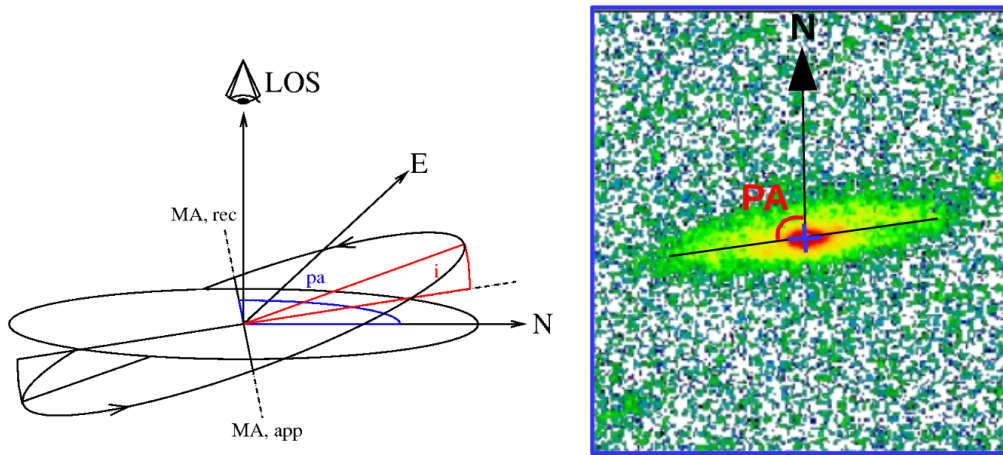


Figure 4.4: Graphic schemes of projection parameters of disk galaxies, inclination (i) and Position Angle (PA). Left: Diagram showing a galaxy disk plane, the perpendicular plane to the line of sight (the sky plane) and the angular separation between them corresponding to the inclination measured by the observer, credits: [Titled Ring Fitting Code \(TiRiFiC\)](#). Right: F814W HST image of galaxy CGr34-59 used to illustrate the PA, which corresponds to the angle between the North direction and the semi-major axis of the apparent plane of the disk galactic disk. In this image the barycentre is also indicated by a blue cross.

The fundamental parameters to be recovered from the morphological model are:

- The morphological center is the nearest point to the barycentre of the distribution and that with maximum luminosity (see right Figure 4.4). I highlight at this point that both components of the SB profile share the same center as input in order to trace the profile from the barycentre with both functions.
- Ellipticity accounts for the elongation of a disk due to its apparent orientation on the sky and it is defined as $\varepsilon = 1 - b/a$, being b and a the semi-minor and semi-major axes respectively. In order to account for the projection effects and to recover the physical

properties at the galaxy frame, it is necessary to determine the inclination (i) of the disk, which corresponds to the angle between the plane of the disk and the sky plane perpendicular to the line of sight (see left Figure 4.4). Inclination has a direct dependency on the b/a and therefore on ellipticity. Besides, if the thickness of the disk is taken into account, the i angle is given by the oblate spheroid established by Holmberg (1946) as follows:

$$i = \cos^{-1} \left[\frac{(b/a)^2 - q_0^2}{1 - q_0^2} \right]^{1/2} \quad (4.7)$$

where $q_0 = c/a$ is the axial ratio of a disk viewed in edge-on orientation between the semi-minor axis of the oblate spheroid c (vertical extension of the disk) and the semi-major axis a . In this case an infinitely thin disk is assumed with $q_0 = 0$, so the inclination depends exclusively on the b/a so Eq. 4.7 is simplified to $i = \cos^{-1}(b/a)$.

→ The Position angle. To fully characterize the disk orientation is necessary to determine the position angle (PA) that corresponds to the angular separation between the North direction and the semi-major axis on the apparent plane of the galaxy (see right Figure 4.4). PA can be measured from the photometrical SB profile and also from the velocity maps from neutral or ionized gas (when available), they correspond to the morphological (PA_m) and kinematic (PA_k) position angles respectively. Morphological PA is commonly expressed as modulo π whereas the kinematic PA as modulo 2π .

Non-axisymmetric structures like spiral arms, bars, etc, were also modeled in few exceptional cases in which they represented a dominant component biasing the recovered geometrical parameters. In most cases, the bulge-disk decomposition is sufficient to effectively trace the global features. Besides, at intermediate redshifts galaxies seem to show more fragmented structures sometimes dominated by giant clumps of star formation that were also modeled. I was more focused on retrieving a global reliable morphological modeling retrieving luminosity, geometrical distribution and average size; so modeling internal structures were not inside the scope of this study. This can be done in the future taking as initial constraints the morphological models of this study, specifically the residual maps where the non-axisymmetric structures are extracted (See Figure 4.3). I give some examples of particular cases in the next subsection.

4.2.1 Galfit Modeling of galaxies and some Results

The GALFIT algorithm was written in C, with the main objective to be fast and flexible allowing to simultaneously fit an arbitrary number of structural components and other objects present in one FoV. It is not automatized so I generated a series of simple batch codes in order to run GALFIT in all the 328 galaxies of the sample in groups. In order to take into account the PSF effects, models are convolved with the user-defined PSF in fits format using a fast Fourier Transform. The convolution is adapted to the extent of the object setting the size of the convolution window in pixels in the input file. In fields with additional objects in the FoV, all the neighbor galaxies and/or stars in the sky plane were also modeled using one disk, sersic or PSF component (depending on the object morphology), with the purpose of improving the fit convergence.

Originally GALFIT was designed to study the morphology of high resolution images of nearby galaxies for which substructures can be studied in detail. In the case of this study the high-resolution images from HST-COSMOS allow me to extract spatially resolved information of different structures as arms, bars, prominent HII regions among others which are registered in the residuals or are modeled as additional components in other cases. Here I present some outstanding cases to explain the successful bulge-disk decomposition and how this method is closely related with the morphological type of the studied galaxies.

Below, I provide some examples of the morphological modeling along with the retrieved parameters for the central object, for which I used the analytic functions previously described in Eq. 4.6, sharing the same center for the bulge and disk components and convolved with the PSF determined in Table 4.1. All the Figures show in consecutive panels from left to right: the F814W HST image, the GALFIT model and the corresponding residual.

1. Early type vs. Late type models. The bulge-disk model was applied to all galaxies in the sample even for early type morphologies that are expected to be dominated by a spheroidal component. Exploring the output parameters I can determine which galaxies have early-type morphology based on the size and light contribution of each component to the total profile. I computed the B/D ratio as it is explained in subsection 4.2.2 in order to establish the dominant component for each case. Figure 4.5 shows galaxies CGr61-45, CGr51-27 and CGr32-312, all with $B/D > 1$ and small disk radii. The most relevant parameters for each galaxy are summarized as follows:

- CGr61-45 has a disk effective radius of $R_{ed} = 0.21''$ which corresponds the 23% compared with the size of the bulge $R_{eb} = 0.91''$. The relative magnitude difference between the output integrated magnitudes for the disk and bulge components from GALFIT is $m_b - m_d = -2.6$. This galaxy has light ratios: $B/D_{Re} = 9.78$ and $B/T_{Re} = 0.91$, so the disk component contributes in less than 10% to the SB profile.
- CGr51-27 has $R_{ed} < 0.1''$ while the bulge size is equivalent to $R_{eb} = 0.48''$. The output integrated magnitude of the disk is $m_d = 30$ – which is the maximum allowed value for a magnitude in GALFIT –, representing a very faint or non-existing object with a null contribution to the light profile. These results on size and magnitude are then compatible with the absence of a disk component. This is confirmed by the light ratios obtained for this galaxy with values: $B/D_{Re} = 1.56 \times 10^6$ and $B/T_{Re} = 1$.

- CGr32-312 has $R_{ed} = 0.09''$ which represents 10% of the bulge size $R_{eb} = 0.89''$. The relative magnitude between disk and bulge components is $m_b - m_d = -2.3$. The bulge-disk ratio computed at effective radius is equivalent to $B/D_{Re} = 8.1$ and the bulge-to-total ratio corresponds to $B/T_{Re} = 0.89$.

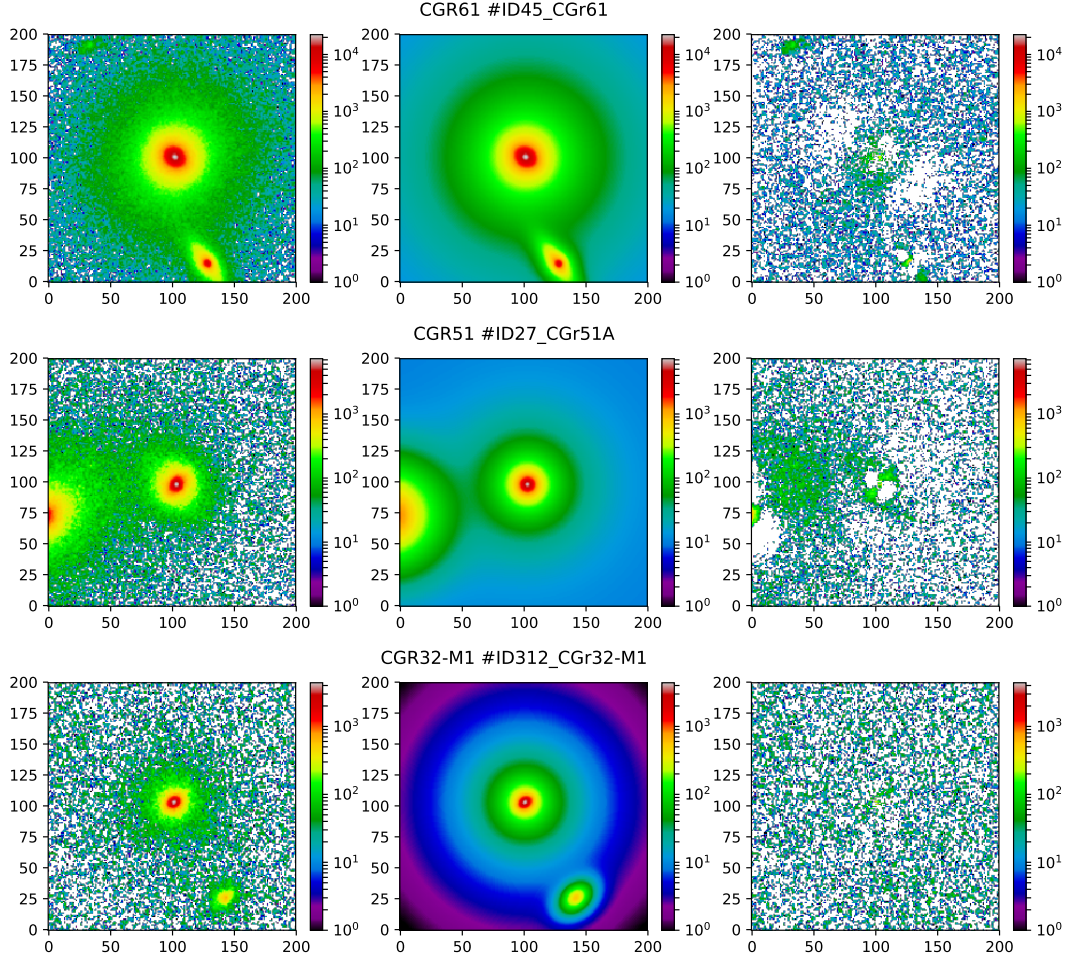


Figure 4.5: Morphological models for Early type galaxies in arbitrary flux units at logarithmic scale. For each row from left-to right in consecutive panels: HST F814W image, GALFIT output model and residual image. Top row: Galaxy CGr61-45. Middle row: CGr51-27. Bottom row: CGr32-312.

Now for disk dominated galaxies, I present three examples corresponding to galaxies: CGr84b-276, CGr23-119 and CGr34-59 in Figure 4.6. All of them are dominated by the disk component showing spiral arms or bars within their disks in different orientations being CGr84b-276 almost face-on and CGr34-59 close to an edge-on orientation. In opposition to the results obtained for early type galaxies, for these late type counterparts it is evident that the dominant component is the disk, retrieving small B/D values, specially for CGr23-119 for which the bulge component is negligible. The B/D ratio is calculated at the effective radius R_e . The most relevant features and parameters for each galaxy are summarized as follows:

- CGr84b-276 presents well defined spiral arms and a bar which are more clearly observable in the residual image after the bulge-disk modeling. In this case neither the arms, nor

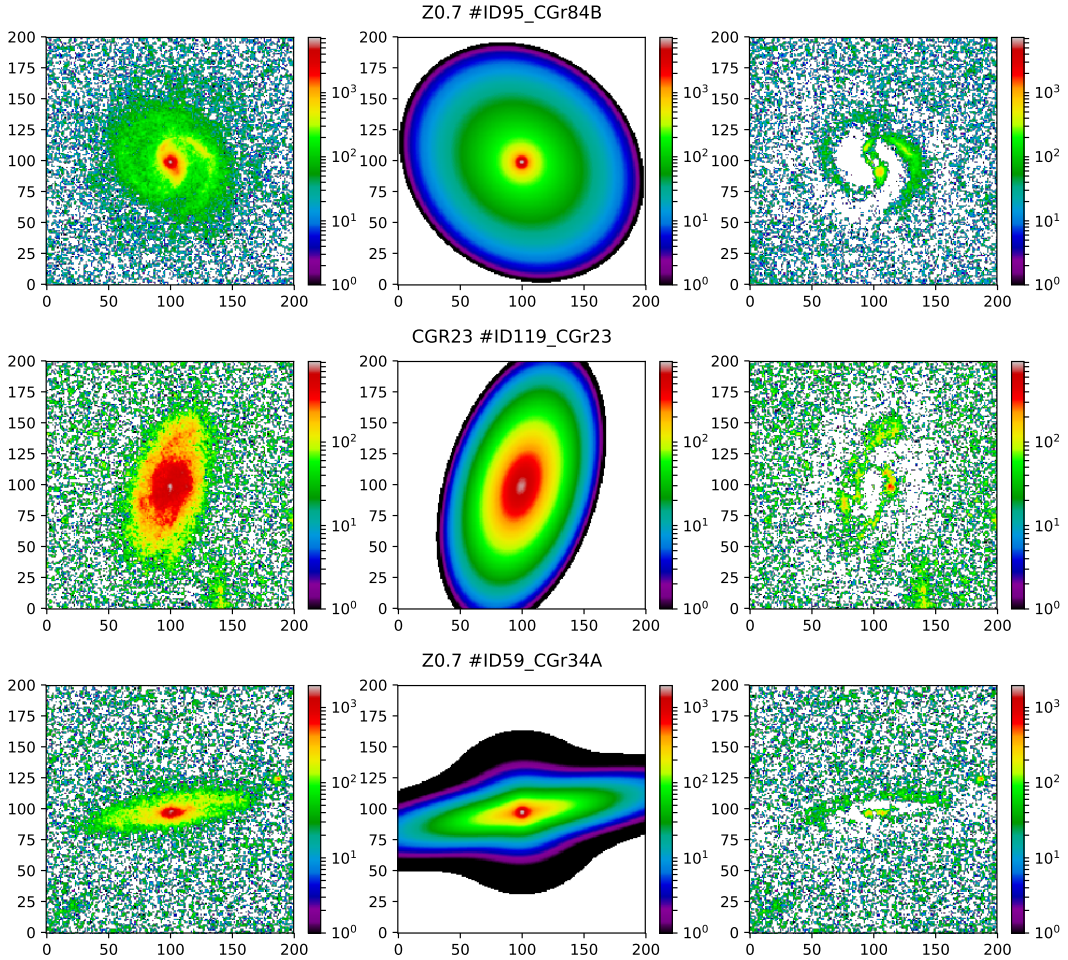


Figure 4.6: Morphological models for Late type galaxies in arbitrary flux units at logarithmic scale. For each row from left-to right in consecutive panels: HST F814W image, GALFIT output model and residual image. Top row: Galaxy CGr84b-276 (ID 95 in the sub-field). Middle row: CGr23-119. Bottom row: CGr34-59.

the bar seem to affect the global SB profile. This galaxy has a low inclination of $i = 33^\circ$, a B/D_{Re} ratio of 0.4 and a $D/T_{Re} = 0.72$. The sizes of the bulge and disk are $R_{eb} = 0.19''$ and $R_{ed} = 1.49''$ respectively.

- CGr23-119 is a disk galaxy with spiral arms, very luminous in the central part but with no evidence of the presence of a bulge. In the residual the spiral arms are more clearly visible as well as some SF clumps. The inclination of the disk corresponds to $i = 59^\circ$, with sizes $R_{eb} < 0.1''$ and $R_{ed} = 1.08''$ and a relative magnitude $m_b - m_d = 15.5$, with maximum $m_b = 30$, corresponding to a lower limit of $B/D_{Re} < 6.3 \times 10^{-7}$ and $D/T_{Re} = 1$, which is compatible with the absence of a bulge. The integrated spectrum of this galaxy is showed in Figure 2.14 in Chapter 2.
- CGr34-59 has an edge-on orientation with $i = 80^\circ$ due to its elongated appearance. The B/D_{Re} ratio is 0.3 denoting the disk is the dominant component with disk to Total luminosity ratio equivalent to $D/T_{Re} = 0.77$. A faint structure is observed in the residuals contouring the disk, and a small 'central bar' which can be related to dust extinction whose

effect is more pronounced for highly inclined galaxies. The sizes of each component are $R_{eb} \sim 0.17''$ and $R_{ed} = 1.28''$.

2. Clumpy disks and foreground objects. Figure 4.7 shows two cases of galaxies at intermediate redshift with luminous star-forming clumps and one with a small foreground galaxy which is visible in front of the disk of the studied galaxy. I modeled the most brilliant clumps and bright features like foreground galaxies or stars since they can affect the estimations of the morphological center, the size of the disk and the inclination. I used exponential disk functions to model this small concentrated regions.

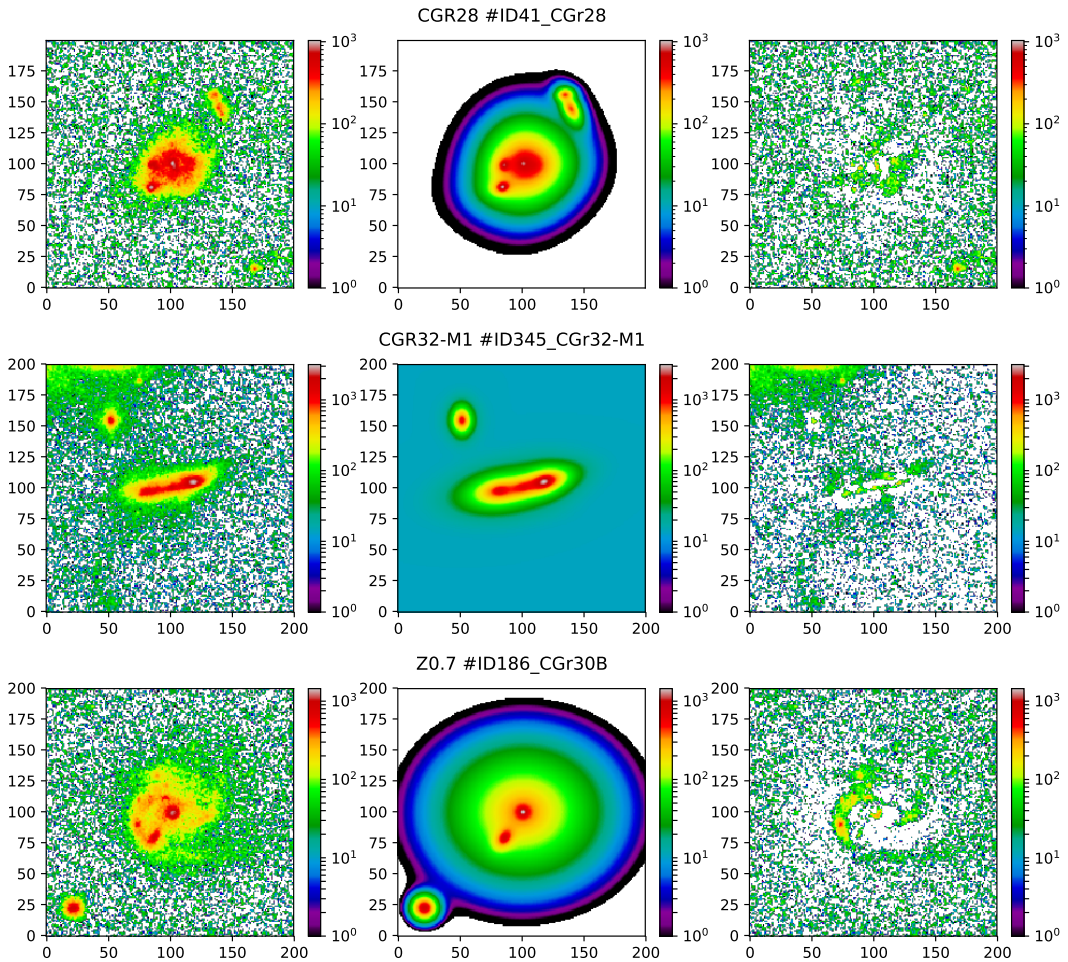


Figure 4.7: Morphological models of clumpy disks in which each the strongest SF regions were modeled as components to avoid bias in the output parameters. For each row from left-to right in consecutive panels: HST F814W image, GALFIT output model and residual image. Top row: Galaxy CGR28-41. Middle row: CGR32-345. Bottom row: CGR30-186.

As I mentioned before distant galaxies present fragmented morphologies with strong SF regions and bars or arms are not still well developed in some of them. In Figure 4.7, galaxies CGR28-41 and CGR30-186 are both near face-on cases with inclinations of 41° and 33° respectively. If the clump or foreground components are not added the parameters of inclination, size and center vary considerably letting models that even visually, differ considerably from

the observed morphologies. In the Middle panel galaxy CGr32-345 is an edge-on galaxy with $i = 75.5^\circ$, with no bulge ($B/D_{Re} = 1.6 \times 10^{-6}$) and the presence of a very prominent clump in its disk. If the clump is not modeled GALFIT takes it as the bulge of the galaxy, fixing the center in the most luminous location of the clump or bright feature. All these cases indicate that modeling of SF clumps and foreground objects is fundamental to retrieve reliable values on the output parameters.

3. Crowded Fields \Rightarrow Multi-Object Modeling. Some fields have multiple objects so it is important to model all of them in order to account for the influence of their SB on the central galaxy. I present two fields in Fig. 4.8: CGr32-289 and CGr79-46 with multiple objects nearby the central galaxy. I assigned a separated component for each object giving their coordinates in the input file for GALFIT. The modeling is then performed simultaneously so the morphological parameters for the surrounding objects are also recovered. In most of the cases I used a single exponential disk for late type galaxies or a single de Vaucouleurs profile for early type ones. The composite bulge-disk model is only performed on the central galaxy in each convolved field. In the case of stars in the fields, I use the PSF profile I provide to GALFIT in the input file.

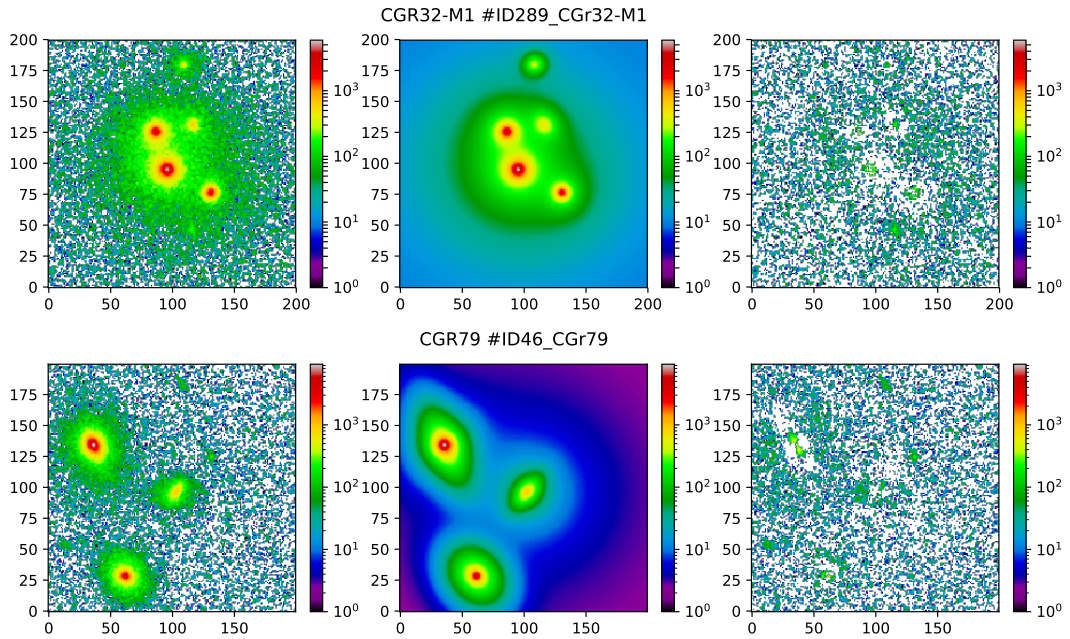


Figure 4.8: Morphological models of crowded fields applying a simultaneous Multi-Object modeling. For each row from left-to right in consecutive panels: HST F814W image, GALFIT output model and residual image. Top row: Galaxy CGr32-289. Bottom row: CGr79-46.

4. Cases with strong stellar bars, rings or prominent arms. In the sample there are some cases of large spiral galaxies with very well defined internal structures like bars, arms or rings that are prominent and in some cases can bias the model, a possible solution is to model this structures separately (like was done with CGr84-24 below) and to evaluate the difference in the projection parameters with respect to the simple bulge-disk decomposition. Further study can be done on this respect in a near future given the fact that for the low redshift sample the analysis is still ongoing and the morphological decomposition and residuals allow to identify asymmetries, perturbations, interactions, etc. In Figure 4.9 I present the models for galaxies CGr32-268, CGr84-24 and CGr61-140 showing a dominant bar, bright arms and a bar-ring system respectively. The most prominent features for each galaxy are summarized as follows:

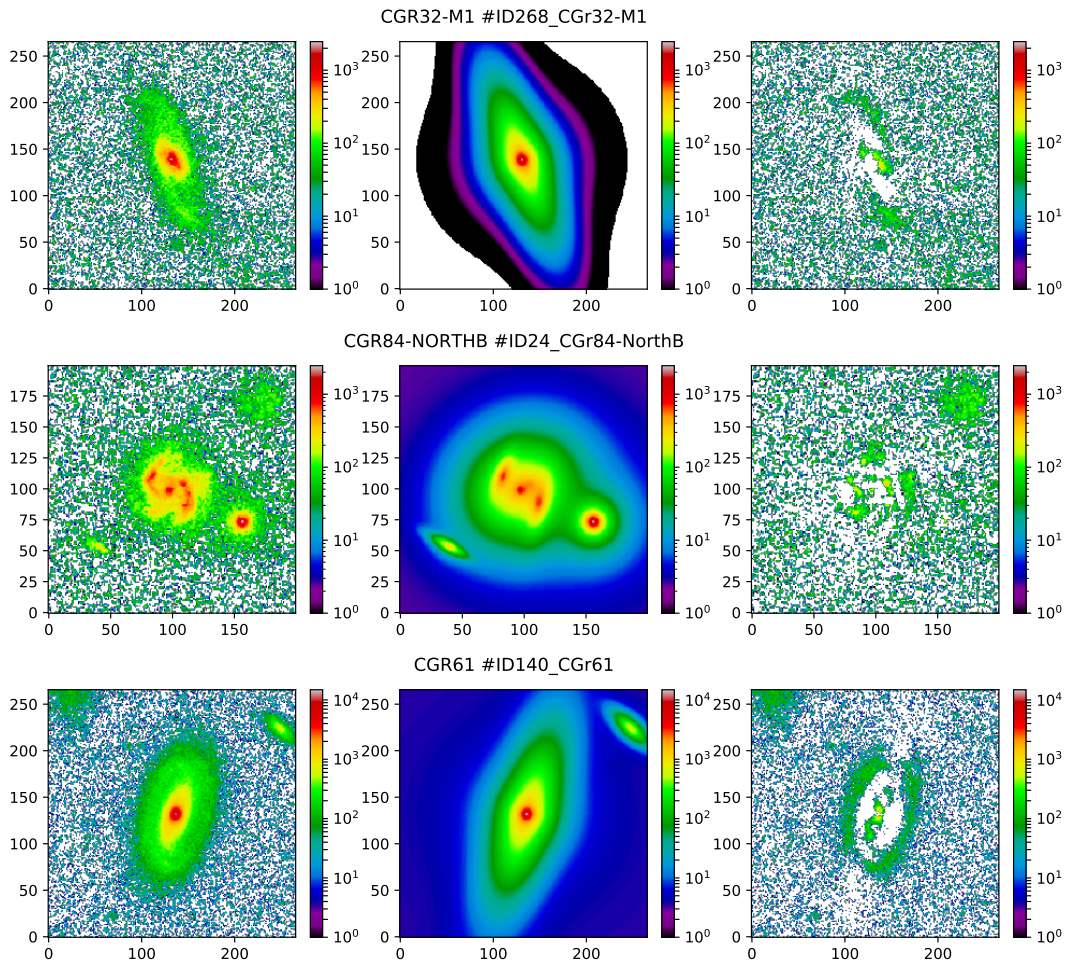


Figure 4.9: Morphological models of extended disks containing prominent non-axisymmetric components like bars, arms and rings. For each row from left-to right in consecutive panels: HST F814W image, GALFIT output model and residual image. Top row: Galaxy CGr32-268. Middle row: CGr84-24. Bottom row: CGr61-140.

- Galaxy CGr32-268 presents a strong bar. The arms are quite open and are faint with respect to the bar. The elongated arms and the bar are clearly visible in the residual. This morphology is typical of a perturbed galaxy probably due to an interaction with another galaxy or with the gravitational potential of group in which it is part. Despite the fact the

bar is bright I achieved a model that traces all along the disk and it is not limited to the bar. The PA of the disk seems to be well modeled and was not biased by the orientation of the bar like in some few cases in which the arms are too faint and the SB profile only follows the bar. The inclination of the disk is $i = 72.5^\circ$ and the PA_m corresponds to 19° measured from the North direction to the semi-major axis being positive towards the East [0° – 90°] and negative towards the West, according to the conventions used by GALFIT. The size of the bulge is $R_{eb} = 0.46''$ which is small compared to the size of the disk $R_{ed} = 1.5''$. The light ratios are to $B/D_{Re} = 0.55$ and $D/T_{Re} = 0.64$, corresponding to a disk galaxy with an important bulge component (representing the 36% of the SB profile).

- CGr84b-23 has a face-on orientation with bright arms and represents an extreme case for retrieving the morphological parameters. Modeling only the bulge-disk components I recover an inclination of $i = 50^\circ$ which is clearly overestimated for a face-on orientation. Adding the two components to model the SB of the arms the estimation of inclinations is reduced to $i = 26^\circ$. The bulge component is found to be almost null with a $B/D_{Re} < 0.1$ and $D/T_{Re} = 0.97$.
- CGr61-140 (from the low redshift sample) shows a bar-ring system in the residual image. It is well modeled by a bulge-disk strategy and unlike the other two galaxies the bulge component in this galaxy does contribute to the SB general profile with $B/D_{Re} = 0.58$ and $B/T_{Re} = 0.37$. This galaxy has an extended disk with a size of $R_{ed} = 1.29''$, an inclination of $i = 72^\circ$ and a smaller bulge component with a size of $R_{eb} = 0.23''$. The internal structures namely the bar and the ring, are not dominant in the SB profile so they were not modeled in this case, nevertheless by modeling the bar possible bias effects on the projection parameters could be identified.

4.2.2 Determination of Global Properties: R_e and B/D, B/T ratios

The outputs from GALFIT provide essentially the bulge-disk morphological decomposition parameters and the residuals of the models for all the galaxies in the parent sample. In order to derive global properties like the total luminosity (at certain radius), the global effective radius (R_e) and the corresponding bulge-to-disk (B/D), bulge-to-total (B/T) and disk-to-total (D/T) luminosity ratios for each galaxy, it is necessary to integrate the parameters of individual profile components. To compute the global properties I used a python routine written by W. Mercier (IRAP), which takes as input the bulge and disk integrated magnitudes (magnitudes of reference, m_b and m_d) and sizes (effective radii R_{eb} and R_{ed}) from the GALFIT modeling described above.

From the individual integrated magnitudes a total integrated magnitude is computed, using the general definition of magnitude as follows:

$$m = -2.5 \log(F) + C \quad (4.8)$$

where F is the flux of the object and C a constant term linked to the used photometric band. The flux in turn is defined as $F = L/4\pi D^2$ where L is the luminosity and D is the luminosity distant to the object described by magnitude m . The integrated magnitude is equivalent to the sum individual component magnitudes and considering that the morphological components have different luminosities but are at the same distance (as part of the same object) the total magnitude is expressed as the sum of the individual fluxes, as follows:

$$m_T = -2.5 \log[F_b + F_d] + C \quad (4.9)$$

We can further express the individual fluxes in terms of m_b and m_d by reversing Eq. 4.8, such that:

$$m_T = -2.5 \log[10^{-\frac{m_b}{2.5}} + 10^{-\frac{m_d}{2.5}}] \quad (4.10)$$

From the total flux $F_T = F_b + F_d$ is then possible to compute the total Luminosity L_T which is an intrinsic parameter for the studied galaxies. The global luminosity at certain radius ($L(r)_T = T$), can also be obtained from the integration (from 0 to r) of the sum of de Vaucouleurs and exponential profiles for the bulge and disk respectively ($\Sigma_b(r) + \Sigma_d(r)$), computed using equations Eq. 4.3 and Eq. 4.6), into a projected circular area. In order to retrieve the value of the integrated half-light R_e from an exponential disk and a bulge, the total luminosity obtained from the integrated magnitudes (fluxes) is equalized with the integration of the total surface brightness profile, such that:

$$f(r) = 2\pi \int_0^{r'} [\Sigma_b(r) + \Sigma_d(r)] r dr + L_T \quad (4.11)$$

Using the definitions for $\Sigma_b(r)$ and $\Sigma_d(r)$ from Eq. 4.6, Eq. 4.11 is expressed as follows:

$$f(r) = 2\pi \int_0^{r'} \left[\Sigma_b(R_{eb}) e^{-b_4 \left[\left(\frac{r}{R_{eb}} \right)^{1/4} - 1 \right]} + \Sigma_d(0) e^{-r/R_{ed}} \right] r dr + L_T \quad (4.12)$$

where R_{eb} and R_{ed} are the effective radii obtained from the morphological modeling for the bulge and the disk respectively. The algorithm uses two methods, one semi-analytical and the

other numerical to solve Eq. 4.12 for $r' = R_e$ when $f(r) = 0$. Applying this methodology I computed the global effective radius for all the galaxies in the intermediate redshift sample.

The luminosities for each component ($L_b = B$ and $L_d = D$) are determined by integrating the corresponding surface brightness $\Sigma_n(r)$ profile with index n inside a projected circular area up to certain radius (as it was explained in Section 4.2), or to a list of radii (e.g. R_d , R_e , $R_{2.2}$). I use the global luminosity ($L_T = T$) from the integration of the sum of the bulge and disk SBs, presented in first the term of Eq. 4.11. The estimation of the errors associated to these computations are also obtained. I performed the computation of individual component luminosities and integrated luminosities up to the effective radius R_e , the scale length radius R_d and $2.2 R_d$ for all the galaxies in groups at low and intermediate redshifts.

Luminosity ratios are important to determine the dominant structure from the decomposition, which is directly related to the morphological type. For passive galaxies the bulge component has more weight in the light profile whereas for late type the disk component is brighter or represents at least the same ratio as the spherical component, as can be seen in Figure 3 of [Abril-Melgarejo et al. 2021](#) (5.5, Credit: W. Mercier). This Figure shows the comparison of the distribution of the morphological types (Spiral, Elliptical and Irregular) from morphological Catalogs in the COSMOS field ([Cassata et al. 2007](#) and [Tasca et al. 2009](#)) in function of the B/T distribution from our morphological decomposition. The results obtained show that most of the galaxies dominated by the bulge component are classified as Ellipticals and those dominated by the disk are classified as Irregular or Spirals, in agreement with our two-component profile decomposition strategy.

4.3 Inclination distribution of a randomly selected sample

Inclination of the disk is a fundamental parameter in the determination of the kinematic features. The computation of the rotation velocity depends directly on the inclination of the gaseous disk. From observations we measure the component of velocity along the line of sight (observed velocity) given by: $V_{obs} = V_{rot} \times \sin i$ (this is true when the velocity is measured on the major axis with reference azimuth $\theta = 0^\circ$ and when only rotation is assumed, see the complete expression in Section 1.3, Equation 1.3). Due to this link between rotation velocity and inclination we have to take into account the factor of correction is larger for low inclined galaxies. Likewise, the uncertainty increases for galaxies with high and low inclination depending on the morphological modeling, being small inclinations those with greatest uncertainties as is shown by [Epinat et al. \(2012\)](#), from 2000 Montecarlo simulated disks and later modeled with GALFIT (Fig. 1). By definition the MAGIC sample was built with no preselection criteria based on constrained disk orientations nor on other conditions on the physical observational parameters. As described in Chapter 3 this sample is built as a random survey composed of deep IFS observations on the previous observed HST-COSMOS fields where some dense structures reside.

In order to evaluate if there is any bias on the inclination parameter for this sample, I extracted the distributions of inclinations for the parent and kinematic samples for galaxies at intermediate redshift from the morphological modeling with GALFIT. I present here the distribution of the parent sample of galaxies in groups from the MAGIC survey corresponding to 257 galaxies, the corresponding distribution for the kinematic sample is presented in the article [Abril-Melgarejo et al. \(2021\)](#) in Section 5.5. In contrast, I compare the observed distribution with the theoretical distribution for randomly oriented disks. This theoretical distribution is derived from the fact that the probability to observe a thin disk with certain orientation between θ_1 and θ_2 is equivalent to $|\cos \theta_1 - \cos \theta_2|$, which corresponds to the cumulative distribution function (CDF). Then the total CDF evaluated from $\theta = 0$ to any orientation, corresponds to the function $F(\theta) = 1 - \cos \theta$. Since θ is a continuous random variable the probability density function (PDF) corresponds to $f(\theta) = \sin \theta$. Now, to determine the mean distribution and its corresponding error bars, I used the inverse transform sampling theorem on the CDF to obtain random inclinations of the size of our samples to produce simulated distributions, as follows:

$$\theta = F(\theta)^{-1} = \cos^{-1}(1 - U) \quad (4.13)$$

where U is a random number over the interval $[0,1]$.

From 5000 realizations I obtained median value in intervals of 5° (black step-function), with upper and lower error bars as shown in Figure 4.10. The errors were obtained by computing the standard deviations of all the inclination values (among the 5000 simulated distributions) over the mean value in each interval (5°) for the upper error, and the standard deviation for all the values under the mean for the lower error. The distribution of inclinations shown in Fig. 4.10 illustrates the fact that the construction of the MAGIC sample is done without any prior. The median value of the sample of inclinations is 65.2° which is close to the theoretical median inclination of 60° . Indeed, the inclination distribution resembles a random pick up of disks. The distribution has an increasing number of galaxies from 0° to 60° , mostly under the theoretical median distribution, then it reaches the maximum between 70° and 75° . From 60°

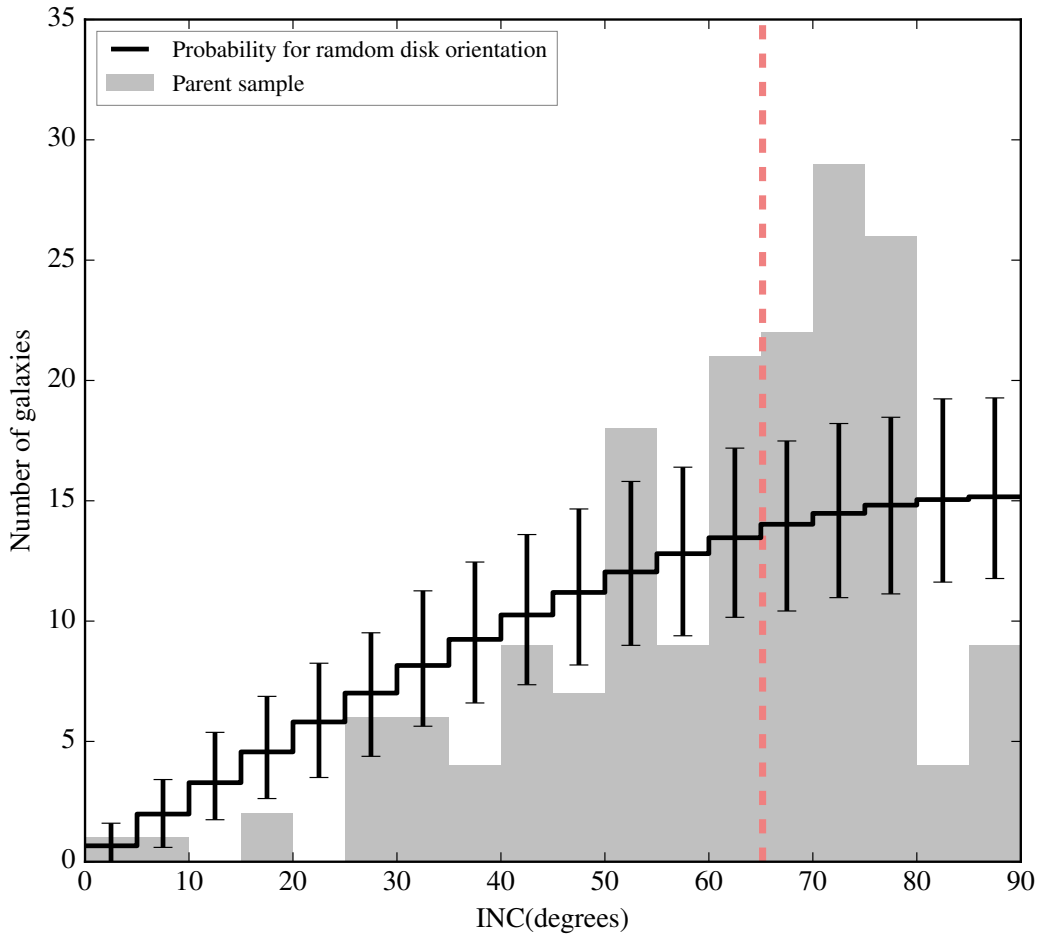


Figure 4.10: Distribution of Inclinations obtained with the GALFIT modeling for the MUSE parent sample of intermediate redshift galaxies composed of 257 galaxies with a bin of 5° (filled gray histogram). The theoretical distribution is overplotted in black step-function with the uncertainties corresponding to 5000 realizations of simulated random inclination distributions. The dashed orange line indicates the median value of the sample $i_{MEDIAN} = 65.2^\circ$ which is close to the median theoretical value of 60° .

to 80° the observed distribution overpasses that of the theoretical expected histogram. Then the MAGIC sample misses galaxies at very low inclinations ($0^\circ < i < 5^\circ$ and $10^\circ < i < 15^\circ$) and some at high ($i > 80^\circ$) inclinations. This is due to the high uncertainties associated to the morphological modeling of almost face-on or edge-on galaxies leading to over or underestimations of inclinations respectively. It is therefore more difficult to retrieve realistic projection parameters in these extreme cases which explains the lack of galaxies at the edges of the distribution. In the case of edge-on galaxies the disk is normally obscured for the high levels of dust extinction that might reduce the detection of emission lines. The second reason is that null thickness is assumed for the modeling, so for galaxies with thick disks real inclination can be underestimated. The lack of face-on galaxies could be due in principle to the small quantities expected from the theoretical CDF. Another reason could be that some galaxies present irregular morphological features along their disks like bright clumps, bars or deformed arms that dominate the surface brightness distribution resulting in an overestimated inclination (see Figure 4.9 middle panel).

As explained in section 4.2.1 I tried to reduce these effects at maximum by modeling separately strong features in order to retrieve the best model surface brightness distribution of the disk.

Using this same methodology I obtained the inclination distribution for the kinematics sample which is directly compared with the parent sample in Fig. 4.10. Both distributions are presented in Fig. 5 of the article [Abril-Melgarejo et al. 2021](#) (presented in Chapter 5) in which I present the results derived from the morpho-kinematic analysis on the intermediate redshift subsample.

This sample differs from samples with observational constrains based on preselected physical parameters. An example case come from the study made by [Epinat et al. \(2012\)](#), on a sample of 40 star-forming galaxies from the MASSIV survey that were preselected by a minimum threshold of [OII] line equivalent width and their photometric multiband spectral energy distribution to ensure a sample of only star-forming galaxies. Another important difference with this study is the resolution of the CFHT I-band imaging used to derive the morphology, since it was not enough to differentiate the clumpy contributions and there could be emission line contamination since the spectral range of the i-band filters corresponds to the redshifted [OII] λ 3727 line at the redshift range of the galaxies in their study. For MAGIC the HST F814W images allow to clearly differentiate the strong morphological features and interacting galaxies. Their inclination distribution (Fig. 2) is clearly constrained to intermediate inclinations, with the maximum around 60° , an important lack of high inclined galaxies and no galaxies with low inclinations ($i < 20^\circ$). They attribute the lack of face-on galaxies to the existence of irregular morphologies they can not resolve, computational bias and the fact GALFIT can not recover extreme inclinations. In contrast, in the MAGIC inclination distribution there are galaxies all along the range of inclinations and following the growing of the theoretical CDF.

4.4 MUSE LSF and PSF determination

Since one of the main objectives of this study is to determine the kinematics of the ionized gas, it is important to have into account the detection range of different nebular lines within the MUSE spectral coverage, depending on the redshift of the studied galaxies, as I described in Section 2.5.1. In this study the extraction of kinematic information is concentrated on the [OII] doublet and a combination of [OIII] and H β emission lines which are observable by MUSE at intermediate redshifts. Additionally, for the low redshift sample where other emission lines are still observable, I also performed the kinematics extraction for the combination of H α – [NII] and the [SII] doublet.

The determination of the Point Spread Function (PSF) in each band is of paramount importance since it is the measure of the MUSE spatial resolution at the analyzed wavelengths. The PSF of MUSE includes the instrumental response to a point source and the seeing effects in the spatial plane. Likewise, I also have taken into account the instrumental response to an infinite narrow spectral line through the determination of the Line Spread Function (LSF), which is equivalent to the spatial PSF but in the spectral dimension. The LSF accounts for the variation (broadening) of the FWHM of a spectral line at different observed wavelengths that is characteristic of the instrument. In the case of MUSE, the LSF was characterized in the studies performed by Bacon et al. (2017) and (Gu erou et al., 2017) using deep observations from the Hubble Ultra Deep Field (HUDF) and the Hubble Deep Field South (HDFS) MUSE surveys, respectively. In these studies the MUSE LSF is defined as,

$$FWHM_{\lambda} = \lambda^2 \times 5.866 \times 10^{-8} - \lambda \times 9.187 \times 10^{-4} + 6.040 \quad (4.14)$$

where λ is in Angstroms. So with this formulation I computed the LSF (spectral FWHM) for each emission line at the observed wavelength at the mean redshift of the studied galaxy group in each field. Since spectral resolution limits the ability to measure properly velocity dispersion, then its computation depends on the power of resolution in the spectral dimension as I introduce below. In general, the observed wavelength depends on the redshift of the source as $\lambda_{obs} = (1+z)\lambda_{em}$. A source in movement with respect to the median redshift of the system, like the ionized gas orbiting in the disk of a galaxy, produces a variation (shift) in wavelength that can be translated into a variation of velocity as it is described in terms of the Doppler effect, such that:

$$\frac{\Delta v}{c} = \frac{\Delta \lambda}{\lambda_{obs}} \rightarrow \Delta v = c \frac{\Delta \lambda}{\lambda_{obs}} \quad (4.15)$$

where $\Delta \lambda$ corresponds to the shift in wavelength due to the motion of the system. In the case of non circular motions the velocity dispersion of a system is related to the broadening of the spectral lines so it is important to establish the effects of spectral resolution in terms of velocity dispersion, i.e. to determine how much of the observed broadening is due to the spectral resolution and how much to the velocity dispersion of the system. Taking Eq. 4.15 to evaluate the velocity dispersion variation due to spectral resolution, where Δv corresponds to σ_v and the spectral resolution $\Delta \lambda \rightarrow \sigma_{\lambda}$ is expressed in terms of the $FWHM_{\lambda}$ corresponding to $\sigma_{\lambda} = FWHM_{\lambda} \times (2\sqrt{2\ln 2})^{-1}$, then Eq. 4.15 takes the form:

$$\sigma_v = \frac{c\sigma_{\lambda}}{(1+z)\lambda_{emit}} \quad (4.16)$$

from which I estimated the threshold velocity dispersion, which is the minimum resolved velocity dispersion by MUSE, corresponding to the observable most prominent nebular lines for each galaxy group. The threshold velocity dispersion σ_v and the spectral resolution σ_λ for each group are presented in Table 4.2. The computation was done for [OII] and H β -[OIII] for intermediate redshift galaxy groups. Within the low redshift sample constituted by 5 galaxy groups, there are 3 groups for which H α and [SII] are still observable, so σ_v and σ_λ were also computed at those wavelengths as it is shown in Table 4.2. From the values of Table 4.2 it is observed that spectral resolutions are higher (as well as spatial resolution as it is shown below) and the velocity dispersion threshold is lower for lines at longer wavelengths. Despite this we use the bluest lines corresponding to the [OII] doublet given the fact that these lines have the highest signal-to-noise ratio after H α as was discussed in Section 2.5.1.

Regarding the determination of the MUSE PSF I extracted several narrow band images for all stars, in fields of 30×30 pix² centered on each star observed at the redshifted wavelengths (λ_{obs}) of different emission lines, according to the median redshift of each galaxy group.. This was done by collapsing the MUSE datacube around λ_{obs} using 48 channels for [OII] 261 for H β - [OIII] 117 for H α - [NII] and 96 for [SII]. All the used stars used to compute the PSF were identified thanks to the MUSE high confidence spectroscopic redshifts (Inami et al., 2017) and confirmed as stars by cross-checking each object with the SIMBAD catalog (strategy that was described in Section 4.1), this in order to avoid using unresolved galaxies that could lead to overestimation of the PSF values.

For the computation of the PSF I used the strategy and all the formulations presented for SB profiles in Section 4.1 concerning the PSF of HST images. In this case, I fitted different images at different narrow bands using the analysis algorithm GALFIT with Gaussian and Moffat profiles in each case. I had from 2 to 4 stars per field, and alike what was done for HST data I only used the stars in each field to calculate the median PSF since each observation was integrated with exposures at different dates with different seeing conditions. Therefore there is a PSF estimation per wavelength, per field and per profile function. The average PSF values for each group are summarized in Table 4.3. The PSF calculation was also performed on the three low redshift groups for which there is detection of H α and [SII] emission lines but this sample is composed of few galaxies. As I show in Section I performed also the kinematics extraction for H α and [SII] but I did not go further in the analysis since this sample is too small, I just used these velocity maps for performing a visual comparison with the [OII] and H β - [OIII] maps. In Table 4.3 the notations -D, -BS and MD correspond to Deep, Best seeing and mid-deep observations. For group CGr32 was observed employing three subfields with a datacube for each one denoted as M1, M2 and M3. Group CGr84 was observed employing 2 subfields denoted as South (S) and North (N). Finally in CGr51 there are two groups structures identified as a and b. All these notations are described in Chapter 3.

As expected, the FWHM is lower for the Moffat profiles which are by definition sharper than the Gaussian profiles (see Section 4.1). The average difference between the FWHM between the two type of profiles is of $\sim 0.1''$, which corresponds to ~ 0.5 pix. Since the profiles of the stars are quite symmetric and to be sure to include all the seeing effects, given that the spatial resolution of MUSE is one order of magnitude lower compared to the HST spatial sampling, for which I used Moffat profiles I take the wider Gaussian profile values for characterizing the PSF

Table 4.2: Threshold velocity dispersion and instrumental spectral dispersion computed from the MUSE LSF (Eqs. 4.14 and 4.16), for the most prominent nebular lines. σ_v corresponds to the velocity dispersion (in km s^{-1}) and σ_λ (in \AA) to the spectral response at the given wavelength. These two parameters are given per group for [OII] and H β -[OIII] for intermediate redshift galaxy groups and additionally for H α and [SII] for the low redshift sample (listed from CGr23 on).

Group	z	[km s ⁻¹] [\AA]	σ_v [OII] σ_λ [OII]	σ_v H β -[OIII] σ_λ H β -[OIII]	σ_v H α σ_λ H α	σ_v [SII] σ_λ [SII]
CGr28	0.530	60.5 2.44	41.3 2.71	---	---	
CGr30	0.725	50.7 2.6	37 2.5	---	---	
CGr32	0.730	50.4 2.47	36.9 2.55	---	---	
CGr34	0.732	50.4 2.55	36.8 2.47	---	---	
CGr79	0.531	60.4 2.71	41.3 2.45	---	---	
CGr84	0.697	51.9 2.57	37.4 2.46	---	---	
CGr84b	0.681	52.6 2.59	37.7 2.45	---	---	
CGr114	0.659	53.6 2.6	38.1 2.45	---	---	
CGr23	0.355	73.14 2.89	48.06 2.52	35.9 2.51	35.61 2.54	
CGr26	0.440	66.5 2.47	44.4 2.79	---	---	
CGr51	0.340	74.3 2.53	48.7 2.91	36.2 2.49	35.7 2.52	
CGr51b	0.480	64 2.76	43.1 2.46	---	---	
CGr61	0.364	72.5 2.88	47.7 2.52	35.8 2.51	35.7 2.55	

to later perform the kinematics extraction. The median [OII] PSF computed for all the fields is $\sim 0.664''$, the median for the intermediate redshift and the median for the low redshift sample are $0.652''$ and $0.776''$ respectively. The sharpest profile has a PSF of $\sim 0.578''$ corresponding to field CGr84-N and the highest PSF value corresponds to $0.833''$ in field CGr23. The values with large PSF are linked to the observing strategy since for the first observations in snapshot mode (1hr exposure), the seeing constrains were relaxed in order to produce preliminary datacubes on which to decide if it was suitable to apply deeper observations depending on the existence of overdense structures in the observed field.

In the case of the PSF for the interval $H\beta$ -[OIII] the median for all groups corresponds to $0.625''$, for the intermediate redshift groups is of $0.607''$ and for the low redshift sample is equivalent to $0.668''$. The sharpest profile has a PSF of $\sim 0.508''$ corresponding to group CGr32-M2 and the highest PSF corresponds to $0.733''$ in field CGr23.

Table 4.3: Results of the PSF computation in for all galaxy groups. The number of stars used to compute the median PSF is indicated in the second column. The PSF values are given in arcsec for [OII] and $H\beta$ -[OIII] narrow ranges using a Gaussian (columns 3 and 4) and a Moffat profile (columns 5 and 6). For groups 30 and 34 the -D, -BS and -MD labels correspond respectively to the Deep, Best-Seeing and Mid-Deep MUSE datacubes (this notation was introduced in Section 3.3).

Group	N stars	Gaussia Profile		Moffat Profile	
		PSF [OII]	PSF $H\beta$ -[OIII]	PSF [OII]	PSF $H\beta$ -[OIII]
CGr28	3	0.654	0.664	0.636	0.626
CGr30-D	4	0.704	0.625	0.594	0.533
CGr30-BS	4	0.641	0.564	0.553	0.487
CGr32-M1	2	0.596	0.516	0.492	0.380
CGr32-M2	3	0.624	0.508	0.529	0.400
CGr32-M3	2	0.722	0.660	0.609	0.559
CGr34-MD	4	0.664	0.614	0.575	0.531
CGr34-BS	4	0.649	0.602	0.561	0.522
CGr79	2	0.658	0.539	0.579	0.457
CGr84	2	0.620	0.611	0.567	0.543
CGr84-North	2	0.578	0.516	0.498	0.442
CGr114	2	0.741	0.663	0.623	0.562
CGr23	3	0.833	0.733	0.794	0.650
CGr26	1	0.736	0.668	0.632	0.58
CGr51	2	0.776	0.658	0.740	0.597
CGr51b	2	0.718	0.655	0.630	0.584
CGr61	3	0.783	0.669	0.640	0.560

Table 4.4: Results of the PSF computation for three low redshift galaxy groups: CGr23, CGr51a and CGr61 at $z \sim 0.355$, ~ 0.340 and ~ 0.364 respectively. The same conventions for the columns in Table 4.3 are applicable.

Group	N stars	Gaussia Profile		Moffat Profile	
		PSF $H\alpha$ -[NII]	PSF [SII]	PSF $H\alpha$ -[NII]	PSF [SII]
CGr23	3	0.661	0.671	0.580	0.578
CGr51-a	2	0.587	0.579	0.538	0.521
CGr61	3	0.631	0.594	0.538	0.519

In Table 4.4 I present the results of the PSF determination for three low redshift groups: CGr23, CGr51a and CGr61 at $z \sim 0.355$, ~ 0.340 and ~ 0.364 respectively, for which lines $H\alpha$, [NII] and [SII] are observable. for the interval $H\alpha$ -[NII] narrow images the meadian PSF for

these three groups is $0.631''$ whereas for doublet [SII] the median PSF corresponds to $0.594''$. The sharpest profiles for H α -[NII] and [SII] correspond to $0.587''$ and $0.579''$ respectively, both in group CGr51a. The widest profiles for H α -[NII] and [SII] are $0.661''$ and $0.671''$ respectively, in group CGr23.

The PSF value mainly depends on the seeing conditions during the observations for each field and also on the total exposure time for each field. In Table 4.3 it is observed that in general the PSF is larger for low redshift groups which are in turn the fields observed in snapshot mode with relaxed seeing conditions whereas most of the observations for the intermediate redshift sample have exposures from 2.2 to 9.75 hours (see Chapter 3), observed with better seeing conditions.

4.5 Kinematics Extraction

The next step in the analysis is the extraction of the spatially resolved kinematics and distribution of the ionized gas by means of a careful fitting of the nebular emission lines in all the sample. From MUSE data cubes I performed a modeling around different emission lines using CAMEL⁵, a python code devoted to the fitting of any nebular line using a combination of 2D-Gaussian profiles and a polynomial continuum, whose strategy is described in detail by [Epinat et al. \(2012\)](#). The most relevant outputs for the analysis are the line flux map, the distribution of the signal-to-noise ratio (S/N) and the rotation velocity and velocity dispersion maps, this for each of the modeled emission lines (or groups of emission lines), see [Figure 4.12](#).

The fitted lines for which the observed velocity and velocity dispersion maps were extracted are: [OII] $\lambda\lambda$ 3727,3729 doublet, H β λ 4861 – [OIII] λ 5007, H α λ 6563 – [NII] $\lambda\lambda$ 6548, 6583 and [SII] $\lambda\lambda$ 6716,6731 (see [Figure 2.14](#) in [Chapter 2](#)). For each galaxy and each narrow band range a sub-databcube was extracted around the central coordinates with a spatial extension of 30×30 pixels. A spatial smoothing was applied by implementing a two-dimensional FWHM of 2 pixels size (smaller than the PSF) in order to increase the S/N per pixel without affecting the spatial resolution. The fitting was performed spaxel by spaxel using a constant continuum to account for the stellar continuum contribution. Each emission line within each narrow range was modeled separately using a Gaussian profile at the rest-frame wavelengths corresponding to each line. For each combination of lines CAMEL uses the flux ratios from the photo-ionization mechanisms established by [Osterbrock & Ferland \(2006\)](#), this to constrain ranges of values for the different flux ratios like in the case of the [OII] doublet CAMEL uses: $0.35 \leq F[\text{OII}]\lambda 3727 / F[\text{OII}]\lambda 3729 \leq 1.5$.

In summary, the velocity map is computed from the relative difference between the systemic velocity (given by the Hubble law and the redshift of the galaxy) and the measured velocity given by the position of the maximum of the Gaussian fit at each spaxel. The velocity dispersion map corresponds to the Gaussian dispersion (FWHM_λ) taking into account the threshold velocity dispersion σ_v related to the spectral resolution (see [Table 4.2](#)) of the fitted line in the spectral dimension for each spaxel. The detailed process and formalism used by the algorithm CAMEL to extract the observed rotation velocity and velocity dispersion maps from the flux moments approach and the Doppler effect is presented in [appendix C](#) and of the PhD Thesis [Epinat \(2009\)](#).

Having the fitted observed maps, I proceed to apply a systematic cleaning setting a limit of $\text{S/N} \geq 5$ for each spaxel using a python routine that removes all the spaxels with lower S/N values than the limit or having velocity dispersion lower than the 80% the dispersion of the spectral resolution (LSF), like it is shown in [Figure 4.11](#). The relaxation on the LSF limit is made with the objective to maintain the detection of even slightly narrower lines than the LSF that might be present in the spectra due to e.g. a low S/N. This limit in spectral resolution also avoids to include noise in the line fitting. Following the automatized cleaning process, I performed a careful visual inspection checking one by one the cleaned velocity maps (for each galaxy at each narrow band) in order to remove spurious spaxels, isolated spaxels or spaxels with low S/N and atypical velocity values with respect to their neighbors (with a discrepancy

⁵<https://bitbucket.org/bepinat/camel.git>

of more than 50km s^{-1} , see Figure 4.11). For two SF galaxies in the same modeling window (could be interacting pairs), the two velocity fields appear in the output of the cleaning process, so when possible they are carefully separated by manually erasing the pixels corresponding to the accompanying galaxy. After the visual inspection, for each velocity field I created a mask that is applied when the cleaning routine is run for a second time.

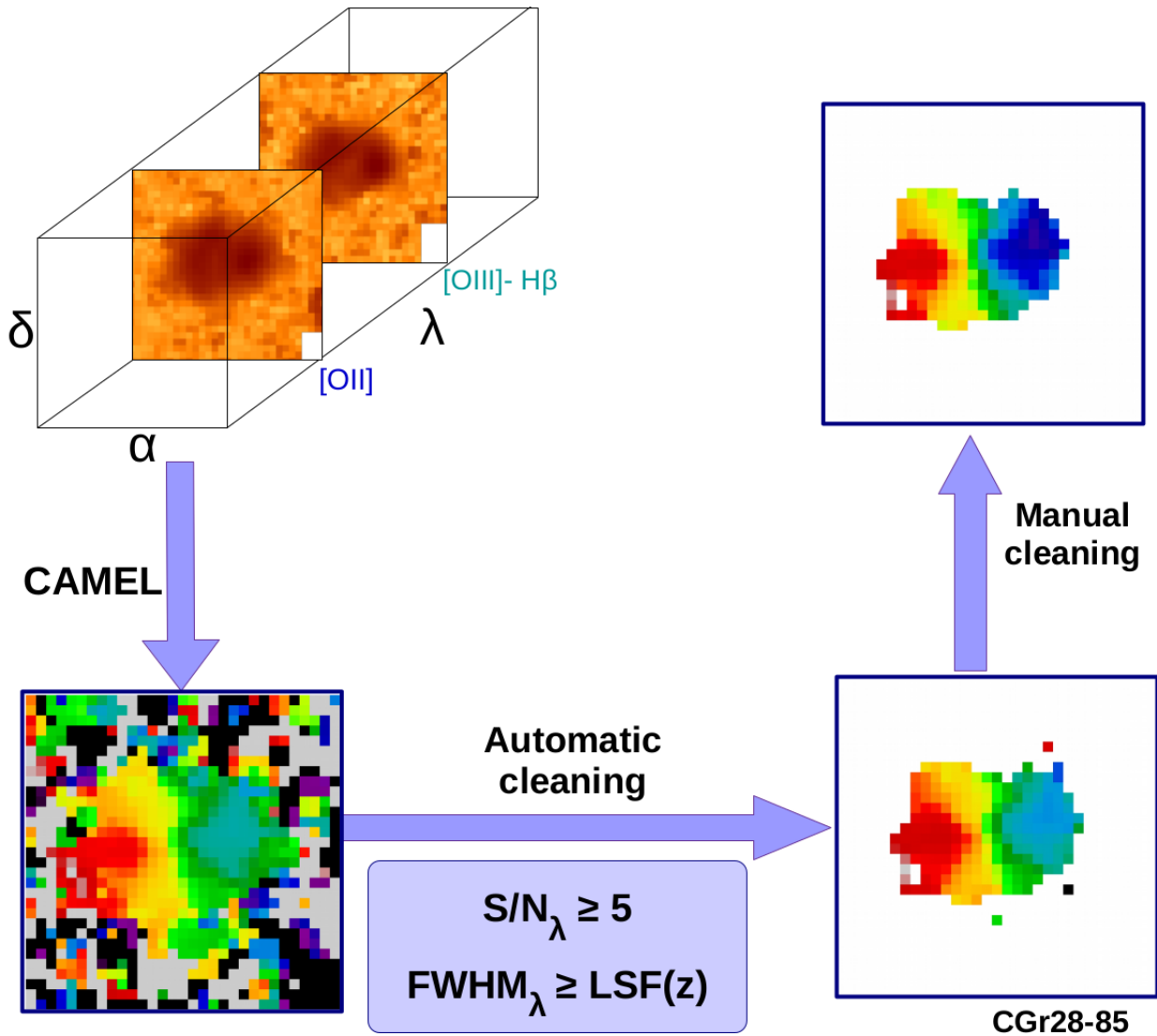


Figure 4.11: Diagram explaining the 2D kinematic extraction based on an spaxel by spaxel emission-line modeling and the corresponding cleaning process. From the reduced datacube (left superior corner) the observed flux, SNR, rotation velocity and velocity dispersion maps are extracted by modeling the emission lines with Gaussian profiles, using the fitting code **CAMEL** (model of galaxy CGr28-85 is used as example, left-inferior corner). These maps present the resulting value in all the pixels. Then, a pixel by pixel cleaning process is subsequently applied assuring to keep the pixels with enough SNR (>5) and those for which the emission-line is resolved ($\text{FWHM} > \text{LSF}$), (right-inferior corner). Finally, a manual cleaning is performed for all the models in each of the narrow line regimes for each galaxy (right-superior corner).

Finally, I obtain the clean maps at the different observable narrow bands as is shown in Figure 4.12. This figure shows the extraction of flux, S/N, rotation velocity and velocity dispersion maps for galaxy CGr23-19 at $z=0.354$ for which all the narrow bands are observable with MUSE (see Figure 2.14 in Chapter 2 showing the integrated spectrum of this galaxy). This is an example of the potential that MUSE observations have to trace the distribution in different emission lines identifying differences and common features among the maps.

According to Tiley et al. 2016, the choice of the emission line used to trace the dynamics of the gas is significant since different lines trace different phases of the gas and this can be visually confirmed in Figure 4.12. In this case just visually we can see all the ionized components are rotating approximately at the same orientation (the kinematic PAs are approximately similar) but there are differences in the extension of the maps and in the velocity gradients. In the case of the velocity dispersion maps considerably differ from one to another but an objective comparison only can be done after the kinematics modeling to take into account the beam-smearing effect by which the central velocity dispersion tends to be overestimated, as it is discussed in the kinematics modeling Section 4.6. The most extended maps correspond to those showing the Balmer lines and the [OII] doublet probably due to their stronger signal. The signal for the [SII] doublet is more limited to the internal parts of the disk since the S/N in this band is considerably lower.

Another interesting aspect that can be determined at this stage, just with the observable kinematic maps is that in principle two types of galaxies can be recognized. In first place those galaxies with high S/N and well defined velocity maps which are related to gas rich star-forming galaxies and those with no emission coherent signal related to passive or quenched galaxies with few gas budget. This separation of passive and Star-forming galaxies is explored in detail in the article Abril-Melgarejo et al. 2021 (see Section 5.5) where we relate the S/N of the ionized gas with the B/D light ratio from morphology and the SFR vs. Mass diagram, finding that not all the galaxies classified as star-forming from the SED fitting have coherent signal in emission, denoting a lack of ionized gas and perhaps indicating an active quenching process. For the smallest galaxies this can not be defined clearly because of the size limit in detection (see Section 5.5).

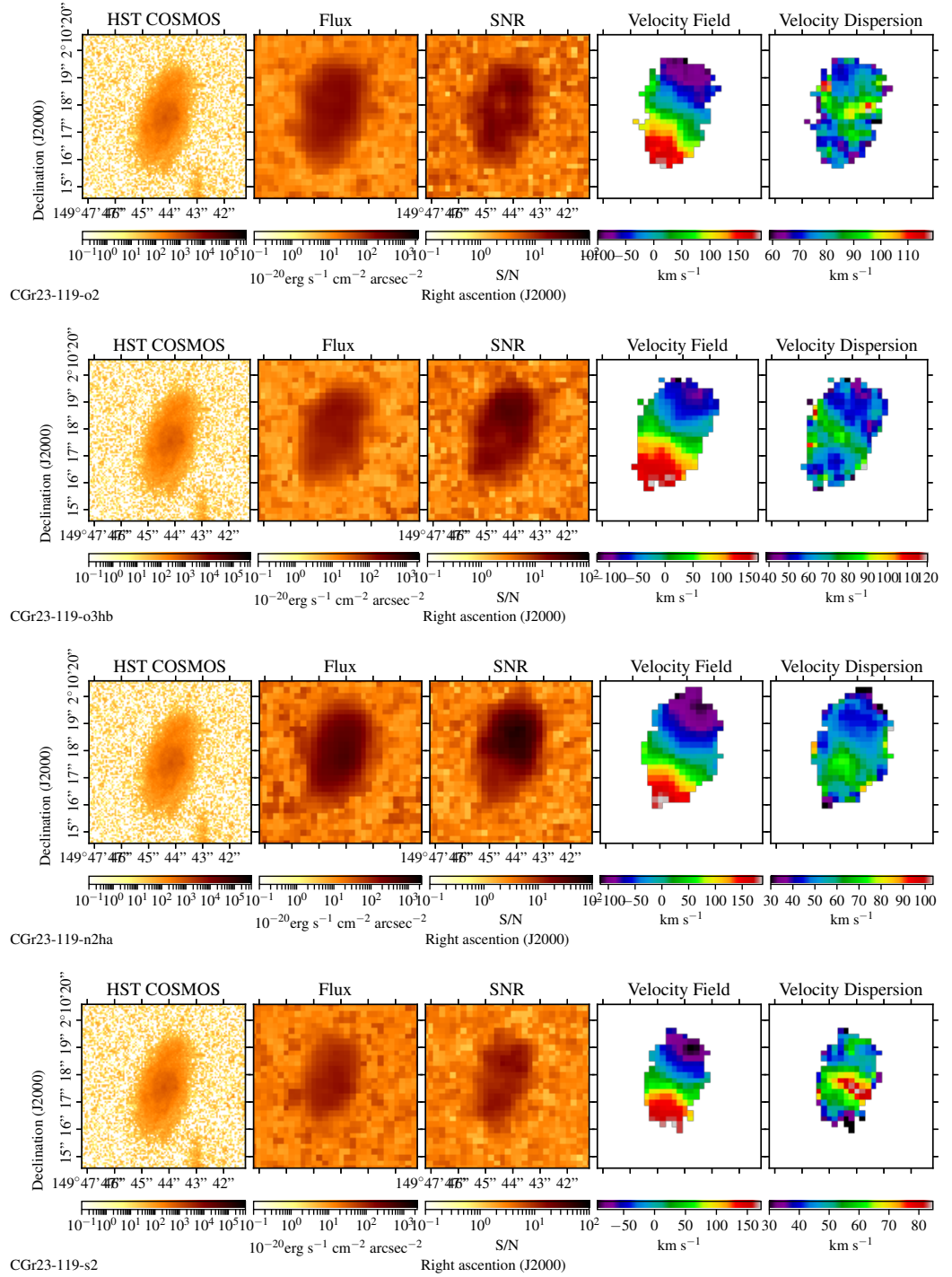


Figure 4.12: Kinematics extraction for spiral galaxy CGr23-119 in four different narrow bands, each one corresponding to one row of the Figure. For each row from left-to right in consecutive panels: HST F814W image, flux map, S/N map, and the clean rotation velocity and velocity dispersion maps. First row: maps corresponding to the [OII] doublet narrow band. Second row: H α -[NII] band. Third row: H β -[OIII] band. Fourth row: [SII] doublet

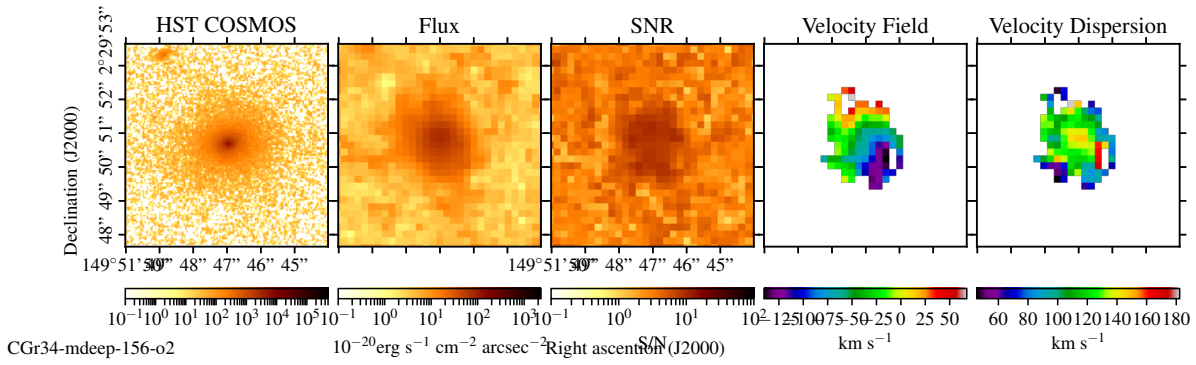


Figure 4.13: Kinematics extraction for ETG CGr34-156, a massive galaxy with very low SFR and bulge-dominated, showing a clear extended distribution of emission from the ionized gas at [OII] band with high S/N. From left-to right in consecutive panels: HST F814W image, flux map, S/N map, and the clean rotation velocity and velocity dispersion maps corresponding to the [OII] doublet narrow band.

Other exceptions to the general assumption of passive galaxies presenting a null or very low star-formation come from 4 large early type galaxies (ETG) for which I recover coherent [OII] signal showing extended velocity maps. The ionizing mechanism of these galaxies was checked looking for possible AGN activity which is described in detail in Section 5.4 but there was no evidence of high level ionization characteristic of the presence of an AGN. The early type galaxies showing Star-formation activity (nebular emission) are: CGr34-156, CGr32-288, CGr84-329 and CGr114-66. These galaxies have $B/D > 1$ and low SFR according to the SED fitting, but they present extended coherent emission in [OII]. From them CGr32-288 and CGr34-156 are elliptical galaxies and galaxies CGr84-329 and CGr114-66 correspond to disk galaxies with no spiral internal structures, probably corresponding to S0 type (lenticular), all of them with high [OII] S/N. As an example I present the maps corresponding to galaxy CGr34-156 in Fig 4.13 where the coherent emission from the ionized gas is clearly visible and is extended along the galaxy. This galaxy has a $B/D = 1.36$, a Mass of $10^{11.17} M_{\odot}$ and an $\log(\text{SFR}) = -2.58 M_{\odot} \text{yr}^{-1}$, typical characteristics of a passive early type galaxy.

4.6 Kinematics modeling

After the careful cleaning process described above, the observed velocity and velocity dispersion maps were modeled using a two-dimensional rotating disk applying an IDL routine developed by B. Epinat based on the Markwardt MPFIT IDL library. The gas is assumed to follow a circular rotation so a velocity map is distorted by projection effects which produce the appearance of a "spider-diagram", like the velocity maps observed in Figures 1.6 and 4.12. In literature there are different models to fit a velocity distribution (field), some are based on the observed shape of rotation curves fitted with Arc-tangent functions (Courteau, 1997), others use an exponential infinitely thin disk as the mass distribution proposed by Freeman (1970) and others apply a linear ramp model described by Wright et al. (2009) and Epinat et al. (2012). All these models might recover slightly different output parameters, so when comparisons are done with other studies it is very important to consider the kinematic model used in each case.

The kinematic modeling routine considers the spatial and spectral resolution limits of the observations computed in Section 4.4. This algorithm produces a high resolution model by first smoothing the observed field by the spatial PSF and then taking the emission line flux distribution as proxy to weight the velocity contribution in each spaxel (see the formalism presented in Section 4.6.1) of the observed velocity field (low resolution field). In order to minimize the number of free parameters and to decrease the level of degeneracy in the output model parameters, the center coordinates and the inclination of the disk are fixed, since these parameters were derived from the Morphological modeling on high resolution HST images (see Section 4.2). The model used for the kinematic characterization in this study is a ramp model in which the rotation velocity linearly increases from the center of the galaxy until it reaches the maximum value and then it remains constant, this last is known as the plateau velocity. The choice of the ramp models to describe the velocity fields in this study relies on the fact that from simulations ramp models have proved to better characterize the velocity fields of distant galaxies (Epinat et al., 2010). The point of inflection or change between the two velocity functions is known as the turnover point at r_t , the position at which the plateau V_t is reached. Then the rotation curve has the form:

$$V_{rot} = \begin{cases} V_t \times \frac{r}{r_t} & \text{if } r \leq r_t \\ V_t & \text{if } r > r_t \end{cases} \quad (4.17)$$

From this formulation then the main parameters to be determined are r_t and V_t , but the algorithm also computes the kinematic position angle (PA_k) and the systemic redshift (z_s) obtained from the computed cosmological systemic velocity of the center of mass (or rotation) of the galaxy. The algorithm also takes into account the velocity uncertainty map to weight the error in each spaxel. To determine the best model it uses a χ^2 minimization strategy based on the Levenberg-Marquardt algorithm. With the velocity curve and the kinematic parameters defined for each galaxy I performed the computation of the velocity at 2.2 times the disk scale length radius $V(2.2R_d)=V_{2.2}$. This is a characteristic value of the disk size extended enough for the maximum rotation velocity to be reached inside it ($R_{2.2} \geq r_t$), for the majority of the galaxies in the sample. The computation of the uncertainties in different cases, depending if V_t is reached inside $R_{2.2}$ or not, is described in detail in Abril-Melgarejo et al. (2021) in Section 5.5.

Another output parameter derived from the model is the intrinsic or local velocity disper-

sion (inherent to the system), which is one of the most important kinematic parameters since it accounts for the non-circular motions related to pressure support. However, this parameter is difficult to determine with accuracy due to three observational effects, one from the turbulent motions in the line-of-sight, the second is the beam smearing effect and the last is related with an additional component of dispersion from the instrument (the LSF effect). All these effects strongly affect the observations producing wrong estimations of the velocity dispersion. The effect of beam smearing is measurable as an over-estimation of the velocity dispersion in the central parts of galaxies. So in order to minimize this effect the fitting routine performs an estimation of the beam smearing producing a correction map which is subtracted in quadrature to the observed velocity dispersion in a spaxel by spaxel basis. The spectral resolution effect related to the LSF is computed as described in Section 4.4, obtaining the velocity dispersion threshold and the spectral resolution values for our sample which are presented in Table 4.2. The instrumental dispersion is then taken into account by quadratic subtraction of threshold velocity dispersion and the dispersion measured by CAMEL in each spaxel. Therefore, the result of applying these corrections is the estimation of the intrinsic velocity dispersion. This intrinsic velocity dispersion is fundamental for the kinematics analysis to determine for example the dynamical support of each galaxy in the sample given by the $V(R)/\sigma_v$ ratio, as it is presented in Chapter 5.

The kinematic parameters derived from the model allow not only to obtain the Tully-Fisher relation (M_\star vs. V_{rot}) as it is the main goal of this study, but also allow to make interesting comparisons between morphological and kinematics parameters such as the position angle. It is very common for studies performed with long-slit, complemented with additional photometry, to assume the morphological PA_m indicates the same orientation of the gas kinematic configuration (PA_k), so slits are often oriented matching the morphological PA_m (Pelliccia et al., 2019). In contrast, from the advent of IFS data and high resolution radio data, now it is possible to determine the kinematic distribution of the different studied components (ionized gas, neutral gas or stars) and non negligible variations have been observed in the disk orientations and distributions of the different components (Epinat et al. 2012, Contini et al. 2016), therefore the assumption that $PA_m=PA_k$ must be taken with care.

For the galaxies analyzed in this study I evaluated the difference between the PA_m from the stellar continuum of HST morphology and the PA_k from the kinematic modeling of the ionized gas. The absolute difference $|PA_m - PA_k|$ in function of the kinematic PA was obtained for 174 disk SF galaxies in groups, as it is shown in Figure 4.14. I found that 30% of the sample of SF galaxies used in the comparison has a difference above the $\pm 40^\circ$, which is the typical average maximum difference (between 30° and 45°) assumed by the long-slit studies between PA_m and PA_k to extract velocity curves (Pelliccia et al. 2019). This assumed threshold of 40° for the PA estimation is quite wide and leads to high uncertainties for the kinematics obtained with long-slit spectroscopy. For smaller thresholds between PA estimations, I found 60.3% of SF galaxies have smaller differences than 30° and 42.5% with absolute differences smaller than 15° . The difference $PA_m - PA_k$ considerably diminishes for the kinematic sample composed of 77 galaxies having only 7 galaxies (9%) with a difference of $\pm 40^\circ$ between the two PA estimations, this effect is shown by the histograms on the left panel of Figure 4.14, corresponding to the PA absolute difference distribution for the SF and kinematic samples (green and purple histograms respectively). Likewise, I found that for the kinematic sample 84% of galaxies

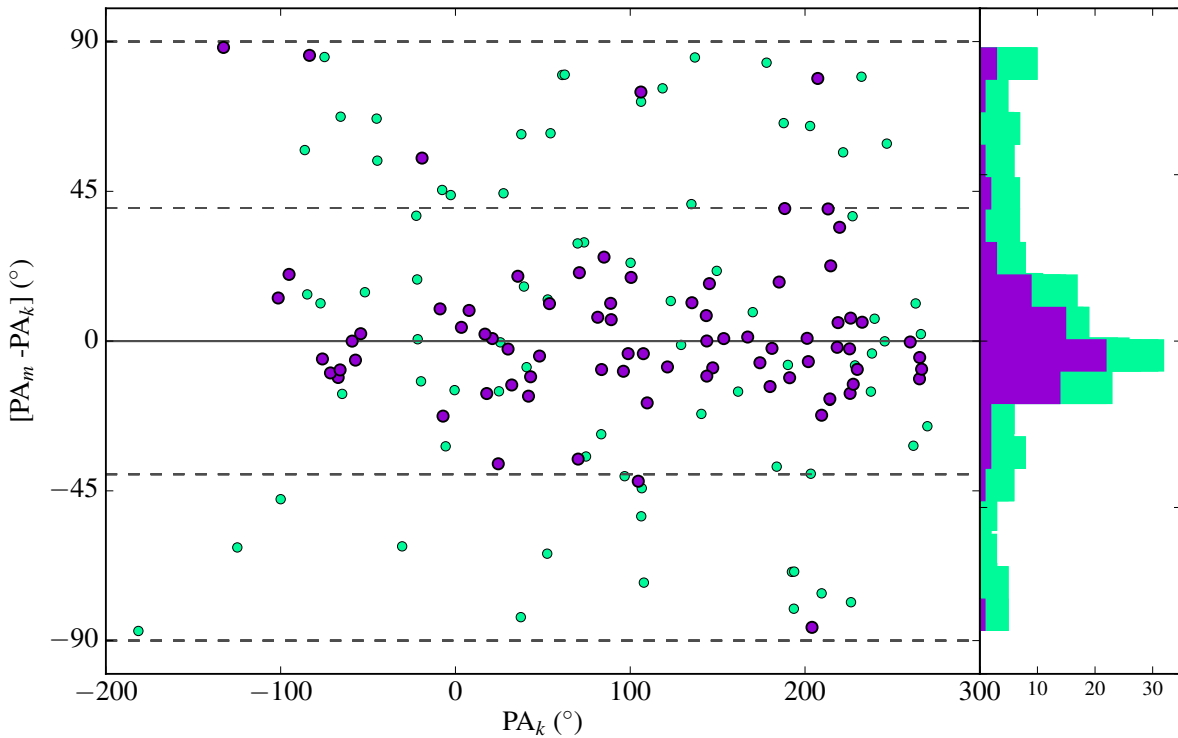


Figure 4.14: Absolute difference between the morphological and kinematic Position Angles. This result shows the orientation of the disks for different components (stars and ionized gas) changes above 40° for the 30% of the disk galaxy sample composed of 174 SF galaxies (purple and green circles). Whereas for the 77 galaxies part of the kinematic sample (purple circles) the difference in PA is above $\pm 40^\circ$ only for 9% of the rotation dominated galaxies. The dashed lines mark $\pm 40^\circ$ and $\pm 90^\circ$. The corresponding distributions (with bins of size 10°) are presented on the left panel, showing a narrower distribution around small PA differences for the kinematic sample (purple histogram), while an important part of the SF galaxies have a considerable absolute difference between PA values (green histogram).

have smaller differences than 30° and 65% with differences smaller than 15° . The distribution for the SF galaxies (green histogram) extends beyond $\pm 40^\circ$ while the distribution for the kinematic sample (purple histogram) is more concentrated towards smaller relative differences. This is due to the fact that the kinematic sample is composed of well resolved, rotation dominated galaxies (with a clear velocity gradient from the ionized gas), with enough S/N as it is established by the selection criteria presented in Section 5.2, so more precise estimations of the kinematic PA can be made and consequently more reliable comparison with the PA_m values.

Alike for what was done in morphology, modeling different internal components to determine their light contribution, in kinematics it is not possible to model internal structures like spiral arms, bars, rings or clumps since MUSE data does not have enough spatial resolution to separate the kinematic contributions of such structures at sub-kiloparsec scales. So it is important to highlight the kinematics analysis assumes a dominant global rotation system.

4.6.1 Recovering velocity and velocity dispersion maps from Light distribution

I present a summary of the Mathematical formalism of dynamical moments applied by the IDL routine used to model the kinematics described in [Epinat et al. \(2010\)](#), from spectral emission lines in three dimensions, one spectral and two spatial. The spectral light distribution is composed of the continuum surface brightness and the spectral emission line light distribution denoted by $L(x, y, \lambda)$. Then the spectral light distribution is defined as:

$$S(x, y, \lambda) = L(x, y, \lambda) + C(x, y) \quad (4.18)$$

Using the zero order moment corresponding to the monochromatic line flux on the spatial dimensions that is defined as $M(x, y) = \int_{\lambda} L d\lambda$, the velocity or first moment of the emission line is expressed as:

$$V(x, y) = \overline{V(x, y)} = \frac{\int_{\lambda} L(x, y, \lambda)v(\lambda)d\lambda}{M(x, y)} \quad (4.19)$$

Now the second order moment is equivalent to σ_v^2 . Like this the velocity dispersion is defined as:

$$\sigma_v = \sqrt{\overline{V^2(x, y)} - \overline{V(x, y)}^2} \quad (4.20)$$

where $\overline{V^2(x, y)}$ is equivalent to Eq. 4.19 with $v^2(\lambda)$. The sampling is done by pixels and by spectral elements so the distribution of light should be recovered with discrete functions. Consequently, the spectral sampling is made through n adjacent spectral elements each centered at λ_i considering that the spectral line should be well resolved and that there is no loss of light because of the LSF or PSF effects, then the monochromatic flux can be expressed as a summation of the contribution of light from each channel as $M(x, y) \approx \sum_i L_i(x, y, \lambda_i)$, With this Equations 4.19 and 4.20 can be expressed in a discrete form as:

$$\overline{V(x, y)} \approx \frac{\sum_{i=1}^n L_i(x, y, \lambda_i)v(\lambda_i)}{M(x, y)} \quad (4.21)$$

$$\overline{V(x, y)}^2 \approx \frac{\sum_{i=1}^n L_i(x, y, \lambda_i)v^2(\lambda_i)}{M(x, y)} \quad (4.22)$$

Accounting for PSF and LSF Effects.

All this formulation applies to the ideal case in which there is a continuous sampling and lines are infinitely thin (described by Dirac functions), but as I presented in section 4.4 the PSF and the LSF (linked to the velocity dispersion threshold) strongly affect the spatial and spectral resolutions respectively. In order to account for the effects of the PSF and LSF, the light distribution is convolved in first place by the LSF and then by the PSF so $S_{i,0}(x, y, \lambda_i) = S_i \otimes_{\lambda_i} LSF \otimes_{xy} PSF$, then $M_0 = \sum_i S_{i,0}$. The measurement of the moments will be also affected by the PSF convolution such that for a moment of order α :

$$\overline{V_0^\alpha} = \frac{(\overline{V^\alpha} M) \otimes_{xy} PSF}{M_0} \quad (4.23)$$

And the effect of the PSF on the second moment is expressed as:

$$\sigma_{v0}^2 = \overline{V_0^2} - \overline{V_0}^2 = \frac{(\sigma_v + \overline{V}^2)M \otimes_{xy} PSF}{M_0} - \left[\frac{(\overline{V}M) \otimes_{xy} PSF}{M_0} \right]^2 \quad (4.24)$$

Spatial Sampling and the beam smearing effect

The effect of spatial sampling is also accounted by convolving each pixel by a rectangular function to reproduce the discrete observed light distribution as follows:

$$S_{obs}(X, Y, \lambda_i) = \int_{pix} S_{i,0}(x, y, \lambda_i) dx dy \quad (4.25)$$

where $\int_{pix} = \int_{X+\Delta x/2}^{X+\Delta x/2} \int_{y+\Delta y/2}^{y+\Delta y/2} dx dy$.

Using the definition of bracket average as $\langle x \rangle = (a - b)^{-1} \int_a^b f(x) dx$ applied to \int_{pix} Eq. 4.25 can be simplified as:

$$S_{obs}(X, Y, \lambda_i) = \frac{1}{\Delta x \Delta y} \int_{pix} S_{i,0}(x, y, \lambda_i) dx dy \quad (4.26)$$

$$= \langle S_{i,0}(x, y, \lambda_i) \rangle \quad (4.27)$$

Eq. 4.26 corresponds to the average integrated light in a pixel of dimensions Δx Δy and centered at (X, Y) . The total observed flux is obtained by performing the summing on all the pixels as $M_{obs} = \sum_i S_{obs}(X, Y, \lambda_i)$ which is expressed as average in the form:

$$M_{obs}(X, Y) = \langle M(x, y) \otimes_{xy} PSF \rangle \quad (4.28)$$

Then a velocity moment of order α will be expressed as:

$$\overline{V^\alpha}(X, Y) = \frac{\langle [\overline{V^\alpha} M] \otimes_{xy} PSF \rangle}{M_{obs}} \quad (4.29)$$

The second moment is given by $\sigma_{obs}^2 = \overline{V_{obs}^2}(X, Y) - \overline{V_{obs}}(X, Y)^2$, therefore the observed velocity dispersion will be defined as:

$$\sigma_{obs} = \left[\frac{\langle [(\sigma_v^2 + \overline{V}^2)M] \otimes_{xy} PSF \rangle}{M_{obs}} - \frac{\langle \overline{V}M \otimes_{xy} PSF \rangle}{M_{obs}} \right]^{1/2} \quad (4.30)$$

The expressions in Eqs. 4.30 and 4.29 give the estimation of velocity and velocity dispersion including the beam smearing effect for which it is fundamental to determine the PSF. From equation 4.30 the value of intrinsic velocity dispersion $\sigma_v(x, y)$ can be recovered by inverting this equation taking into account all the implemented instrumental and seeing effects. The same is applicable to recover the rotation velocity. These estimations of intrinsic kinematic values is in turn related with the velocity curve model ramp model I presented above, since the computed r_t is the input parameter from which a high resolution 2D model is created. The spatially resolved model is then adjusted to the data using the formalism introduced in this subsection 4.6.1. From the best fit model, it is possible then to estimate the beam smearing correction.

4.7 Summary of the Morpho-Kinematics Analysis

The strategy followed to retrieve the morphological and kinematics parameters of galaxies in dense environments presented along this Chapter is summarized in a complete and simple diagram listing all the parameters and steps followed in order to obtain the stellar-mass Tully-Fisher relation in Figure 4.15.

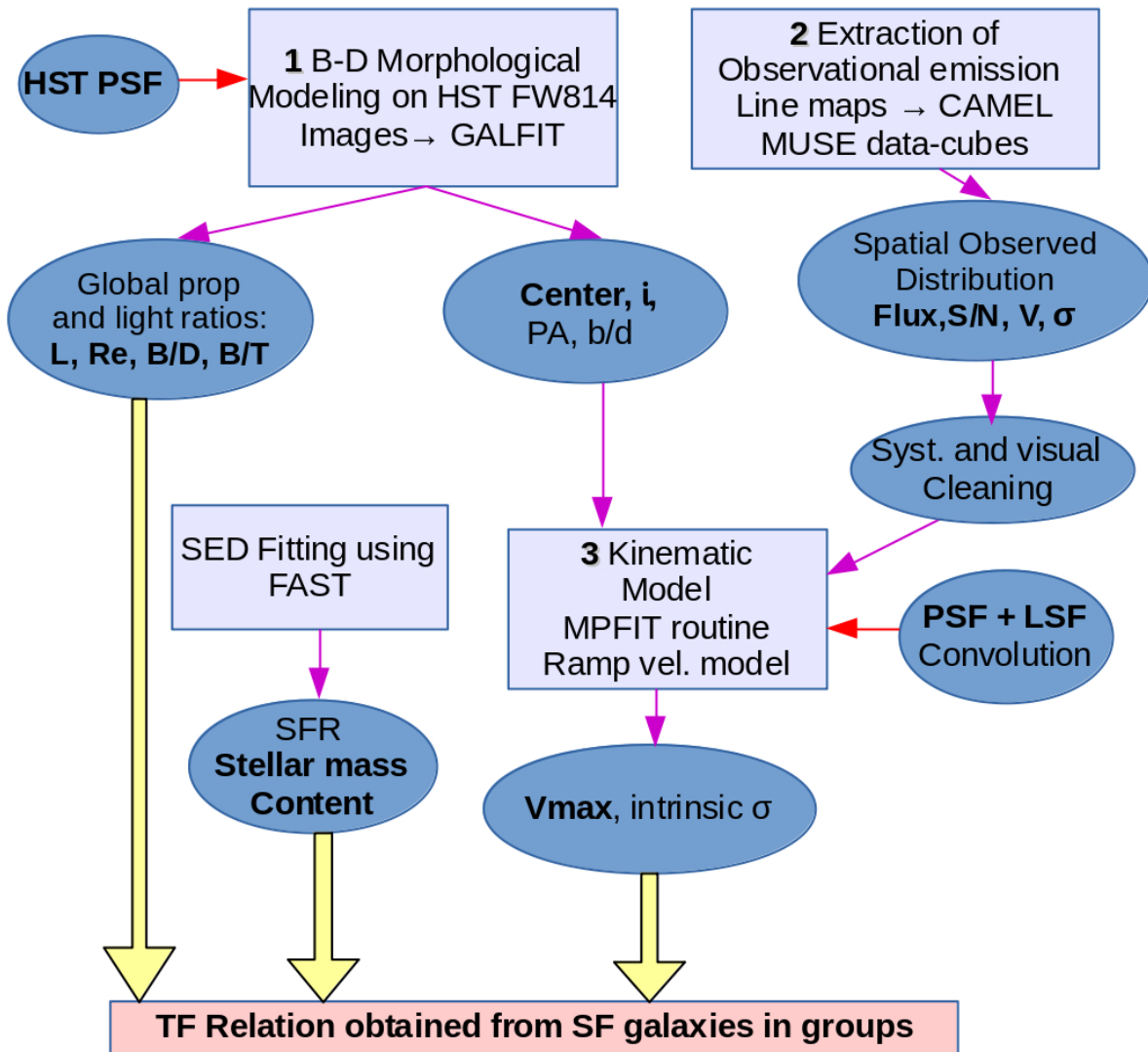


Figure 4.15: Summary Diagram of the followed Morpho-Kinematics analysis in order to retrieve different physical features from morphology using high resolution imaging and dynamical properties recovered from the IFS data.

→ I started by computing the PSF modeling the SB of all the available non-saturated stars in the COSMOS fields. Providing the HST-PSF I computed the SB distribution of galaxies using a composite bulge-disk morphological decomposition to retrieve in each case the center coordinates, and for the disk the ellipticity (b/a), the PA and the inclination. I also performed a computation of the global Luminosity, effective radius and luminosity

ratios (B/D, B/T and D/T) between the bulge and disk components having their sizes and magnitudes from the morphological modeling using the fitting algorithm GALFIT.

- The second step consisted in the Extraction of the observed emission line maps (Flux, S/N, V and σ) by fitting the continuum and emission lines with polynomial and Gaussian functions respectively using the fitting python code CAMEL. The maps were recovered for various emission lines ([OII], $H\beta$ -[OIII], $H\alpha$ -[NII], [SII]) as far as they were observable according to the redshift of the galaxies. The maps are systematically cleaned with an automatic routine and then by a visual inspection.

- Before proceeding with the kinematics modeling the MUSE PSF was determined per field and per emission line (the results are presented in Table 4.3) and the LSF was computed per emission line at the observed wavelength per group (see Table 4.2). The input morphological parameters fundamental for the kinematic modeling are the center coordinates and the inclination of the disk which are set as fixed parameters. A ramp velocity model is then applied on the clean observed maps convolved with the PSF and LSF in order to account for seeing and instrumental effects (beam smearing, spatial and spectral dispersion), retrieving as result the intrinsic velocity dispersion and rotation velocity distributions, applying the formalism presented in Subsection 4.6.1. The beam smearing effect is taken into account in the computation of the average velocity dispersion and maximum rotation velocity. Finally the maximum rotation velocity at $R_{2.2}$ ($2.2R_d$, see Section 1.4) is recovered.

- Finally, with the kinematic parameters and the estimations of stellar Mass and SFR from the SED fitting (described in Chapter 3), I was able to produce the relation between stellar Mass and Maximum rotation velocity of the disk (the Tully-Fisher Relation) of SF galaxies in dense structures at intermediate redshift. This was done mainly using the [OII] doublet light distribution. The completion of the morphological characterization, the kinematic extraction and the features obtained from the SED fitting allow me to study the kinematics structure and support of the galaxies in the sample and the relation of their evolution state with the environment in which they are embedded, this is one of the main objectives of the extensive analysis presented in the article [Abril-Melgarejo et al. \(2021\)](#), described in detail in Chapter 5.

Chapter 5

The Tully-Fisher relation and the determination of Dark Matter content

5.1 Methodology

I performed a detailed morpho-kinematics modeling of the sub-sample described in Section 3.4, in order to obtain spatially resolved kinematics and the dark matter and baryonic mass contents. The parent sample from MUSE was randomly selected, there were no apriori conditions on size or magnitude, only the COSMOS pre-established fields. Below I list the main steps of our research strategy that led to the publication of the most important results in the study [Abril-Melgarejo et al. \(2021\)](#) in Section 5.5.

- The selection of group members was made based on the redshift spectroscopic determination from MUSE using the robust methodology established in [Inami et al. \(2017\)](#). Then we performed a Friends of Friends (FoF) algorithm that assign the membership of a galaxy if it is below certain threshold of velocity separation (measured from the MUSE spectra) and of angular separation in sky (measured in the HST high resolution images). We used a projected separation of 450Mpc and a velocity separation of 500 Km s⁻¹.
- I performed a morphological modeling of the surface brightness using a two-component model, separating the light contribution of the bulge (central region) and the disk. This was done for ~ 330 galaxies in total including the low redshift galaxy groups. We used the HST images in the F814W band that correspond to the continuum emission of the underlined dominant stellar populations. The modeling was obtained using the GALFIT algorithm with which we recovered geometrical parameters like inclination (i), Position Angle (PA), ellipticity (b/a) and the morphological center.
- From data cubes I extracted narrow band emission sub-datacubes (for the [OII] doublet and for the region of [OIII] and H β), I then modeled the emission lines by single Gaussian curves. For each emission line regime I applied a systematic cleaning of residual and spurious pixels in the velocity maps. With this I obtained the observed velocity and velocity dispersion (σ)fields (see Figure 6 of the paper in Section 5.5).
- With the morphological parameters as input values (center, PA and i), I proceed to perform the kinematic modeling of the velocity and σ maps, corrected by beam-smearing

effect (that accounts for the wrong estimation of σ due to the rapidly changing velocities in the central regions).

- I recovered the maximum rotation velocity at $R_{2.2}$. I also analytically combined the two surface brightness components to obtain the value of the integrated effective radius (R_{eff}), that corresponds to the radius at which we have the half of the total luminosity from HST images.
- Using the vast photometry available for the COSMOS fields the Spectral Energy distribution (SED) was modeled in order to characterize the continuum emission of the stars to determine the stellar mass and the SFR, which are fundamental parameters to establish the stellar mass TFR.

Determination of the kinematic sample. I developed a robust new method based on the combined information extracted from morphology (performing a bulge-disk decomposition modeling), kinematics and SED fitting; instead of mainly using the V/σ ratio for the selection of the rotation-dominated galaxies, as it is commonly done in the literature. In order to have a more objective and physical selection and since we need galaxies to be spatially resolved, we study the impact of the size of the stellar distribution compared to the size of the MUSE PSF, and of the S/N of the [OII] doublet used to derive meaningful kinematics maps, as it is described below in Section 5.2. We also evaluated the effects of such selection criteria on the TFR, and the results match well with the dynamical and visual properties of the velocity fields of rotation-dominated disks. We obtained 77 galaxies fulfilling the SNR and size requirements to be part of the kinematic sample. We further eliminated bulge-dominated galaxies and those presenting dominant AGN activity giving a final kinematic sample of 67 galaxies.

Determination of gas and dynamical Masses. Assuming a spherical mass distribution and with the values of $R_{2.2}$ and the velocity at that radius $V_{2.2}$ I computed the dynamical mass which accounts the contribution to rotation velocity from the baryonic mass (stars, gas, dust) and the dark matter halo. Now, to compute the gas mass and the gas fraction of the galaxies in the kinematic sample, I computed the flux from the [OII] emission corrected by dust extinction and we then made use of the Kennicutt Schimidt (KS) law (Kennicutt, 1998), that is the relation between the SFR and the gas surface density, assuming a constant gas density. We adapted the original law made for $H\alpha$ to [OII] which is explained in detail in Abril-Melgarejo et al. (2021).

5.2 Selection Criteria to define the Kinematic sample using the Integrated spectral Flux

In this section I will describe the selection criteria using the integrated flux from the photometry available. After the systematic and manual cleaning of the extracted observed velocity maps (Section 4.5), I perform a preliminary visual inspection and classification of the velocity fields according to its extension and the presence of a clear velocity gradient. From the morphological bulge-disk decomposition, I compute the total effective radius as global indicator of size for each galaxy, as was described in Section 4.2.2. Then I obtain the ratio between the effective radius the MUSE PSF and. The SNR is computed based on the quadratic sum of the fluxes corresponding to each of the [OII] lines over the error associated to the fitting of the lines. In this case the value of the flux corresponds to the individual spectral line fitting (of the [OII] lines) performed on the integrated spectrum inside a circular aperture of 3" diameter.

Below I make a summary of all the information included for the selection criteria applied to SF galaxies:

- ▷ Preliminary visual inspection and classification of the velocity fields by size and presence of a velocity gradient.
- ▷ Morphological bulge-disk decomposition → Computation of the total effective radius.
- ▷ Determination of the MUSE PSF.
- ▷ Computation of the SNR for the [OII] doublet.

The selection criteria used to effectively segregate the SF and rotation-dominated galaxies from the parent sample is the result of the implementation of different constrains on different parameters derived from both the morphological and kinematic modeling. With this mutually complementary information in hand, we were able to find the most suitable combination of parameters in order to effectively build the kinematic sample.

I first made a classification of the velocity fields (VF) based on a rigorous visual inspection, taking into account the size of the minor by the major kinematic axis and the existence or absence of a rotation velocity gradient within them. The classification gave us eight types of velocity fields determined as follows:

- FLAG = 0: No coherent [OII] signal
- FLAG = 1: Coherent flux information but very small VF $<4 \times 4$ pixels
- FLAG = 2 Coherent flux information but small VF ($\lesssim 8 \times 8$ pixels) and no velocity gradient.
- FLAG = 3 Coherent flux information but small VF ($\lesssim 8 \times 8$ pixels) and with velocity gradient.
- FLAG = 4 Larger VF ($\lesssim 10 \times 10$ pixels) but no velocity gradient.
- FLAG = 5 Larger VF ($\lesssim 10 \times 10$ pixels) with clear velocity gradient.
- FLAG = 6 Larger VF ($\lesssim 13 \times 13$ pixels) and no velocity gradient.

- FLAG = 7 Larger VF ($\lesssim 13 \times 13$ pixels) with clear velocity gradient.
- FLAG = 8 Very large velocity field and clear velocity gradient.

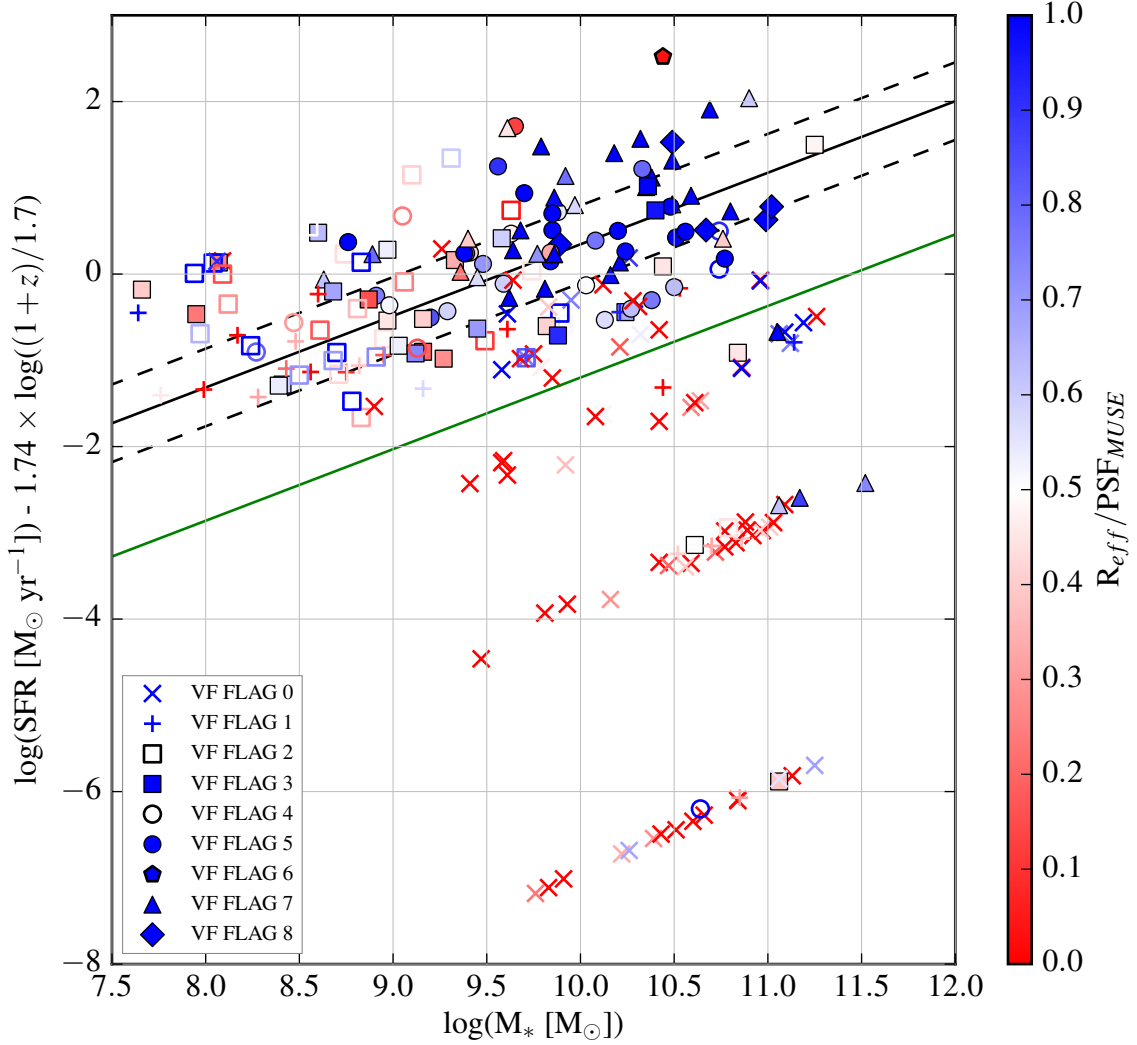


Figure 5.1: SFR versus Mass_* diagram for the parent sample in color scatter function of their size represented by the $R_{eff}/\text{PSF}_{MUSE}$ ratio. All the VF classification is presented with different symbols, in general open symbols correspond to galaxies with no coherent [OII] signal and no velocity gradient and filled symbols are those galaxies with well defined VFs of different sizes. The black lines correspond to the z correction on the SFR for MUSE data from (Boogaard et al., 2018). The green line corresponds to the separation between SF and quiescent galaxies explained in section 3.3 (Figure 1) at Abril-Melgarejo et al. 2021 (see Section 5.5).

In Figure 5.1 I present the SFR vs. Stellar Mass diagram for the parent sample at intermediate redshift assigning different symbols for the VF classification mentioned above in color scatter function of the $R_{eff}/\text{PSF}_{MUSE}$ ratio. Regarding galaxies flagged with absence of velocity gradient or with no coherent emission signal (0,1,2,4 and 6), we can determine that the galaxies that are visually excluded are mainly small galaxies with $R_{eff}/\text{PSF} < 1$. It is observed that those galaxies with no emission or very few signal (0 and 1) correspond to passive galaxies

with low SFR or to low mass galaxies. Those with small velocity fields (2) correspond mostly to small galaxies with stellar masses $\leq 10^{9.5} M_{\odot}$. Larger galaxies (4) are few and they are located in the inferior part of the main sequence. There is only one galaxy with VF_FLAG=6 (CGr84-50) which corresponds to a galaxy identified as QSO with high SFR but with no clear rotation velocity gradient in [OII] emission, in this case the dominant ionizing source is the AGN (see Figure 5.4) which leads to an overestimation of the SFR. Besides, this galaxy is dominated by the bulge component (B/D = 12.8) and represents a peculiar case.

From MUSE data, I determined the SNR level for the [OII] doublet, taking into account the sum in quadrature of the intensities of each line over the noise, estimated from the errors associated to the emission line fitting as follows:

$$N = \sqrt{\sum_i^{N_i} (eflux1)^2 + \sum_i^{N_i} (eflux2)^2} \quad (5.1)$$

where *eflux1* corresponds to the error associated to flux of line [OII] λ 3727 and *eflux2* associated to [OII] λ 3729 flux. I also computed the MUSE seeing from the modeling of the PSF of stars from narrow band images around the [OII] emission line at the mean redshift of each group as described in Section 4.4, with this I built a diagram to evaluate the selection criteria. The selection effects diagram consists of the [OII] SNR in function of the resolution indicator, the R_{eff}/PSF_{MUSE} ratio.

From such diagram I established optimal minimum values for the SNR and the R_{eff}/PSF_{MUSE} ratio as SNR=5 and 10 and a $R_{eff}/PSF_{MUSE}=0.5$, that is the R_{eff} is half of the MUSE PSF which is the minimum requirement for the galaxies to be resolved in MUSE data. Around these values we set some upper and lower limits which are showed in Figure 5.2 as discontinuous lines: $5 \leq SNR \leq 15$ and $0.25 \leq R_{eff}/PSF_{MUSE} \leq 1$. Most of the galaxies over the limits are galaxies dominated by the disk component ($B/D \leq 1$) and with VF Flags 3,5,7 and 8 corresponding to velocity fields with clear velocity gradient. Most of VF flags with values 0,1,2 and 4 are confined under the limits.

Nevertheless, I identified 12 galaxies with well defined velocity gradients and extended velocity fields (with VF flags 5 or 7) that are below the established limits in SNR and/or R_{eff}/PSF but from their physical properties (mass and SFR), their position in the TFR and the visual inspection of their velocity fields, they should be included in the Kinematic sample. Then there is a discrepancy between the selection method and the physical properties recovered from the morpho-kinematic modeling since these are extended disk and massive galaxies with well defined velocity fields. This issue is due to the method from which the flux is determined since for galaxies with high rotation velocity (VF 5 or 7) the line fitting could be not efficient to sample the broadening of the spectral lines and the aperture used to extract the integrated spectra might not be representative of the extension of the ionized gas disk.

In the next Section 5.3 I give a description of the origin of this discrepancy and another method to compute the flux that gives a better estimation and allows one to determine the definitive selection threshold values.

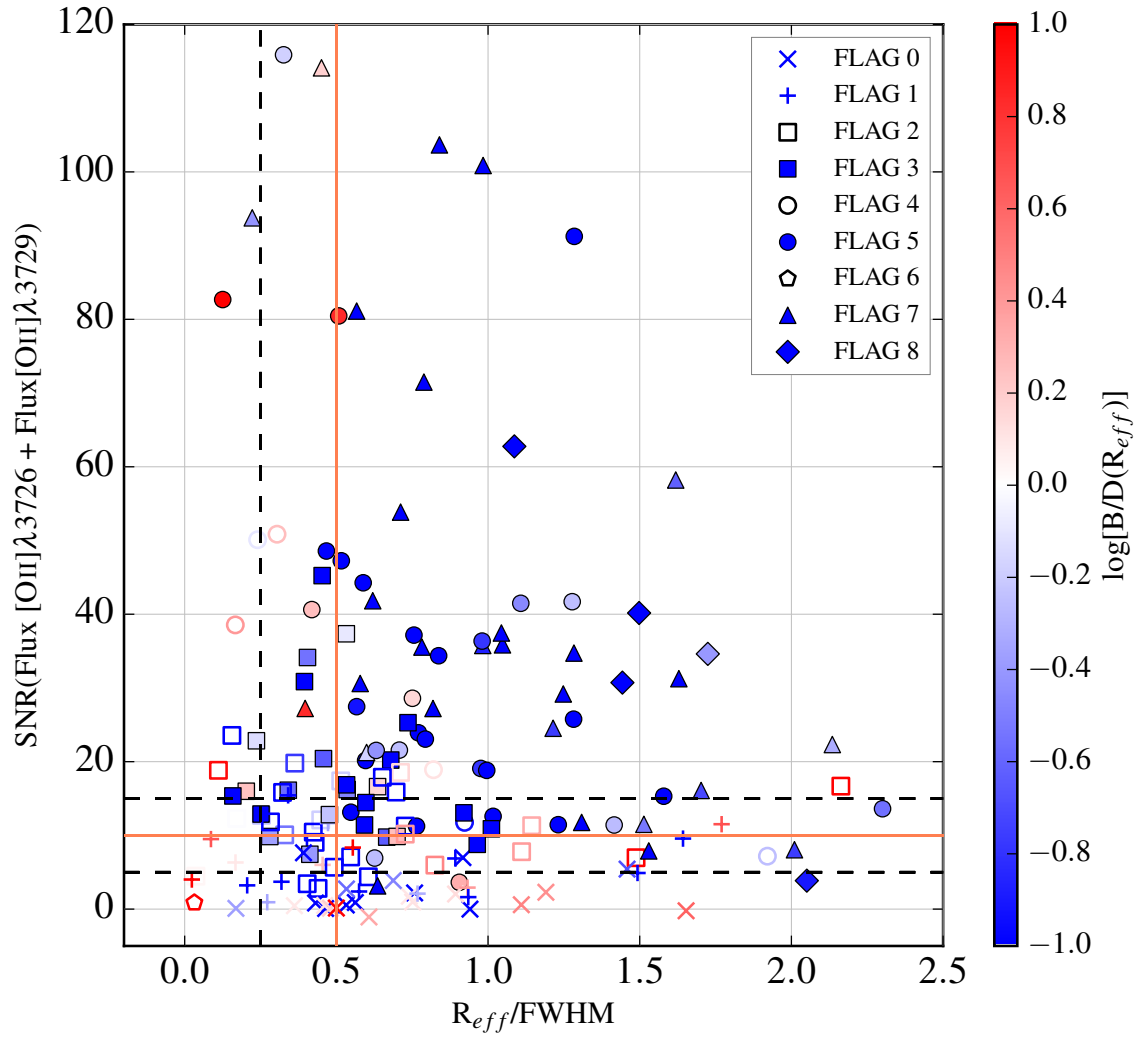


Figure 5.2: Selection effects diagram (SNR vs. $R_{\text{eff}}/\text{PSF}_{\text{MUSE}}$) using the flux estimations from the integrated spectrum for SNR. The diagram is in scatter function of the B/D ratio to visually link the morphological results with the selection criteria.

5.3 Definitive Selection Criteria using the [OII] Flux from MUSE narrow band images

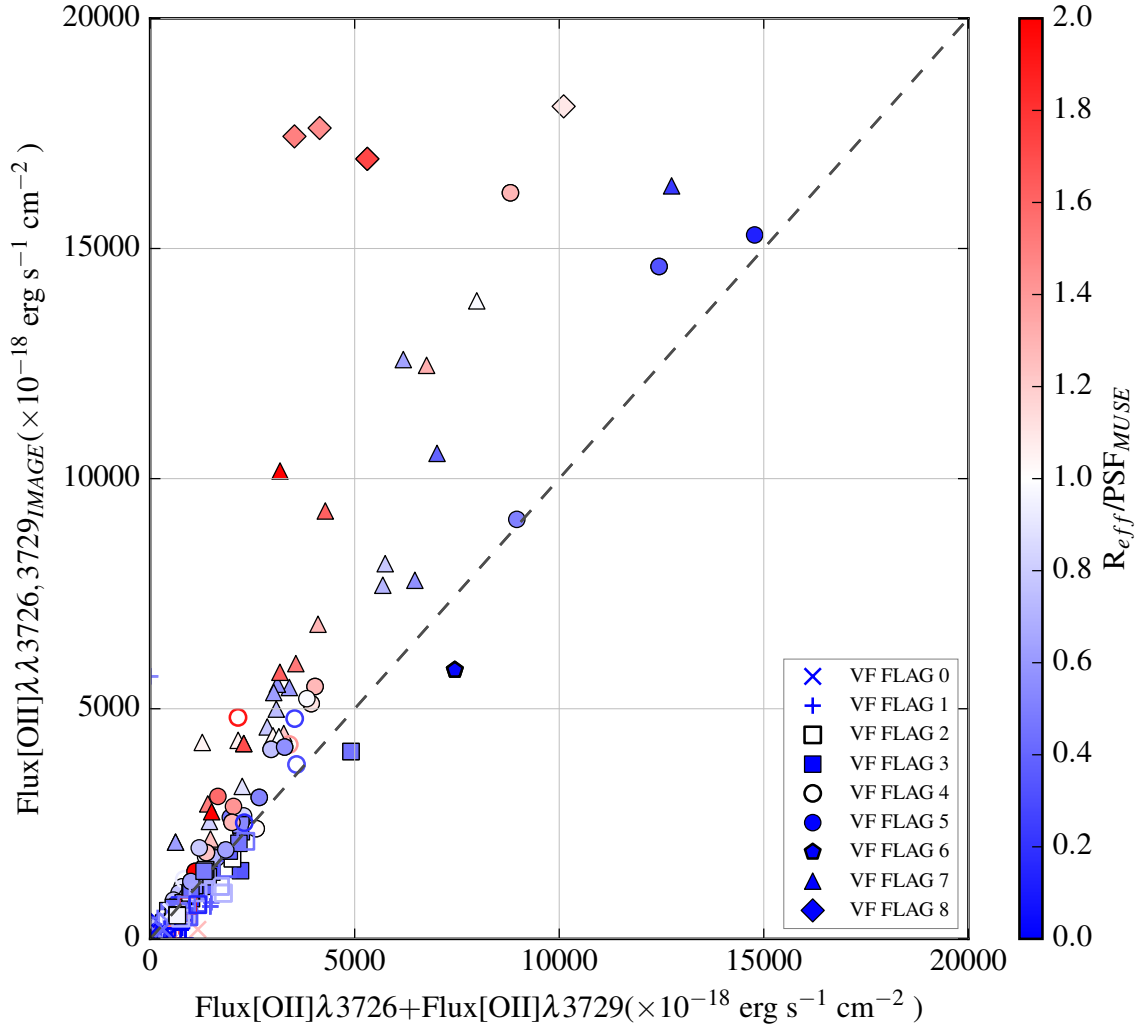


Figure 5.3: Comparison between the [OII] Flux extracted using narrow band images from MUSE in function of the [OII] flux derived from the integrated spectral line fitting. The diagonal representing the 1–1 relation is plotted as a discontinuous line. Most of the galaxies agree with the values of flux from the two methods. The outliers are mainly due to large galaxies with well defined velocity fields and fast rotators (VF_FLAGS 7 and 8).

As a second strategy, I computed the fluxes for each galaxy using narrow images extracted from the MUSE data cubes and centered on each of the lines of the [OII] doublet. The narrow images are produced by stacking the datacube in the spectral axis in an interval around each of the lines of the [OII] doublet (I used the CAMEL algorithm to produce these narrow images). To ensure the sampling of the extension of the ionized gas disk, I used the mask produced for the cleaned velocity maps (see Section 4.5) to limit the computation to the regions with enough S/N. I then computed the photometric flux values and compared them with the flux derived from the integrated spectra, and as we can see in Figure 5.3 most of the galaxies agree

for the two estimations very closed to the 1–1 relation. Nevertheless there is an important number of outliers for which we can see all the flux values using the integrated spectra are underestimated with respect to the flux from the narrow images. Most of these discrepancies come mostly from large galaxies with extended Velocity fields (VF_FLAGS 7 and 8) and high rotation velocities ($>150 \text{ km s}^{-1}$). We suspect this underestimation of the flux is product of the broadening of the lines due to their high rotation, so the Gaussian line profile fitting is insufficient in these cases. The low values for the fluxes might also be due to the usage of small apertures which do not include the contribution of emission from the outer parts of the galaxies.

As a result of what was described above, with the estimation of the SNR using the flux from the integrated spectra, some large galaxies have an atypical low SNR values and as consequence lie outside the kinematic sample when they own very well defined velocity fields. It turns out evident that these galaxies should be added to the final sample. For this reason we favor the usage of the photometric estimation for the [OII] flux which represents better what we obtain from the visual inspection and from the recovered physical properties of these fast rotator systems. In this case, we obtain a richer kinematic sample matching very well with the visual inspection.

Regarding the SNR, I recover higher values by a factor of 3 to 5 times higher since the flux values are more adapted to the extension of the ionized gas disks. The resulting selection diagram is presented in Figure 7 of my article (see Section 5.5). The definitive threshold values to define our kinematic sample are $S/N \geq 40$ and $R_{eff}/FWHM_{MUSE} \geq 0.5$, limits that ensure to have enough resolved galaxies with high signal values to compute reliable kinematic parameters.

Most of the passive galaxies from the parent sample are removed from the kinematic sample using our selection criteria. Nevertheless, we identified four passive galaxies which have important emission in [OII] and present a defined rotation velocity gradient. These galaxies correspond to ETG I presented in Section 4.5 which are massive galaxies with $10^{11} \leq M_{\odot} \leq 10^{11.6}$ with extended [OII] emission. To avoid passive galaxies to be added to the kinematic sample, we also imposed a limit on SFR which corresponds to the green line in Figure 5.1.

Then applying our selection method we are effectively discarding galaxies that are not well resolved in our sample and those whose properties do not agree with star-forming and rotation dominated galaxies.

5.4 Ionization mechanisms: AGN identification

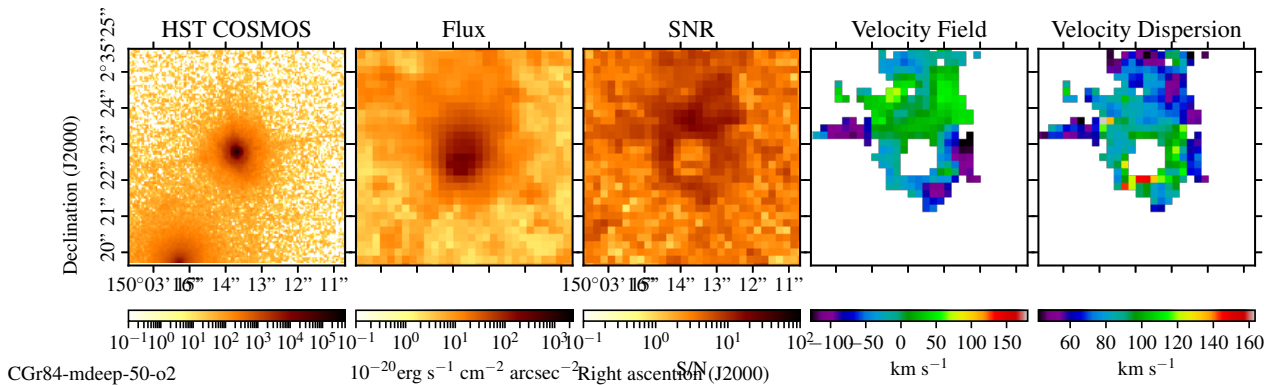


Figure 5.4: Kinematics extraction for the QSO CGr84-50, a compact luminous galaxy with extended emission from the ionized gas mainly dominated by the ionizing mechanisms from the AGN in the center. From left-to right in consecutive panels: HST F814W image, flux map, S/N map, and the clean rotation velocity and velocity dispersion maps corresponding to the [OII] doublet narrow band.

Galaxies hosting AGNs are dominated by high ionization levels causing big uncertainties in the determination of both stellar mass and SFR. One example of such objects is galaxy CGr84-50 presented in Figure 5.4, which we identified as a QSO for being compact ($R_{eff} < 0.1''$) and very luminous with an extended region of ionized gas. In order to identify AGNs inside our sample I performed a method based on the usage of diagnostic diagrams adapted to the emission line ratios [OIII]/ $H\beta$ [OII]/ $H\beta$ and the stellar mass, suitable for intermediate redshifts and the MUSE spectral range, complemented with a careful visual inspection of the spectra of AGN candidates to recognize broad emission lines and/or emission lines with a high ionizing level typical of AGN activity like [NeIII] $\lambda 3868$ and [MgII] $\lambda 2800$. At intermediate redshift and with the lack of near infrared observations we can not use the traditional nebular emission BPT diagram (Baldwin et al., 1981), so the determination of the ionizing mechanism of galaxies classified in our sample as star forming from the SED fitting is made with two adapted diagnostic curves: the first is the diagnostic diagram that combines the [OIII] $\lambda 5007/H\beta$ and [OII] $\lambda\lambda 3727, 3729/H\beta$ line ratios (see Figure 5.5 upper panel), proposed by Lamareille (2010) (hereafter, L10) and the second is the Mass-Excitation diagram (MEx) that compares the [OIII] $\lambda 5007/H\beta$ line ratio with the stellar mass (see Figure 5.5 lower panel) from the study of Juneau et al. (2011).

Both L10 and MEx are empirical curves based on photo-ionization models, fitted to a considerable quantity of emission line fluxes and stellar masses from reference samples in the local Universe and applied to galaxies at intermediate redshifts. The MEx curve was defined first using a low redshift sample of reference from the Sloan Digital Sky Survey (SDSS) that was separated into SFGs and AGNs using the BPT diagram. Since the [NII] $\lambda 6584/H\alpha$ is used to estimate the metallicity of the gas-phase for SFGs, and given the Mass-metallicity relation, the stellar mass can be used as substitute of the red line ratio parameter in a diagnostic diagram for intermediate redshift galaxies. The distribution of the SFGs and AGNs from the low redshift on the MEx diagram sample shows a clear separation between the two types. Two curves were fitted in order to maximize the separation setting the boundaries of classification. The MEx diagnostic was also applied to a sample of 2812 galaxies at $0.3 < z < 1$ from the Great

Observatories Origins Deep Survey North (GOODS-N). Their results are in agreement with an independent AGN classification based in X-ray data.

The L10 was defined using data of 89379 emission-line galaxies at low redshift ($0 < z < 0.2$) from the SDSS. With this statistically significant sample they first used the classical BPT diagram to separate SFG, Seyfert2, Liners and composites and then they evaluated the distribution of each of the classified emission-type groups on the blue diagram ($[\text{OIII}]\lambda 5007/\text{H}\beta$ vs. $[\text{OII}]\lambda\lambda 3727, 3729/\text{H}\beta$). Based on this distribution they defined the boundary curve to separate star-forming galaxies from AGNs, reporting an efficiency of 99.7% to separate SFG, and an average of 88% to separate AGNs. At the same time this diagram is not useful to differentiate galaxies in the composite zone of the BPT diagram and there is a considerable proportion ($\sim 1/3$) of Seyfert2 galaxies residing in the SF region for which they also provide an empirical line that separates the transition region in which SFGs are mixed with the Seyfert2 galaxies. They applied this diagnostic method on a sample of VVDS galaxies at $0.5 < z < 0.8$ to effectively determine the SF and AGNs samples.

Considering the advantages and limitations of the two classification methods, I built both the L10 and MEx diagnostic diagrams (see Figure 5.5) for our sample sample of Star forming galaxies (determined in Section 3.4). I then identified as candidates those galaxies above at least one of the diagnostic curves in order to avoid the composite zones and taking into account the uncertainty thresholds near the curves. 25 candidates were obtained from which 7 belong to the kinematic sample. We extracted the integrated spectra over the full extent of the galaxies weighted by the white-light flux, in turn obtained by collapsing the MUSE data cube in λ direction. We performed a detailed visual inspection of these integrated spectra to look for broadening features and/or high level emission lines. Like this we identified 9 AGNs in the SF sample and 4 ambiguous cases that show some broadening in some cases or high ionization levels. The ambiguous objects can be due to low-level AGN activity or SF galaxies with multiple kinematic components. Among these results we have 3 AGNs (CGr30-71, CGr32-454 and CGr32-268) and 2 ambiguous cases (CGr32-345 and CGr32-132). Galaxy CGr30-71 was studied and identified as AGN by [Epinat et al. \(2018\)](#). The ambiguous cases might be due to low AGN activity and/or to complex kinematics structure (different components). Then we carefully identified among the AGN candidates for which the AGN affected the velocity fields of host galaxies. We then removed from the analysis CGr32-268 and CGr32-454, whose AGN activity dominates over the ionized emission from the SF disk.

I also applied this method to the early type galaxies (ETGs) in groups identifying some of them above the diagnostic curves, but since these diagnostic curves were constrained using only SFGs, I computed the errors in the emission line ratios to identify the candidates having anomalous high ionization levels. We identified some candidates but after the visual inspection of their spectra we did not find any clear indication of AGN activity.

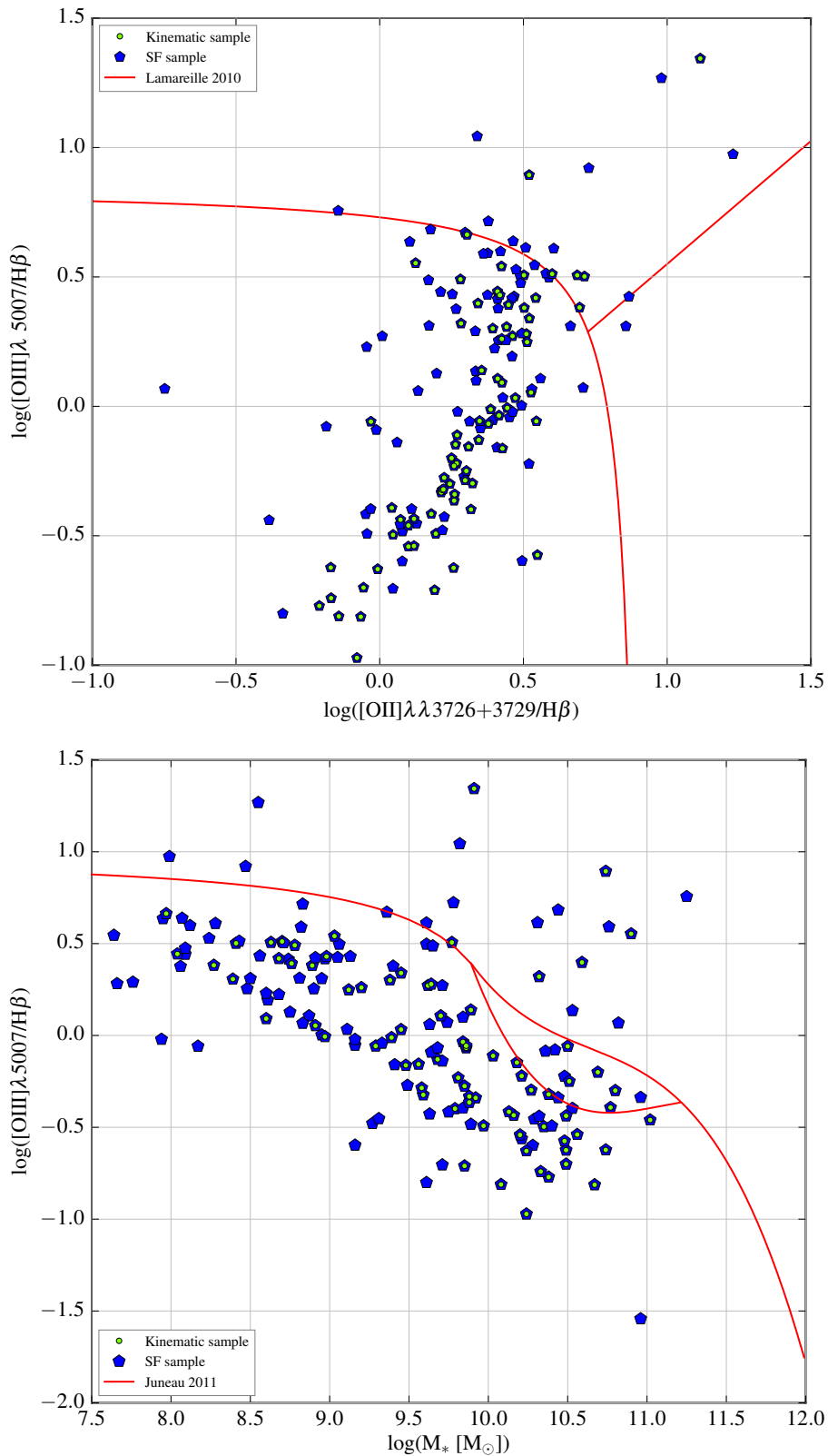


Figure 5.5: **Top panel:** Blue diagnostic diagram ($[\text{OIII}]\lambda 5007/\text{H}\beta$ vs. $[\text{OII}]\lambda\lambda 3727, 3729/\text{H}\beta$). The red curve corresponds to the empirical curve computed by Lamareille (2010). Galaxies in the SF sample from the SED fitting are represented by blue pentagons. Likewise, green circles correspond to galaxies in the kinematic sample. **Bottom panel:** Mass Excitation diagnostic diagram and the red curves separating the SFGs from AGNs, defined by Juneau et al. (2011). The symbols are the same than in the top panel representing the SF and kinematic sample.

5.5 Paper I: TFR in dense environments at $z \sim 0.7$ in the MAGIC survey

From the parent sample carefully selected, in the previous chapters, we performed detailed morpho-kinematics modeling in building spatially resolved kinematics maps with the goal to study the dark matter and baryonic mass contents, in analyzing the Tully-Fisher relationship (TFR). The TFR links the maximum rotation velocity of galaxies – a proxy of dark matter halo mass distribution – to their stellar and/or baryonic mass content. This relation provides key information on the dynamical support, and on formation and evolutionary state of galaxies. We obtained a kinematic sample which consists of 77 star-forming galaxies in 8 groups, spanning a redshift range of $0.5 < z < 0.8$, fulfilling the SNR in $[\text{OII}]\lambda\lambda 3727, 3729$ and size requirements requested in order to study the TFR of galaxies in dense environments. Additionally, we have applied an additional selection removing bulge-dominated galaxies and those presenting strong AGN activity, resulting in a definitive kinematic sample of 67 galaxies. Those galaxies are subject to interactions and mechanisms affecting their evolution by lowering their gas fractions and consequently reducing their star-forming capacity earlier than their isolated counterparts.

In this chapter, we show that our selection criteria considerably reduces the number outliers in the TFR, which are predominantly dispersion-dominated galaxies. We find that mainly galaxies with low rotation velocities are affected by the inclusion of the velocity dispersion in the velocity budget. The scatter of the TFR has also been reduced while the slope and the zero-point have been shifted. The significant offset of the TFR zero-point between galaxies in low- and high-density environments is interpreted as a decrease of either stellar mass or an increase of rotation velocity for galaxies in groups. We also studied the stellar and baryon mass fractions within stellar disks and found they both increase with stellar mass. The evolution of the TFR in dense environments could be due to a combination of quenching of star-formation and of contraction of the baryonic content, depending on the mass regime. These hypotheses are supported by evidences presented in this chapter and by previous environmental studies in literature also described in this chapter.

The Tully-Fisher relation in dense groups at $z \sim 0.7$ in the MAGIC survey ^{★,★★}

Valentina Abril-Melgarejo¹, Benoît Epinat^{1,2}, Wilfried Mercier², Thierry Contini², Leindert A. Boogaard³, Jarle Brinchmann^{3,4}, Hayley Finley², Léo Michel-Dansac⁵, Emmy Ventou², Philippe Amram¹, Davor Krajnović⁶, Guillaume Mahler⁷, Juan C. B. Pineda⁸, and Johan Richard⁵

¹ Aix Marseille Univ, CNRS, CNES, LAM, Laboratoire d'Astrophysique de Marseille, Marseille, France
e-mail: valentina.abril@lam.fr

² Institut de Recherche en Astrophysique et Planétologie (IRAP), Université de Toulouse, CNRS, UPS, CNES, Toulouse, France

³ Leiden Observatory, Leiden University, PO Box 9513, NL-2300 RA Leiden, The Netherlands

⁴ Instituto de Astrofísica e Ciências do Espaço, Universidade do Porto, CAUP, Rua das Estrelas, PT4150-762 Porto, Portugal

⁵ Univ Lyon, Univ Lyon1, Ens de Lyon, CNRS, Centre de Recherche Astrophysique de Lyon UMR5574, F-69230, Saint-Genis-Laval, France

⁶ Leibniz-Institut für Astrophysik Potsdam (AIP), An der Sternwarte 16, D-14482 Potsdam, Germany

⁷ Department of Astronomy, University of Michigan, 1085 South University Ave, Ann Arbor, MI 48109, USA

⁸ Escuela de Física, Universidad Industrial de Santander, Bucaramanga 680002, Colombia

Received 2 July 2020 / Accepted 19 January 2021

ABSTRACT

Context. Galaxies in dense environments are subject to interactions and mechanisms that directly affect their evolution by lowering their gas fractions and consequently reducing their star-forming capacity earlier than their isolated counterparts.

Aims. The aim of our project is to get new insights into the role of environment in the stellar and baryonic content of galaxies using a kinematic approach, through the study of the Tully-Fisher relation (TFR).

Methods. We study a sample of galaxies in eight groups, over-dense by a factor larger than 25 with respect to the average projected density, spanning a redshift range of $0.5 < z < 0.8$ and located in ten pointings of the MAGIC MUSE Guaranteed Time Observations program. We perform a morpho-kinematics analysis of this sample and set up a selection based on galaxy size, $[\text{O II}]\lambda\lambda 3727, 3729$ emission line doublet signal-to-noise ratio, bulge-to-disk ratio, and nuclear activity to construct a robust kinematic sample of 67 star-forming galaxies.

Results. We show that this selection considerably reduces the number of outliers in the TFR, which are predominantly dispersion-dominated galaxies. Similar to other studies, we find that including the velocity dispersion in the velocity budget mainly affects galaxies with low rotation velocities, reduces the scatter in the relation, increases its slope, and decreases its zero-point. Including gas masses is more significant for low-mass galaxies due to a larger gas fraction, and thus decreases the slope and increases the zero-point of the relation. Our results suggest a significant offset of the TFR zero-point between galaxies in low- and high-density environments, regardless of the kinematics estimator used. This can be interpreted as a decrease in either stellar mass by $\sim 0.05 - 0.3$ dex or an increase in rotation velocity by $\sim 0.02 - 0.06$ dex for galaxies in groups, depending on the samples used for comparison. We also studied the stellar and baryon mass fractions within stellar disks and found they both increase with stellar mass, the trend being more pronounced for the stellar component alone. These fractions do not exceed 50%. We show that this evolution of the TFR is consistent either with a decrease in star formation or with a contraction of the mass distribution due to the environment. These two effects probably act together, with their relative contribution depending on the mass regime.

Key words. galaxies: evolution – galaxies: kinematics and dynamics – galaxies: groups – galaxies: high-redshift

1. Introduction

Galaxies mainly assemble their mass and evolve inside dark matter halos (DMHs) via continuous accretion of cold gas (e.g., Dekel et al. 2009) and by the merging of galaxies. However, the way baryons are accreted on galaxies inside these DMHs along cosmic time is still a matter of debate. Additionally, it is not yet clear if DMHs evolve simultaneously with the baryonic content

of galaxies or if they are first settled before baryons are accreted. Estimating dark matter mass inside galaxies is necessary to solve this, which is only possible through the study of galaxy dynamics.

The Tully-Fisher relation (TFR, Tully & Fisher 1977) can be used to answer these questions since it links the total mass content of a population of star-forming galaxies to their luminosity, or to their stellar content. If DMHs are already settled we expect a strong evolution of the TFR zero-point, whereas if the baryonic and dark matter contents evolve simultaneously, the evolution is expected to depend mainly on the gas fraction.

Significant efforts to solve this question have been made by studying how the TFR evolves with cosmic time using various samples of star-forming galaxies, but the evolution of this rela-

* Tables B.1 and B.2 are also available at the CDS via anonymous ftp to cdsarc.u-strasbg.fr (130.79.128.5) or via <http://cdsarc.u-strasbg.fr/viz-bin/cat/J/A+A/647/A152>

** Based on observations made with ESO telescopes at the Paranal Observatory under programs 094.A-0247, 095.A-0118, 096.A-0596, 097.A-0254, 099.A-0246, 100.A-0607, 101.A-0282.

tion with redshift is still a matter of debate. In the local Universe, many studies of the TFR have been performed on spiral galaxies (e.g., Bell & de Jong 2001; Masters et al. 2006; Pizagno et al. 2007; Sorce et al. 2014; Gómez-López et al. 2019). However, one difficulty in comparing these studies comes from the heterogeneous datasets (H I or ionized gas spectroscopy, magnitudes in diverse spectral bands) and methods (integral field and long-slit spectroscopy data, H I widths, or velocity maps). Nevertheless, it seems clear that the TFR slope and zero-point depend on the mass range (McGaugh et al. 2000; McGaugh 2005). Simons et al. (2015) show that there is a transition in the TFR at a stellar mass of around $10^{9.5} M_{\odot}$ at $0.1 < z < 0.4$.

The population of star-forming galaxies at intermediate to high redshift, during and after the peak of cosmic star formation ($0.5 < z < 3$, Madau & Dickinson 2014), has been the topic of several kinematics studies using integral field spectrographs on 10m class telescopes. The first was obtained at $z \sim 0.6$ from the IMAGES (Intermediate-mass Galaxy Evolution Sequence) sample. Puech et al. (2008) found an evolution in both near infrared luminosity and stellar mass TFR zero-point, which implies that disks double their stellar content between $z \sim 0.6$ and $z = 0$. On the other hand, taking into account the gas content and using the same sample, Puech et al. (2010) found no evolution in the baryonic TFR. They also found a high scatter in the TFR that they attributed to galaxies with perturbed or peculiar kinematics, mainly based on visual inspection of their velocity fields. At higher redshift, an evolution in the stellar mass TFR was also found by Cresci et al. (2009) using the SINS (Spectroscopic Imaging survey in the near-infrared with SINFONI) sample at $z \sim 2$, with a similar amplitude as IMAGES, and more marginally by Gnerucci et al. (2011) from the LSD (Lyman-break galaxies Stellar population and Dynamics) and AMAZE (Assessing the Mass-Abundance redshift Evolution) samples at $z \sim 3$. However, Vergani et al. (2012) did not find such an evolution using the MASSIV (Mass Assembly Survey with SINFONI in VVDS) sample at $z \sim 1.2$. Other studies using long-slit spectroscopy on samples at $z \sim 1$ did not find any evolution of the stellar mass TFR either (e.g., Miller et al. 2012; Pelliccia et al. 2017). All these samples contained fewer than ~ 100 galaxies.

Recently, the multiplexing power of the multi-object integral field unit spectrograph KMOS (K-band Multi Object Spectrograph) has led to new, much larger samples of around a thousand galaxies (Wisnioski et al. 2015; Stott et al. 2016). Still, despite samples being larger, the debate has not been closed. Indeed, using the KROSS (KMOS Redshift One Spectroscopic Survey) sample, Tiley et al. (2019) found no evolution of the stellar mass TFR between $z = 0$ and $z = 1$, whereas Übler et al. (2017), using the KMOS3D sample, found some evolution. Indeed, in their first analysis of the KROSS sample Tiley et al. (2016), Tiley et al. did find an evolution as well, but in Tiley et al. (2019), they refined their analysis by making a careful comparison at $z \sim 0$ with the SAMI (Sydney-AAO Multi-object Integral-field spectrograph) Galaxy Survey (e.g., Bryant et al. 2015). This allowed them to minimize the potential methodological biases arising from sample selection, analysis methods, and data quality. Indeed, the differences in instrumental set-ups and the methodologies to extract kinematics and, more generally, to select the samples make comparisons problematic. Most of these intermediate redshift samples of star-forming galaxies have been preselected from large spectroscopic samples based on color or magnitude. Therefore, they are most often limited to the most massive galaxies ($M_{*} > 10^{10} M_{\odot}$), whereas most of the galaxies in the Universe are below this limit. A few TFR studies on smaller samples at $z > 0.5$ have, however, considered galaxies down

to low masses using either the MUSE (Multi Unit Spectrograph Explorer) integral field instrument (Contini et al. 2016) or the DEIMOS (DEep Imaging Multi-Object Spectrograph) multi-slit spectrograph (Simons et al. 2017).

On the other hand, the environment also plays an important role in the mass assembly of galaxies and in the transformation of star-forming galaxies into passive ones. Indeed, it has been observed in the Local Universe that the quenching of star formation and the buildup of the red sequence happen earlier in dense environments than in the field (e.g., Peng et al. 2010; Muzzin et al. 2012). This could be induced by direct interactions among galaxies, by interactions between galaxies and the gravitational potential of the group or cluster, or by interactions with intra-group or cluster media, which either prevent gas accretion onto galaxies or remove their gas content (e.g., Boselli & Gavazzi 2006). Environment might also have an impact on the baryonic content of underlying DMHs. However, studying the kinematics of disks is more challenging in dense environments than in the field due to the reduced gas fraction. In the local Universe, the population of disks is larger in the outskirts of such structures, which probably means that they are just entering these structures or that they are less affected by the environment. This is supported by the fact that studies using local cluster galaxies do not show evidence for variation of the TFR with environment (e.g., Masters et al. 2006, 2008). In addition, a comparison of the TFR between galaxies in the field (Torres-Flores et al. 2011) and in compact groups (Torres-Flores et al. 2013), where galaxy interactions are supposed to be more important, provides a similar conclusion.

At higher redshift, and most specifically at $z \sim 1$ when the cosmic star formation starts its decrease, the densest structures have already started their relaxation but still contain a large fraction of star-forming galaxies (e.g., Muzzin et al. 2013), probably because galaxies had more gas at that time and because the environmental processes that turn off star formation operate on fairly long timescales (e.g., Cibinel et al. 2013; Wetzel et al. 2013). This means that disks might survive longer before being devoid of gas and could therefore be more severely impacted by the environment than in the local Universe.

However, despite the new large samples presented above, studying the impact of environment on the TFR is not yet possible at intermediate redshift since very little is known about the density field in which those galaxies reside, due to incomplete spectroscopic coverage. Some studies have, however, targeted a few dozen galaxies in groups and (proto-)clusters at intermediate redshift with KMOS and FORS2 (e.g., Sobral et al. 2013; Pérez-Martínez et al. 2017; Böhm et al. 2020). So far, the most complete study of the TFR as a function of environment has been performed from long-slit spectroscopy observations by Pelliccia et al. (2019), using a sample of 94 galaxies at $z \sim 1$, a fraction of which were members of clusters. They do not report significant modification of the TFR with environment.

Focusing on star-forming galaxies along the main sequence is essential to analyze and compare the TFR for similar populations of galaxies in various environments. In this paper, we present the study of the spatially resolved ionized gas kinematics and of the TFR for a sample of star-forming galaxies in dense environments at intermediate redshifts ($z \sim 0.7$) from the MUSE gAlaxy Groups In Cosmos (MAGIC) dataset (Epinat et al., in prep), using data from MUSE (Bacon et al. 2015). At these redshifts, the MUSE field of view corresponds to a linear physical size of more than 400 kpc, which is the typical size for groups. This allows us to study the properties of star-forming galaxies in groups without any other preselection besides targeting known

over-densities, leading to samples not limited in magnitude nor in color (Contini et al. 2016).

The structure of the paper is as follows. In Sect. 2 we present the MUSE observations of the MAGIC program and the data reduction. Identification of groups and their properties, detailed group galaxies physical properties, including their morphological and kinematics modeling, and kinematic sample selection criteria are described in Sect. 3. Section 4 is focused on the detailed analysis of the TFRs and their comparison with reference samples, whereas the interpretation of the results is conducted in Sect. 5 before concluding the analysis in Sect. 6. Throughout the paper, we assume a Λ CDM cosmology with $H_0 = 70 \text{ km s}^{-1} \text{ Mpc}^{-1}$, $\Omega_M = 0.3$, and $\Omega_\Lambda = 0.7$.

2. MUSE observations in dense environments and data reduction

The sample of galaxies located in dense environment that is analyzed in this paper is a subsample of the MAGIC Survey (MUSE gAlaxy Groups In Cosmos). We focus on eight groups of the COSMOS field (Scoville et al. 2007) selected in the COSMOS group catalog of Knobel et al. (2012) with redshifts $0.5 < z < 0.8$ observed during MUSE Guaranteed Time Observations (GTO) as part of an observing program focusing on the effect of the environment on galaxy evolution over the past 8 Gyrs (PI: T. Contini). All the details on group selection, observations and data reduction will be presented in the MAGIC survey paper (Epinat et al. in prep), so here we give a summary of the most important steps.

The observations presented in this paper were spread over seven periods. For each targeted field, observing blocks of four 900 seconds exposures including a small dithering pattern and a rotation of the field of 90° between each, were combined to obtain final datacubes with depths from one to ten hours. In order to be able to perform kinematics analysis, good seeing conditions providing a point spread function full width at half maximum (PSF FWHM) lower than $0.8''$ were required unless the adaptive optics system was used in the last observing runs.

The basic data reduction was applied for each OB separately using the MUSE standard pipeline (Weilbacher et al. 2020). Version v1.6 was used for all seeing limited observations except for CGr30 (v1.2), whereas v2.4 was used for AO observations. A default sky subtraction was applied to each science exposure before aligning and combining them using stars in the field. The Zurich Atmosphere Purge software (ZAP; Soto et al. 2016) was then applied to the final combined cube to further improve sky subtraction. Version 0.6 was used for CGr30, CGr34, and the one hour exposure cube on CGr84, version 1.1 was used for CGr28, the deepest cube on CGr84, and CGr114, whereas version 2.0 was used for the two other groups observed with AO.

In the end, each cube has a spatial sampling of $0.2''$ and a spectral sampling of 1.25 \AA over a 4750 \AA to 9350 \AA spectral range and an associated variance datacube is also produced.

The knowledge of both point spread function (PSF) and line spread function (LSF) are essential to derive accurate kinematic measurements. In order to compute the MUSE PSF, we modeled the surface brightness profiles of all the stars in each field using the GALFIT software (Peng et al. 2002). Gaussian luminosity profiles were used to model all the stars since their observed profiles are quite symmetric. We have from three to five stars per field and since all the galaxies in a given group are within a narrow redshift range, we extracted narrow-band images of each star around the wavelength of the [O II] doublet (used to extract

kinematics, see Sect. 3.5) redshifted at the median redshift of each group. We then computed the median FWHM of the stars for each group in each field to evaluate the corresponding PSF. The median PSF FWHM value for all the fields is $\sim 0.66''$, the smallest PSF value corresponds to $0.58''$ and the largest to $0.74''$.

We determined the LSF FWHM using the prescriptions from Bacon et al. (2017) and Guérou et al. (2017), in which they analyzed the variation of the MUSE LSF with wavelength in the Hubble Ultra Deep Field and in the Hubble Deep Field South. The MUSE LSF is described as:

$$\text{FWHM} = \lambda^2 \times 5.866 \times 10^{-8} - \lambda \times 9.187 \times 10^{-4} + 6.040, \quad (1)$$

where FWHM and λ are both in Angstroms. The corresponding dispersion is then estimated assuming the LSF is Gaussian.

Table 1 summarizes the main observational properties of the eight studied galaxy groups: group ID, coordinates of the center, exposure time per field, median redshift, MUSE PSF FWHM, total number of galaxy members and number of galaxies belonging to the kinematic sample (see Sect. 3.6). Medium-deep data ($> 4\text{h}$) are used for most of the groups.

3. Physical properties of galaxies in dense environments

3.1. Redshift determination and group membership

The groups have been targeted in the COSMOS field (Scoville et al. 2007), therefore, all galaxies in the field have already been identified in broad-band photometry up to a limiting magnitude of ~ 26 at 3σ in the z_{++} band (COSMOS2015; Laigle et al. 2016). The spectroscopic redshifts for all objects in the photometric COSMOS2015 catalog located inside the MUSE fields were estimated using the redshift finding algorithm MARZ (Hinton et al. 2016; Inami et al. 2017) based on their absorption and emission spectral features. At the redshift range of our groups (average $z \sim 0.7$), the most prominent emission lines are the [O II] $\lambda\lambda 3727, 3729$ doublet, [O III] $\lambda 5007$, and the Balmer lines starting with H β . The main absorption lines are Ca II H $\lambda 3968.47$, Ca II K $\lambda 3933.68$, G band at 4100 \AA , and the Balmer absorption lines. For each source in each field a PSF-weighted spectrum was extracted (as described in Inami et al. 2017) and then the strongest absorption and emission lines were identified giving a robust redshift determination. We attributed confidence flags for all these objects, following the procedure described in Inami et al. (2017).

We used secure spectroscopic redshifts to identify dense structures and galaxies within them using a friends of friends (FoF) algorithm, which will be described in the MAGIC survey paper (Epinat et al. in prep.). This method is intended to assign the membership of galaxies to a certain group or cluster if they are below given thresholds of angular separation on the sky plane and of velocity separation in the redshift domain from the nearest neighbors. We used a projected separation of 450 kpc and a velocity separation of 500 km s^{-1} between neighbors, as suggested by Knobel et al. (2009). Such conservative separations ensure that we do not miss any group galaxy in the process. Using this technique allowed us to find other structures than the targeted ones in the redshift range $0.5 < z < 0.8$. However, except in one case (CGr84 fields), the number of galaxies in secondary structures is small and we therefore concentrated our efforts on the densest structures containing at least ten members. This led us with a sample of 277 galaxies inside eight galaxy groups. Due

Table 1: General properties of the galaxy groups in the parent sample.

ID COSMOS Group (1)	R.A. (J2000) (2)	Dec. (J2000) (3)	Exp. Time (h) (4)	Redshift (5)	PSF FWHM " (6)	Number of galaxies (all/SED/MS/KS) (7)	M_{vir} $10^{13} M_{\odot}$ (8)
CGr28	150°13'32"	1°48'42"	1	0.530	0.654	10/10/9/3	7.1
CGr30	150°08'30"	2°04'01"	9.75	0.725	0.700	44/39/33/15	6.5
CGr32	149°55'19"	2°31'16"	$3 \times (1 + \mathbf{3.35})^{(a)}$	0.730	0.596-0.624-0.722 ^(a)	106/92/50/13	81.4
CGr34	149°51'32"	2°29'28"	5.25	0.732	0.664	20/20/17/9	10.4
CGr79	149°49'15"	1°49'18"	4.35	0.531	0.658	19/19/15/8	11.2
CGr84	150°03'24"	2°36'09"	5.25 + 1 ^(b)	0.697	0.620-0.578 ^(b)	31/26/21/8	8.2
CGr84b	150°03'28"	2°36'32"	5.25 + 1 ^(b)	0.681	0.620-0.578 ^(b)	35/32/25/9	8.8
CGr114	149°59'50"	2°15'33"	2.2	0.659	0.740	12/12/8/2	3.5
Median				0.689	0.656		8.5
Total			41.9			277/250/178/67	

Notes. (1) COSMOS Group ID. (2) and (3) J2000 coordinates of the centers of the galaxy groups. (4) Exposure time per field. Exposure using adaptive optics are marked in bold. (5) Median redshift of the group. (6) MUSE PSF FWHM of the narrow band image around the observed wavelength of the [O II] doublet at the group redshift (7) Number of galaxies (i) all: total in each group; (ii) SED: with SED fitting information (SFR and stellar mass); (iii) MS: on the main sequence of star-forming galaxies; (iv) KS: in the final kinematic sample. (8) Virial mass of the groups. ^(a) CGr32 has been observed within a mosaic of three adjacent MUSE fields having the same exposure time (1h without and 3.35h with adaptive optics). The three PSF FWHM values correspond to each field. ^(b) CGr84 and CGr84b are both observed in the same two adjacent MUSE fields. The two values of exposure times and of seeing correspond to each field.

to blending or due to the absence of photometry in the COSMOS2015 catalog, we discarded 27 galaxies from the analysis, leading to a parent sample of 250 galaxies in groups.

3.2. Groups properties

The eight groups studied in this paper are quite dense and massive. Their virial mass was estimated from the velocity dispersion of members computed using the gapper method discussed in Beers et al. (1990) and used in Cucciati et al. (2010):

$$\sigma_v = \frac{\sqrt{\pi}}{N(N-1)} \sum_{i=1}^{N-1} i(N-i)(v_{i+1} - v_i), \quad (2)$$

where v_i are the velocities of the N members sorted in ascending order, computed with respect to the median redshift of the group. The mass was then computed as:

$$M_{\text{vir}} = \frac{3\sqrt{3}\sigma_v^3}{11.4GH(z)}, \quad (3)$$

where G is the gravitational constant and $H(z)$ is the Hubble parameter at redshift z (see Lemaux et al. 2012). These masses are provided in Table 1. They span a range between 3.5 and $81.4 \times 10^{13} M_{\odot}$, with a median mass of $8.5 \times 10^{13} M_{\odot}$. For some of the groups presented here, masses were also estimated using X-ray data from XMM and *Chandra* (Gozaliasl et al. 2019). We checked the consistency between the two estimates and found an agreement within ~ 0.5 dex. The most massive group contains more than 100 members and is most likely a cluster (CGr32; cf. Boselli et al. 2019). We will, however, refer to all the structures as groups. More detail will be provided in the survey paper (Epinat et al. in prep). The typical projected galaxy density in the MUSE fields ranges between 65 and 220 galaxies per Mpc^2 , with a median of around 100 galaxies per Mpc^2 (20 galaxies per squared arcminute). The typical galaxy density ranges between 130 and 500 galaxies per Mpc^3 , with a median of around 200 galaxies per Mpc^3 assuming that the third dimension equal the projected one. This is 200 times denser than the typical galaxy density that is around 0.5 galaxy per Mpc^3 (e.g., Conselice et al.

2016) at $z \sim 0.5 - 0.7$, converting comoving volume to proper one. We also made similar typical galaxy density estimates from the MUSE data in order to have a consistent selection. Indeed, the galaxy density provided by Conselice et al. (2016) is based on photometric redshifts, whereas we only used galaxies with secure MUSE spectroscopic redshifts¹. We considered all the galaxies between $z = 0.5$ and $z = 0.75$ with secure redshifts and we estimated the average density including and excluding the studied groups. We obtained a similar density as in Conselice et al. (2016) when we included the groups, and a value four times lower when groups were excluded. This result is not surprising, because of the different sample selections and since the study of Conselice et al. (2016) does include some groups. We can therefore consider that our groups are at least 200 times denser than the average density within the considered redshift range. Since the sizes of the groups in the third dimension are not well constrained, we also compared the surface densities and found that our groups are on average 25 times denser than the field, assuming a typical redshift bin of 0.025 ($\sim 4500 - 5000 \text{ km s}^{-1}$) for the groups, which is an upper limit. Given the size of the group sample studied here, we do not refine further the density estimate. We can nevertheless claim that our groups are much denser than the average environments encountered in the Universe.

3.3. Global galaxy properties

Using the extensive photometry available in the COSMOS field (Laigle et al. 2016), stellar mass, star formation rate (SFR), and extinction were estimated for all the galaxies in the selected groups within MUSE fields. Apertures of $3''$ were used over 32 bands from the COSMOS2015 catalog to obtain photometric constraints on the stellar population synthesis (SPS) models. Instead of using the properties derived from the purely photometric redshift catalog of Laigle et al. (2016), we remodeled the photometry taking advantage of the robust spectroscopic redshift measurements from MUSE spectra to introduce additional constraints into the SPS models. To model the spectra we

¹ Around half of the galaxies detected in our MUSE cubes have such secure redshifts.

used the spectral energy distribution (SED) fitting code FAST (Kriek et al. 2009) with a synthetic library generated by the SPS model of Conroy & Gunn (2010), assuming a Chabrier (2003) initial mass function (IMF), an exponentially declining SFR ($\text{SFR} \propto \exp(-t/\tau)$, with $8.5 < \log(\tau[\text{yr}^{-1}]) < 10$), and a Calzetti et al. (2000) extinction law. We used the same method as in the previous studies by Epinat et al. (2018) and Boselli et al. (2019) on the COSMOS Groups 30 and 32, respectively, using MUSE data, to derive the uncertainties on the SED by adding in quadrature a 0.05 dex uncertainty to each band that account for residual calibration uncertainties.

The distributions of stellar mass (M_*) and SFR extracted from the SED fitting are presented in Fig. 1. The whole sample of galaxies in groups covers a wide range of masses from $\sim 10^{7.5} M_\odot$ to $\sim 10^{11.5} M_\odot$. The parent sample includes a large fraction of galaxies lying on the main-sequence of star-forming galaxies and some passive galaxies. In this study, we are interested in the kinematic properties of star-forming galaxies in groups. We therefore need to distinguish between passive and star-forming galaxies. To do that, we used the prescription of Boogaard et al. (2018) to account for the SFR evolution with redshift at a given stellar mass and we identified galaxies along the main sequence of star-forming galaxies as those for which

$$\log(\text{SFR}) - 1.74 \times \log((1+z)/1.7) \geq 0.83 \times \log(M_*) - 9.5, \quad (4)$$

where M_* is the stellar mass in M_\odot and SFR is the star formation rate in $M_\odot \text{ yr}^{-1}$. This subsample contains 178 galaxies and is referred to as the parent sample of star-forming galaxies. It spreads over a wide range of masses ($\sim 10^{7.5} M_\odot$ to $\sim 10^{11.5} M_\odot$) and SFRs ($10^{-2} M_\odot \text{ yr}^{-1}$ to $10^2 M_\odot \text{ yr}^{-1}$). Masses and SFRs for the kinematic sample (see Sect. 3.6) are presented in Table B.2 of Appendix B.

3.4. Morphological analysis

In order to constrain efficiently geometrical parameters required for the kinematics analysis, a homogeneous extraction of the surface brightness distribution using high resolution images is highly desirable. In addition, studying galaxy morphology is instructive of their type and size. Ideally one should probe the old stellar populations better traced by rest-frame red images. For the COSMOS sample, the publicly available images with the best spatial resolution are the *Hubble* Space Telescope (HST) Advanced Camera for Surveys (ACS) images observed with the F814W filter, which corresponds to rest-frame wavelengths around 5000 \AA at $z \sim 0.7$, and that have a spatial resolution better than $0.1''$ (corresponding to $\sim 700 - 600 \text{ pc}$ in the galaxies frame). These images were produced using the MultiDrizzle software (Koekemoer et al. 2007) on the COSMOS field (Scoville et al. 2007), with a spatial sampling of $0.03''/\text{pixel}$ and a median exposure time of 2028 seconds.

Models for the surface brightness distribution of the stellar continuum and the determination of the geometrical parameters were performed for all the galaxies in groups on these HST-ACS images, using the data analysis algorithm GALFIT (Peng et al. 2002). First, with the purpose of determining the PSF in these images, we identified 27 non saturated stars present over 14 fields corresponding to groups observed with MUSE in the COSMOS field before October 2018. These stars were modeled using a circular Moffat profile. We then built with GALFIT the theoretical PSF taking the median value of each parameter derived from the 27 stars: $\text{FWHM} = 0.0852''$ and $\beta = 1.9$ (Moffat index).

We followed the same method as in Contini et al. (2016) for galaxies in the Hubble Deep Field South, and in Epinat et al.

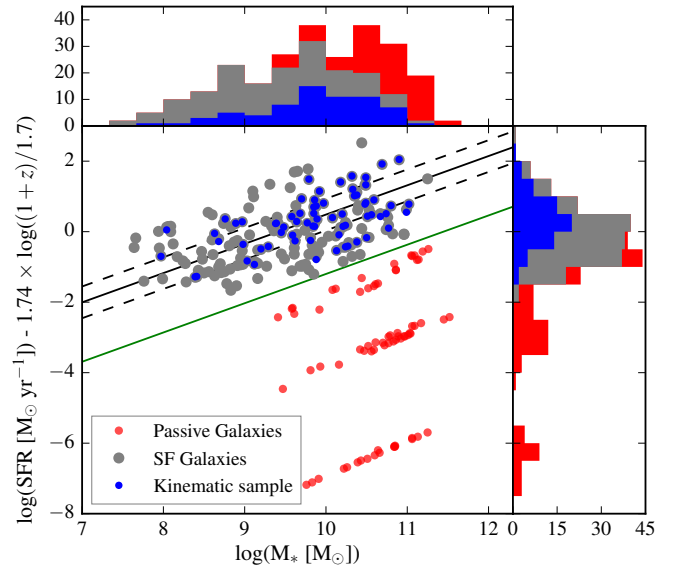


Fig. 1: Distribution of the whole sample on the M_* - SFR plane. The green line represents the separation defined in Eq. 4 used to distinguish between galaxies on the red sequence (red dots) and galaxies along the main sequence of star-forming galaxies (gray dots). The solid black line represents the best fitting of SFR - M_* empirical relation for star-forming galaxies derived by Boogaard et al. (2018), with SFR normalized to redshift $z = 0.7$ to account for the evolution with redshift, whereas the dashed lines represent the $1-\sigma$ intrinsic scatter of this relation. Blue dots correspond to the 67 galaxies in the final kinematic sample ($S/N \geq 40$, $R_{eff}/\text{FWHM} \geq 0.5$). The histograms show the stellar mass and SFR distributions for the passive galaxies (red), for the parent sample of star-forming galaxies (gray) and for the kinematic sample (blue).

(2018) for the galaxies in the group COSMOS-Gr30: The galaxies in our sample were modeled with a composite of bulge and disk model profiles. The bulge is spheroidal and is described by a classical de Vaucouleurs profile (Sersic index $n = 4$),

$$I(r) = I_b(r_e) e^{-7.67[(r/r_e)^{1/4} - 1]}, \quad (5)$$

where r_e is the bulge effective radius and $I_b(r_e)$ is the bulge intensity at the effective radius. The disk is described by an exponential disk,

$$I(r) = I_d(0) e^{-r/R_d}, \quad (6)$$

where $I_d(0)$ is the disk central intensity and R_d the disk scale length. Both profiles share a common center. For the bulge the free parameters are the total magnitude and the effective radius. For the disk we let free the position angle (PA_m), axis ratio, total magnitude and scale length.

When necessary, additional components were introduced to account for extra features (nearby faint galaxies in the field, strong bars, star-forming clumps, etc.) and avoid the bias they could cause in the resulting parameters. This was very obvious in some cases where strong star-forming clumps biased the center of the galaxy closer to the clump than to the actual center. Therefore, modeling them as individual components allowed us to have better geometrical determinations of the bulge and of the disk. We performed morphological modeling the full parent

sample, that includes passive galaxies, with the aim at statistically characterizing the galaxy groups and the ratio of passive to star-forming galaxies. Morphological parameters for the kinematic sample (see Sect. 3.6) are presented in Appendix B.

We compared our morphological decomposition with morphological catalogs in the COSMOS field to assess its robustness. Several morphological catalogs are publicly available and provide, among others, galaxy sizes, axis ratios and morphological types (Tasca int catalog: Tasca et al. 2009, Tasca linee catalog: Abraham et al. 1996 and Tasca SVM catalog: Huertas-Company et al. 2008²; Cassata catalog Cassata et al. 2007³; Zurich catalog Scarlata et al. 2007; Sargent et al. 2007⁴). In all these catalogs, morphological measurements based on SExtractor (Bertin & Arnouts 1996) segmentation maps are provided. Whereas our forward modeling approach corrects the size and the axis ratio for the PSF of the HST-ACS images, this is not the case for methods based on segmentation maps. For this analysis we used data on four additional MUSE fields targeting groups at redshifts $0.3 < z < 0.5$, and we included the morphological analysis performed on field galaxies, leading to a total sample of 659 galaxies, in order to increase the intersection of our sample with that of the COSMOS catalogs. We present the comparison with the Cassata et al. (2007) catalog, for which the intersection with our sample is large (471 galaxies in common) and for which the dispersion between their effective radius measurements and ours is the smallest. It is however worth noticing that the trends presented hereafter are the same whatever the catalog used.

We first compared the effective radii (see Fig. 2). Our method provides effective radii for both bulge and disk components. In order to do a fair comparison, we used our models to infer a global effective radius (R_{eff}). GALFIT effective radii are smaller than those in the COSMOS catalogs for galaxies with radii smaller than $\sim 0.2''$. The relative difference increases when the effective radius decreases, which clearly demonstrates that the difference is due to the fact that we compare a forward model that takes into account the PSF to SExtractor based measurements that are limited by the image spatial resolution. For larger radii, GALFIT effective radii are larger but the relative difference is lower than 50% and depends on the catalog used for comparison. In addition, this does not impact the total magnitude of our model that is in good agreement with that of those catalogs. We also computed the bulge to disk ratio inside R_{eff} and checked that this correlates with the COSMOS morphological classification (see Fig. 3), in order to assess the validity of our bulge/disk decomposition. Clearly, elliptical galaxies have a larger fraction of bulge-dominated galaxies and spiral galaxies have a larger fraction of disk-dominated galaxies. We also see such an agreement in the distribution of galaxies inside the M_* - SFR plot for the present parent sample of galaxies in groups. Last, we compared the axis ratio from GALFIT to the one determined by Cassata et al. (2007) (see Fig. 4) and found that, on average, it is lower using GALFIT. This is expected since the COSMOS catalog provides a global axis ratio while we determined it for the disk with GALFIT. We can see that most of the scatter comes from bulge-dominated galaxies. The agreement for disk-dominated galaxies is fairly good, despite GALFIT still leads to lower values. For very low disk axis ratios, this can be explained by the fact that GALFIT corrects the ratio for the HST-ACS PSF, whereas SExtractor

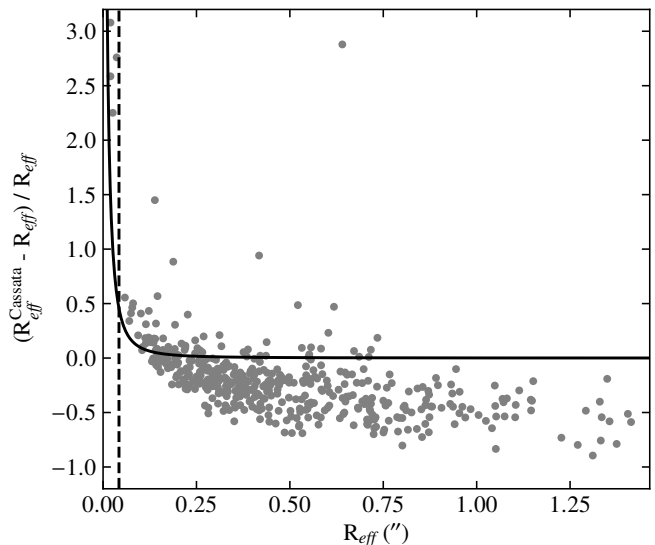


Fig. 2: Relative difference between the global effective radius inferred from our GALFIT models and the Cassata et al. (2007) morphological catalog as a function of the GALFIT effective radius. The solid black line represents the limiting effective radius measurable when not taking into account the PSF, and the dashed vertical line marks the value of half the HST-ACS PSF FWHM.

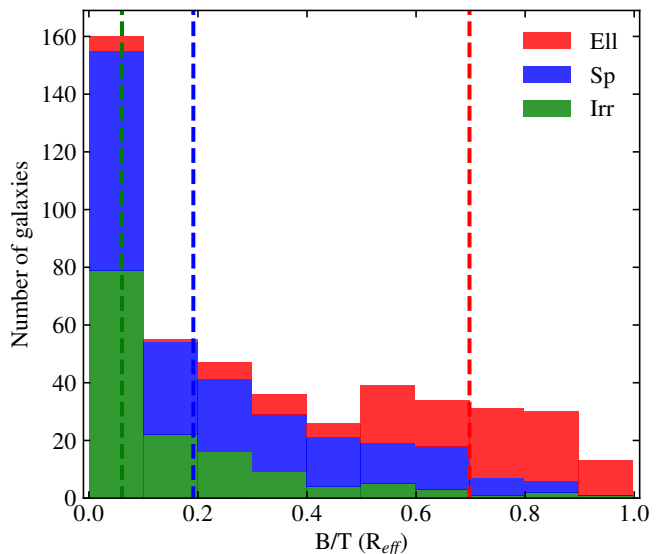


Fig. 3: Distribution of the three morphological classes defined in the Cassata et al. (2007) catalog as a function of the bulge to total flux ratio estimated at the effective radius. Green, blue, and red stacked histograms correspond to galaxies classified, respectively, as irregular, spiral, and elliptical. The median values for those three classes are 0.06, 0.19, and 0.70, respectively, and are indicated by dashed colored vertical lines.

does not. These results underline the reliability of our morphological analysis that is homogeneous for the whole sample of galaxies.

By construction, our group sample should display a distribution compatible with random disk orientation since there is no galaxy preselection. In order to evaluate if there is any bias on

² https://irsa.ipac.caltech.edu/data/COSMOS/gator_docs/cosmos_morph_tasca_colDescriptions.html

³ https://irsa.ipac.caltech.edu/data/COSMOS/gator_docs/cosmos_morph_cassata_colDescriptions.html

⁴ https://irsa.ipac.caltech.edu/data/COSMOS/gator_docs/cosmos_morph_zurich_colDescriptions.html

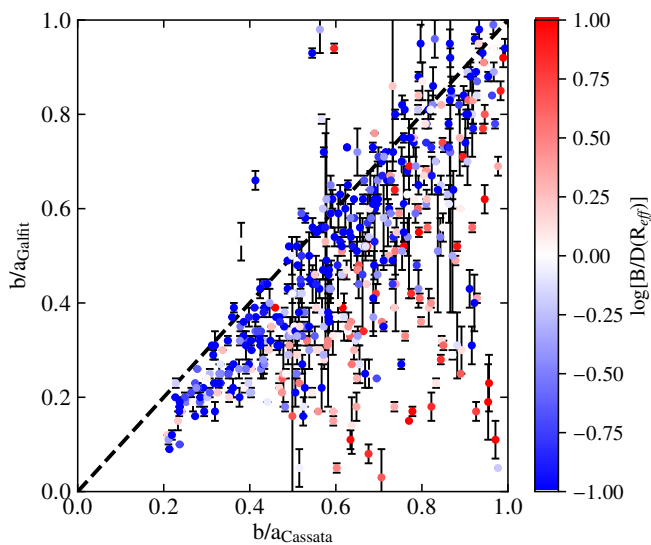


Fig. 4: Axis ratio for the disk determined using GALFIT as a function of the global axis ratio from the Cassata et al. (2007) catalog. The color indicates the luminosity ratio of the bulge with respect to the disk inside the effective radius, red and blue colors corresponding, respectively, to bulge- and disk-dominated galaxies.

the inclination parameter for our sample, we extracted the distributions of inclinations of our sample from our morphological modeling with GALFIT, assuming razor-thin disks. In this analysis, we only use the parent sample of star-forming galaxies (see Sect. 3.3) since red sequence galaxies are supposed to be ellipticals. We compared our observed distribution with the theoretical distribution for randomly oriented disks. This theoretical distribution is derived from the fact that the probability to observe a thin disk with an orientation between θ_1 and θ_2 is equal to $|\cos \theta_1 - \cos \theta_2|$. The distribution of inclinations shown in Fig. 5 illustrates the fact that the construction of our sample is done without any prior. The median value of inclination for our sample is 65.2° , which is close to the theoretical median inclination of 60° . Our sample misses low inclination systems ($i < 40^\circ$) and highly inclined ones ($i > 80^\circ$) with respect to the expected distribution of inclinations for randomly oriented disks (orange curve). On the one hand, at low inclination, this may be due to the small number of galaxies expected from the theoretical distribution function. Moreover, despite we modeled separately some strong features in the light distributions, residual features, such as bars or arms, may have persisted, affecting the models of the disks and biasing the estimated inclination toward higher values. On the other hand, the lack of edge-on galaxies, could be due to high levels of dust extinction that could reduce the detection of such galaxies. However, this could also be due to the fact that we assume a null thickness for the modeling, so for galaxies with thick disks we may underestimate their real inclination. Using an intrinsic axial ratio of the scale height to the scale length different than zero would mainly fill the histogram at high inclination without changing it much at low inclination. For bulge-dominated galaxies, the morphological decomposition may lead to unconstrained disk parameters. We therefore also studied the inclination distribution after removing bulge-dominated galaxies from the distribution. This resulted in removing almost all galaxies with disk inclinations larger than 80° . Nevertheless, this did not impact much the rest of the distribution. This shows that our

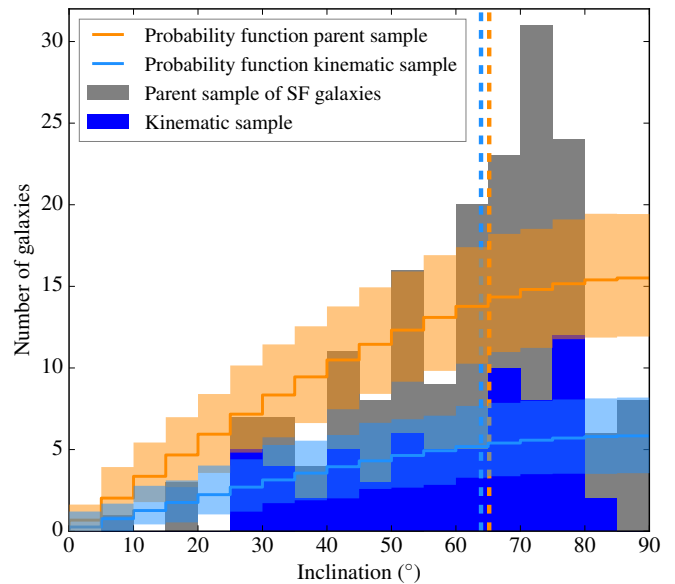


Fig. 5: Distribution of disk inclinations for the parent sample on the main sequence of star-forming galaxies with a bin of 5° (gray). The orange curve and shadow area represent the expected theoretical distribution for random orientations and the 1σ uncertainties computed from 5000 realizations of such a random distribution with the same number of 178 galaxies as the parent sample. The distribution of the final kinematic sample ($S/N > 40$, $R_{eff}/FWHM > 0.5$) of 67 galaxies is also displayed (filled blue histogram) along with the associated theoretical distribution and the corresponding 1σ uncertainties (light blue curve and shadow area). The dashed orange and blue vertical lines indicate the median value for the parent ($i = 65.2^\circ$) and final kinematic ($i = 63.9^\circ$) samples, respectively.

bulge-disk decomposition provides meaningful measurements of disk inclinations for disk-dominated galaxies.

3.5. Kinematics of the ionized gas

We extracted the spatial distribution and kinematics of the ionized gas for all galaxies in the parent sample⁵. In this study, in order to have an homogeneous analysis, we focus on kinematics derived from the $[\text{O II}]\lambda\lambda 3727, 3729$ doublet. From the MUSE datacubes, we extracted the line flux, signal-to-noise ratio (S/N), velocity field and velocity dispersion map by modeling the $[\text{O II}]\lambda\lambda 3727, 3729$ line doublet using the python code CAMEL⁶ described in Epinat et al. (2012), which fits any emission line with a Gaussian profile and uses a polynomial continuum. For each galaxy we extracted a sub-datacube around its center with a total size of 30×30 pixels and, in order to increase the S/N per pixel without lessening the resolution, a 2D spatial Gaussian smoothing with a FWHM of two pixels was applied. To perform the fitting around the $[\text{O II}]$ doublet spaxel by spaxel, we use a constant continuum. Each line was modeled separately by a Gaussian profile at different rest-frame wavelengths, but assuming the same velocity and velocity dispersion. The ratio between the flux of the two $[\text{O II}]$ doublet lines was constrained between $0.35 \leq F_{[\text{O II}]\lambda 3727}/F_{[\text{O II}]\lambda 3729} \leq 1.5$, according to the expected

⁵ We were able to extract $[\text{O II}]$ kinematics for only six galaxies considered as passive, two of which show signs of AGN activity.

⁶ <https://bitbucket.org/bepinat/camel.git>

photo-ionization mechanism (Osterbrock & Ferland 2006). We then run a cleaning routine to remove all the spaxels with S/N below a threshold of 5 or having a velocity dispersion lower than 0.8 times the dispersion corresponding to the spectral resolution (see Sect. 2). The latter ensures to avoid fitting noise while keeping detection even of narrow lines that might be present. After the automatic cleaning we visually inspected all the resulting velocity fields with the goal to remove isolated spaxels or spaxels with both low S/N and atypical velocity values with respect to their neighbors.

The kinematics of each galaxy was then modeled as a rotating disk in two dimensions. This model is taking into account properly the effect of the limited spatial resolution of observations. It produces a high resolution model and uses the observed line flux distribution to weight the velocity contribution within each spaxel of the low resolution velocity field after smoothing by the MUSE PSF, as described in Epinat et al. (2010). We fixed the inclination (i) and center (x, y) to those derived from the morphological analysis of the high resolution HST-ACS images (see Sect. 3.4) in order to suppress the degeneracy with the rotation velocity amplitude and with the systemic velocity, respectively. This degeneracy in the kinematic model is strong when the data is severely affected by beam smearing (Epinat et al. 2010). The rotation curve used in the model is linearly rising up to a constant plateau and has two parameters: V_t , the velocity of the plateau and r_t , the radius at which the plateau is reached:

$$V_r = V_t \times \frac{r}{r_t} \quad \text{when } r \leq r_t \quad \text{or} \quad V_r = V_t \quad \text{when } r > r_t. \quad (7)$$

The other fitted parameters are the systemic redshift (z_s) and the kinematic position angle of the major axis (PA_k). This procedure fits the observed velocity field, taking the velocity uncertainty into account to weight the contribution of each spaxel. It uses a χ^2 minimization based on the Levenberg-Marquardt algorithm. It also produces a map of the beam smearing correction to be subtracted in quadrature to the observed velocity dispersion map. For the pixels where the measured velocity dispersion is lower than the LSF, the LSF corrected dispersion is set to zero. Similarly, when the LSF corrected dispersion is lower than the beam smearing correction, the beam smearing corrected dispersion map is null. This method has been used in several studies (Epinat et al. 2009, 2010, 2012; Vergani et al. 2012; Contini et al. 2016).

The goal of this modeling is the derivation of V_{r22} , the rotation velocity at $R_{22} = 2.2 \times R_d$, and of σ , the velocity dispersion (see Sect. 4.1). For the final kinematic sample (see Sect. 3.6), the cleaned kinematic maps are more extended than R_{22} , except for two galaxies for which the data extends up to 96% and 87% of R_{22} . For the less extended one, the plateau is reached within the data. We therefore kept both in the analysis. When the plateau is reached within the data but not reached within R_{22} , the uncertainty on the velocity is estimated from the uncertainty on V_t , r_t , and R_d . When the plateau is not reached within the data, uncertainties on both r_t and V_t are large due to a degeneracy in the model. However, the slope might be well constrained. In those cases, the uncertainty on V_{r22} is deduced from the one on R_{22} , estimated as the mean of the MUSE PSF standard deviation ($\text{FWHM} / 2 \sqrt{2 \log 2}$) and of the uncertainty on $2.2 \times R_d$. In the other cases, we use the formal uncertainty on V_t . The velocity dispersion is estimated on the beam smearing corrected velocity dispersion map as the median of the spaxels where the S/N is above 5. It therefore equals to zero when more than half of those spaxels have a measured line width lower than the quadratic combination of LSF plus beam smearing correction

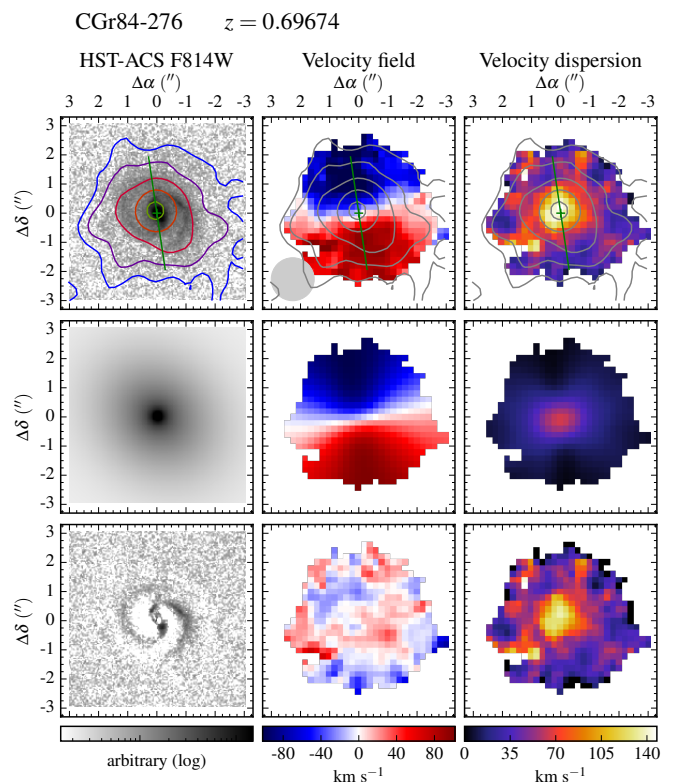


Fig. 6: Example of maps and models for galaxy ID276 in CGR84. Top row, from left to right: HST-ACS F814W images, MUSE velocity fields and velocity dispersion maps corrected for spectral resolution. Middle row: Associated models. The velocity dispersion (third column) corresponds to a beam smearing correction map. Bottom row: Residuals, except for the third column that shows the beam smearing corrected velocity dispersion map. On each observed map, the green cross indicates the center derived from the morphology, whereas the green segment indicates the kinematic major axis and has a length corresponding to R_{22} . The $[\text{O II}]$ flux distribution is shown with contours at levels of surface brightness $\Sigma([\text{O II}]) = 2.5, 5.0, 10.0, 20.0, 40.0, 80.0 \times 10^{-18} \text{ erg s}^{-1} \text{ cm}^{-2} \text{ arcsec}^{-2}$. The MUSE spatial resolution is indicated with a gray disk of diameter FWHM in the bottom-left corner of the velocity field.

widths. We present model parameters and their uncertainties for the kinematic sample in Table B.1. Quantities derived from these models are stored in Table B.2. Appendix A shows the maps obtained for the full kinematic sample, whereas Fig. 6 shows one example of the maps obtained.

3.6. Kinematic sample selection criteria

Our parent sample of 178 star-forming galaxies in groups covers a broad mass range from $\sim 10^{7.5} M_\odot$ to $\sim 10^{11.5} M_\odot$ (see Fig. 1). Six galaxies of this parent sample are embedded in a large structure of ionized gas in the group CGR30 (Epinat et al. 2018), which prevents their kinematics to be retrieved unambiguously from the ionized nebula. They are therefore removed from this analysis. Galaxies with low SFR are not expected to provide detailed and accurate kinematics information from ionized gas emission lines. In addition, low-mass galaxies are expected to be small and may be potentially unresolved in our MUSE observa-

tions. Therefore, a first visual inspection allowed us to identify the sample of galaxies with spatially resolved kinematics. We attributed flags corresponding to the quality of the velocity fields (VF) based on its extent and on the presence of a smooth velocity gradient. We ended up with eight flags: 0 when no signal is detected, 1 when the size of the cleaned VF does not exceed 4×4 pixels ($\sim 6 \times 6 \text{ kpc}^2$ at $z = 0.7$), 2 and 3 when the VF is smaller than 8×8 pixels ($\sim 11 \times 11 \text{ kpc}^2$), 4 and 5 when it is smaller than 10×10 pixels ($\sim 14 \times 14 \text{ kpc}^2$), 6 and 7 when it is smaller than 13×13 pixels ($\sim 19 \times 19 \text{ kpc}^2$), and 8 when it is larger than 13 pixels. Flags 3, 5, 7, and 8 correspond to galaxies with clear velocity gradients whereas galaxies with flags 2, 4, and 6 do not show such gradients. There are 28 flag 0 galaxies in the parent sample of star-forming galaxies. These galaxies are probably galaxies with no further star formation and would appear as red sequence galaxies if we had used [O II] flux to estimate the SFR. They are mainly located at the bottom of the main sequence, despite some of them are above. One of them is a quasar, whereas neither active galactic nucleus (AGN) nor quasar templates were used, so its mass and SFR may be incorrect. For the others, since no clear sign of AGN was observed (see Sect. 4.2), this could mean that they have been quenched recently.

In order to have a more objective and physical selection, we used the combined information extracted from morphology, kinematics and SED fitting. Since we need the kinematics of galaxies to be spatially resolved, a first criterion is used to quantify the size of the ionized gas distribution with respect to that of the spatial resolution. Since the limited spatial resolution of MUSE data might prevent to measure robustly the size of the [O II] flux distribution, we define the first criterion as the ratio of the effective radius of the stellar distribution with respect to the size of the MUSE PSF. It seems reasonable to assume that the ionized gas disk is closely related to the underlying stellar distribution⁷, which contains the newly formed stars that photo-ionize the gas (e.g., Epinat et al. 2008; Vergani et al. 2012). The higher HST-ACS spatial resolution makes measurements of stellar distributions much more accurate, especially for galaxies with optical sizes close to, or less extended than the seeing in MUSE data. Moreover, the extent of kinematics maps where the S/N is above 5 might overestimates the true extent of ionized gas disks and might gets larger than the MUSE PSF FWHM, especially for bright compact [O II] emitters. We define a second criterion as the S/N of the [O II] doublet in the MUSE data in order to derive meaningful kinematic maps. We estimated the flux in the [O II] doublet using the cleaned line flux maps, where the individual S/N per pixel is at least 5 (see Sect. 3.5). This ensures to optimize the aperture over which the flux is computed and to increase the S/N with respect to using integrated spectra that might show strong deviation to Gaussian lines due to the underlying galaxy kinematics. The noise was estimated as the quadratic sum of the uncertainty on the flux of individual pixels. We plot the S/N as a function of the ratio between the global effective radius (R_{eff}) divided by the MUSE PSF FWHM in Fig. 7 and used various symbols depending on the visual flags. As expected, all the flag 1 galaxies have a S/N lower than 40 (17/18 have $S/N < 30$) and are very small (10/18 have $R_{eff}/FWHM < 0.5$). Most of the flag 2 galaxies are also either small or with rather low S/N. Only five of them (three excluding bulge-dominated galaxies) have disk effective radii larger than half the MUSE PSF FWHM and a S/N larger than 40. Around half flag 3 galaxies are above these thresholds, whereas higher flags are almost all within these constraints. There is only one flag 6 galaxy that is the quasar. It

has a very small effective radius but has some diffuse extended emission around it. This galaxy is therefore outside the thresholds. Based on this quantitative agreement with the visual classification, we conclude that these objective criteria are a good way of performing a robust selection. The PSF FWHM is an estimate of the half light radius of a point source, it therefore makes sense that galaxies with disk effective radii lower than half the MUSE PSF FWHM are not resolved within the MUSE data. On the other hand, assuming a constant surface brightness and a S/N above a threshold of 8 per pixel over a circular surface up to the effective radius, the global S/N might be above the dotted line shown in Fig. 7. We see that using the S/N threshold of 40 leads to a very small difference. We checked each galaxy between these two limits. In most of the cases, the ionized gas is less extended than the stellar disk, or it is patchy, therefore not covering uniformly the stellar disk. In other cases, the galaxies are quite edge-on, leading to a lower spatial coverage than when assuming a circular galaxy. For only one galaxy, it is clear that its velocity field only covers the central region of a very extended disk. We therefore use the global S/N threshold as selection criterion. Hereafter, we opt as a baseline for strict selection criteria with a S/N limit of 40 and a $R_{eff}/FWHM$ limit of 0.5, which leads to a sample of 77 galaxies. In Sect. 4, we also use relaxed selection criteria with a S/N limit of 30 and a $R_{eff}/FWHM$ limit of 0.25, leading to a sample of 112 galaxies, in order to investigate the impact of selection on the analysis.

We further removed the eight galaxies for which the bulge to disk ratio within R_{eff} is larger than unity (red symbols in Fig. 7). Indeed, we found that those galaxies have less accurate morphological parameters, with usually very small disk scale lengths, and therefore inaccurate estimates of their stellar mass within R_{22} (see Sect. 4.1) or bad estimates of the rotation velocity because it is inferred at too small radii. This interpretation is more relevant for low-mass systems for which we do not expect strong bulges. Nonetheless, this indicates that the morphology is not accurate due, most of the time, to galaxies being faint.

Last, we identified galaxies hosting AGN, for which the strong signal from the central region can dominate the ionized gas emission and prevent secure disk kinematics measurements by underestimating the rotation and overestimating the velocity dispersion. Their high ionization levels may also cause large uncertainties in the determination of both stellar mass and SFR. In order to identify AGN inside our sample, we used the diagnostic diagram that combines the [O III] $\lambda 5007/H\beta$ and [O II] $\lambda 3727,3729/H\beta$ line ratios, proposed by Lamareille (2010), and the mass-excitation diagram that compares the [O III] $\lambda 5007/H\beta$ line ratio with the stellar mass (Juneau et al. 2011). These two diagnostic diagrams are based on the emission lines available in the optical spectra of intermediate redshift galaxies. We obtained seven AGN candidates in the kinematic sample identified as such in at least one of these two diagnostic diagrams. We then visually inspected their integrated spectra to look for broader features and/or high-level emission lines typical of AGN activity like [Ne III] $\lambda 3868$ and [Mg II] $\lambda 2800$. We finally identified three secure AGN (CGr30-71, CGr32-268 and CGr32-454) and two ambiguous cases (CGr32-132 and CGr32-345) in the kinematic sample. The ambiguous objects can be due to low-level AGN activity or star-forming galaxies with multiple kinematic components. Among the secure AGN, we excluded CGr32-268 and CGr32-454 (identified with stars in Fig. 7) because their AGN affected the velocity fields of the host galaxy. Using these two additional selection criteria leads to a final kinematic sample containing 67 galaxies. Half of the galaxies removed with these criteria were classified as potentially nonrotat-

⁷ In the case of nonresonant lines

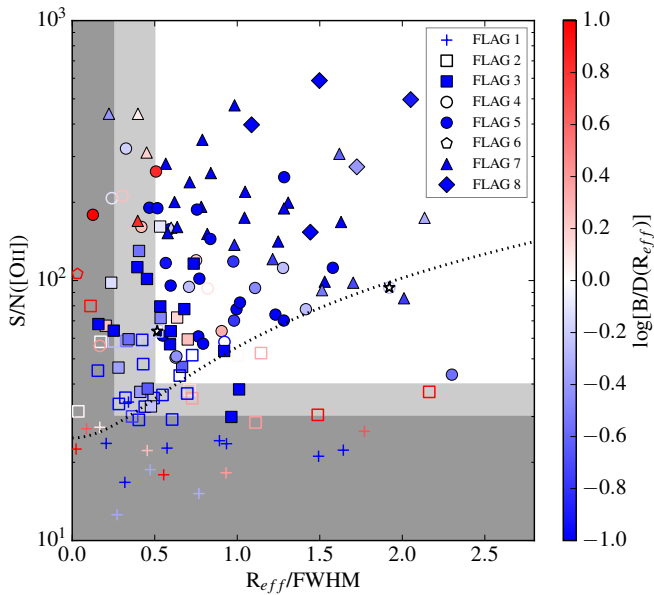


Fig. 7: S/N of the total [O II] flux as a function of the global effective radius divided by the MUSE PSF FWHM for the parent sample of galaxies located in the main sequence of star-forming galaxies. The white area corresponds to the parameter space used for the strict selection ($S/N > 40$ and $R_{eff}/FWHM > 0.5$), whereas the light gray area also contains galaxies within the relaxed selection ($S/N > 30$ and $R_{eff}/FWHM > 0.25$) used in Sect. 4 to study the impact of the selection on the analysis. The dotted black line corresponds to the limit for a constant S/N of 8 over the effective radius. The symbols correspond to the visual velocity field flags from 1 to 8. Crosses and empty symbols correspond to galaxies with no obvious velocity shear, whereas filled symbols correspond to galaxies with evidence for rotation. The color indicates the ratio of the bulge luminosity with respect to the disk one inside the global effective radius, red and blue colors corresponding, respectively, to bulge- and disk-dominated galaxies. The two problematic AGN hosts rejected in the final sample are identified with stars.

ing, leaving only three such galaxies within the final sample. In the next section, we will discuss the impact of the thresholds on the TFR.

The distributions corresponding to the final kinematic sample are overplotted on the parent sample distributions in Fig. 1. The kinematic sample is covering the galaxies with the largest SFR. Nevertheless, the median SFR ($1.95 M_{\odot} \text{ yr}^{-1}$) is only twice as large as the median SFR of the parent sample of star-forming galaxies ($0.85 M_{\odot} \text{ yr}^{-1}$). It covers the same mass range as the parent sample of star-forming galaxies but has a lower fraction of low-mass galaxies ($< 10^{8.5} M_{\odot}$) than the parent sample since they are less extended than more massive ones. The median stellar mass is $7.6 \times 10^9 M_{\odot}$, which is slightly higher than the median stellar mass of the parent sample of star-forming galaxies of $4.4 \times 10^9 M_{\odot}$. In the end, the kinematic sample represents around 38% of the parent sample in the main sequence. However, removing galaxies with very low ionized gas fluxes that may be passive (flags 0 and 1), and excluding the quasar and the galaxies embedded in the extended nebula in CGr30, the kinematic sample represents more than 50% of the population of star-forming galaxies. Most of the galaxies that are not in the kinematic sam-

ple are low-mass ones because they are too small to be properly resolved.

Finally, we also checked that the inclination distribution of the final kinematic sample is still compatible with that of a randomly selected sample (see Fig. 5). The kinematic sample better follows a random orientation distribution. This is probably due to the removal of the smallest galaxies and of bulge-dominated galaxies for which morphology may be more difficult to retrieve with accuracy. This means that the inclination is not affecting much our ability to retrieve kinematics information. We thus decide not to put any constraint on inclination since very few galaxies have an inclination below 30° . For some of these galaxies, inclination may be overestimated, leading to an underestimation rather than to an overestimation of their rotation velocity. Only one galaxy (CGr84b-23) seems to be potentially in this case.

4. Stellar and baryonic mass Tully-Fisher relations

Our aim is to study the impact of environment on the TFR by comparing this relation obtained for the MAGIC group sample to the one derived for other samples of either field (KMOS3D, Übler et al. 2017; KROSS, Tiley et al. 2019) or cluster (ORELSE, Pelliccia et al. 2019) galaxies over a similar redshift range. The whole KMOS3D sample covers a wider redshift range. In the following analysis, we focus on the lowest redshift subsample with $z < 1.1$. We also consider separately the KROSS rotation dominated ($V_{r22}/\sigma > 1$) and disk ($V_{r22}/\sigma > 3$) subsamples. We decided to compare our dataset to the KMOS3D and the KROSS samples since they are the two largest ones observed with integral field spectroscopy, and to the ORELSE sample because it is currently the only one exploring the impact of environment, despite it has been observed using long-slit spectroscopy. The average redshift is around 0.9 for all comparison samples used, slightly higher than the average redshift around 0.7 of the MAGIC sample. We first ensure that methodology biases, due to uncertainties, fitting methods (Sect. 4.1), and sample selection (Sect. 4.2), are minimized before analyzing and comparing the TFR for the MAGIC and the comparison samples with the same procedure.

4.1. Fitting methods and uncertainties

The TFR is a relation that connects either the magnitude or the mass of a galaxy to its rotation velocity. This relation is commonly fitted with the following expression:

$$\log M = \alpha \left[\log V - \log V_{ref} \right] + \beta, \quad (8)$$

where $\log V_{ref}$ is set to a non-null value to reduce the correlation between α and β and therefore reduce uncertainties on the latter. To reach this goal, $\log V_{ref}$ has to be set accordingly to the sample, as the mean or median of the velocity distribution. In order to be able to make comparisons between various samples, we use $\log(V_{ref} [\text{km s}^{-1}]) = 2.2$, which is the median value of the rotation velocity for the final kinematic sample of 67 galaxies defined in Sect. 3.6. We will study the cases where M is either the stellar or the baryonic mass and where V is either the rotation velocity or a velocity that includes both the rotation and the velocity dispersion components.

The velocity can either be a terminal, an asymptotic velocity or a velocity within a given radius. At intermediate redshift, it is common to measure the velocity at $R_{22} = 2.2 \times R_d$ because this radius is usually within kinematic measurements coverage and because the maximum rotation is expected to be reached in most

of the cases. For a purely exponential disk mass distribution, it is the radius where the maximum circular velocity is reached, but for real distributions, this is not necessarily the case and we could expect that the maximum rotation might quite often not be reached in low-mass galaxies, based on rotation curves observed in the local Universe (e.g., Persic et al. 1996; Epinat et al. 2008).

It is also common to add an asymmetric drift correction to the rotation velocity measurement in TFR studies in order to account for the gas pressure support (e.g., Meurer et al. 1996; Burkert et al. 2010) and estimate the circular velocity that the gas would have in absence of pressure. This correction is usually performed assuming that the gas is in dynamical equilibrium, has axisymmetric kinematics, an exponential surface density and an isotropic velocity ellipsoid, that the velocity dispersion is constant with radius, and that it predominantly traces the pressure of the gas⁸. When no dispersion term is added, we will refer to rotation velocity V_r , whereas we will talk about corrected velocity V_c when it is included. For comparison purposes with the work of Übler et al. (2017), we use the corrected velocity defined as:

$$V_c(r) = \sqrt{V_r(r)^2 + 2\sigma^2 \times \frac{r}{R_d}}. \quad (9)$$

In this equation, we assume that the gas and stellar disks have the same scale length. We decide to estimate the velocity at R_{22} , therefore:

$$V_{c22} = V_c(R_{22}) = \sqrt{V_{r22}^2 + 4.4\sigma^2}. \quad (10)$$

The uncertainty on this velocity takes into account the uncertainty on both $V_{r22} = V_r(R_{22})$ and σ . The velocity dispersion and its associated uncertainty are estimated, respectively, as the median and as the standard deviation of the beam smearing corrected dispersion map (see Sect. 3.5). Uncertainties on the corrected velocity are therefore larger than those on the rotation velocity alone. Equation 9 was derived by Burkert et al. (2010), assuming that the velocity dispersion does not depend on the height with respect to the disk plane. Whereas this assumption may be unrealistic, because it theoretically predicts gas disks with an exponentially growing thickness with radius, other authors (e.g., Meurer et al. 1996; Pelliccia et al. 2019) assumed the disk scale height to be constant with radius, leading to a similar relation, but with a weight twice lower for the velocity dispersion (i.e., a factor of 2.2 in Eq. 10). Such equations are also comparable to the combined velocity scale introduced by Weiner et al. (2006) in order to refine the agreement between kinematics inferred from integrated spectra and from spatially resolved spectroscopy. They found the best agreement using the parameter:

$$S_{0.5}^2 = 0.5V_r^2 + \sigma^2. \quad (11)$$

This parameter is very similar to half the squared velocity corrected for the asymmetric drift of Meurer et al. (1996), estimated at R_{22} . Equation 9 might therefore over-estimate the contribution of the dispersion.

Since the velocity is measured within a given size, it is also necessary to estimate masses at the same radius. Stellar masses at intermediate redshifts are derived from photometric measurements inside circular apertures. In principle this has to be taken

into account. In Pelliccia et al. (2017, 2019), a global lowering of the stellar mass by a factor of 1.54 was inferred assuming that the apertures are large with respect to galaxy sizes and that their mass distribution follows that of an exponential disk. For the MAGIC group sample, we have refined this correction since galaxies are not always well described by a disk alone and because large galaxies can be as large as the photometric apertures. In order to have estimates of the stellar mass inside R_{22} , for each galaxy, we used the morphological decomposition performed with GALFIT in order to estimate a correction defined as the ratio of the flux within R_{22} in the galaxy plane over the flux within a $3''$ diameter circular aperture centered on the galaxy, using a Gaussian smoothing of $0.8''$ to mimic the methodology used to extract the photometry. On average, for the kinematic sample, the stellar masses at R_{22} are 1.4 times smaller than inside the $3''$ diameter apertures used to extract photometry. In some studies, the TFR is determined without considering any mass correction. We have therefore made an analysis of the difference we obtain depending on the correction (see Sect. 4.2).

Several linear regressions or fitting methods are commonly used to adjust the TFR on galaxy samples. The simplest methods are the Ordinary Least Square linear fits (direct, inverse or bisector) that consider one of the variable to depend on a fixed one. This method only takes into account the uncertainty on the dependent parameter. Usually, because the selection is performed on the mass or luminosity of galaxies, inverse fits, considering the velocity as the dependent variable, are used. However, uncertainties on both mass and velocity should be accounted for. Therefore, more sophisticated methods have been developed, such as (i) the Orthogonal Distance Regression (Boggs & Rogers 1990), that minimizes the distance of the data points orthogonal to the linear function, (ii) MPFITEXY⁹ (Williams et al. 2010), based on the Levenberg-Marquardt algorithm and that additionally takes into account, and eventually adjusts, the intrinsic scatter in the weighting scheme, (iii) HYPERFIT¹⁰ (Robotham & Obreschkow 2015), which has the same capabilities as MPFITEXY, but which can use various optimization algorithms, including bayesian methods, or (iv) other bayesian methods. The HYPERFIT method was used for the KROSS sample (Tiley et al. 2019), whereas MPFITEXY was used for the ORELSE (Pelliccia et al. 2019) and KMOS3D (Übler et al. 2017) samples. Übler et al. (2017) used both MPFITEXY and bayesian methods and showed that the agreement is good. We have further taken the public values available online of masses and velocities provided by Pelliccia et al. (2019) and Tiley et al. (2019) to study the agreement of the results obtained by HYPERFIT and MPFITEXY. We found in both ORELSE and KROSS a perfect agreement. We therefore use MPFITEXY in the following analysis, using the inverse linear fit approach with the adjustment of the intrinsic scatter to the relation, as done by other authors mentioned above. We use the formal uncertainties provided by the fit since they are comparable to those obtained using bootstrapping methods by other authors.

In order to make appropriate comparisons with other surveys and to avoid peculiar galaxies with very small uncertainties to drive the fit of the TFR, we introduce systematic uncertainties on both stellar masses and velocities. For the uncertainties on stellar masses, we adopt a similar strategy as Pelliccia et al. (2019) for the MAGIC group sample by adding in quadrature a systematic uncertainty of 0.2 dex to the uncertainties delivered by the SED fits described in Sect. 3.3. This is rather similar to what is done in

⁸ This hypothesis may not be verified in practice due to the coarse spatial resolution that might prevent the correction of deviations from rotation by our model (see Sect. 3.5) or of unresolved large-scale motions.

⁹ <https://github.com/williamsnj/mpfitexy>

¹⁰ <http://hyperfit.icrar.org>

Tiley et al. (2019) on the KROSS sample where the uncertainty is constant and equal to 0.2 dex, or in Übler et al. (2017), where the uncertainty is around 0.15 dex. For the velocities, we similarly add in quadrature several systematic uncertainties (see Sect. 4.2). We use a systematic uncertainty of 20 km s^{-1} as a reference. In order to ensure a proper comparison with other samples, we use the same unique methodology to fit TFR for all the samples.

Lastly, the disk thickness used to infer inclination impacts the deprojected rotation velocity. We use a null thickness whereas Pelliccia et al. (2019), Tiley et al. (2019) and Übler et al. (2017) use an intrinsic axial ratio of the scale height to the scale length q_0 of 0.19, 0.20, and 0.25 for all galaxies in the ORELSE, KROSS, and KMOS3D samples, respectively. Using such values reduces $\log(V_r)$ by $\log(\sqrt{1 - q_0^2}) = 0.008, 0.009, \text{ and } 0.014$ dex, respectively, for all galaxies, regardless of inclination. This therefore does not add any dispersion in the relations and only modifies the zero-point, by about +0.03-0.05 dex on the mass. The impact on the corrected velocity V_c is lower since the correction only applies on the rotation velocity and not on the velocity dispersion term. These offsets are small compared to the offset we observe between MAGIC and other samples (see Table 4). We further stress that in these studies, no bulge-disk decomposition is performed, which means that the considered thickness also accounts for the bulge. It therefore makes sense to use a lower thickness in our study. Using $q_0 = 0.1$ instead of $q_0 = 0$ would lead to a decrease in velocity by ~ 0.002 dex only (increase in mass zero-point by ~ 0.01 dex), which is negligible. We therefore use a null disk thickness for MAGIC to compare with other studies.

4.2. Impact of selection, uncertainties, and aperture correction on the stellar mass Tully-Fisher relation

In this subsection, we study the impact of sample selection, of uncertainties, and of the stellar mass aperture correction on the stellar mass TFR (smTFR) using the rotation velocity. In many studies published so far, the selection is based on the V_r/σ ratio (e.g., Übler et al. 2017; Tiley et al. 2019; Pelliccia et al. 2019). Without such a selection, a significant fraction of galaxies appears as outliers in the TFR, with many galaxies having lower rotation velocities than expected at a given stellar mass (or magnitude or baryonic mass).

In a first attempt to draw the smTFR, we included all the star-forming galaxies with velocity field flags larger than or equal to 2. In Fig. 8, where colors indicate the ratio of V_{r22}/σ , we see, as in other TFR studies, that most of the outliers have a low ratio. This does not necessarily mean that the velocity dispersion is large but rather that the rotation velocity is low. For low-mass systems, this can be due to the shape of the rotation curves or to a lack of spatial resolution. We further identified in this figure galaxies in the kinematic sample defined in Sect. 3.6 with both relaxed ($S/N > 30$ and $R_{eff}/FWHM > 0.25$) and strict ($S/N > 40$ and $R_{eff}/FWHM > 0.5$) selection conditions, as well as galaxies removed due to large bulge-to-disk ratio or AGN. Our selection criteria mainly discard low-mass galaxies and most of the strong outliers to the relation, except at low stellar masses, without any prior on the kinematic measurements. We therefore also studied the smTFR using various thresholds in mass. A first threshold of $10^{8.5} M_\odot$ seems necessary in terms of completeness and provides a sample of 61 galaxies. A second threshold of $10^9 M_\odot$ enables us to keep galaxies with more robust mass and velocity estimates and leads to 55 galaxies. Finally, a threshold of $10^{10} M_\odot$ produces a sample of 28 galaxies that is more similar to the KROSS

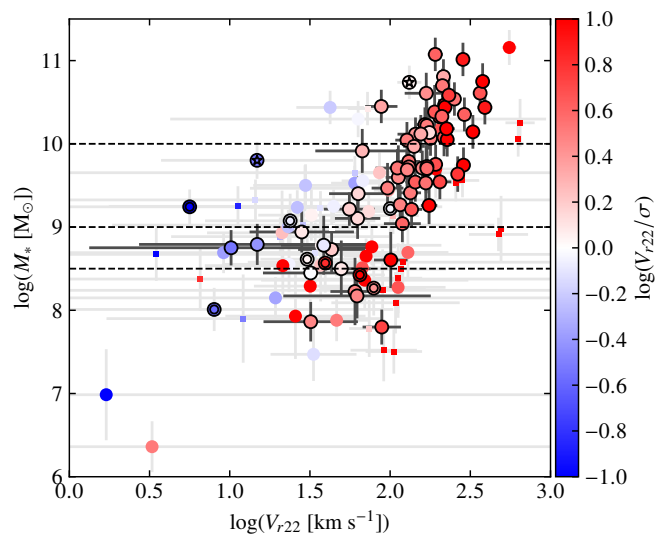


Fig. 8: Stellar mass TFR for the MAGIC group sample, using the rotation velocity. The black circles correspond to galaxies fulfilling the strict conditions ($S/N > 40$ and $R_{eff}/FWHM > 0.5$), whereas circles without contours indicate additional galaxies with more relaxed conditions ($S/N > 30$ and $R_{eff}/FWHM > 0.25$). Small squares show all other galaxies on the main sequence with velocity flags larger than or equal to 2. The color indicates the values of V_{r22}/σ . The three horizontal dashed lines indicate the threshold in mass used. For galaxies in the kinematic sample, we also identify bulge-dominated galaxies (double circles) and problematic AGN (circled stars) that are discarded from the analysis of the final sample.

disky and KMOS3D samples. For the 10^9 ($10^{8.5}$) M_\odot limit, the agreement between morphological and kinematic position angles is better than 40° for all but one (two) galaxies. Under the reasonable assumption that the ionized gas is rotating within the same plane as the stellar disk, this indicates that both morphology and kinematic measurements are robust. These results are clearly in favor of observational biases to explain outliers to the smTFR rather than to a change of dynamical support.

We perform fits of the smTFR for all those various samples both without and with constraints on the slope (see Table 2, second panel). When no constraint is set on the slope, we observe that the slope and the zero-point are correlated but that both intrinsic and total scatter reduce when increasingly stringent selection criteria are used. The absence of a monotonic trend on the slope seems to indicate that a few galaxies can have a significant impact on the slope. Because the choice of a proper V_{ref} impacts the observed variations of the zero-point when the slope is free, we use fixed slopes to compare zero-points. We decided to fix the slope to the one we find for the KROSS rotation dominated sample since it is the closest to the slope we find on average without constraint (see Sect. 4.3 and Table 3). Using this fixed slope still provides the same result for the scatter. The zero-point seems to slightly decrease by about 0.1 dex when outliers are removed, which is expected since outliers have on average large masses with respect to the expectations from their rotation velocity. These variations of the zero-point are within the uncertainties. Nevertheless, the zero-point increases by about 0.1 dex when we only keep galaxies with masses larger than $10^{10} M_\odot$. The free slope for this subsample is lower than for the other ones but this could be due to the stellar mass range of this sample be-

Table 2: Fits of the stellar mass TFR using the rotation velocity for various MAGIC kinematic sample selections, various uncertainties on the velocity and with or without stellar mass correction.

Sample (1)	Mass correction (2)	$\log(M_* [M_\odot])$ (3)	Slope (4)	ΔV [km s ⁻¹] (5)	α (6)	β (7)	σ_{int} (8)	σ_{tot} (9)	d.o.f./N _{gal} (10)
Final	Yes	> 9.0	Free	20	4.03 ± 0.63	9.79 ± 0.09	0.43	0.55	53 / 55
Final	Yes	> 9.0	Fixed	20	3.61	9.82 ± 0.07	0.38	0.50	54 / 55
Relaxed	Yes		Free	20	3.66 ± 0.35	9.93 ± 0.07	0.53	0.77	110 / 112
Strict	Yes		Free	20	3.75 ± 0.40	9.86 ± 0.07	0.42	0.60	75 / 77
Final	Yes		Free	20	3.81 ± 0.43	9.82 ± 0.07	0.41	0.56	65 / 67
Final	Yes	> 8.5	Free	20	3.67 ± 0.50	9.83 ± 0.07	0.40	0.54	59 / 61
Final	Yes	> 10.0	Free	20	3.49 ± 1.17	9.93 ± 0.19	0.39	0.47	26 / 28
Relaxed	Yes		Fixed	20	3.61	9.92 ± 0.07	0.52	0.76	111 / 112
Strict	Yes		Fixed	20	3.61	9.86 ± 0.07	0.40	0.58	76 / 77
Final	Yes		Fixed	20	3.61	9.83 ± 0.07	0.38	0.54	66 / 67
Final	Yes	> 8.5	Fixed	20	3.61	9.83 ± 0.07	0.39	0.53	60 / 61
Final	Yes	> 10.0	Fixed	20	3.61	9.91 ± 0.09	0.40	0.49	27 / 28
Final	Yes	> 9.0	Free		3.69 ± 0.54	9.86 ± 0.08	0.47	0.53	53 / 55
Final	Yes	> 9.0	Free	10	3.81 ± 0.57	9.84 ± 0.08	0.46	0.54	53 / 55
Final	Yes	> 9.0	Fixed		3.61	9.87 ± 0.07	0.46	0.52	54 / 55
Final	Yes	> 9.0	Fixed	10	3.61	9.85 ± 0.07	0.44	0.52	54 / 55
Final	No	> 9.0	Free	20	3.56 ± 0.55	9.94 ± 0.08	0.38	0.49	53 / 55
Final	No	> 9.0	Fixed	20	3.61	9.94 ± 0.07	0.37	0.50	54 / 55

Notes. The relaxed (strict) selection corresponds to all galaxies fulfilling $S/N > 30$ (40) and $R_{\text{eff}}/\text{FWHM} > 0.25$ (0.5), whereas problematic AGN and bulge-dominated galaxies are further removed from the strict selection in the final sample (defined in Sect. 3.6). The two first rows correspond to the TFR fits used as reference. The fixed slope corresponds to the slope we derived for the KROSS rotation dominated sample. (1) Identification of the MAGIC group sample used. (2) Indication about mass correction with R_{22} . (3) Threshold used on the stellar mass. (4) Constraint on the slope. (5) Systematic uncertainty on velocity added in quadrature. (6) Value of the TFR slope. (7) Value of the TFR zero-point. (8) Intrinsic dispersion around the TFR obtained by enforcing the χ^2 to be equal to unity. (9) Total dispersion around the TFR. (10) Number of degrees of freedom/number of galaxies.

ing of the same order of magnitude as the intrinsic scatter. We decide to use, as a reference, the sample with a mass limit of $10^9 M_\odot$ that represents a good compromise between the accuracy of measurements and the statistics since it contains 55 galaxies. We reached similar conclusions using slopes fixed to the ones found using the KROSS disk and ORELSE samples.

We further studied the impact of the uncertainties on the velocity to the fits of the smTFR. To do that, we added in quadrature a systematic value of 10 or 20 km s⁻¹ to the uncertainty derived from the kinematics modeling (see Table 2, third panel). When this systematic uncertainty increases, the slope increases whereas the zero-point decreases. Since the zero-point variation can be due to the slope variation, we also fixed the slope to that found for the KROSS rotation dominated sample. In that case, the decrease in the zero-point is less and is around 0.05 dex for the case of a systematic uncertainty of 20 km s⁻¹, which is within the typical uncertainty of 0.07 dex. We checked that the impact is similar whatever the MAGIC subsample used. We also tried to add a relative uncertainty rather than an absolute one, but this provides the same behavior. It is also interesting to notice that this does not affect significantly the intrinsic and total scatters. We decided to use the 20 km s⁻¹ value because it is in better agreement with the typical uncertainties observed or used for other published samples.

Last, we also investigated the impact of the stellar mass aperture correction within the R_{22} radius (see Table 2, bottom panel). Using a fixed slope shows that the mass correction reduces the zero-point by about 0.12 dex, which is expected since on average the mass is reduced by a factor of 1.4, corresponding to a correction of -0.15 dex. Correcting the masses also clearly increases

the slope. This reflects the fact that the mass correction is larger for low-mass galaxies than for high-mass ones since the size of a galaxy correlates with its mass. It is worth noticing that for this same reason, the zero-point decrease observed when we use more stringent sample selection constraints is stronger when the mass is not corrected, which means that correcting the mass is necessary to avoid over-estimating the zero-point variation with mass. The scatter is not much affected when the slope is fixed whereas it is increased when it is free. The same conclusions are reached whatever the sample used. In conclusion, we can expect a rise of the zero-point of around 0.25 dex at maximum depending on the uncertainties (0.05 dex), on the stellar mass correction (0.15 dex) and sample selection (0.05 dex) with respect to the reference we adopt in the following analysis.

4.3. Stellar mass Tully-Fisher relation

We showed in the previous section that not correcting the mass for the limited photometric apertures possibly biases the slope of the relation in addition to obviously shifting the zero-point. The studies we are comparing to use similar initial mass functions to compute their stellar mass but do not make any correction for this aperture effect. We will assume that, at fixed slope, the main impact is a shift of the zero-point by 0.15 dex, although it depends on the size of the apertures used. The results we are discussing here and in Sect. 4.4 are summarized in Tables 3 and 4.

We fitted the smTFR for the KROSS rotation dominated and disk samples as well as for the ORELSE sample with the same fitting routine as for the MAGIC group sample and letting the

Table 3: Results of the fits of the various TFR for reference samples and for MAGIC using fixed and free slopes.

Sample (1)	$\log(M_* [M_\odot])$ (2)	TFR (3)	Tracer (4)	Slope (5)	α (6)	β (7)	σ_{int} (8)	σ_{tot} (9)	d.o.f/ N_{gal} (10)
MAGIC	> 9.0	smTFR	V_{r22}	Free	4.03 ± 0.63	9.79 ± 0.09	0.43	0.55	53 / 55
ORELSE		smTFR	V_{r22}	Free	3.18 ± 0.41	10.23 ± 0.09	0.48	0.63	75 / 77
MAGIC	> 9.0	smTFR	V_{r22}	Fixed	3.18	9.85 ± 0.06	0.34	0.46	54 / 55
KROSS rot dom		smTFR	V_{r22}	Free	3.61 ± 0.31	10.61 ± 0.07	0.66	0.71	257 / 259
MAGIC	> 9.0	smTFR	V_{r22}	Fixed	3.61	9.82 ± 0.07	0.38	0.50	54 / 55
KROSS disk		smTFR	V_{r22}	Free	4.42 ± 0.43	10.21 ± 0.04	0.34	0.45	110 / 112
MAGIC	> 9.0	smTFR	V_{r22}	Fixed	4.42	9.76 ± 0.08	0.46	0.60	54 / 55
MAGIC	> 9.0	smTFR	V_{c22}	Free	4.35 ± 0.59	9.51 ± 0.10	0.33	0.48	53 / 55
MAGIC	> 10.0	smTFR	V_{c22}	Free	3.97 ± 1.32	9.65 ± 0.27	0.37	0.47	26 / 28
ORELSE		smTFR	V_{c22}	Free	3.24 ± 0.33	9.96 ± 0.06	0.37	0.51	75 / 77
MAGIC	> 9.0	smTFR	V_{c22}	Fixed	3.24	9.65 ± 0.05	0.27	0.41	54 / 55
KMOS3D		smTFR	V_{c22}	Free	2.91 ± 0.28	9.96 ± 0.06	0.12	0.27	63 / 65
MAGIC	> 9.0	smTFR	V_{c22}	Fixed	2.91	9.69 ± 0.05	0.26	0.39	54 / 55
MAGIC	> 10.0	smTFR	V_{c22}	Fixed	2.91	9.85 ± 0.07	0.26	0.38	27 / 28
KMOS3D		smTFR	V_{c22}	Fixed	$3.60^{(a)}$	9.84 ± 0.04	0.17	0.32	64 / 65
MAGIC	> 9.0	smTFR	V_{c22}	Fixed	3.60	9.60 ± 0.06	0.28	0.43	54 / 55
MAGIC	> 10.0	smTFR	V_{c22}	Fixed	3.60	9.72 ± 0.08	0.32	0.44	27 / 28
MAGIC	> 9.0	bmTFR	V_{r22}	Free	3.55 ± 0.49	9.99 ± 0.07	0.35	0.45	53 / 55
MAGIC	> 9.0	bmTFR	V_{c22}	Free	3.74 ± 0.45	9.76 ± 0.08	0.25	0.38	53 / 55
MAGIC	> 10.0	bmTFR	V_{c22}	Free	3.64 ± 1.06	9.83 ± 0.22	0.31	0.41	26 / 28
KMOS3D		bmTFR	V_{c22}	Free	2.21 ± 0.22	10.26 ± 0.05	0.01	0.23	63 / 65
MAGIC	> 9.0	bmTFR	V_{c22}	Fixed	2.21	9.95 ± 0.04	0.21	0.31	54 / 55
MAGIC	> 10.0	bmTFR	V_{c22}	Fixed	2.21	10.11 ± 0.06	0.20	0.30	27 / 28
KMOS3D		bmTFR	V_{c22}	Fixed	$3.75^{(b)}$	10.00 ± 0.04	0.19	0.33	64 / 65
MAGIC	> 9.0	bmTFR	V_{c22}	Fixed	3.75	9.75 ± 0.05	0.24	0.38	54 / 55
MAGIC	> 10.0	bmTFR	V_{c22}	Fixed	3.75	9.81 ± 0.08	0.31	0.42	27 / 28

Notes. For KMOS3D, we use uncertainties on stellar mass of 0.2 dex rather than the 0.15 dex used in Übler et al. (2017) in order to provide a better comparison to the other samples. The results for reference samples are provided without correction of the velocity due to the intrinsic axial ratio and without correction of the stellar mass. The latter correction would generate an offset of their zero-point of -0.15 dex. The average redshift is around 0.9 for all comparison samples used, slightly higher than the average redshift around 0.7 of the MAGIC final kinematic sample. (1) Identification of the sample used. Bold font indicates the MAGIC group TFR we consider as references. (2) Threshold used on the stellar mass. (3) Type of TFR studied. (4) Tracer used to infer the TFR. (5) Constraint on the slope. When fixed, the value of the slope used is the one indicated in column (6) and corresponds to the free slope of one of the comparison samples. (6) Value of the TFR slope. (7) Value of the TFR zero-point. (8) Intrinsic dispersion around the TFR obtained by enforcing the χ^2 to be equal to unity. (9) Total dispersion around the TFR. (10) Number of degrees of freedom/number of galaxies. ^(a) Value from Reyes et al. (2011) used in Übler et al. (2017) to compare with local Universe. ^(b) Value from Lelli et al. (2016) used in Übler et al. (2017) to compare with local Universe.

slope free. We then fixed the slope for the MAGIC group sample to those reference slopes to infer a possible zero-point shift (see Fig. 9). We find a significant evolution of the zero-point toward lower values for the MAGIC group sample with respect to each reference sample. The decrease in the zero-point is more significant compared to the KROSS samples (Tiley et al. 2019) that are supposed to have less galaxies in dense environments than the ORELSE sample (Pelliccia et al. 2019) dominated by cluster galaxies. The offset with the KROSS rotation dominated sample is about 0.79 dex, whereas it reduces to 0.45 dex with the KROSS disk sample. This is expected from the selection function of those two samples, which is based on two different thresholds of V_{r22}/σ (1 and 3, respectively). Our sample selection seems to better match that of the rotation dominated sample since its average stellar masses is identical to that of the MAGIC final sample ($10^{10.0} M_\odot$) and because they have a very similar standard deviation. It is however instructive to observe that the offset is still significant with respect to the KROSS disk sample that has an average stellar mass of $10^{10.2} M_\odot$. The offset with respect to the ORELSE sample is 0.38 dex. The ORELSE

and MAGIC group samples are also rather similar despite the ORELSE sample has a slightly lower average stellar mass, in better agreement with the MAGIC group sample with a cut in stellar mass of $10^{8.5} M_\odot$, however, using this subsample still gives an offset of 0.37 dex. If we consider the correction of the mass for apertures, these shifts lower to 0.64 dex, 0.30 dex and 0.23 dex. These offsets are not within the uncertainties on the parameter.

The slope we obtain for the MAGIC group sample is in between the two KROSS samples. If we use a stellar mass threshold of $10^{8.5} M_\odot$, the slope $\alpha = 3.67$ decreases and agrees well with that of the KROSS rotation dominated sample, and is in better agreement with that of the ORELSE sample, despite it remains larger. This difference could be due to the stellar mass correction that increases the slope (see Sect. 4.2 and Table 2). However, in any case, the intrinsic and total scatters for the MAGIC group sample are lower than for the KROSS rotation dominated and ORELSE samples, regardless of whether the slope is free or fixed. These scatters are nevertheless higher than for the KROSS disk sample and are the highest when the slope is fixed to that

Table 4: TFR zero-point difference between various reference samples and the MAGIC final kinematic sample, with a mass threshold of $10^9 M_{\odot}$, using similar slopes.

Sample (1)	TFR (2)	Tracer (3)	α (4)	$\Delta \log M$ (5) (6)		$\Delta \log V$ (7) (8)	
ORELSE	smTFR	V_{r22}	3.18	0.38	0.23	-0.119	-0.072
KROSS rottdom	smTFR	V_{r22}	3.61	0.79	0.64	-0.219	-0.177
KROSS diskly	smTFR	V_{r22}	4.42	0.45	0.30	-0.102	-0.068
ORELSE	smTFR	V_{c22}	3.24	0.31	0.16	-0.096	-0.049
KMOS3D	smTFR	V_{c22}	2.91	0.27	0.12	-0.093	-0.041
KMOS3D	smTFR	V_{c22}	3.60 ^(b)	0.24	0.09	-0.067	-0.025
KMOS3D ^(a)	smTFR	V_{c22}	2.91	0.11	-0.04	-0.038	0.014
KMOS3D ^(a)	smTFR	V_{c22}	3.60 ^(b)	0.12	-0.03	-0.033	-0.008
KMOS3D	bmTFR	V_{c22}	2.21	0.31	0.16	-0.140	0.072
KMOS3D	bmTFR	V_{c22}	3.75 ^(c)	0.26	0.11	-0.069	-0.029
KMOS3D ^(a)	bmTFR	V_{c22}	2.21	0.15	0.00	-0.068	0.000
KMOS3D ^(a)	bmTFR	V_{c22}	3.75 ^(c)	0.19	0.04	-0.051	-0.011

Notes. (1) Identification of the comparison sample. (2) Type of TFR studied. (3) Tracer used to infer the TFR. (4) Value of the slope used. Zero-point difference in mass / velocity: (5) / (7) with no correction; (6) / (8) taking into account the -0.15 dex offset for the correction of stellar masses within R_{22} . ^(a) These lines correspond to the difference between the KMOS3D sample and the MAGIC sample with a mass threshold of $10^{10} M_{\odot}$. ^(b) Value from Reyes et al. (2011) used in Übler et al. (2017) to compare with local Universe. ^(c) Value from Lelli et al. (2016) used in Übler et al. (2017) to compare with local Universe.

of this sample. For the latter sample, the slope is steep and the scatter is reduced due to the selection function that naturally removes slow rotators.

In order to ensure that the different selection does not bias the comparisons, we checked that the median value of $V_r(R_{22})/\sigma$ for our sample is not larger than that of the other samples that used a limit of either 1 or 3. The MAGIC final kinematic sample is clearly not biased toward very high values of this parameter since the lowest value is 0.3 and the median is 3.6. As a comparison, the median value for the ORELSE sample is 3.0.

We did a similar analysis including the contribution of the dispersion term, that is, using the corrected rather than the rotation velocity. We used the KMOS3D (Übler et al. 2017) and the ORELSE samples, for which the dispersion contribution is available, as references for the slope. For the KMOS3D sample, we used both the fixed slope they employed in their analysis, taken from Reyes et al. (2011) in the local Universe, and the one resulting from the fit with a free slope we performed on their dataset (see Fig. 10). The primary effect of the inclusion of the dispersion is to increase the rotation velocity, to increase the slope of the relation and to decrease the scatter around the smTFR even for galaxies below the mass threshold. The median velocity dispersion in our sample is $\sim 40 \text{ km s}^{-1}$. Using it to infer the corrected velocity therefore mainly impacts galaxies with a low rotation velocity, which is the reason for the slope to be steeper and for the zero-point at $\log(V_{ref} [\text{km s}^{-1}]) = 2.2$ to be reduced. Several studies assume that the ratio of the rotation velocity to the velocity dispersion inferred from the ionized gas indicates the dynamical support of galaxies (see, e.g., Burkert et al. 2010; Wuyts et al. 2016; Turner et al. 2017; Übler et al. 2019), although it is theoretically valid only for collisionless systems. Whereas this is not the scope of this paper, we stress that a high velocity dispersion associated with a small disk size might mean that the galaxy ionized gas kinematics are not correctly resolved. Indeed, if a galaxy has an intrinsic rotation but its ionized gas distribution is not resolved, the observed line will be enlarged. In other words, the rotation will be encoded in the ve-

locity dispersion. This is the typical beam smearing effect that affects mainly the central parts of galaxies at intermediate to high redshift. Our analysis of the impact of selection on the smTFR seems to support this. Indeed, our final sample, which is constructed without any prior on the dynamical support, contains very few outlying and dispersion-dominated galaxies, whereas such galaxies are included when the constraints on galaxy sizes are relaxed, similarly to what is observed in other samples. We also note that the uncertainties on velocity dispersion are usually large due (i) to the limitation of the beam smearing correction, (ii) to the limited spectral resolution of the various spectrographs used since $R = 3000$ corresponds to an instrumental dispersion of 40 km s^{-1} , and (iii) to the lesser accuracy to retrieve the second order moment with respect to the first order moment.

As for the previous smTFR determined using the rotation velocity, we find a significant decrease in the zero-point with respect to the other samples when a fixed slope is used. The offset with respect to the KMOS3D sample is 0.27 dex or 0.24 dex when we use either the value of the fit with a free slope we performed on the KMOS3D dataset, or the fixed slope from Lelli et al. (2016) that Übler et al. (2017) used to compare with local Universe. We stress that the KMOS3D sample is mainly composed of massive galaxies since its median stellar mass is $10^{10.5} M_{\odot}$. Using a stellar mass threshold of $10^{10} M_{\odot}$ rather than $10^9 M_{\odot}$ for the MAGIC sample reduces the offset by more than 0.1 dex. Further assuming a correction for the stellar mass would make the zero-point for MAGIC compatible with the KMOS3D sample. However, we emphasize that this MAGIC subsample contains only 27 galaxies. The offset for the ORELSE sample is 0.31 dex, rather similar to the offset found using the rotation velocity, reduced to 0.16 dex accounting for the mass correction. The better agreement with KMOS3D, which is supposed to be dominated by galaxies in low-density environment seems to point toward methodological differences, either in the mass estimation or in the kinematics extraction.

Similarly to the smTFR determined with the rotation velocity, the intrinsic and total scatters are lower in the MAGIC group

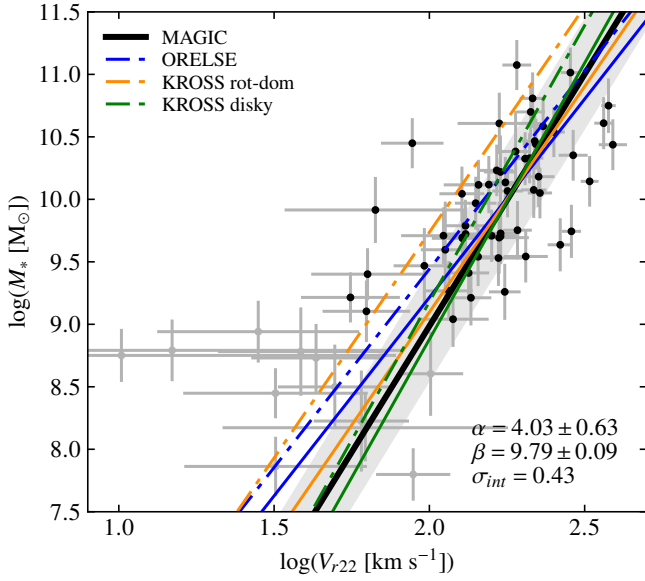


Fig. 9: Stellar mass TFR for the MAGIC final kinematic sample, using the rotation velocity. The black dots indicate galaxies used for the reference subsample with stellar masses above $10^9 M_\odot$, whereas gray dots indicate the other galaxies for information. The black line corresponds to the fit to the MAGIC group sample with a free slope and the intrinsic scatter is represented with the gray shaded area. The parameters of this fit are indicated in the figure. Colored dotted-dashed lines correspond to fits on other samples, with an offset of -0.15 dex for the correction of the stellar mass. The slopes of these fits are used to perform additional fits of the smTFR on the MAGIC group sample. The corresponding fits are shown with continuous lines having the same colors as the samples used as reference for the slope.

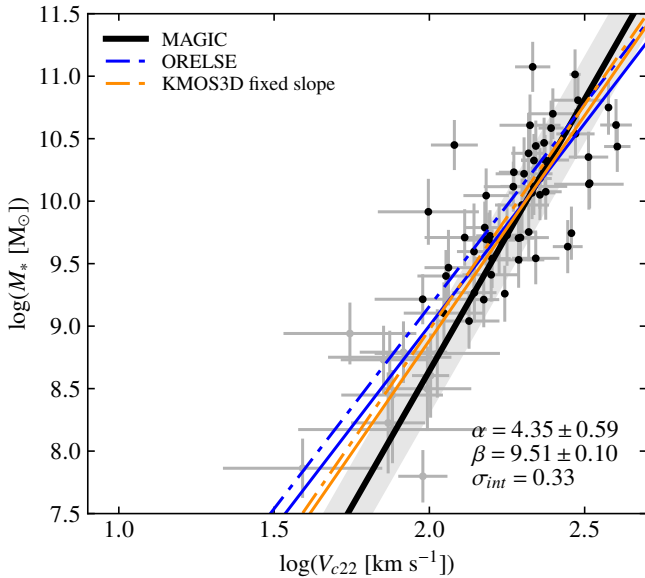


Fig. 10: Stellar mass TFR for the MAGIC final kinematic sample, using the corrected velocity. See Fig. 9 for the description of lines and symbols. An offset of -0.15 dex has been applied for the comparison samples to account for the stellar mass correction within R_{22} .

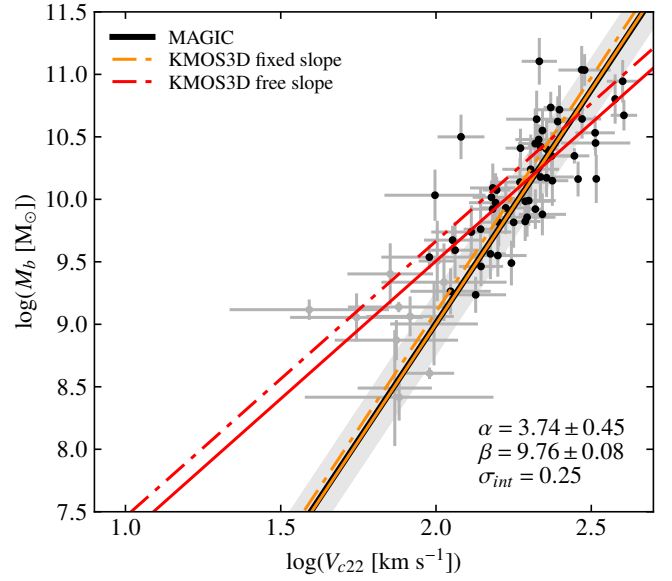


Fig. 11: Baryonic mass TFR for the MAGIC final kinematic sample, using the corrected velocity. See Fig. 9 for the description of lines and symbols. An offset of -0.15 dex has been applied for the comparison samples to account for the stellar mass correction within R_{22} .

sample than in the ORELSE sample. On the contrary, the scatter in the KMOS3D sample is lower than for the MAGIC group sample. This probably indicates strong differences in sample selections among the various samples discussed here.

4.4. Baryonic mass Tully-Fisher relation

In order to complement the previous smTFR analysis, we also tried to include the gas mass in the mass budget in order to infer the baryonic mass TFR (bmTFR) because the gas content of galaxies is supposed to differ depending on their environment. We have estimated gas masses for our sample from the Kennicutt-Schmidt relation between the SFR surface density and the gas surface density (Kennicutt 1998b), assuming the gas density to be constant over R_{22} , leading to:

$$M_g = (4 \times 10^9 \times \text{SFR})^{5/7} \times (\pi R_{22}^2)^{2/7}, \quad (12)$$

where M_g is the mass of gas in M_\odot , R_{22} is in pc, and SFR is in $M_\odot \text{ yr}^{-1}$. SFR can be deduced either from SED fitting or from $[\text{O II}]$ flux. For the latter, we derived the average SFR per square parsec using the (Kennicutt 1998a) relation, assuming that the flux is emitted within R_{22} . Combining these laws, the relation between the $[\text{O II}]$ flux, $F_{[\text{O II}]}$, in $\text{erg s}^{-1} \text{ cm}^{-2}$, and the gas mass, M_g , in M_\odot is:

$$M_g = (4.756 \pm 1.944) \times 10^{-23} \times (\pi R_{22}^2)^{2/7} \times (4\pi D_L^2 F_{[\text{O II}]})^{5/7}, \quad (13)$$

where D_L is the luminosity distance at the redshift of the source in cm, and R_{22} is in pc. In this relation, we used the $[\text{O II}]$ flux corrected for galactic extinction, assuming the Milky Way dust attenuation curve from Cardelli et al. (1989), and for internal dust-extinction, using the absorption deduced from the SED fitting and the Calzetti et al. (2000) dust attenuation law. We find a good correlation between those two estimates. For our final kinematic sample, masses of gas inferred from the $[\text{O II}]$ doublet

are ~ 0.15 dex larger than those inferred from SED fitting on average, the difference being larger at low mass. In Table B.2, we provide the mass of gas inferred from SED fitting that is used as a reference in the following analysis, despite it corresponds to SFR integrated over longer timescales (~ 1 Gyr) compared to SFR derived from the [O II] doublet (~ 10 Myr). Indeed, nebular lines might not be the best proxy to infer gas masses, especially in dense environments where ionization could arise from other mechanisms than photo ionization (e.g., Epinat et al. 2018; Boselli et al. 2019) but also because SFR could be enhanced temporarily by environment/interactions, therefore biasing gas mass measurements. Similarly, gas masses inferred from scaling relations (e.g., Scoville et al. 2017; Tacconi et al. 2018), might also be inappropriate for our sample since such scaling relations have been obtained independently from environment.

The impact of including gas masses is more pronounced for low-mass galaxies that have a larger gas fraction on average. This is reflected in the bmTFR fit, that has a less steep slope ($\alpha = 3.55$) than for the smTFR fit ($\alpha = 4.03$), in agreement with previous studies. Including gas mass also increases the overall mass, and therefore increases the zero-point. The samples we used for the comparison of the smTFR using the rotation velocity in Sect. 4.3 do not provide both rotation velocities and baryonic masses. Nevertheless, the KMOS3D sample enables us to make a comparison of the bmTFR using the corrected velocity (see Fig. 11). The inclusion of the velocity dispersion contribution induces a steeper slope, as for the smTFR. When we fix the slope, we find a zero-point offset with respect to the KMOS3D sample of 0.31 dex or 0.25 dex depending on the slope used. This difference is larger than for the smTFR because the difference between fixed and free slopes on the KMOS3D data is larger. We also checked that using a threshold of $10^{10} M_{\odot}$ for the selection and no correction of the stellar mass for the MAGIC group sample leads to lower offsets of 0.15 dex ($\alpha = 2.21$) and 0.19 dex ($\alpha = 3.75$), which reverses the difference. This offset is slightly more important than the one for the smTFR, meaning that the MAGIC zero-point is lower than for other samples, which probably reflects a difference in the gas mass estimates. Using gas masses obtained from Eq. 13 leads to lower free slopes and to lower offsets of the zero-point at fixed slope for the $10^9 M_{\odot}$ mass threshold, whereas it provides substantially similar results with the $10^{10} M_{\odot}$ mass threshold. As for the smTFR, the intrinsic and total scatters are larger for the MAGIC group sample than for the KMOS3D sample.

5. Interpretation of the TFR evolution

It seems clear from the previous section that for any TFR studied, the stellar mass for a given rotation velocity is lower for the MAGIC group sample than for other samples used as reference, by at least 0.1 dex, or reversely that the rotation velocity at a given stellar mass is larger for MAGIC. Among these samples, MAGIC is the only one that only contains galaxies in dense groups or clusters, the ORELSE sample being composed of both cluster and field galaxies. Our findings might therefore point to an effect of environment on the baryonic content of galaxies. In this section we are first investigating the baryon fraction before exploring two main hypotheses, either the quenching of star formation or the contraction of baryons, to interpret these results.

5.1. Stellar and baryonic matter fraction

In order to do a fair interpretation of the TFR variation with environment, understanding the stellar mass and baryonic mass frac-

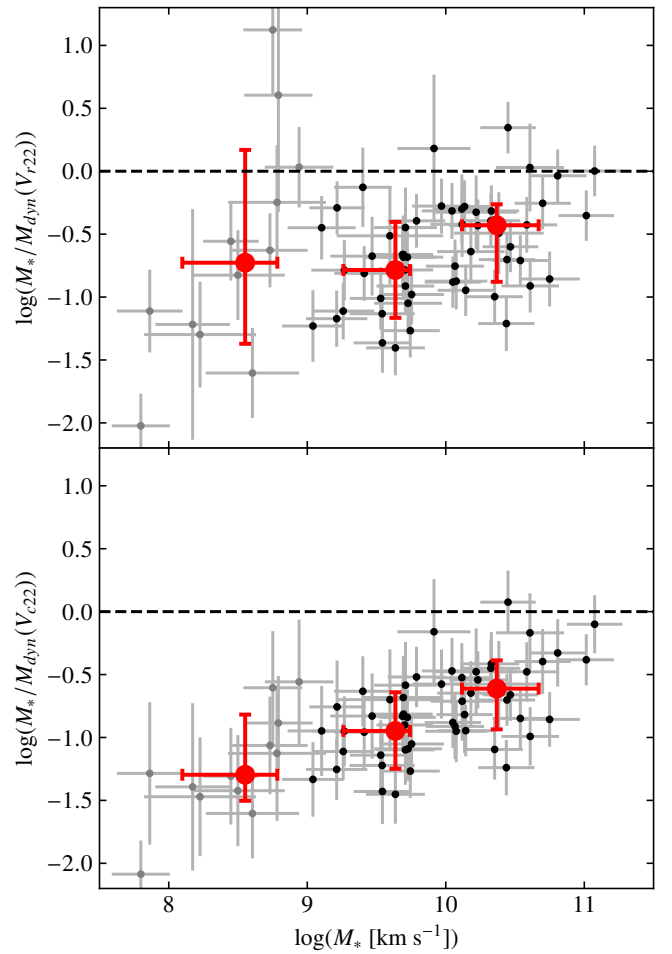


Fig. 12: Stellar mass fraction as a function of the stellar mass, within R_{22} . Black dots correspond to the final MAGIC kinematic sample with stellar masses above $10^9 M_{\odot}$, whereas the gray dots are for galaxies with masses below this limit. The black horizontal dashed line marks the theoretical upper limit of a fraction unity. The three red dots correspond to median values for the three following stellar mass bins: $M_* \leq 10^9 M_{\odot}$, $10^9 M_{\odot} < M_* \leq 10^{10} M_{\odot}$ and $M_* > 10^{10} M_{\odot}$. They contain, respectively, 12, 27, and 27 galaxies. The errors bars indicate the 16th and 84th percentiles in each bin. The dynamical mass is computed either using the rotation (top) or corrected (bottom) velocities.

tion is necessary. Indeed, the dynamical mass might measure the total mass within a given radius and is related to both this considered radius and the velocity measured at this radius. If the mass within R_{22} is dominated by baryons, the interpretation might differ from the hypothesis that the mass is dominated by dark matter. We therefore estimated the dynamical mass for the galaxies in the MAGIC kinematic sample in order to search for a dependence of the stellar and baryonic content of galaxies in groups as a function of the stellar mass. In this work, we assume that at large distance, one can consider that the mass distribution is spherical:

$$M_{\text{dyn}}(r) = \frac{rV(r)^2}{G}. \quad (14)$$

We computed this mass at R_{22} using both the rotation velocity and the corrected velocity that includes the velocity dispersion

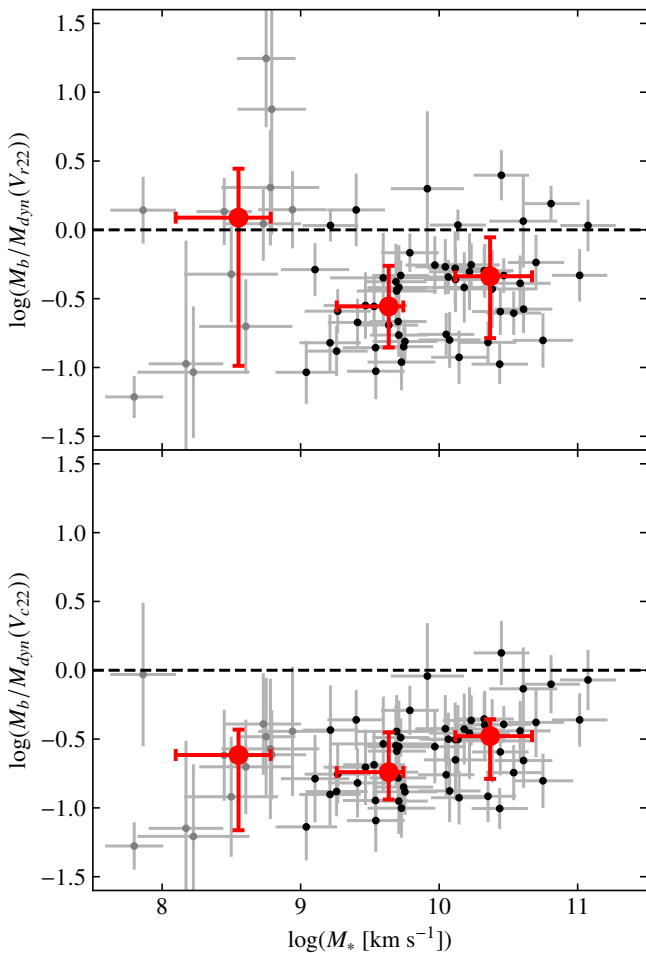


Fig. 13: Baryonic mass fraction as a function of the stellar mass, within R_{22} . See Fig. 12 for the description of symbols.

(Eq. 9). These dynamical masses are provided in Table B.2. We then derived the stellar mass fraction within R_{22} and the baryonic mass fraction within the same radius, using the stellar masses corrected for the photometric apertures (see Sect. 4.1) and assuming the gas mass is within this radius. Figures 12 and 13 show these fractions as a function of stellar mass. Because we believe that galaxies with masses lower than $10^9 M_\odot$ have kinematic measurements less reliable than more massive ones, we have split the sample in three stellar mass bins, one for masses below $10^9 M_\odot$, another for masses above $10^{10} M_\odot$ and the last one for stellar masses in between those two values. We have measured median masses and mass fractions for those three bins and show them as red dots in these figures.

Whatever the velocity estimator used, the stellar mass fraction is more important at high mass, similarly to the results of Pelliccia et al. (2019) for both low and high-density environments. This trend is more pronounced when the velocity dispersion is accounted for since using the corrected velocity clearly increases the dynamical mass for low-mass systems.

When the gas content is included, the baryon fraction seems to increase with stellar mass. The baryon fraction seems however slightly higher for low-mass systems than for high-mass ones, nevertheless, the lowest stellar mass bin clearly has a large dispersion linked to dynamical measurements. This possibly indicates either that the gas mass is, as expected, contributing more

to the total baryonic mass in galaxies with low stellar mass or that the gas mass is overestimated for low stellar mass galaxies, at least within R_{22} .

Taking or not into account the velocity dispersion to compute the dynamical mass, the median baryon fractions change, although both estimates remain consistent within the error bars. As already discussed in Sect. 4.3, it is not yet clear whether the velocity dispersion really traces the dynamical mass rather than local star formation or feedback mechanisms. Figures 12 and 13 tend to indicate that dispersion should be included since more galaxies are close or even above the theoretical limit of a fraction of unity when using only rotation (upper panels). Nevertheless, only a few galaxies with stellar masses above $10^9 M_\odot$ are above this theoretical limit within the large associated uncertainties, one of which (CGr84b-23) having a low inclination, and therefore probably an underestimated rotation. Moreover, for barely resolved objects that are more common at low mass where the impact of including velocity dispersion is the largest, velocity dispersion might contain some information on the rotation velocity not measurable from velocity fields.

We find a typical stellar mass fraction below 50%, even for massive galaxies. The fraction in the low-mass regime can be as low as $\sim 10\%$. Similarly, we find a baryonic mass fraction lower than 50%, even for massive galaxies. This indicates that, at low mass, kinematic measurements probe DMHs and that at high mass, they trace equally the potential of baryons and dark matter. This means that the interpretation of the TFR offset could differ between high-mass and low-mass systems. For low-mass systems, it seems clear that the baryonic content of galaxies in dense groups is less important for a given DMH, whereas for high-mass systems, velocities could be higher either due to a higher dark matter fraction than expected in this mass regime or because the baryon distribution in galaxies has been contracted, as expected from Eq. 14 at fixed dynamical mass.

We cannot compare robustly the results found with our sample to others. Indeed, the work done for KROSS in Stott et al. (2016) is limited in terms of stellar mass range (above $10^{9.5} M_\odot$) and does not discuss the evolution of the fraction of baryons as a function of the stellar mass but as a function of the dynamical mass. The only comparison we could perform is with the stellar mass fraction computed in Pelliccia et al. (2019) on the ORELSE sample. However, many discrepancies between their study and the present one makes such a comparison difficult. Indeed, our size measurements rely on a bulge-disk decomposition, our stellar masses are corrected with individual corrections, the combination of rotation and dispersion are different and they used both dispersion and rotation-dominated galaxies.

Studying the impact of environment on the stellar and baryonic fractions would require a sample on which a similar methodology would be adopted for (i) the measurements of galaxy sizes, (ii) the kinematics modeling, (iii) the stellar mass estimates and corrections for photometric apertures and (iv) for sample selection. This will be the scope of a specific study using foreground and background galaxies observed in the MAGIC dataset, ensuring a robust comparison.

5.2. Quenching timescale in groups

One impact of dense environment is a decrease in star formation in galaxies. Grützbauch et al. (2011) found that galaxies in overdensities, where density is larger by a factor of 5 with respect to the mean density, have their SFR lowered by a factor of $\sim 2 - 3$ up to $z = 2$. Similarly, Tomczak et al. (2019), focusing on star-forming galaxies, found that there is a decrease of around

0.2–0.3 dex of the SFR in the highest-density environments with respect to the lowest-density ones, more pronounced for galaxies with stellar masses between $\sim 10^{10}$ and $\sim 10^{11} M_{\odot}$, this decrease being larger in the lowest redshift bin ($0.6 < z < 0.9$). We find a similar trend with stellar mass for our final kinematic sample when comparing the SFR to the relation provided by Boogaard et al. (2018) displayed in Fig. 1 in various mass bins. Such a lowering of the SFR (ΔSFR) might reduce the stellar mass content of DMHs by an amount ΔM_* that should depend on the time ΔT when galaxies entered into dense structures:

$$\Delta T = \frac{\Delta M_*}{\Delta SFR}. \quad (15)$$

Given the baryonic mass fraction derived for our sample in Sect. 5.1, we can assume that the velocity traces the large-scale mass of the underlying DMH. This is further reinforced by the fact that the plateau velocity is reached within R_{22} for 48/77 galaxies of the kinematic sample with strict criteria, for 43/67 galaxies using the final kinematic sample (no bulge-dominated galaxies and no problematic AGN), and for 40/55 galaxies when the mass threshold of $10^9 M_{\odot}$ is applied, that is, from two thirds to three quarters of the sample for an increasingly stringent selection. We can thus expect that the offset of the zero-point we observed in the smTFR in dense groups with respect to low-density environments results from an impact of the environment on SFR, and it is therefore possible to estimate the time at which the groups formed.

$$\Delta T = \frac{\Delta(\log M_*)}{\alpha \times \Delta(\log SFR)}, \quad (16)$$

where we assume that the main sequence relation is linear between stellar mass and SFR with $SFR = \alpha \times M_*$, with $\alpha = 10^{-9.5} \text{ s}^{-1}$. This approximation provides a description of the relation provided in Boogaard et al. (2018) better than 0.2 dex in the mass range between 10^9 and $10^{11} M_{\odot}$.

Assuming a lowering of the SFR by $\Delta(\log SFR) = 0.3$ dex, as suggested by the studies mentioned above, the offsets in zero-point of 0.64, 0.30, 0.23 and ~ 0.1 we found in Sects. 4.3 and 4.4 (see Table 4) lead to times since galaxies entered the structures of 6.7 Gyr, 3.2 Gyr, 2.4 Gyr, and 1 Gyr for the KROSS rotation dominated, KROSS disk, ORELSE, and KMOS3D samples, respectively. Depending on the sample, the difference is quite large. The result is unlikely for the KROSS rotation dominated sample since it would mean that groups formed right after the big bang. This discrepancy, even between the two KROSS subsamples, probably points to a methodology bias either in the sample selection or in the way kinematics are derived. The comparison with KMOS3D would lead to a formation of groups at redshift around $z \sim 0.9$. It is worth emphasizing that the KMOS3D subsample we use as reference has a median redshift of 0.9. Nevertheless, we assume there is no significant evolution of the TFR between $z \sim 0.7$ and $z \sim 0.9$. The difference with ORELSE could be interpreted in line with the environment selection. Indeed, in case quenching is most efficient in clusters, galaxies that enters the structures might stop their star formation in a much shorter amount of time. Therefore, star-forming galaxies observed in clusters might be galaxies that just entered the clusters. In addition, the ORELSE sample is not exclusively composed of cluster galaxies, which means that the results from this sample may be more similar to that for field galaxies. Making this assumption, the comparison with ORELSE would lead to a formation of groups from the MAGIC sample at redshift around $z \sim 1.2$.

In order to check whether these timescales are realistic, we have also estimated the typical depletion time for the galaxies in our sample, based on our gas mass and SFR estimates. The depletion time seems rather constant with stellar mass. This timescale is on the order of ~ 1 Gyr for masses above $10^9 M_{\odot}$. Therefore, if our interpretation is correct, this means that either gas accretion remains possible after galaxies enter groups or that they entered in groups with a larger gas fraction, by a factor of around 2.

It is interesting to notice that the zero-point offset is slightly less important for high-mass galaxies than for low-mass ones, by about 0.1 dex. This is compatible with these galaxies being less dark matter dominated, hence their rotation velocity is not only tracing the underlying DMH potential.

In any cases, these results are subject to large uncertainties on the lowering of the SFR. Ideally, one would need to compute this lowering from a reference sample of galaxies in low-density environments.

5.3. Mass distribution contraction in groups

Another consequence of dense environments is that the distribution of baryons is more concentrated than in low-density environments. In the local Universe, several studies show evidence for this contraction, which is more pronounced for low-mass late-type galaxies (e.g., Maltby et al. 2010; Fernández Lorenzo et al. 2013; Cebrián & Trujillo 2014). At higher redshift a similar trend is also found between field and cluster galaxies (e.g., Kuchner et al. 2017; Matharu et al. 2019; Pelliccia et al. 2019). Matharu et al. (2019) found a contraction of 0.07 dex for late-type cluster galaxies at $z \sim 1$, consistent with size growth being inhibited for about 1 Gyr by cluster environment, whereas Pelliccia et al. (2019) found a more pronounced decrease of 0.13 dex for the ORELSE sample. Kuchner et al. (2017) interpret the decrease in the contraction with mass as quenching timescale being longer for high-mass galaxies.

If the mass is dominated by baryons, or dark matter distribution contracts similarly to baryons, then one expects from Eq. 14 that the rotation velocity is larger when a galaxy is contracted. If we assume the mass within R_{22} remains identical, then we have

$$\Delta(\log V) = -0.5\Delta(\log R_{22}). \quad (17)$$

Depending on the expected contraction, the variation in velocity might be around 0.035 and 0.065 dex. This can be compared to the offset in zero-point of the TFR. This offset in mass can be converted into an offset in velocity using the corresponding slope for each comparison sample. We found velocity offset of 0.177, 0.068, 0.025, and 0.072 for the KROSS rotation dominated, KROSS disk, KMOS3D, and ORELSE samples, respectively (see Table. 4). Except for the KROSS rotation dominated sample, these offsets are compatible with contraction. The discrepancy with KROSS might be explained by a difference of methodology in either sample selection or kinematics extraction, as already proposed in Sect. 5.2. The difference found with respect to the ORELSE sample may be due to a differential contraction since ORELSE galaxies already have smaller radii than field (Pelliccia et al. 2019) and because cluster galaxies should even be smaller than group ones. It can either be explained by this sample not containing only cluster galaxies, by the methodology to extract velocities or by DMHs in groups and clusters not being impacted similarly by environment.

Contraction of baryons is supposed to be more pronounced at low mass, which is also the regime where dark matter dominates.

In this regime we therefore expect that kinematics trace the DMH distribution. The observed increase in velocity in groups may indicate that for a given baryonic mass, the ratio of the DMH mass over the radius is larger in groups than at low density, which could be induced either by dynamical processes contracting DMHs or by galaxies living in more massive halos in dense environments, or by a combination of both. At high mass, contraction seems insufficient to explain the zero-point offset, except if we compare with KMOS3D. In addition, we assumed a similar galaxy contraction in groups and clusters whereas it is expected to be less important in groups. It is therefore difficult to explain the offset at high mass with contraction only. Proper mass models would be required to understand what component drives the large rotations depending on the mass of galaxies.

6. Conclusions

We investigated the impact of environment on the stellar mass and baryonic mass TFR using a sample of 67 star-forming galaxies located in eight groups at redshift $0.5 < z < 0.8$ with projected densities at least 25 times larger than the average galaxy densities in the same redshift range. These groups were observed as part of the 70h on-source MAGIC MUSE-GTO project (PI: T. Contini) inside the COSMOS field. We performed a bulge-disk decomposition on 250 galaxies in those groups to infer accurate bulge-to-disk ratios, galaxy sizes and projection parameters. We built a robust kinematic sample of galaxies on the main sequence of star-forming galaxies based on their size with respect to MUSE observations spatial resolution as well as on the signal-to-noise ratio of the [O II] doublet used to derive galaxy kinematic maps. Some AGN and bulge-dominated galaxies were also discarded from our analysis. We extracted rotation velocities at 2.2 times the disk scale lengths (R_{22}) as well as the velocity dispersion from these maps using kinematic models that take into account the limited spatial resolution of our observations. Our selection lead to a sample spanning a wide range of stellar masses between 10^8 and $10^{11} M_{\odot}$, and mainly composed of rotation-dominated galaxies without requiring a prior condition on the ratio of rotation over dispersion velocities, in contrast with selection functions used in most of such kinematics studies. We derived both the stellar and baryonic mass TFR for our sample, studied the impact of selection and methodology, and compared it to KROSS, KMOS3D and ORELSE, major surveys at similar redshifts. We summarize here the main results.

- Methodology biases can induce a change of the zero-point of 0.05 dex depending on how velocities uncertainties are estimated and of 0.05 dex depending on the selection criteria for the MAGIC sample, that is, by removing or including peculiar galaxies and by modifying the stellar mass range. Not correcting stellar masses to have estimates at the same radius where the velocity is measured introduces an additional increase of 0.15 dex. Methodology biases with respect to other studies have been reduced as much as possible and, whereas we have estimated stellar masses within R_{22} , we have taken into account this in the subsequent comparisons with other samples.
- Using the rotation velocity alone, the MAGIC groups best fit smTFR (bmTFR) computed assuming a reference velocity $\log(V_{ref} [\text{km s}^{-1}]) = 2.2$ has a slope $\alpha = 4.03 \pm 0.63$ (3.55 ± 0.49), a zero-point $\beta = 9.79 \pm 0.09$ (9.99 ± 0.07), and an intrinsic scatter $\sigma_{\text{int}} = 0.43$ (0.35). Taking also into account an asymmetric drift correction, we found that the best fit smTFR (bmTFR) has a slope $\alpha = 4.35 \pm 0.59$ (3.74 ± 0.45),

a zero-point $\beta = 9.51 \pm 0.10$ (9.76 ± 0.08), and an intrinsic scatter $\sigma_{\text{int}} = 0.33$ (0.25).

- The inclusion of the velocity dispersion in the dynamics budget has a more significant impact on galaxies with low rotation velocities and reduces the intrinsic scatter of the various TFR. It increases the slope and decreases the zero-point, however the effect is the same for any sample.
- Using the rotation velocity either alone or corrected for an asymmetric drift, smTFR slopes for the various samples are compatible within the fitting uncertainties. However, using fixed slopes, we systematically find a zero-point in terms of mass that is lower for the MAGIC sample than for the other samples used for comparison. This decrease in the zero-points is about 0.05 – 0.3 dex depending on the sample used, except for the KROSS rotation dominated sample where it reaches 0.6 dex, which we interpret as a combination of sample selection and methodology biases. The offset is the lowest when comparing to KMOS3D, which targeted essentially galaxies more massive than $10^{10} M_{\odot}$. Finally, this evolution of the zero-point with environment contrasts with the result of Pelliccia et al. (2019) for the ORELSE sample. The non-evolution of the zero-point for this sample containing cluster galaxies may be due to the fact that this sample includes also field galaxies and to quenching being more efficient in clusters, which might bias the sample toward star-forming galaxies that just entered dense structures.
- Similarly, we studied the bmTFR relation, by including gas masses, estimated by reversing the Kennicutt-Schmidt law. The impact of gas mass is more pronounced for the low-mass regime than for the high-mass one because low-mass galaxies have a larger gas fraction.
- We find a reduction of the bmTFR zero-point similar to that of the smTFR for KMOS3D sample for which this comparison was possible.

We also derived stellar and baryonic mass fraction for the MAGIC group sample and found that the stellar mass fraction increases from around 10% in the low-mass regime up to 50% at maximum in the high-mass regime, in line with previous studies. A similar but weaker trend is observed for the baryon fraction that remains below 50%.

We then interpreted the differences we observe in the TFR with two main hypotheses. On the one hand, we made the hypothesis that kinematics trace the DMH mass and therefore interpreted the difference in zero-point as resulting from quenching. Assuming a decrease in the SFR by 0.3 dex due to environment, we could infer that the bulk of galaxies we observe in groups would have entered the over-density between 1 to 3 Gyr ago. On the other hand, we studied the impact of a contraction of the mass distribution within R_{22} to infer the expected increase in velocity. The hypothesis that environment contracts the stellar content of galaxies by 0.07 to 0.13 dex, seems able to justify from half to the whole offset we observe in the TFR with respect to other samples. Since dark matter fraction is large, it would therefore indicate that dark matter is also contracted or that DMHs are more massive. It is therefore likely that both contraction of the mass distribution and star-formation quenching participate in the observed differences in the TFR between dense groups and low-density environments and that the contribution of each mechanism depends on the mass regime.

Nevertheless, despite our efforts to minimize systematics, the results we obtained might still depend on the comparison samples and on the methodology used (i) to perform sample selection, (ii) to measure galaxy sizes, (iii) to infer stellar and gas

masses within a given radius and (iv) to derive kinematics properties. Combining all these source of uncertainties make difficult to extract robust comparisons that could serve as the basis for an estimation of each process and link this to star-formation quenching mechanisms, such as ram-pressure stripping, gravitational interactions between galaxies or between galaxy and group potential wells, merging, or starvation.

We therefore need a comparison sample of field galaxies with a dataset very similar to the MAGIC group sample so that we can estimate within stellar mass bins the variation with environment of (i) the SFR, (ii) the disk scale length, (iii) the velocity, and therefore study the impact of environment on both the TFR and the baryon mass fraction as a function of mass. Such a sample will be built from the MAGIC dataset itself. Ideally, mass models constrained with observed stellar distribution should be used to determine if halos have been contracted depending on the stellar mass or on the asymptotic halo mass.

Acknowledgements. We dedicate this article in memory of Hayley Finley. This work has been carried out thanks to the support of the Ministry of Science, Technology and Innovation of Colombia (MINCIENCIAS) PhD fellowship program No. 756-2016. This work has been carried out through the support of the ANR FOGHAR (ANR-13-BS05-0010-02), the OCEVU Labex (ANR-11-LABX-0060), and the A*MIDEX project (ANR-11-IDEX-0001-02), which are funded by the “Investissements d’avenir” French government program managed by the ANR. This work was supported by the Programme National Cosmology et Galaxies (PNCG) of CNRS/INSU with INP and IN2P3, co-funded by CEA and CNES. JB acknowledges support by FCT/MCTES through national funds by the grant UID/FIS/04434/2019, UIDB/04434/2020 and UIDP/04434/2020 and through the Investigador FCT Contract No. IF/01654/2014/CP1215/CT0003. JCBP acknowledges financial support of Vicerrectoría de Investigación y Extensión de la Universidad Industrial de Santander under project 2494. This research has made use of MATPLOTLIB (Hunter 2007). We acknowledge David Carton for his investment in the build-up of the project. The authors thank the referee for the useful and constructive comments that enabled to significantly improve the paper.

References

- Abraham, R. G., Tanvir, N. R., Santiago, B. X., et al. 1996, *MNRAS*, 279, L47
- Bacon, R., Brinchmann, J., Richard, J., et al. 2015, *A&A*, 575, A75
- Bacon, R., Conseil, S., Mary, D., et al. 2017, *A&A*, 608, A1
- Beers, T. C., Flynn, K., & Gebhardt, K. 1990, *AJ*, 100, 32
- Bell, E. F. & de Jong, R. S. 2001, *ApJ*, 550, 212
- Bertin, E. & Arnouts, S. 1996, *A&AS*, 117, 393
- Boggs, P. T. & Rogers, J. E. 1990, in *Statistical analysis of measurement error models and applications: proceedings of the AMS-IMS-SIAM joint summer research conference held June 10-16, 1989*, Vol. 112, *Contemporary Mathematics*, 186
- Böhm, A., Ziegler, B. L., Pérez-Martínez, J. M., et al. 2020, *A&A*, 633, A131
- Boogaard, L. A., Brinchmann, J., Bouché, N., et al. 2018, *A&A*, 619, A27
- Boselli, A., Epinat, B., Contini, T., et al. 2019, *A&A*, 631, A114
- Boselli, A. & Gavazzi, G. 2006, *PASP*, 118, 517
- Bryant, J. J., Owers, M. S., Robotham, A. S. G., et al. 2015, *MNRAS*, 447, 2857
- Burkert, A., Genzel, R., Bouché, N., et al. 2010, *ApJ*, 725, 2324
- Calzetti, D., Armus, L., Bohlin, R. C., et al. 2000, *ApJ*, 533, 682
- Cardelli, J. A., Clayton, G. C., & Mathis, J. S. 1989, *ApJ*, 345, 245
- Cassata, P., Guzzo, L., Franceschini, A., et al. 2007, *ApJS*, 172, 270
- Cebrián, M. & Trujillo, I. 2014, *MNRAS*, 444, 682
- Chabrier, G. 2003, *PASP*, 115, 763
- Cibinel, A., Carollo, C. M., Lilly, S. J., et al. 2013, *ApJ*, 777, 116
- Conroy, C. & Gunn, J. E. 2010, *ApJ*, 712, 833
- Conselice, C. J., Wilkinson, A., Duncan, K., & Mortlock, A. 2016, *ApJ*, 830, 83
- Contini, T., Epinat, B., Bouché, N., et al. 2016, *A&A*, 591, A49
- Cresci, G., Hicks, E. K. S., Genzel, R., et al. 2009, *ApJ*, 697, 115
- Cucciati, O., Marinoni, C., Iovino, A., et al. 2010, *A&A*, 520, A42
- Dekel, A., Birnboim, Y., Engel, G., et al. 2009, *Nature*, 457, 451
- Epinat, B., Amram, P., Balkowski, C., & Marcelin, M. 2010, *MNRAS*, 401, 2113
- Epinat, B., Amram, P., & Marcelin, M. 2008, *MNRAS*, 390, 466
- Epinat, B., Contini, T., Finley, H., et al. 2018, *A&A*, 609, A40
- Epinat, B., Contini, T., Le Fèvre, O., et al. 2009, *A&A*, 504, 789
- Epinat, B., Tasca, L., Amram, P., et al. 2012, *A&A*, 539, A92
- Fernández Lorenzo, M., Sulentic, J., Verdes-Montenegro, L., & Argudo-Fernández, M. 2013, *MNRAS*, 434, 325
- Gnerucci, A., Marconi, A., Cresci, G., et al. 2011, *A&A*, 528, A88
- Gómez-López, J. A., Amram, P., Epinat, B., et al. 2019, *A&A*, 631, A71
- Gozali, G., Finoguenov, A., Tanaka, M., et al. 2019, *MNRAS*, 483, 3545
- Grützbauch, R., Conselice, C. J., Bauer, A. E., et al. 2011, *MNRAS*, 418, 938
- Guérou, A., Krajnović, D., Epinat, B., et al. 2017, *A&A*, 608, A5
- Hinton, S. R., Davis, T. M., Lidman, C., Glazebrook, K., & Lewis, G. F. 2016, *Astronomy and Computing*, 15, 61
- Huertas-Company, M., Rouan, D., Tasca, L., Soucail, G., & Le Fèvre, O. 2008, *A&A*, 478, 971
- Hunter, J. D. 2007, *Computing in Science & Engineering*, 9, 90
- Inami, H., Bacon, R., Brinchmann, J., et al. 2017, *A&A*, 608, A2
- Janeau, S., Dickinson, M., Alexander, D. M., & Salim, S. 2011, *ApJ*, 736, 104
- Kennicutt, Robert C., J. 1998a, *ARA&A*, 36, 189
- Kennicutt, Robert C., J. 1998b, *ApJ*, 498, 541
- Knobel, C., Lilly, S. J., Iovino, A., et al. 2012, *ApJ*, 753, 121
- Knobel, C., Lilly, S. J., Iovino, A., et al. 2009, *ApJ*, 697, 1842
- Koekemoer, A. M., Aussel, H., Calzetti, D., et al. 2007, *ApJS*, 172, 196
- Kriek, M., van Dokkum, P. G., Labbé, I., et al. 2009, *ApJ*, 700, 221
- Kuchner, U., Ziegler, B., Verdugo, M., Bamford, S., & Häußler, B. 2017, *A&A*, 604, A54
- Laigle, C., McCracken, H. J., Ilbert, O., et al. 2016, *ApJS*, 224, 24
- Lamareille, F. 2010, *A&A*, 509, A53
- Lelli, F., McGaugh, S. S., & Schombert, J. M. 2016, *ApJ*, 816, L14
- Lemaux, B. C., Gal, R. R., Lubin, L. M., et al. 2012, *ApJ*, 745, 106
- Madau, P. & Dickinson, M. 2014, *ARA&A*, 52, 415
- Maltby, D. T., Aragón-Salamanca, A., Gray, M. E., et al. 2010, *MNRAS*, 402, 282
- Masters, K. L., Springob, C. M., Haynes, M. P., & Giovanelli, R. 2006, *ApJ*, 653, 861
- Masters, K. L., Springob, C. M., & Huchra, J. P. 2008, *AJ*, 135, 1738
- Matharu, J., Muzzin, A., Brammer, G. B., et al. 2019, *MNRAS*, 484, 595
- McGaugh, S. S. 2005, *ApJ*, 632, 859
- McGaugh, S. S., Schombert, J. M., Bothun, G. D., & de Blok, W. J. G. 2000, *ApJ*, 533, L99
- Meurer, G. R., Carignan, C., Beaulieu, S. F., & Freeman, K. C. 1996, *AJ*, 111, 1551
- Miller, S. H., Ellis, R. S., Sullivan, M., et al. 2012, *ApJ*, 753, 74
- Muzzin, A., Wilson, G., Demarco, R., et al. 2013, *ApJ*, 767, 39
- Muzzin, A., Wilson, G., Yee, H. K. C., et al. 2012, *ApJ*, 746, 188
- Osterbrock, D. E. & Ferland, G. J. 2006, *Astrophysics of gaseous nebulae and active galactic nuclei*
- Pelliccia, D., Lemaux, B. C., Tomczak, A. R., et al. 2019, *MNRAS*, 482, 3514
- Pelliccia, D., Tresse, L., Epinat, B., et al. 2017, *A&A*, 599, A25
- Peng, C. Y., Ho, L. C., Impey, C. D., & Rix, H.-W. 2002, *AJ*, 124, 266
- Peng, Y.-j., Lilly, S. J., Kovač, K., et al. 2010, *ApJ*, 721, 193
- Pérez-Martínez, J. M., Ziegler, B., Verdugo, M., Böhm, A., & Tanaka, M. 2017, *A&A*, 605, A127
- Persic, M., Salucci, P., & Stel, F. 1996, *MNRAS*, 281, 27
- Pizagno, J., Prada, F., Weinberg, D. H., et al. 2007, *AJ*, 134, 945
- Puech, M., Flores, H., Hammer, F., et al. 2008, *A&A*, 484, 173
- Puech, M., Hammer, F., Flores, H., et al. 2010, *A&A*, 510, A68
- Reyes, R., Mandelbaum, R., Gunn, J. E., Pizagno, J., & Lackner, C. N. 2011, *MNRAS*, 417, 2347
- Robotham, A. S. G. & Obreschkow, D. 2015, *PASA*, 32, e033
- Sargent, M. T., Carollo, C. M., Lilly, S. J., et al. 2007, *ApJS*, 172, 434
- Scarlata, C., Carollo, C. M., Lilly, S., et al. 2007, *ApJS*, 172, 406
- Scoville, N., Aussel, H., Brusa, M., et al. 2007, *ApJS*, 172, 1
- Scoville, N., Lee, N., Vanden Bout, P., et al. 2017, *ApJ*, 837, 150
- Simons, R. C., Kassim, S. A., Weiner, B. J., et al. 2017, *ApJ*, 843, 46
- Simons, R. C., Kassim, S. A., Weiner, B. J., et al. 2015, *MNRAS*, 452, 986
- Sobral, D., Swinbank, A. M., Stott, J. P., et al. 2013, *ApJ*, 779, 139
- Sorce, J. G., Tully, R. B., Courtois, H. M., et al. 2014, *MNRAS*, 444, 527
- Soto, K. T., Lilly, S. J., Bacon, R., Richard, J., & Conseil, S. 2016, *MNRAS*, 458, 3210
- Stott, J. P., Swinbank, A. M., Johnson, H. L., et al. 2016, *MNRAS*, 457, 1888
- Tacconi, L. J., Genzel, R., Saintonge, A., et al. 2018, *ApJ*, 853, 179
- Tasca, L. A. M., Kneib, J. P., Iovino, A., et al. 2009, *A&A*, 503, 379
- Tiley, A. L., Bureau, M., Cortese, L., et al. 2019, *MNRAS*, 482, 2166
- Tiley, A. L., Stott, J. P., Swinbank, A. M., et al. 2016, *MNRAS*, 460, 103
- Tomczak, A. R., Lemaux, B. C., Lubin, L. M., et al. 2019, *MNRAS*, 484, 4695
- Torres-Flores, S., Epinat, B., Amram, P., Plana, H., & Mendes de Oliveira, C. 2011, *MNRAS*, 416, 1936
- Torres-Flores, S., Mendes de Oliveira, C., Plana, H., Amram, P., & Epinat, B. 2013, *MNRAS*, 432, 3085
- Tully, R. B. & Fisher, J. R. 1977, *A&A*, 500, 105
- Turner, O. J., Cirasuolo, M., Harrison, C. M., et al. 2017, *MNRAS*, 471, 1280
- Übler, H., Förster Schreiber, N. M., Genzel, R., et al. 2017, *ApJ*, 842, 121
- Übler, H., Genzel, R., Wisnioski, E., et al. 2019, *ApJ*, 880, 48
- Vergani, D., Epinat, B., Contini, T., et al. 2012, *A&A*, 546, A118
- Weilbacher, P. M., Palsa, R., Streicher, O., et al. 2020, *A&A*, 641, A28
- Weiner, B. J., Willmer, C. N. A., Faber, S. M., et al. 2006, *ApJ*, 653, 1027
- Wetzel, A. R., Tinker, J. L., Conroy, C., & van den Bosch, F. C. 2013, *MNRAS*, 432, 336
- Williams, M. J., Bureau, M., & Cappellari, M. 2010, *MNRAS*, 409, 1330
- Wisnioski, E., Förster Schreiber, N. M., Wuyts, S., et al. 2015, *ApJ*, 799, 209
- Wuyts, S., Förster Schreiber, N. M., Wisnioski, E., et al. 2016, *ApJ*, 831, 149

Appendix A: Morpho-kinematics maps for individual galaxies with $S/N \geq 40$ and $R_{eff}/FWHM \geq 0.5$

Appendix A.1: Galaxies of the final kinematic sample

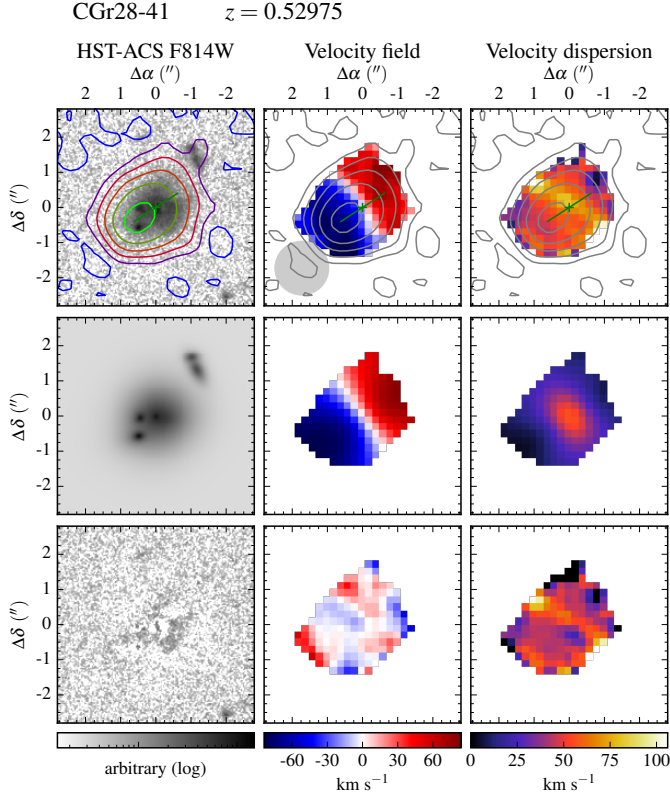


Fig. A.1: Morpho-kinematics maps for galaxy CGr28-41. Top row, from left to right: HST-ACS F814W images, MUSE velocity fields and velocity dispersion maps corrected for spectral resolution. Middle row: Associated models. The velocity dispersion (third column) corresponds to a beam smearing correction map. Bottom row: Residuals, except for the third column that shows the beam smearing corrected velocity dispersion map. On each observed map, the green cross indicates the center derived from the morphology, whereas the green segment indicates the kinematic major axis and has a length corresponding to R_{22} . The $[O II]$ flux distribution is shown with contours at levels of surface brightness $\Sigma([O II]) = 2.5, 5.0, 10.0, 20.0, 40.0, 80.0 \times 10^{-18} \text{ erg s}^{-1} \text{ cm}^{-2} \text{ arcsec}^{-2}$. The MUSE spatial resolution is indicated with a gray disk of diameter FWHM in the bottom-left corner of the velocity field.

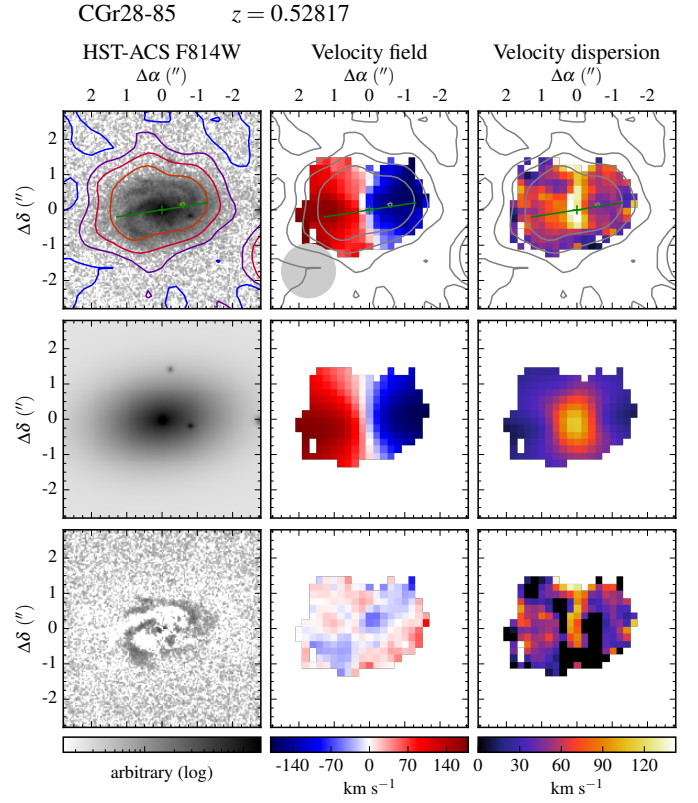


Fig. A.2: Morpho-kinematics maps for galaxy CGr28-85. See caption of Fig. A.1 for the description of figure.

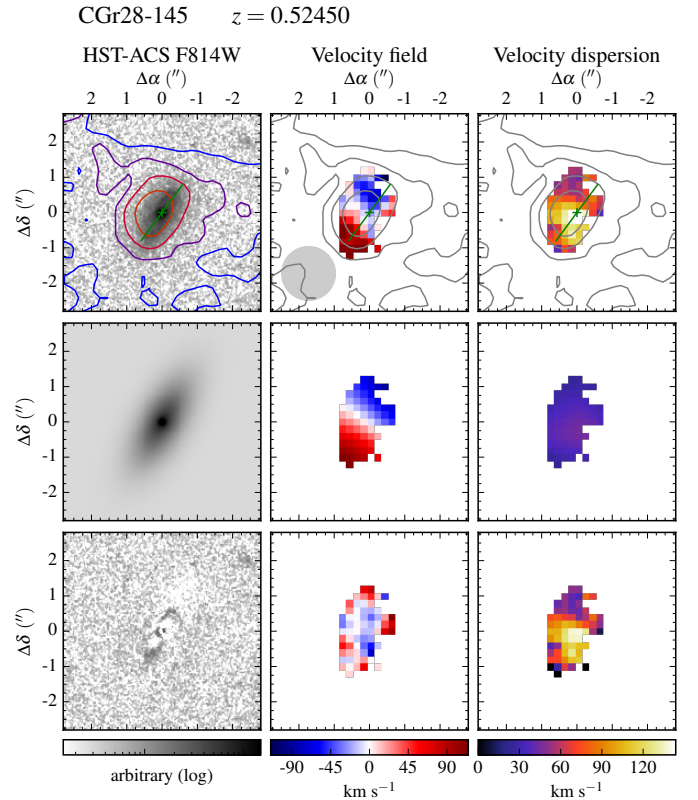


Fig. A.3: Morpho-kinematics maps for galaxy CGr28-145. See caption of Fig. A.1 for the description of figure.

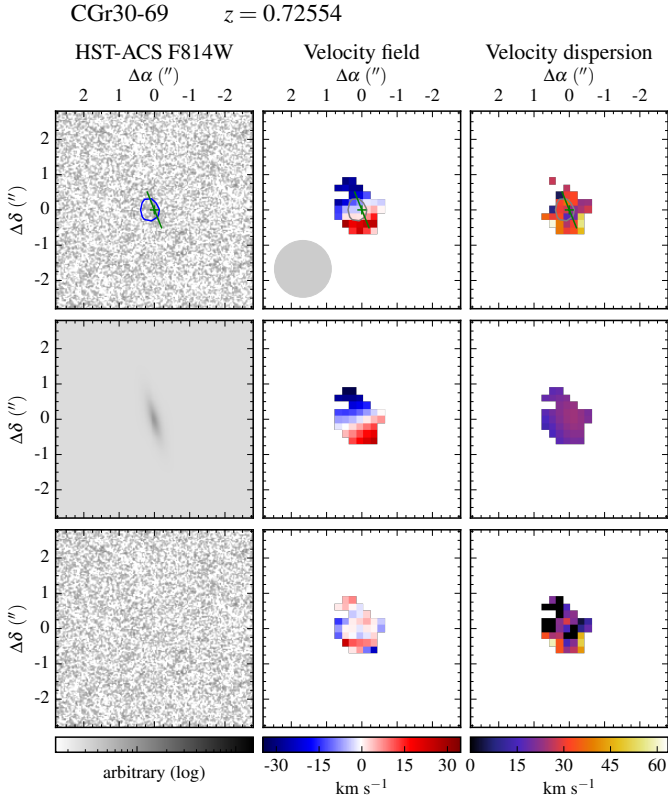


Fig. A.4: Morpho-kinematics maps for galaxy CGr30-69. See caption of Fig. A.1 for the description of figure.

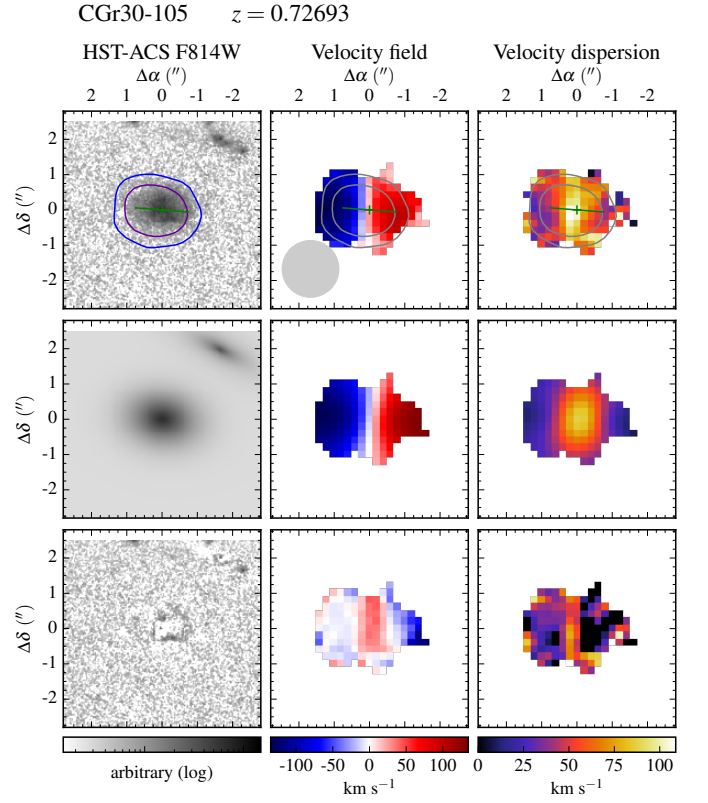


Fig. A.6: Morpho-kinematics maps for galaxy CGr30-105. See caption of Fig. A.1 for the description of figure.

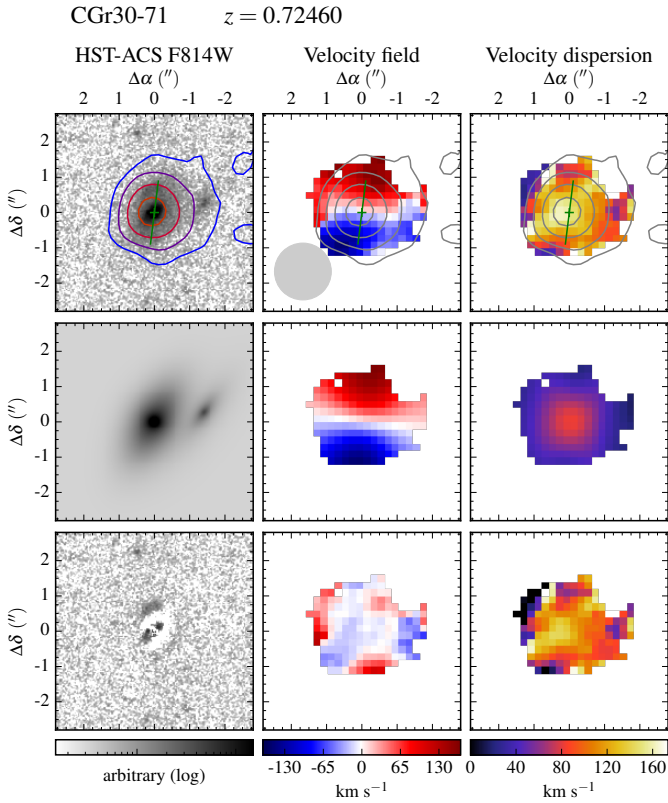


Fig. A.5: Morpho-kinematics maps for galaxy CGr30-71. See caption of Fig. A.1 for the description of figure.

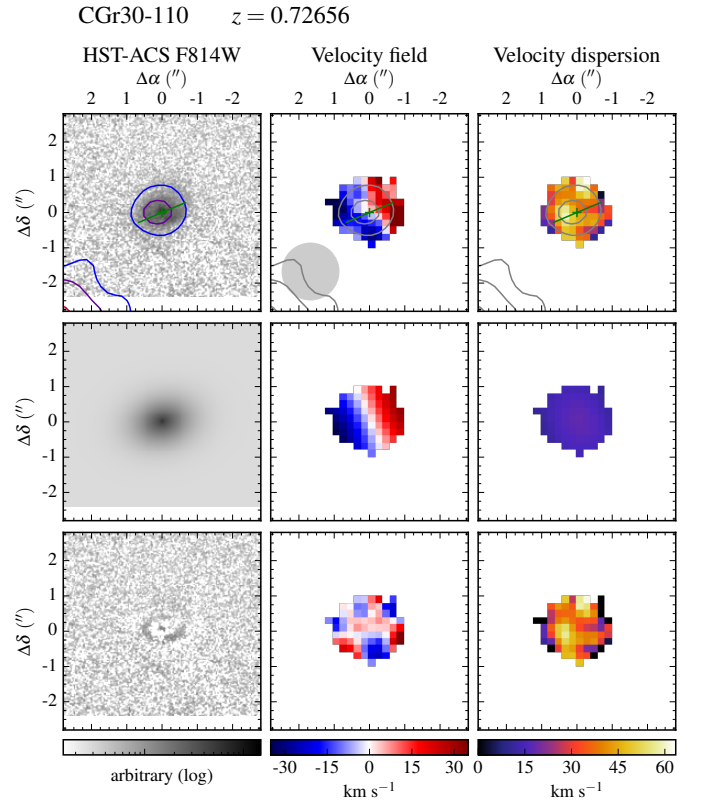


Fig. A.7: Morpho-kinematics maps for galaxy CGr30-110. See caption of Fig. A.1 for the description of figure.

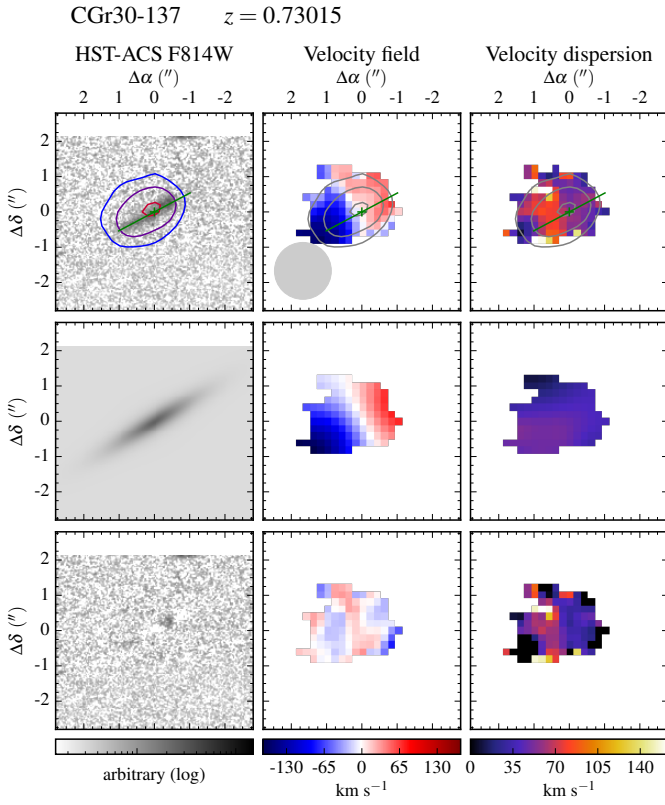


Fig. A.8: Morpho-kinematics maps for galaxy CGr30-137. See caption of Fig. A.1 for the description of figure.

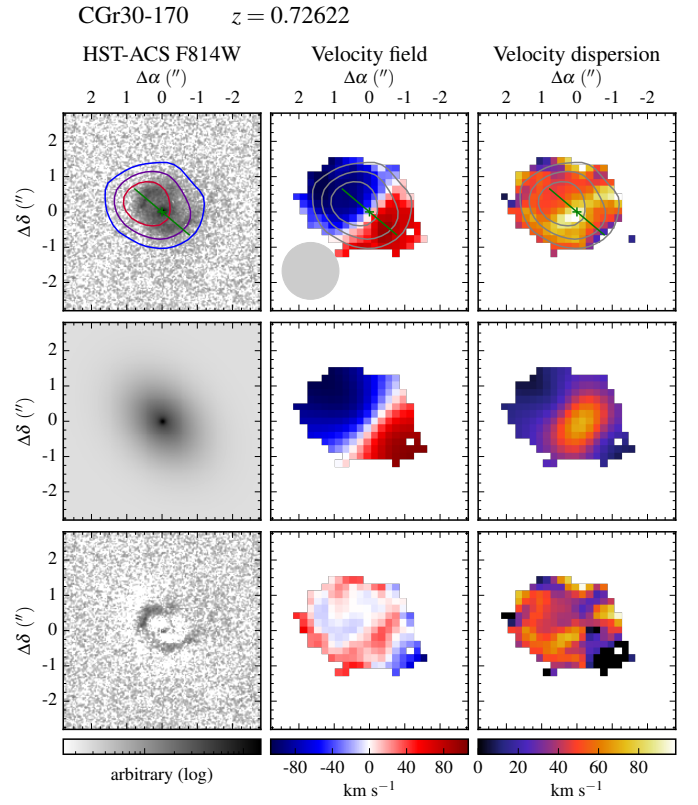


Fig. A.10: Morpho-kinematics maps for galaxy CGr30-170. See caption of Fig. A.1 for the description of figure.

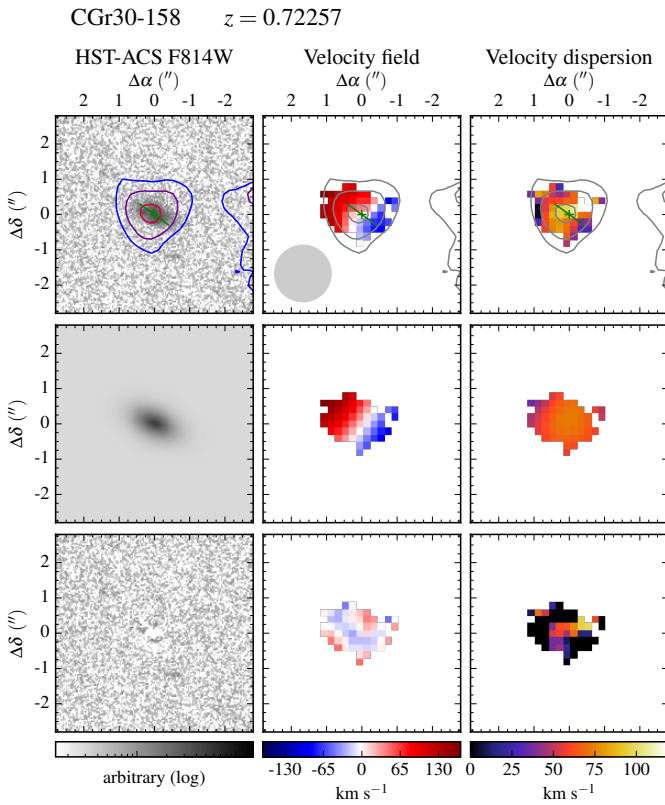


Fig. A.9: Morpho-kinematics maps for galaxy CGr30-158. See caption of Fig. A.1 for the description of figure.

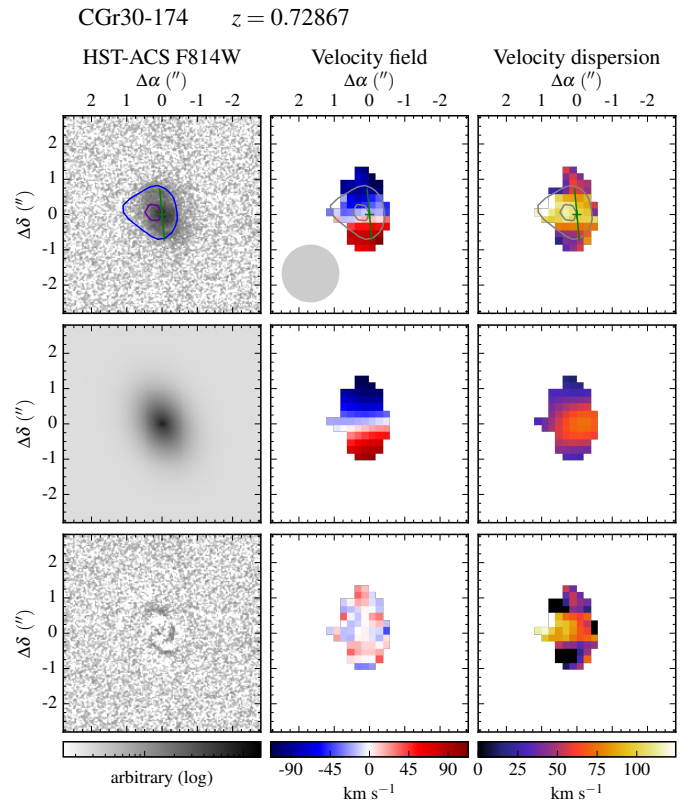


Fig. A.11: Morpho-kinematics maps for galaxy CGr30-174. See caption of Fig. A.1 for the description of figure.

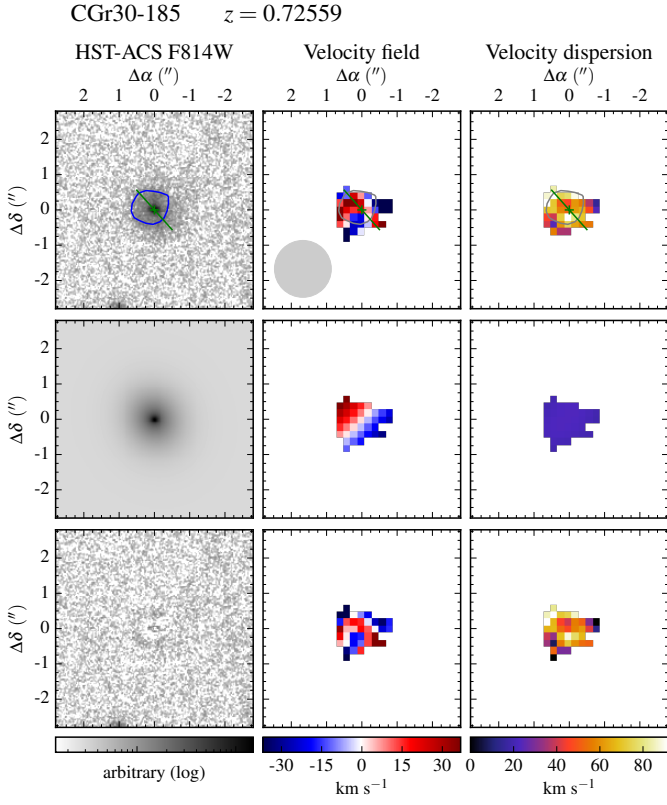


Fig. A.12: Morpho-kinematics maps for galaxy CGr30-185. See caption of Fig. A.1 for the description of figure.

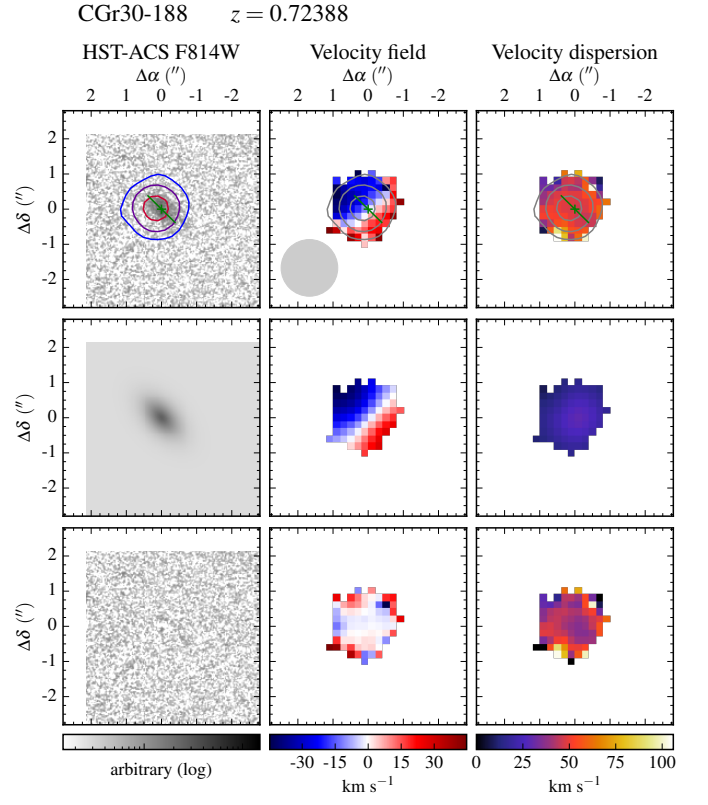


Fig. A.14: Morpho-kinematics maps for galaxy CGr30-188. See caption of Fig. A.1 for the description of figure.

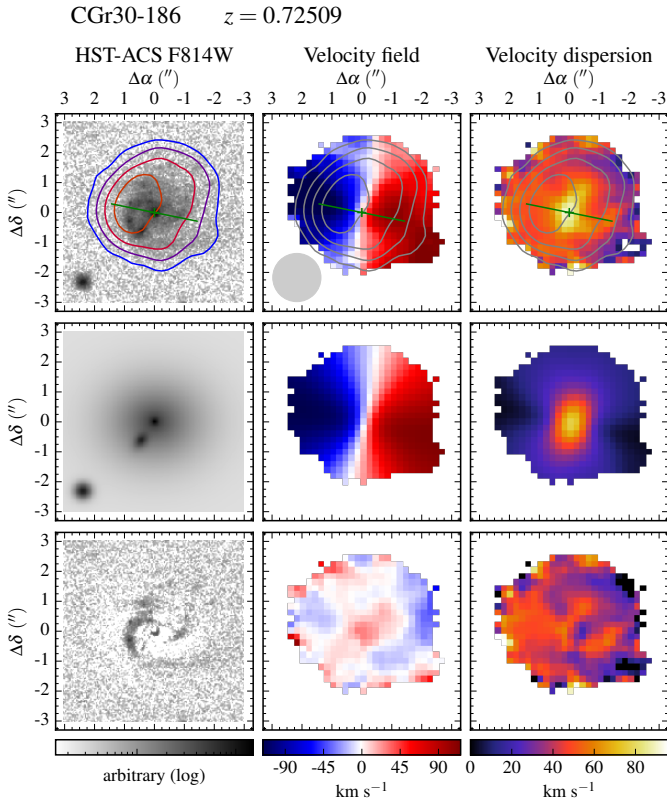


Fig. A.13: Morpho-kinematics maps for galaxy CGr30-186. See caption of Fig. A.1 for the description of figure.

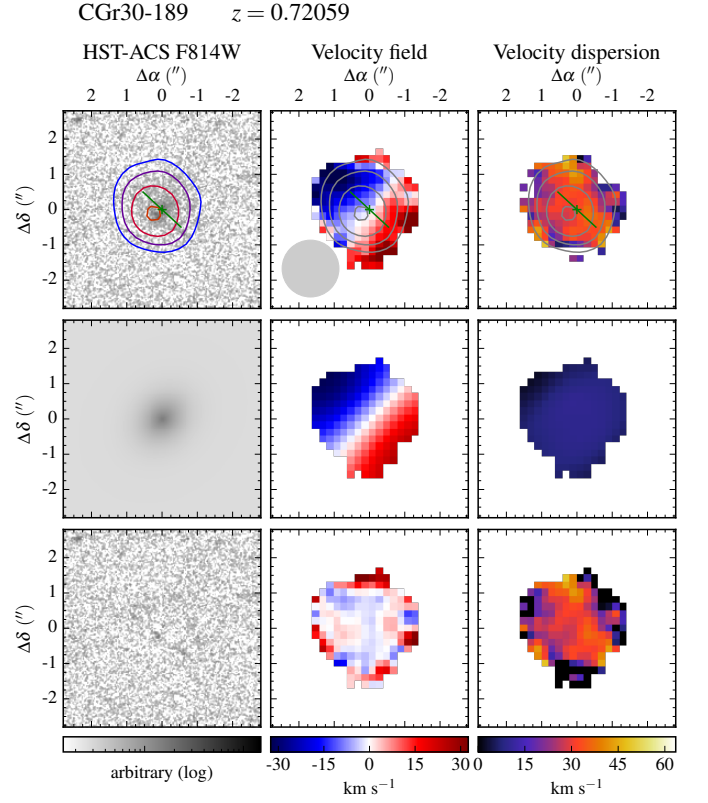


Fig. A.15: Morpho-kinematics maps for galaxy CGr30-189. See caption of Fig. A.1 for the description of figure.

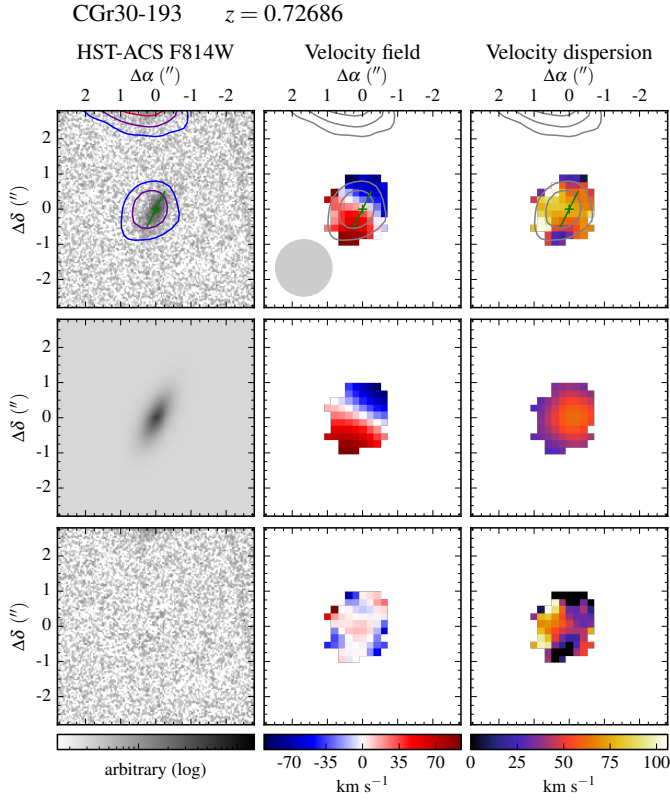


Fig. A.16: Morpho-kinematics maps for galaxy CGr30-193. See caption of Fig. A.1 for the description of figure.

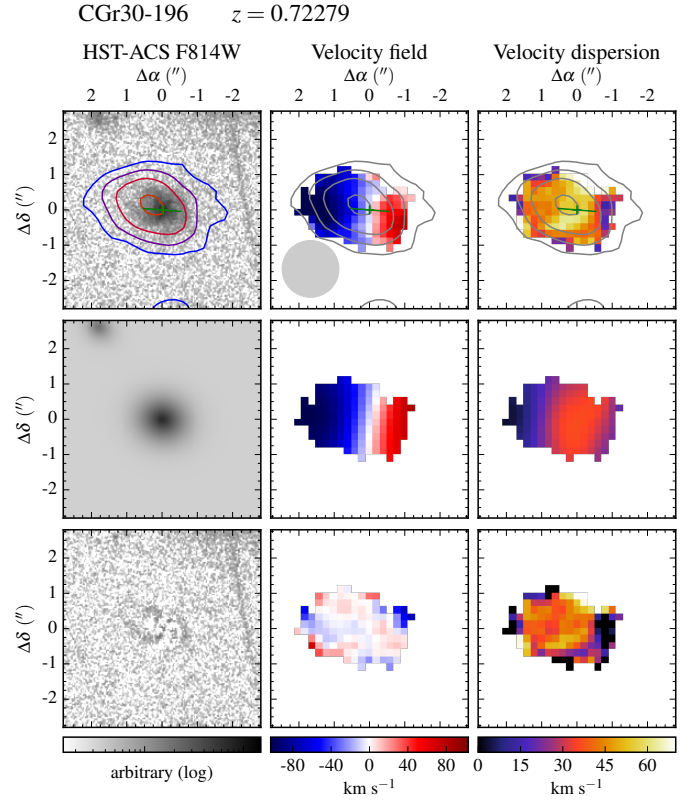


Fig. A.18: Morpho-kinematics maps for galaxy CGr30-196. See caption of Fig. A.1 for the description of figure.

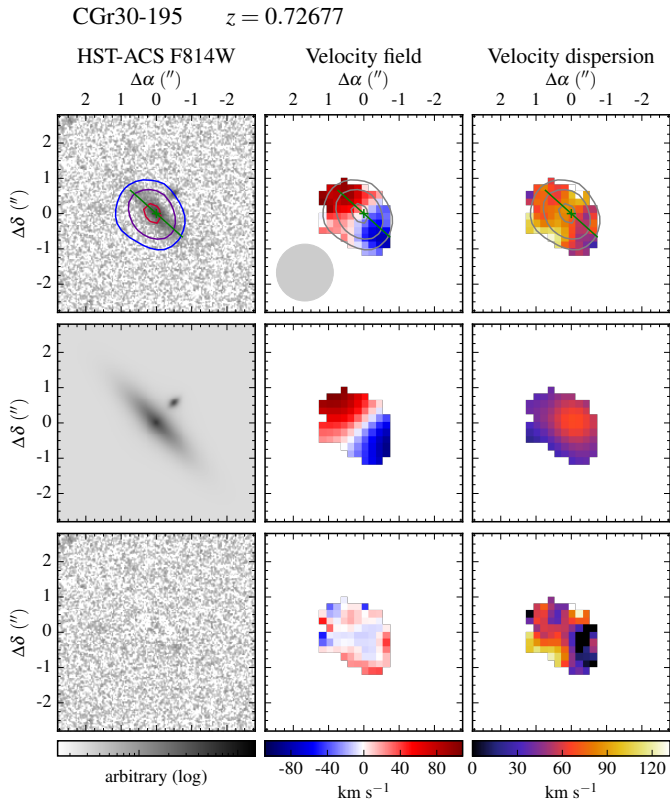


Fig. A.17: Morpho-kinematics maps for galaxy CGr30-195. See caption of Fig. A.1 for the description of figure.

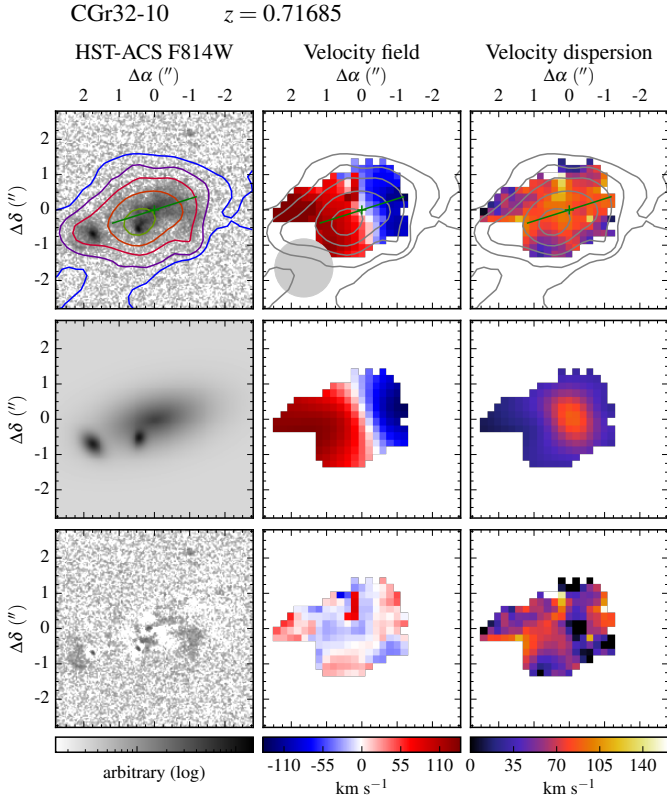
Valentina Abril-Melgarejo et al.: TFR in dense groups $z \sim 0.7$ in the MAGIC survey

Fig. A.19: Morpho-kinematics maps for galaxy CGr32-10. See caption of Fig. A.1 for the description of figure.

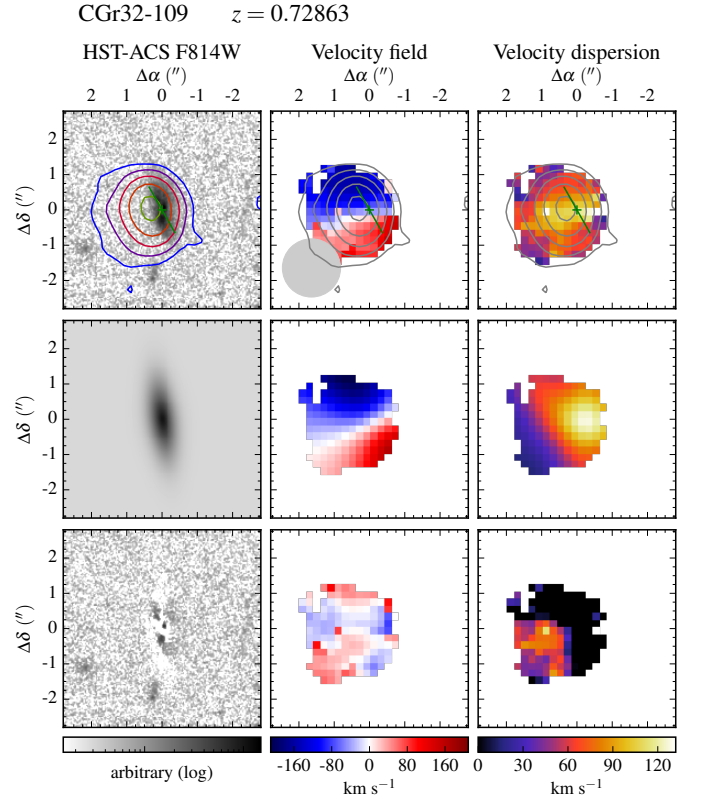


Fig. A.21: Morpho-kinematics maps for galaxy CGr32-109. See caption of Fig. A.1 for the description of figure.

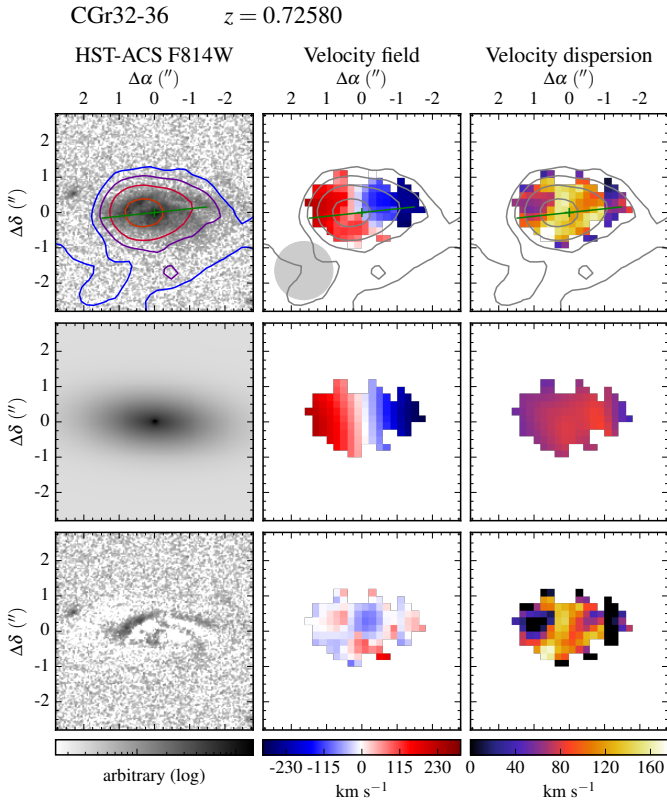


Fig. A.20: Morpho-kinematics maps for galaxy CGr32-36. See caption of Fig. A.1 for the description of figure.

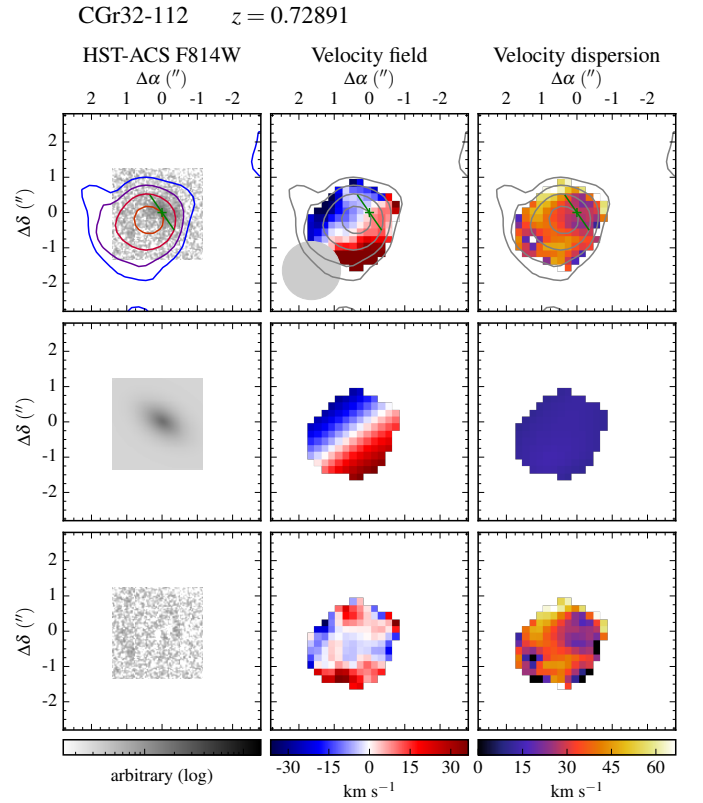


Fig. A.22: Morpho-kinematics maps for galaxy CGr32-112. See caption of Fig. A.1 for the description of figure.

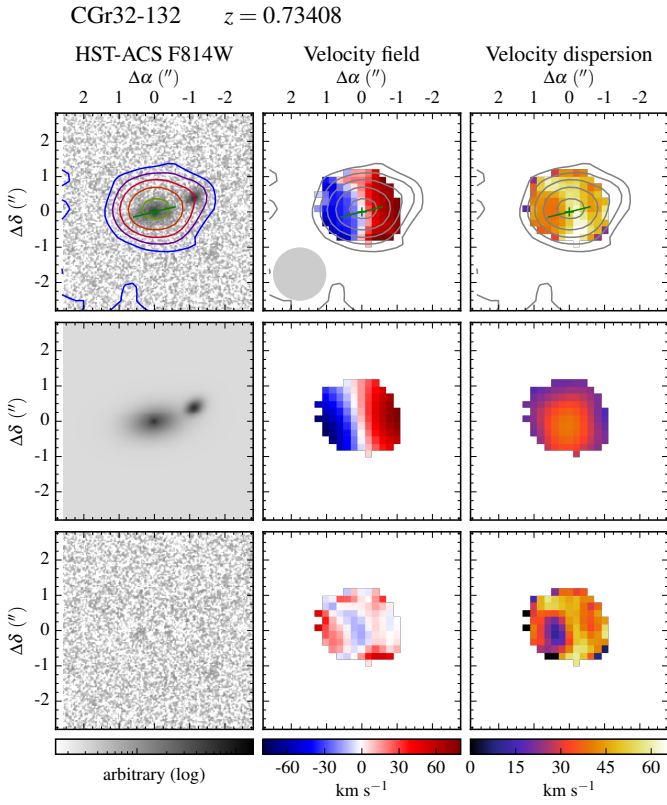


Fig. A.23: Morpho-kinematics maps for galaxy CGr32-132. See caption of Fig. A.1 for the description of figure.

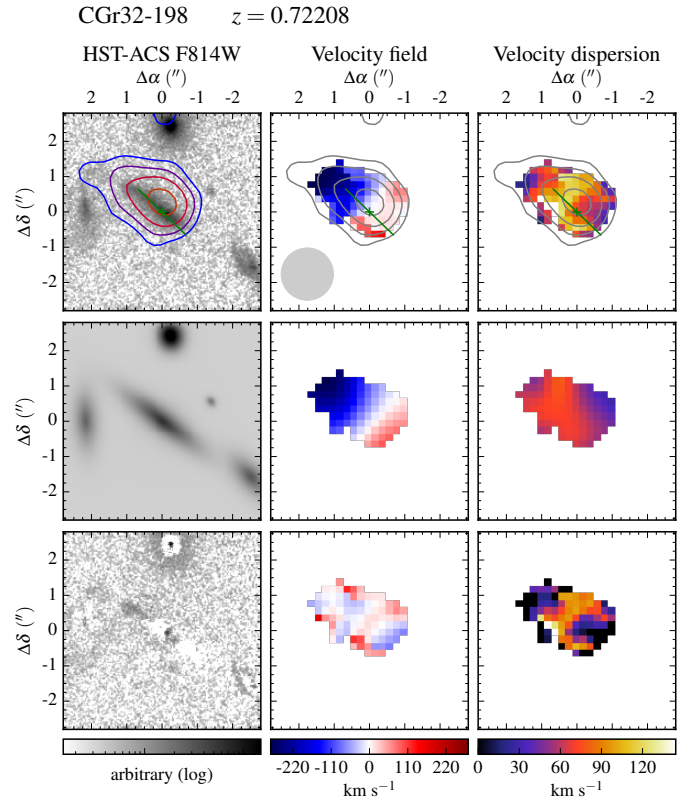


Fig. A.25: Morpho-kinematics maps for galaxy CGr32-198. See caption of Fig. A.1 for the description of figure.

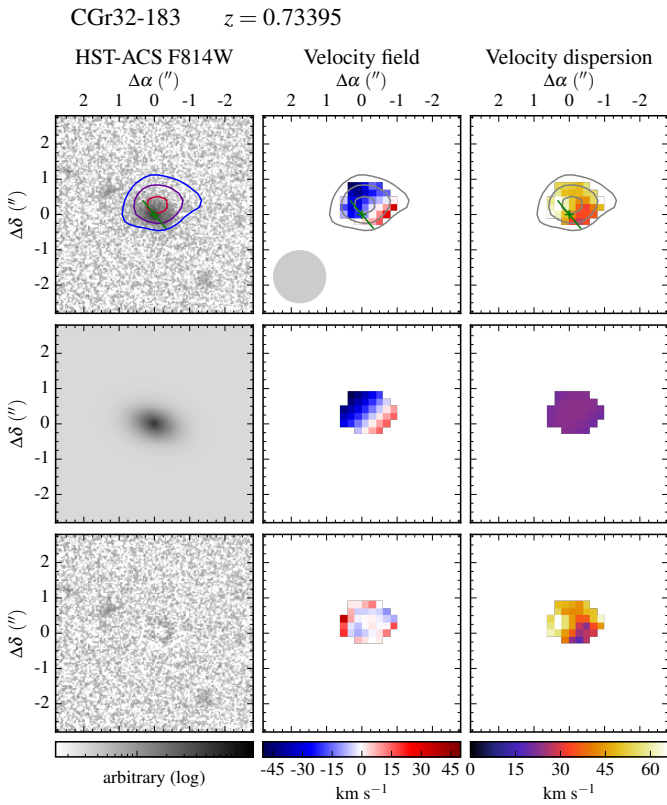


Fig. A.24: Morpho-kinematics maps for galaxy CGr32-183. See caption of Fig. A.1 for the description of figure.

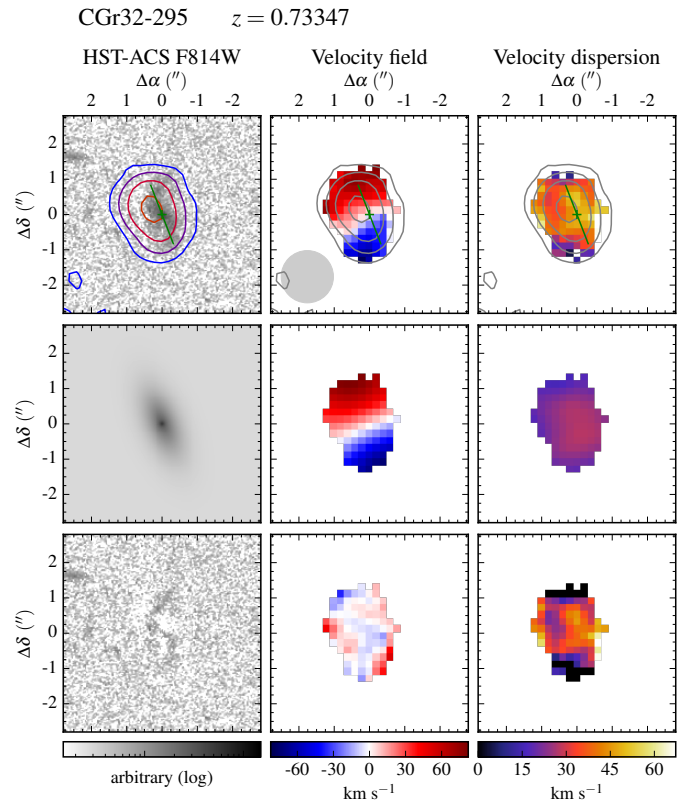


Fig. A.26: Morpho-kinematics maps for galaxy CGr32-295. See caption of Fig. A.1 for the description of figure.

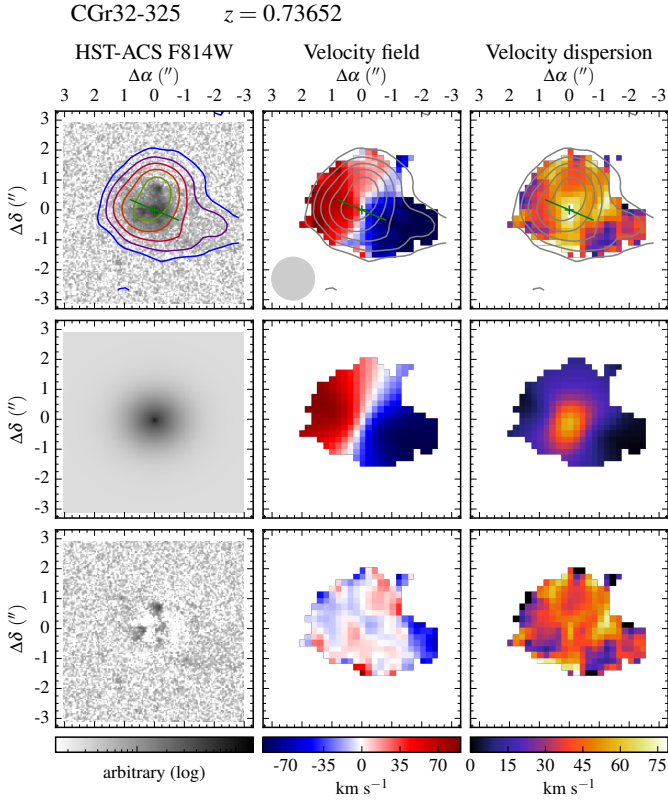


Fig. A.27: Morpho-kinematics maps for galaxy CGr32-325. See caption of Fig. A.1 for the description of figure.

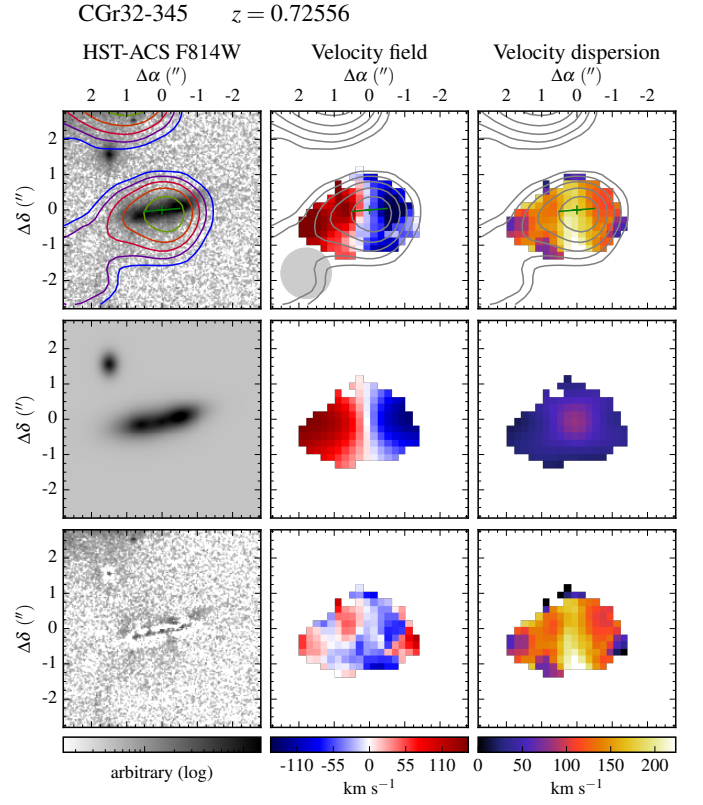


Fig. A.29: Morpho-kinematics maps for galaxy CGr32-345. See caption of Fig. A.1 for the description of figure.

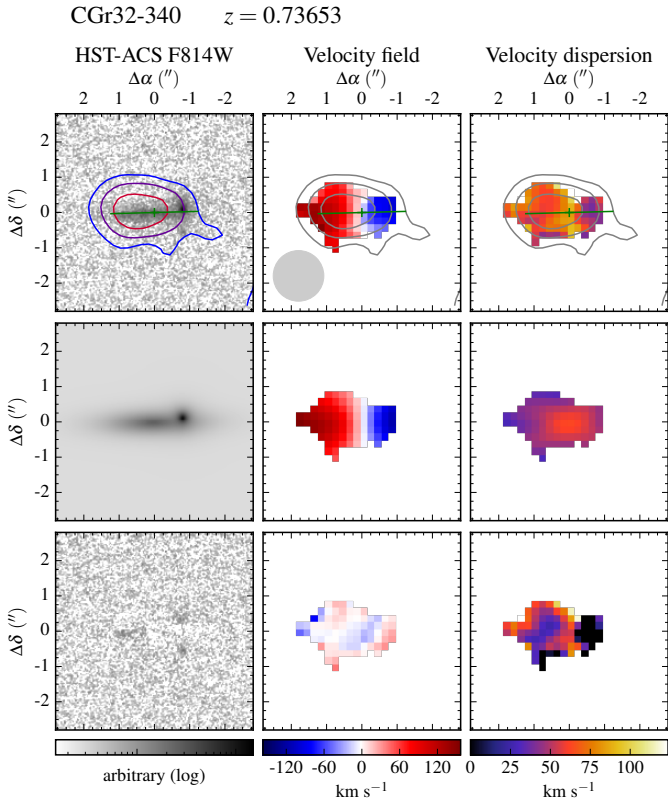


Fig. A.28: Morpho-kinematics maps for galaxy CGr32-340. See caption of Fig. A.1 for the description of figure.

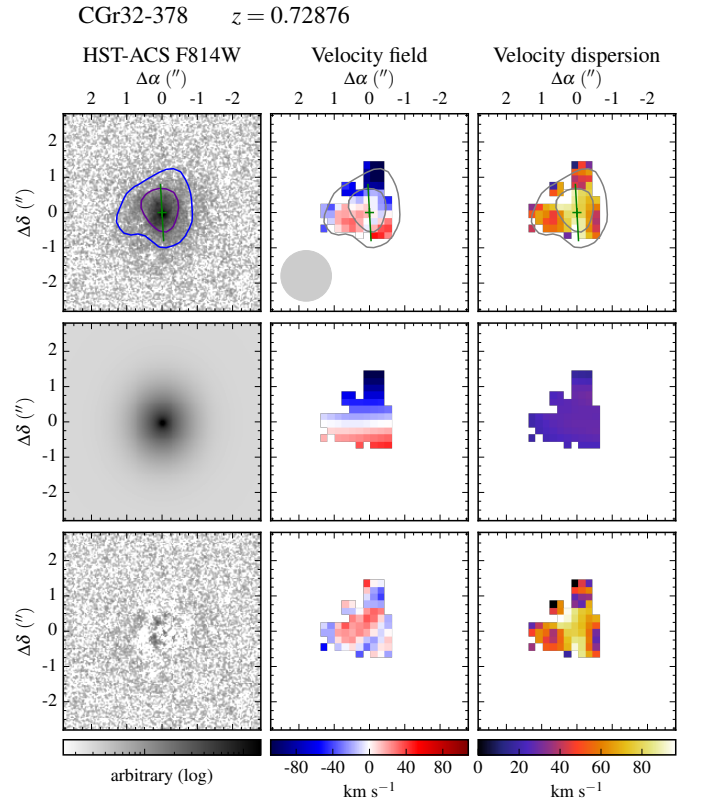


Fig. A.30: Morpho-kinematics maps for galaxy CGr32-378. See caption of Fig. A.1 for the description of figure.

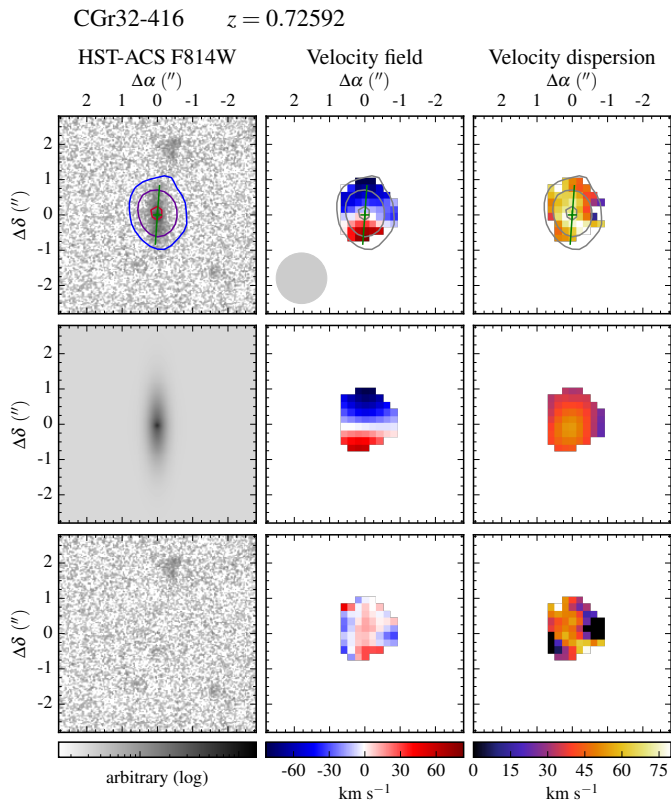


Fig. A.31: Morpho-kinematics maps for galaxy CGr32-416. See caption of Fig. A.1 for the description of figure.

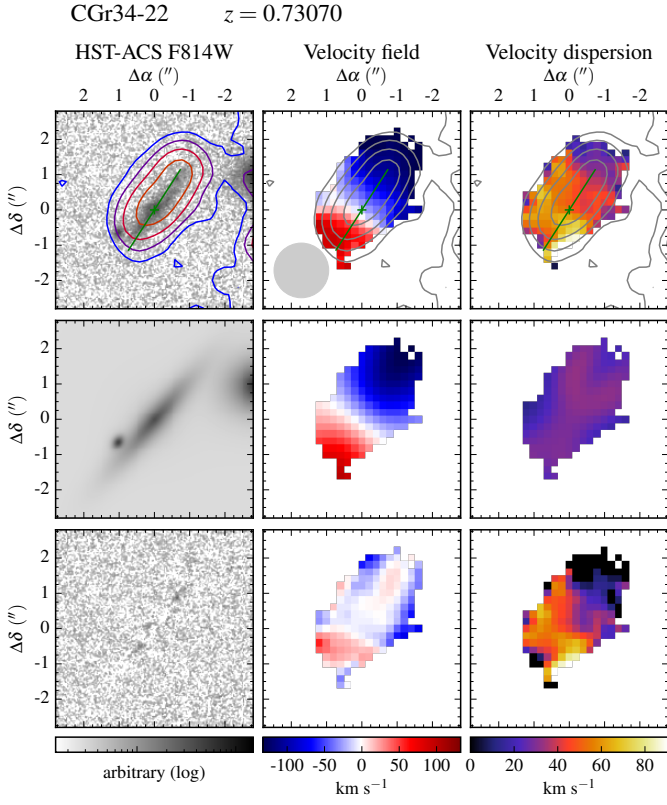


Fig. A.32: Morpho-kinematics maps for galaxy CGr34-22. See caption of Fig. A.1 for the description of figure.

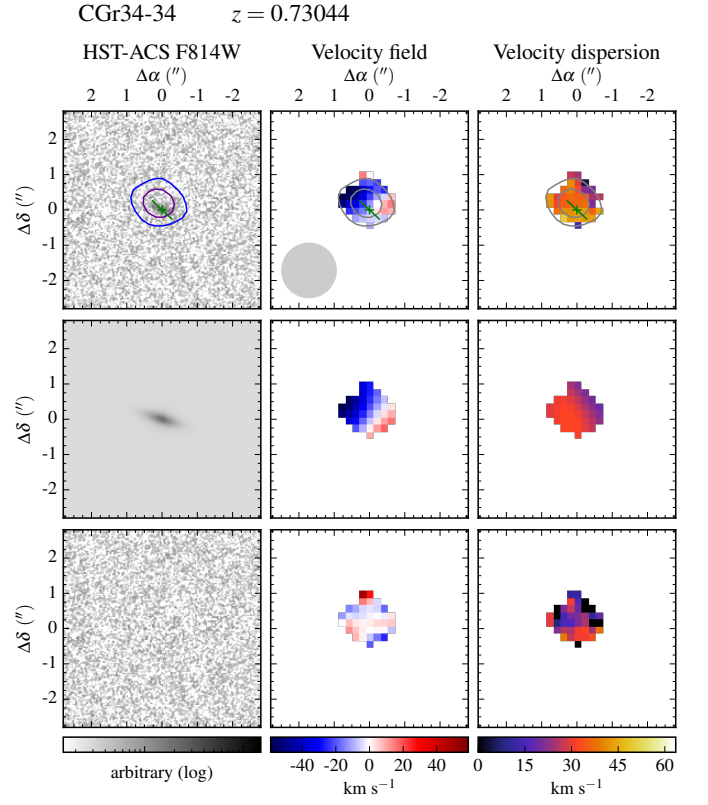


Fig. A.34: Morpho-kinematics maps for galaxy CGr34-34. See caption of Fig. A.1 for the description of figure.

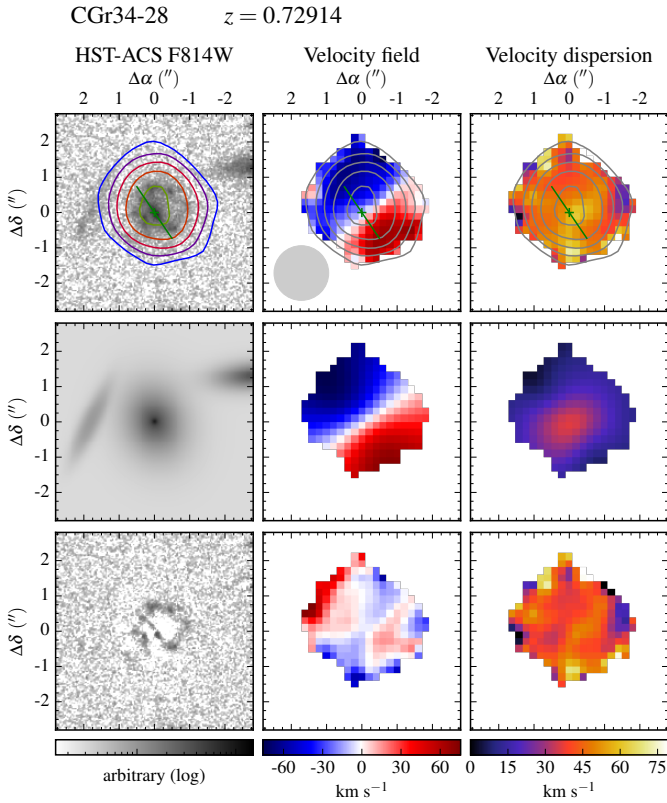


Fig. A.33: Morpho-kinematics maps for galaxy CGr34-28. See caption of Fig. A.1 for the description of figure.

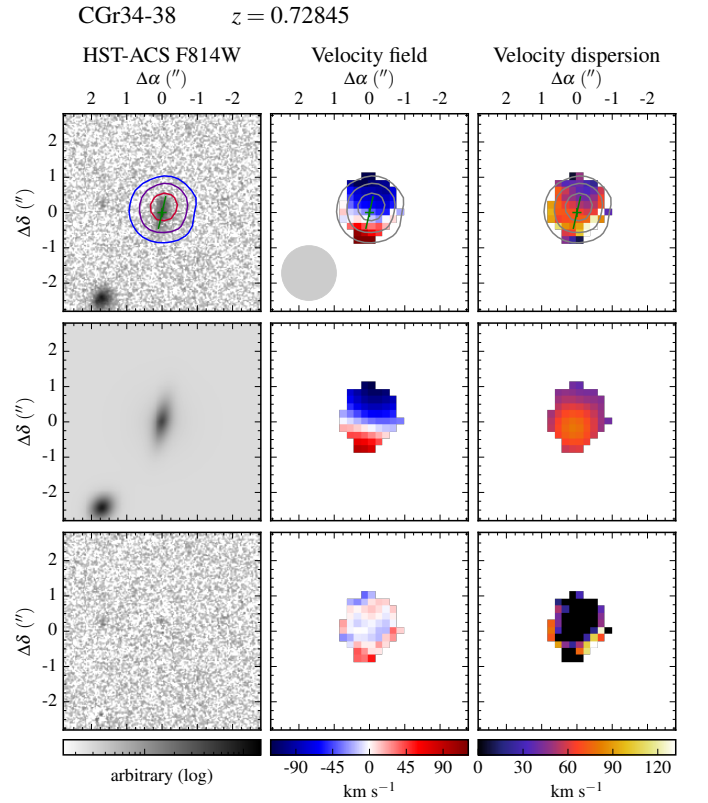


Fig. A.35: Morpho-kinematics maps for galaxy CGr34-38. See caption of Fig. A.1 for the description of figure.

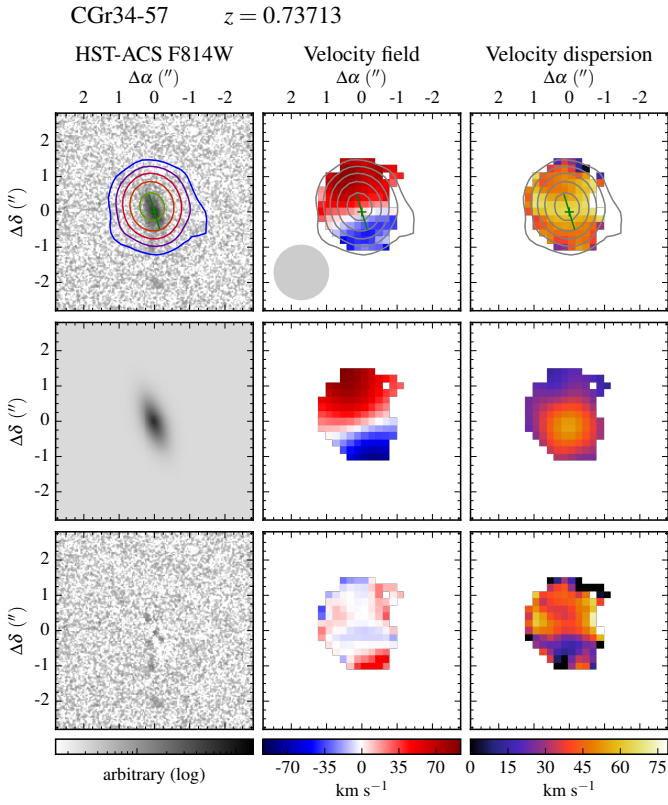


Fig. A.36: Morpho-kinematics maps for galaxy CGr34-57. See caption of Fig. A.1 for the description of figure.

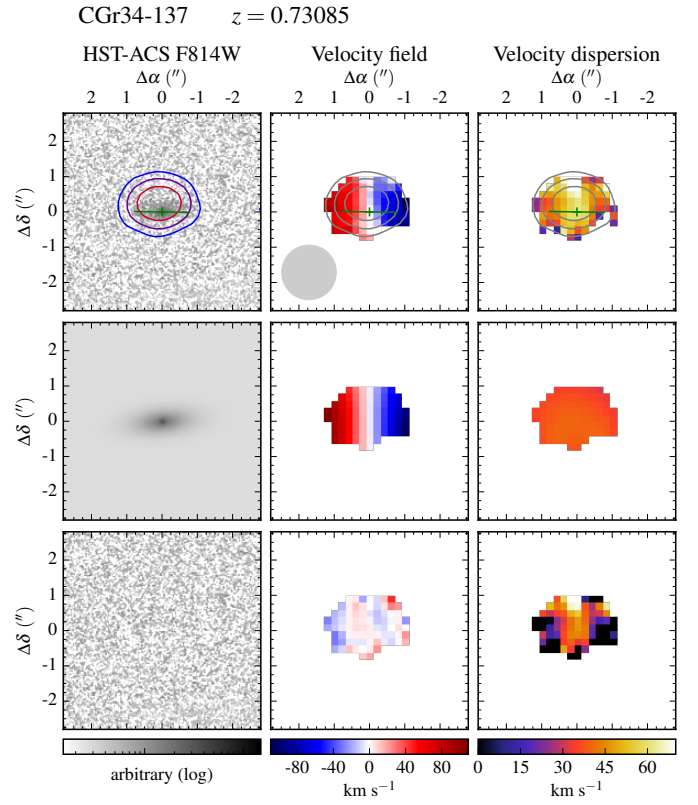


Fig. A.38: Morpho-kinematics maps for galaxy CGr34-137. See caption of Fig. A.1 for the description of figure.

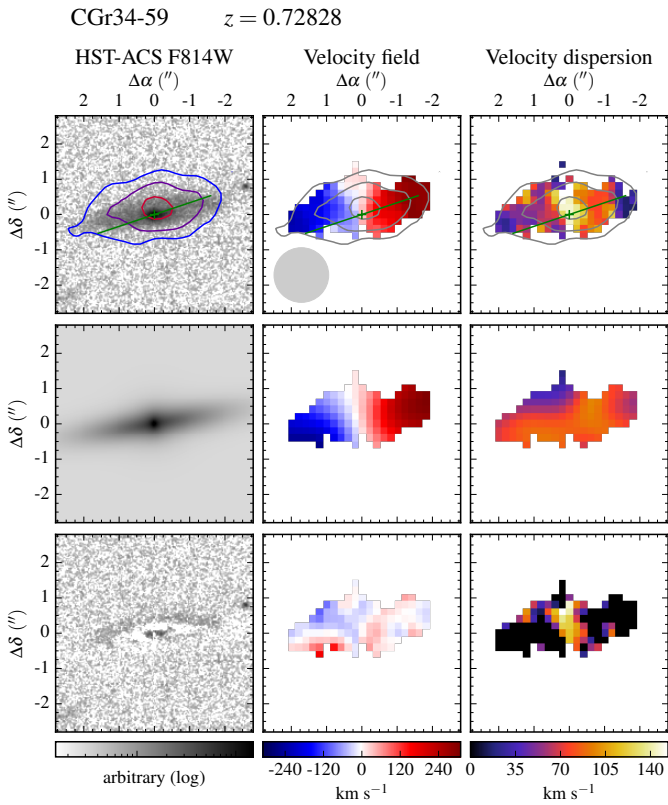


Fig. A.37: Morpho-kinematics maps for galaxy CGr34-59. See caption of Fig. A.1 for the description of figure.

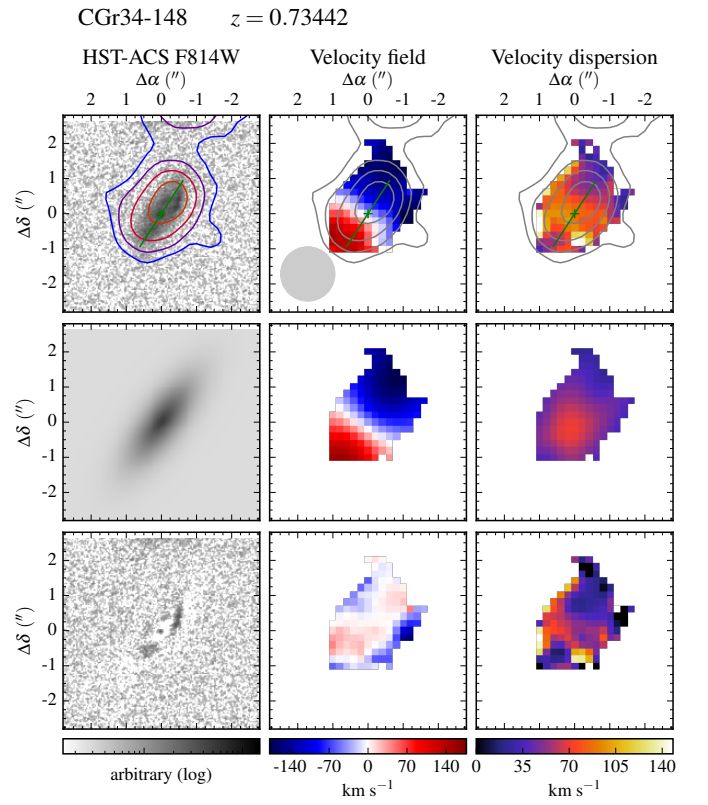


Fig. A.39: Morpho-kinematics maps for galaxy CGr34-148. See caption of Fig. A.1 for the description of figure.

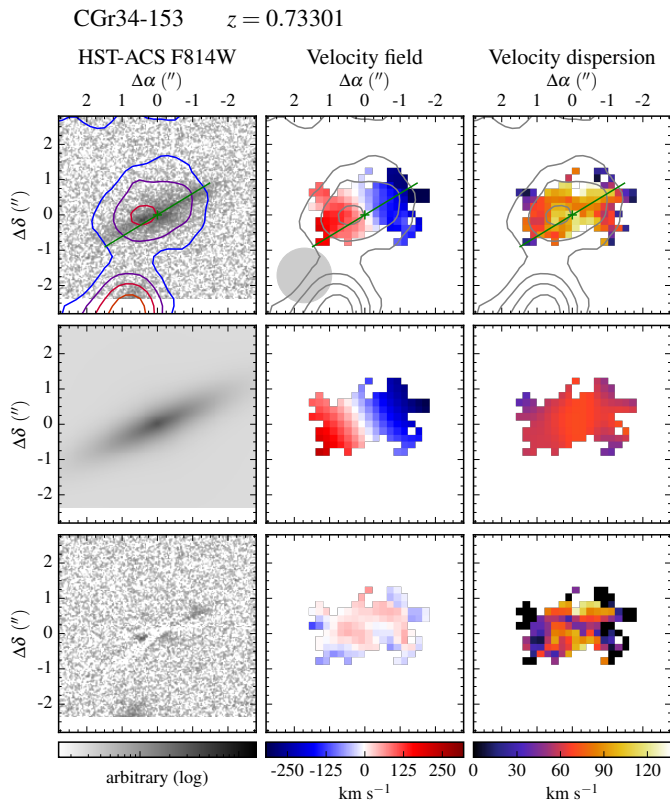


Fig. A.40: Morpho-kinematics maps for galaxy CGr34-153. See caption of Fig. A.1 for the description of figure.

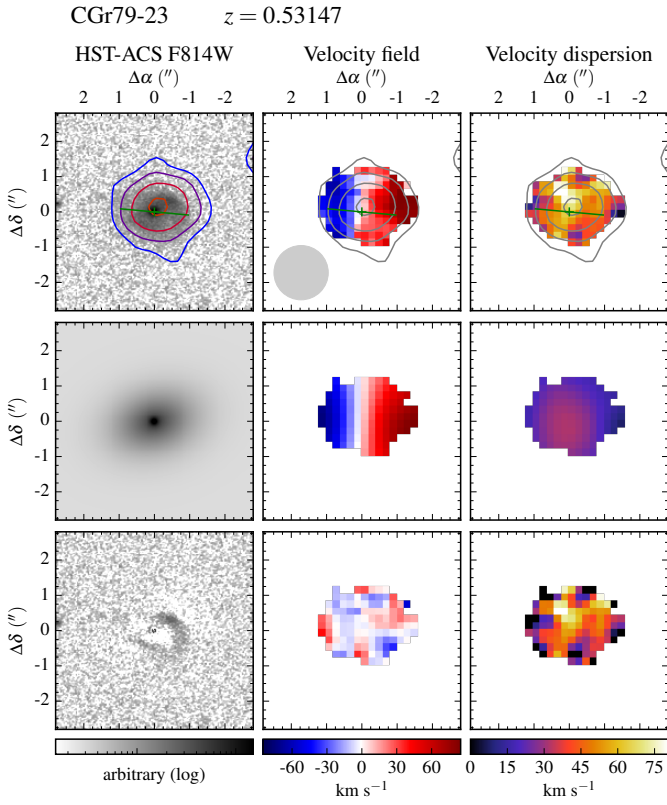


Fig. A.41: Morpho-kinematics maps for galaxy CGr79-23. See caption of Fig. A.1 for the description of figure.

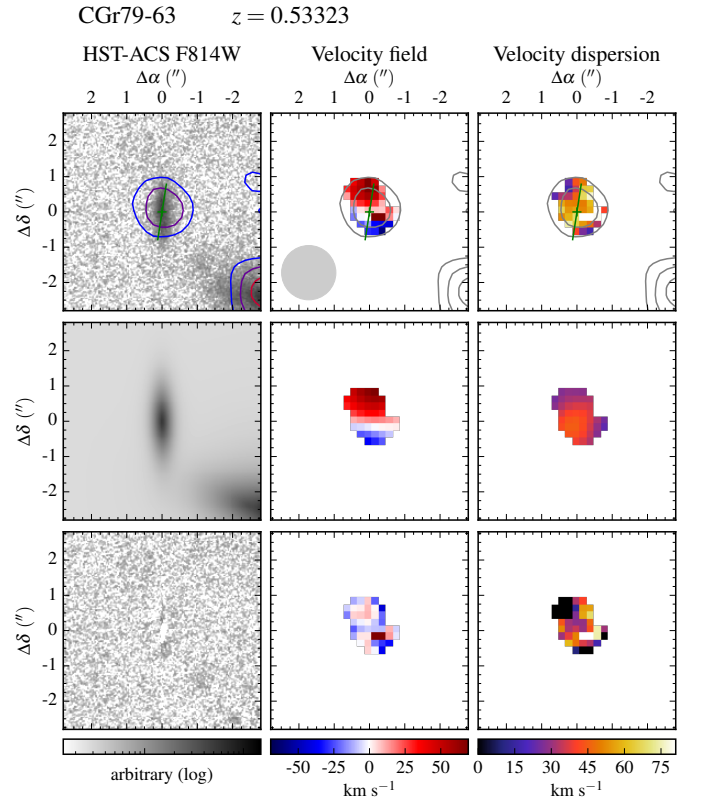


Fig. A.43: Morpho-kinematics maps for galaxy CGr79-63. See caption of Fig. A.1 for the description of figure.

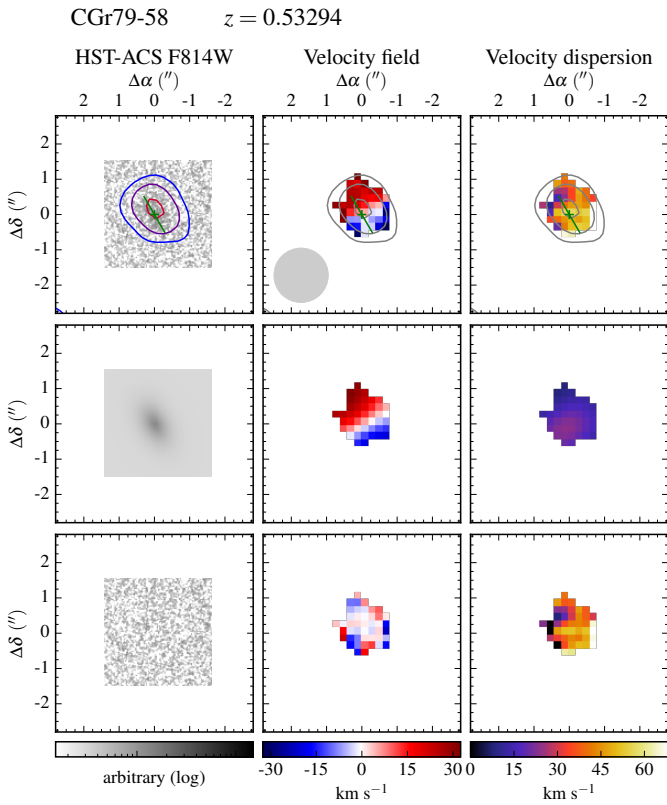


Fig. A.42: Morpho-kinematics maps for galaxy CGr79-58. See caption of Fig. A.1 for the description of figure.

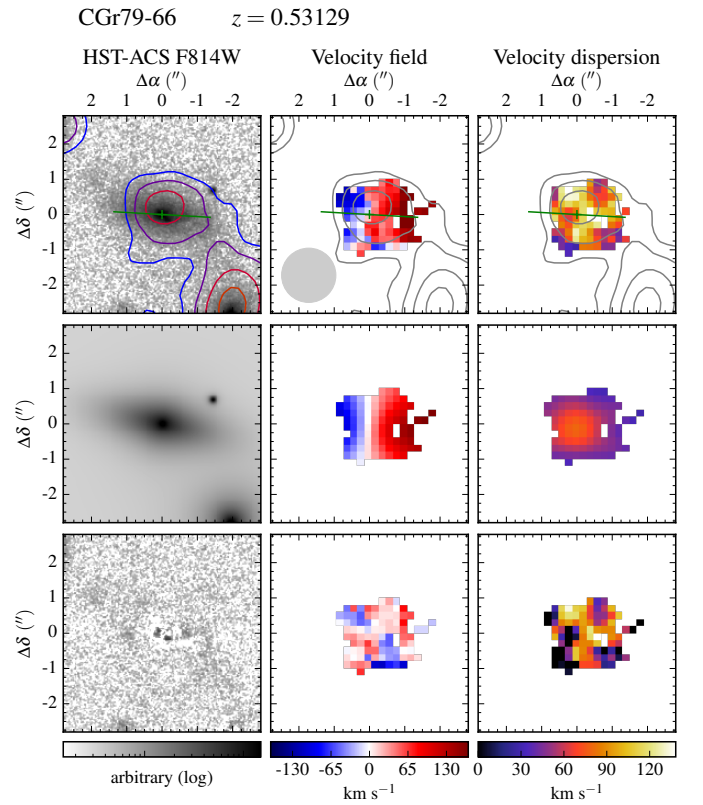


Fig. A.44: Morpho-kinematics maps for galaxy CGr79-66. See caption of Fig. A.1 for the description of figure.

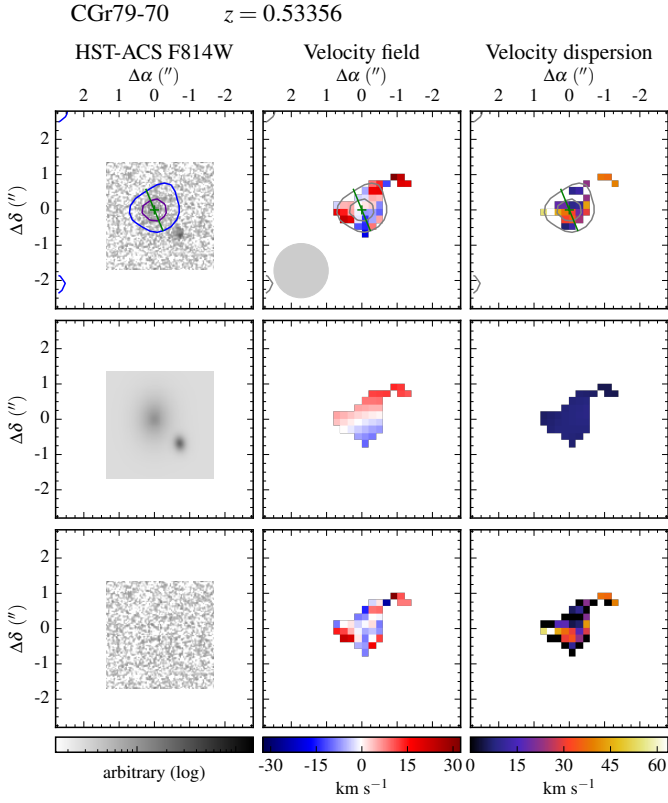


Fig. A.45: Morpho-kinematics maps for galaxy CGr79-70. See caption of Fig. A.1 for the description of figure.

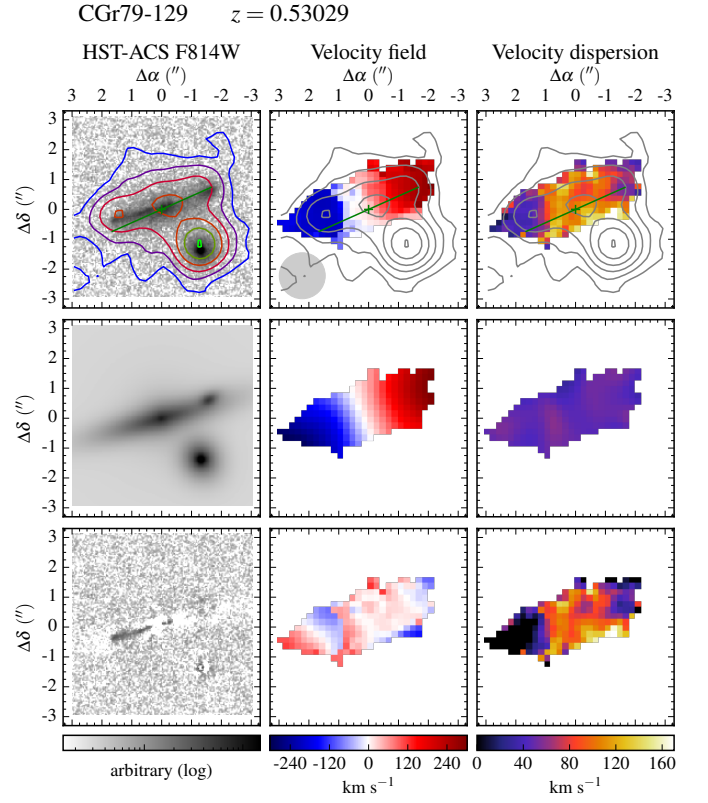


Fig. A.47: Morpho-kinematics maps for galaxy CGr79-129. See caption of Fig. A.1 for the description of figure.

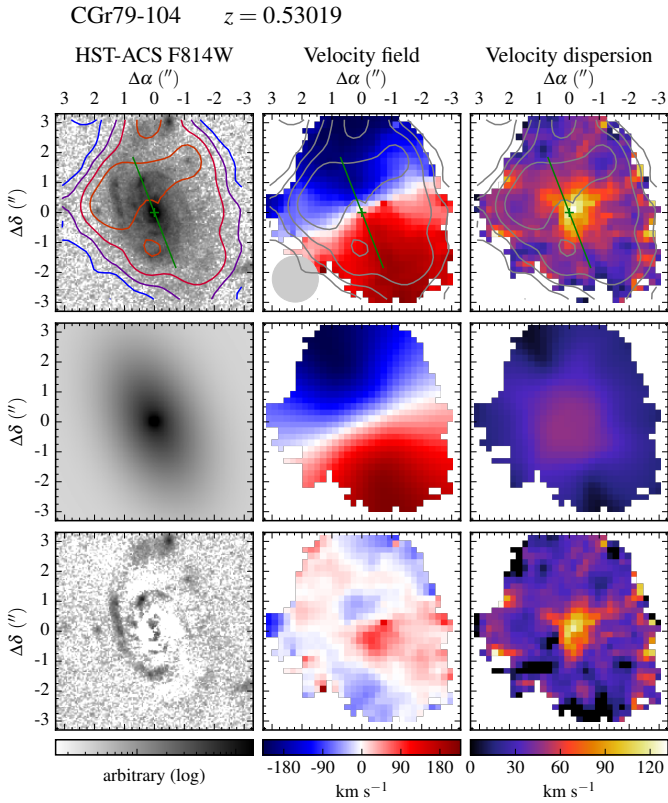


Fig. A.46: Morpho-kinematics maps for galaxy CGr79-104. See caption of Fig. A.1 for the description of figure.

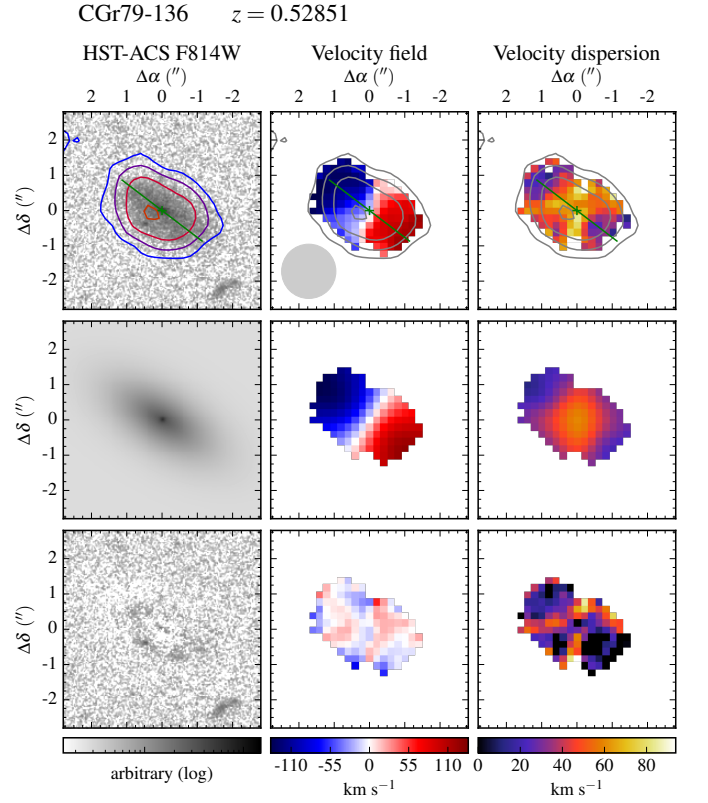


Fig. A.48: Morpho-kinematics maps for galaxy CGr79-136. See caption of Fig. A.1 for the description of figure.

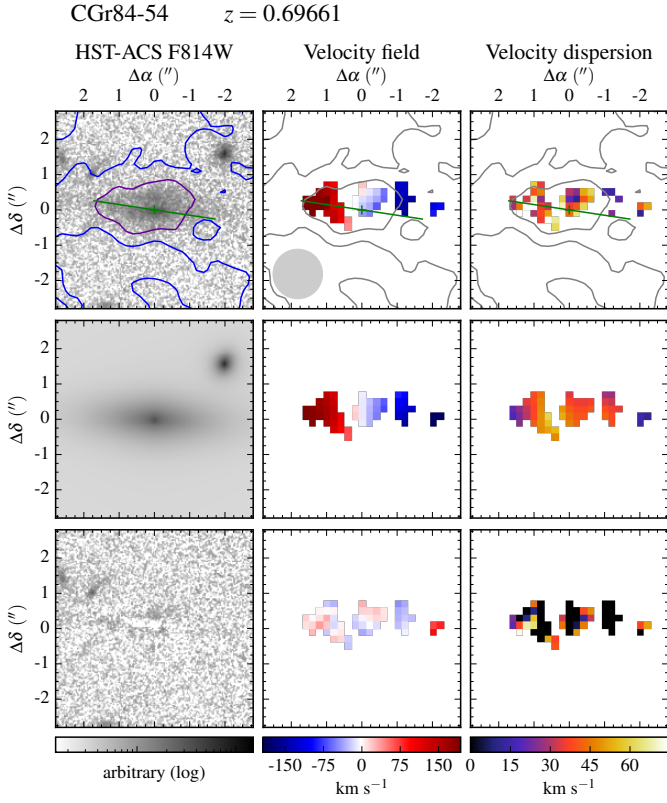


Fig. A.49: Morpho-kinematics maps for galaxy CGr84-54. See caption of Fig. A.1 for the description of figure.

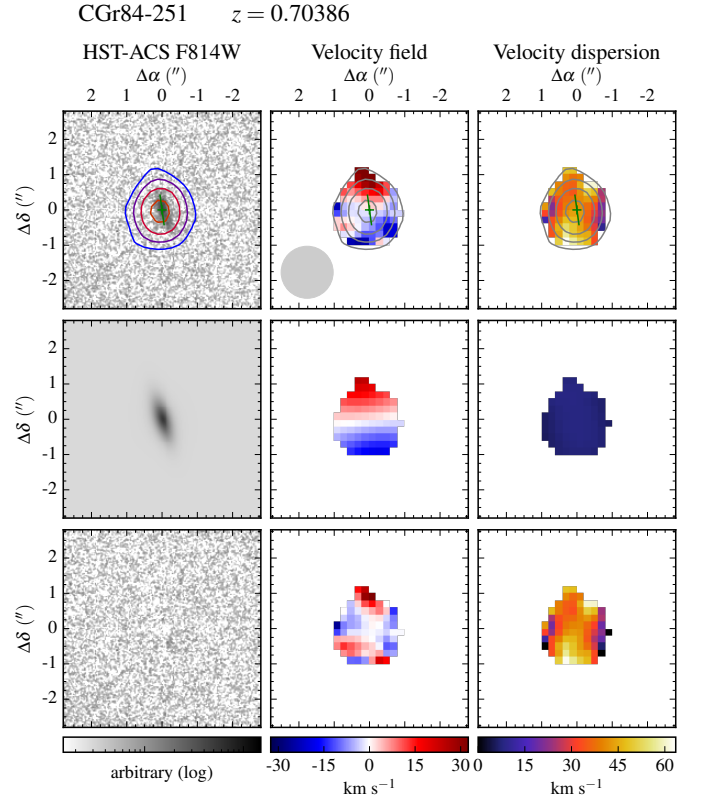


Fig. A.51: Morpho-kinematics maps for galaxy CGr84-251. See caption of Fig. A.1 for the description of figure.

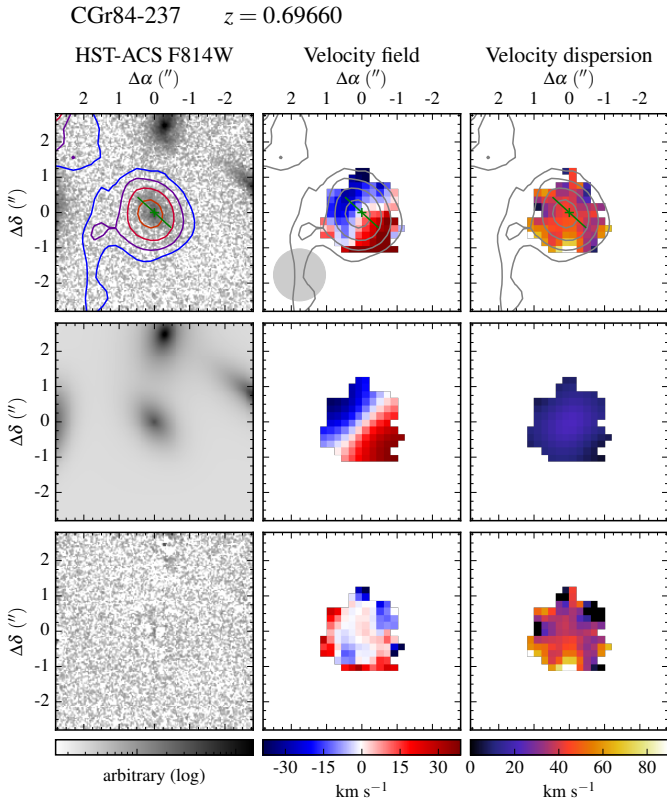


Fig. A.50: Morpho-kinematics maps for galaxy CGr84-237. See caption of Fig. A.1 for the description of figure.

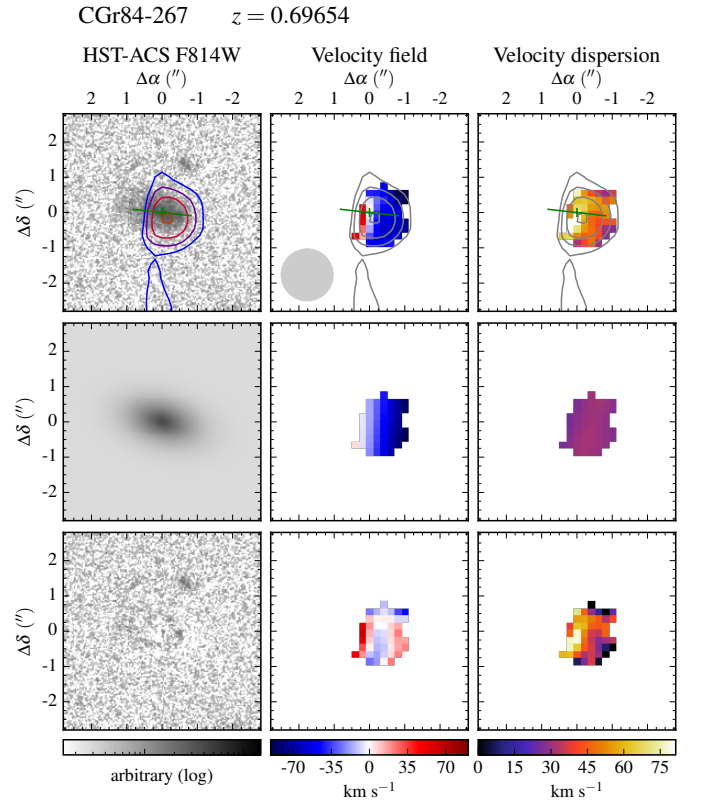


Fig. A.52: Morpho-kinematics maps for galaxy CGr84-267. See caption of Fig. A.1 for the description of figure.

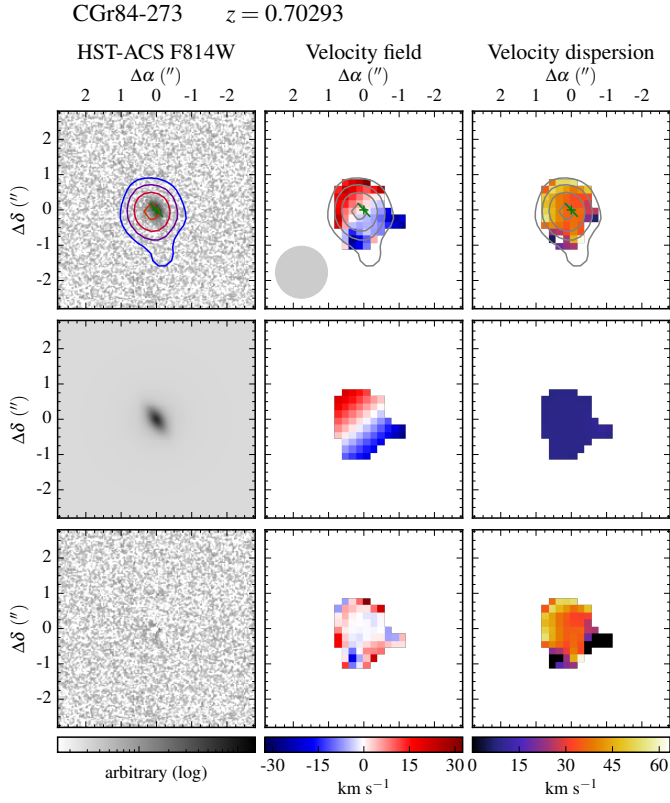


Fig. A.53: Morpho-kinematics maps for galaxy CGr84-273. See caption of Fig. A.1 for the description of figure.

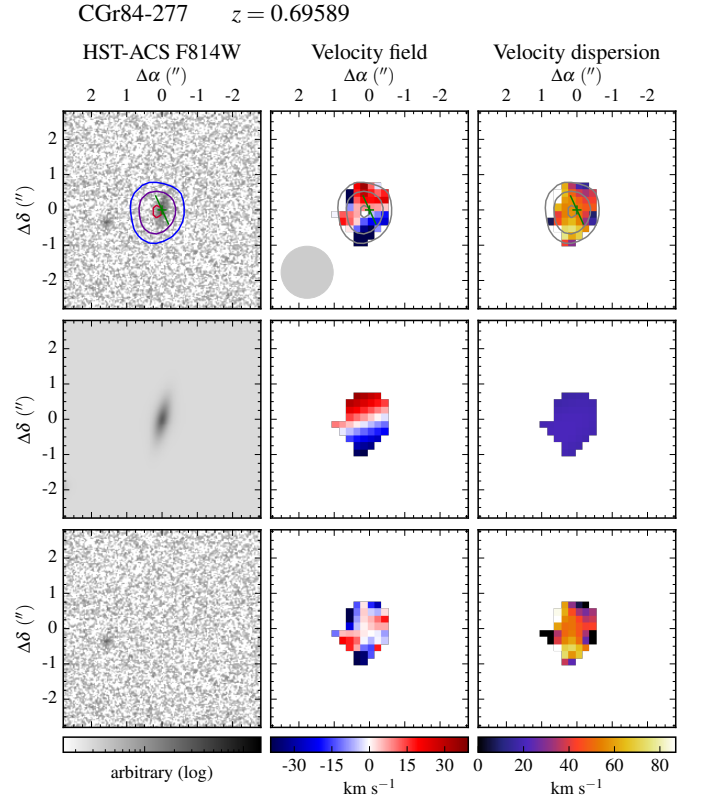


Fig. A.55: Morpho-kinematics maps for galaxy CGr84-277. See caption of Fig. A.1 for the description of figure.

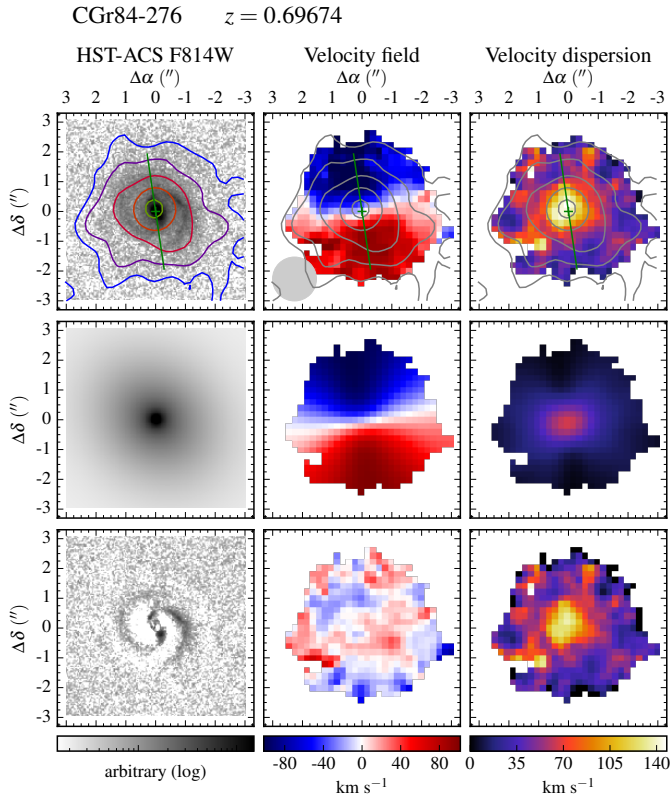


Fig. A.54: Morpho-kinematics maps for galaxy CGr84-276. See caption of Fig. A.1 for the description of figure.

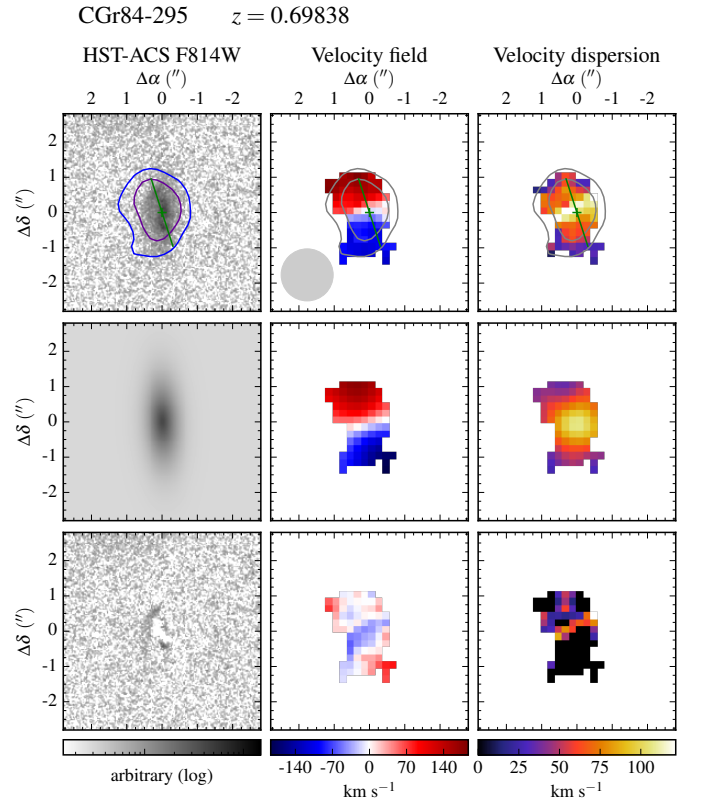


Fig. A.56: Morpho-kinematics maps for galaxy CGr84-295. See caption of Fig. A.1 for the description of figure.

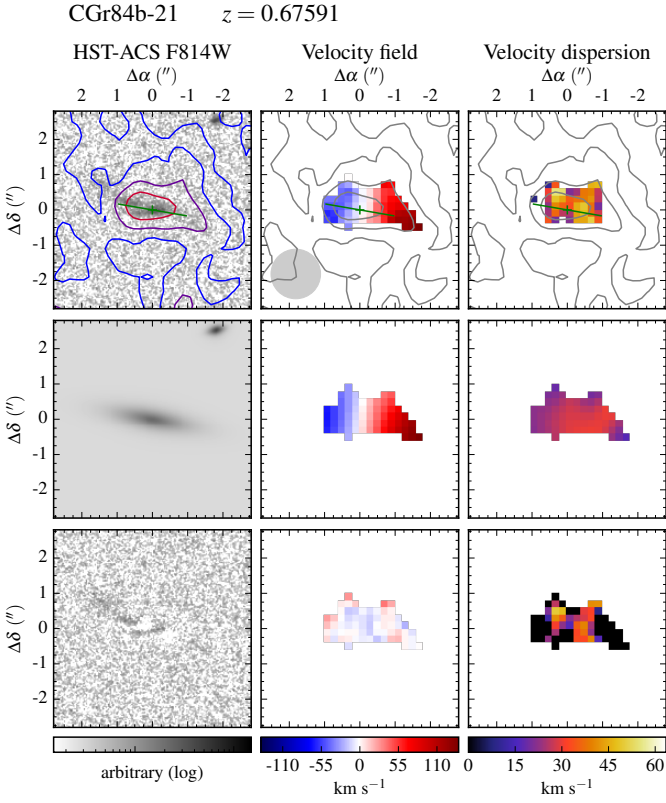


Fig. A.57: Morpho-kinematics maps for galaxy CGr84b-21. See caption of Fig. A.1 for the description of figure.

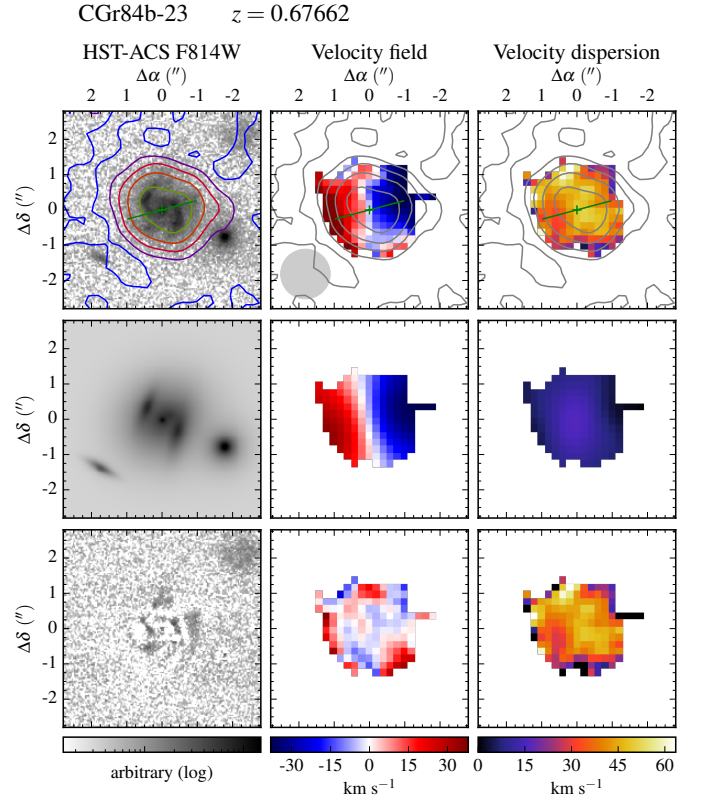


Fig. A.59: Morpho-kinematics maps for galaxy CGr84b-23. See caption of Fig. A.1 for the description of figure.

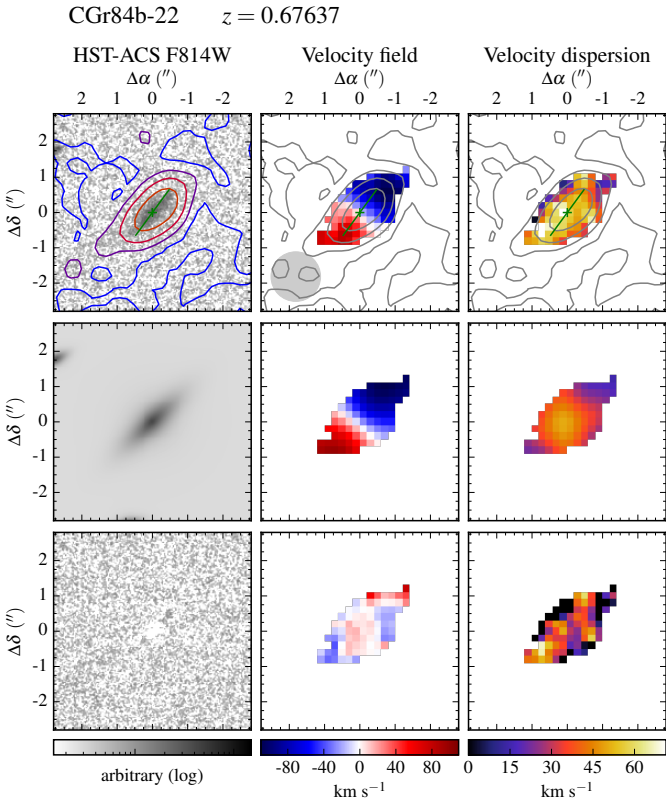


Fig. A.58: Morpho-kinematics maps for galaxy CGr84b-22. See caption of Fig. A.1 for the description of figure.

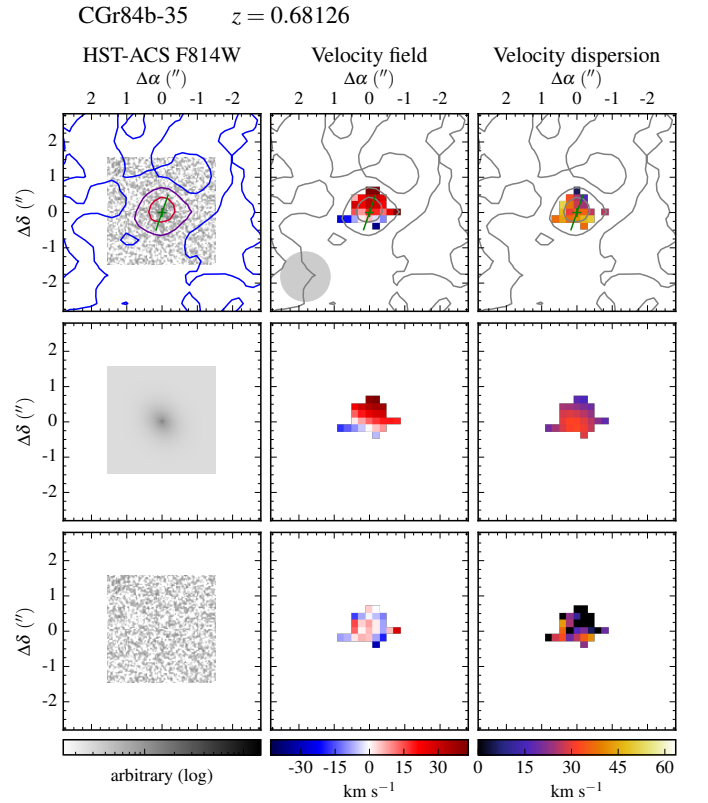


Fig. A.60: Morpho-kinematics maps for galaxy CGr84b-35. See caption of Fig. A.1 for the description of figure.

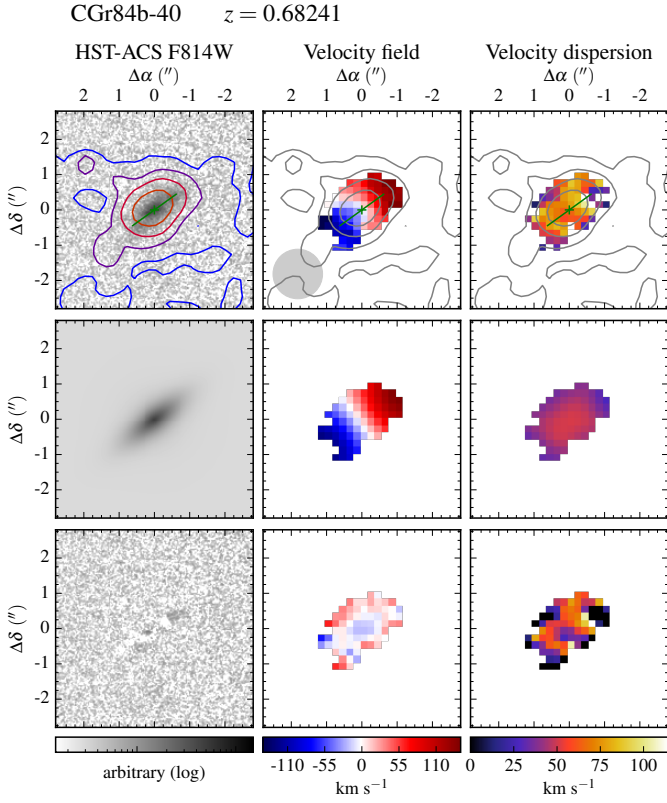


Fig. A.61: Morpho-kinematics maps for galaxy CGr84b-40. See caption of Fig. A.1 for the description of figure.

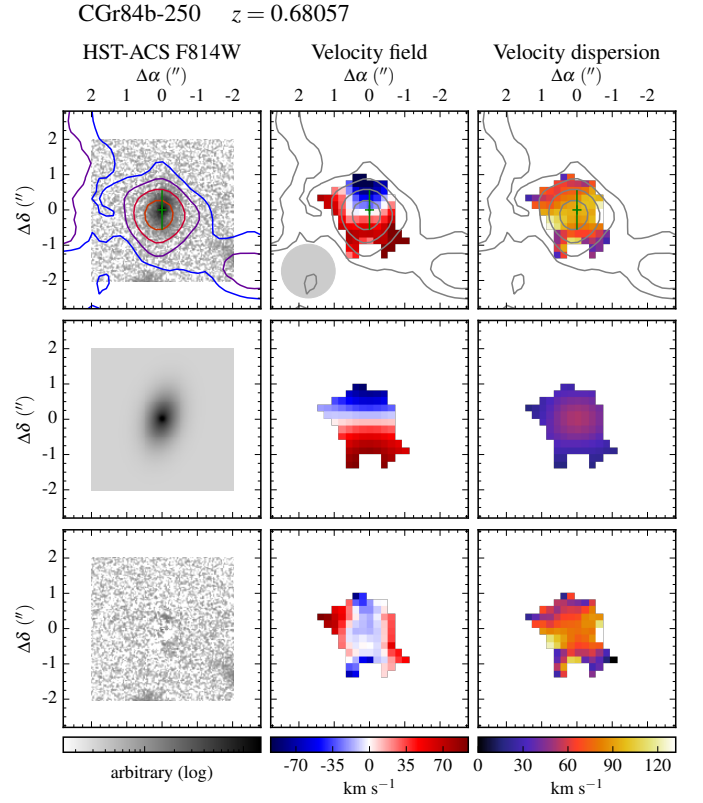


Fig. A.63: Morpho-kinematics maps for galaxy CGr84b-250. See caption of Fig. A.1 for the description of figure.

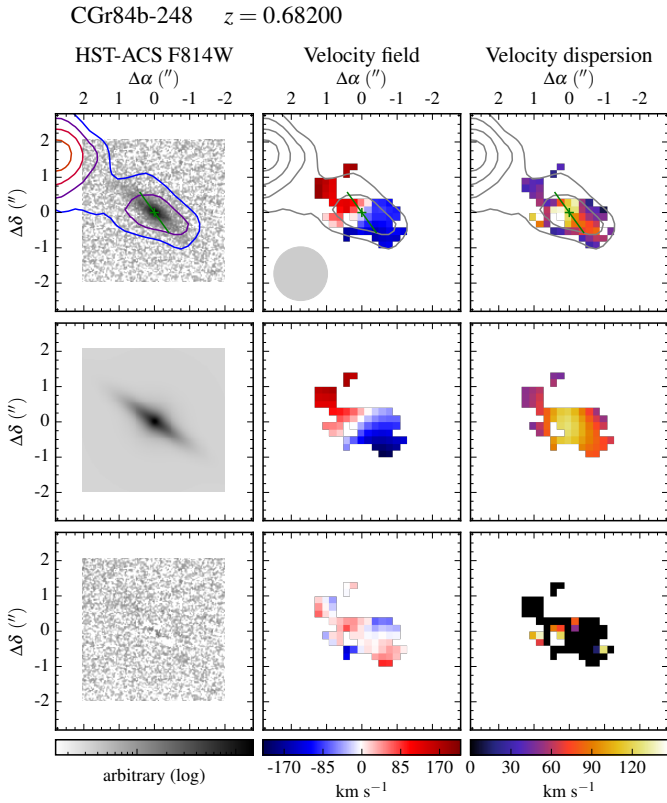


Fig. A.62: Morpho-kinematics maps for galaxy CGr84b-248. See caption of Fig. A.1 for the description of figure.

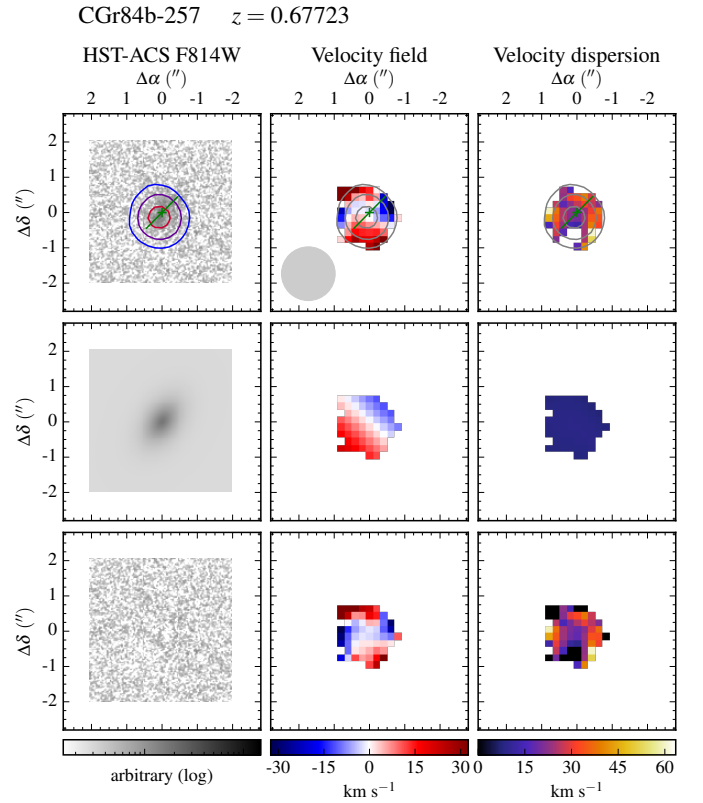


Fig. A.64: Morpho-kinematics maps for galaxy CGr84b-257. See caption of Fig. A.1 for the description of figure.

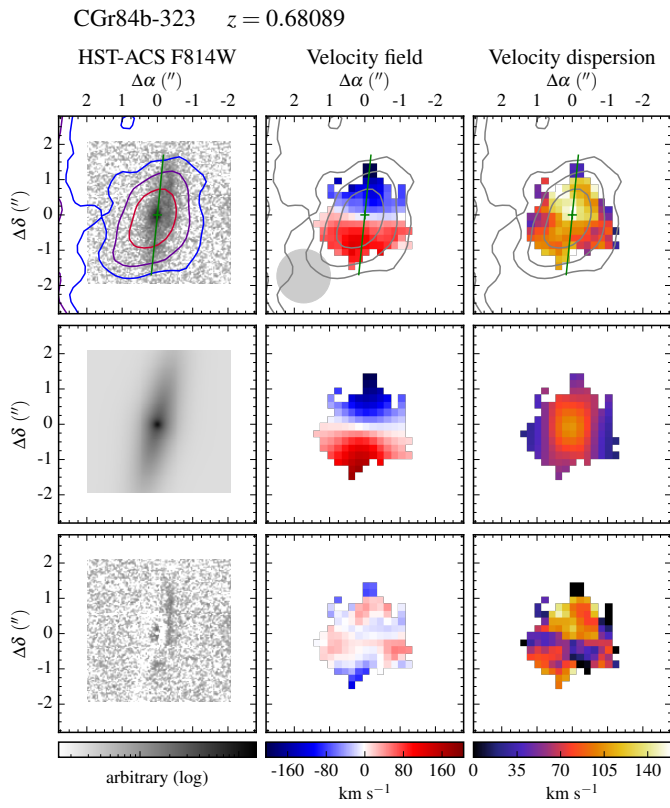


Fig. A.65: Morpho-kinematics maps for galaxy CGr84b-323. See caption of Fig. A.1 for the description of figure.

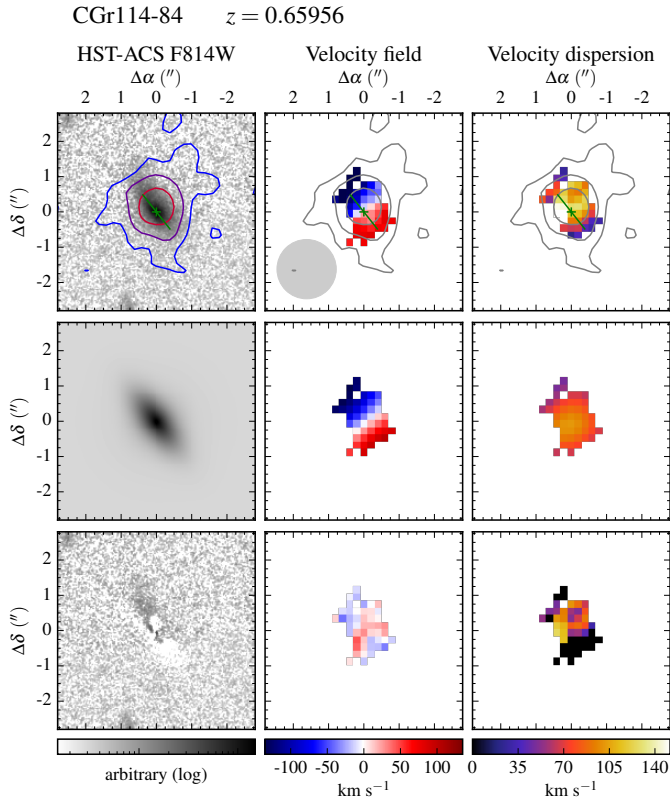


Fig. A.66: Morpho-kinematics maps for galaxy CGr114-84. See caption of Fig. A.1 for the description of figure.

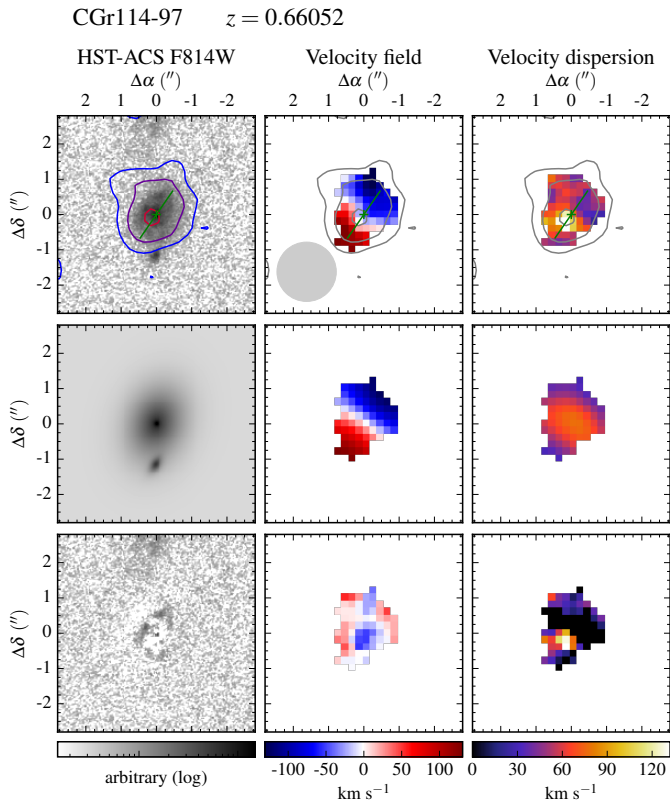


Fig. A.67: Morpho-kinematics maps for galaxy CGr114-97. See caption of Fig. A.1 for the description of figure.

Appendix A.2: Galaxies with kinematics biased by an AGN

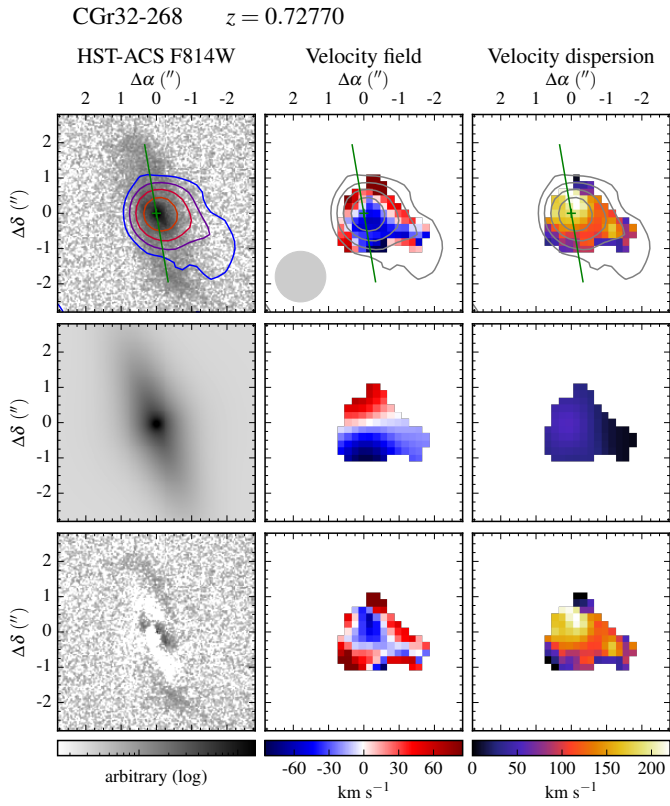


Fig. A.68: Morpho-kinematics maps for galaxy CGr32-268. See caption of Fig. A.1 for the description of figure.

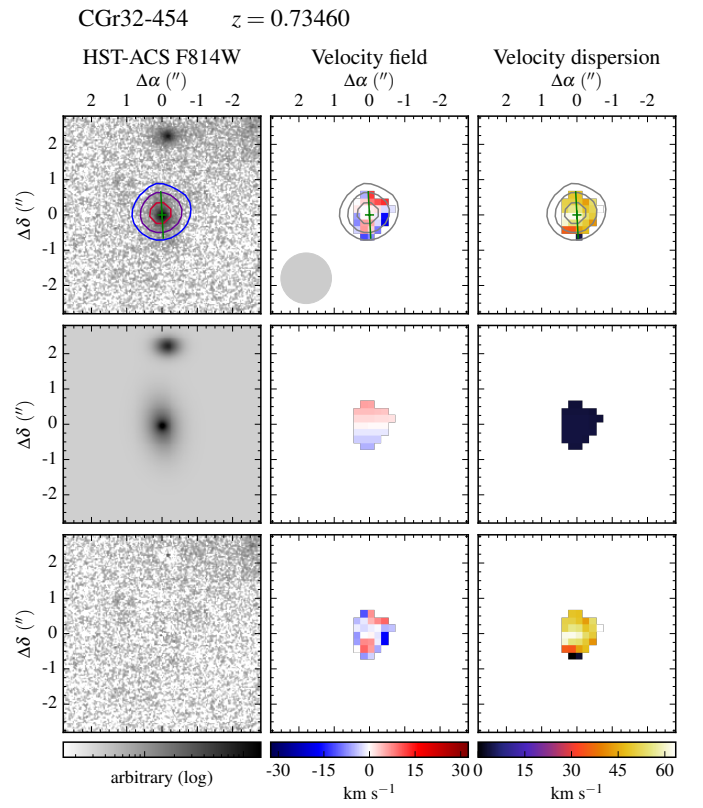


Fig. A.69: Morpho-kinematics maps for galaxy CGr32-454. See caption of Fig. A.1 for the description of figure.

Appendix A.3: Galaxies with a dominant bulge within the effective radius

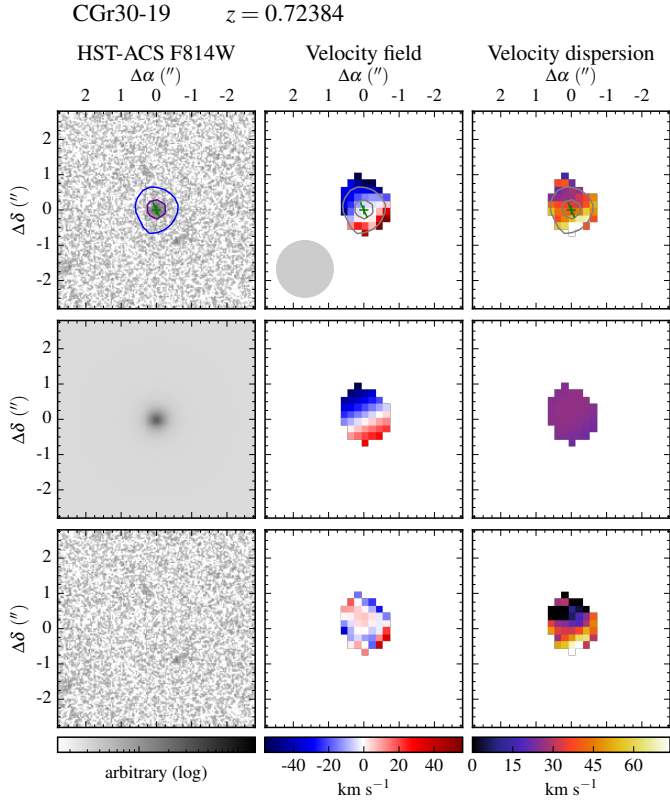


Fig. A.70: Morpho-kinematics maps for galaxy CGr30-19. See caption of Fig. A.1 for the description of figure.

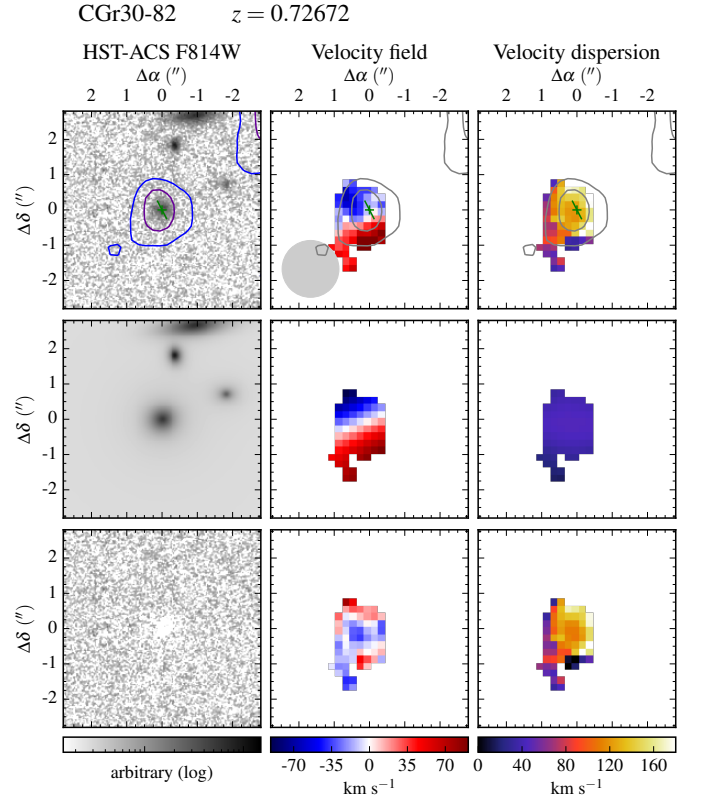


Fig. A.71: Morpho-kinematics maps for galaxy CGr30-82. See caption of Fig. A.1 for the description of figure.

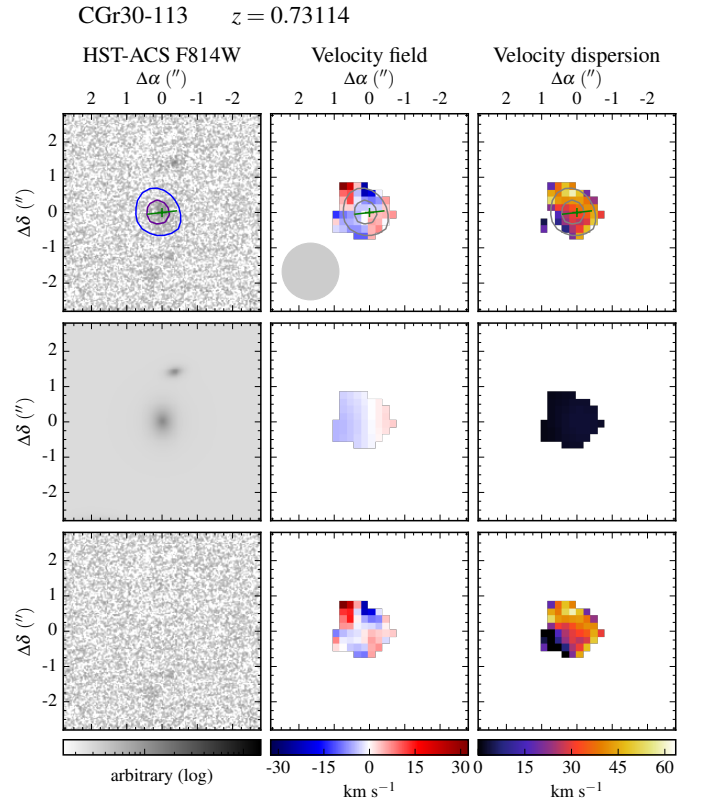


Fig. A.72: Morpho-kinematics maps for galaxy CGr30-113. See caption of Fig. A.1 for the description of figure.

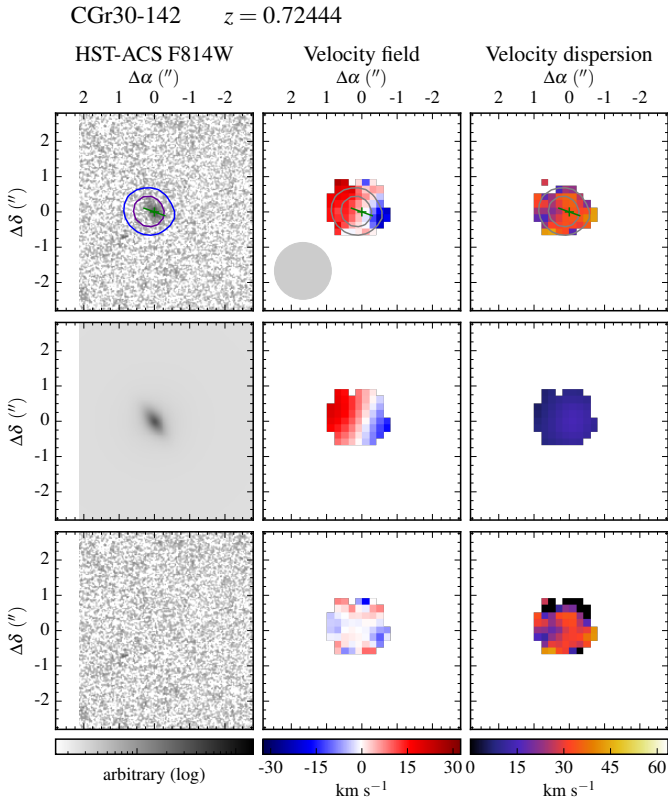


Fig. A.73: Morpho-kinematics maps for galaxy CGr30-142. See caption of Fig. A.1 for the description of figure.

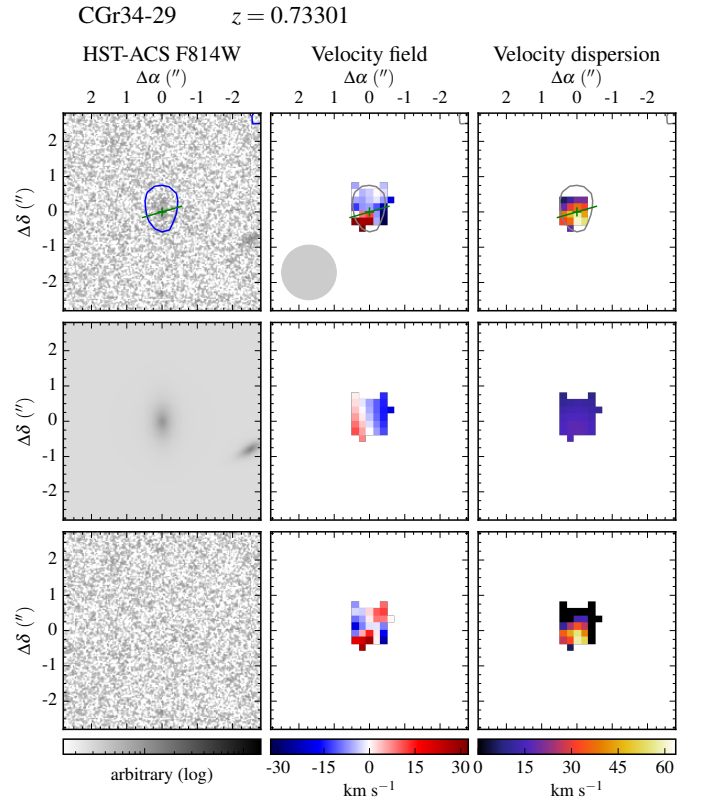


Fig. A.75: Morpho-kinematics maps for galaxy CGr34-29. See caption of Fig. A.1 for the description of figure.

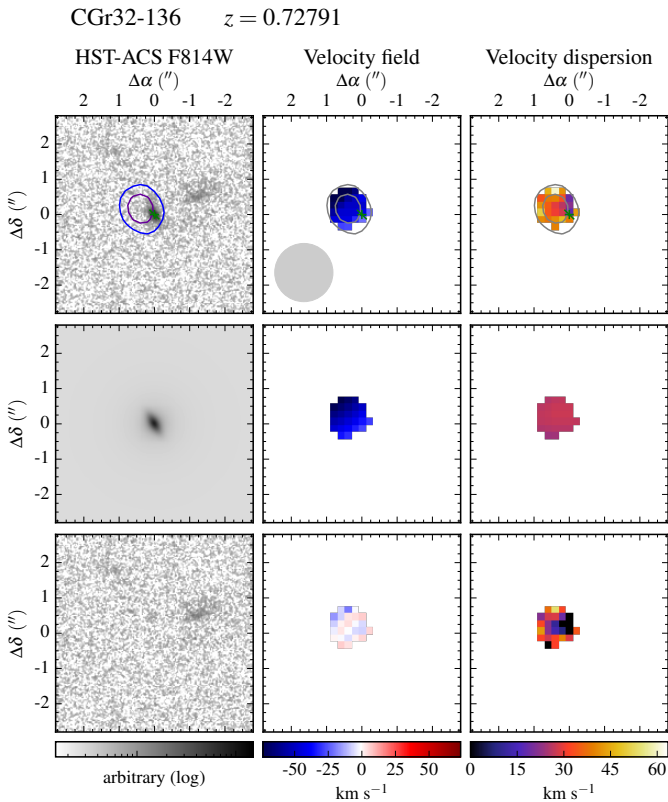


Fig. A.74: Morpho-kinematics maps for galaxy CGr32-136. See caption of Fig. A.1 for the description of figure.

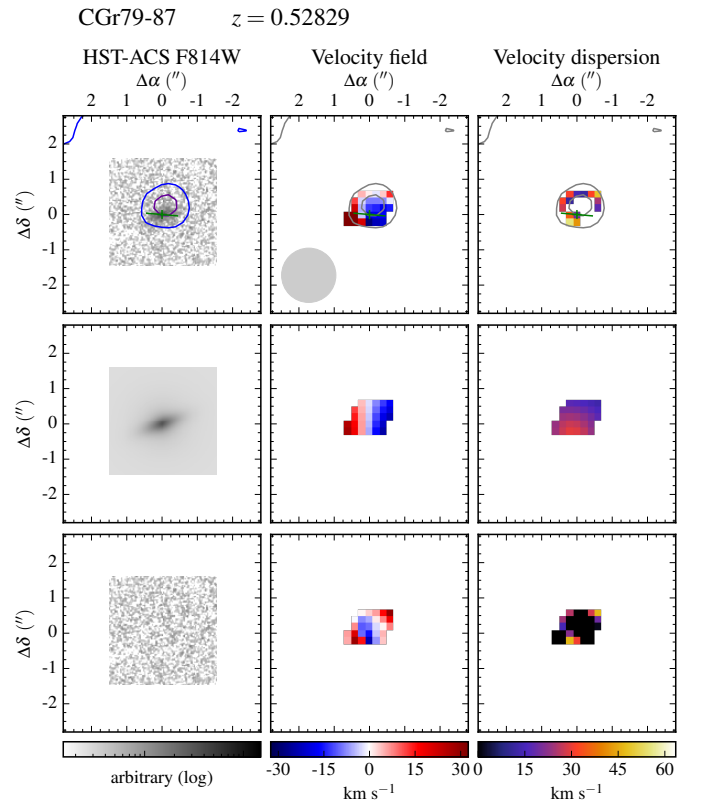


Fig. A.76: Morpho-kinematics maps for galaxy CGr79-87. See caption of Fig. A.1 for the description of figure.

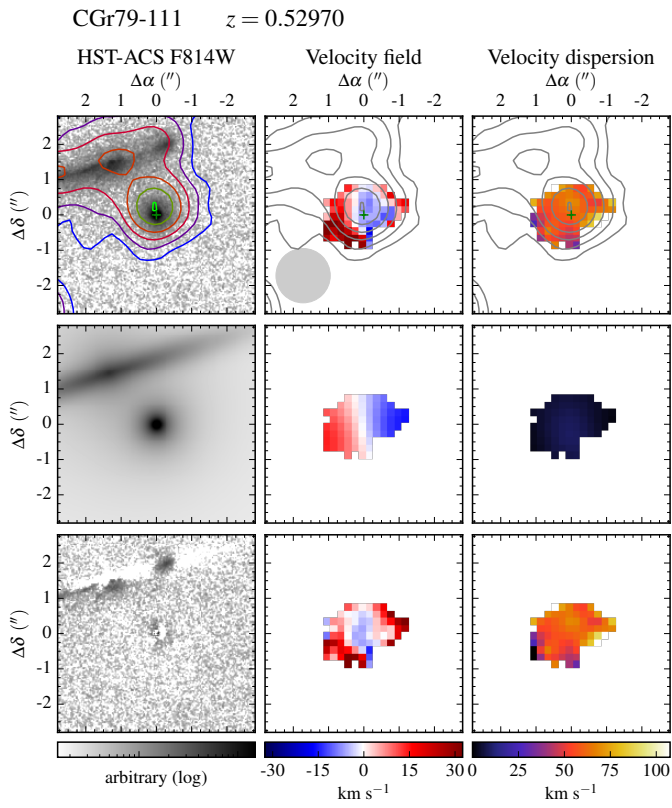


Fig. A.77: Morpho-kinematics maps for galaxy CGr79-111. See caption of Fig. A.1 for the description of figure.

**Appendix B: Tables: Physical and
morpho-kinematic properties of the kinematics
sample**

Table B.1: Observational information, morphological and kinematic model parameters for the 77 galaxies with $S/N \geq 40$ and $R_{eff}/FWHM \geq 0.5$.

Gr ID	ID	z	R.A. [J2000]	Dec. [J2000]	FWHM ["]	[O II] flux [10^{-20} erg s^{-1} cm^{-2}]	b/a	PA _m [°]	R _d [kpc]	PA _k [°]	r _t [kpc]	V _t [km s^{-1}]
(1)	(2)	(3)	(4)	(5)	(6)	(7)	(8)	(9)	(10)	(11)	(12)	(13)
CGr28	41	0.52975	150°08'12.0"	2°03'33.1"	0.654	24421 ± 94	0.86 ± 0.01	175 ± 3	2.10 ± 0.04	303 ± 1	1.3 ± 0.1	170 ± 2
CGr28	85	0.52817	150°08'37.3"	2°03'49.0"	0.654	17617 ± 115	0.59 ± 0.01	96 ± 0	3.72 ± 0.01	99 ± 1	1.3 ± 0.1	232 ± 2
CGr28	145	0.52450	150°08'55.5"	2°03'38.1"	0.654	5219 ± 74	0.42 ± 0.01	151 ± 1	2.81 ± 0.02	144 ± 5	5.5 ± 1.5	155 ± 22
CGr30	69	0.72554	150°08'37.3"	2°03'49.0"	0.700	341 ± 6	0.19 ± 0.03	16 ± 2	1.79 ± 0.19	202 ± 11	1.4 ± 0.1	60 ± 7
CGr30	71	0.72460	150°08'55.5"	2°03'38.1"	0.700	5461 ± 34	0.50 ± 0.01	150 ± 1	2.95 ± 0.04	353 ± 1	3.5 ± 0.6	215 ± 5
CGr30	105	0.72693	150°08'37.0"	2°03'53.1"	0.700	2552 ± 17	0.72 ± 0.01	81 ± 1	2.48 ± 0.01	266 ± 1	1.6 ± 1.6	203 ± 2
CGr30	110	0.72656	150°08'43.2"	2°03'54.2"	0.700	1000 ± 10	0.73 ± 0.01	102 ± 2	2.36 ± 0.02	293 ± 5	5.4 ± 2.8	69 ± 22
CGr30	137	0.73015	150°08'28.9"	2°04'06.1"	0.700	2170 ± 15	0.16 ± 0.01	121 ± 1	3.78 ± 0.06	298 ± 2	9.9 ± 1.2	243 ± 14
CGr30	158	0.72257	150°07'59.7"	2°04'14.9"	0.700	1542 ± 25	0.55 ± 0.01	65 ± 1	1.65 ± 0.02	54 ± 3	5.2 ± 0.9	240 ± 19
CGr30	170	0.72622	150°08'19.4"	2°04'10.6"	0.700	4314 ± 20	0.74 ± 0.01	41 ± 1	3.32 ± 0.03	230 ± 1	1.4 ± 0.1	165 ± 1
CGr30	174	0.72867	150°08'24.5"	2°04'15.3"	0.700	842 ± 14	0.70 ± 0.01	23 ± 1	2.39 ± 0.02	185 ± 4	1.5 ± 0.1	169 ± 5
CGr30	185	0.72559	150°08'05.2"	2°04'20.7"	0.700	413 ± 9	0.89 ± 0.01	25 ± 5	2.46 ± 0.05	42 ± 10	14.3 ± 1 × 10 ⁸	381 ± 3 × 10 ⁹
CGr30	186	0.72509	150°08'18.8"	2°04'17.1"	0.700	17436 ± 30	0.84 ± 0.01	92 ± 2	4.79 ± 0.05	259 ± 1	1.4 ± 0.1	218 ± 0
CGr30	188	0.72388	150°08'50.5"	2°04'26.7"	0.700	1781 ± 11	0.55 ± 0.01	43 ± 2	1.78 ± 0.06	226 ± 3	1.4 ± 0.1	63 ± 3
CGr30	189	0.72059	150°08'27.6"	2°04'28.1"	0.700	4605 ± 13	0.82 ± 0.02	136 ± 6	2.40 ± 0.09	227 ± 2	7.1 ± 0.7	58 ± 4
CGr30	193	0.72686	150°08'07.0"	2°04'29.1"	0.700	1219 ± 13	0.39 ± 0.01	154 ± 1	1.83 ± 0.03	154 ± 3	1.5 ± 0.1	134 ± 4
CGr30	195	0.72677	150°08'12.4"	2°04'27.0"	0.700	1783 ± 15	0.25 ± 0.01	44 ± 1	3.24 ± 0.06	48 ± 2	1.5 ± 0.1	159 ± 4
CGr30	196	0.72279	150°08'07.4"	2°04'32.4"	0.700	5532 ± 36	0.88 ± 0.01	74 ± 3	1.75 ± 0.01	266 ± 2	6.5 ± 0.3	222 ± 6
CGr32	10	0.71685	150°08'12.0"	2°03'33.1"	0.722	12461 ± 62	0.46 ± 0.01	104 ± 1	4.06 ± 0.03	108 ± 1	1.4 ± 0.1	179 ± 2
CGr32	36	0.72580	150°08'37.3"	2°03'49.0"	0.722	5981 ± 60	0.39 ± 0.01	87 ± 1	4.89 ± 0.03	96 ± 2	9.9 ± 0.7	364 ± 16
CGr32	109	0.72863	150°08'55.5"	2°03'38.1"	0.722	8152 ± 42	0.30 ± 0.01	7 ± 1	2.44 ± 0.02	210 ± 1	1.5 ± 0.1	287 ± 3
CGr32	112	0.72891	150°08'53.3"	2°03'45.4"	0.722	5353 ± 27	0.56 ± 0.02	57 ± 2	1.94 ± 0.06	215 ± 2	22.5 ± 0.1	169 ± 6
CGr32	132	0.73408	150°08'37.0"	2°03'53.1"	0.624	7683 ± 32	0.53 ± 0.01	99 ± 1	1.99 ± 0.04	284 ± 1	4.2 ± 0.4	112 ± 4
CGr32	183	0.73395	150°08'19.6"	2°03'59.5"	0.624	1206 ± 19	0.62 ± 0.01	74 ± 1	1.65 ± 0.03	220 ± 7	22.6 ± 0.1	392 ± 48
CGr32	198	0.72208	150°08'28.9"	2°04'06.1"	0.624	4461 ± 37	0.23 ± 0.01	53 ± 1	3.08 ± 0.03	226 ± 1	8.8 ± 0.4	344 ± 8
CGr32	295	0.73347	150°07'59.7"	2°04'14.9"	0.624	4412 ± 25	0.44 ± 0.01	22 ± 1	2.93 ± 0.06	21 ± 2	7.6 ± 0.6	113 ± 6
CGr32	325	0.73652	150°08'19.4"	2°04'10.6"	0.596	18088 ± 46	0.88 ± 0.01	91 ± 3	2.86 ± 0.02	67 ± 1	1.3 ± 0.1	192 ± 1
CGr32	340	0.73653	150°08'24.5"	2°04'15.3"	0.596	3095 ± 28	0.22 ± 0.01	91 ± 1	4.09 ± 0.07	92 ± 1	4.4 ± 0.7	190 ± 5
CGr32	345	0.72556	150°08'05.2"	2°04'20.7"	0.596	12586 ± 78	0.32 ± 0.02	104 ± 1	1.65 ± 0.16	95 ± 1	1.3 ± 0.1	176 ± 3
CGr32	378	0.72876	150°08'18.8"	2°04'17.1"	0.596	1293 ± 22	0.87 ± 0.01	179 ± 2	2.62 ± 0.02	183 ± 4	8.6 ± 1.9	249 ± 45
CGr32	416	0.72592	150°08'50.5"	2°04'26.7"	0.596	1353 ± 17	0.25 ± 0.01	0 ± 1	2.73 ± 0.06	176 ± 3	1.3 ± 0.1	128 ± 7
CGr34	22	0.73070	150°08'12.0"	2°03'33.1"	0.664	9297 ± 30	0.19 ± 0.01	139 ± 1	4.47 ± 0.06	147 ± 1	10.8 ± 0.3	157 ± 1
CGr34	28	0.72914	150°08'37.3"	2°03'49.0"	0.664	13863 ± 29	0.80 ± 0.01	17 ± 2	2.91 ± 0.03	214 ± 1	4.2 ± 0.1	131 ± 1
CGr34	34	0.73044	150°08'53.3"	2°03'45.4"	0.664	784 ± 11	0.21 ± 0.02	73 ± 2	1.24 ± 0.07	227 ± 6	5.2 ± 4.9	119 ± 42
CGr34	38	0.72845	150°08'37.0"	2°03'53.1"	0.664	1758 ± 19	0.33 ± 0.01	168 ± 1	1.50 ± 0.04	167 ± 2	1.5 ± 0.1	175 ± 5
CGr34	57	0.73713	150°08'43.2"	2°03'54.2"	0.664	7791 ± 28	0.39 ± 0.01	19 ± 1	1.66 ± 0.02	17 ± 1	1.5 ± 1.5	116 ± 2
CGr34	59	0.72828	150°08'19.6"	2°03'59.5"	0.664	2933 ± 32	0.17 ± 0.01	99 ± 1	5.55 ± 0.06	288 ± 1	7.7 ± 0.4	377 ± 4
CGr34	137	0.73085	150°08'28.9"	2°04'06.1"	0.664	2673 ± 18	0.35 ± 0.01	96 ± 1	2.57 ± 0.12	89 ± 2	11.8 ± 2.0	248 ± 36
CGr34	148	0.73442	150°08'47.9"	2°04'12.1"	0.664	6836 ± 36	0.36 ± 0.01	144 ± 1	3.70 ± 0.03	147 ± 1	5.7 ± 0.3	217 ± 3
CGr34	153	0.73301	150°07'59.7"	2°04'14.9"	0.664	2763 ± 32	0.22 ± 0.01	114 ± 1	5.72 ± 0.11	121 ± 2	18.8 ± 1.5	581 ± 40
CGr79	23	0.53147	150°08'12.0"	2°03'33.1"	0.658	4392 ± 32	0.70 ± 0.01	105 ± 1	2.76 ± 0.02	265 ± 3	5.0 ± 0.6	127 ± 7
CGr79	58	0.53294	150°08'37.3"	2°03'49.0"	0.658	1349 ± 17	0.59 ± 0.04	28 ± 4	1.68 ± 0.10	30 ± 10	1.3 ± 0.1	50 ± 6

Table B.1: continued

Gr ID	ID	z	R.A. [J2000]	Dec. [J2000]	FWHM ["]	[O II] flux [10 ⁻²⁰ erg s ⁻¹ cm ⁻²]	b/a	PA _m [°]	R _d [kpc]	PA _k [°]	r _i [kpc]	V _r [km s ⁻¹]
(1)	(2)	(3)	(4)	(5)	(6)	(7)	(8)	(9)	(10)	(11)	(12)	(13)
CGr79	63	0.53323	150°08'55.5"	2°03'38.1"	0.658	998 ± 19	0.27 ± 0.01	1 ± 1	2.28 ± 0.02	351 ± 7	2.1 ± 7.3	111 ± 28
CGr79	66	0.53129	150°08'53.3"	2°03'45.4"	0.658	2878 ± 37	0.35 ± 0.01	78 ± 1	3.91 ± 0.03	267 ± 2	3.5 ± 1.4	212 ± 10
CGr79	70	0.53356	150°08'37.0"	2°03'53.1"	0.658	662 ± 13	0.72 ± 0.05	178 ± 6	1.80 ± 0.13	22 ± 14	14.8 ± 2×10 ⁸	119 ± 2×10 ⁹
CGr79	104	0.53019	150°08'19.6"	2°03'59.5"	0.658	41536 ± 84	0.58 ± 0.01	22 ± 1	5.63 ± 0.03	201 ± 1	10.4 ± 0.1	284 ± 1
CGr79	129	0.53029	150°08'47.9"	2°04'12.1"	0.658	10166 ± 58	0.20 ± 0.01	105 ± 1	5.18 ± 0.06	294 ± 1	18.0 ± 0.5	459 ± 9
CGr79	136	0.52851	150°07'59.7"	2°04'14.9"	0.658	5792 ± 34	0.48 ± 0.01	58 ± 1	4.07 ± 0.05	233 ± 1	4.4 ± 0.4	170 ± 2
CGr84	54	0.69661	150°08'12.0"	2°03'33.1"	0.578	1467 ± 34	0.32 ± 0.01	89 ± 1	5.62 ± 0.13	81 ± 3	7.4 ± 1.1	220 ± 8
CGr84	237	0.69660	150°08'37.3"	2°03'49.0"	0.620	4118 ± 22	0.65 ± 0.01	35 ± 2	2.02 ± 0.04	228 ± 2	2.6 ± 1.3	56 ± 4
CGr84	251	0.70386	150°08'55.5"	2°03'38.1"	0.620	3074 ± 16	0.32 ± 0.01	17 ± 1	1.37 ± 0.03	8 ± 6	7.6 ± 6.3	38 ± 23
CGr84	267	0.69654	150°08'53.3"	2°03'45.4"	0.620	2395 ± 29	0.56 ± 0.01	75 ± 1	2.68 ± 0.03	84 ± 3	13.6 ± 2×10 ⁷	294 ± 4×10 ⁸
CGr84	273	0.70293	150°08'37.0"	2°03'53.1"	0.620	2477 ± 15	0.44 ± 0.01	32 ± 1	0.80 ± 0.01	43 ± 6	22.2 ± 0.1	129 ± 11
CGr84	276	0.69674	150°08'43.2"	2°03'54.2"	0.620	16947 ± 62	0.84 ± 0.01	48 ± 2	6.32 ± 0.10	188 ± 1	1.3 ± 0.1	191 ± 1
CGr84	277	0.69589	150°08'19.6"	2°03'59.5"	0.620	1158 ± 15	0.26 ± 0.01	168 ± 1	1.41 ± 0.07	24 ± 6	22.1 ± 0.1	276 ± 28
CGr84	295	0.69838	150°08'28.9"	2°04'06.1"	0.620	1874 ± 25	0.37 ± 0.01	2 ± 1	3.25 ± 0.03	18 ± 1	1.3 ± 0.1	227 ± 3
CGr84b	21	0.67591	150°08'12.0"	2°03'33.1"	0.578	2531 ± 36	0.23 ± 0.01	80 ± 1	3.10 ± 0.07	260 ± 3	12.2 ± 2.7	181 ± 32
CGr84b	22	0.67637	150°08'37.3"	2°03'49.0"	0.578	5483 ± 49	0.31 ± 0.01	133 ± 1	2.55 ± 0.06	144 ± 2	4.1 ± 0.7	136 ± 5
CGr84b	23	0.67662	150°08'55.5"	2°03'38.1"	0.578	16211 ± 65	0.90 ± 0.01	128 ± 3	3.19 ± 0.03	105 ± 2	4.5 ± 0.6	88 ± 3
CGr84b	35	0.68126	150°08'53.3"	2°03'45.4"	0.578	1143 ± 27	0.79 ± 0.06	36 ± 14	1.65 ± 0.19	341 ± 8	1.3 ± 0.1	89 ± 14
CGr84b	40	0.68241	150°08'37.0"	2°03'53.1"	0.578	5111 ± 55	0.35 ± 0.01	128 ± 1	2.44 ± 0.03	306 ± 2	6.1 ± 0.7	189 ± 9
CGr84b	248	0.68200	150°08'43.2"	2°03'54.2"	0.648	1247 ± 25	0.20 ± 0.01	55 ± 1	2.23 ± 0.03	36 ± 1	1.4 ± 0.1	328 ± 8
CGr84b	250	0.68057	150°08'19.6"	2°03'59.5"	0.648	4168 ± 36	0.59 ± 0.01	166 ± 1	1.73 ± 0.02	180 ± 2	3.2 ± 1.0	141 ± 9
CGr84b	257	0.67723	150°08'28.9"	2°04'06.1"	0.648	1503 ± 13	0.62 ± 0.01	147 ± 3	2.00 ± 0.06	135 ± 7	21.4 ± 1×10 ⁸	137 ± 7×10 ⁸
CGr84b	323	0.68089	150°08'47.9"	2°04'12.1"	0.648	4243 ± 43	0.24 ± 0.01	168 ± 1	5.46 ± 0.13	174 ± 1	1.4 ± 0.1	252 ± 5
CGr114	84	0.65956	150°08'12.0"	2°03'33.1"	0.740	1934 ± 38	0.42 ± 0.01	37 ± 1	1.95 ± 0.01	218 ± 3	1.4 ± 0.1	210 ± 8
CGr114	97	0.66052	150°08'37.3"	2°03'49.0"	0.740	1977 ± 35	0.73 ± 0.01	163 ± 1	2.56 ± 0.02	145 ± 3	3.8 ± 1.4	225 ± 17
CGr32	268	0.72770	150°08'47.9"	2°04'12.1"	0.596	4812 ± 51	0.30 ± 0.01	19 ± 1	6.48 ± 0.07	10 ± 3	1.6 ± 7.0	132 ± 11
CGr32	454	0.73460	150°08'27.6"	2°04'28.1"	0.596	1036 ± 16	0.55 ± 0.01	8 ± 2	2.17 ± 0.08	3 ± 89	7.9 ± 7×10 ²	24 ± 2×10 ³
CGr30	19	0.72384	150°08'12.0"	2°03'33.1"	0.700	639 ± 9	0.96 ± 0.04	118 ± 49	0.72 ± 0.03	204 ± 6	11.0 ± 4×10 ⁷	549 ± 2×10 ⁹
CGr30	82	0.72672	150°08'53.3"	2°03'45.4"	0.700	1131 ± 18	0.89 ± 0.02	106 ± 9	0.91 ± 0.03	207 ± 5	6.1 ± 1.2	304 ± 45
CGr30	113	0.73114	150°08'19.6"	2°03'59.5"	0.700	745 ± 8	0.69 ± 0.04	2 ± 7	1.34 ± 0.15	276 ± 32	1.5 ± 0.1	8 ± 5
CGr30	142	0.72444	150°08'47.9"	2°04'12.1"	0.700	930 ± 8	0.43 ± 0.03	35 ± 2	1.03 ± 0.06	70 ± 6	1.4 ± 0.1	30 ± 3
CGr32	136	0.72791	150°08'43.2"	2°03'54.2"	0.722	597 ± 10	0.33 ± 0.02	30 ± 1	0.58 ± 0.01	226 ± 24	7.7 ± 10.9	144 ± 148
CGr34	29	0.73301	150°08'55.5"	2°03'38.1"	0.664	417 ± 8	0.46 ± 0.06	1 ± 5	1.90 ± 0.25	106 ± 15	1.5 ± 0.1	39 ± 10
CGr79	87	0.52829	150°08'43.2"	2°03'54.2"	0.658	553 ± 11	0.32 ± 0.02	110 ± 2	1.25 ± 0.07	85 ± 17	1.3 ± 0.1	65 ± 12
CGr79	111	0.52970	150°08'28.9"	2°04'06.1"	0.658	9115 ± 35	0.83 ± 0.05	120 ± 10	0.11 ± 0.00	100 ± 8	1.3 ± 0.1	29 ± 3

Notes. (1) COSMOS group ID; (2) galaxy ID; (3) spectroscopic redshift; (4) and (5) J2000 coordinates; (6) median PSF FWHM, corresponding to narrow band [O II] MUSE observations; (7) [O II] flux derived from MUSE flux maps; (8), (9) and (10) axis ratio, position angle of the major axis and disk scale length from morphological modeling; (11) kinematic position angle of the major axis; (12) radius at which the plateau is reached; (13) velocity of the plateau. Galaxies with large uncertainties on both r_i and V_r are those for which the plateau is not reached within the data, nevertheless their slope might be well constrained (see Sect. 3.5). The table is split in three parts to identify (i) the final kinematic sample, (ii) galaxies having their kinematics biased by an AGN, and (iii) those with a dominant bulge within the effective radius.

Valentina Abril-Melgarejo et al.: TFR in dense groups $z \sim 0.7$ in the MAGIC surveyTable B.2: Physical properties of the 77 galaxies with $S/N \geq 40$ and $R_{eff}/FWHM \geq 0.5$.

Gr ID	ID	R_{eff} [kpc]	$\log(B/D)$	i [°]	V_{r22} [km s ⁻¹]	σ [km s ⁻¹]	V_{c22} [km s ⁻¹]	$\log(M_*)$ [M_\odot]	$\log(M_*(R_{22}))$ [M_\odot]	$\log(SFR)$ [$M_\odot \text{ yr}^{-1}$]	$\log(M_g)$ [M_\odot]	$\log(M_{dyn}(V_{r22}))$ [M_\odot]	$\log(M_{dyn}(V_{c22}))$ [M_\odot]
(1)	(2)	(3)	(4)	(5)	(6)	(7)	(8)	(9)	(10)	(11)	(12)	(13)	(14)
CGr28	41	3.46	-1.68	31 ± 2	170 ± 4	45 ± 21	194 ± 22	9.86 ^{+0.06} _{-0.13}	9.70 ± 0.20	0.15 ^{+0.07} _{-0.01}	9.20 ± 0.04	10.49 ± 0.02	10.61 ± 0.10
CGr28	85	5.93	-1.27	54 ± 1	232 ± 4	39 ± 32	247 ± 23	10.67 ^{+0.13} _{-0.13}	10.58 ± 0.22	0.43 ^{+0.07} _{-0.07}	9.54 ± 0.04	11.01 ± 0.02	11.06 ± 0.08
CGr28	145	4.01	-0.78	65 ± 1	155 ± 22	72 ± 35	217 ± 54	10.24 ^{+0.14} _{-0.07}	10.12 ± 0.23	0.18 ^{+0.06} _{-0.06}	9.30 ± 0.20	10.54 ± 0.12	10.83 ± 0.21
CGr30	69	3.01	-4.14	79 ± 2	60 ± 7	20 ± 16	74 ± 20	8.41 ^{+0.33} _{-0.38}	8.23 ± 0.40	-1.27 ^{+0.54} _{-0.54}	8.15 ± 0.90	9.52 ± 0.12	9.70 ± 0.24
CGr30	71	3.04	-0.18	60 ± 1	215 ± 5	100 ± 40	301 ± 58	10.90 ^{+0.08} _{-0.01}	10.81 ± 0.21	2.05 ^{+0.08} _{-0.01}	10.64 ± 0.08	10.84 ± 0.02	11.14 ± 0.17
CGr30	105	4.16	-5.67	44 ± 1	203 ± 4	36 ± 28	217 ± 21	10.49 ^{+0.01} _{-0.19}	10.33 ± 0.21	0.82 ^{+0.01} _{-0.15}	9.72 ± 0.07	10.72 ± 0.02	10.78 ± 0.08
CGr30	110	3.91	-1.89	43 ± 1	67 ± 40	35 ± 16	99 ± 37	10.08 ^{+0.33} _{-0.08}	9.91 ± 0.26	0.40 ^{+0.23} _{-0.23}	9.41 ± 0.17	9.73 ± 0.52	10.08 ± 0.33
CGr30	137	6.35	-5.09	81 ± 1	204 ± 27	39 ± 38	220 ± 39	9.68 ^{+0.08} _{-0.01}	9.54 ± 0.21	0.52 ^{+0.23} _{-0.23}	9.61 ± 0.26	10.91 ± 0.11	10.97 ± 0.15
CGr30	158	2.77	-5.18	57 ± 1	168 ± 31	0 ± 30	168 ± 31	9.88 ^{+0.09} _{-0.09}	9.69 ± 0.29	0.73 ^{+0.25} _{-0.25}	9.56 ± 0.30	10.38 ± 0.16	10.38 ± 0.16
CGr30	170	5.32	-1.32	42 ± 1	165 ± 4	42 ± 21	187 ± 21	10.35 ^{+0.01} _{-0.07}	10.23 ± 0.21	1.02 ^{+0.01} _{-0.43}	9.94 ± 0.22	10.66 ± 0.02	10.77 ± 0.10
CGr30	174	3.88	-1.36	46 ± 1	169 ± 5	52 ± 37	202 ± 43	10.38 ^{+0.30} _{-0.01}	10.22 ± 0.29	-0.29 ^{+0.55} _{-0.55}	8.92 ± 0.28	10.54 ± 0.03	10.70 ± 0.18
CGr30	185	3.38	-0.64	27 ± 2	144 ± 31	56 ± 25	186 ± 41	10.24 ^{+0.01} _{-0.01}	10.12 ± 0.20	-0.43 ^{+0.01} _{-0.01}	8.83 ± 0.01	10.42 ± 0.19	10.64 ± 0.19
CGr30	186	7.60	-1.19	33 ± 2	218 ± 4	40 ± 16	234 ± 12	10.49 ^{+0.01} _{-0.03}	10.47 ± 0.20	1.54 ^{+0.15} _{-0.22}	10.40 ± 0.13	11.07 ± 0.02	11.13 ± 0.05
CGr30	188	2.98	-4.95	57 ± 1	63 ± 4	44 ± 19	111 ± 33	9.29 ^{+0.17} _{-0.11}	9.10 ± 0.25	-0.42 ^{+0.44} _{-0.44}	8.75 ± 0.23	9.55 ± 0.06	10.05 ± 0.26
CGr30	189	3.99	-1.92	35 ± 3	43 ± 6	27 ± 13	71 ± 23	8.89 ^{+0.18} _{-0.19}	8.73 ± 0.27	0.24 ^{+0.37} _{-0.47}	9.30 ± 0.30	9.36 ± 0.11	9.79 ± 0.28
CGr30	193	3.03	-1.88	67 ± 1	134 ± 4	40 ± 30	158 ± 34	9.59 ^{+0.11} _{-0.02}	9.41 ± 0.22	-0.10 ^{+0.58} _{-0.29}	8.99 ± 0.24	10.22 ± 0.03	10.37 ± 0.19
CGr30	195	4.95	-0.79	76 ± 1	159 ± 4	55 ± 33	196 ± 41	9.84 ^{+0.07} _{-0.08}	9.71 ± 0.21	0.16 ^{+0.07} _{-0.31}	9.32 ± 0.16	10.62 ± 0.02	10.81 ± 0.18
CGr30	196	2.93	-4.87	28 ± 2	131 ± 7	36 ± 19	151 ± 21	9.97 ^{+0.08} _{-0.09}	9.79 ± 0.21	0.81 ^{+0.22} _{-0.22}	9.63 ± 0.11	10.18 ± 0.05	10.31 ± 0.12
CGr32	10	6.81	-3.11	63 ± 1	179 ± 4	56 ± 32	214 ± 37	10.18 ^{+0.09} _{-0.01}	10.07 ± 0.21	1.41 ^{+0.16} _{-0.16}	10.27 ± 0.15	10.82 ± 0.02	10.98 ± 0.15
CGr32	36	8.01	-1.57	67 ± 1	364 ± 16	78 ± 52	399 ± 47	10.69 ^{+0.01} _{-0.04}	10.61 ± 0.21	1.92 ^{+0.03} _{-0.03}	10.68 ± 0.26	11.52 ± 0.04	11.60 ± 0.10
CGr32	109	4.10	-5.61	73 ± 1	287 ± 4	0 ± 31	287 ± 4	9.92 ^{+0.04} _{-0.07}	9.74 ± 0.21	1.15 ^{+0.28} _{-0.28}	9.95 ± 0.18	11.01 ± 0.01	11.01 ± 0.01
CGr32	112	3.25	-4.86	56 ± 2	32 ± 9	33 ± 15	76 ± 29	8.63 ^{+0.01} _{-0.01}	8.45 ± 0.20	-0.05 ^{+0.16} _{-0.16}	9.04 ± 0.01	9.00 ± 0.24	9.76 ± 0.33
CGr32	132	3.23	-1.45	58 ± 1	112 ± 4	39 ± 14	139 ± 18	9.77 ^{+0.15} _{-0.48}	9.60 ± 0.38	0.25 ^{+0.16} _{-0.16}	9.26 ± 0.61	10.11 ± 0.03	10.30 ± 0.11
CGr32	183	2.71	-1.62	52 ± 1	63 ± 17	45 ± 13	113 ± 24	9.58 ^{+0.48} _{-0.01}	9.40 ± 0.21	0.43 ^{+0.69} _{-0.11}	9.34 ± 0.07	9.53 ± 0.24	10.03 ± 0.18
CGr32	198	5.48	-0.76	77 ± 1	264 ± 15	43 ± 41	279 ± 31	9.79 ^{+0.02} _{-0.10}	9.64 ± 0.21	1.49 ^{+0.11} _{-0.02}	10.25 ± 0.06	11.04 ± 0.05	11.09 ± 0.10
CGr32	295	4.74	-1.42	64 ± 1	96 ± 9	30 ± 16	115 ± 20	9.62 ^{+0.01} _{-0.37}	9.47 ± 0.30	-0.26 ^{+0.17} _{-0.03}	8.99 ± 0.09	10.14 ± 0.08	10.30 ± 0.15
CGr32	325	4.72	-1.74	28 ± 2	192 ± 4	39 ± 15	209 ± 13	9.89 ^{+0.01} _{-0.01}	9.75 ± 0.23	0.36 ^{+0.01} _{-0.01}	9.43 ± 0.00	10.73 ± 0.02	10.81 ± 0.05
CGr32	340	6.86	-5.24	77 ± 1	190 ± 5	42 ± 30	209 ± 27	10.51 ^{+0.01} _{-0.36}	10.38 ± 0.32	0.44 ^{+0.13} _{-0.34}	9.57 ± 0.18	10.88 ± 0.02	10.96 ± 0.11
CGr32	345	2.75	-2.06	71 ± 2	176 ± 4	131 ± 48	326 ± 84	10.32 ^{+0.01} _{-0.05}	10.14 ± 0.20	1.58 ^{+0.03} _{-0.19}	10.16 ± 0.06	10.42 ± 0.05	10.95 ± 0.23
CGr32	378	3.99	-0.94	30 ± 2	168 ± 48	61 ± 22	211 ± 48	10.74 ^{+0.17} _{-0.11}	10.61 ± 0.25	0.51 ^{+0.19} _{-0.07}	9.51 ± 0.22	10.58 ± 0.25	10.78 ± 0.20
CGr32	416	4.30	-1.18	76 ± 1	128 ± 7	39 ± 22	152 ± 26	9.85 ^{+0.01} _{-0.09}	9.69 ± 0.21	0.52 ^{+0.19} _{-0.39}	9.53 ± 0.22	10.36 ± 0.05	10.51 ± 0.15
CGr34	22	7.81	-0.62	79 ± 1	144 ± 5	33 ± 24	159 ± 22	9.64 ^{+0.16} _{-0.07}	9.54 ± 0.24	0.29 ^{+0.62} _{-0.01}	9.49 ± 0.31	10.67 ± 0.03	10.76 ± 0.12
CGr34	28	4.74	-1.51	37 ± 1	131 ± 4	41 ± 14	157 ± 16	9.86 ^{+0.05} _{-0.14}	9.72 ± 0.21	0.90 ^{+0.14} _{-0.14}	9.82 ± 0.10	10.41 ± 0.03	10.56 ± 0.09
CGr34	34	2.58	-0.48	78 ± 2	62 ± 63	21 ± 12	76 ± 53	8.39 ^{+0.19} _{-0.19}	8.17 ± 0.27	-1.28 ^{+0.49} _{-0.49}	8.05 ± 0.25	9.39 ± 0.88	9.57 ± 0.61
CGr34	38	3.41	-0.25	71 ± 1	175 ± 5	0 ± 41	175 ± 5	9.48 ^{+0.03} _{-0.13}	9.26 ± 0.22	0.13 ^{+0.58} _{-0.03}	9.10 ± 0.29	10.37 ± 0.03	10.37 ± 0.03
CGr34	57	2.74	-1.84	67 ± 1	116 ± 4	37 ± 19	140 ± 23	9.45 ^{+0.13} _{-0.07}	9.27 ± 0.24	-0.02 ^{+0.19} _{-0.09}	9.02 ± 0.11	10.05 ± 0.03	10.22 ± 0.14
CGr34	59	7.29	-0.52	80 ± 1	377 ± 4	0 ± 44	377 ± 4	10.80 ^{+0.07} _{-0.10}	10.75 ± 0.22	0.74 ^{+0.09} _{-0.71}	9.86 ± 0.36	11.61 ± 0.01	11.61 ± 0.01
CGr34	137	4.04	-1.16	70 ± 1	119 ± 24	29 ± 22	134 ± 30	9.20 ^{+0.10} _{-0.11}	9.04 ± 0.22	-0.49 ^{+0.40} _{-0.40}	8.79 ± 0.07	10.27 ± 0.18	10.37 ± 0.20
CGr34	148	6.20	-5.61	69 ± 1	217 ± 4	46 ± 33	237 ± 28	10.21 ^{+0.11} _{-0.09}	10.08 ± 0.22	0.15 ^{+0.84} _{-0.07}	9.34 ± 0.45	10.95 ± 0.02	11.03 ± 0.10

A&A proofs: manuscript no. MAGIC_TFR

Table B.2: continued

Gr ID	ID	R_{eff} [kpc]	$\log(B/D)$	i [$^\circ$]	V_{r22} [km s^{-1}]	σ [km s^{-1}]	V_{c22} [km s^{-1}]	$\log(M_*)$ [M_\odot]	$\log(M_*(R_{22}))$ [M_\odot]	$\log(\text{SFR})$ [$M_\odot \text{ yr}^{-1}$]	$\log(M_g)$ [M_\odot]	$\log(M_{dyn}(V_{r22}))$ [M_\odot]	$\log(M_{dyn}(V_{c22}))$ [M_\odot]
(1)	(2)	(3)	(4)	(5)	(6)	(7)	(8)	(9)	(10)	(11)	(12)	(13)	(14)
CGr34	153	9.71	-0.76	77 ± 1	390 ± 35	48 ± 37	403 ± 39	10.49 ^{+0.05} _{-0.01}	10.44 ± 0.20	1.33 ^{+0.01} _{-0.12}	10.29 ± 0.07	11.65 ± 0.08	11.68 ± 0.09
CGr79	23	4.07	-0.88	46 ± 1	127 ± 7	40 ± 22	152 ± 26	10.16 ^{+0.01} _{-0.01}	10.04 ± 0.22	-0.09 ^{+0.02} _{-0.05}	9.10 ± 0.03	10.36 ± 0.05	10.52 ± 0.15
CGr79	58	2.82	-4.64	54 ± 3	50 ± 6	41 ± 18	99 ± 32	8.68 ^{+0.01} _{-0.01}	8.50 ± 0.34	-0.28 ^{+0.05} _{-0.07}	8.84 ± 0.46	9.33 ± 0.11	9.92 ± 0.28
CGr79	63	3.82	-5.32	74 ± 1	111 ± 28	32 ± 28	130 ± 39	9.88 ^{+0.01} _{-0.01}	9.71 ± 0.23	-0.79 ^{+0.01} _{-0.01}	8.55 ± 0.34	10.16 ± 0.22	10.29 ± 0.26
CGr79	66	5.87	-0.26	70 ± 1	212 ± 10	63 ± 40	250 ± 46	10.77 ^{+0.01} _{-0.01}	10.70 ± 0.20	0.10 ^{+0.01} _{-0.01}	9.32 ± 0.03	10.95 ± 0.04	11.10 ± 0.16
CGr79	70	3.02	-4.68	44 ± 5	32 ± 8	11 ± 18	39 ± 23	8.04 ^{+0.01} _{-0.01}	7.86 ± 0.24	0.05 ^{+0.01} _{-0.01}	9.09 ± 0.09	8.97 ± 0.23	9.15 ± 0.51
CGr79	104	8.49	-0.90	55 ± 1	284 ± 4	36 ± 21	295 ± 12	10.99 ^{+0.01} _{-0.01}	11.01 ± 0.20	0.55 ^{+0.01} _{-0.01}	9.73 ± 0.00	11.37 ± 0.01	11.40 ± 0.04
CGr79	129	8.84	-0.32	78 ± 1	290 ± 24	70 ± 45	325 ± 48	10.38 ^{+0.01} _{-0.01}	10.35 ± 0.20	1.04 ^{+0.01} _{-0.01}	10.06 ± 0.07	11.35 ± 0.07	11.45 ± 0.13
CGr79	136	6.74	-1.84	61 ± 1	170 ± 4	26 ± 22	178 ± 14	9.81 ^{+0.01} _{-0.01}	9.73 ± 0.25	-0.25 ^{+0.01} _{-0.01}	9.08 ± 0.20	10.78 ± 0.02	10.82 ± 0.07
CGr84	54	9.48	-0.56	71 ± 1	220 ± 8	0 ± 23	220 ± 8	10.48 ^{+0.01} _{-0.01}	10.44 ± 0.20	0.78 ^{+0.01} _{-0.01}	9.90 ± 0.25	11.14 ± 0.03	11.14 ± 0.03
CGr84	237	3.34	-1.79	49 ± 1	56 ± 4	37 ± 20	95 ± 34	9.39 ^{+0.01} _{-0.01}	9.22 ± 0.20	0.24 ^{+0.01} _{-0.01}	9.26 ± 0.01	9.51 ± 0.06	9.97 ± 0.31
CGr84	251	2.29	-4.96	71 ± 1	15 ± 15	39 ± 13	83 ± 27	8.98 ^{+0.01} _{-0.01}	8.79 ± 0.25	-0.36 ^{+0.01} _{-0.01}	8.73 ± 0.20	8.19 ± 0.90	9.68 ± 0.28
CGr84	267	4.50	-5.43	56 ± 1	128 ± 21	42 ± 21	155 ± 31	9.85 ^{+0.01} _{-0.01}	9.69 ± 0.22	0.70 ^{+0.01} _{-0.01}	9.66 ± 0.43	10.35 ± 0.14	10.52 ± 0.17
CGr84	273	2.36	-0.09	64 ± 1	10 ± 6	35 ± 16	75 ± 34	9.03 ^{+0.01} _{-0.01}	8.75 ± 0.21	-0.83 ^{+0.01} _{-0.01}	8.26 ± 0.04	7.63 ± 0.47	9.36 ± 0.40
CGr84	276	7.63	-0.40	33 ± 2	191 ± 4	47 ± 29	215 ± 28	11.02 ^{+0.01} _{-0.01}	11.07 ± 0.20	0.78 ^{+0.01} _{-0.01}	9.93 ± 0.00	11.07 ± 0.02	11.17 ± 0.11
CGr84	277	2.36	-4.63	75 ± 1	39 ± 13	47 ± 25	106 ± 49	8.97 ^{+0.01} _{-0.01}	8.78 ± 0.35	0.28 ^{+0.01} _{-0.01}	9.20 ± 0.41	9.03 ± 0.28	9.91 ± 0.40
CGr84	295	5.45	-5.45	68 ± 1	227 ± 4	0 ± 27	227 ± 4	10.20 ^{+0.03} _{-0.03}	10.05 ± 0.20	0.50 ^{+0.03} _{-0.03}	9.56 ± 0.03	10.93 ± 0.02	10.93 ± 0.02
CGr84b	21	5.20	-4.98	77 ± 1	101 ± 14	0 ± 16	101 ± 14	8.76 ^{+0.01} _{-0.01}	8.60 ± 0.34	0.36 ^{+0.01} _{-0.01}	9.45 ± 0.36	10.21 ± 0.12	10.21 ± 0.12
CGr84b	22	5.20	-0.25	72 ± 1	136 ± 5	30 ± 19	150 ± 17	9.38 ^{+0.01} _{-0.01}	9.21 ± 0.22	0.23 ^{+0.01} _{-0.01}	9.31 ± 0.32	10.38 ± 0.03	10.47 ± 0.10
CGr84b	23	5.23	-1.61	26 ± 2	88 ± 4	39 ± 14	120 ± 21	10.56 ^{+0.01} _{-0.01}	10.45 ± 0.20	0.48 ^{+0.01} _{-0.01}	9.54 ± 0.00	10.10 ± 0.04	10.37 ± 0.15
CGr84b	35	2.66	-1.37	38 ± 6	89 ± 14	17 ± 15	95 ± 17	7.97 ^{+0.01} _{-0.01}	7.80 ± 0.21	-0.70 ^{+0.01} _{-0.01}	8.54 ± 0.04	9.82 ± 0.15	9.88 ± 0.17
CGr84b	40	4.53	-0.47	70 ± 1	167 ± 21	47 ± 30	194 ± 37	9.70 ^{+0.01} _{-0.01}	9.53 ± 0.22	0.93 ^{+0.01} _{-0.01}	9.80 ± 0.24	10.54 ± 0.11	10.67 ± 0.17
CGr84b	248	2.87	-0.26	78 ± 1	328 ± 8	0 ± 35	328 ± 8	10.27 ^{+0.04} _{-0.04}	10.14 ± 0.20	-0.41 ^{+0.04} _{-0.04}	8.82 ± 0.03	11.09 ± 0.02	11.09 ± 0.02
CGr84b	250	2.60	-0.92	54 ± 1	141 ± 9	67 ± 27	199 ± 40	10.13 ^{+0.01} _{-0.01}	9.97 ± 0.21	-0.54 ^{+0.01} _{-0.01}	8.66 ± 0.05	10.25 ± 0.05	10.54 ± 0.17
CGr84b	257	3.36	-4.88	52 ± 1	28 ± 7	23 ± 15	55 ± 27	9.12 ^{+0.01} _{-0.01}	8.94 ± 0.25	-0.93 ^{+0.01} _{-0.01}	8.42 ± 0.13	8.91 ± 0.20	9.50 ± 0.43
CGr84b	323	7.79	-0.72	76 ± 1	252 ± 5	74 ± 38	295 ± 42	10.59 ^{+0.01} _{-0.01}	10.54 ± 0.20	0.90 ^{+0.01} _{-0.01}	9.97 ± 0.01	11.25 ± 0.02	11.39 ± 0.12
CGr114	84	3.26	-0.42	65 ± 1	210 ± 8	51 ± 44	236 ± 42	10.50 ^{+0.02} _{-0.02}	10.33 ± 0.20	-0.17 ^{+0.01} _{-0.01}	8.96 ± 0.01	10.64 ± 0.03	10.74 ± 0.15
CGr114	97	4.10	-1.31	43 ± 1	225 ± 17	15 ± 34	227 ± 20	10.33 ^{+0.01} _{-0.01}	10.18 ± 0.24	1.20 ^{+0.01} _{-0.01}	10.00 ± 0.50	10.82 ± 0.07	10.83 ± 0.08
CGr32	268	8.31	-0.26	73 ± 1	132 ± 11	118 ± 56	280 ± 104	10.74 ^{+0.02} _{-0.02}	10.74 ± 0.20	0.07 ^{+0.02} _{-0.02}	9.42 ± 0.49	10.76 ± 0.07	11.42 ± 0.32
CGr32	454	2.23	-0.20	57 ± 1	15 ± 4	51 ± 15	108 ± 31	9.91 ^{+0.01} _{-0.01}	9.80 ± 0.22	-0.57 ^{+0.01} _{-0.01}	8.70 ± 0.06	8.39 ± 0.24	10.11 ± 0.25
CGr30	19	3.22	0.16	16 ± 9	79 ± 56	30 ± 27	101 ± 56	8.60 ^{+0.01} _{-0.01}	8.27 ± 0.33	0.49 ^{+0.01} _{-0.01}	9.18 ± 0.49	9.36 ± 0.61	9.57 ± 0.48
CGr30	82	4.60	0.32	27 ± 3	100 ± 24	109 ± 47	250 ± 91	9.56 ^{+0.01} _{-0.01}	9.22 ± 0.33	1.26 ^{+0.01} _{-0.01}	9.79 ± 0.36	9.67 ± 0.21	10.47 ± 0.32
CGr30	113	4.17	0.11	46 ± 4	8 ± 5	30 ± 16	64 ± 34	8.27 ^{+0.01} _{-0.01}	8.01 ± 0.26	-0.89 ^{+0.01} _{-0.01}	8.35 ± 0.09	7.64 ± 0.52	9.45 ± 0.46
CGr30	142	3.81	0.16	65 ± 2	30 ± 4	27 ± 13	65 ± 23	8.91 ^{+0.01} _{-0.01}	8.61 ± 0.32	-0.24 ^{+0.01} _{-0.01}	8.75 ± 0.33	8.69 ± 0.12	9.35 ± 0.31
CGr32	136	3.67	0.25	71 ± 2	24 ± 21	28 ± 15	64 ± 30	9.45 ^{+0.01} _{-0.01}	9.07 ± 0.32	-0.62 ^{+0.01} _{-0.01}	8.33 ± 0.18	8.22 ± 0.77	9.08 ± 0.41
CGr34	29	4.84	0.02	63 ± 4	39 ± 10	6 ± 20	41 ± 16	8.78 ^{+0.01} _{-0.01}	8.57 ± 0.35	-1.46 ^{+0.01} _{-0.01}	8.03 ± 0.96	9.18 ± 0.23	9.22 ± 0.34
CGr79	87	4.73	0.33	71 ± 2	65 ± 12	0 ± 15	65 ± 12	8.70 ^{+0.01} _{-0.01}	8.42 ± 0.21	-0.99 ^{+0.01} _{-0.01}	8.26 ± 0.14	9.43 ± 0.16	9.43 ± 0.16
CGr79	111	2.10	0.84	34 ± 6	6 ± 4	59 ± 18	124 ± 38	10.03 ^{+0.01} _{-0.01}	9.24 ± 0.21	-0.21 ^{+0.01} _{-0.01}	8.21 ± 0.05	6.25 ± 0.62	8.94 ± 0.27

Notes. (1) COSMOS group ID; (2) galaxy ID; (3) global effective radius; (4) logarithm of the bulge-to-disk ratio at R_{22} ; (5) disk inclination; (6) rotation velocity at R_{22} ; (7) median velocity dispersion; (8) corrected velocity at R_{22} as described in Eq. 10; at logarithmic scale; (9) stellar mass within an aperture of $3''$; (10) corrected stellar mass inside R_{22} ; (11) SFR from the SED fitting; (12) gas mass computed using the Kennicutt-Schmidt law, from SED SFRs; (13) and (14) dynamical masses computed from the rotation velocity V_{r22} and the corrected velocity V_{c22} respectively. The table is split in three parts to identify (i) the final kinematic sample, (ii) galaxies having their kinematics biased by an AGN, and (iii) those with a dominant bulge within the effective radius.

Chapter 6

Summary and Conclusions

Galaxies are the building blocks of the large scale structures of the Universe, distributed along filaments, walls, groups, clusters and voids; all shaped by the distribution of dark matter halos which constitute most of the matter budget of the Universe. Galaxies have suffered significant morphological and kinematic transformations from the maximum of the Cosmic SFR density at $z \sim 2$ to today, from clumpy disks and perturbed galaxies with complex kinematics (different components) to regular well defined spirals and passive elliptical galaxies. It has been observed that there is a strong correlation between the environment in which a galaxy forms and evolves with different physical properties, like its capacity to form new stars, its size, kinematics and baryonic content. Therefore the epoch between $z \sim 1.5$ to $z \sim 0.3$ is a fundamental transformation period during which galaxies actively evolved.

Galaxy groups were formed, assembled their mass and got virialized, after the maximum of cosmic SFR density strongly affecting the star formation activity and morphology of galaxies residing inside them. This due to the fact that in dense environments there is a larger probability that a galaxy interacts with other galaxies and with its environment by means of different mechanisms, implying galaxies in dense environments to quench their star-formation activity before galaxies in field for the low to intermediate mass galaxies regimes ($10^9 M_{\odot} < M_{\star} < 10^{11} M_{\odot}$, Peng et al. 2010b).

Galaxy kinematics is a fundamental tool in the understanding of the processes and mechanisms that govern formation and evolution of galaxies, as for rotation dominated systems it traces the distribution of the total mass content, including the baryonic and dark matter components. Then comparing kinematic and physical features at different redshifts represents a robust strategy to trace the evolution of galaxies. From kinematics it is also possible to separate the dynamical components (baryonic and dark), by modeling the rotation curve, if one has access to the total baryonic content (including the gas fraction). Velocity maps give information about interactions in the evolution history of galaxies by the identification of complex kinematics originated from internal disturbances or external interactions.

High resolution HST observations and IFS exposures of a total of ~ 330 galaxies in dense structures were obtained in the redshift interval $0.3 < z < 0.8$, from the MAGIC MUSE-GTO survey, whose observations are performed inside the HST COSMOS field (Scoville et al., 2007a). The ionized gas is used to extract dynamics of galaxies in the sample, and taking into ac-

count the detection limits of nebular lines for MUSE, the $[\text{OII}]\lambda\lambda 3727, 3729 \text{ \AA}$ doublet is used as kinematic tracer since is the brightest spectral emission feature available in all the redshift interval. Since the aim of my PhD Thesis project is to determine the influence of environment and the mechanisms conducting the earlier quenching of the star-formation activity in dense environments, I performed an extensive morpho-kinematic study and a further analysis of the stellar-mass TFR (smTFR) and the baryonic TFR (bmTFR) of galaxies in dense groups at $z \sim 0.7$. The results were later compared to the smTFR derived from other studies performed on samples at different environments in literature: two in low density environments (KMOS^{3D}, Übler et al. 2017; and KROSS, Tiley et al. 2019) and the other from galaxies in clusters (ORELSE, Pelliccia et al. 2019).

I mainly applied the analysis on the intermediate z sub-sample composed of 250 galaxies at $0.5 < z < 0.8$ from 8 dense groups (Section 3.4), since this sample traces the period of cosmic evolution after the maximum of cosmic SF, with the deepest MUSE observations containing the largest/densest structures. The results are mainly derived from the morpho-kinematics analysis performed on these 250 galaxies and the determination of dynamical and structural features of 77 star-forming rotation dominated galaxies. Below, I summarize the main results of this research project whose core analysis is detailed in the article Abril-Melgarejo et al. 2021 (Section 5.5).

- The study was performed on dense and massive groups with a projected density at least 25 larger than the average galaxy densities at the redshift interval of the sample, computed using the method established by Beers et al. (1990) and Cucciati et al. (2010). The virial masses range between 3.1 and $81.4 \times 10^{13} M_{\odot}$ with an average median mass of $8.5 \times 10^{13} M_{\odot}$.
- With the results from the SED fitting applied on the available photometry in COSMOS for MAGIC fields, I obtained the SFR vs. stellar Mass diagram to consistently separate the population of galaxies into passive and star-forming, located in the red and main sequence (MS) of the diagram respectively. The sample of star-forming galaxies is composed of 178 galaxies which covers a wide range of masses between $10^{7.5} M_{\odot}$ to $10^{11.5} M_{\odot}$ and SFR from $10^{-2} M_{\odot} \text{ yr}^{-1}$ to $10^2 M_{\odot} \text{ yr}^{-1}$. All the galaxies in the kinematic sample are part of the MS (representing 43% of the SF galaxies) whose median mass is of $7.2 \times 10^9 M_{\odot}$ and the median SFR is equivalent to $1.74 M_{\odot} \text{ yr}^{-1}$.
- Using the high resolution HST-ACS F814W images available for MAGIC fields, I performed a bulge-disk morphological decomposition analysis to model the surface brightness of 330 galaxies including the low-redshift sample. I computed the the global size (global effective radius R_{eff}), global luminosity and the luminosity ratios from the bulge-disk decomposition. In cases of complex morphology I included the modeling of some internal structures and for crowded fields I also modeled other nearby galaxies in order to minimize the influence of the additional light profiles.
- I estimated the bulge-to-disk ratios in order to establish the contribution of each component to the light profile. The B/D, B/T and D/T light ratios are important to determine the dominant component and to check relations with the SFR and the dynamical support. There are 34 bulge dominated galaxies ($B/D > 1$) in the red-sequence representing 53% of the quiescent galaxies. For galaxies in main sequence 44 galaxies have $B/D > 1$ representing 25% of the star-forming galaxies. From a comparison of these morphological

results of galaxies in groups and others in field (from the MAGIC sample) with COSMOS morphological catalogs (performed by W. Mercier), an agreement was found between the morphological decomposition with morphological type, being spirals and irregulars mostly composed by disk dominated galaxies and ellipticals by bulge-dominated profiles. I then use this result to discard bulge dominated galaxies from the final kinematic sample.

- I obtained the distribution of inclinations of the parent and kinematic samples from the morphological modeling, showing they approximately follow (inside the errors) the theoretical probability function of random disks orientations. The median inclination of the parent sample is $i_{MEDIAN} = 65.2^\circ$ and for the kinematic sample is equivalent to $i_{MEDIAN} = 63.9^\circ$, values that are close to the median inclination $i_{MEDIAN} = 60^\circ$ of the theoretical distribution. I demonstrated then the random nature of the sample with no bias due to pre-selection.
- I investigated the difference between the morphological and kinematic estimations of the PA and found for 174 galaxies that the absolute difference $|PA_m - PA_k| > 40^\circ$ for the 30% of the SF sample. This result shows the advantages of IFS data allowing to extract spatially resolved kinematics over long-slit observations.

I effectively extracted and modeled the kinematics of 178 SF galaxies in the sample using the formalism of dynamical moments (Epinat et al., 2012) applied on the [OII] flux map, to obtain the velocity and velocity dispersion maps respectively. I then extracted the rotation velocity at 2.2 times the disk scale length ($R_{2.2}$) using a ramp model to fit the rotation curve, taking into account the effect of spatial resolution (PSF and LSF). The rotation velocity and the intrinsic velocity dispersion were obtained for the kinematic sample at $z \sim 0.7$ being 92% rotation dominated systems ($V/\sigma > 1$) and 8% dispersion dominated (6 galaxies). I list below the results concerning the kinematic analysis.

- I implemented a new selection strategy for the building of the kinematic sample, based on the global size (R_{eff} from morphology) with respect to MUSE spatial resolution, as well as on the S/N ratio of the [OII] doublet flux used to derive meaningful kinematics maps. The selection is then based on the threshold values $S/N \geq 40$ and $R_{eff}/FWHM_{MUSE} \geq 0.5$, limits that ensure to constrain the sample to sufficiently resolved galaxies and with enough emission from the ionized gas, in order to recover robust kinematic measurements. This selection widely agrees with a visual inspection performed on the clean velocity maps by identifying the extension of the ionized disk and the presence of a clear velocity gradient. After applying this method, 77 galaxies are above the selection limits which correspond to 43% of the sample of star-forming galaxies. The fact that only 6 galaxies from the kinematic sample are dispersion dominated shows the effectiveness of the selection method, which directly selects the systems supported by rotation without any a posteriori assumption as it is typically done when the velocity-to-dispersion (V/σ) ratio is used.
- I applied two diagnostic diagrams (Lamareille 2010, Juneau et al. 2011), effective at intermediate redshift to determine the ionizing mechanisms with the aim to identify galaxies with Active Galactic Nuclei (AGN) in the kinematic sample. Three galaxies were confirmed as AGNs and two ambiguous cases, probably due to a low AGN activity. One AGN was discarded since it is dominated by the bulge component. The others were kept in the kinematic sample since they present extended disks for which we can differentiate

the ionizing emission coming from the HII regions, hence the rotation velocity can be determined.

- I used the limit $B/D > 1$ to identify possible early type galaxies (ETGs) in the sample, as was previously discussed. I then removed 8 ETGs from the final kinematics sample. Now, taking into account the spatial resolution limitation that mainly affect small galaxies an additional limit was set on stellar mass for galaxies with $M_* \geq 10^9 M_\odot$, letting the analysis robustly constrained to 54 rotation dominated star-forming galaxies. This limit also allows to perform a more suitable comparison with other studies in literature that are limited to massive galaxies.
- The gas mass fraction for the kinematic sample was computed employing the inverse form of the Kennicutt-Schmidt (KS) law (Kennicutt, 1998), using the SFR from SED fitting corrected by dust extinction. The median gas mass of the sample corresponds to $\log(\overline{M_g}) \sim 9.45 M_\odot$, while the median value of the stellar mass is $\log(\overline{M_*}) \sim 9.71 M_\odot$. The results confirm that gas fractions in galaxies at intermediate redshift are in average larger than those at low redshifts. Related to this, some galaxies in the main sequence (whose SFR was computed from the SED fitting using multiband photometry), do not present or have very few emission from the ionized gas, suggesting these galaxies might be passing through a quenching of their star formation. Other galaxies are too small to reliability determine their emission flux. In contrast, among the massive ETGs I found 4 cases with active star formation in their centers showing they have localized SF activity. AGN emission was discarded for these galaxies.
- Both the stellar and baryonic mass TFR were derived studying the impact of the selection methodology. To obtain the TFR in each case a linear bisector fitting was performed and the obtained slope and zero point parameters were compared with other studies on the TFR at similar redshifts from major IFS surveys like KROSS (Tiley et al., 2019) and KMOS^{3D} (Übler et al., 2017) and with long slit using ORELSE (Pelliccia et al., 2019). Two different dynamical estimators were used, $V_{2.2}$ the rotation velocity at $R_{2.2}$ and V_{circ} the circular velocity from (Übler et al., 2017) including a term to account for velocity dispersion. Using $V_{2.2}$ alone, the best fit obtained for the smTFR (bmTFR) for MAGIC groups (assuming a reference velocity $V_{ref} = 100 \text{ km s}^{-1}$) corresponds to a slope $\alpha = 3.65 \pm 0.52$ (3.20 ± 0.49), a zero point $\beta = 9.11 \pm 0.15$ (9.46 ± 0.14), and an intrinsic scatter $\sigma = 0.38$ (0.36). Taking also into account an asymmetric drift correction given by V_{circ} , the best fit smTFR (bmTFR) corresponds to a slope $\alpha = 4.02 \pm 0.49$ (3.63 ± 0.49), a zero point $\beta = 8.75 \pm 0.17$ (9.11 ± 0.17), and an intrinsic scatter $\sigma = 0.25$ (0.28).
- When V_{circ} is used the intrinsic scatter in the TFR considerably diminishes in special for small galaxies, this due to the fact that V_{circ} includes the velocity dispersion in the dynamical budget and small galaxies are mostly dominated by dispersion presenting low rotation velocities. For any sample used the effect is the same, using V_{circ} increases the slope and decreases the zero-point of the TFR.
- The free slope fitting from MAGIC is quite consistent with the three comparison studies for the smTFR, using both $V_{2.2}$ or V_{circ} . However, when fixed slopes are used, the zero-point is systematically shifted towards smaller Mass values and larger velocities for the MAGIC sample with respect to the other comparison samples. The decrease of the

zero-point in all comparisons ranges between $\Delta M_* = 0.05 - 0.3$ dex, depending on the comparison sample being the KROSS sample that with the biggest offset with respect to MAGIC.

- In the case of the bmTFR the MAGIC results could only be compared with the bmTFR from KMOS^{3D} using two different fitting methods (fixed and free slope). Using V_{circ} , for the free slope KMOS^{3D} fitting a shift towards a lower zero-point (0.26 dex) was found while for the fixed KMOS^{3D} there a small offset (0.18 dex) with respect to MAGIC.
- [By comparing the stellar and baryonic masses](#) with the dynamical mass (computed using both $V_{2.2}$ and V_{circ}) the corresponding fractions were computed for the MAGIC sample. It was found that stellar fractions clearly increase in function of stellar mass from 10% for low mass galaxies up to 50% for massive galaxies. For the baryon fraction a global comparable trend is found remaining below 50% even for massive galaxies, this could be due to uncertainties in the estimation of gas mass for small galaxies where high scatter is present in the baryonic fraction.

The most relevant result from this study is the shift of the zero-point TFR of the MAGIC sample with respect to other samples at the same redshift regime, for which two hypotheses have been proposed. In the first assuming that kinematics traces DMH mass – i.e that for a given velocity, DMH mass is constant– then the shift to lower masses in groups is the result of active quenching mechanisms inside dense environments (Described in Section 1.5). Assuming a decline of the SFR by 0.3 dex due to environment ([Tomczak et al., 2019](#)), the time of interaction in which galaxies have entered into the structures is estimated between 1 to 3 Gyrs. In a second scenario, the effect of the contraction of the mass distribution within $R_{2.2}$ (for a given M_*) implies an increase of rotation velocity. A contraction [factor](#) ranging between 0.07 to 0.13 was found and seems to account for at least half of the observed offsets. Since dark matter fraction is large, it would therefore indicate that dark matter is also contracted or that dark matter halos are more massive. The environmental contraction of baryons have been documented in literature from several studies ([Weinmann et al. 2009](#), [Maltby et al. 2010](#) and [Fernández Lorenzo et al. 2013](#) and [Matharu et al. 2019](#)) which agrees with this hypothesis.

Then the differences in the smTFR and bmTFRs among samples in environments of different densities are likely related to both the star-formation quenching and the contraction of the mass distribution in dense environments. Likewise, the influence of each mechanism depends on the mass regime (different mass fractions). Nevertheless, in order to obtain a most robust comparison, without the effects of selection and data systematics from the different involved instruments, we highlight the necessity of a suitable comparison sample which implies to use the same data quality, similar kinematic extraction and modeling, similar selection strategy and analysis. This is the next step to implement, in order to robustly characterize the role of environment in galaxy evolution and to contrast the results from this project with a similar study, using the same strategy on the MAGIC field galaxies lead by W. Mercier (IRAP), in which I actively participate.

Chapter 7

Perspectives

The results presented in this PhD Thesis correspond to the first study using the MAGIC sample to investigate the role of environment in the dynamical properties of galaxies. This project has shown the high potential and advantages 3D spectroscopy surveys have on the study of the spatially resolved properties of large samples which allow to perform statistically meaningful analysis. In the case of MUSE its exceptional capacity to gather deep IFS observations inside its extended FoV allows the investigation of the properties and evolution of large and dense structures like groups and clusters at intermediate redshifts. I am interested in the characterization of such structures by studying their mass distribution, density (number of galaxies per Mpc^2), determination of the barycenter position, projected radial density, dynamics and interactions at large scales (accretion of gas and in-falling galaxies). This is currently in progress with the description of the MAGIC Survey and the characterization of this galaxy groups sample in the article [Epinat et al. in prep.](#), in which I actively participate. Follow-up observations in the high energy regime (X-rays with observations from Chandra and XMM) are particularly useful to perform this kind of studies.

Parallel to the obtention of the stellar TFR using the [OII] doublet as dynamical tracer, I have been working in the computation of rotation velocity in other narrow bands ($\text{H}\alpha$ -[NII] for the low redshift sample and [OIII]- $\text{H}\beta$ for the the entire sample). This is an ongoing project with the aim to determine the consistency among the estimations of the kinematic parameters using different phases of the ionized gas by evaluating the level of agreement among the different TFRs at these bands.

Moreover, the morphological decomposition I performed for this study offers the possibility to perform several complementary studies like the characterization of the morphological residuals to quantify asymmetries (lopsidedness), concentration of the profiles, to identify structures like rings, arms and bars and computing statistics on the ratio of galaxies with perturbed morphologies in function of redshift. It would also be interesting to characterize the clumpiness of the disks by performing histograms on the radial distribution of surface brightness profiles. Then, on the basis of our bulge-disc decomposition and structural analysis on asymmetries, clumpiness and internal components (bars, rings, arms, etc), it will be possible to obtain our own morphological classification on the MAGIC sample and to perform the comparison with other morphological catalogs.

The results derived from this work show the high efficiency of our methodology to consis-

tently select rotation dominated galaxies within a sample, based on the capacity to extract reliable information using resolution and S/N limits criteria. As was introduced in Section 3.3 the MAGIC survey includes other galaxy groups (CGr35, CGr87, CGr172) and new observations on the existing groups, whose data was recently reduced. Additionally, as part of the MUSE-GTO programs there are observations of dense structures in other fields like the UDFS and the HUDF. These additional datasamples enrich the diversity of environments on which the analysis proposed in this Thesis can be applied.

The study of environmental effects in galaxy evolution, using a dynamical approach has been the main objective of this work, so currently I'm participating in the analysis and identification of substantial differences between the TFR of galaxies in dense structures and that of galaxies in field in the MAGIC sample, this by applying the same methodology as the one proposed in this pioneering study. This will prove the consistency of the results of our comparison with other IFS samples with different instrumental systematics and using different methods to extract kinematics. With this groups vs. field comparison involving galaxies in the MAGIC sample, we will be able to obtain robust indicators on the role of environment and differences in the distributions of stellar mass, baryonic mass and dark-matter halos, inside well determined redshift and mass bins. For this study of galaxies in field, I extracted the velocity and velocity dispersion maps for all the objects in the MAGIC fields (except for the three newly reduced fields mentioned above), including galaxies in field and I modeled the kinematics of galaxies in the selected densest structures.

Since the debate on the evolution of the stellar mass TFR is still open, I am interested in further study the differences between the smTFR in the local Universe and galaxies at intermediate redshift using IFS data (e.g. WEAVE, SAMI and MaNGA in the local Universe vs. KMOS and MUSE at higher redshift). There is besides a lack of characterization of the environment in local Universe samples which has a lot of potential to be investigated.

From the kinematic modeling, another possibility is to construct the radial distribution of the dark matter component, based on the baryonic and dynamic mass distributions obtained in this study. This will complement the structural study on the sample of galaxies in dense structures.

I also envisage to pursue this research project by studying the distribution of the angular momentum for the MAGIC sample. This study will give a complete kinematic characterization on the support and structure of these galaxies. Additionally, it will allow to characterize the evolution processes of these galaxies and to better understand the way in which environment impacts such evolution.

Appendix A

Research in collaboration

I list here all the research projects in which I participated and contributed during my PhD and others that are in progress. Likewise, I give the links to the publications derived from the concluded projects.

- 1. Evidence for ram-pressure stripping in a cluster of galaxies at $z=0.7$**
A. Boselli, B. Epinat, T. Contini, V. Abril-Melgarejo et al. 2019, A&A.
<http://adsabs.harvard.edu/abs/2019A&A...631A.114B>
- 2. The MUSE Hubble Ultra Deep Field Survey XX. The angular momentum of low-mass star-forming galaxies. A cautionary tale and insights from TNG50.**
Nicolas F. Bouché, Shy Genel, Alisson Pellissier, Cédric Dubois et al. 2021, A&A.
<https://ui.adsabs.harvard.edu/abs/2021arXiv210112250B/abstract>
- 3. The MUSE Extremely Deep Field: the Cosmic Web in Emission at High Redshift**
Roland Bacon, David Mary, Thibault Garel, Jeremy Blaizot et al. 2021, A&A.
<https://ui.adsabs.harvard.edu/abs/2021arXiv210205516B/abstract>
- 4. MAGIC: MUSE - gALaxy Groups In Cosmos - I. A survey of galaxies in groups at intermediate redshift**
B. Epinat, T. Contini, V. Abril-Melgarejo, W. Mercier et al. (in prep.)
- 5. Galaxy kinematics of intermediate redshift field galaxies in the COSMOS area**
W. Mercier, T. Contini, B. Epinat, V. Abril-Melgarejo et al. (in prep.)
- 6. Census of galaxy gas kinematics in MUSE–UDF up to $z\sim 1.5$**
T. Contini, B. Epinat et al. (in prep.)

A.1 Paper II. Evidence for ram-pressure stripping in a cluster of galaxies at $z = 0.7$

In this Appendix I present a study performed on the interaction of two star-forming galaxies with the intra-cluster medium (ICM) of the dense structure CGr32, using data from the MUSE-gAlaxy Groups In Cosmos (MAGIC) GTO programme, in which I participate as co-author. CGr32 is a cluster structure containing 106 galaxy members and a virial mass of $M_{vir}=8.14\times 10^{14} M_{\odot}$ at $z=0.73$. MUSE observations reveal the presence of two massive galaxies ($M_{star} \sim 10^{10} M_{\odot}$) with extended low-surface brightness tails of diffuse gas detected in the [OII] emission-line doublet, with a typical surface brightness of a few $10^{-18} \text{ erg s}^{-1} \text{ cm}^{-2} \text{ arcsec}^{-2}$. The tails with cometary shape have a maximum extension of $\simeq 100$ kpc (projected distance) from the galaxy discs, and the lack of detection of any diffuse stellar counterpart in very deep infrared images (from the Suprime-Cam), clearly indicate that these two galaxies are undergoing a ram-pressure stripping event which is removing gas from them, meanwhile they traverse the intra-cluster medium (ICM). This result is thus the first evidence that the dynamical interaction between the cold galaxy interstellar medium (ISM) with the hot and dense ICM was already active when the Universe was only half its present age and it is probably one of the dominant perturbing mechanism in dense environments. Since this phenomenon has been also observed in the local Universe these observations open the possibility to study the evolution of dense structures at different cosmic epochs by performing comparisons of the different physical features of galaxies and mechanisms in play.

My contribution specifically consisted in the computation of the MUSE FWHM for the field CGr32 of the MAGIC survey where we have identified a cluster structure at $z\sim 0.7$ (See Section 3.3), and also the extraction of the observational flux, velocity and velocity dispersion maps for the two star-forming galaxies and also for their tails of diffuse ionized gas using the algorithm CAMEL, with the strategy described in Section 4.5. For the kinematic extraction I used two different smoothing coefficients using a two-dimensional FWHM of 2 and 5 pixels size. I also provided the morphological models for these two galaxies, accounting for the brightness contribution of the field bright star close to galaxy ID-473, using a free parameter to account for the gradient of the sky background in both spatial directions.

Evidence for ram-pressure stripping in a cluster of galaxies at $z = 0.7$ ^{★,★★}

A. Boselli¹, B. Epinat^{2,1}, T. Contini², V. Abril-Melgarejo¹, L. A. Boogaard³, E. Pointecouteau², E. Ventou², J. Brinchmann^{3,4}, D. Carton⁵, H. Finley^{6,2}, L. Michel-Dansac⁵, G. Soucail², and P. M. Weilbacher⁷

¹ Aix Marseille Univ., CNRS, CNES, LAM, Marseille, France

e-mail: alessandro.boselli@lam.fr, benoit.epinat@lam.fr

² IRAP, Université de Toulouse, CNRS, CNES, UPS, Toulouse, France

³ Leiden Observatory, Leiden University, PO Box 9513, 2300 RA Leiden, The Netherlands

⁴ Instituto de Astrofísica e Ciências do Espaço, Universidade do Porto, CAUP, Rua das Estrelas, 4150-762 Porto, Portugal

⁵ Univ Lyon, Univ. Lyon1, ENS de Lyon, CNRS, Centre de Recherche Astrophysique de Lyon UMR5574, 69230 Saint-Genis-Laval, France

⁶ Stockholm University, Department of Astronomy and Oskar Klein Centre for Cosmoparticle Physics, AlbaNova, University Centre, 10691 Stockholm, Sweden

⁷ Leibniz-Institut für Astrophysik Potsdam (AIP), An der Sternwarte 16, 14482 Potsdam, Germany

Received 19 June 2019 / Accepted 11 September 2019

ABSTRACT

Multi-Unit Spectroscopic Explorer (MUSE) observations of the cluster of galaxies CGr32 ($M_{200} \simeq 2 \times 10^{14} M_{\odot}$) at $z = 0.73$ reveal the presence of two massive star-forming galaxies with extended tails of diffuse gas detected in the [O II] $\lambda\lambda 3727-3729$ Å emission-line doublet. The tails, which have a cometary shape with a typical surface brightness of a few 10^{-18} erg s⁻¹ cm⁻² arcsec⁻², extend up to $\simeq 100$ kpc (projected distance) from the galaxy discs, and are not associated with any stellar component. All this observational evidence suggests that the gas was removed during a ram-pressure stripping event. This observation is thus the first evidence that dynamical interactions with the intracluster medium were active when the Universe was only half its present age. The density of the gas derived using the observed [O II] $\lambda 3729$ /[O II] $\lambda 3726$ line ratio implies a very short recombination time, suggesting that a source of ionisation is necessary to keep the gas ionised within the tail.

Key words. galaxies: clusters: general – galaxies: clusters: individual: CGr32 – galaxies: evolution – galaxies: interactions – galaxies: ISM – galaxies: high-redshift

1. Introduction

Since the seminal work of Dressler (1980), it has become evident that the environment plays a major role in shaping galaxy evolution. High-density regions such as rich clusters of galaxies are mainly composed of early-type objects, (ellipticals and lenticulars) while the field is dominated by late-type, star-forming systems. In these dense regions, the fraction of quiescent galaxies increases with decreasing redshift (e.g. Dressler et al. 1997). It is still unclear which, among the different mechanisms proposed in the literature – gravitational interactions (Merritt 1983; Byrd & Valtonen 1990; Moore et al. 1998) or hydrodynamic interactions with the hot ($T \simeq 10^7-10^8$ K) and dense ($\rho_{\text{ICM}} \simeq 10^{-3}$ cm⁻³, e.g. Sarazin 1986) intracluster medium, (ICM; Gunn & Gott 1972; Cowie & Songaila 1977; Nulsen 1982; Larson et al. 1980) whose contribution might change at different cosmic epochs, is at the origin of these observed differences (Boselli & Gavazzi 2006, 2014).

In the local Universe, where high sensitivity multi-frequency observations are available, allowing the detection of the differ-

ent stellar components and gas phases (cold, ionised, hot) with a spectacular angular resolution, it is becoming evident that within structures as massive as $M_{200} \geq 10^{14} M_{\odot}$, ram-pressure stripping is the dominant process responsible for the quenching of the star-formation activity of disc galaxies (Boselli & Gavazzi 2006). The most convincing evidence comes from the recent, very deep observations of nearby clusters using narrow-band filters centred around the H α Balmer recombination line, which revealed the presence of extended (up to $\simeq 100$ kpc) low surface brightness ($\Sigma(\text{H}\alpha) \simeq 10^{-18}$ erg s⁻¹ cm⁻¹ arcsec⁻²) tails of ionised gas. The cometary shape of the tails and the lack of any associated diffuse tidal structure rule out any gravitational perturbation, which would affect the gaseous and the stellar component at the same time. This undoubtedly means that the ionised gas tail is formed after the interaction of the galaxy interstellar medium (ISM) with the ICM. The most striking examples were first found in the nearby cluster, A1367, by Gavazzi et al. (2001), (see also Boselli & Gavazzi 2014; Gavazzi et al. 2017; Consolandi et al. 2017) and are now becoming common in other clusters such as Norma (Zhang et al. 2013), Coma (Yagi et al. 2007, 2010, 2017; Fossati et al. 2012; Gavazzi et al. 2018), and Virgo (Yoshida et al. 2002; Kenney et al. 2008; Boselli et al. 2016a, 2018a,b; Fossati et al. 2018). Tails of stripped material have also been observed in HI (Chung et al. 2007; Scott et al. 2012), in CO (Jáchym et al. 2013, 2014, 2017), and in X-rays (Sun et al. 2006, 2007, 2010),

* The reduced datacube is also available at the CDS via anonymous ftp to cdsarc.u-strasbg.fr (130.79.128.5) or via <http://cdsarc.u-strasbg.fr/viz-bin/cat/J/A+A/631/A114>

** Based on observations made with ESO telescopes at the Paranal Observatory under programmes 097.A-0254, 100.A-0607, 101.A-0282.

indicating that the other gas phases can also be perturbed during the interaction. Ram-pressure stripping as the dominant mechanism is also suggested by the relative distribution in clusters of gas-deficient and star-forming galaxies (Gavazzi et al. 2013; Boselli et al. 2014b), by the outside-in radial truncation of the different components of the ISM (Cayatte et al. 1990, 1994; Cortese et al. 2010, 2012; Boselli et al. 2014a), and the star-forming disc (Koopmann et al. 2001; Boselli & Gavazzi 2006; Boselli et al. 2006, 2015; Fossati et al. 2013), and by the abrupt truncation of the star-formation activity of cluster galaxies (Boselli et al. 2016b; Fossati et al. 2018).

The statistical importance of ram-pressure stripping, which is proportional to $\rho_{\text{ICM}} V^2$ (where V is the velocity of the galaxy within the cluster, and ρ_{ICM} is the density of the ICM), was expected to decrease at earlier epochs, when clusters of galaxies were first assembling through the accretion of smaller groups (Gnedin 2003; De Lucia et al. 2012). At this time, the reduced density of the ICM and lower velocity dispersion typical of lower-mass dark matter halos would have favoured gravitational interactions able to modify the structural properties of the perturbed galaxies. These gravitationally perturbed objects are probably the progenitors of massive lenticulars observed in nearby clusters (e.g. Boselli & Gavazzi 2006). The transformation of galaxies at higher redshift via gravitational perturbations in lower-density structures before their accretion into massive clusters (pre-processing) is also corroborated by the typical age of the stellar populations of lenticulars, their perturbed star-formation history, and their distribution in high-density regions at different epochs (Dressler et al. 1997; Dressler 2004; Poggianti et al. 1999, 2006).

Despite the fact that the aforementioned evolutionary picture is now becoming clearer, we still do not know at which epoch and under which conditions gravitational perturbations were superseded by hydrodynamic interactions of galaxies with the ICM. Although massive clusters were significantly less numerous in the past, the physical conditions encountered by infalling systems were similar to those present in local clusters, characterised by similar ρ_{ICM} gas densities (Giodini et al. 2013; McDonald et al. 2017). It is thus conceivable that ram-pressure episodes were already present at early epochs. Due to obvious observational limits, direct evidence for ongoing ram-pressure stripping at higher redshift is still lacking. Cortese et al. (2007) discovered two galaxies in two clusters at $z \approx 0.2$ with extended tails of star-forming regions that are now generally referred to as jellyfish galaxies (e.g. Poggianti et al. 2017). Since then, another ~ fifty objects with similar characteristics have been found in deep *Hubble* Space Telescope (HST) images of clusters at $0.3 \leq z \leq 0.7$ (Owers et al. 2012; Ebeling et al. 2014; McPartland et al. 2016). Since it is selected in the optical bands, however, where the emission is dominated by stars of intermediate age, a jellyfish morphology is not direct proof of an ongoing ram-pressure stripping episode (Cortese et al. 2007). In ram-pressure stripped galaxies, star-formation in the tail is not ubiquitous (e.g. Boselli et al. 2016a), and whenever observed, it is generally localised in very compact H II regions dominated by young stellar populations mainly emitting in the UV bands. Extended and asymmetric low surface brightness structures in the optical bands are due to tidal tails. The only clear example of galaxies undergoing ram-pressure stripping at intermediate redshift comes from deep Subaru narrow-band imaging observations of the cluster Abell 851 at $z = 0.4$ (Yagi et al. 2015). Indirect evidence at $z = 0.7$ comes from the reduced gas content (Betti et al. 2019), and the extended H α ionised gas emission (Vulcani et al. 2016) observed in galaxies located in high-density regions.

The search for galaxies undergoing a ram-pressure stripping event in high- z clusters is now possible thanks to the advent of new-generation instruments in the radio millimetric and optical domains. The extraordinary sensitivity of ALMA allows the detection of low-column density tails of molecular gas stripped from perturbed cluster galaxies. The results obtained in the local Universe, however, suggest that the cold gas, once stripped and in contact with the hot surrounding ICM, rapidly changes phase, becoming ionised via different possible mechanisms, such as heat conduction, shocks, or magneto hydrodynamic waves (Tonnesen & Bryan 2010, 2012; Boselli et al. 2016a; Gavazzi et al. 2018). The ionised gas phase can be detected by IFU spectrographs, provided that their sensitivity is sufficient to reach a surface brightness as low as $\sim 10^{-18}$ erg s $^{-1}$ cm $^{-1}$ arcsec $^{-2}$, the typical limiting surface brightness of Multi-Unit Spectroscopic Explorer (MUSE) after ~ one hour of exposure.

As part of the MUSE Guaranteed Time Observations (GTO), we recently undertook a spectroscopic survey of intermediate redshift ($0.25 < z < 0.85$) groups and clusters (MAGIC: MUSE-gALaxy Groups In Cosmos, Epinat et al., in prep.). During this survey, we detected two star-forming galaxies in the COSMOS cluster 32 (Knobel et al. 2012) at $z = 0.73$ with extended (up to ≈ 100 kpc in projected distance) tails of ionised gas, without any stellar counterpart in the deep optical images. This observation is thus the first evidence of an ongoing ram-pressure stripping event at $z > 0.5$. This paper is structured as follows; in Sect. 2, we briefly describe the cluster, in Sect. 3, the observations, and the data reduction. The analysis of the MUSE data is given in Sect. 4, and the results are discussed in Sect. 5, and summarised in the conclusion. We assume a Λ CDM cosmology with $H_0 = 70$ km s $^{-1}$, $\Omega_M = 0.7$, and $\Omega_\Lambda = 0.3$.

2. The galaxies ID 345 and ID 473 in the cluster CGr32

Initially identified as a group, the COSMOS cluster 32 (CGr32; Knobel et al. 2012) shows properties typical of cluster of galaxies (Table 1) CGr32 is located at a redshift of $z = 0.73$, and is part of the COSMOS Wall described by Iovino et al. (2016) (see Fig. 1). Thanks to the new MUSE observations, 105 galaxies have been identified as cluster members. We determined cluster membership based on the spatial and redshift distributions thanks to a friends-of-friends algorithm using a linking length of 450 kpc, and a velocity separation of 500 km s $^{-1}$ (Epinat et al., in prep.). The cluster has a velocity dispersion of ≈ 930 km s $^{-1}$ using all galaxies detected with MUSE, a radius of $R_{200} \approx 1.0$ Mpc, and a dynamical mass of $M_{200} \approx 2.3 \times 10^{14} M_\odot$ inferred from X-ray observations (ID 10220 in Gozaliasl et al. 2019), and is thus comparable to a fairly massive cluster like Virgo in the local Universe. The fraction of star-forming galaxies ($\sim 50\%$)¹ is close to the typical fraction observed in similar clusters at that redshift (Dressler et al. 1997), and to that of the spiral-rich Virgo cluster (48%, Boselli et al. 2014b). The galaxies studied in this work (ID 345 and ID 473) are two edge-on spirals located at ≈ 200 – 220 kpc from the cluster centre (see Table 2) coherently identified as the peak of galaxy and hot-gas density in both the MUSE data (Epinat et al., in prep.), and in the *XMM-Newton/Chandra* X-rays data (Finoguenov et al. 2007;

¹ The distinction between quiescent and star-forming galaxies is made from their distribution in the main sequence diagram as suggested by Barro et al. (2017), and consistently with Boselli et al. (2014b). Stellar masses and star-formation rates have been derived as described in Sect. 3.2.

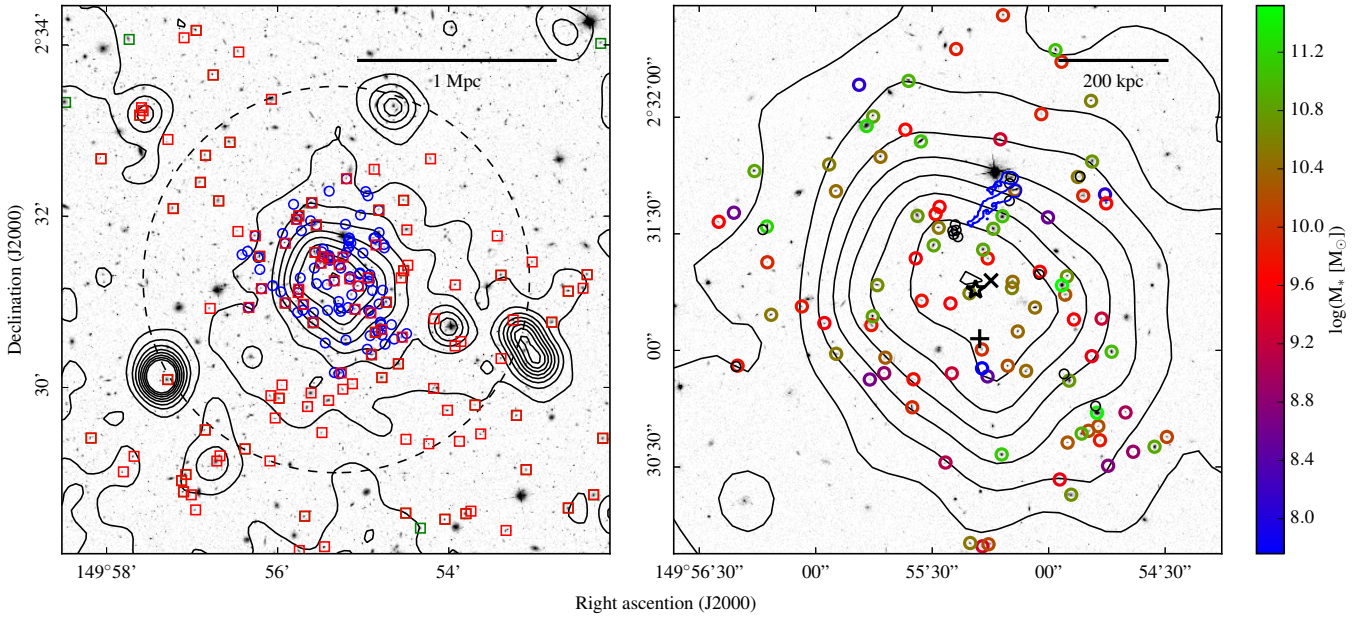


Fig. 1. Distribution of galaxies within the cluster CGr32. *Left panel:* $6' \times 6'$ HST ACS (F814W filter, logarithmic scale, arbitrary units) map of COSMOS region, including the CGr32 cluster of galaxies. Spectroscopically identified cluster members within the MUSE data are indicated with blue circles, and galaxies in the Iovino et al. (2016) and Knobel et al. (2012) catalogues within the same redshift range ($0.71685 \leq z \leq 0.74378$) are indicated with red squares. Contours show the X-ray gas distribution (XMM-Newton, 0.5–2 keV, Finoguenov et al. 2007), smoothed with a two-pixel Gaussian. The grey dashed circle represents R_{200} . *Right panel:* close-up of the region mapped with MUSE. Galaxies are colour coded according to their stellar mass (Epinat et al., in prep.), and those without mass estimates due to blending in broad-band images are shown with black circles. The black star indicates the barycentre of the MUSE cluster members, the black plus sign is the centre quoted by Iovino et al. (2016), and the black cross indicates the X-ray centre of Gozaliasi et al. (2019). The tails of ionised gas are indicated with a blue contour ($\Sigma([\text{O II}]) = 1.5 \times 10^{-18} \text{ erg s}^{-1} \text{ cm}^{-2} \text{ arcsec}^{-2}$).

George et al. 2011; Gozaliasi et al. 2019, and this work – see Table 1 and Sect. 3.2). The asymmetric velocity distribution of galaxy members and a significantly larger velocity dispersion of the star-forming galaxies ($\sigma_{\text{SF}} = 1085 \text{ km s}^{-1}$) with respect to the quiescent objects ($\sigma_{\text{Q}} = 697 \text{ km s}^{-1}$) suggest infall into the cluster (Colless & Dunn 1996), as is expected for a cluster still in formation (Fig. 2). The galaxies ID 345 and ID 473 (Fig. 3) have a relative line-of-sight velocity with respect to the cluster of $\Delta V_{\text{ID 345}} = -824 \text{ km s}^{-1}$ and $\Delta V_{\text{ID 473}} = -1903 \text{ km s}^{-1}$, and are thus crossing the cluster from the back. Despite its large line-of-sight velocity, ID 473 has a high probability of being a real member of the cluster. Using more stringent parameters for the friends-of-friends algorithm as low as 375 kpc and 400 km s^{-1} , as suggested by Iovino et al. (2016), it still remains a member.

3. Observations and data reduction

3.1. MUSE spectroscopy

Details of the MUSE observations and data reduction will be presented in a dedicated paper (MAGIC survey paper, Epinat et al., in prep.). Here, we briefly summarise the main steps. The observations of CGr32 were obtained during MUSE-GTO as part of the MAGIC project (Epinat et al., in prep., PI: T. Contini). Three fields were necessary to map the cluster core. An equal observing time of 4.35 h was spent on each field over three observing runs: 1 h per field without adaptive optics (AO) in April 2016 (Programme ID 097.A-0254), 3.3 h per field with AO in March (3.3 h in total, Programme ID 100.A-0607) and April 2018 (6.7 h in total, Programme ID 101.A-0282). For each run, the observing block sequence consisted of four 900 s exposures, each taken after rotating the field by 90° .

Table 1. Properties of the cluster CGr32.

Variable	Value	Ref.	Comment
RA ($J2000$)	149°55'19.0''	TW	MUSE barycentre
Dec ($J2000$)	2°31'15.5''	TW	MUSE barycentre
RA ($J2000$)	149°55'14.8''	1	From X-rays data
Dec ($J2000$)	2°31'18.0''	1	From X-rays data
z	0.7303	1	
σ	931 km s^{-1}	TW	Full sample
σ_{Q}	697 km s^{-1}	TW	Quiescent galaxies
σ_{SF}	1085 km s^{-1}	TW	Star-forming galaxies
R_{200}	1.53 Mpc	TW	From MUSE data
M_{200}	$8.14 \times 10^{14} M_{\odot}$	TW	From MUSE data ^(a)
R_{200}	0.983 Mpc	1	From X-rays data
M_{200}	$2.33 \times 10^{14} M_{\odot}$	1	From X-rays data

Notes. ^(a)This mass reduces to $M_{200} = 3.41 \times 10^{14} M_{\odot}$ if derived using the velocity dispersion of the quiescent population only, rather than the full sample.

References. TW: this work, (1) Gozaliasi et al. (2019).

For each of the three fields, we produced a single reduction combining all exposures with and without AO. The reduction was performed using the MUSE standard pipeline v1.6 (Weilbacher et al. 2012, 2014; Weilbacher 2015). The data reduction process generates data cubes with a spatial sampling of $0.2''$ and a spectral sampling of 1.25 \AA . The spatial extent of each field is of one square arcminute, and the spectrum ranges from 4750 \AA to 9350 \AA .

The point spread function (PSF) of the combined exposures was estimated on each field from a Gaussian fit to the stars

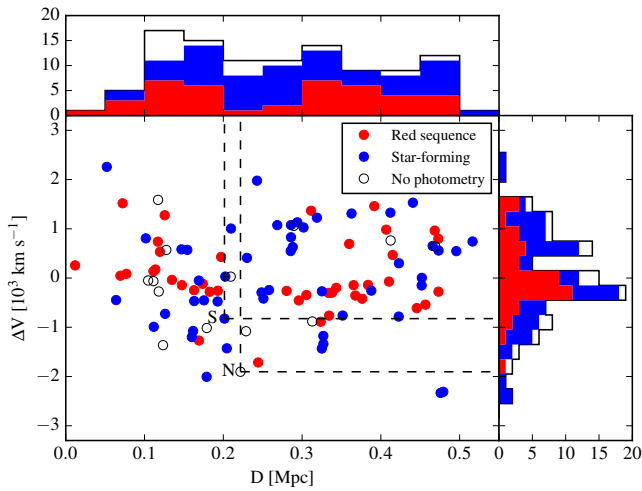


Fig. 2. Phase-space diagram of galaxies in cluster CGr32 determined using the barycentre of the cluster members identified spectroscopically with MUSE as the cluster centre. Quiescent galaxies are indicated with red-filled dots, star-forming objects with blue-filled dots. Black open circles show blended galaxies with unavailable broad-band photometry. The galaxies ID 345 and ID 473 are indicated with “S” and “N”, respectively.

present in each datacube. The average full width at half maximum (FWHM) at $\lambda = 6450 \text{ \AA}$ ranges from $0.60''$ to $0.72''$ depending on the field. The two galaxies with tails are visible on the same field, which has an FWHM of $0.60''$.

We derived $[\text{O II}]^2$ flux (Fig. 3) and kinematics (Fig. 4) maps for the two galaxies with tails using CAMEL³ (Epinat et al. 2012), which fits any emission line using a Gaussian function and a polynomial continuum to any pixel of a datacube, after a Gaussian spatial smoothing with an FWHM of 3×3 pixels and using a continuum of degree one, mainly to account for the continuum of the strong star in the field, which is close to the two galaxies. We also extracted the same maps with a Gaussian spatial smoothing of 4×4 pixels FWHM in order to define masks where the tails are detected in $[\text{O II}]$. The masks were defined using both a flux threshold of $7.5 \times 10^{-19} \text{ erg s}^{-1} \text{ cm}^{-2} \text{ arcsec}^{-2}$ (1.5 times the surface brightness limit in the smoothed $[\text{O II}]$ map) and a criterion on kinematics of the detected structure to remove regions with velocity discontinuities larger than $\approx 200 \text{ km s}^{-1}$. An additional mask was applied to hide the emission from other galaxies in the group. These final masks were used to produce integrated spectra (and their variance spectra) for both galaxies and associated tails (cf. Fig. 5). The velocity amplitude over these galaxies and tails is $\sim 400 \text{ km s}^{-1}$, which would broaden emission lines in the spectra integrated over the masks, and thus decrease the signal to noise ratio. Therefore, in order to remove large-scale velocity variations, each pixel is set, before integration, at rest wavelengths using the spatially resolved velocity field shown in Fig. 4. The residual broadening resulting from the uncertainties in the velocity field is $\sim 30\text{--}50 \text{ km s}^{-1}$, which is below the spectral resolution of the MUSE data (see Bacon et al. 2017) over the whole spectral range shown in Fig. 5. The continuum resulting from the bright star was removed from the galaxy ID 473 and its tail spectra by scaling the absorption lines of the star spectrum. For the tail, a residual continuum signal from both the star and a

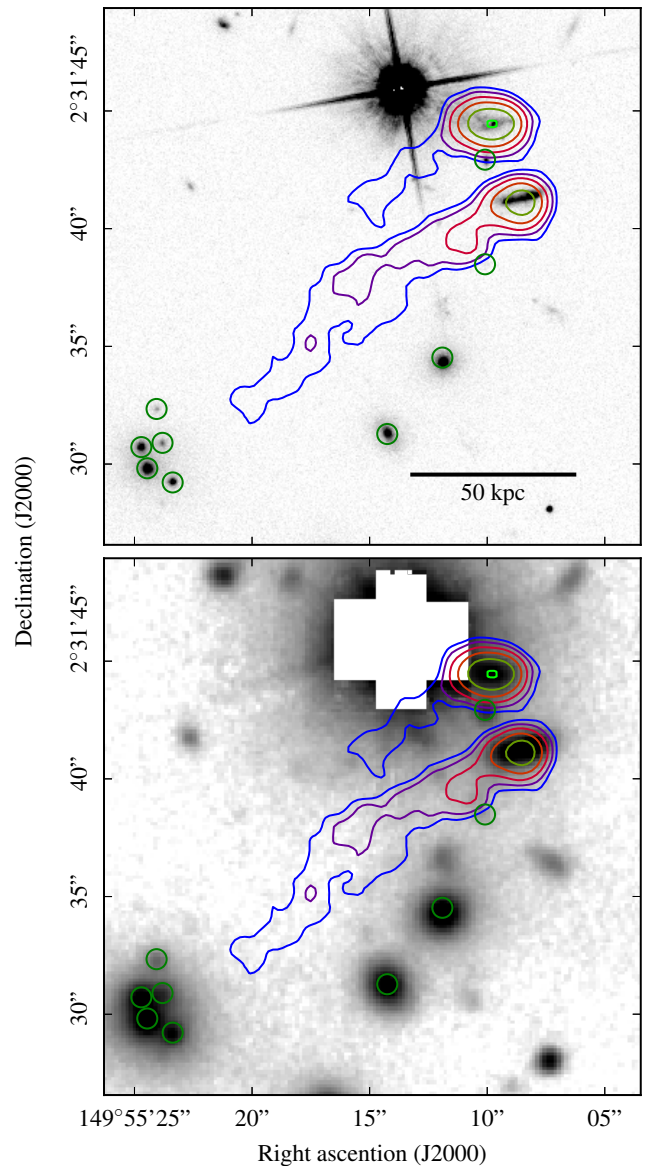


Fig. 3. F814W HST ACS (top) and i' -band Suprime-Cam (bottom) images of galaxies ID 345 (south) and ID 473 (north) in cluster CGr32. Other cluster members are shown with green circles. Contours show the $[\text{O II}]$ flux map obtained using a Gaussian smoothing of 3 pixels FWHM at a level of $\Sigma([\text{O II}]) = 1.5, 3.3, 7.4, 16.3, 36.1, 80.0 \times 10^{-18} \text{ erg s}^{-1} \text{ cm}^{-2} \text{ arcsec}^{-2}$. Both images (oriented as in the sky, north is up, east on the left) show the lack of any optical counterpart along the tail.

background galaxy was also removed. In the tails, the $[\text{O II}]$ doublet flux was then measured as the sum of the spectrum around a narrow spectral window centred on the line, which corresponds to a velocity amplitude of 600 km s^{-1} around each side of the lines. Uncertainties were determined over the same range from the variance spectrum. The observed fluxes in the tail are given in Table 2. We also measured the mean $[\text{O II}]$ doublet ratio within the tail. The mean ratio in the tail of ID 345, the only one where the signal is sufficiently high to make this velocity correction possible, is $[\text{O II}]\lambda 3729/[\text{O II}]\lambda 3726 = 1.15 \pm 0.06$. It is important to remember, however, that this is a light-weighted mean, probably biased towards the emission of the brightest regions, possibly associated with compact, but unresolved, H II regions. If we

² Hereafter $[\text{O II}]$ refers to the $[\text{O II}]\lambda 3727\text{--}3729 \text{ \AA}$ emission-line doublet.

³ <https://gitlab.lam.fr/bepinat/CAMEL.git>

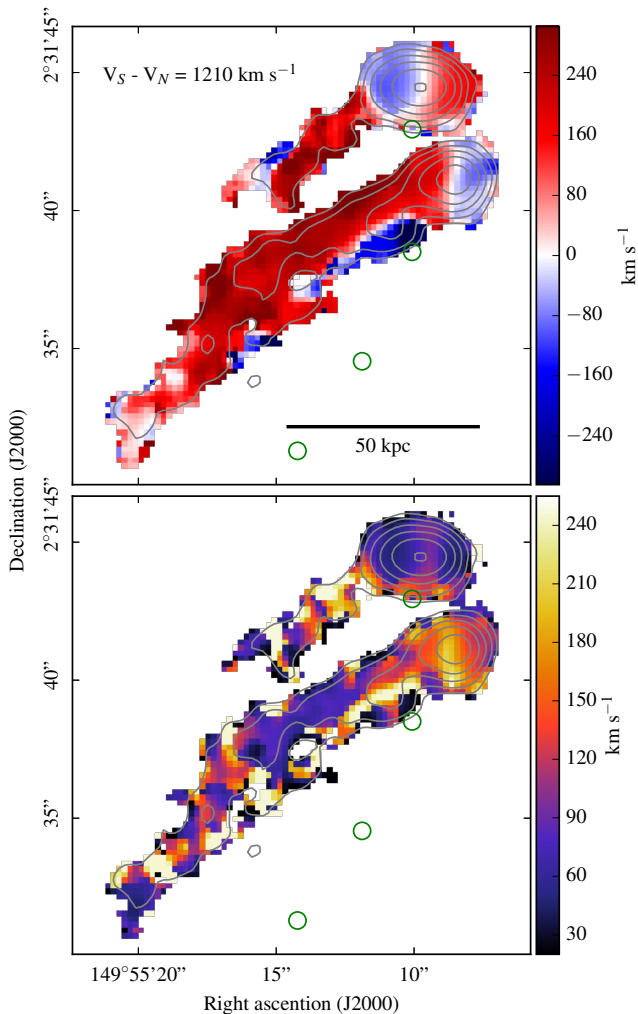


Fig. 4. *Top panel:* velocity fields of the tails obtained using a Gaussian smoothing of 3 pixels FWHM. The two subsystems have been put at rest frames, so that they can be compared on the same figure. *Bottom panel:* velocity dispersion map of the tail obtained using a Gaussian smoothing of 3 pixels FWHM. The contours correspond to [O II] flux emission as in Fig. 3. The green circles indicate the position of other cluster member galaxies.

try to measure the [O II] doublet ratio pixel per pixel along the tail, its ratio is $[\text{O II}]\lambda 3729/[\text{O II}]\lambda 3726 \approx 1.5$ in more than 50% of the pixels. We also tried to measure $\text{H}\beta$ and $[\text{O III}]\lambda 5007 \text{ \AA}$ line fluxes in the tails using the masks defined for the [O II] doublet. We obtained a $\sim 1.5\text{-}\sigma$ detection of $\text{H}\beta$ on the integrated spectrum of the tail associated to ID 345 ($f_{\text{ID 345}}(\text{H}\beta) = 7.76 \pm 5.25 \times 10^{-18} \text{ erg s}^{-1} \text{ cm}^{-2}$), and an upper limit in the tail of ID 473 ($\sigma_{\text{ID 473}}(\text{H}\beta) = 1.92 \times 10^{-18} \text{ erg s}^{-1} \text{ cm}^{-2}$), as well as upper limits in both tails for the [O III] line ($\sigma_{\text{ID 345}}([\text{O III}]) = 5.23$ and $\sigma_{\text{ID 473}}([\text{O III}]) = 2.03$ in units of $10^{-18} \text{ erg s}^{-1} \text{ cm}^{-2}$).

For the two galaxies, we first removed the stellar continuum using pPXF (Cappellari & Emsellem 2004) with the MILES stellar population synthesis library (Falc3n-Barroso et al. 2011). We then determined fluxes of $\text{H}\beta$, $\text{H}\gamma$, [O II] and [O III] using the same method as for the tails.

3.2. Other data

CGr32 is inside the COSMOS field (Scoville et al. 2007) and has therefore been observed in many bands. We used the

HST Advanced Camera for Surveys (ACS) image of the field observed with the F814W filter for a morphological analysis of the two galaxies with GALFIT (Peng et al. 2002), while the Subaru Prime Focus Camera (Suprime-Cam) image in the i' -band (Taniguchi et al. 2007), the deepest available for this field with a limiting surface brightness of $28 \text{ mag arcsec}^{-2}$, was used to search for any possible red stellar population counterpart in the galaxy tails. We also used the *XMM-Newton* data for the determination of the density profile of the hot ICM. For this purpose, we used the COSMOS mosaic image in the 0.5–2 keV band (Hasinger et al. 2007; Finoguenov et al. 2007) for illustration purposes in Fig. 1, and the OBSID 0203361701 archive data for the extraction of the hot gas density distribution. This is the longest exposure ($\sim 32 \text{ ksec}$) covering CGr32 within the inner 10 arcmin of the FoV. The data were processed following the methodology presented in Pratt et al. (2007) and Bartalucci et al. (2017). The 3D density profile is derived from the surface brightness profile (extracted at the position of the X-ray centre reported in Table 1) using a non-parametric deconvolution and deprojection method with regularisation (Croston et al. 2006, see Fig. 6 and Sect. 5).

We determined galaxy parameters, such as stellar mass, star-formation rate (SFR), and extinction, from spectral energy distribution models using the FAST code (Kriek et al. 2009) as described in Epinat et al. (2018) for a similar dataset in the COSMOS field with deep imaging data from the UV to the near-IR. Stellar masses and SFRs are calculated assuming a Chabrier (2003) IMF. The spectrum of ID 345 exhibits asymmetric shapes of the emission lines $[\text{O III}]\lambda 4959, 5007$ and $\text{H}\beta$, which could be explained by a contribution from an AGN. The presence of an AGN is also suggested by its strong observed radio emission at 1.4 GHz (0.115 mJy – Schinnerer et al. 2010 – corresponding to a rest-frame luminosity $L(1.4 \text{ GHz}) = 4 \times 10^{23} \text{ W Hz}^{-1}$ derived assuming a nonthermal spectral index $\alpha = 0.8$ – Condon 1992). Should such an AGN indeed be present, this could bias the SFR derived from the SED fitting. For the galaxy ID 473, where the photometry is highly contaminated by a nearby star, the stellar mass is just a rough estimate. For this galaxy, the SFR was determined using two different methods, the first one from the $\text{H}\beta$ emission line corrected for dust attenuation using the Balmer decrement, the second one from the observed [O II] line using the Moustakas et al. (2006) calibration.

4. Analysis

4.1. Physical properties

The MUSE observations of the cluster reveal the presence of an extended tail of ionised gas detected in the [O II] line associated with the two galaxies ID 345 and ID 473, as depicted in Fig. 3. The two tails, which extend from the galaxy discs in the south-east direction, are $13.4''$ (97 kpc) and $4.7''$ (34 kpc) long (projected distance), and $2.9''$ (21 kpc) and $2.1''$ (15 kpc) wide (see Table 2). The deep optical images of the cluster do not show any stellar counterpart associated with the extended ionised gas tail (Fig. 3) down to a surface brightness limit of $\approx 28 \text{ mag arcsec}^{-2}$ in the i' -band. The orientation of the tails, which in both cases is parallel to the stellar disc major axis, also indicates that the gas stripping occurs edge-on. Figure 5 shows the spectra of the galaxies and their tails.

We can compare the properties of the tails to those observed in local galaxies. Unfortunately, at this redshift, the $\text{H}\alpha$ line is outside the spectral domain of MUSE, while $\text{H}\beta$ is only barely detected ($1.5\text{-}\sigma$ detection) in the tail of ID 345 and undetected in

A&A 631, A114 (2019)

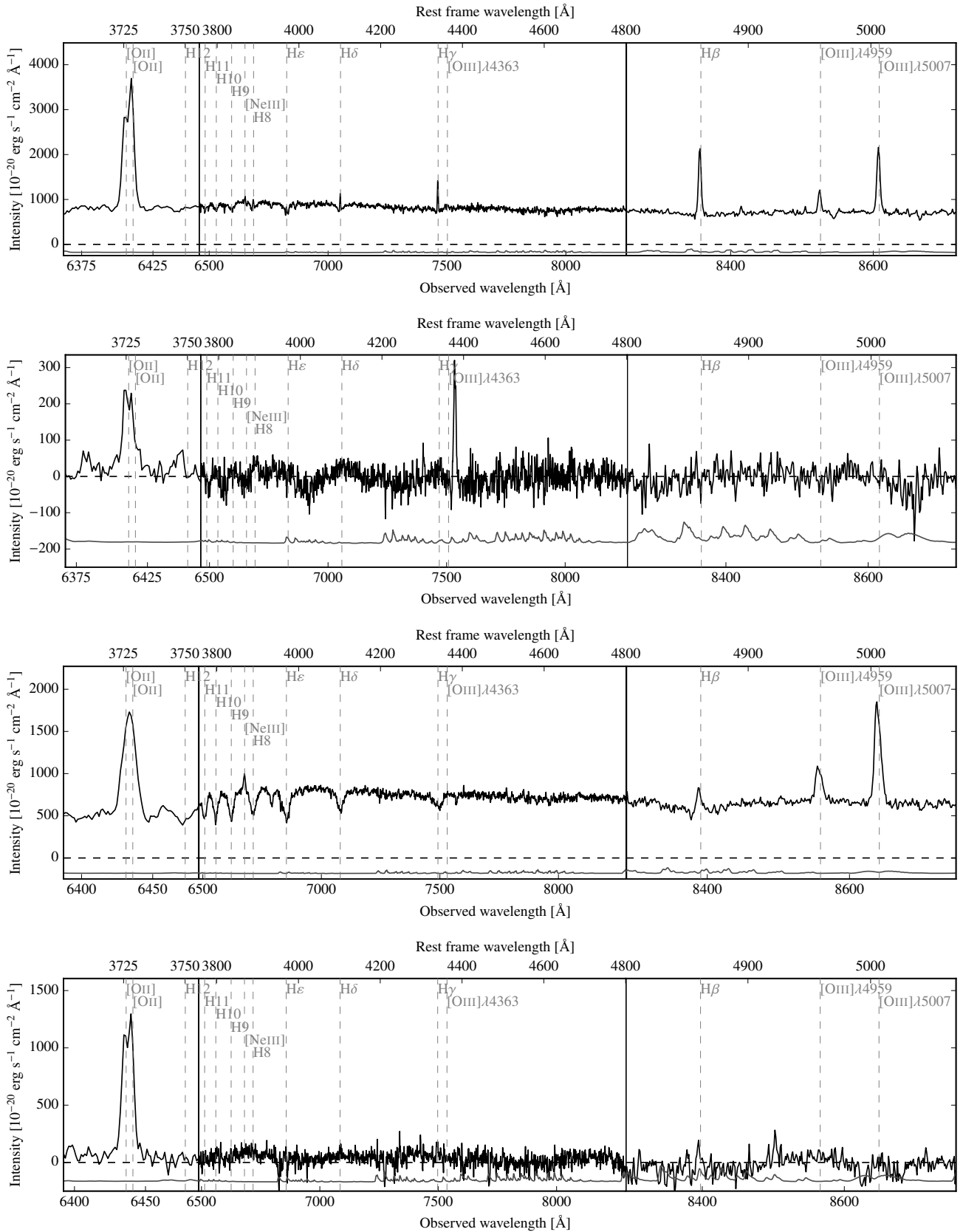


Fig. 5. MUSE integrated spectra corrected for variations in the velocity field of galaxy ID 473 (*upper panel*), its tail (*upper middle panel*), galaxy ID 345 (*lower middle panel*), and its tail (*lower panel*). The associated standard deviation, which is shifted below zero for clarity, is shown in grey. The main lines at the redshift of the sources are indicated with grey dotted vertical lines. An emission around 7500 Å associated with a background [O II] emitter is observed in the spectra of ID 473's tail. Fluctuations in the spectra of the tails are due to imperfect bright-star continuum subtraction and faint background sources.

Table 2. Properties of the two galaxies with tails.

Variable	ID 345	ID 473
RA ($J2000$)	149°55′8.6″	149°55′9.7″
Dec ($J2000$)	2°31′41.2″	2°31′44.6″
$V_{\text{gal}} - V_{\text{CGr32}}$	-824 km s ⁻¹	-1903 km s ⁻¹
$R^{(a)}$	201 kpc	222 kpc
M_{star}	$2.0 \times 10^{10} M_{\odot}$	$\sim 10^{10} M_{\odot}$
$M_{\text{dyn}}^{(b)}$	$1.0 \times 10^{11} M_{\odot}$	$9.7 \times 10^{10} M_{\odot}$
σ	131 ± 48 km s ⁻¹	41 ± 34 km s ⁻¹
SFR	$38 M_{\odot} \text{ yr}^{-1}$ ^(c)	$10\text{--}24 M_{\odot} \text{ yr}^{-1}$ ^(d)
tail proj. length	97 kpc	34 kpc
tail proj. width	21 kpc	15 kpc
$f([\text{O II}]_{\text{tail}})$	$113.4 \pm 2.3 \times 10^{-18}$ erg s ⁻¹ cm ⁻²	$26.4 \pm 1.2 \times 10^{-18}$ erg s ⁻¹ cm ⁻²

Notes. ^(a)Projected distance from the cluster centre. ^(b)Dynamical masses were estimated using the extent measured in the [O II] distribution, and the velocity amplitude of a rotating disc model, which takes into account the beam smearing as done in [Contini et al. \(2016\)](#). The velocity dispersion was corrected for beam smearing and for the instrumental spectral resolution. ^(c)Possibly overestimated due to the presence of an AGN. ^(d)The first value has been measured from the H β line using a dust attenuation estimate derived from the Balmer decrement, the second one has been derived from the observed [O II] line using the calibration of [Moustakas et al. \(2006\)](#).

ID 473, we thus have to derive the intensity of the [O II] line and convert it into H α assuming a standard [O II]/H α ratio. Spectroscopic observations of the tails of ionised gas in ram-pressure stripped galaxies of the local Universe are limited to the spectral domain $\lambda \geq 4000\text{--}9000 \text{ \AA}$ ([Yoshida et al. 2004, 2012; Fossati et al. 2016; Poggianti et al. 2017](#)), preventing any estimate of this ratio from local measurement. The only direct measurement of the [O II]/H α ratio in the stripped material of local galaxies is the value derived by [Cortese et al. \(2006\)](#) around some gravitationally perturbed galaxies in the cluster A1367 ([O II]/H $\alpha \approx 2$). We do not expect the physical properties of the stripped gas, which is not associated with any stellar component and is probably embedded in a similarly hot and dense ICM, to differ significantly from those observed in A1367. This value is consistent with the value derived using the $1.5\text{-}\sigma$ detection of H β in the tail of ID 345 ([O II]/H $\beta = 14.6$) and the $3\text{-}\sigma$ upper limit in ID 473 ([O II]/H $\beta \geq 4.6$), and adopting H α /H $\beta = 2.86$, if we make the reasonable assumption that the dust attenuation is negligible. We thus derive the H α luminosity assuming [O II]/H $\alpha = 2$ ($L(\text{H}\alpha) = 1.3 \times 10^{41} \text{ erg s}^{-1}$ for ID 345 and $L(\text{H}\alpha) = 2.5 \times 10^{40} \text{ erg s}^{-1}$ for ID 473) and the mean surface brightness of the tails ($\Sigma(\text{H}\alpha) = 1.5 \times 10^{-18} \text{ erg s}^{-1} \text{ arcsec}^{-2}$ for ID 345 and $\Sigma(\text{H}\alpha) = 1.3 \times 10^{-18} \text{ erg s}^{-1} \text{ arcsec}^{-2}$ for ID 473). These numbers, which are close to the detection limits of modern instrumentation, are comparable to those observed in the nearby Universe. Due to cosmological surface brightness dimming, however, when transformed to physical units, both H α luminosities and surface brightnesses are a factor of ~ 10 higher than those measured in local systems.

We can also use the [O II] $\lambda 3729$ /[O II] $\lambda 3726$ line ratio to derive the gas density within the tails. For a mean value of [O II] $\lambda 3729$ /[O II] $\lambda 3726 = 1.15 \pm 0.06$ measured on the integrated spectrum of the tail of ID 345, the corresponding electron density is $n_e \approx 200 \text{ cm}^{-3}$. As mentioned in Sect. 3.1, however, this is a light-weighted mean, and is thus probably biased towards the brightest and highest density regions, unresolved in

the MUSE data. Indeed, this gas density perfectly matches that observed in star-forming regions of galaxies at $z \approx 2$ ([Sanders et al. 2016](#)). The typical line ratio measured pixel per pixel in the diffuse tail is [O II] $\lambda 3729$ /[O II] $\lambda 3726 \approx 1.5$, corresponding to a gas density $n_e \lesssim 10 \text{ cm}^{-3}$ ([Osterbrock & Ferland 2006](#)). This upper limit is consistent with the gas density derived from the [S II] $\lambda 6716$ /[S II] $\lambda 6731$ line ratio measured in the diffuse tails of local galaxies, or independently with geometrical considerations (e.g. [Fossati et al. 2016; Boselli et al. 2016a](#)). As in [Boselli et al. \(2016a\)](#) and [Fossati et al. \(2016\)](#), we can also estimate the typical recombination time of the ionised gas,

$$\tau_{\text{rec}} = \frac{1}{n_e \alpha_A}, \quad (1)$$

where α_A is the total recombination coefficient ($\alpha_A = 4.2 \times 10^{-13} \text{ cm}^3 \text{ s}^{-1}$; [Osterbrock & Ferland 2006](#)). For $n_e = 10 \text{ cm}^{-3}$, $\tau_{\text{rec}} \approx 10^4 \text{ yr}$, a very short time compared to the travel time of the tail ($\tau_{\text{travel}} \approx 10^8 \text{ yr}$).

This very short recombination time suggests that, as in local galaxies, a source of gas excitation within the tail must be present. In the case where photoionisation, which requires the presence of star-forming regions within the tail, is lacking, other ionising mechanisms include thermal conduction, magneto hydrodynamics waves, and shocks ([Fossati et al. 2016; Boselli et al. 2016a](#)). The presence of shock-ionised gas is suggested by the high [O II]/[O III] $\lambda 5007$ ratio observed in the tails ([O II]/[O III] $\lambda 5007 \gtrsim 7$ and 4.5 in ID 345 and ID 473, respectively, [Dopita & Sutherland 1995](#)). Part of the stripped gas might still be in other phases such as cold H I, or hot-gas emitting in X-rays, as suggested by simulations ([Tonnesen & Bryan 2010, 2012](#)).

4.2. Kinematical properties

Figure 4 shows the velocity field and the velocity dispersion map of the ionised gas over the two perturbed galaxies and along the tails. The velocity field of both galaxies is very symmetric, and the difference between the receding and approaching sides of both almost edge-on rotating ($>70^\circ$) discs is $\sim 300 \text{ km s}^{-1}$. In addition, the size of the two galaxies is quite similar, which suggests that they have a comparable dynamical mass (cf. Table 2). The velocity of the gas is fairly constant along the tails, and is a bit higher than that of the associated galaxies, which means that the gas is decelerated in the tail, confirming its stripped-gas origin. This difference is higher for the northern galaxy ID 473 ($\Delta V \sim 100 \text{ km s}^{-1}$). The low velocities (in blue) associated with a higher velocity dispersion in the southern tail are caused by the overlap of the tail with a galaxy of the cluster with a lower velocity than the tail (cf. Fig. 3). The velocity dispersion of the gas is high in the southern galaxy ID 345 ($\sim 131 \text{ km s}^{-1}$), which seems to host an active galactic nucleus (based on broad lines and a high [O III] $\lambda 5007$ /H β ratio around 3.5 on the integrated spectrum). It is lower ($\sim 75 \text{ km s}^{-1}$) in the northern galaxy ID 473, while the velocity dispersion of the gas along both tails is fairly high ($\sim 80 \text{ km s}^{-1}$). It should be noted, however, that this is a light-weighted estimate of the velocity dispersion of the gas within the tails. It is comparable to the median dispersion along tails ($\sim 90 \text{ km s}^{-1}$) determined on the velocity dispersion map (see Fig. 4), but much more uncertain, due to the low signal-to-noise. Similar velocity dispersions have been observed within the tail of local galaxies (e.g. ESO 137-001, [Fumagalli et al. 2014](#).)

5. Discussion

The presence of long tails of ionised gas without any old stellar counterpart suggests that the two galaxies are now undergoing a

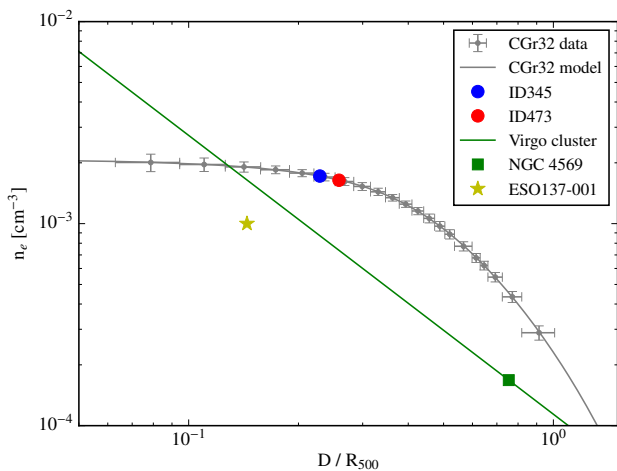


Fig. 6. Normalised radial profile of intra-cluster electron density of CGr32 (data as grey points and best fit as a grey solid line) derived from *XMM-Newton* observation compared to that of the Virgo cluster (green solid line) derived from *Suzaku* and *Planck* data (Simionescu et al. 2017). The blue and red dots, the green square, and the yellow star indicate the position of the galaxies ID 345, ID 473 in CGr32, NGC 4569 in Virgo, and ESO 137-001 in Norma, respectively. Norma R_{500} was estimated using the Sun et al. (2009) mass-temperature relation with $kT = 6$ keV.

ram-pressure stripping episode. The derived density, mass, and recombination time of ionised gas stripped during the interaction, as well as the shape and size of the tail associated to the two galaxies ID 345 and ID 473, are very similar to those observed in the massive spiral NGC 4569 in the Virgo cluster, or ESO 137-001 in the Norma (A3627) cluster. The conditions for gas stripping via ram pressure, $\rho_{\text{ICM}} V^2 > 2\pi G \Sigma_{\text{gas}} \Sigma_{\text{star}}$ (Gunn & Gott 1972), where Σ_{gas} and Σ_{star} are the density of gas and stars over the disc of the galaxy, can be compared to those encountered in these nearby counterparts. Indeed, the velocity dispersion of the cluster CGr32 ($\langle V_{\text{cluster}} \rangle \approx 930 \text{ km s}^{-1}$) is close to that of Virgo ($\langle V_{\text{cluster}} \rangle \approx 800 \text{ km s}^{-1}$, Boselli et al. 2014b) and Norma ($\langle V_{\text{cluster}} \rangle \approx 925 \text{ km s}^{-1}$, Sun et al. 2010), where ram-pressure stripping is active.

We use the radial profile of the intracluster electron density, n_e , derived from *XMM-Newton* data (see Sect. 3.2) to estimate n_e at the position of the two target galaxies (Fig. 6). The azimuthal mean densities of the hot intracluster gas at the position of the two galaxies ID 345 and ID 473, are $n_e = 1.7 \times 10^{-3}$ and $n_e = 1.6 \times 10^{-3} \text{ cm}^{-3}$, respectively. These densities are comparable to those encountered in similar clusters in the redshift range $z = 0.7$ to $z = 0$ (Giodini et al. 2013; McDonald et al. 2017).

These electron densities can also be compared to those measured in the Virgo cluster at a similar radial distance from the cluster core ($n_e \approx 2 \times 10^{-3} \text{ cm}^{-3}$ at 100 kpc, $n_e \approx 10^{-3} \text{ cm}^{-3}$ at 200 kpc), or at the distance of NGC 4569 ($n_e \approx 2 \times 10^{-4} \text{ cm}^{-3}$ at 500 kpc)⁴ as derived from *Suzaku* and *Planck* data by Simionescu et al. (2017). They can also be compared to those in the Norma cluster at the distance of ESO 137-001 ($n_e \approx 10^{-3} \text{ cm}^{-3}$ at 180 kpc, Sun et al. 2010). The conditions encountered by the galaxies ID 345 and ID 473 in the cluster CGr32, very similar to those observed in similar objects in the local Universe, are optimal for an efficient ram-pressure stripping event. The gas column density over the disc of the two galaxies is prob-

ably higher than those present in ESO 137-001 and NGC 4569, while the stellar density is probably lower, just because they are observed at much earlier epochs ($z = 0.7$). In particular, we recall that NGC 4569 is a bulge-dominated Sa galaxy. The relative absolute line-of-sight velocities with respect to the mean velocity of the cluster are $V_{\text{ID 345}} - \langle V_{\text{CGr32}} \rangle = -824 \text{ km s}^{-1}$ and $V_{\text{ID 473}} - \langle V_{\text{CGr32}} \rangle = -1903 \text{ km s}^{-1}$. The projected extension of the ionised gas tails suggests that the galaxies are also moving on the plane of the sky, thus these values should be considered as lower limits. These numbers can also be compared to the relative line-of-sight velocity of NGC 4569 with respect to Virgo, $V_{\text{NGC 4569}} - \langle V_{\text{Virgo}} \rangle = 1176 \text{ km s}^{-1}$, ESO 137-001 with respect to Norma, $V_{\text{ESO 137-001}} - \langle V_{\text{Norma}} \rangle = 191 \text{ km s}^{-1}$, and UGC 6697 with respect to A1367, $V_{\text{UGC 6697}} - \langle V_{\text{A1367}} \rangle = 132 \text{ km s}^{-1}$. This simple comparison suggests that, as in their local counterparts, ID 345 and ID 473 are suffering a ram-pressure stripping event. It is also worth mentioning that one of the two galaxies, ID 345, shows prominent Balmer absorption lines (see Fig. 5), typical in objects suffering an abrupt variation in star-formation activity. Its position above the main sequence (at $z = 0.7$ main sequence galaxies of $M_{\text{star}} \sim 10^{10} M_{\odot}$ have star-formation rates $\text{SFR} \sim 10 M_{\odot} \text{ yr}^{-1}$, Whitaker et al. 2014) suggests that this galaxy might have undergone a moderate starburst phase induced by the compression of the gas along the disc (e.g. Bekki 2014). The decrease in activity indicated by the prominent Balmer absorption lines might result after gas ablation, which in a ram-pressure stripping event occurs outside-in, and reduces the activity of star-formation in the outer disc, as indeed observed in local galaxies (e.g. Boselli et al. 2006, 2016b; Fossati et al. 2018). We can also mention that the edge-on orientation of the galaxies on the plane of the sky, and in the direction of the stripping, favours the detection of the optically thin ablated gas just for projection effects.

The parallel orientation of the tails of the two galaxies is, however, striking. It is very unlikely that these two objects are members of a group, and are thus gravitationally interacting while infalling into the cluster. Their relative velocity is very high ($V_{\text{ID 473}} - V_{\text{ID 345}} = 1079 \text{ km s}^{-1}$), thus the duration of the tidal encounter is too short to induce important modifications (Boselli & Gavazzi 2006). Furthermore, if both galaxies were members of the same infalling group, they would be spiralling around the centre of gravity, producing twisted tails, as observed in the blue infalling group in A1367 (Cortese et al. 2006; Fossati et al. 2019). We remark that both tails are oriented from the galaxies to the south-east, the same direction of the filamentary structure joining the cluster CGr32 to the COSMOS Wall (Iovino et al. 2016). This might indicate that both galaxies have been accreted from this structure and have just crossed the cluster. Their difference in velocity might just indicate that they come from a different region of the COSMOS Wall, which seems to extend over several Mpc along the line-of-sight (Iovino et al. 2016).

If the gas keeps the dynamical imprint of the region from where it has been stripped and is decelerated by the interaction with the hot ICM, as observed in local edge-on galaxy UGC 6697 in A1367 (Consolandi et al. 2017), Fig. 4 can be interpreted as follows: in the northern galaxy ID 473 the gas is decelerated in the tail with respect to the galaxy, which means that the trajectory of the galaxy within the cluster is not on the plane of the sky, but rather on the line of sight, thus, the galaxy is crossing the cluster from the background. This could explain why the tail is relatively short compared to that of ID 345. In the southern galaxy ID 345, the less pronounced velocity offset between the galaxy and the tail, and the extension of the tail,

⁴ The electron density of the ICM at the distance of NGC 4569 is significantly different to the one reported in Boselli et al. (2016a), which was based on old ROSAT data.

suggest that the trajectory of the galaxy within the cluster is mainly on the plane of the sky. The observed large velocities along the tail may be due to a combination of gas in the tail being decelerated, and gas being stripped from the receding side of the galaxy. The two galaxies show a relatively high velocity dispersion of gas both in their discs and in the tails ($\sim 100 \text{ km s}^{-1}$). Given their almost edge-on trajectories, this could result from the contribution of gas stripped from both the approaching and receding sides of the rotating disc, whose contribution cannot be resolved because of beam smearing, as observed in the edge-on galaxy UGC 6697 in A1367 (Consolandi et al. 2017). We notice, however, that the velocity dispersion of the gas in the tail is smaller than the maximal rotational difference between the two sides of both galaxies ($\sim 150\text{--}200 \text{ km s}^{-1}$). To conclude, ID 345 has probably already passed the pericentre, while ID 473 is a fresh infaller as suggested by its position in the phase-space diagram. Galaxies with properties similar to ID 345 (eccentric position in the phase-space and tails oriented toward the cluster centre), although unusual, are also present in local clusters (e.g. NGC 4569, Boselli et al. 2014b, 2016a).

We can also compare the properties of the two galaxies to the most recent results from cosmological hydrodynamic simulations, and in particular to the predictions of IllustrisTNG (Yun et al. 2019), which are perfectly tuned for a comparison with our target, since they have been obtained for simulated galaxies ($M_{\text{star}} \geq 10^{9.5} M_{\odot}$) and clusters ($10^{13} M_{\odot} \leq M_{200} \leq 10^{14.6} M_{\odot}$) of similar mass. These simulations indicate that galaxies with tails of stripped gas due to ram-pressure stripping are frequent in clusters with a redshift $z < 0.6$. About 30% of the disc galaxies have such a cometary shape in the gaseous component⁵, with a very weak dependence on redshift. They also show that these objects are more frequent at intermediate to large clustercentric radii ($r/R_{200} \geq 0.25$, which corresponds to $\approx 250\text{--}400 \text{ kpc}$ for the cluster CGr32), in galaxies with a high velocity with respect to the mean velocity of the cluster, and in more massive clusters. The simulations also show that the orientation of the tail, which generally traces the trajectory of the galaxy within the high-density region, does not depend on the relative position of the galaxy with respect to the cluster centre. ID 345 and ID 473 are located at $\approx 200 \text{ kpc}$ in projection from the cluster core, and have tails oriented almost towards the cluster centre, and a high velocity along the line of sight with respect to that of the cluster, and thus match all the properties of perturbed galaxies in the simulations.

6. Conclusion

As part of the MUSE-gALaxy Groups In Cosmos (MAGIC) GTO programme, we observed the cluster of galaxies CGr32 ($M_{200} \approx 2 \times 10^{14} M_{\odot}$) at $z = 0.73$. The MUSE observations reveal the presence of two massive ($M_{\text{star}} \approx 10^{10} M_{\odot}$) galaxies with extended low-surface brightness tails of diffuse gas detected in the [O II] emission-line doublet. The cometary shape of the tails, and the lack of any diffuse stellar counterpart in the very deep Suprime-Cam images, clearly indicate that the two galaxies are undergoing a ram-pressure stripping event. This result is thus the first evidence that the dynamical interaction between the cold galaxy ISM with the hot and dense ICM, which is probably the dominant perturbing mechanism in high-density environments

in the local Universe, was also active at earlier epochs, when the Universe was only half its present age. This result is consistent with the predictions of the most recent cosmological simulations of galaxy evolution.

The density of the gas within the tail derived using the [O II] $\lambda 3729$ /[O II] $\lambda 3726$ line ratio indicates that the recombination time, $\tau_{\text{rec}} \approx 10^4 \text{ yr}$, is very short compared to the travel time of the tail, $\tau_{\text{travel}} \approx 10^8 \text{ yr}$, as is often observed in local galaxies. This suggests that a source of gas excitation must be present within the tail. To conclude, this work is further confirmation that the extraordinary IFU capabilities of MUSE in terms of field of view and sensitivity can be successfully used to extend local studies to the high redshift Universe, thus opening a new era in the study of the role of the environment on galaxy evolution.

Acknowledgements. We thank the anonymous referee for constructive comments and suggestions. This work was supported by the Programme National Cosmology et Galaxies (PNCG) of CNRS/INSU with INP and IN2P3, co-funded by CEA and CNES. This work has been carried out thanks to the support of the ANR FOGHAR (ANR-13-BS05-0010-02), the OCEVU Labex (ANR-11-LABX-0060) and the A*MIDEX project (ANR-11-IDEX-0001-02) funded by the ‘‘Investissements d’Avenir’’ French government programme managed by the ANR. VA acknowledges the COLCIENCIAS (Colombia) PhD fellowship programme No. 756-2016. JB acknowledges support by FCT/MCTES through national funds by grant UID/FIS/04434/2019 and through Investigador FCT Contract No. IF/01654/2014/CP1215/CT0003. This work made use of observations obtained with *XMM-Newton*, an ESA science mission with instruments and contributions directly funded by ESA Member States and NASA.

References

- Bacon, R., Conseil, S., Mary, D., et al. 2017, *A&A*, 608, A1
 Barro, G., Faber, S. M., Koo, D. C., et al. 2017, *ApJ*, 840, 47
 Bartalucci, I., Arnaud, M., Pratt, G. W., et al. 2017, *A&A*, 598, A61
 Bekki, K. 2014, *MNRAS*, 438, 444
 Betti, S. K., Pope, A., Scoville, N., et al. 2019, *ApJ*, 874, 53
 Boselli, A., & Gavazzi, G. 2006, *PASP*, 118, 517
 Boselli, A., & Gavazzi, G. 2014, *A&ARv*, 22, 74
 Boselli, A., Boissier, S., Cortese, L., et al. 2006, *ApJ*, 651, 811
 Boselli, A., Cortese, L., Boquien, M., et al. 2014a, *A&A*, 564, A67
 Boselli, A., Voyer, E., Boissier, S., et al. 2014b, *A&A*, 570, A69
 Boselli, A., Fossati, M., Gavazzi, G., et al. 2015, *A&A*, 579, A102
 Boselli, A., Cuillandre, J. C., Fossati, M., et al. 2016a, *A&A*, 587, A68
 Boselli, A., Roehly, Y., Fossati, M., et al. 2016b, *A&A*, 596, A11
 Boselli, A., Fossati, M., Consolandi, G., et al. 2018a, *A&A*, 620, A164
 Boselli, A., Fossati, M., Ferrarese, L., et al. 2018b, *A&A*, 614, A56
 Byrd, G., & Valtonen, M. 1990, *ApJ*, 350, 89
 Cappellari, M., & Emsellem, E. 2004, *PASP*, 116, 138
 Cayatte, V., van Gorkom, J. H., Balkowski, C., & Kotanyi, C. 1990, *AJ*, 100, 604
 Cayatte, V., Kotanyi, C., Balkowski, C., & van Gorkom, J. H. 1994, *AJ*, 107, 1003
 Chabrier, G. 2003, *PASP*, 115, 763
 Chung, A., van Gorkom, J. H., Kenney, J. D. P., & Vollmer, B. 2007, *ApJ*, 659, L115
 Colless, M., & Dunn, A. M. 1996, *ApJ*, 458, 435
 Condon, J. J. 1992, *ARA&A*, 30, 575
 Consolandi, G., Gavazzi, G., Fossati, M., et al. 2017, *A&A*, 606, A83
 Contini, T., Epinat, B., Bouché, N., et al. 2016, *A&A*, 591, A49
 Cortese, L., Gavazzi, G., Boselli, A., et al. 2006, *A&A*, 453, 847
 Cortese, L., Maricall, D., Richard, J., et al. 2007, *MNRAS*, 376, 157
 Cortese, L., Davies, J. I., Pohlen, M., et al. 2010, *A&A*, 518, L49
 Cortese, L., Ciesla, L., Boselli, A., et al. 2012, *A&A*, 540, A52
 Cowie, L. L., & Songaila, A. 1977, *Nature*, 266, 501
 Croston, J. H., Arnaud, M., Pointecouteau, E., & Pratt, G. W. 2006, *A&A*, 459, 1007
 De Lucia, G., Weinmann, S., Poggianti, B. M., Aragón-Salamanca, A., & Zaritsky, D. 2012, *MNRAS*, 423, 1277
 Dopita, M. A., & Sutherland, R. S. 1995, *ApJ*, 455, 468
 Dressler, A. 1980, *ApJ*, 236, 351
 Dressler, A. 2004, in *Clusters of Galaxies: Probes of Cosmological Structure and Galaxy Evolution*, eds. J. S. Mulchaey, A. Dressler, & A. Oemler, 206
 Dressler, A., Oemler, A., Couch, W. J., et al. 1997, *ApJ*, 490, 577
 Ebeling, H., Stephenson, L. N., & Edge, A. C. 2014, *ApJ*, 781, L40

⁵ Since these simulations do not discriminate between the different gas phases, it is not astonishing that the fraction of galaxies with observed tails in the ionised gas is significantly lower than 30%.

- Epinat, B., Tasca, L., Amram, P., et al. 2012, *A&A*, **539**, A92
- Epinat, B., Contini, T., Finley, H., et al. 2018, *A&A*, **609**, A40
- Falcón-Barroso, J., Sánchez-Blázquez, P., Vazdekis, A., et al. 2011, *A&A*, **532**, A95
- Finoguenov, A., Guzzo, L., Hasinger, G., et al. 2007, *ApJS*, **172**, 182
- Fossati, M., Gavazzi, G., Boselli, A., & Fumagalli, M. 2012, *A&A*, **544**, A128
- Fossati, M., Gavazzi, G., Savorgnan, G., et al. 2013, *A&A*, **553**, A91
- Fossati, M., Fumagalli, M., Boselli, A., et al. 2016, *MNRAS*, **455**, 2028
- Fossati, M., Mendel, J. T., Boselli, A., et al. 2018, *A&A*, **614**, A57
- Fossati, M., Fumagalli, M., Gavazzi, G., et al. 2019, *MNRAS*, **484**, 2212
- Fumagalli, M., Fossati, M., Hau, G. K. T., et al. 2014, *MNRAS*, **445**, 4335
- Gavazzi, G., Boselli, A., Mayer, L., et al. 2001, *ApJ*, **563**, L23
- Gavazzi, G., Fumagalli, M., Fossati, M., et al. 2013, *A&A*, **553**, A89
- Gavazzi, G., Consolandi, G., Yagi, M., & Yoshida, M. 2017, *A&A*, **606**, A131
- Gavazzi, G., Consolandi, G., Gutierrez, M. L., Boselli, A., & Yoshida, M. 2018, *A&A*, **618**, A130
- George, M. R., Leauthaud, A., Bundy, K., et al. 2011, *ApJ*, **742**, 125
- Giodini, S., Lovisari, L., Pointecouteau, E., et al. 2013, *Space Sci. Rev.*, **177**, 247
- Gnedin, O. Y. 2003, *ApJ*, **589**, 752
- Gozaliasl, G., Finoguenov, A., Tanaka, M., et al. 2019, *MNRAS*, **483**, 3545
- Gunn, J. E., & Gott, III, R., 1972, *ApJ*, **176**, 1
- Hasinger, G., Cappelluti, N., Brunner, H., et al. 2007, *ApJS*, **172**, 29
- Iovino, A., Petropoulou, V., Scodreggio, M., et al. 2016, *A&A*, **592**, A78
- Jáchym, P., Kenney, J. D. P., Ržuička, A., et al. 2013, *A&A*, **556**, A99
- Jáchym, P., Combes, F., Cortese, L., Sun, M., & Kenney, J. D. P. 2014, *ApJ*, **792**, 11
- Jáchym, P., Sun, M., Kenney, J. D. P., et al. 2017, *ApJ*, **839**, 114
- Kenney, J. D. P., Tal, T., Crawl, H. H., Feldmeier, J., & Jacoby, G. H. 2008, *ApJ*, **687**, L69
- Knobel, C., Lilly, S. J., Iovino, A., et al. 2012, *ApJ*, **753**, 121
- Koopmann, R. A., Kenney, J. D. P., & Young, J. 2001, *ApJS*, **135**, 125
- Kriek, M., van Dokkum, P. G., Labbé, I., et al. 2009, *ApJ*, **700**, 221
- Larson, R. B., Tinsley, B. M., & Caldwell, C. N. 1980, *ApJ*, **237**, 692
- McDonald, M., Allen, S. W., Bayliss, M., et al. 2017, *ApJ*, **843**, 28
- McPartland, C., Ebeling, H., Roediger, E., & Blumenthal, K. 2016, *MNRAS*, **455**, 2994
- Merritt, D. 1983, *ApJ*, **264**, 24
- Moore, B., Lake, G., & Katz, N. 1998, *ApJ*, **495**, 139
- Moustakas, J., Kennicutt, R. C., & Tremonti, C. A. 2006, *ApJ*, **642**, 775
- Nulsen, P. E. J. 1982, *MNRAS*, **198**, 1007
- Osterbrock, D. E., & Ferland, G. J. 2006, *Astrophysics of Gaseous Nebulae and Active Galactic Nuclei* (Sausalito: University Science Books)
- Owers, M. S., Couch, W. J., Nulsen, P. E. J., & Randall, S. W. 2012, *ApJ*, **750**, L23
- Peng, C. Y., Ho, L. C., Impey, C. D., & Rix, H.-W. 2002, *AJ*, **124**, 266
- Poggianti, B. M., Smail, I., Dressler, A., et al. 1999, *ApJ*, **518**, 576
- Poggianti, B. M., von der Linden, A., De Lucia, G., et al. 2006, *ApJ*, **642**, 188
- Poggianti, B. M., Moretti, A., Gullieuszik, M., et al. 2017, *ApJ*, **844**, 48
- Pratt, G. W., Böhringer, H., Croston, J. H., et al. 2007, *A&A*, **461**, 71
- Sanders, R. L., Shapley, A. E., Kriek, M., et al. 2016, *ApJ*, **816**, 23
- Sarazin, C. L. 1986, *Rev. Mod. Phys.*, **58**, 1
- Schinnerer, E., Sargent, M. T., Bondi, M., et al. 2010, *ApJS*, **188**, 384
- Scott, T. C., Cortese, L., Brinks, E., et al. 2012, *MNRAS*, **419**, L19
- Scoville, N., Aussel, H., Brusa, M., et al. 2007, *ApJS*, **172**, 1
- Simionescu, A., Werner, N., Mantz, A., Allen, S. W., & Urban, O. 2017, *MNRAS*, **469**, 1476
- Sun, M., Jones, C., Forman, W., et al. 2006, *ApJ*, **637**, L81
- Sun, M., Donahue, M., & Voit, G. M. 2007, *ApJ*, **671**, 190
- Sun, M., Voit, G. M., Donahue, M., et al. 2009, *ApJ*, **693**, 1142
- Sun, M., Donahue, M., Roediger, E., et al. 2010, *ApJ*, **708**, 946
- Taniguchi, Y., Scoville, N., Murayama, T., et al. 2007, *ApJS*, **172**, 9
- Tonnesen, S., & Bryan, G. L. 2010, *ApJ*, **709**, 1203
- Tonnesen, S., & Bryan, G. L. 2012, *MNRAS*, **422**, 1609
- Vulcani, B., Treu, T., Schmidt, K. B., et al. 2016, *ApJ*, **833**, 178
- Weilbacher, P. 2015, in *Science Operations 2015: Science Data Management – An ESO/ESA Workshop*, 1
- Weilbacher, P. M., Streicher, O., Urrutia, T., et al. 2012, in *Software and Cyberinfrastructure for Astronomy II*, SPIE Conf. Ser., 8451, 84510B
- Weilbacher, P. M., Streicher, O., Urrutia, T., et al. 2014, in *Astronomical Data Analysis Software and Systems XXIII*, eds. N. Manset, & P. Forshay, *ASP Conf. Ser.*, **485**, 451
- Whitaker, K. E., Franx, M., Leja, J., et al. 2014, *ApJ*, **795**, 104
- Yagi, M., Komiyama, Y., Yoshida, M., et al. 2007, *ApJ*, **660**, 1209
- Yagi, M., Yoshida, M., Komiyama, Y., et al. 2010, *AJ*, **140**, 1814
- Yagi, M., Gu, L., Koyama, Y., et al. 2015, *AJ*, **149**, 36
- Yagi, M., Yoshida, M., Gavazzi, G., et al. 2017, *ApJ*, **839**, 65
- Yoshida, M., Yagi, M., Okamura, S., et al. 2002, *ApJ*, **567**, 118
- Yoshida, M., Ohyama, Y., Iye, M., et al. 2004, *AJ*, **127**, 90
- Yoshida, M., Yagi, M., Komiyama, Y., et al. 2012, *ApJ*, **749**, 43
- Yun, K., Pillepich, A., Zinger, E., et al. 2019, *MNRAS*, **483**, 1042
- Zhang, B., Sun, M., Ji, L., et al. 2013, *ApJ*, **777**, 122

Appendix B

Conferences, Meetings and Schools

- **14th, 15th, 17th and 19th MUSE BUSY WEEK:** MUSE Consortium Collaboration meetings. Volendam - Netherlands (20th – 24th November 2017), Hendaye - France (18th – 22nd June 2018), Goslar - Germany (13th – 17th May 2019) and Cyberspace (5th – 8th May 2020). Speaker. **Summarizing Talks:** Presentation of the GTO paper research project of 10 mins, and update talks of 4mins.
- **4th Indo-French Astronomy School (IFAS4), Spectroscopy 3D 2D (9th – 16th July 2018):** Research project on techniques and analysis. **Talk presenting the results:** Identifying emission-line objects and understanding the detection limits. Centre de Recherche Astrophysique de Lyon (CRAL)/ Université de Lyon. Lyon, France.
- **XXX IAU General Assembly (20rd – 31th August 2018):** Participant. **Poster:** Galaxy Evolution in Groups Observed by the IFS MUSE. Vienna, Austria. I was awarded a Grant of 600€ to be part of the selected volunteers to participate in the logistics organization of the IAU General Assembly 2018.
- **European Week of Astronomy and Space Science (EWASS) 2019 (24th – 28th June 2019):** Participant. **Symposium 6:** Dynamics of disk galaxies in the era of large surveys. **Poster:** Galaxy evolution in groups at intermediate redshift observed by the IFS MUSE, a dynamical approach; as part of the project: Impact of environment at intermediate redshift, first results of the MAGIC project. Lyon, France.
- **European Astronomical Society Annual Meeting (EAS) 2020 (29th June – 3rd July 2019):** Speaker. **Symposium 6:** Stellar & Gas kinematics in galaxies across cosmic time, connecting observations with theory. **Contributing Talk:** Galaxy evolution in dense environments observed by the IFS MUSE, a dynamical approach. Virtual.

Bibliography

- Abril-Melgarejo V., et al., 2021, *A&A*, 647, A152
- Babcock H. W., 1939, *Lick Observatory Bulletin*, 498, 41
- Bacon R., Monnet G., 2017, *Optical 3D-Spectroscopy for Astronomy*. Wiley, <https://books.google.fr/books?id=u08GCwAAQBAJ>
- Bacon R., et al., 1995, *A&AS*, 113, 347
- Bacon R., et al., 2006, *Proceedings of SPIE - The International Society for Optical Engineering*, 6269
- Bacon R., et al., 2015, *A&A*, 575, A75
- Bacon R., et al., 2017, *A&A*, 608, A1
- Baldwin J. A., Phillips M. M., Terlevich R., 1981, *PASP*, 93, 5
- Bassett R., et al., 2017, *MNRAS*, 470, 1991
- Beckwith S. V. W., et al., 2006, *AJ*, 132, 1729
- Beers T. C., Flynn K., Gebhardt K., 1990, *AJ*, 100, 32
- Begeman K. G., Broeils A. H., Sanders R. H., 1991, *MNRAS*, 249, 523
- Bell E. F., de Jong R. S., 2001, *ApJ*, 550, 212
- Bialas D., Lisker T., Olczak C., Spurzem R., Kotulla R., 2015, *A&A*, 576, A103
- Blanton M. R., et al., 2003, *ApJ*, 592, 819
- Bloom J. V., et al., 2017, *MNRAS*, 472, 1809
- Boogaard L. A., et al., 2018, *A&A*, 619, A27
- Boselli A., et al., 2019, *A&A*, 631, A114
- Bosma A., 1978, PhD thesis, -
- Boulanger F., et al., 2009, *Experimental Astronomy*, 23, 277
- Cassata P., et al., 2007, *ApJS*, 172, 270

- Ciesla L., et al., 2012, *A&A*, 543, A161
- Conselice C. J., Bundy K., Ellis R. S., Brichmann J., Vogt N. P., Phillips A. C., 2005, *ApJ*, 628, 160
- Contini T., et al., 2012, *A&A*, 539, A91
- Contini T., et al., 2016, *A&A*, 591, A49
- Courteau S., 1997, *AJ*, 114, 2402
- Courtès G., 1960, *Annales d’Astrophysique*, 23, 115
- Cresci G., et al., 2009, *ApJ*, 697, 115
- Cucciati O., et al., 2010, *A&A*, 520, A42
- Davies R. I., et al., 2013, *A&A*, 558, A56
- Dekel A., et al., 2009, *Nature*, 457, 451
- Delgado-Serrano R., Hammer F., Yang Y. B., Puech M., Flores H., Rodrigues M., 2010, *A&A*, 509, A78
- Dressler A., 1980, *ApJ*, 236, 351
- Eisenhauer F., et al., 2003, SINFONI - Integral field spectroscopy at 50 milli-arcsecond resolution with the ESO VLT. pp 1548–1561, doi:10.1117/12.459468
- Epinat B., 2009, PhD thesis, -
- Epinat B., Amram P., Marcelin M., 2008, *MNRAS*, 390, 466
- Epinat B., Amram P., Balkowski C., Marcelin M., 2010, *MNRAS*, 401, 2113
- Epinat B., et al., 2012, *A&A*, 539, A92
- Epinat B., et al., 2018, *A&A*, 609, A40
- Erb D. K., 2008, *ApJ*, 674, 151
- Faber S. M., et al., 2003, The DEIMOS spectrograph for the Keck II Telescope: integration and testing. pp 1657–1669, doi:10.1117/12.460346
- Feng G., Xu K., Xuan-Bin L., Wei Z., Jun-Rong L., 2010, *Chinese Astronomy and Astrophysics*, 34, 234
- Fernández Lorenzo M., Sulentic J., Verdes-Montenegro L., Argudo-Fernández M., 2013, *MNRAS*, 434, 325
- Förster Schreiber N. M., et al., 2006, *ApJ*, 645, 1062
- Förster Schreiber N. M., et al., 2009, *ApJ*, 706, 1364

- Freedman W. L., 1990, *ApJ*, 355, L35
- Freeman K. C., 1970, *ApJ*, 160, 811
- Frenk C. S., et al., 2000, arXiv e-prints, pp astro-ph/0007362
- Giavalisco M., et al., 2004, *ApJ*, 600, L93
- Gnerucci A., et al., 2011, *A&A*, 528, A88
- Gómez-López J. A., et al., 2019, *A&A*, 631, A71
- Graham A. W., 2013, Elliptical and Disk Galaxy Structure and Modern Scaling Laws. p. 91, doi:10.1007/978-94-007-5609-0_2
- Graham A. W., Driver S. P., 2005, *PASA*, 22, 118
- Guérou A., et al., 2017, *A&A*, 608, A5
- Hinton S. R., Davis T. M., Lidman C., Glazebrook K., Lewis G. F., 2016, *Astronomy and Computing*, 15, 61
- Holmberg E., 1946, Meddelanden fran Lunds Astronomiska Observatorium Serie II, 117, 3
- Hopkins A. M., Beacom J. F., 2006, *ApJ*, 651, 142
- Hopkins P. F., et al., 2010, *ApJ*, 724, 915
- Hubble E. P., 1926, *ApJ*, 64, 321
- Hubble E., 1936, The Realm of the Nebulae. Mrs. Hepsa Ely Silliman memorial lectures, Yale University Press, <http://books.google.com.mx/books?id=kgiXdDGLpFUC>
- Hunter D., 1997, *PASP*, 109, 937
- Inami H., et al., 2017, *A&A*, 608, A2
- Jones T. A., Swinbank A. M., Ellis R. S., Richard J., Stark D. P., 2010, *MNRAS*, 404, 1247
- Juneau S., Dickinson M., Alexander D. M., Salim S., 2011, *ApJ*, 736, 104
- Kennicutt Robert C. J., 1998, *ApJ*, 498, 541
- King I., 1962, *AJ*, 67, 471
- King I. R., 1966, *AJ*, 71, 64
- Knobel C., et al., 2009, *ApJ*, 697, 1842
- Knobel C., et al., 2012, *ApJ*, 753, 121
- Koekemoer A. M., et al., 2007, *ApJS*, 172, 196
- Kriek M., van Dokkum P. G., Labbé I., Franx M., Illingworth G. D., Marchesini D., Quadri R. F., 2009, *ApJ*, 700, 221

- Laigle C., et al., 2016, *ApJS*, **224**, 24
- Lamareille F., 2010, *A&A*, **509**, A53
- Law D. R., Steidel C. C., Erb D. K., Larkin J. E., Pettini M., Shapley A. E., Wright S. A., 2007, *ApJ*, **669**, 929
- Le Fèvre O., et al., 2003, Commissioning and performances of the VLT-VIMOS instrument. pp 1670–1681, doi:10.1117/12.460959
- Lemaux B. C., et al., 2014, *A&A*, **572**, A90
- Liller M. H., 1966, *ApJ*, **146**, 28
- Lubin L. M., Gal R. R., Lemaux B. C., Kocevski D. D., Squires G. K., 2009, *AJ*, **137**, 4867
- Madau P., Dickinson M., 2014, *ARA&A*, **52**, 415
- Maillard J. P., Drissen L., Grandmont F., Thibault S., 2013, *Experimental Astronomy*, **35**, 527
- Maiolino R., et al., 2008, *A&A*, **488**, 463
- Maltby D. T., et al., 2010, *MNRAS*, **402**, 282
- Mannucci F., et al., 2009, *MNRAS*, **398**, 1915
- Masters K. L., 2013, arXiv e-prints, p. arXiv:1303.7118
- Masters K. L., Springob C. M., Haynes M. P., Giovanelli R., 2006, *ApJ*, **653**, 861
- Matharu J., et al., 2019, *MNRAS*, **484**, 595
- McGaugh S. S., 2005, *ApJ*, **632**, 859
- McGaugh S. S., Schombert J. M., Bothun G. D., de Blok W. J. G., 2000, *ApJ*, **533**, L99
- McGaugh S. S., Lelli F., Schombert J. M., 2016, *Phys. Rev. Lett.*, **117**, 201101
- Mediavilla E., Arribas S., Roth M., Cepa-Nogué J., Sánchez F., 2011, 3D Spectroscopy in Astronomy
- Miller S. H., Bundy K., Sullivan M., Ellis R. S., Treu T., 2011, *ApJ*, **741**, 115
- Miller S. H., Ellis R. S., Sullivan M., Bundy K., Newman A. B., Treu T., 2012, *ApJ*, **753**, 74
- Miller S. H., Sullivan M., Ellis R. S., 2013, *ApJ*, **762**, L11
- Mouhcine M., Lewis I., Jones B., Lamareille F., Maddox S. J., Contini T., 2005, *MNRAS*, **362**, 1143
- Neichel B., et al., 2008, *A&A*, **484**, 159
- Osterbrock D. E., 1989, Astrophysics of gaseous nebulae and active galactic nuclei

- Osterbrock D. E., Ferland G. J., 2006, *Astrophysics of gaseous nebulae and active galactic nuclei*
- Pease F. G., 1918, [Proceedings of the National Academy of Science](#), **4**, 21
- Peebles P. J. E., 1993, *Principles of Physical Cosmology*
- Pelliccia D., Tresse L., Epinat B., Ilbert O., Scoville N., Amram P., Lemaux B. C., Zamorani G., 2017, [A&A](#), **599**, A25
- Pelliccia D., et al., 2019, [MNRAS](#), **482**, 3514
- Peng C. Y., Ho L. C., Impey C. D., Rix H.-W., 2002, [AJ](#), **124**, 266
- Peng C. Y., Ho L. C., Impey C. D., Rix H.-W., 2010a, [AJ](#), **139**, 2097
- Peng Y.-j., et al., 2010b, [ApJ](#), **721**, 193
- Perlmutter S., et al., 1999, [ApJ](#), **517**, 565
- Pizagno J., et al., 2007, [AJ](#), **134**, 945
- Planck Collaboration et al., 2016, [A&A](#), **594**, A13
- Puech M., 2010, [MNRAS](#), **406**, 535
- Puech M., et al., 2008, [A&A](#), **484**, 173
- Raichoor A., et al., 2012, [ApJ](#), **745**, 130
- Ravikumar C. D., et al., 2007, [A&A](#), **465**, 1099
- Renault E., et al., 2010, in *Proc. SPIE*. p. 77394R, [doi:10.1117/12.857198](#)
- Reyes R., Mandelbaum R., Gunn J. E., Pizagno J., Lackner C. N., 2011, [MNRAS](#), **417**, 2347
- Richard J., et al., 2019, arXiv e-prints, p. [arXiv:1906.01657](#)
- Riess A. G., et al., 1998, [AJ](#), **116**, 1009
- Rix H.-W., et al., 2004, [ApJS](#), **152**, 163
- Rosado M., et al., 1995, in Pena M., Kurtz S., eds, *Revista Mexicana de Astronomia y Astrofisica Conference Series Vol. 3*, *Revista Mexicana de Astronomia y Astrofisica Conference Series*. p. 263
- Rubin V. C., 1983, [Science](#), **220**, 1339
- Rubin V. C., Ford W. K. J., Strom K. M., Strom S. E., Romanishin W., 1978a, [ApJ](#), **224**, 782
- Rubin V. C., Ford W. K. J., Thonnard N., 1978b, [ApJ](#), **225**, L107
- Rubin V. C., Ford W. K. J., Thonnard N., 1980, [ApJ](#), **238**, 471
- Sakai S., et al., 2000, [ApJ](#), **529**, 698

- Schawinski K., et al., 2014, *MNRAS*, 440, 889
- Schmidt K. H., Boller T., 1993, *Astronomische Nachrichten*, 314, 361
- Schneider P., 2007, *Extragalactic Astronomy and Cosmology: An Introduction*. Springer Berlin Heidelberg, <https://books.google.fr/books?id=V2h10nb29RUC>
- Scoville N., et al., 2007a, *ApJS*, 172, 1
- Scoville N., et al., 2007b, *ApJS*, 172, 38
- Sérsic J., 1963, *Boletin de la Asociacion Argentina de Astronomia La Plata Argentina*, 6, 41
- Sharpley R., et al., 2006, *New Astr. Rev.*, 50, 370
- Sheth K., et al., 2008, *ApJ*, 675, 1141
- Sorce J. G., et al., 2013, *ApJ*, 765, 94
- Sparke L. S., Gallagher John S. I., 2007, *Galaxies in the Universe*
- Springel V., et al., 2005, *Nature*, 435, 629
- Springel V., Frenk C. S., White S. D. M., 2006, *Nature*, 440, 1137
- Stott J. P., et al., 2016, *MNRAS*, 457, 1888
- Tacconi L. J., et al., 2013, *ApJ*, 768, 74
- Tasca L. A. M., et al., 2009, *A&A*, 503, 379
- Tiley A. L., et al., 2016, *MNRAS*, 460, 103
- Tiley A. L., et al., 2019, *MNRAS*, 485, 934
- Tomczak A. R., et al., 2019, *MNRAS*, 484, 4695
- Torres-Flores S., Epinat B., Amram P., Plana H., Mendes de Oliveira C., 2011, *MNRAS*, 416, 1936
- Trujillo I., Aguerri J., Cepa J., Gutiérrez C., 2001, *MNRAS*, 328, 977
- Trussler J., Maiolino R., Maraston C., Peng Y., Thomas D., Goddard D., Lian J., 2020, *MNRAS*, 491, 5406
- Tully R. B., Fisher J. R., 1977, *A&A*, 500, 105
- Tully R. B., Pierce M. J., 2000, *ApJ*, 533, 744
- Turner O. J., et al., 2017, *MNRAS*, 471, 1280
- Übler H., et al., 2017, *ApJ*, 842, 121
- Vergani D., et al., 2012, *A&A*, 546, A118

- Verheijen M. A. W., 1997, PhD thesis, -
- Verheijen M. A. W., 2001, [ApJ](#), **563**, 694
- Vogt F. P. A., et al., 2017, [Physical Review X](#), **7**, 021044
- Walter F., et al., 2007, [ApJ](#), **661**, 102
- Walter F., Brinks E., de Blok W. J. G., Bigiel F., Kennicutt Robert C. J., Thornley M. D., Leroy A., 2008, [AJ](#), **136**, 2563
- Weinmann S. M., Kauffmann G., van den Bosch F. C., Pasquali A., McIntosh D. H., Mo H., Yang X., Guo Y., 2009, [MNRAS](#), **394**, 1213
- Wisnioski E., et al., 2015, [ApJ](#), **799**, 209
- Wisnioski E., et al., 2019, [ApJ](#), **886**, 124
- Wright S. A., Larkin J. E., Law D. R., Steidel C. C., Shapley A. E., Erb D. K., 2009, [ApJ](#), **699**, 421
- de Vaucouleurs G., 1948, *Annales d'Astrophysique*, **11**, 247
- de Vaucouleurs G., 1953, [MNRAS](#), **113**, 134
- de Vaucouleurs G., 1957, [AJ](#), **62**, 69
- van den Bergh S., 2002, [PASP](#), **114**, 797

Résumé

Les galaxies se forment et évoluent dans différents environnements, façonnées par la distribution des halos de matière noire. L'évolution des galaxies dans les environnements à faible densité (EFD) diffère considérablement de celles des structures denses (SD), où les facteurs environnementaux réduisent la teneur en gaz en éteignant leur capacité de formation stellaire plus tôt que leurs homologues isolées. Le but de ce travail est d'étudier la Relation Tully Fisher (RTF) des galaxies en groupes à décalages spectraux vers le rouge (z) intermédiaires. Cette relation fournit des informations clés sur le support dynamique, ainsi que sur la formation et l'état évolutif des galaxies. L'avènement des spectrographes à champ intégral (IFS) comme MUSE, permet d'effectuer des études spatialement résolues à z intermédiaires. Cette recherche est basée sur l'exploitation d'un échantillon unique de 12 groupes de galaxies sélectionnés du sondage GTO MUSE gAlaxy Groups In Cosmos (MAGIC), à $0,3 < z < 0,8$. La cinématique a été extraite à l'aide du doublet $[\text{OII}]\lambda\lambda 3726,3729 \text{ \AA}$. Une décomposition bulbe-disque et une modélisation cinématique 2D ont été appliquées pour récupérer la vitesse de rotation maximale à 2.2 fois la longueur de l'échelle du disque ($R_{2.2}$), la dispersion des vitesses (σ) intrinsèque et la masse dynamique. J'ai effectué une sélection d'échantillons en fixant des limites sur la résolution spatiale et sur le rapport signal sur bruit (S/B), notre méthode réduit le nombre de galaxies dominées par σ . J'ai trouvé que les fractions de masse stellaire et baryonique augmentent avec la masse stellaire, et un décalage du point zéro (z_0) de la RTF entre différents environnements qui implique que les galaxies dans des SD tournent plus vite que dans des EFD. L'évolution du RTF en milieu dense pourrait être due à une combinaison d'extinction de la formation stellaire et la contraction du contenu baryonique.

Mots-clés: *Évolution des galaxies, Dynamique des Galaxies, Gaz ionisé, redshift intermédiaire, échantillons IFS, Analyse morpho-cinématique*

Abstract

Galaxies form and evolve in different environments, shaped by the distribution of dark matter halos. The evolution of galaxies in low-density environments significantly differs from those in dense structures, where environmental drivers reduce the gas content quenching their star formation capacity earlier than their isolated counterparts. The goal of this work is to study the TFR for galaxies at intermediate z groups. This relation provides key information on the dynamical support, and on formation and evolutionary state of galaxies. The advent of powerful IFS instruments like MUSE, allows to perform spatially resolved studies at intermediate redshifts (z). This research is based on the exploitation of an unique sample of 12 dense galaxy groups selected in the COSMOS field, from the GTO MUSE gAlaxy Groups In Cosmos (MAGIC) Survey, at $0.3 < z < 0.8$. The kinematics was extracted using the $[\text{OII}]\lambda\lambda 3726,3729 \text{ \AA}$ doublet. A bulge-disk decomposition and a 2D kinematic modeling were applied to recover the maximum rotation velocity at 2.2 disk scale lengths ($R_{2.2}$), the intrinsic velocity dispersion (σ) and the dynamical mass. I performed a rigorous sample selection in setting limits on the spatial resolution and on the signal-to-noise ratio (SNR). I compared my results with previous studies in different environments finding our method reduces the outliers in the TFR. I found the stellar and baryonic mass fractions increase with stellar mass. I also found a clear offset of the TFR zero-point between different environments implying that at fixed stellar mass, galaxies in dense environments rotate faster than in low-density environments. The evolution of the TFR in dense environments could be due to a combination of quenching of SF and contraction of the baryonic content.

Keywords: *Galaxy Evolution, Galaxy Dynamics, Ionized gas, Intermediate redshift, IFS samples, morpho-kinematics analysis*

Laboratoire d'Astrophysique de Marseille

38, rue Frédéric Joliot-Curie
13388 Marseille Cedex 13 - France
